

Evaluation form for external referees of PhD theses

Personal information of the referee

First names	Gerardo
Last name	Herrera Garcia
Academic degree	PhD
Position	Resarcher
Institute / Division	Instituto Geológico y Minero de España/ Geohazards InSAR laboratory and modeling group
Street address / number	Calle Alenza 1
Zip code / Town / (Country)	Madrid 28003
E-mail	g.herrera@igme.es

Name (family and given) of PhD candidate:

Sara Frangioni

Title of thesis:

APPLICATIONS OF SAR INTERFEROMETRY FOR MONITORING GROUND DEFORMATIONS AND ENGINEERING INFRASTRUCTURES

Note:

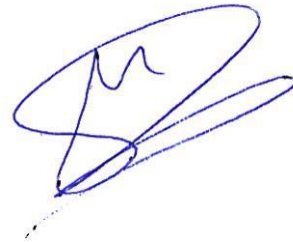
The PhD thesis is submitted as a manuscript, with an already published article.

Report:

The title and the abstract of the thesis “Application of SAR Interferometry for monitoring ground deformations and Engineering Structures” well reflect the content of and adequately to a PhD research. The use of English fulfils the international standards required for papers in SCI journals. References cover reasonably well the wide spectrum of previous studies were InSAR is applied to terrain motion mapping and monitoring. The quality of the illustrations, the provided information and the captions are well placed in the text and help to understand the performed research. Ground displacement data

retrieved from the PSI processing of both C- and X- band SAR datasets is described at the beginning of every test site, followed by a scientific interpretation on the results based on geo-thematic layers and in situ data. It is impressive to acknowledge the inclusion of 10 different test sites within this PhD. The methods presented to estimate ground displacements are adequate and broadly accepted by the scientific community. The quality of the results and the interpretation of the data are correct and consistent with the available ground truth information used for every test site. The greatest importance of this scientific work is how the combination of InSAR and geomorphologic tools to improve hydrogeological risk assessment both at regional and local scale. Consequently the scientific content of the work adequately correspond to the standard of a doctoral dissertation, showing evidence of a substantial achievement made by the candidate enhancing the prevention and mitigation strategies of civil protection and environmental managers.

Madrid, 12th January 2015



Gerardo Herrera Garcia

Geohazards InSAR laboratory and modeling group

Área de Riesgos Geológicos

Departamento de Investigación Geocientífica

Instituto Geológico y Minero de España

Evaluation form for external referees of PhD theses

Personal information of the referee

First names	Oriol
Last name	Montserrat
Academic degree	PhD
Position	Senior Researcher
Institute / Division	Centre Tecnològic de Telecomunicacions de Catalunya (CTTC) Remote Sensing Department (RSE)
Street address / number	Parc Mediterrani de la Tecnologia (PMT) - Building B4 Av. Carl Friedrich Gauss 7
Zip code / Town / (Country)	08860 - Castelldefels (Spain)
E-mail	oriol.monserrat@cttc.cat

Name (family and given) of PhD candidate:

Sara Frangioni

Title of thesis:

APPLICATIONS OF SAR INTERFEROMETRY FOR MONITORING GROUND DEFORMATIONS AND ENGINEERING INFRASTRUCTURES

Note:

The PhD thesis is submitted as a manuscript, with an already published article.

Report:

This thesis work aims to demonstrate the potentials of SAR interferometry as a tool for detecting and monitoring hydrogeological instability's. This goal is achieved by means of a compilation of interesting results obtained applying different DInSAR methodologies and analysed at different scale levels: from single infrastructures up to regional maps. The thesis is generally well written and the title of the work and the abstract are both in accordance with the content of the thesis.

The structure of the work allows an easy and profitable reading: the rationale of the whole work is well presented and analyzed. The first three chapters are used to introduce the techniques used

within the work and to present a short review of the applications of SAR techniques for deformation measurement purposes. The most original part of the work is concentrated between chapters 4 and 9. These chapters consist on a set of interesting examples of how to analyse and interpret deformation maps and time series derived from SAR interferometry and how to use them to generate different products like for instance actualized landside inventory maps. Again, the structure of each of these chapters eases the reading and understanding of the work. Moreover, the figures are well located and the quality of both the figure and the caption are adequate according to the scientific international standards.

For all these reasons I understand that the scientific content of the work fully meets the standard of a doctoral thesis and it definitely shows evidence of a major scientific achievement by the candidate.

Location, Date:

Castell de l'ob, 15/12/2014

Signature: Oriol Monserrat





UNIVERSITÀ
DEGLI STUDI
FIRENZE

DOTTORATO DI RICERCA IN

Scienze della Terra

CICLO XXVII

COORDINATORE Prof. Lorenzo Rook

**APPLICATIONS OF SAR INTERFEROMETRY FOR
MONITORING GROUND DEFORMATIONS AND
ENGINEERING INFRASTRUCTURES**

Settore Scientifico Disciplinare GEO/05

Dottorando

Dott. Geol. Sara Frangioni

(firma)

Tutore

Prof. Nicola Casagli

(firma)

CoTutore

Ing. Michele Crosetto

(firma)

Coordinatore

Prof. Lorenzo Rook

(firma)

Anni 2012/2014

ACKNOWLEDGMENTS

I would like to express my gratitude to my supervisor, Prof. Nicola Casagli, whose expertise, understanding, and patience, added considerably to my research experience.

The work done for this thesis was made in collaboration with the IG (Instituto de Geomatica) within the CTTC (Centre Tecnològic Telecomunicacions Catalunya) in Castelldefels (Barcelona).

Very special thanks goes out to Dr. Michele Crosetto for taking time out from his busy schedule to serve as my external supervisor.

I would like to thank all the members of the Institute of Geomatics, for the assistance they provided at all levels of the project. In particular tanks to Marta Agudo, Maria Cuevas, Guido Luzi and Oriol Montserrat.

TABLE OF CONTENTS

ABSTRACT.....	1
INTRODUCTION.....	5
1. OBJECTIVE AND STRUCTURE OF THE RESEARCH.....	8
1.1 STUDY SCOPE AND CONTENTS.....	9
1.2 STRUCTURE.....	10
2. REMOTE SENSING TECHNIQUES.....	13
2.1 RADAR REMOTE SENSING AND SAR.....	16
2.1.1 Acquisition Mode.....	19
2.1.2 Acquisition Geometry.....	20
2.1.3 Radar image.....	22
2.1.4 Prospective distortion.....	24
2.1.5 SAR resolution.....	26
2.2 INTERFEROMETRIC SYNTHETIC APERTURE RADAR.....	27
2.3 DIFFERENTIAL INTERFEROMETRY.....	30
2.3.1 Temporal and geometrical decorrelation.....	32
2.4 PSI: PERSISTENT SCATTERERS INTERFEROMETRY.....	33
2.4.1 Soil deformation measurements.....	37
2.4.2 Measures along the L.O.S.....	39
3. SAR DATA AND THEIR APPLICATIONS.....	41
3.1 REMOTE SENSING TECHNOLOGIES.....	42
3.2 DIFFERENT RADAR SENSORS AND SAR DATA.....	44
3.2.1 SAR data in C-band: ERS 1/2, ENVISAT, RADARSAT satellites.....	46
3.2.2 SAR data in X-band: TerraSAR-X and COSMO-SkyMed satellites.....	48
3.2.3 Compared evaluation of different wavelength SAR data.....	50
3.3 A REVIEW OF THE BENEFIT OF SAR DATA.....	54
3.4 APPLICATIONS FOR GROUND DEFORMATION MONITORING.....	60
3.4.1 Landslide.....	60
3.4.2 Subsidence and Uplift.....	63

3.4.3 Sinkhole.....	64
3.4.4 Regional Mapping.....	64
3.4.5 Emergency Preparedness.....	65
3.5 APPLICATIONS TO ENGINEERING INFRASTRUCTURES.....	66
3.5.1 Single Buildings.....	66
3.5.2 Roads and Railways.....	66
3.5.3 Tunnelling activities.....	67
3.5.4 Bridges.....	68
3.5.5 Airports.....	68
4. C-BAND DATA FOR LOCAL-SCALE MONITORING.....	69
4.1 GENERAL CONSIDERATIONS.....	69
4.2 SqueeSAR™ PROCESSING METHOD.....	70
4.2.1 Input Data.....	72
4.3 TEST SITE.....	78
4.3.1 Geological Setting.....	78
4.3.2 Results and Discussion.....	82
5. C-BAND DATA FOR BASIN-SCALE MONITORING.....	98
5.1 GENERAL CONSIDERATIONS.....	98
5.2 PSInSAR™ PROCESSING METHOD.....	100
5.3 SPATIAL CHARACTERIZATION.....	102
5.3.1 Detection of “new” landslides and of change of boundaries.....	104
5.3.2 Classification of the state of activity.....	106
5.3.3 Detect buildings potentially damaged by landslides.....	112
5.4 AN EXAMPLE OF AN UPDATING OF A LANDSLIDE INVENTORY.....	116
5.4.1 Basin scale: Setta Basin.....	116
>5.5 ATTACHED PAPER.....	117
“Landslide inventory updating by means of Persistent Scatterer interferometry (PSI): the Setta basin (Italy) case study.” - Geomatics, Natural Hazards And Risk 2014	
6. X-BAND DATA FOR LOCAL-SCALE MONITORING.....	139
6.1 GENERAL CONSIDERATIONS.....	139
6.2 THE IG PROCESSING CHAIN FOR SMALL AREAS.....	140

6.2.1 Input data.....	143
6.2.2 Methodology.....	147
6.3 OVERVIEW OF THE STUDY AREA.....	157
6.3.1 General Geological Setting.....	157
6.3.2 Stratigraphy.....	159
6.3.3 Geomorphological Setting.....	161
6.4 TEST SITES.....	167
6.4.1 El Papiol.....	169
6.4.1.1 Geological Setting.....	170
6.4.1.2 Results and Discussion.....	172
6.4.1.3 Field Trip Validation.....	176
6.4.2 Montjuïc.....	177
6.4.2.1 Geological Setting.....	177
6.4.2.2 Results and Discussion.....	180
6.4.2.3 Field Trip Validation.....	182
6.4.2.4 Real Velocity Calculation.....	184
6.4.3 Castellbisbal.....	186
6.4.3.1 Geological Setting.....	186
6.4.3.2 Results and Discussion.....	187
6.4.3.3 Field Trip Validation.....	189
6.4.3.4 Real Velocity Calculation.....	191
7. X-BAND DATA FOR BASIN-SCALE MONITORING.....	193
7.1 GENERAL CONSIDERATIONS.....	193
7.2 IG PROCESSING CHAIN FOR WIDE AREAS.....	194
7.2.1 Input data.....	195
7.2.2 Methodology.....	196
7.3 TEST SITES.....	201
7.3.1 Burgos.....	202
7.3.1.1 Geological Setting.....	203
7.3.1.2 Results and Discussion.....	205
7.3.2 Barcelona.....	212
7.3.2.1 Geological Setting.....	213
7.3.2.2 Results and Discussion.....	216

8. C-AND X-BAND DATA FOR LOCAL-SCALE MONITORING.....	225
8.1 GENERAL CONSIDERATIONS.....	225
8.2 OVERVIEW OF THE STUDY AREA.....	226
8.3 TEST SITES.....	228
8.3.1 Naso.....	229
8.3.1.1 Geological Setting.....	229
8.3.1.2 Results and Discussion.....	230
8.3.2 Castell'Umberto.....	239
8.3.2.1 Geological Setting.....	239
8.3.2.2 Results and Discussion.....	240
9. C- AND X-BAND DATA FOR BASIN-SCALE MONITORING.....	249
9.1 GENERAL CONSIDERATIONS.....	249
9.2 SPATIAL CHARACTERIZATION.....	250
9.2.1 A method for the landslide susceptibility map.....	251
9.2.2 Predisposing factors.....	252
9.2.3 Data analysis and results.....	264
9.3 TEST SITE.....	268
9.3.1 Geological Setting.....	269
9.3.2 Results and Discussion.....	274
10. DISCUSSION AND CONCLUSION.....	285
REFERENCES.....	297

LIST OF FIGURES

Figure 1: Flowchart of the thesis roadmap.

Figure 2: Remote sensing using passive or active sensor From <http://en.wikipedia.org>.

Figure 3: The electromagnetic spectrum. From <http://en.wikipedia.org>.

Figure 4: A SAR system from a satellite. Taken from COLESANTI et al., 2006.

Figure 5: Simplified geometry of a side looking radar sensor. (Roth, 2001).

Figure 6: SAR sensor acquisition geometries: the two acquisition orbits. From <http://treuropa.com/technique/sar-imagery>.

Figure 7: Amplitude image.

Figure 8: Phase image (known modulo 2π).

Figure 9: Distortions caused by the radar inherent side-looking geometry. Layover (a) results in a reversion of the terrain geometry. [From Roth, 2001].

Figure 10: Distortions caused by the radar inherent side-looking geometry. Foreshortening causes compression of slopes facing towards the sensor. [From Roth, 2001].

Figure 11: Distortions caused by the radar inherent side-looking geometry. Points in the shadow (c) of an object are not visible in the radar image. [From Roth, 2001].

Figure 12: Relationship between that ground movement and the corresponding shift in signal phase. From <http://treuropa.com/technique/insar-evolution/>.

Figure 13: Interferogram of the L'Aquila earthquake that occurred in Italy, on 6th April 2009. [From <http://treuropa.com/technique/insar-evolution/>].

Figure 14: Examples of interferogram and the subsequently deformation map created for the areas that are coherent. From <http://treuropa.com/technique/insar-evolution/>.

Figure 15: Schematic representation of the PSInSARTM approach.

Figure 16: Examples of artificial and natural stable reflectors.

Figure 17: Schematic representation of the PS technique theory [Modified from T.R.E.s.r.l, 2004].

Figure 18: Sign of the velocity component recorded by the sensor depending on the direction of motion; the recorded movement (blue) is close to the satellite (positive).

Figure 19: Sign of the velocity component recorded by the sensor depending on the direction of motion; the recorded movement (red) is moving away from the satellite.

Figure 20: Image shows a schematic of SAR satellites that have acquired / are acquiring / will acquire SAR images use in Historic and Ongoing Monitoring analysis. Satellites have varied resolutions, signal wavelengths and repeat cycles; a summary of each satellites is described below. [Taken by T.R.E.].

Figure 21: Application of multi - frequency SAR data (L-, C-, X-band) in relation to different phenomena and analysis features.

Figure 22: Track of Verduno gallery, forthcoming excavation, projected onto an optical image (Google Earth).

Figure 23: Scheme of SqueeSAR™ analysis. The pixels of the SAR image that are radar target points, i.e. the PS, are shown in red; the pixels corresponding to distributed radar targets, i.e. the DS, are shown in blue; the pixels that are discarded due to the low coherence of the signal, are shown in orange. Each DS, in particular, summarizes the information contained in the group of pixels that fall within "effective area", which is the area that is used during the filtering operation (TRE Srl).

Figure 24: Distribution of measurement points identified and displayed with an annual average velocity value.

Figure 25: Dataset ERS ascending for the period 1992-2000. The orange boxes indicate the areas selected for a detailed analysis in the neighborhood of the track; the white circles show the significant targets, discussed in the text.

Figure 26: Dataset ERS descending for the period 1992-2000. The orange boxes indicate the areas selected for a detailed analysis in the neighborhood of the track; the white circles show the significant targets, discussed in the text.

Figure 27: Dataset ENVISAT ascending for the period 2004-2010. The orange boxes indicate the areas selected for a detailed analysis in the neighborhood of the track; the white circles show the significant targets, discussed in the text.

Figure 28: Dataset ENVISAT descending for the period 2003-2010. The orange boxes indicate the areas selected for a detailed analysis in the neighborhood of the track; the white circles show the significant targets, discussed in the text.

Figure 29. Location of Verduno site.

Figure 30: Geological scheme of BTP (Gelati and Gnaccolini, 1988).

Units of substrate: 1 = Units of Pidimont, Brianzonesi unit; 2 = Ligurian units. Cenozoic cover; 3 = Upper Eocene Tortonian; 4 = Messinian; 5 = Pliocen. Quaternary deposits; 6 = Front of allocton; 7 = Villalvernia-Varzi Line; 8 = BM: Low Monferrato e Torino hill; AM: High Monferrato; BG = Borbera-Grue Area; F = Ligurian end.

Figure 31: IFFI Landslide inventory maps (source WEBGIS Cart @ net-IFFI) on satellite photos with high detail (source Visual Earth).

Figure 32: IFFI Landslide inventory maps (source WEBGIS Cart @ net-IFFI) on a IGM map on a 1: 25.000 scale.

Figure 33: Mapping of landslides classified in the PAI of the Piedmont region (source <http://www.regione.piemonte.it/disuw>) on IGM map on a scale of 1: 25.000.

Figure 34: Delimitation of identified areas along the area interested by the future tunnel.

Figure 35: Localization of radar targets in the areas 1 and 2.

Figure 36: Time series of Radarsat targets selected for Area 1.

Figure 37: Time series of Radarsat targets selected for Area 2.

Figure 38: Time series of Radarsat targets selected for Area 2.

Figure 39: Time series of ENVISAT targets with descending geometry (Figure 18) in the Area 2.

Figure 40: Localization of radar targets in the areas 3 and 4.

Figure 41: Time series of Radarsat targets selected for Area 3.

- Figure 42:** Time series of ERS targets with descending geometry (figure 26) falling in the Area 3.
- Figure 43:** Time series of Radarsat targets selected for Area 3.
- Figure 44:** Localization of radar targets in the areas 5 and 6.
- Figure 45:** Time series of Radarsat targets selected for Area 5.
- Figure 46:** Time series of Radarsat targets selected for Area 6.
- Figure 47:** Localization of radar targets in the area 7.
- Figure 48:** Time series of Radarsat targets selected for Area 7A.
- Figure 49:** Time series of Radarsat targets selected for Area 7B.
- Figure 50:** Localization of radar targets in the area 8.
- Figure 51:** Time series of Radarsat targets selected for Area 8.
- Figure 52:** Localization of radar targets in the area 9.
- Figure 53:** Time series of Radarsat targets selected for Area 8.
- Figure 54:** Localization of radar targets in the area 10.
- Figure 55:** Time series of Radarsat targets selected for Area 10.
- Figure 56:** Localization of radar targets in the area 11.
- Figure 57:** Time series of Radarsat targets selected for Area 11.
- Figure 58:** Localization of radar targets in the area 12.
- Figure 59:** Time series of Radarsat targets selected for Area 12.
- Figure 60:** Time series of ERS targets with ascending orbit selected for Area 12.
- Figure 61:** Time series of ERS targets with descending orbit selected for Area 12.
- Figure 62:** Time series of ENVISAT targets with ascending orbit selected for Area 12.
- Figure 63:** Time series of ENVISAT targets with descending orbit selected for Area 12.
- Figure 64:** Entrance of the highway in the side of Alba: comparison between 2000 and 2012 orthophotos.
- Figure 65:** Localization of radar targets in the area 13.
- Figure 66:** Time series of Radarsat targets selected for Area 13.
- Figure 67:** Area of the new hospital Alba-Bra: comparison between 2000 and 2012 orthophotos.
- Figure 68:** Localization of radar targets in the area 14.
- Figure 69:** Time series of Radarsat targets selected for Area 14.
- Figure 70:** Flow chart describing the mapping of landslides and the evaluation of their state of activity.
- Figure 71:** A new landslide mapped for the presence of moving PS away from other areas mapped as landslides.
- Figure 72:** Change of boundaries of a landslide for the presence of moving PS, due to the same phenomenon mapped.
- Figure 73:** cases of correlation between the activity state of the landslide indicated in the existing inventory and the information provided by the PSs. A) Confirmation of an active landslide. B) Confirmation of a landslide inactive.

Figure 74: cases of non-correlation between the activity state of the landslide indicated in the existing inventory and the information provided by the PS. The activity status of the landslide shown in the preexisting inventory is changed from active to inactive (A) and from inactive to active (B).

Figure 75: cases of non-correlation between the activity status of the landslide indicated in the existing inventory and the information provided by the PSs. Both stable and instable PSs are concentrated in two distinct areas of the existing landslides; the two portions are separated varying the activity status. Case A: an active landslide is separated from an inactive portion. Case B: an inactive landslide is separated from an active portion.

Figure 76: Activity matrix and intensity scale.

Figure 77: Symbols used by Alexander, 1989 for a description of the fractures caused by the impact of a landslide on a building. From the top left, there are fractures for cutting; for expansion; for compression, unidirectional, in the direction of the arrow largest.

Figure 78: Building on which the analysis by impact is carried out. The numbers indicate the four sides taken into account for the analysis of fractures by impact. ERS data are represented.

Figure 79: Building on which the analysis by impact is carried out. The numbers indicate the four sides taken into account for the analysis of fractures by impact. ENVISAT data are represented.

Figure 80: fractures present on each of the four sides of the building. The symbols used to represent the type of fracture refers to the one adopted by Alexander, shown in Figure 51.

Figure 81: Graphic representation of numeric arrays that have been used to verify the type of prevalent fracture. The fracture is classified with two parameters: the first is the type of stress (relaxing, compressive, shear); the second is the type of the fracture (sub-horizontal, sub-vertical diagonal). The numbers in red indicate the predominant type of fracture.

Figure 82: Area of study. The area covers some urban settlements surrounding the city of Barcelona. These fall within the Llobregat delta.

Figure 83: Schematic representation of the methodology adopted for the preparation of this work.

Figure 84: Topographic Map on a 1:5000 scale acquired by the Institute Cartographic of Catalunya.

Figure 85: Ortophoto in scale 1:5000 acquired by the Institute Cartographic of Catalunya.

Figure 86: Google map image.

Figure 87: Geological Map on a 1:50.000 scale acquired by the Institute Cartographic of Catalunya.

Figure 88: TerraSAR-X detected image of Castellbisball (Barcelona, Spain). Image of the average amplitude. Light colors indicate high reflectivity of the signal. Conversely, dark colors indicate low reflectivity signal.

Figure 89: Image of the D_A . Dark colors are associated with low amplitude dispersion and therefore the signal is of good quality. Conversely, light colors are signs of a high amplitude dispersion; the signal is not good.

Figure 90: TerraSAR-X detected image of Castellbisball (Barcelona, Spain). Image of differential interferogram. From this image, you cannot find the shift, too small for differential interferometry.

Figure 91: Pixels connection; example of Delaunay triangulations. The selected pixels are connected by edges. The differential wrapped phase value over each edge is calculated by

subtracting the wrapped phase values over its extremes. Each edge has one differential phase value for each of the N interferograms. [Adapted from Mora et al., 2003].

Figure 92: Estimation of the differential velocity and the differential topographic error. For each edge, γ is a function which depends on the variables Δv and $\Delta \mathcal{E}$. To find the maximum value of γ several pairs $(\Delta v, \Delta \mathcal{E})$ are proved. The estimated values $(\Delta v_{\text{estimated}}, \Delta \mathcal{E}_{\text{estimated}})$ are given by the pair which gives the maximum value of γ . This solution doesn't give exactly the absolute maximum γ_{max} but the best approximation γ_{max} due to the used discrete network. As much dense is the discrete network, the better is the approximation, but at the same time, more expensive is the computation time [Taken from Biescas, 2007].

Figure 93: Example of geocoded deformation map. The colour scale is saturated between -5 and +5 mm/year.

Figure 94: Schematic Geologic map of the Llobregat delta region (modified from Almera, 1891) [SIMÒ et al. 2005].

Figure 95: Landslide susceptibility map in Catalonia with the localization of major events with recorded damage sometime in history [Taken from RISKCAT: Els riscos naturals a Catalunya].

Figure 96: Susceptibility map to the collapses and subsidences in Catalonia. The most affected zones are highlighted. [Taken from RISKCAT: Els riscos naturals a Catalunya].

Figure 97: Colorscale for the ground deformation map visualization in Google Earth

Figure 98: El Papiol.

Figure 99: Mean Amplitude image.

Figure 100: Geological map on a 1:50.000 scale of El Papiol. Taken from the cartographic portal of ICC (Institut Cartogràfic de Catalunya).

Figure 101: Deformation map. The PS that indicate significant movements are in four different areas. In particular, PS with negative velocity values characterizes the area labeled as one as result of a west-facing slope; this implies that the movement is detected moving away from the satellite. The other 3 areas show positive values, because the motion is detected approaching the satellite. The velocity values refer to the Line of Sight of the SAR; there is a minimum value of -8.5 mm / year and a maximum of 12.2 mm / year. The color scale is saturated between - 5 mm / year and + 5 mm / year.

Figure 102: Image of Google Earth of the Les Escletxes (zone A).

Figure 103: Cross section of the Les Escletxes landslides.

Figure 104: Pictures of the trenches in the geotope of Les Escletxes.

Figure 105: Slope processes delimited on the village of El Papiol. The pictured were taken during a field survey when diffuse damages to the buildings and roads have been detected.

Figure 106: Jardins Costa i Llobera and Mountjuïc and Mean Amplitude image of Mountjuïc.

Figure 107: Geological map on a 1:50.000 scale. Taken from the cartographic portal of ICC (Institut Cartogràfic de Catalunya).

Figure 108: Layout of the lithostratigraphic units of the Miocene. Adapted from [Pacerisa, 1999](#).

Figure 109: Land deformation map after the processing. The orange spot indicates the stable area in which all the points refer. The velocity value are saturated within a range between -5 mm / year and $+5$ mm / year. The velocity values refer to the Line of Sight of the SAR; there is a minimum value of -6.9 mm / year and a maximum of 1.2 mm / year.

Figure 110: two different sites have been detected as interested by deformation. The first one interests the Carretera Miramar and a portion of the underlying gardens. The mean velocity is $4 - 5$ mm / year. The second site, placed near a small car park next to the entrance of the tunnel on Carretera Miramar has a mean velocities are around 4.8 mm / year.

Figure 111: In A in the interferometric data indicate that the area affected by soil deformation. The area is under a scarp. In B is visible the alternation of clay lithology's resting upon cementified sandstone layers. In C the effects of the soil movement on the sidewalk.

Figure 112: In A in the interferometric data indicate that the area affected by soil deformation. In B and in C the effects of the soil movement on the scarp.

Figure 113: Aspect Image of Montjuïc

Figure 114: Slope image of Montjuïc

Figure 115: Pictures explain the procedure to correct the measured velocity along the line of sight to calculate the real velocity. It takes into account the two components of movement: horizontal and vertical.

Figure 116 Geological map on a 1:50.000 scale of Castellbisbal. Taken from the cartographic portal of ICC (Institut Cartogràfic de Catalunya).

Figure 117: Image of Castellbisbal.

Figure 118: Mean Amplitude image of Castellbisbal.

Figure 119: Land deformation map after the processing. The orange point indicate the stable area in which all the points refer. The velocity value are saturated within a range between -5 mm / year and $+5$ mm / year. The PS that indicate significant movements are in three different areas. In particular, the area labeled as A shows positive values. The other areas are characterized by PS with negative velocity values as result of a probably subsidence. This implies that the movement is detected moving away from the satellite.

Figure 120: image of the slope on which a real velocity calculation was made; the PS used to estimate the value are in the red area. They show positive values; this implies that the movement is detected moving close to the satellite. The velocity value are saturated within a range between -5 mm / year and $+5$ mm / year.

Figure 121: Image of the scarp; near the escarpment is visible an alteration of plant tissue.

Figure 122: Image of building conditions. In correspondence of PS were found fractures along the road and the walls surrounding the house.

Figure 123: Aspect Image of Castellbisbal

Figure 124: Slope image of Castellbisbal

Figure 125: Pictures explain the procedure to correct the measured velocity along the line of sight to calculate the real velocity. It takes into account the two components of movement: horizontal and vertical.

Figure 126: Flow diagram of the methodology used for the data processing in the wide areas.

Figure 127: Mean amplitude image of the interested area of Burgos and location of the seed chosen for the propagation step within the interferometric procedure.

Figure 128: Mean amplitude image and results of the seed propagation along the frame using the Kd-tree propagation for the interested area of Burgos.

Figure 129: Image of the 2D Phase Unwrapping step conducted in IDL environment. In particular the IDL unwrapping general window and the IDL window for procedure setting are shown in the image.

Figure 130: Flux diagram that shows the different passages useful to obtain a deformation map without the atmosphere contribution.

Figure 131: Images show the different passages useful to obtain a deformation map without the atmospheric contribution. The first image correspond to the original image with the atmosphere contribution; the second image is the filter that is used to remove the atmosphere. The third image is the first image without the atmosphere contribution.

Figure 132: Burgos city; location of the interested area of study.

Figure 133: Geological set of Burgos city.

Figure 134: Deformation maps of Burgos. The PS that indicate significant movements are in three different areas. The color scale is saturated between -10 mm / year and $+10$ mm / year.

Figure 135: Mean amplitude image of the study area and localization of radar targets in the area A. The velocity value are saturated within a range between -10 mm / year and $+10$ mm / year. The velocity values refer to the Line of Sight of the SAR.

Figure 136: Time series of the interested points for the area A.

Figure 137: Mean amplitude image of the study area and localization of radar targets in the area B. The velocity value are saturated within a range between -10 mm / year and $+10$ mm / year. The velocity values refer to the Line of Sight of the SAR.

Figure 138: Time series of the interested points for the area B.

Figure 139: Mean amplitude image of the study area and localization of radar targets in the area B. The velocity value are saturated within a range between -10 mm / year and $+10$ mm / year. The velocity values refer to the Line of Sight of the SAR.

Figure 140: Time series of the interested points for the area C.

Figure 141: Onshore–offshore geographical and geological settings of the Llobregat and Besòs deltas (northeast Spain, north-western Mediterranean Sea). After ICC (2005), Medialdea et al. (1986, 1989), and Perea (2006).

Figure 142: Cross-sectional structural sketch of the Catalan Coastal Ranges showing the tectonic structure of central plain and shelf off Barcelona. See Fig. 1 for location. From Parcerisa (2002).

Figure 143: Previous geologic cross section of the onshore and offshore of the Llobregat deltas base on [Ministerio de Obras Públicas \(1966\)](#), [Marques \(1984\)](#), and [Medialdea et al. \(1986, 1989\)](#). The lower Quaternary deltas (Q1–3) correlate with the Lower Detrital Complex and the Holocene delta (Q4) with the Upper Deltaic Complex. After [Simó et al \(2005\)](#).

Figure 144: El Prat del Llobregat airport taken from Google Earth.

Figure 145: Geological setting of the airport area. Taken from <http://siurana.icgc.cat/visorIGC/geotreballs.jsp>.

Figure 146: Mean amplitude image and deformation map after the TerraSAR-X processing data on El Prat Airport of Barcelona. The velocity value are saturated within a range between -10 mm / year and $+10$ mm / year. The PS that indicate significant movements in four different sectors. The PS are characterized by negative velocity values. This implies that the movement is detected moving away from the satellite. The registered movement can be due to the construction of new structures as well as some subsidence phenomena.

Figure 147: Geological setting of the harbour area. Taken from <http://siurana.icgc.cat/visorIGC/geotreballs.jsp>.

Figure 148: Image of the Barcelona Harbour taken from Google Earth.

Figure 149: Mean amplitude image and Deformation map after the TerraSAR-X processing data on Barcelona Harbour. The velocity value are saturated within a range between -10 mm / year and $+10$ mm / year. The PS that indicate significant movements in the eastern part of the harbor. The PS are characterized by negative velocity values because of a probably subsidence. This implies that the movement is detected moving away from the satellite.

Figure 150: Geological setting of the industrial polygon. Taken from <http://siurana.icgc.cat/visorIGC/geotreballs.jsp>

Figure 151: Image of the Industrial Polygon of Pratenc taken from Google Earth.

Figure 152: Mean amplitude image and Deformation map after the TerraSAR-X processing data on the industrial Polygon of Barcelona. The velocity value are saturated within a range between -10 mm / year and $+10$ mm / year. The PS that indicate significant movements are in two different areas. In particular, the area along the track of the Llobregat River shows positive values. The other areas are characterized by PS with negative velocity values as result of a probably subsidence. This implies that the movement is detected moving away from the satellite.

Figure 153: Tectonic scheme of Sicily [Gasperi \(1995\)](#). 1. Etna volcanic rocks; 2. Succession of the Pliocene and Pleistocene; 3. Succession of the Tortonian and Pliocene; 4. Unit of the Arco Calabro-Peloritano; 5. Unit of Sicilidi; 6. Flysch Numidico; 7. Unit Panormidi; 8. Imeresi units; 9. Sicane units 10. Unit of Trapani; 11. Iblee and Saccensi units.

Figure 154: Analyzed areas within Messina province, Sicily (Italy).

Figure 155: carta geomorfologica tratta dall'Atlante del Progetto AVI (<http://avi.gndci.cnr.it/docs/schedes3/sicilia/>).

Figure 156: Geological map (stralcio CARG – ISPRA, 2009). CALCARENITI DI SAN CORRADO: ORDa e ORDb: alternating of yellowish limestones and ocher sands, etheropic each

other in layers of 20 50 cm, fossils, containing sometimes decimeter levels of quartz micro-conglomerates grayish uncemented (ORDc); maximum thickness of 130 m. FLYSCH DI CAPO D'ORLANDO: CODb: predominantly sandstone facies (Oligocene)

Figure 157: Ascending ERS data in the Naso area.

Figure 158: Time series of ascending ERS targets.

Figure 159: Descending ERS data in the Naso area.

Figure 160: Time series of descending ERS targets.

Figure 161: Ascending ENVISAT data in the Naso area

Figure 162: Time series of ascending ENVISAT targets.

Figure 163: Descending ENVISAT data in the Naso area.

Figure 164: Time series of ascending ENVISAT targets.

Figure 165: Ascending RADARSAT data in the Naso area.

Figure 166: Time series of ascending RADARSAT target selected.

Figure 167: Time series of ascending RADARSAT target selected.

Figure 168: Descending RADARSAT data in the Naso area.

Figure 169: Time series of descending RADARSAT target selected.

Figure 170: Ascending COSMO-SkyMed data in the Naso area.

Figure 171: Descending COSMO-SkyMed data in the Naso area.

Figure 172: Geological Map (stralcio CARG – ISPRA, 2009) and location of the area affected by the landslide.

Figure 173: Geomorphological map from the Atlante of the AVI Project (<http://avi.gndci.cnr.it/docs/schedes3/sicilia/>).

Figure 174: Ascending ERS data in the Sfaranda area.

Figure 175: Time series of ascending ERS targets selected.

Figure 176: Descending ERS data in the Sfaranda area.

Figure 177: Time series of descending ERS targets selected.

Figure 178: Ascending ENVISAT data in the Sfaranda area.

Figure 179: Time series of ascending ENVISAT targets selected.

Figure 180: Descending ENVISAT data in the Sfaranda area.

Figure 181: Time series of descending ENVISAT targets selected.

Figure 182: Ascending RADARSAT data in the Sfaranda area.

Figure 183: Time series of ascending RADARSAT targets selected.

Figure 184: Descending RADARSAT data in the Sfaranda area.

Figure 185: Time series of descending RADARSAT targets selected.

Figure 186: Ascending COSMO-SkyMed data in the Sfaranda area.

Figure 187: Descending COSMO-SkyMed data in the Sfaranda area.

Figure 188: Histogram of the type of landslides in the area.

Figure 189: Digital terrain model (DTM) with 20m resolution of the mountain-hilly area of Messina Province; it was used to derive the topographic attributes of the terrain at a resolution of 100m.

Figure 190: Image of the Aspect map derived from digital terrain model (DTM) with 20m resolution of the Messina Province.

Figure 191: Image of the Slope map derived from digital terrain model (DTM) with 20m resolution of the mountain-hilly area of Messina Province.

Figure 192: Planar curvature.

Figure 193: Planar curvature: convergence and divergence of the flow according to the trend of contour lines

Figure 194: Image of the TWI map derived from digital terrain model (DTM) with 20m resolution.

Figure 195: Lithological map of the Messina Province obtained after the work of unification and reclassification.

Figure 196: Land Use map in the Messina Province after the reclassification work of the Corine Land Cover map (CLC).

Figure 197: Susceptibility map of Messina Province.

Figure 198: Frequency histogram of the values of susceptibility classified according to the Natural Breaks.

Figure 199: Outline of the major structural domains of the Apennine-Maghrebian orogen; identifies a thrust system composed of the unit of foreland to the South, from the Maghrebids units and the from the Kabilo-Calabridi units to north ([Lentini et al., 1995](#)).

Figure 200: Landslide Inventory in Sicily; IFFI, 2004.

Figure 201: Ground deformation velocity map: PS ERS data in ascending pass.

Figure 202: Ground deformation velocity map: PS ERS data in descending pass.

Figure 203: Ground deformation velocity map: PS ENVISAT data in ascending pass.

Figure 204: Ground deformation velocity map: PS ENVISAT data in descending pass.

Figure 205: Ground deformation velocity map: PS RADARSAT data in ascending pass.

Figure 206: Ground deformation velocity map: PS RADARSAT data in descending pass.

Figure 207: Ground deformation velocity map: PS COSMO-SkyMed data in ascending pass.

Figure 208: Ground deformation velocity map: PS COSMO-SkyMed data in descending pass.

LIST OF TABLES

Table 1: List of commonly used microwave bands.

Table 2 and Table 3: technical parameters and operational features of the main satellite sensors. Different colours distinguish different signal wavelength band of acquisition.

Table 4: Application of the satellite SAR sensors spectral bands related to the land use classes, as defined by Level 1 of CORINE Land Cover 2000.

Table 5: Application of different microwave bands SAR data in relation to the landslide velocity class (Cruden and Varnes, 1996).

Table 6: Application of satellite DInSAR and PSInSAR analyses related to the landslide velocity scale as proposed by Cruden & Varnes (1996). Mod. From Metternich et al., 2005.

Table 7: Applicability of Advanced InSAR to landslide phenomena in relation to the material type and movement type, as classified by Cruden and Varnes (1996).

Table 8: Landslide classification after Varnes (1978).

Table 9: Landslide velocity classes, as proposed by Cruden & Varnes (1996).

Table 10. Specifications of the dataset analyzed.

Table 11: Table of the classes in which the Aspect map is divided.

Table 12: Application of the satellite SAR sensors spectral bands related to the landslide velocity scale as proposed by Cruden & Varnes (1996).

Table 13: Application of the satellite SAR sensors spectral bands related to the land use classes, as defined by Level 1 of CORINE Land Cover 2000.

ABSTRACT

The government, the state, the regions and local authorities are increasingly put in place tools for risk analysis aimed at its reduction. These systems should result in a gradual improvement of risk assessment, of the measures undertaken to mitigate it and of a greater awareness, on the part of those involved, on the risks involved and on the different levels of reductions.

An advanced and innovative monitoring system governed by a law that would give guidelines for the management of risk is a starting point on which to base the analysis for the landslide risk.

Currently, the regulations at both national and regional level in the field of spatial planning and land protection, has as its objective the analysis of hydrogeological risk in terms of prediction, prevention and mitigation of risk.

In particular, the national legislation concerning the protection of the soil with a policy of prediction and prevention of flood and landslide risk is born by the Framework Law 183/89.

In particular, river basins are divided into basins of national, inter-regional and regional level and are imposed Basin Authority that are required to prepare the plans of basin.

Then the law 267/98 followed to disaster of Sarno states that the national and inter-regional authority of basin of adopt plans for the hydrogeological asset; they must contain in particular the perimeter of the areas exposed to hydrogeological risk to provide safeguards measures. Three phases must be practiced: identifying areas prone to landslide risk; define the perimeter, assess the levels of risk, determine the protective measures; schedule risk mitigation.

The hydrogeological disest is one of the main causes of risk for the social and economic structure of our country. Heavily influenced by human activity and the ongoing changes in the territory that have increased the possibility of occurrence of catastrophic phenomena, as well as by the increased presence of elements at risk and people in areas where these events are more likely, this occurs now with increasingly catastrophic effects.

Deforestation due to anthropization of the territory, the opening of quarries, the pumping from underground aquifers, the lack of maintenance of the slopes and the river valleys in addition to a general default to the current planning legislation on construction, highlighted the fragility the Italian territory with a present need for emergency interventions to stop landslides.

The increasing number of landslides that have occurred in recent decades in Italy, offered a great opportunity to study and investigate, by encouraging the emergence of a culture of anticipation and prevention, which is based on the identification of areas susceptible to landslide risk and on development of interventions aimed at reducing the impact of these phenomena.

Interferometric radar approach represents a powerful tool to detect movements on the Earth's surface. Thus, mapping and monitoring slope instability can greatly benefit from remote sensing and satellite data analysis due to the cost-effectiveness, great accuracy (up to 1 mm), high spatial resolution, non-invasiveness, good temporal coverage and measurement sampling.

In particular, advanced multi-temporal interferometric techniques, i.e. Persistent Scatterer Interferometry (PSI) have been successfully used in the last years for investigating natural hazards and, in particular, landslide processes.

This PhD research aims at give some applications of SAR interferometry for monitoring ground deformation and engineering infrastructures at basin and local scale, and for quantitatively and qualitatively analysis of slow-moving landslide phenomena.

The work is mainly based on the combined use of ground motion rates provided by PS radar data with conventional geomorphologic tools such as optical data, geo-thematic and *in situ* information, and further ground-truth data.

In particular, the research takes advantage of the potentials of PSI techniques for the spatial and temporal characterization of landslide ground displacements, in order to identify the most unstable areas and spatially and temporally monitor them. The spatial detection of landslides is performed through the mapping and the evaluation of phenomena, combined with the improving procedures for landslide activity and intensity assessment, exploiting more accurate PSI-based methodological tools. The temporal characterization of landslides is carried out through an advanced analysis of PS displacement time series and the integration of PS temporal information with other monitoring data.

RIASSUNTO

Le amministrazioni pubbliche, lo Stato, le Regioni e gli enti locali sempre più spesso predispongono strumenti per l'analisi del rischio finalizzate alla sua riduzione. Questi sistemi dovrebbero comportare un miglioramento progressivo della valutazione del rischio, delle misure intraprese per la mitigazione e della maggiore consapevolezza, da parte dei soggetti coinvolti, sui rischi che si corrono e sui diversi livelli di abbattimento.

Un avanzato ed innovativo sistema di monitoraggio regolato da una normativa che possa dare linee guida per la gestione del rischio è un punto di inizio su cui fondare l'analisi per il rischio idrogeologico.

Attualmente, la normativa vigente sia a livello nazionale che regionale in materia di pianificazione territoriale e di difesa del suolo, si pone come obiettivo l'analisi del rischio idrogeologico in termini di previsione, prevenzione e mitigazione del rischio stesso.

In particolare, la normativa nazionale relativa alla difesa del suolo con una politica di previsione e prevenzione del rischio da frana ed alluvioni nasce con la legge quadro 183/89. Tale legge individua nel bacino idrografico l'ambito geografico fondamentale per la difesa del suolo; in particolare i bacini idrografici vengono suddivisi in bacini di rilievo nazionale, interregionale e regionale e vengono istituite le Autorità di Bacino che devono redigere i piani di Bacino.

Successivamente la legge 267/98 seguita al disastro Sarno, prevede che le Autorità di Bacino di rilievo nazionale ed interregionale adottino piani di Stralcio per l'Assetto Idrogeologico; questi devono contenere in particolare la perimetrazione delle aree a rischio idrogeologico per prevedere misure di salvaguardia. In particolare devono essere praticate tre fasi: individuare le aree soggette a rischio idrogeologico; perimetrare, valutare i livelli di rischio, definire le misure di salvaguardia; programmare la mitigazione del rischio.

Il dissesto idrogeologico è una delle cause di rischio principali per l'assetto sociale ed economico del nostro paese. Fortemente condizionato dall'azione dell'uomo e dai continui cambiamenti del territorio che hanno incrementato la possibilità di accadimento di fenomeni disastrosi, oltre che dall'aumentata presenza di beni e di persone in zone ove tali eventi sono più probabili, questo si manifesta ormai con effetti sempre più catastrofici. Il disboscamento dovuto all'antropizzazione del territorio, l'apertura di cave, l'emungimento dalle falde sotterranee, la mancata manutenzione dei versanti e delle valli fluviali in aggiunta ad una generale inadempienza all'attuale legislazione urbanistica in materia

edilizia, ha evidenziato la fragilità del territorio italiano con una sempre più presente necessità di ricorrere a interventi di emergenza per arginare dissesti idrogeologici.

Il crescente numero di fenomeni franosi che sono avvenuti negli ultimi decenni in Italia, ha offerto una grande opportunità di studio ed approfondimento, stimolando la nascita di una cultura di previsione e prevenzione, fondata sia sull'individuazione delle aree più suscettibili al rischio idrogeologico sia sulla messa a punto di interventi mirati alla riduzione dell'impatto di questi fenomeni.

L'approccio radar interferometrico rappresenta un potente strumento per rilevare i movimenti sulla superficie terrestre. Pertanto, la mappatura e il monitoraggio dell'instabilità dei versanti possono trarre grandi vantaggi dal telerilevamento e dall'analisi di dati satellitari, grazie al buon rapporto costo-beneficio, la grande precisione (fino ad 1 mm), l'alta risoluzione spaziale, la non invasività, buona copertura temporale ed il campionamento delle misure. In particolare, le tecniche interferometriche multi-temporali avanzate, come la tecnica Persistent Scatterer Interferometry (PSI), sono state utilizzate con successo negli ultimi anni per investigare i rischi naturali ed in particolare, i fenomeni franosi.

Questa tesi di Dottorato mira a fornire alcune applicazioni dell'interferometria SAR per il monitoraggio delle deformazioni del suolo e delle strutture a scala regionale e locale, oltre che per l'analisi quantitativa e qualitativa dei fenomeni franosi lenti.

Il lavoro si basa sull'uso combinato dei valori di velocità fornite da dati radar PS con strumenti geomorfologici convenzionali quali dati ottici ed informazioni geo-tematiche.

In particolare, la ricerca analizza e usa le potenzialità della tecnica PSI per la caratterizzazione spaziale e temporale di movimenti franosi, al fine di individuare le aree più instabili e di monitorarle spazialmente e temporalmente.

L'individuazione spaziale delle frane viene eseguita attraverso la mappatura e la valutazione dei fenomeni, combinata con procedure per migliorare la valutazione della loro attività e intensità, sfruttando le più accurate metodologie basate sull'approccio PSI. La caratterizzazione temporale delle frane è effettuata attraverso l'analisi avanzata delle serie temporali di spostamento dei PS e l'integrazione delle informazioni temporali PS con altri dati di monitoraggio.

INTRODUCTION

Hydrogeological phenomena are one of the most widespread geological hazards and cause every year a lot of human losses and damages to infrastructure (Glade et al., 2005).

Ground instability ranges from devastating landslides, involving the chaotic mass movement of large quantities of rock or soil along steep, unstable slopes, to the progressive downward surface movements, commonly referred as subsidence, produced by ground water withdrawal, mineral extraction, underground storage and engineering works, and to the collapse of buried natural or man-made cavities and settlement of loose sediments.

The hazard depends on velocity, mass and time frequency of the event. One of the most important actions for the mitigation of the risk is to have updated inventories and much information as possible. The detection, mapping and studying of these phenomena are complex processes that can be made with different methodologies like field survey, remote sensing, historical information, modelling and a monitoring system.

The best methodology to detect and studying landslide and subsidence depends on the typology of the process, on the velocity, on the scale of analysis, on the geological and geomorphological settings, on the economical resource available and the associated risk.

Van Westen describes some good guidelines on the methodologies of detection, monitoring and studying Van Westen et al., (2008) and Fell et al., (2008).

The experience suggests that the best way to point out inventories is to use a multidisciplinary approach in order to exploit the advantages of each technique and to reduce the limitations. In this sense, the remote sensing is one of the most used methodologies to study landslides and subsidence (Mantovani et al., 1996; Singhroy, 2005; Metternich, 2005) and it has shown its capabilities in providing precise measurements of ground displacement on earth surface.

Thanks to the availability of historical archive datasets of SAR images acquired by ERS1/2 and ENVISAT satellites (ESA-European Spatial Agency), spanning from 1992 to 2010, and images by RADARSAT 1/2 (CSA-Canadian Spatial Agency) sensors, as well as satellite data from current X-band high resolution satellite systems, i.e. COSMO-SkyMed (ASI-Italian Space Agency) and TerraSAR-X (DL-German Aerospace Centre), PSI techniques can be applied to provide back analysis and monitoring of ground displacements with high precision up to about 1 mm/year (depending on the number of available images, the phase stability of each PS and its distance from the reference point on a single measure.

In addition to the traditional optical sensors (aerial photos), it is possible to use new sensors that allow analysing different aspects of investigations: multispectral images for land use and geology classifications, LiDAR for precise digital elevation models (DEM), radar images and SAR (Synthetic Aperture Radar) interferometry for the detection of ground movements. In each aspect of landslides and subsidence analysis all, the remote sensing tools can assume an important role. Some considerations, based on the paper of [Van Westen et al., \(2008\)](#), are reported in the following points.

Creation or updating of an inventory. It consists in to define the presence, the dimension, the typology, the state of activity of the landslides and all the other information available about landslides. These operations may be done from a single small basin scale to a national scale. The remote sensing has an important role because as many instruments may be used to map landslides. The analysis may be made through classical visual interpretation of aerial stereoscopic photos. For instance, the interpretation of aerial stereoscopic photos and the consulting of archive material are the techniques most used to produce the Italian Inventory of landslides (IFFI) ([APAT, 2007](#)). In addition, the high resolutions satellite images (Ikonos, Quikbird) may be used to detect landslides. The high resolutions DEM from LiDAR or SAR interferometry may use to create precise 3D models of terrain that facilitate the individuation of landslides geometries. The information of ground movement deriving from photogrammetry, overlaying of LiDAR DEM or SAR interferometry may be used to determine the state of activity of the landslides.

Susceptibility maps. It consist into individuate the areas that are potentially affected by landslides or subsidence by means of model that take in accounts some parameters (i.e. slope, land use, lithology, thickness of unstable material, geotechnical parameters, soil moisture). In addition, this operation may be made from a single basin to wide area. The remote sensing is important in this case too. For instance may be used in the definition of land use by means of the use of multi-spectral images. DEM derived from LiDAR or SAR interferometry are used to create slope and aspect that can be used in models of landslides susceptibility.

Monitoring. Monitor the movements, the piezometry, the triggering factor (rainfall) of a phenomenon. The monitoring is made at scale of single landslide or subsidence but on regional planning, many processes can be monitored at the same time. The real-time monitoring can be used to create an early-warning system. The remote sensing has a role also in the monitoring. For instance, the SAR interferometry can be used to register the movement of landslides and subsidence phenomena in real time (GB-SAR) or not real time (PSI techniques).

Modelling. At a scale of single process, a model that predict the possible evolution of a phenomenon or reproduce landslide kinematics may be pointed out. This is a deterministic approach that uses some defined and measured parameters (geological, geotechnical, topographic) to calculate the slope stability. The remote sensing, even if with a little importance, can be used also in this step. For instance, a good DEM derived from a remote sensing can be used in a model for slope stability calculation.

Mapping the element at risk. It consists in to individuate all the human elements potentially affected by landslides or subsidence. The remote sensing can be used, for instance, for the visual detection of buildings or for an automatic land use classification to individuate the anthropic settlement.

The potential hazard of ground instability phenomena can be reduced or even prevented especially in highly settled and susceptible areas; this by performing a proper identification and mapping of such ground movements, in order to support an appropriate land use planning and to facilitate the risk mitigation design.

Prevention and prediction of hydrogeological processes and failures need to be carried out for improving risk management activities and focusing resources according the distribution and intensity of the hazard.

In this PhD programme, remote sensing technique, and in particular PSI analysis, are exploited for studying and characterize ground deformations and engineering infrastructures.

PSI data are firstly analysed for spatial detection in order to identify priority areas where detailed analysis and additional in situ investigations can be focused. Then, PSI data are implemented to achieve a qualitative and quantitative interpretation and reliable characterization of phenomena and related landslides-prone and-affected areas.

The analysis aims at better understanding the distribution, activity and evolution of the investigated hydrogeological events and at assessing related damages and elements at risk, in order to assign a confidence degree and to potentially provide a preliminary tool for further hazard risk analysis.

1. OBJECTIVE AND STRUCTURE OF THE RESEARCH

Hydrogeological instability events represent the major geological hazards, occurring worldwide more frequently than any other natural disasters, including earthquakes, floods and volcanic eruptions.

Landslides and subsidence phenomena cause fatalities and injured people, but also produce direct and indirect socio-economic losses, in terms of property and infrastructure damage and environmental degradation.

Remote-sensing techniques represent a powerful tool to measure and map ground displacement as they offer a synoptic view that can be repeated at different time intervals and that is available at various scales.

Earth Observation and remote-sensing have a major role for studying geo hazard related events at different stages, such as detection, mapping, monitoring, hazard zonation, modelling and prediction.

The capability of PSI techniques in developing ground movement's inventories relies on the possibility of assigning a spatial meaning to the point with respect to ground displacement measurements provided by the PS technique, through the interpretation of aerial-photos and optical satellite imagery, topographic maps and ancillary data.

Due to the remote-sensing character of the above approach, which allows the acquisition of data over wide areas, and the extremely high precision of the radar measurements, this method is applicable at different scales.

This PhD thesis work deals with satellite Earth Observation (EO) tools that contribute to geo hazards analysis and characterizations in landslide-prone and landslide-affected areas. In this thesis, in order to detect slow moving processes, an approach based on radar interferometric data processed with the PSI approach, is proposed.

This thesis contains the main results of some works carried out at the Earth Sciences Department of the University of Firenze (DST-UNIFI, Centre of Competence of the Italian Civil Protection for geo-hazards) and at the Institute of Geomatics (Institut de Geomàtica) within the CTTC (Centre Tecnològic Telecomunicacions Catalunya) in Castelldefels (Spain).

The work wants to explore the potential of more recent remote-sensing techniques commonly applied in hydrogeological risk analysis, such as radar interferometric techniques.

1.1 STUDY SCOPE AND CONTENTS

This work aims at exploiting and improving new procedures and capabilities for detection, mapping, monitoring and forecasting ground deformation phenomena, mainly landslides and land subsidence and engineering infrastructures.

Persistent Scatterers Interferometry (PSI) is a well-known powerful advanced multi-interferometric SAR technique that allows measuring centimetre and sub-centimetre ground displacements occurred during a defined range of time, with millimetre accuracy. Accordingly, it has been fruitfully applied in the fields of geology (subsidence, landslides, earthquakes, volcanic activities), for scientific studies and for hazard and risk assessment strategies.

In the last few years, some new approaches have been developed to improve standard PSI analysis and try to overcome some problems and limitations within this technique.

This work fully exploits the existing ESA satellite systems operating in the microwave C-band as ERS, ENVISAT and RADARSAT. Moreover, SAR data provided by the new recent space missions, which are mainly X-band, as COSMO-SkyMed and TerraSAR-X, are deeply investigated to take advantage from their innovative characteristics such as the exploited microwave wavelength, shorter revisiting time and higher spatial and temporal resolution. Therefore, these modern generation SAR data can represent an effective tool for the rapid updating of landslide inventory maps and for hazard and risk studies.

The analysis of the benefits introduced by the new satellite missions with respect to the previous ones, in terms of technical performances and improvements in applications, is investigated in this thesis. In particular, SAR data acquired in X-band by the new sensors COSMO-SkyMed and TerraSAR-X, due to their different operational characteristics, imply a thorough investigation to assess their procedural use in combination with C-band interferometric data.

Such techniques have been exploited in several test sites in order to explore their effectiveness in detection and mapping of some areas affected by ground movements.

The present research is focused on evaluating the application of PSI SAR interferometry for monitoring ground deformations and engineering infrastructures, taking into account the site-specific investigation features and the satellite acquisition parameters and characteristics.

The radar interferometry has been used in presence of slow kinematic movements; TerraSAR-X data have been exploited for a rapid detection of landslides and subsidence phenomena. The potential applications, general problems and specific issues related to the combined use of different radar sensors are also addressed in this thesis.

1.2 STRUCTURE OF THE RESEARCH

This thesis represents the outcome of the PhD activity at the Earth Sciences Department of the University of Firenze (Centre of Competence of the Italian Civil Protection) and at the Institute of Geomatics (Institut de Geomàtica) within the CTTC (Centre Tecnològic Telecomunicacions Catalunya) in Castelldefels (Spain). The PS data were analysed over wide areas and in some local case histories in order to test the potential and limitation of these techniques in geological process detection with particular focus on landslides. The studies analysis were conducted in the test site of Verduno, in some areas within and near Barcelona city, in Burgos (Castilla y Leon), and in some areas within the province of Messina. This allows analysing many geological environments, to manage radar data from different type of satellite and to use different types of Persistent Scatterers products.

After an introduction where the PS techniques and their main problematic are described, a methodological procedure for the PS data processing and interpretation from basin to local scale was set up and focused for each case of study. The procedure to extract PS from raw data is explained for the different cases and all the areas detected were geologically interpreted comparing it with the other geo-databases available or other ancillary data. After, the check of the advantages and the limitation of PS data in the updating of landslides inventories in terms of adding new processes, boundaries and state of activity updating is explained. In this step the work was made over some areas at basin scale (Setta Basin, Barcelona city, Burgos and the Province of Messina) using PS data from traditional SAR satellite (ERS 1-2 and ENVISAT) and over some small areas (areas near Barcelona city and some areas of the Messina Province) using data from high resolution satellite (TerraSAR-X and COSMO-SkyMed). For all the areas the PS were tested with a multidisciplinary approach; field survey, ancillary geological data, photo interpretation were combined with PS information in order to understand the behaviour of the ground deformations monitoring. Finally, the conclusions resume and discuss the main results obtained during the research period.

This thesis is organized as in figure 1 and it includes eleven chapters, outlined as follows.

- * Chapter 1 introduces contents, objectives and outline of this PhD thesis.
- * Chapter 2 describes the basic principles of space-born radar remote sensing and renders a review of radar interferometry techniques, both classical and advanced approaches.
- * Chapter 3 deals with a review of remote sensed SAR data applications for monitoring ground deformations and engineering infrastructures; the chapters also provides a

- state of art of the sensors used up to date and of the applicability of PSI techniques to landslide phenomena.
- * Chapter 4 gives an application of C-Band SAR data for monitoring ground deformation and engineering infrastructures at a local scale. In particular, the subject of this chapter is the SqueeSAR™ analysis carried out in the area where it is planned the construction of the Verduno gallery (CN).
 - * Chapter 5 provides an application of C-Band SAR data for monitoring ground deformation and engineering infrastructures at a basin scale. In particular the chapter describes the applications of interferometric data for the spatial characterization of landslide phenomena and the updating of a landslides inventory at basin scale. The Landslide Inventory Mapping (LIM) procedures for detection and mapping, and the matrix-based approach for defining the landslide state of activity are here explicated. A case of study demonstrate the applicability of this methodology at basin scale: the Setta basin (Emilia-Romagna Region, Italy). The outcomes of the performed work for the test site are shown in the related Annex at the end of the thesis.
 - * Chapter 6 explains about the use of X-Band SAR data for monitoring ground deformation and engineering infrastructures at a local scale. The chapter first describes the IG interferometric processing chain for small areas and subsequently the PS data analysis. Three case studies are shown: El Papiol (Catalunya, Spain), Mountjuic (Barcelona, Spain) and the Castellbisbal (Catalunya, Spain). The whole efforts and results on these test sites are shown in the work.
 - * Chapter 7 describes some applications of X-Band SAR data for monitoring ground deformation and engineering infrastructures at a basin scale. Initially, the chapter explains the IG interferometric full frame processing chain for wide areas. Two case of study are shown: Burgos (Castilla y Leon, Spain) and some applications of SAR data for engineering infrastructures within Barcelona city. The whole efforts and results on this test sites are presented in the thesis.
 - * Chapter 8 gives some applications of the contribution of X-band SAR data in addition to C-band SAR data for the spatial characterization of ground deformations at a local scale. After some general considerations, the interpretation of PS data on landslides at a local scale is explained. Two case of study are shown: Naso and Castell'Umberto Sfaranda within the province of Messina, Italy.
 - * Chapter 9 provides an application of the contribution of X-band SAR data in addition to C-band SAR data for the spatial characterization of ground deformations at a basin scale. In this chapter, a methodology used for the spatial prediction with a landslides

- * susceptibility map in the province of Messina is given. These represent the probability of occurrence of a certain type of landslides in a given area, but without taking into account the time factor. In this context, an essential element is the use of interferometric data. For this, the data acquired in C-band are compared with those available in X-band to have an idea of what are the deformations occurred in the time.
- * Chapter 10 deals with discussion issues regarding applicability, limitations and uncertainties of PSI data and techniques, as well as advantages, potentials and future potential improvements. This chapter also summarizes the main findings of this thesis.
- * Chapter 11 gives the references cited in this work.

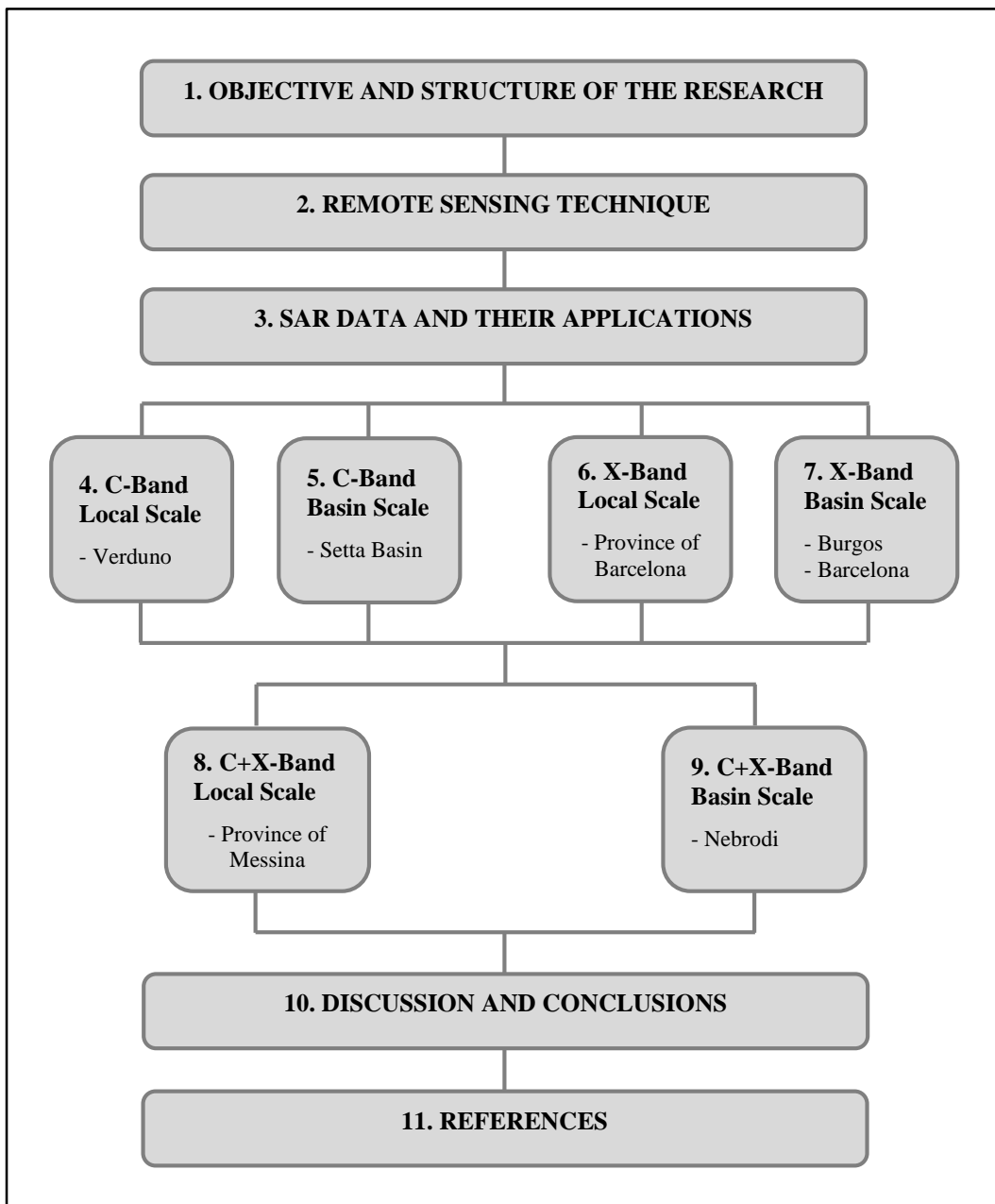


Figure 1: Flowchart of the thesis roadmap

2. REMOTE SENSING TECHNIQUES

Remote sensing is simply defined as the approach of obtaining information without physical contact with the object and thus in contrast to in situ observation (Lillesand and Kiefer, 1987). In modern usage, the term generally refers to the use of aerial sensor technologies to detect and classify objects on Earth (both on the surface, and in the atmosphere and oceans) by means of propagated signals (e.g. electromagnetic radiation). It may be split into active remote sensing, when a signal is first emitted from aircraft or satellites) (Schowengerdt and Robert A., 2007; Schott and John Robert, 2007; Guo Huadong et al., 2013) or passive (e.g. sunlight) when information is merely recorded (figure 2).

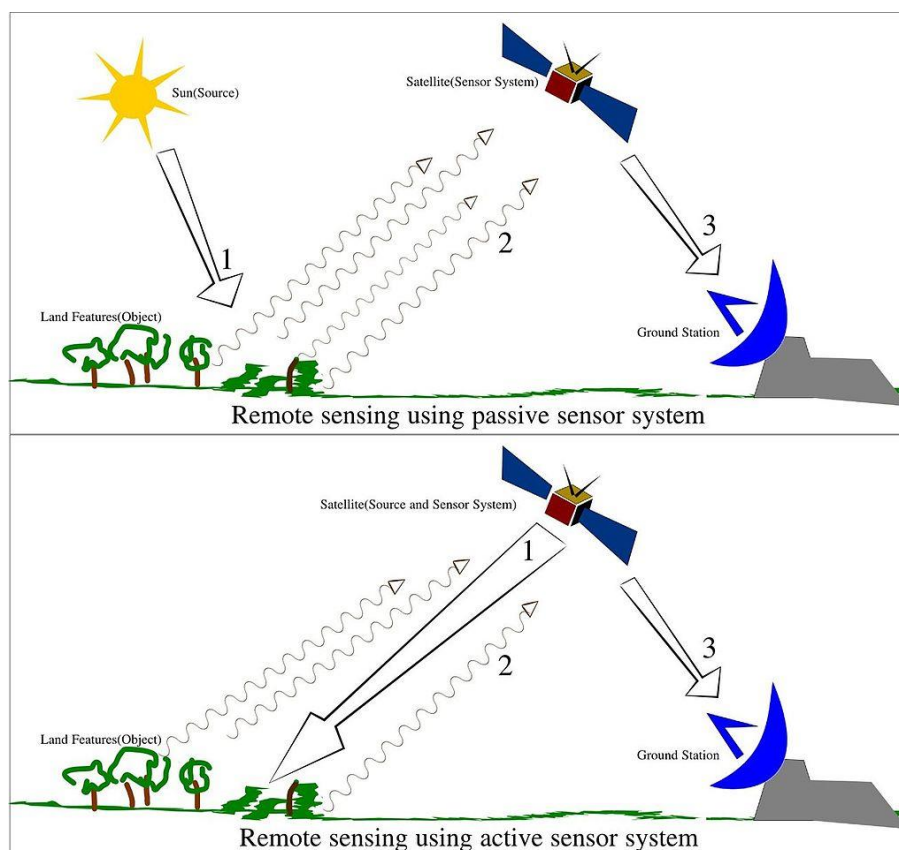


Figure 2: Remote sensing using passive or active sensor From <http://en.wikipedia.org>.

Passive sensors gather natural radiation that is emitted or reflected by the object or surrounding areas. Reflected sunlight is the most common source of radiation measured by passive sensors. Examples of passive remote sensors include film photography, infrared, charge-coupled devices, and radiometers.

Active collection, on the other hand, emits energy in order to scan objects and areas whereupon a sensor then detects and measures the radiation that is reflected or backscattered from the target. RADAR and LiDAR are examples of active remote sensing where the time delay between emission and return is measured, establishing the location, speed and direction of an object. Remote sensing makes it possible to collect data on dangerous or inaccessible areas. Remote sensing also replaces costly and slow data collection on the ground, ensuring in the process that areas or objects are not disturbed. Orbital platforms collect and transmit data from different parts of the electromagnetic spectrum (figure 3), which in conjunction with larger scale aerial or ground-based sensing and analysis, provides researchers with enough information to monitor trends of natural long and short term phenomena.

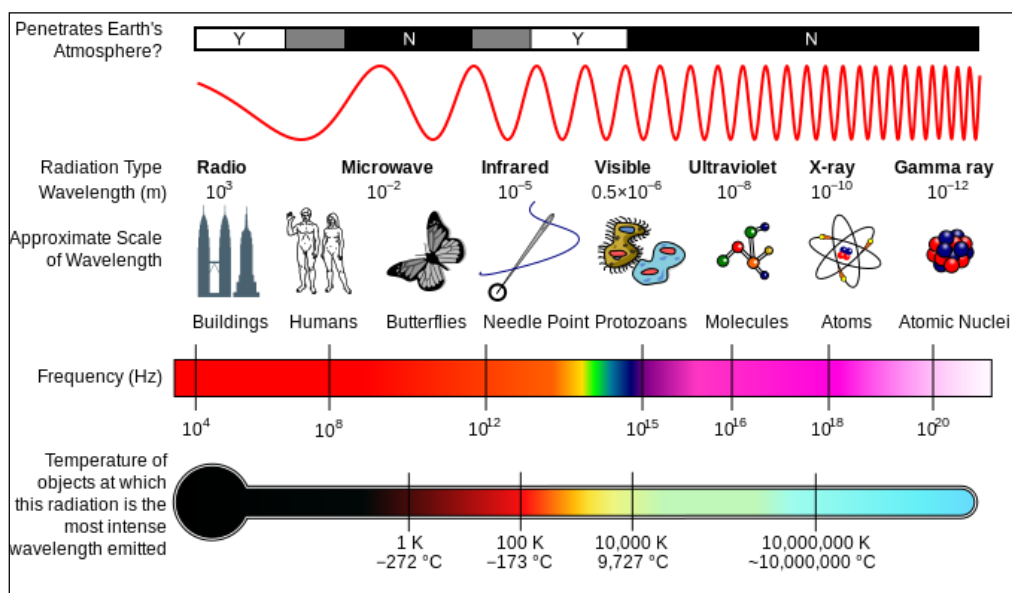


Figure 3: The electromagnetic spectrum. From <http://en.wikipedia.org>.

The basis for multispectral collection and analysis is that of examined areas or objects that reflect or emit radiation that stand out from surrounding areas.

Conventional radar is mostly associated with aerial traffic control, early warning, and certain large scale meteorological data. Doppler radar is used by local law enforcements' monitoring of speed limits and in enhanced meteorological collection such as wind speed and direction within weather systems in addition to precipitation location and intensity.

Other types of active collection includes plasmas in the ionosphere. Interferometric synthetic aperture radar is used to produce precise digital elevation models of large scale terrain (RADARSAT, TerraSAR-X, Magellan).

Laser and radar altimeters on satellites have provided a wide range of data. By measuring the bulges of water caused by gravity, they map features on the seafloor to a resolution of a mile or so. By measuring the height and wavelength of ocean waves, the altimeters measure wind speeds and direction, and surface ocean currents and directions.

Light detection and ranging (LIDAR) is well known in examples of weapon ranging, laser illuminated homing of projectiles. LIDAR is used to detect and measure the concentration of various chemicals in the atmosphere, while airborne LIDAR can be used to measure heights of objects and features on the ground more accurately than with radar technology. Vegetation remote sensing is a principal application of LIDAR.

Radiometers and photometers are the most common instrument in use, collecting reflected and emitted radiation in a wide range of frequencies. The most common are visible and infrared sensors, followed by microwave, gamma ray and rarely, ultraviolet. They may also be used to detect the emission spectra of various chemicals, providing data on chemical concentrations in the atmosphere.

Stereographic pairs of aerial photographs have often been used to make topographic maps by imagery and terrain analysts in trafficability and highway departments for potential routes.

Simultaneous multi-spectral platforms such as Landsat have been in use since the 70's.

These thematic mappers take images in multiple wavelengths of electro-magnetic radiation (multi-spectral) and are usually found on Earth observation satellites, including (for example) the Landsat program or the IKONOS satellite.

Maps of land cover and land use from thematic mapping can be used to prospect for minerals, detect or monitor land usage, deforestation, and examine the health of indigenous plants and crops, including entire farming regions or forests (Guo Huadong et al., 2013).

Landsat images are used by regulatory agencies such as KYDOW to indicate water quality parameters including Secchi depth, chlorophyll a density and total phosphorus content.

Weather satellites are used in meteorology and climatology.

Hyperspectral imaging produces an image where each pixel has full spectral information with imaging narrow spectral bands over a contiguous spectral range. Hyperspectral imagers are used in various applications including mineralogy, biology, defence, and environmental measurements.

Within the scope of the combat against desertification, remote sensing allows to follow-up and monitor risk areas in the long term, to determine desertification factors, to support decision-makers in defining relevant measures of environmental management, and to assess their impacts (Begni G. et al., 2005).

2.1 RADAR REMOTE SENSING AND SAR (Synthetic Aperture Radar)

The word “RADAR” itself is an acronym for *Radio Detection And Ranging*. Radar is nowadays commonly defined as an active object-detection system that operates with a beam of microwaves of the electromagnetic spectrum (figure 4). Radar systems were initially developed in the first half of the 20th century to determine the position or path of a moving object like an ocean-going vessel or an airplane. Pulse compression signal processing techniques have been traditionally used to improve the signal to noise ration and then locate targets with an error of few meters (Cumming and Wong, 2005).

A specific class of radar system is the Synthetic Aperture Radar (SAR), a microwave imaging system. It has cloud - penetrating capabilities because it uses microwaves. It has day and night operational capabilities because it is an active system. Finally, its “interferometric configuration” allows accurate measurements of the radiation travel path because it is coherent. These devices are capable of synthesizing a large antenna that observes the same target on the ground from different angles of view. The SAR along its trajectory repeatedly observes the same area and synthesizes a larger antenna, combining the data acquired in the successive positions, therefore obtaining a high resolution in azimuth direction. Measurements of travel path variations as a function of the satellite positions and the time of acquisition allow the generation of Digital Elevation Model (DEM) and measurement of centimetric surface deformations of the terrain (Ferretti et al., 2007). A space born SAR imaging system is sketched in figure 4.

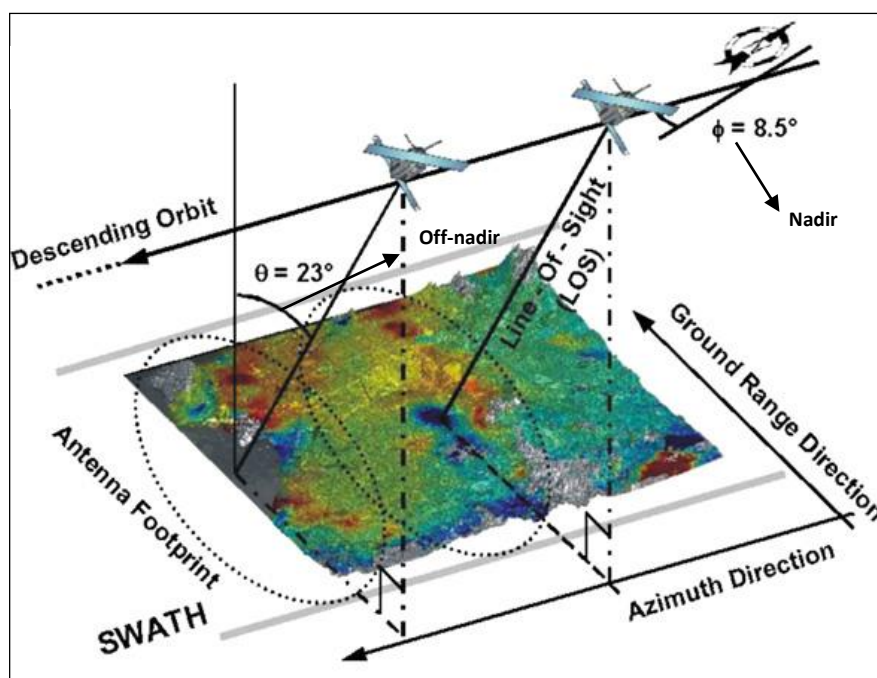


Figure 4: A SAR system from a satellite. Taken from COLESANTI et al., 2006.

A satellite carries a radar with the antenna pointed to the Earth surface in the plane perpendicular to the orbit. The inclination of the antenna with respect to the nadir is called “Off-nadir angle” and it is supposed to be equal to the “incidence angle” of the radiation on an assumed flat horizontal terrain. Space borne SAR systems typically have a fixed right side looking antenna that illuminates an area on the ground (the “antenna footprint”), along the sensor’s track, with a series of monochromatic microwave pulses.

The platform’s flight direction is called the “azimuth direction” and the direction of the main lobe of the transmitting antenna is called the “ground range direction”.

The satellite-to-target direction is usually called the “slant-range” direction (Hooper, 2006).

As the spacecraft moves, SAR sensor emits a stream of radar signals and the illuminated footprint sweeps out and traces a “swath” (area seen on the ground), in the ground range direction, on the earth surface. When detecting targets, the resolution is defined as the capability of a sensor to identify as separate two closely spaced scattering objects. Concerning radar systems, when two objects are too close each other, they are simultaneously within the same radar beam. Thus, they return reflections together and the receiving antenna records their backscattered signals at the same time. Conversely, when two targets are sufficiently far apart different radar beams illuminate one another, so they cause reflections at different times and their echoes are received separately.

The resolution of radar sensor in the direction parallel to the flight of the satellite (azimuth direction) depends on the width of the radar beam (b), which depends on the employed wavelength (λ) and on the physical (i.e. real) length L of the transmitting antenna: $b = \lambda/L$

Taking into account the distance (R) between the sensor and the target, the azimuth resolution (R_{azimuth}) for a real aperture radar system is given by $R_{\text{azimuth}} = R \cdot b$. Real aperture radars hosted by satellite platforms do not provide suitable resolution. For instance, given a beam width of 10 milliradians, at a distance of 400 kilometres, the azimuth resolution will be 4 km. For such systems, azimuth resolution can be improved increasing the length of the physical antenna used to illuminate the target scene or by using a shorter signal wavelength. The decrease of the wavelength would lead to a higher atmosphere and cloud impact on the capability of imaging radars. On the other hand, from antenna theory, the area illuminated on the ground is inversely proportional to the physical shape and dimensions of the antenna (Skolnik, 2001). Therefore, to obtain fine azimuth resolution in real-aperture radar systems (in the order of few meters), it would be necessary a very long physical antenna, e.g. some kilometres long. SAR (Synthetic Aperture Radar) approach was developed to overcome the main limitation of real aperture system. The SAR concept

separates two targets at the same range but different azimuth positions by their different relative velocities with respect to the moving platform.

The reflected monochromatic waves from two different scatterers in the same illuminated beam have different Doppler shifts or phases associated with them. Using the knowledge of the path of the imaging platform, we can compute the exact phase history for every point target on the ground. We combine information from multiple echoes, effectively creating a synthetic longer aperture to separate targets within the same illuminated beam. Resolution is dependent on the total amount of phase information available for each target. The longer a target is illuminated; the better is our ability to resolve it. In other simpler words, SAR system achieves fine azimuth by using a small antenna and “long” wavelengths, approximately few centimetres. Moreover, retrieved information is independent from the sensor-target distance. SAR is usually implemented by exploiting the forward motion of the aircraft or spacecraft. A single beam antenna, few meters long, is used. From different positions in distinct instants, the antenna repeatedly illuminates a target scene. Individual echoes, received successively at the different antenna positions, are recorded, stored, combined and then processed together, simulating a “synthetic aperture”, to provide a finer azimuth resolution (Hooper, 2006).

SAR is an extension of the “classical” radar techniques that create a directional beam using sophisticated signal processing to combine information from multiple echoes to accurately estimate the azimuth position of the target as well. The “synthetic aperture” concept allows a good spatial resolution (i.e. approximately meters) with relatively small physical antennas. Microwave signals emitted by SAR sensors have a specific central frequency, called “operating frequency”, which characterizes signal propagation and penetration features. Hence, sensors work at specific bands of the microwave domain, corresponding to different wavelengths (λ). Currently, the operational satellite SAR systems work in one of these microwave bands, commonly used in space borne radar applications: C-band (4-8 GHz, ≈ 5.6 cm wavelength), X-band (8-12 GHz, ≈ 3.1 cm wavelength) and L-band (1-2 GHz, ≈ 23 cm wavelength). Terrestrial radar remote sensing techniques usually use Ku band (12 – 18 GHz, ≈ 1.8 cm wavelength) (table 1).

Band	Frequency range	Wavelength (λ)	Central λ
L	1 – 2 GHz	30-15 cm	23 cm
S	2 – 4 GHz	15-7.5 cm	10 cm
C	4 – 8 GHz	7.5-3.75 cm	5.6 cm
X	8 – 12 GHz	3.75-2.50 cm	3.1 cm
Ku	12 – 18 GHz	2.5-1.67 cm	1.8 cm

Table 1: List of commonly used microwave bands.

2.1.1 ACQUISITION MODE

There are three operating acquisition modes of SAR system: Strip map, ScanSAR and Spotlight (Franceschetti, 1999). The most simple and popular is the Strip map mode, since has been the acquisition type of early space borne systems (ERS 1/2, and JERS-1). In this case, the radar looking angle is fixed. Antenna points along fixed direction to one side of the flight platform path (cross-track direction). As platform moves, the antenna footprint covers a relatively narrow strip (70 and 100 km wide swath for JERS1 and ERS 1/2, respectively). The more recent family of SAR satellite platforms (Radarsat 1/2, ENVISAT) was designed to acquire images in both Strip map and ScanSAR mode. Space borne radar applications exploiting ScanSAR images are ideally suited for mapping and monitoring large areas displacements. ScanSAR mode can achieve a wide swath coverage, periodically sweeping the antenna look angle. As platform moves, the antenna has the capability to illuminate several sub-swaths (in the cross-track direction), increasing the width of the image swath up to 400–500 km. Moreover, ScanSAR can acquire images for a given target area more frequently than Strip map mode, significantly improving the temporal resolution of deformation mapping. Nevertheless, according to Monti, Guarnieri and Rocca (1999), lower resolution images are obtained by operating in the ScanSAR mode, since the increased coverage led to a loss in the azimuth resolution. Typical swaths widths of Radarasat 1/2, ENVISAT, images are 500 and 400 km respectively. Up to know, ScanSAR, is the established mode in SAR for wide-swath imaging. However, the mode has several drawbacks caused by the focusing of the same target from different portions of the antenna (Meta et al. 2010).

The Spotlight mode is the most modern SAR version of imaging radar and can provide imagery with high spatial resolution. Higher resolution is obtained by pointing the radar look angle to keep the target area within the illumination beam for a longer time. Thanks to a longer synthetic aperture, Spotlight SAR considerably enhances the capability of SAR sensor of acquiring high-resolution imagery, although the expense of spatial coverage. The newest X-band satellite generation is capable of acquiring images in Strip map, ScanSAR and Spotlight mode, achieving in the last case an image pixel resolution of up to 1m.

TOPS (Terrain Observation with Progressive Scan) is a further acquisition mode. It is a wide-swath mode that overcomes the limitations imposed by the ScanSAR mode. During the acquisition, the antenna is steered along the track from backwards to forwards, so that every target on the ground is observed with the complete azimuth antenna pattern. The TOPS mode was first demonstrated in orbit by TerraSAR-X (Meta et al., 2010).

2.1.2 ACQUISITION GEOMETRY

Radar is a distance measuring method, utilising the two-way travel time of an emitted microwave pulse between the antenna and various ground targets. Therefore, radar has to be side looking, otherwise objects with equal distance to the left and to the right of the sensor would give reflections at the same point in time and could not be distinguished. These SAR inherent recording parameters lead to some important terminologies and distortional effects, which are described in the following.

Figure 5 illustrates a simplified geometry of a side-looking radar sensor. The footprint illuminated by the microwave pulse is called radar swath. The swath width is controlled by the look angle (θ). Azimuth direction refers to the along-track dimension parallel to the flight direction, whereas the range direction describes the dimension perpendicular to the sensor path. According to the distance from the flight path (nadir line), the radar swath is subdivided into near range and far range. As radar measures how far objects are from the sensor, distances are recorded in slant range along an imaginary line between the radar antenna and the target. Ground range is the perpendicular distance from the platform ground track to an illuminated object. Another important factor is the incidence angle, which describes the angle between the incident radar beam and the ground surface assuming no topography. The term local incidence angle is used for the angle between the radar beam and the normal to the surface at a particular point. Incidence angle and local incidence angle are only equal over flat terrain respectively.

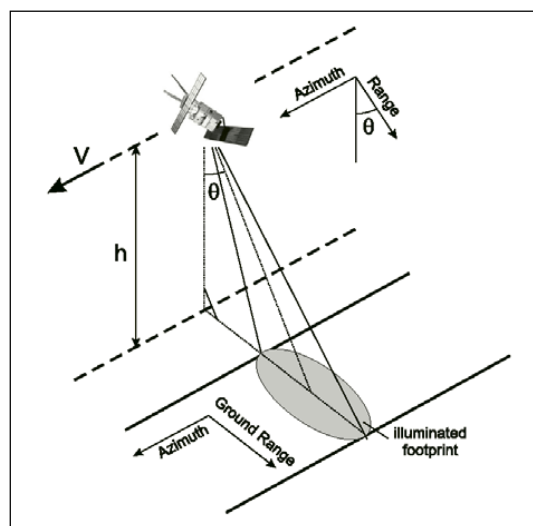


Figure 5: Simplified geometry of a side looking radar sensor. (Roth, 2001).

All satellites equipped with SAR sensors orbit the Earth on a near-polar orbit at an altitude ranging from 500 to 800 km above the Earth's surface, depending on the satellite

platform hosting the SAR sensor. The time taken for a satellite to re-pass over the same area is called the ‘revisiting time’. The angle between true north-south and the satellite orbit varies slightly, depending on the satellite, but in general lies in the range of 10 degrees. The circumpolar orbits of all SAR satellites mean that for half of their trajectory they are travelling from the north pole towards the south pole. This direction is referred to as a descending orbit. Conversely, when the satellite is traveling from the south pole towards the north pole, it is said to be in an ascending orbit. Figure 5 illustrated this concept.

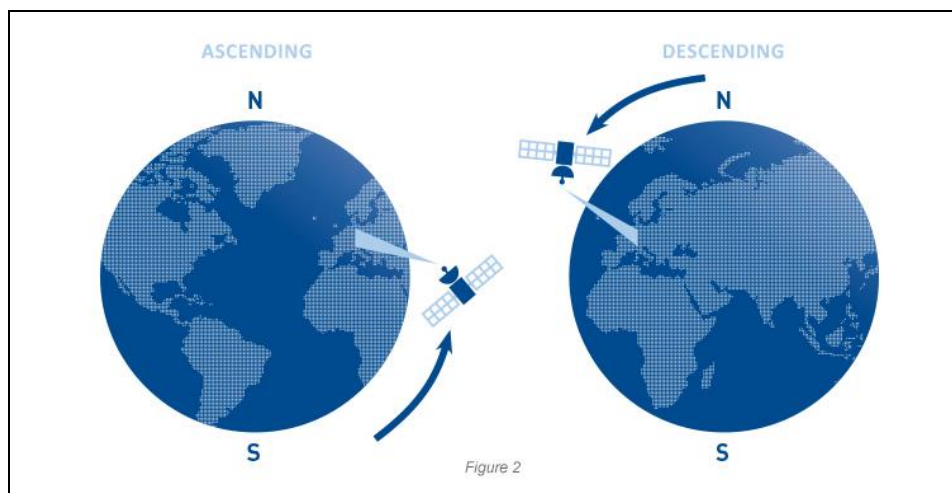


Figure 6: SAR sensor acquisition geometries: the two acquisition orbits. From <http://treuropa.com/technique/sar-imagery>.

A satellite carries a radar with the antenna pointed to the Earth’s surface in the plane perpendicular to the orbit (in practice this is not strictly true, because it is necessary to compensate for the Earth’s rotation). The inclination of the antenna with respect to the nadir is called the off-nadir angle and in contemporary systems is usually in the range between 20° and 50° . Due to the curvature of the Earth’s surface, the incidence angle of the radiation on a flat horizontal terrain is larger than the off-nadir (typically 35° for TerraSAR-X). However, for the sake of simplicity we assume here that the Earth is flat, and hence that the incidence angle is equal to the off-nadir angle, as shown in the figure above. The SAR systems acquires in two different geometries: ascending and descending; the first coincides with the north-south orbit and the second with the south-north orbit.

The direction parallel to the orbit of the satellite is called azimuth direction and coincides with the north-south direction.

The sensor-target direction, perpendicular to the orbit and inclined at an angle off-nadir to the vertical, is called slant range direction or line of sight.

2.1.3 RADAR IMAGE

The SAR processing is the transformation of raw SAR signal data into a spatial image. There are numerous published algorithms (Soumekh, 1999; Cumming and Wong, 2005) that can be used to process the recorded echoes to create high-resolution images using the SAR concept. The output from SAR processing algorithm is a single look complex (SLC) image, a two dimensional array of complex numbers, representing the brightness and phase of the scatterers on the ground. The indices of pixels in the matrix are directly related to the azimuth and range position of the scatterers with respect to a reference point on the platform's path. A digital SAR image can be seen as a mosaic (a two-dimensional array formed by columns and rows) of small picture elements (pixels), whose dimensions are the sensor-target distance (slant range or Line of Sight) and the platform flight direction (azimuth). Each pixel is associated with a small area of the Earth's surface (called a resolution cell) and gives a complex number that carries amplitude and phase information about the microwave field backscattered by all the scatterers (rocks, vegetation, buildings) within the corresponding resolution cell projected on the ground. The location and dimension of the resolution cell in azimuth and slant-range coordinates depend only on the SAR system characteristics, so the resolution depends on the sensor used and its acquisition mode. As pointed out before, pixel dimension ranges from 20x5m for ERS1/2 or ENVISAT satellites, up to 1m for the new X-band satellites. Each SAR image is a matrix made of complex numbers, made of amplitude and phase information about the backscattered microwave signal (figure 7 and 8).



Figure 7: Amplitude image.

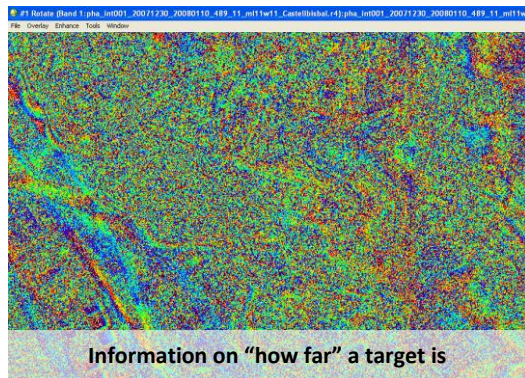


Figure 8: Phase image (known modulo 2π).

The phase refers to the oscillation of electromagnetic waves of the radar signal and mainly depends on the sensor-to-target distance. The phase is not exploitable for a single image. The amplitude of the radiation backscattered by the objects towards the radar and contained in each SAR resolution cell depends on the reflectivity and intensity of the illuminated

objects. Typically, exposed rocks or metal structures have a high capacity to reflect incident radar energy and thus the amplitude of the corresponding pixel is high. Reflectivity of smooth flat surface like water basin or soil is lower, so the amplitude of the reflected signal is lower. Besides the material, amplitude depends on the shape, size, orientation and moisture content of the scatterer, and, last but not least, on the characteristics of the radar beam (frequency, polarization and incident angle of the radar pulses). The terrain area imaged in each SAR resolution cell (called the ground resolution cell) depends on the local topography, in the plane perpendicular to the orbit (ground range direction) and in the azimuth direction. Different rows of the image are associated with different azimuth locations, whereas different columns indicate different slant range locations. Each SAR image pixel represents the coherent sum of all scattering elements within a resolution cell. The amplitude identifies the amount of electromagnetic radiation backscattered towards the satellite, while the phase depends on several factors, including the sensor-target distance. During the various steps along the same orbit, the satellites deviate slightly from the nominal trajectory, so the acquisition geometry for the same area varies of different angles, creating arrays of pixels that do not correspond to the same resolution cell on the ground. To make the analysis it is necessary that the homologous pixels of each image correspond to the same resolution cell; for this, a master image is chosen as reference. The slave images are resampled on the geometry of the master image in order to have the same grid reference for all satellite passages. The detected SAR image is generally visualized by means of grey scale levels, as shown in figure 7, since available sensors operate with a single frequency. Bright pixels correspond to areas of strong back-scattered radiation (urban areas), whereas dark pixels correspond to low backscattered radiation (a quite water basin). Since several scatterers are present within each SAR resolution cell and since echoes can add both constructively and destructively, the amplitude values over a single image fluctuate around the nominal values for each pixel based on its radar brightness, which is known as the “speckle effects” (a visual effect of “salt and pepper” screen). As a result, an individual amplitude image will appear speckled because each resolution cell is composed of many scattering elements, all reflecting incoming signal back to the satellite with different signal strengths and slightly different delays (phases). Thus, pixel phase values for a single image are not useful. If a second image is acquired over the same area, it can be “interfered” with the first image, which entails simply multiplying by complex conjugate. Generally, the second image is acquired from a slightly different position and it is the basis of the SAR interferometry approach, discussed below.

2.1.4 PROSPECTIVE DISTORSION

The side-looking geometry also causes some distortions in radar images especially in mountainous areas known as layover, foreshortening, and shadow. These geometric distortions depend mainly on the relation between terrain slope and the look angle of the radar beam. Since the radar pulse is emitted radially, equal travel times to ground objects are located on a circle centred at the sensor. As a result, objects with different distances on the ground may have the same distance from the satellite sensor.

Figure 9 illustrates the layover effect. The mountaintop (b) is closer to the sensor than the foot of the mountain (a). Therefore, the signal of the mountaintop (b) reaches the sensor before the reflection of the foot of the mountain resulting in layover of the terrain geometry in the slant range image. Generally, layover zones, facing radar illumination, appear as bright features in the image. The ambiguities in these zones cannot be resolved due to the representation of several points on the ground by one single point in the image.

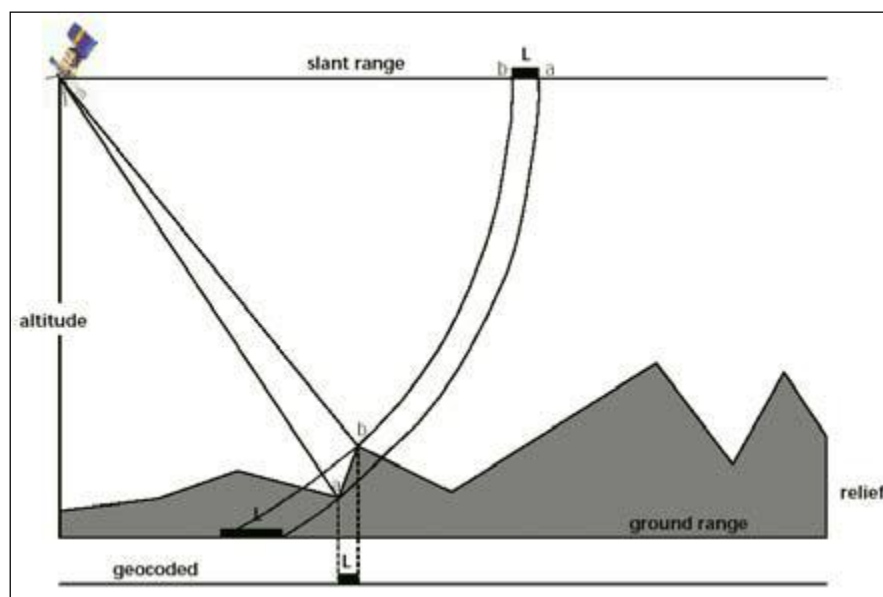


Figure 9: Distortions caused by the radar inherent side-looking geometry. Layover (a) results in a reversion of the terrain geometry. [From Roth, 2001].

In figure 10, the ground distance of the mountain slope is much larger than the recorded distance in the slant range geometry, because the top of the mountain is again relatively close to the sensor. This effect is called foreshortening. Foreshortening is obvious in radar images of mountainous areas, where the mountains seem to lean towards the sensor. The ambiguities of this range compression of the radiometric information backscattered from fore slope areas can be corrected by means of rectification procedures, which use topographic information.

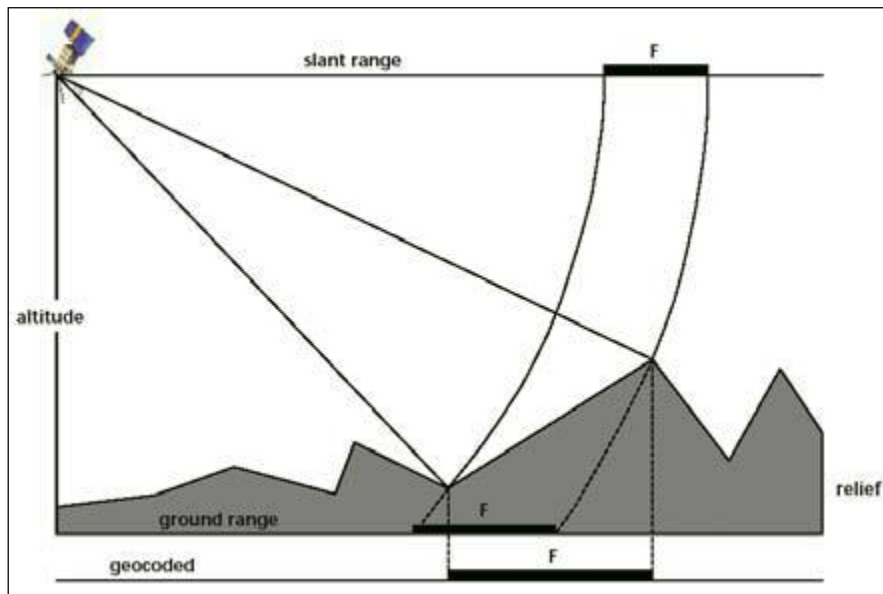


Figure 10: Distortions caused by the radar inherent side-looking geometry. Foreshortening causes compression of slopes facing towards the sensor. [From Roth, 2001].

The shadow effect (figure 12) is caused by slopes facing away from the sensor with an angle that is steeper than the sensor look angle. Therefore such areas cannot be reached by the radar signal and appear dark (zero signal) in the image. Further, the radar shadows of two objects of the same height are longer in the far range than in the near range of an image.

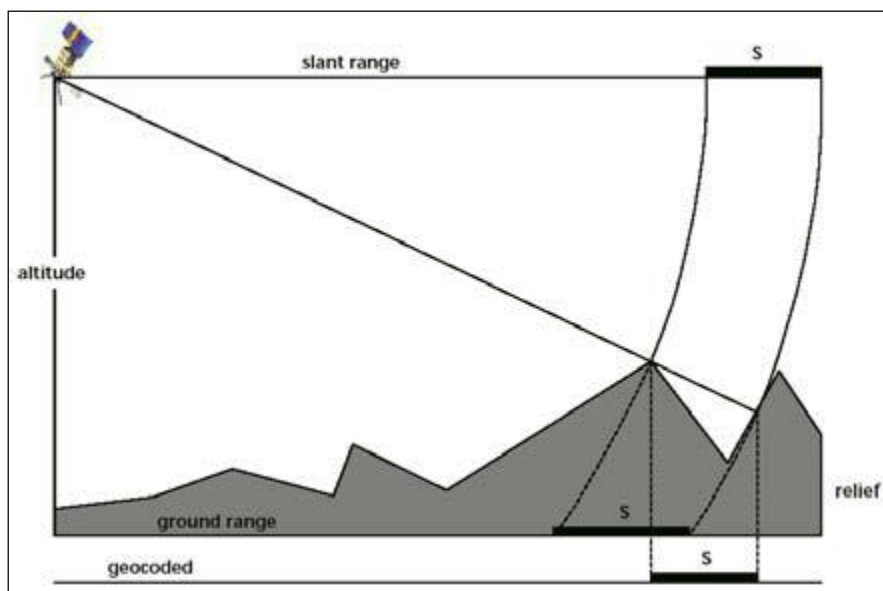


Figure 11: Distortions caused by the radar inherent side-looking geometry. Points in the shadow (c) of an object are not visible in the radar image. [From Roth, 2001].

2.1.5 SAR RESOLUTION

A radar imaging system is characterised by its resolution in azimuth (along-track) and range (across-track) direction. Range resolution in a radar image is mainly controlled by the bandwidth of the emitted microwave pulse. To improve range resolution, pulse duration (τ) should be as short as possible. This would lead to a higher pulse repetition frequency allowing for distinction between more closely spaced objects. However, it is also crucial to transmit enough energy in a pulse to enable the detection of the reflected signals. If the pulse is shortened, its amplitude must be increased to keep the same total energy in the pulse. Technically this is achieved by frequency modulation of the emitted pulses (chirped pulse). Instead of a short pulse with a constant frequency, a long pulse is emitted with a modulated frequency. The frequency modulation must be processed after reception to focus the pulse to a much shorter value. The slant range resolution (r_r) of a radar system and the ground range resolution (r_g), which is the projection of the former to the ground, is given by:

$$r_r = c\tau / 2 \quad \text{and} \quad r_g = c\tau / 2 \sin \theta$$

where c is the propagation velocity and θ the look angle.

The azimuth resolution describes the ability of an imaging radar to separate two closely spaced targets in the direction parallel to the motion of the sensor. For a real aperture radar, the resolution along track (azimuth resolution r_a) depends on the antenna beam width and the distance between the sensor and the observed surface and is given by:

$$r_a = r \cdot (\lambda / L)$$

r = distance between antenna and target; λ = wavelength; L = antenna length

As height and therefore the distance to the target is fixed for satellite based imaging radars, a better resolution can only be achieved by increasing the antenna length. However, assuming a satellite height of about 800 km (like ENVISAT) equipped with a c-band radar ($\lambda = 5.6$ cm), an antenna length of 3 km would be required to obtain a 10 m azimuth resolution. Obviously, this limits the usability of conventional radar and is overcome by a synthetic array approach. A Synthetic Aperture Radar (SAR) utilizes the motion of the sensor to simulate a long antenna. The received signals from subsequent antenna positions are coherently recorded and then added in a processor, using the Doppler principle, to synthesize a long antenna array. With this technique, the 10 meter long ASAR antenna onboard the ENVISAT satellite achieves an azimuth resolution (single look) of about 4.8 m (Rosich et al. 2003).

2.2 InSAR: INTERFEROMETRIC SYNTHETIC APERTURE RADAR

Interferometric synthetic aperture radar, abbreviated InSAR or IfSAR, is a radar technique that uses two or more synthetic aperture radar (SAR) images to generate maps of surface deformation or digital elevation, using differences in the phase of the waves returning to the satellite or aircraft. The technique can potentially measure centimetre-scale changes in deformation over spans of days to years. It has applications for geophysical monitoring of natural hazards, for example earthquakes, volcanoes and landslides, and in structural engineering, in particular monitoring of subsidence and structural stability. When a point on the ground moves, the distance between the sensor and the point also changes and so the phase value recorded by a SAR sensor flying along a fixed orbit will be affected, too. Figure 12 shows the relationship between that ground movement and the corresponding shift in signal phase.

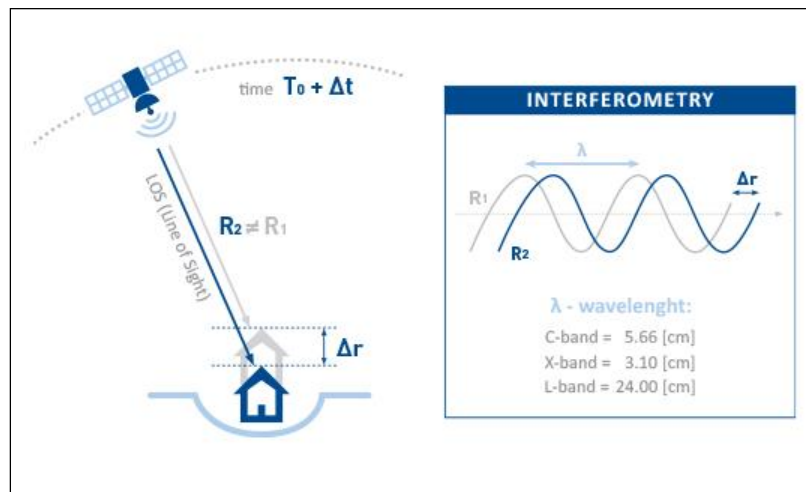


Figure 12: Relationship between that ground movement and the corresponding shift in signal phase. From <http://treuropa.com/technique/insar-evolution/>.

The change in signal phase ($\Delta\phi$) can be expressed in the form of the following simple equation:

$$\Delta\phi = (4\pi/\lambda) \cdot \Delta R + \alpha$$

Where λ is the wavelength, ΔR is the displacement and α is a phase shift due to different atmospheric conditions at the time of the two radar acquisitions. As a consequence, any displacement of a radar target along the LOS creates a phase shift in the radar signal that can be detected by comparing the phase values of two SAR images acquired at different times. Apart from noise and decorrelation effects, interferometric phase values are a blend of different signal contributions.

A single SAR image is no useful, since it is not possible to distinguish the different phase contributions related to reflectivity, topography, atmosphere and noise. The comparison of

two SAR images is needed for InSAR approach and the resulting difference in phase ($\Delta\Phi$) depends only on the change in path length. The difference between the two images is called interferogram; the SAR interferogram is generated by cross-multiplying pixel by pixel the first SAR image with the complex conjugate of the second (Rosen et al., 2000).

Thus, the SAR interferogram amplitude is the amplitude of the first image multiplied by that of the second one, whereas its phase (interferometric phase) is the phase difference between the images. As a result, the interferogram is formed by the complex product of the two SAR images (called the master and the slave) and its phase, which is the most important information, contains contributions referred to atmosphere, topography, terrain deformation and noise. Interferometric phase ($\Delta\phi$) is impacted by four contributions: topographic distortions arising from slightly different viewing angles of the two satellite passes (t); atmospheric effects (α) arising from the wavelength distortion that occurs when signals enter and leave a moisture-bearing layer; any range (distance between the sensor and the target) displacement of the radar target (ΔR); noise.

These factors, expressed more precisely, are given in the equation below:

$$\Delta\phi = (4\pi/\lambda)\cdot\Delta R + \alpha + t + noise$$

It is clear that the difficulties related to the estimation of surface deformation signals from a single SAR interferogram are essentially due to the presence of decorrelation effects (contributing to the noise level), the impact of local topography on phase values and the presence of atmospheric phase components superimposed on the signal of interest. An interferogram is the difference of the phase values corresponding to a certain area, i.e. it is a digital representation of change in surface characterization. It is a matrix of numerical values ranging from $-\pi$ to $+\pi$ (as they correspond to phase variations) and it can be converted to a map, the easiest way to observe whether or not motion has occurred over a certain area. Figure 13 is an interferogram of the L'Aquila earthquake.

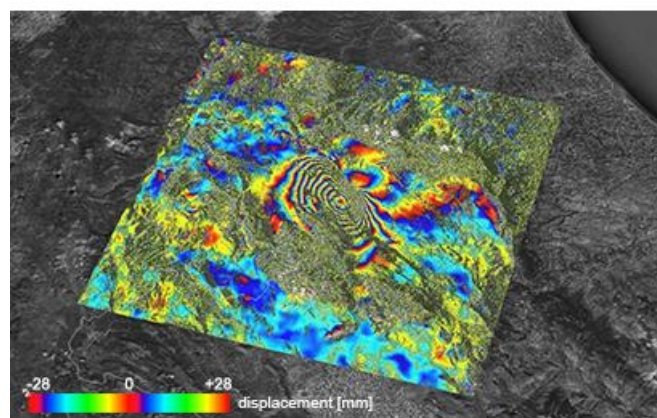


Figure 13: Interferogram of the L'Aquila earthquake that occurred in Italy, on 6th April 2009. [From <http://treuropa.com/technique/insar-evolution>].

The colored bands, referred to as fringes, indicate areas where movement can be measured. The highly speckled areas indicate where some form of decorrelation arose. Here the noise level (mostly due to vegetation) prevents the application of InSAR and no useful information can be extracted. Data were acquired by the ENVISAT satellite for which one phase cycle corresponds to 28 mm of ground deformation along the line of sight (neglecting atmospheric effects).

The fringe visible in figure 13 reveal areas with high coherence while the speckled areas represent very low coherence and noise. Interferometric fringes can only be observed where coherence image prevails. When an area on ground appears to have the same surface characterization in all the acquisition images, then the images are said to be coherent. If the ground surface is disturbed between two acquisitions (for example an agricultural field has been ploughed or tree leaves have moved positions), then those sub-areas will result in noise and no information can be obtained. The term noise is frequently used, standing for non-coherence, or decorrelation.

The coherence of an interferogram is affected by several factors, including: topographic slope angle and orientation (steep slopes lead to coherence), terrain properties, the time between image acquisitions (the longer the time interval, the lower the coherence is), the distance between the satellite tracks during the first and second acquisition, also referred to as the baseline (larger baselines lead to lower coherence). Typical sources of decorrelation can be referred for instance to vegetation and rapid movements, as already mentioned before. Coherence is measured by an index ranging from zero, when the area completely decorrelates, to 1, when the area is completely coherent. Overall, the analysis is successful, within an accurate deformation measurement, when the coherence index is between 0.5 and 1.0.

The main purpose of InSAR is to retrieve and separate the different contributions. The resulting interferogram represents as output very small slant range changes which can be related to topography and/or surface deformation (Klees and Massonet, 1999). The use of InSAR techniques dates back to the 70s, when this approach was exploited for topographic estimation purposes (Graham, 1974; Zebker and Goldstein, 1986).

The distance between two orbits of the satellite in the plane perpendicular to the track direction is called the interferometer baseline, its projection perpendicular to the slant range is the geometrical (perpendicular or normal) baseline. It is also the distance of the slave acquisition orbit with respect to the master. The difference in time between two acquisitions is the temporal baseline.

2.3 DInSAR: DIFFERENTIAL INTERFEROMETRY

Differential interferometry or DInSAR is based on the comparison of synthetic aperture radar images gathered at different times with slightly different looking angles (Gabriel et al., 1989; Rosen et al., 2000; Blamer and Hartl, 1998). The only difference with the InSAR approach is that topographic effects are compensated for by using a Digital Elevation Model (DEM) of the area of interest, creating what is referred to as a differential interferogram (the word ‘differential’ here refers to the subtraction of the topographic phase contribution from the SAR interferogram). This can be expressed as:

$$\Delta\phi = (4\pi/\lambda)\cdot\Delta R + \alpha + \varepsilon + noise$$

where ε is the contribution to phase arising from possible errors in the DEM that was used to remove the topographic effects. Whenever noise levels are low (i.e. decorrelation effects are negligible) and the phase contribution due to the local topography is accurately compensated for (ε is also negligible as well), then the remaining phase will be only due to any deformation of the Earth’s surface between the two acquisitions. This means that the interferometric phase can be referred only to the sole displacement occurred between the first and the second SAR acquisitions. So, the interferometric phase can be simplified as follows:

$$\Delta\phi = (4\pi/\lambda)\cdot\Delta R + \alpha$$

where $\Delta\phi$ is the differential interferometric phase, ΔR is the incremental distance the signal travels from the sensor to the ground and back and α is the atmospheric contribution to phase shift. Unfortunately, with differential interferometry, it is not possible to remove the α component. Although DInSAR may not be the tool for accurate displacement measurements, it is still useful in identifying footprints of progressing movement; DInSAR is the commonly used term for the production of interferograms from which the topographic contribution has been removed.

The basic principle relies on the fact that the phase of SAR images is an ambiguous measure of the sensor-target distance. Distance variations can, therefore, be determined by computing on a pixel-by-pixel basis, the phase difference (interferometric phase) relative to two SAR images.

The interferogram is a matrix of data obtained by comparing the phases of two SAR acquisitions over the same area; the phase of a single SAR image is not usable because it is impossible to distinguish the individual contributions.

With two acquisitions for the same area, it is possible to use the information contained in them. In this case, the interferogram can be generated by subtracting the phase image from

the other. The module of the interferogram is the product of the modules of the two images, while its phase, the interferometric phase, is given by the difference phase of the two images. Once a differential interferogram has been prepared, a deformation map can be created for all areas that are coherent, as shown in Figure 14.

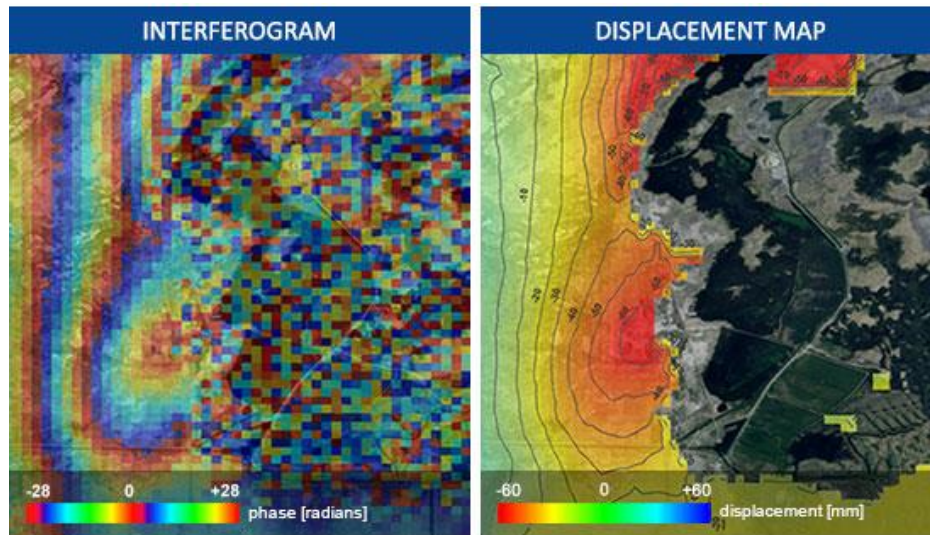


Figure 14: Examples of interferogram and the subsequently deformation map created for the areas that are coherent. From <http://treuropa.com/technique/insar-evolution/>.

On summary, the main contributions to the interferometric phase are shown below.

- Possible ground deformation Δs , affecting directly the sensor-target travel path. Only the projection of the deformation occurring along the sensor-target LOS is appreciated by a SAR system.
- Topographic profiles, in particular the height difference between couples of image pixels. The interferometric sensitivity to topography is much lower and is proportional to the normal baseline of the interferogram at hand (the normal baseline is a measure of how different the two orbits are).
- Phase noise (both temporal and geometric decorrelation).
- Atmospheric artefacts. Although SAR systems are capable of penetrating the cloud cover, the SAR phase signal is significantly influenced by the atmospheric conditions, in particular by the water vapour distribution in the troposphere (Zebker et al., 1997; Hassen, 2001). The atmospheric phase distortion (atmospheric phase screen, APS) is strongly correlated in space within each individual SAR image (i.e. it varies smoothly as a function of range and azimuth).
- Possible imprecisions in the orbital data (in particular baseline errors) translate into a further spatially correlated phase term (Hassen, 2001).

2.3.1 TEMPORAL AND GEOMETRICAL DECORRELATION

Some different factors can reduce or even compromise the quality and reliability of DInSAR results; the most significant limitation is the atmospheric phase delay. There is a variation in the delay of the signal as it propagates through the atmosphere, which leads to the phase term (α) that varies over the image, and that cannot be estimated through conventional DInSAR. Additionally, differential interferograms suffer from temporal and spatial (geometrical) decorrelation, due to the variation of the phase reflectivity ($\Delta\Phi$) of some kinds of radar targets that are not coherent in time. Electromagnetic properties of natural terrain change more rapidly than urban areas or rocks. As the time lag between the two SAR acquisitions increases, the reflectivity cannot be considered identical in the two SAR image acquisitions, and so decorrelation increases. For example, vegetation shows scattering properties that change with time, leading to a loss of interferometric coherence (temporal decorrelation). Temporal decorrelation makes interferometric measurements unfeasible where the electromagnetic profiles and/or the positions of the scatterers change with time within the resolution cell. The use of short revisiting times is not a solution, since slow terrain motion (creeping) cannot be detected. The “geometrical decorrelation” is generally due to reflectivity variations as a function of the incidence angle; if the perpendicular baseline between the two spacecraft positions at the two time acquisitions is non-zero, this difference alters the measurement. This limits the number of image pairs suitable for interferometric applications, unless this phenomenon is reduced due to the point-wise character of the target (a corner reflector). The principal orbital parameter controlling this effect is the so-called normal baseline B_n that is the projection perpendicular to the LOS direction of the distance of the satellite orbits relative to the two images involved in the interferogram. The higher is the absolute value of the baseline, the lower is the bandwidth shared by the two signals and thus the signal-to-noise ratio on the interferogram generated by them is low. Atmospheric heterogeneity superimposes on each SAR acquisition an atmospheric phase screen (APS) that can seriously compromise accurate deformation monitoring (Massonet and Feigl, 1998). Indeed, even considering areas slightly affected by decorrelation, it may be extremely difficult to discriminate displacement phase contributions from the atmospheric signature, at least using individual interferograms (Sandwell and Price, 1998). Some shortcomings of traditional interferometric techniques, such as the effects of the atmosphere and those of geometric and temporal decorrelation, can be removed with the Permanent Scatterers technique. The technique relies on the use of a limited subset of radar targets immune to decorrelation.

2.4 PSI: PERSISTENT SCATTERERS INTERFEROMETRY

The effects due to decorrelation phenomena can be reduced by combining multiple SAR observations using what is called Advanced Multi – temporal DInSAR techniques. Thus, in order to overcome the limits of single pair interferogram analysis (conventional SAR interferometry approach), namely the phase decorrelation and atmospheric effects, the multi–temporal interferometric approach such as Persistent Scatterers Interferometry (PSI) technique was developed. PSI techniques first emerged in 1999 when the Polytechnic University of Milan (POLIMI), in Italy, produced and patented its Permanent Scatterers Interferometry (or PSInSAR™) algorithm.

PSInSAR™ is a significant evolution of conventional InSAR whereby:

- A multi-image data set is used (minimum of 20-25 images)
- Atmospheric and orbital errors are essentially removed
- Sub-pixel radar reflections are analysed
- Linear and non-linear deformation patterns are identified
- Time histories of movement are generated for every radar target (PS)

The use of multi-image datasets makes it possible to identify stable reflectors, referred to as Permanent Scatterers, or PS, which are points on the ground that consistently return stable signals to the satellite sensor, allowing surface displacement velocities to be measured with millimetre accuracy.

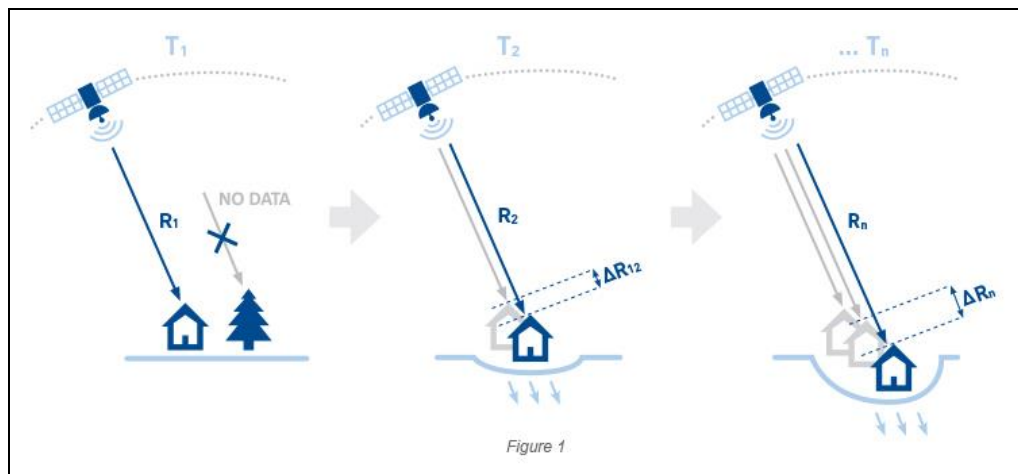


Figure 15: Schematic representation of the PSInSAR™ approach.

The technique of the Persistent Scatterers Interferometry (PSI) uses large stacks of images to generate the differential interferograms with respect a common master image for each available acquisition, even if the baseline is larger than the critical one and the generated interferogram highly affected by spatial decorrelation (Ferretti et al., 2001). The main idea

is to analyse the radar signal backscattered from an observed scene, identifying ground elements characterized by temporally stable electromagnetic features and by high reflectivity. These elements are called PS (Permanent Scatterers or Persistent Scatterers) (Ferretti et al. 2001). The accuracy of the height estimate depends on the normal baseline dispersion of the acquisitions. The wider is the range of the baselines; the better is the digital elevation model (DEM) estimate.

PSI techniques need of many multi-temporal space borne SAR images (at least 15–20), which are co-registered and acquired on the same target area in many different acquisition dates, with a sampling depending on the repeat cycle of the employed satellite. The high dispersion of baseline values and the limited accuracy of the available DEM make impossible the usage of a coherence criterion to select the pixels with good phase quality, since with the largest baselines the topographic component has to be accurately removed from the interferometric phase. With the PS technique, pixels are selected from the study of its amplitude stability along the whole set of images, which requires a minimum of 30 images for a reliable selection; therefore, the maximum resolution of the SAR images is preserved (Ferretti et al., 2001).

Atmospheric artefacts show a strong spatial correlation within each individual SAR acquisition (Hassen, 2001; Williams et al., 1998; Goldstein, 1995), but are uncorrelated in time. Conversely, target motion is usually strongly correlated in time and can exhibit different degrees of spatial correlation depending on the particular displacement phenomenon at hand (e.g. subsidence due to exploitation of ground water resources; (Ferretti et al. 2000) or oil/gas extraction, deformation along seismic faults, localised sliding areas, collapsing buildings). Atmospheric effects can then be estimated and removed combining data from long time series of SAR images.

In order to exploit all the available images and improve the accuracy of APS estimation, only scatterers slightly affected by both temporal and geometrical decorrelation should be selected (Ferretti et al., 2000, 2001). Phase stable point wise targets, hereafter called Permanent Scatterers (PS), can be detected based on a statistical analysis on the amplitudes of their electromagnetic returns (Ferretti et al., 2000, 2001). All available images are focused and co-registered on the reference sampling grid of a unique master acquisition (Basilico, 2000), which should be selected keeping as low as possible the dispersion of the normal baseline values. A correlation is carried out in order to make comparable the amplitude returns relative to different acquisitions.

Amplitude data are analysed on a pixel-by-pixel basis (i.e. without spatial averaging) computing the so-called amplitude stability index (Ferretti et al., 2000, 2001) ratio between

the average amplitude return relative to each individual pixel and its standard deviation. This statistical quantity provides precious information about the expected phase stability of the scattering barycentre of each sampling cell (Ferretti et al., 2001).

Simple thresholding (with a value of 2.5–3.0) on the amplitude stability index allows the identification of a sparse grid of Permanent Scatterers Candidates (PSC), points that are expected having a PS behaviour (Ferretti et al., 2001). PSC are actually a small subset of the PS as a whole since the phase stability of many PS cannot be inferred directly from the amplitude stability index (Ferretti et al., 2001). Their spatial density is usually sufficient (major or equal to 3–4 PS/km²) to carry out the reconstruction and compensation of the APS. Once removed the atmospheric effects, the interferometric data that remain are displacement values (measured along the LOS) and noise, dependent on the quality of the reflector. A Persistent Scatterers (PS) is defined as a radar target that reveals stable amplitude properties and coherent signal phase within a resolution cell, through all of the SAR images within a data stack. Thus, a PS corresponds to a resolution element containing single dominant scatterers. PS point-wise targets exhibit reduced temporal decorrelation due to their electromagnetic reflectivity and their coherent and stable scattering behaviour. Having a stable radar signature, PS are only slightly affected by decorrelation effects and the backscattered radar signal is much higher than the noise of the sensor. Objects that make good PS are usually man-made structures (buildings, dams, bridges, pylons, street lights, above-ground pipelines, any rectilinear structure that can create a dihedral signal reflection back to the satellite), as well as natural reflector (rock outcrops, hard un-vegetated surfaces, boulders) (figure 16)

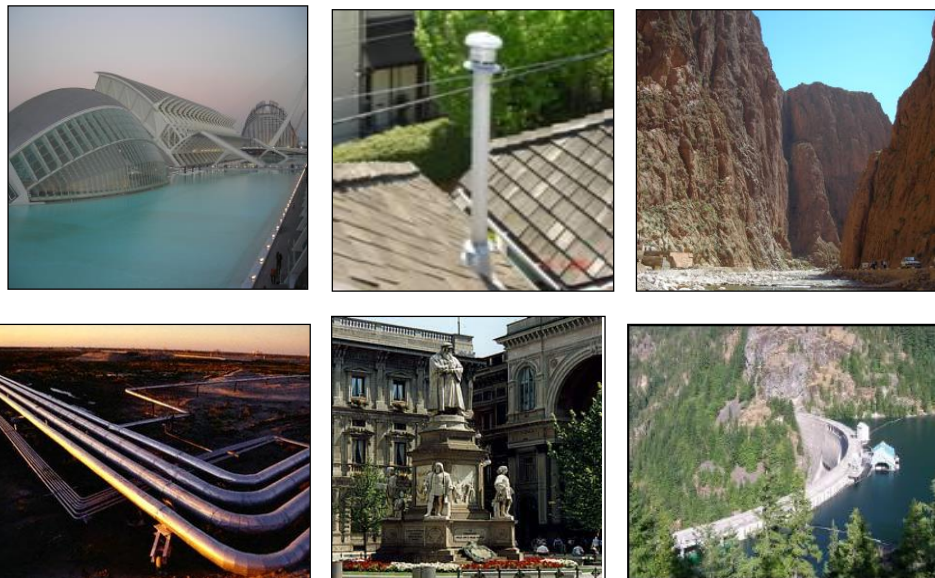


Figure 16: Examples of artificial and natural stable reflectors.

The velocity of each single PS point target can be estimated by performing a statistical analysis on amplitudes of electro-magnetic returns. Signal analysis of the network of coherent PS radar targets, exhibiting high phase stability over the entire observation period; allow estimating the displacements, acquisitions by acquisition, by distinguishing the different contributions related to ground motions from those due to atmosphere, topography and noise. Referring to the equation below:

$$\Delta\phi = (4\pi/\lambda)\cdot\Delta R + \alpha + \varepsilon + noise$$

The subtraction of topographic information (ε) from each interferogram can be performed through a conventional InSAR DEM that can be reconstructed and resampled on the master image grid (Ferretti et al., 1999). Then, for each identified PS, the terms $\Delta\phi$ and noise can be neglected. Therefore, the only problem to overcome is the assessment of atmospheric effect contribution. α is a term strongly correlated in space but not in time. Atmospheric effects are estimated and removed with a statistical analysis of the signals and by applying specific algorithms. As mentioned before, PSI started with the so-called Permanent Scatterers technique proposed by Ferretti et al. (2000). After this initial work, many other interferometric processing approaches were proposed in order to extract long-term stable benchmarks as PSI point targets from multi-interferogram analysis of SAR data (Werner et al., 2003; Hooper et al., 2004; Kampes, 2006). Although these advanced multi-temporal techniques were initially called “Permanent Scatterers techniques”, now all of them, including the original Permanent Scatterers technique, are usually called “PSI techniques” (Persistent Scatterer Interferometry), while the term “Permanent Scatterers” is exclusively associated with the original technique patented by Ferretti et al. (2001). PSI techniques are also called “Advanced multi-temporal DInSAR” to distinguish from the “Classical differential DInSAR”. Actually, all the advanced multi-temporal interferometric approaches can be briefly classified into two groups: Persistent Scatterer Interferometry (PSI) and Small Baseline (SB) methods. PSI methods work by identifying image pixels in a stack of interferograms generated with the same master that are coherent over long time intervals (Hooper et al., 2004; Kampes, 2006). On the other hand, SB methods use SAR image combinations with a short spatial baseline to reduce the effects of spatial and temporal decorrelation (Lanari et al., 2004) and they are used for processing long series of SAR imagery. Each of these methods has its advantages and limitations, and they have both proved to be effective in successfully estimating deformation time series in various regions (Hilley et al., 2004; Hooper et al., 2007). In multi-temporal InSAR processing, both the PS and SB approaches are optimized to obtain ground displacement rates with a nominal accuracy of millimeters per year.

2.4.1 SOIL DEFORMATION MEASUREMENTS

Figure 17 shows a schematic representation of the Persistent Scatterers theory and the disorders present in traditional SAR acquisitions. The basic idea is that the radar sensor mounted on the satellite, sends an electromagnetic pulse toward Earth's surface; the element on the ground surface reflects the signal and returns a part to the satellite. By measuring the elapsed time between sending the signal and receiving the backscattered, the system can determine the distance between sensor and target.

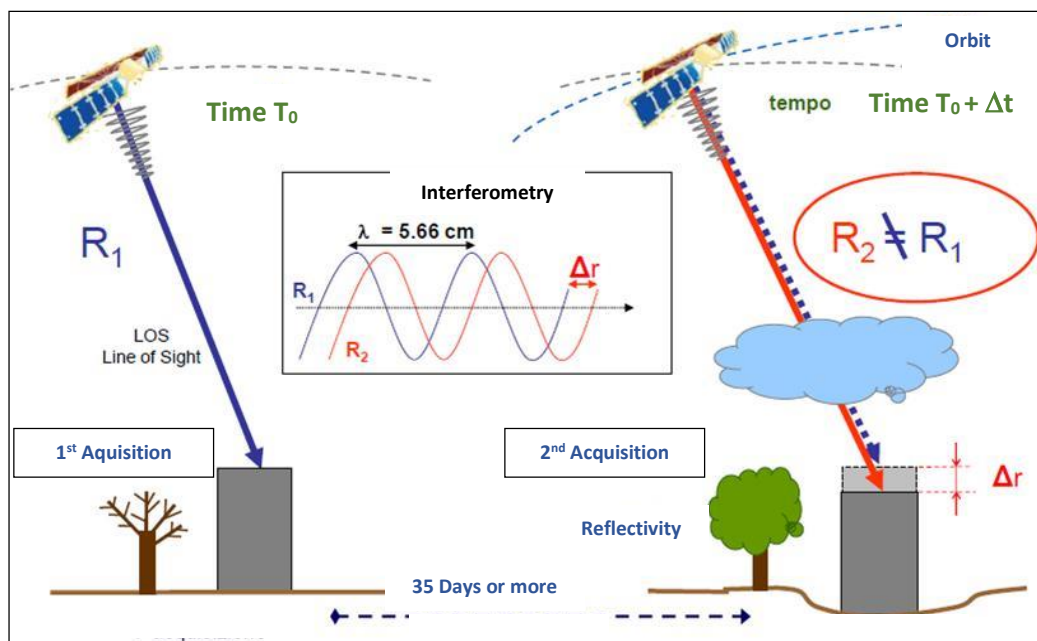


Figure 17: Schematic representation of the PS technique theory [Modified from T.R.E.s.r.l, 2004].

For this it is possible to reconstruct and monitor on large-scale, and with millimeter accuracy, the phenomena of deformation of the Earth's surface because the sensor detects between one and another acquisition, a change of distance and thus the target shift (Casagli et al. 2004). With certain algorithms are estimated for each PS, the degree of atmospheric effects and the surface deformation. The displacement measurements are taken along the line of sight of the sensor and are differential, that is spatially related to a ground point of known coordinates (reference point) and temporally at the acquisition date of the first image; so the measures of movement are relative rather than absolute (Ferretti & Jurine, 2007). Given $N + 1$ SAR data, N differential interferograms can be generated with respect to the common master acquisition. Since Permanent Scatterers are not affected by decorrelation, all interferograms, regardless of their normal and temporal baseline, can be involved in the PS processing. The goal of the PS approach is the separation of these phase terms. The basic idea is to work on the PS grid, computing in each interferogram the phase

difference $\Delta\Phi_i$, relative to pairs of PS within a certain maximum distance (1 km). In fact, since APS is strongly correlated in space, the differential atmospheric phase contributions relative to close PS will be extremely low. Just the phase information is essential for the identification of areas subject to surface movement; it contains various information, as there are many terms that contribute to determining the value, but the most important for the interferometric applications is the sensor-target distance. The phase (of each single pixel) of interferogram is:

$$\Phi_i = \frac{4\pi}{\lambda} r_{Ti} + \alpha_i + n_i + \Phi_{\text{topo-res}}$$

Where λ : is the wavelength; r_{Ti} : is the target motion (with respect to its position at the time of the master acquisition) possibly occurring; α_i : is the atmospheric phase contribution (referred to the master image APS); n_i : is the decorrelation noise ; $\Phi_{\text{topo-res}}$: is the residual topographic phase contribution due to inaccuracy in the reference DEM.

PSI techniques have been primarily exploited for the analysis of ground movements over urbanized areas, where the presence of man-made structures (buildings, roads, bridges, pylons) allow identifying a dense network of strong reflectors (up to several hundred per square kilometre). These stable targets allow retrieving estimates of the displacements along the satellite LOS, with unprecedented accuracy. Thanks to this multi-interferometric approach, the LOS velocity for each PS can be estimated with millimetre precision that is fraction of the operating signal wavelength. It is worth to highlight that all the measurements are made in the satellite's LOS radar beam and that are "relative" measurements, in both space and time. This is because each measurement is referred temporally and spatially to respectively an unique reference image ("Master" image) and to a stable point ("reference point") supposed motionless. The master scene is chosen in order to maximize the total coherence of the interferometric stack and to keep the dispersion of the normal baseline values as low as possible. The selection of the reference point is made within a stable sub-area of the investigated area of interest. The accuracy for the average LOS displacement rate on each PS is 0.1-1 mm/yr. Displacement time series can be retrieved, acquisition per acquisition, with accuracy on single measurements usually ranging from 1 to 3 mm. The geocoding accuracy of PS points depends on the ground pixel resolution (a few meters, depending on the used satellite). For instance, the positioning precision for C – band ERS 1 / 2 (pixel dimension: 20x5 m) is about $\pm 7\text{m}$ in Easting direction, $\pm 2\text{m}$ in Northing direction, and $\pm 1.5\text{m}$ on the vertical axis. For X-band TerraSAR-X (pixel dimension: up to 1x1 m) accuracy is $\pm 4\text{m}$ in Easting and $\pm 1\text{m}$ in Northing and the vertical axis (Colesanti et al., 2003a).

2.4.2 MEASURES ALONG THE L.O.S

The PS-InSAR technique can measure the component of displacement along the line joining sensor-target (line of sight); the acquisition takes place along two different geometries of view:

- Ascending: the satellite moves from S to N and it views a target area looking eastward.
- Descending: the satellite travels from N to S and it views the same target area looking westward

For the geometry of view, the W-facing slopes are detected by sensor in descending mode, while the slopes exposed to E are detected by the ascending mode; the NS-facing slopes are visible from both geometries. The value of the component of the measured displacement is greater the longer the displacement of the soil follows the line of sight. The more the real movement of the ground goes away from the line of sight, the smaller the component of motion recorded, until you reach a recording of motion equal to zero, when it is at perpendicular to the line of sight. In addition to changes in the registration form of the element of motion, you may also have variations of sign, in relation with the convention given. In fact, a ground motion that occurs to the satellite direction will be recorded as towards it (figure 18) and positive by convention (blue vector).

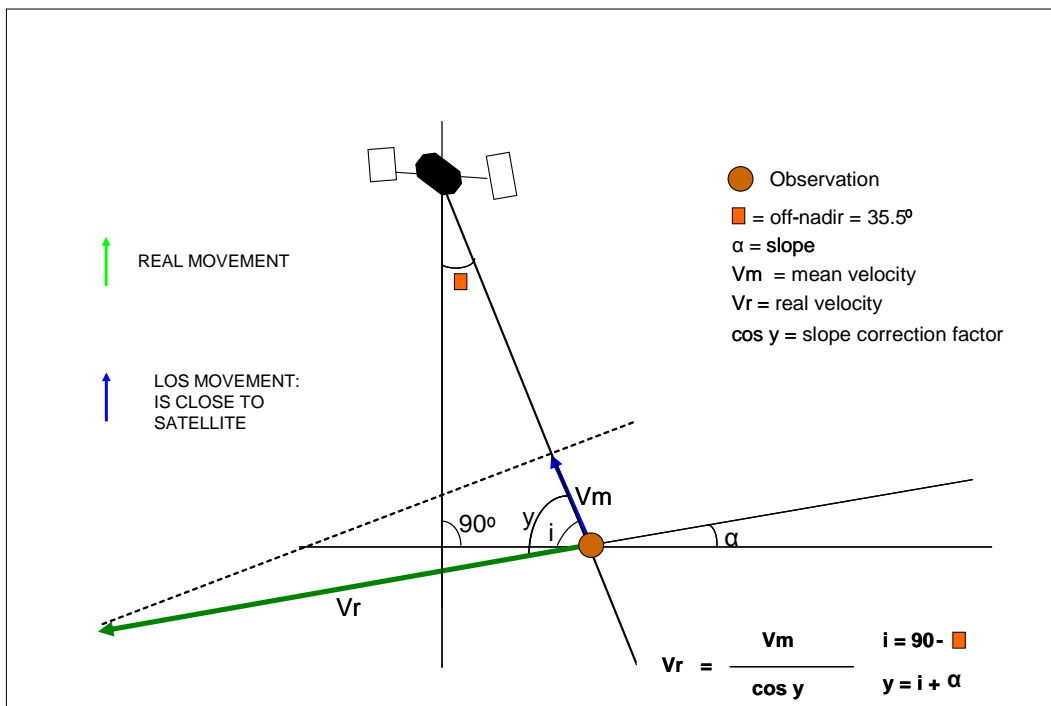


Figure 18: Sign of the velocity component recorded by the sensor depending on the direction of motion; the recorded movement (blue) is close to the satellite (positive).

On the other hand, a movement in the direction of motion of the satellite, will be recorded as moving away from it, and therefore a negative by convention (vector red)

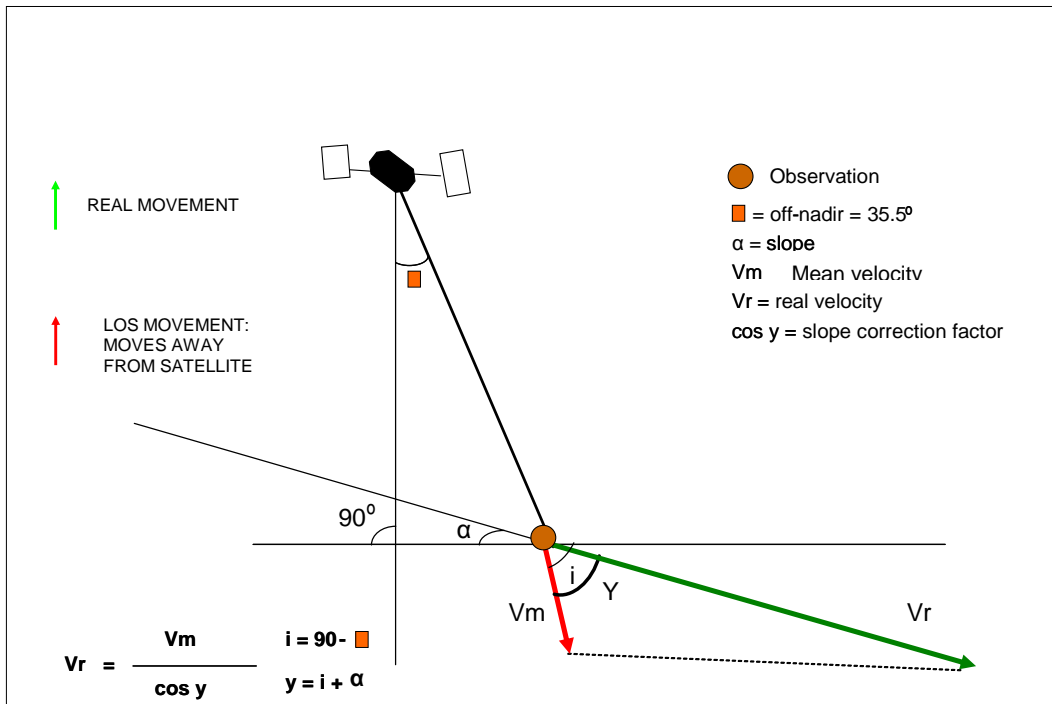


Figure 19: Sign of the velocity component recorded by the sensor depending on the direction of motion; the recorded movement (red) is moving away from the satellite.

A movement that occurs in N-S direction is not recorded because the satellite is able to sense the component of motion along this direction due to the acquisition geometry. It can see only the movement on the LOS direction.

3. SAR DATA AND THEIR APPLICATIONS

In the last decade, satellite radar interferometry has become a very useful remote-sensing tool for the detection and monitoring of active geological processes such as landslides, land subsidence, tectonic motions, and volcanic activity. The reason of the technique success relies on its appeal mainly connected to the capability of measuring ground displacements with a millimetre to centimetre precision even over wide areas (Farina et al., 2006). The application of space-borne InSAR (Synthetic Aperture Radar Interferometry) to landslide research has been improved by the development of the Persistent Scatterers Interferometry (PSI), as well as by the increasing availability of SAR data from different satellite sensors. Landslides studies can greatly take advantages from remote sensing techniques, which allow systematic and easily updatable acquisitions of data over large areas, reducing costs and optimizing field work, thanks to their non-invasiveness, low cost–benefit ratio, wide area coverage and high precision.

The use of remote sensing data, whether air-, satellite- or ground–based radar, has many applications especially if combined with traditional geomorphological tools (field surveys, orthophotos analysis, in situ observations, ground monitoring systems).

Several European research projects exploit traditional and innovative Earth Observation (EO) data and technologies to improve analysis and understanding of ground displacements phenomena and to deliver products tailored on the need of national, regional, and local Civil Protection.

Starting from the exploitation of the long SAR archives of ground deformations of traditional C-band SAR sensors (ERS, ENVISAT, and Radarsat) this work also investigates the opportunities provided by the new SAR missions, including COSMO-SkyMed and TerraSAR-X. With this respect, the innovative characteristics of the new sensors are evaluated, including the different operating microwave band, the significantly reduced revisiting time, and the considerably higher spatial resolution. The new sensors have the potential to become important and primary tools for the rapid production and updating of ground deformation maps, and for associated hazard and risk evaluation. A comparative drawbacks-benefits analysis is performed, investigating advantages and limitations of the new missions, and the related products, when compared to the older missions and products. In this section, a general review of the applications of SAR data is presented, as well as some application examples.

3.1 REMOTE SENSING TECHNOLOGIES

Interferometric radar approach based on EO data acquired by satellite systems represents a powerful tool to detect movements on the Earth's surface. Mapping geomorphologic processes and monitoring slope instability can greatly benefit from satellite data analysis due to the great cost-benefits ratio, non-invasiveness, wide area coverage and high precision of remote sensing techniques.

The first application of SAR Interferometry to the study of natural phenomena was in the 1970s. Afterwards, it has been successfully applied to the observation of different geophysical and geological processes and dynamics, which induce terrain deformations, such as volcanic activity, earthquakes and land subsidence (Zebker et al., 1994; Peltzer and Rosen, 1995; Fornaro et al., 1996; Massonnet and Feigl, 1998). This trend has grown, especially during the last 10 years, due to the availability of a large amount of SAR data acquired from different systems and satellite sensors. Metternicht et al. (2005) provide a further more recent review, analysing the use of remote sensing data in landslides studies during the 1980s, 1990s and 2000s. Metternicht et al. (2005) stated the remote sensing data give a valuable and useful effort to the three main stages of landslides-related studies: detection and mapping; monitoring; spatial analysis and hazard prediction.

For the landslides, detection and mapping the most significant remote sensing tools include optical (multi-and hyper-spectral) and infrared (IR) sensors, active VNIR sensors (LASER altimetry), active microwave sensors (SAR interferometry).

The monitoring of landslides is mostly undertaken applying InSAR and DInSAR techniques (satellite or ground based). For the spatial analysis and hazard prediction, the remote sensed data, such as SAR interferometry, aerial photographs, HR satellite imagery, topographic profiles collected by laser altimeter and digital photogrammetry, can provide landslide diagnostic features for heuristic, statistical, deterministic or inventory methods for landslides hazard works. In particular, remote sensing is useful in landslides hazard and risk assessment for hazard identification, spatial extent prediction and triggering factors detection Metternicht et al. (2005).

Overall, for the landslide studies, Singhroy and Molch (2004) divided the remotely sensed approaches into two different groups: the satellite or air-borne imagery and photo-interpretation, for determining more 'qualitative' phenomena characteristics (distribution and type) and the SAR interferometry or LASER altimetry, for estimating 'quantitative' features (length, thickness, velocity).

Interferometric SAR techniques are suitable for measuring very slow movements of slopes and individual objects. The main advantage over other techniques is the possibility of very

precise and repeated displacement measurements over large areas at reasonable costs (Rott, 2004; Singhroy, 2002).

Space-borne SAR can offer a useful support in the detection and characterization of slow surface displacements, providing rapid and easily updatable ground velocity measurement, along the satellite Line Of Sight (LOS), over large areas with great accuracy (up to 1 mm) and high spatial resolution and sampling (i.e. monthly acquisitions). In the last years, different InSAR techniques have been developed in a great number of applications and research studies to analyse different geological processes from regional to local scales, such as subsidence and landslides, as well as tectonic and volcanic activity (Massonnet and Feigl 1998, Singhroy et al. 1998; Hilley et al. 2004, Bürgmann et al. 2006).

Differential InSAR (DInSAR), that exploits the phase difference of two SAR images gathered at different times on the same area, has been widely used since late 1980s (Zebker et al., 1986; Gabriel et al., 1989) to detect surface deformation over large areas (Costantini et al., 2000). Classical DInSAR analysis is useful to study relatively fast ground deformation and dynamic phenomena occurred in a short period, when compared to the satellite revisiting time, for instance, co-seismic displacements (Carnece et al., 1996; Catani et al., 2005; Biescas et al., 2007; Crosetto et al., 2011). The best results are achieved using several pairs of interferograms and restricting the analysis to small areas e.g., up to a few square kilometres. Atmospheric effects, temporal and geometrical decorrelation, limit the conventional DInSAR.

Advanced multi-temporal interferometric approaches, like PSI, overcome these limitations, analysing long temporal series of SAR data, and providing annual velocities and deformation time series on grids of stable reflective point - wise targets, called Persistent Scatterers or PS (Ferretti et al. 2001). Multi-interferometric InSAR technique has turned out to be a valuable and useful tool to detect and measure surface displacements with millimetre accuracy and to reconstruct the deformation history of the investigated areas. (Farina et al. 2006, Casagli et al. 2009, Bovenga et al. 2006; Cascini et al. 2009; Colesanti and Wasowski 2006; Greif and Vlcko 2011; Hilley et al. 2004;).

PSI analysis, properly integrated with auxiliary data (e.g. aerial imagery), has been mainly used for mapping and monitoring land subsidence, uplifts and slow-moving landslides and for evaluating their state of activity and intensity. (Farina et al. 2003; Ferretti et al. 2005; Meisina et al. 2007, 2008; Casagli et al. 2008; Herrera et al. 2009, 2010; Guzzetti et al. 2009; Lu et al. 2010; Notti et al. 2010; Greif and Vlcko 2011; Frangioni et al. 2014).

3.2 EO DATA: DIFFERENT RADAR SENSORS AND SAR DATA

In the last 20 years, several different radar satellite missions have been launched providing different types of SAR images that can be used for ground movement detection and monitoring. Consequently today, many satellite interferometric data are available, including both historical archives acquired since the early 1990s (e.g. ERS 1/2 and JERS data) and images from currently operating satellites (e.g. ENVISAT, RADARSAT 1/2, TerraSAR-X, COSMO-SkyMed). These, spanning a time interval of more than 19 years and allowing the analysis of both past and recent ground displacements of the observed scenes with millimetre precision. The use of different microwave lengths requires a comparative assessment and illustration of the advantages and disadvantages of these satellites for landslide detection and monitoring.

The main past and present SAR missions are described below in figure 20 and table 2 and table 3, point out respectively the data temporal distribution and the technical parameters of each satellite sensor.

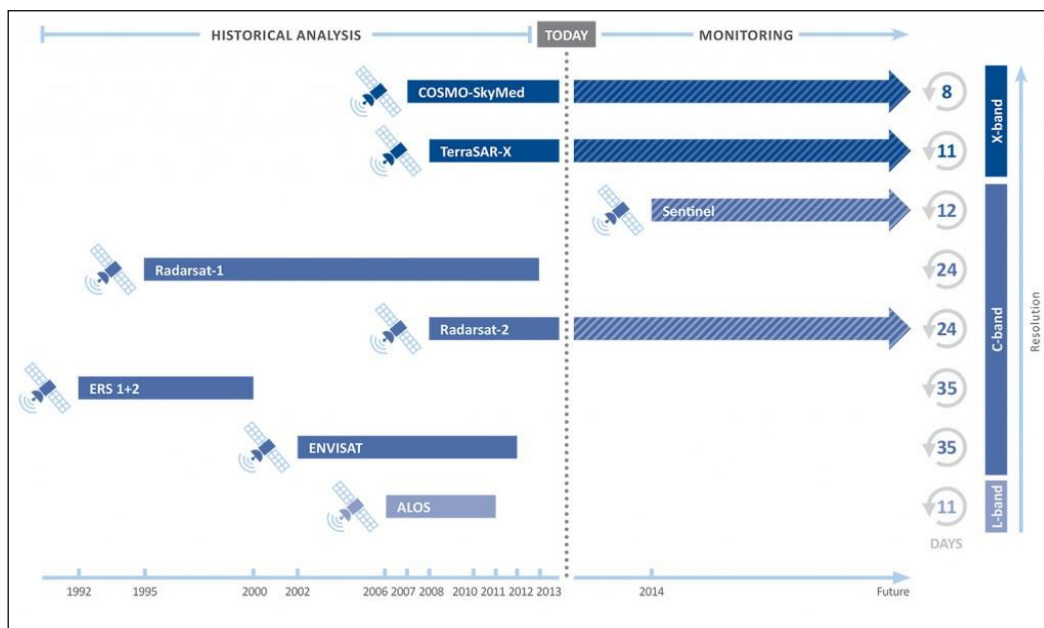


Figure 20: Image shows a schematic of SAR satellites that have acquired / are acquiring / will acquire SAR images use in Historic and Ongoing Monitoring analysis. Satellites have varied resolutions, signal wavelengths and repeat cycles; a summary of each satellites is described below. [Taken by T.R.E.]

First SAR radar images were acquired in C-band. The main satellite systems equipped with C-band sensor are ERS-1, ERS-2, ENVISAT satellites belonging to the European Space Agency (ESA) and RADARSAT-1, RADARSAT-2 of the Canadian Space Agency (CSA).

ESA missions are characterized by a wide area coverage of 100x100 km, a spatial resolution with pixel dimension of 20x5 m, a repeat cycle of 35 days and the availability of extensive historical archives of SAR images beginning in 1992.

The X-band satellite systems are the new generation sensors. The main X-band operating satellites are TerraSAR-X and COSMO-SkyMed, launched in 2007 by the Italian Space Agency (ASI) and the German Aerospace Centre (DLR), respectively.

Concerning L-band, ALOS (Advanced Land Observing Satellite) is a Japanese multi sensor mission, built by the Japan Aerospace Exploration Agency (JAXA) for remote sensing, launched into orbit in 2006 and operating until 2011, equipped with PALSAR (Phased Array type L-band Synthetic Aperture Radar) sensor, which follows JERS- 1 (Japanese Earth Resources Satellite-1) mission finished in 1998.

Satellite	Interval SAR		Resolution		Height	Agency & Nationality
	Initial	End	Range	Azimuth	[km]	
ERS - 1	1992	2002	8	4	745	ESA, Europe
ERS - 2	1995	2001	8	4	745	ESA, Europe
ENVISAT	2002	2010	9	6	820	ESA, Europe
RADARSAT - 1	1995	2000	5-100	5-100	825	CAS/USA, Canada
RADARSAT - 2	2007	2014	5-100	5-100	820	CAS/USA, Canada
JERS - 1	1992	1995	19	19	568	NASDA, Japan
ALOS	2005	2010	10-100	10-100	561	NASDA, Japan
TerraSAR-X	2007	2012	1-4	1-16	514	DLR, Germany
COSMO-SkyMed	2007	2016	1-100	1-100	619	ASI, Italy

Satellite	λ	Freq	Bands	Polarization	Repeat Cycle	θ	Swath
	[cm]	[GHz]			days	degree	km
ERS - 1	5.66	5.3	C	VV	35	23	100
ERS - 2	5.66	5.3	C	VV	35	23	100
ENVISAT	5.65	5.3	C	HH,VV,VH,HV	35	15-45	100
RADARSAT - 1	5.6	5.3	C	HH	24	18-60	45-500
RADARSAT - 2	5.5	5.405	C	HH,VV,VH,HV	24	18-60	20-500
JERS - 1	23.5	1.27	L	HH	44	35	75
ALOS	23.5	1.27	L	HH,VV,VH,HV	46	18-60	20-350
TerraSAR-X	3.1	9.6	X	HH,VV,VH,HV	11	15-65	30-200
COSMOSkyMed	3.1	9.6	X	HH,VV,VH,HV	16	20-50	30-200

Table 2 and Table 3: technical parameters and operational features of the main satellite sensors.

Different colours distinguish different signal wavelength band of acquisition.

3.2.1 SAR DATA IN C-BAND: ERS 1/2, ENVISAT, RADARSAT SATELLITES

First SAR radar images were acquired in C-band, which is characterized by signal frequency of 4-8 Ghz and wavelength (λ) ranging from 7.5 to 3.75 cm.

The main satellite systems equipped with C-band sensor are ERS1, ERS2, ENVISAT satellites belonging to the European Space Agency (ESA) and Radarsat 1, Radarsat 2 of the Canadian Space Agency (CSA).

ESA missions are characterized by a wide area coverage of 100x100 km, a spatial resolution with pixel dimension of 20 x 5 m, a repeat cycle of 35 days and the availability of an extensive historical archive of SAR images beginning in 1992.

Radarsat 1 (which acquires on demand) and Radarsat 2 data show a greater acquisition flexibility due to variable incidence angle and swath range (depending on the seven different acquisition modes and beams) and have a better revisiting time (24 days) with respect to ERS and ENVISAT satellites.

Moreover, within PSI analysis, they guarantee a higher spatial density of radar targets, improving significantly the chance of detecting landslide motions with higher precision and frequency.

In the next future, the RADARSAT Constellation Mission (RCM) will be operative, consisting of three spacecraft fleet of EO satellites, whose launch is scheduled for 2018. Sentinel-1 (ESA) is a two satellite constellation that will provide C-Band SAR data continuity following the retirement of ERS-2 and the end of the ENVISAT mission.

ERS-1 | ERS-2

European Space Agency (ESA) Commissioned: 04/1992 - 02/2001
European Remote Sensing (ERS) satellites 1 and 2, launched in July 1991 and April 1995 respectively, represented the first European satellite-mounted SAR instruments, and have provided a comprehensive archive of imagery for use in interferometric ground movement detection.

ERS-1 failed in March 2001, having far exceeded its life expectancy. Upon losing functionality of on-board gyroscopes, ERS-2 acquired its last usable image for InSAR purposes in February 2001.

The ERS archive is a useful tool for retrospectively monitoring ground movement and has a wide coverage over Europe.

RADARSAT-1

Canadian Space Agency (CSA)

Commissioned: 11/1995 - 03/2013

Radarsat-1, launched in November 1995, is currently the oldest SAR platform still in operation today. Amongst other instrumentation, it mounts a C-band SAR sensor and offers a number of different acquisition modes.

In over 15 years of services, Radarsat-1 has long outlived its design lifetime.

Due to the failure of an on-board tape recorder, Radarsat-1 cannot be used for future monitoring projects in the Middle East, as there is currently no ground station equipped to receive acquired data.

Radarsat-1 has acquired data worldwide, creating a large dataset for retrospective ground movement detection, but is not recommended for future monitoring projects.

RADARSAT-2

Canadian Space Agency (CSA)

Commissioned: 04/2008 - date

Radarsat-2, the sister to Radarsat-1, was launched in 2007 mounting an advanced C-band SAR system and is capable of acquiring higher resolution images than Radarsat-1.

The sensor also performs polar metric acquisitions, suitable for ground target characterization purposes. Radarsat-2 is suitable for use as a long-term monitoring satellite.

ENVISAT

European Space Agency (ESA)

Commissioned: 03/2002 - 10/2010

ENVISAT was launched in March 2002 with an on-board hydrazine capacity designed to last 5 years. Careful management of satellite orbital manoeuvres allowed hydrazine to be saved, extending ENVISAT's operative life by an additional 3.5 years.

Image acquisition continued regularly until ENVISAT was de-orbited in October 2010.

The satellite orbit was lowered to conserve fuel and prolong acquisition life, but at the cost of InSAR processing.

Although ENVISAT continues to acquire, it can no longer be considered reliable for ground movement detection (due to large baselines).

ENVISAT is hence not suggested for long-term monitoring projects, but as a retrospective tool for historical ground movement.

3.2.2 SAR DATA IN X-BAND: TERRASAR-X AND COSMO-SKYMED SATELLITES

The X-band sensors operate with signal frequency of 8-12 Ghz, at nearly 3 cm wavelength ($\lambda =$ from 3.75 to 2.4 cm); the X-band satellite systems are the new generation sensors.

The main new X-band operating satellites are TerraSAR-X and COSMO-SkyMed, launched in 2007 by the Italian Space Agency (ASI) and the German Aerospace Centre (DLR), respectively.

The launch of these new sensors has improved the spatial resolution of the acquired SAR images, being 3x1 m the pixel dimension, with a coverage of about 30x30 km. Other important advantages of both the systems are that the satellite sight angle and the swath can be changed within the configuration mode.

In addition, the acquisition frequency of SAR images is reduced, e.g. the revisiting cycle is 11 days in the case of TerraSAR-X and 16 days in the case of COSMO-SkyMed (that can be reduced to 4 days, if all the four satellites of the system are working).

X-band SAR systems in space aim mostly at facilitating the research and application of terrain - related phenomena with high precision and short revisit cycle compared with the medium resolution SAR system, i.e. ERS , ENVISAT and Radarsat.

Displacement monitoring would much benefit from the advantage of the repeat cycle of few days and from the high ground resolution in azimuth and range, depending on the acquisition mode and incidence angle.

This high spatial resolution and short repeat interval allow studies of highly localized surface displacements with a dynamic temporal evolution that have previously suffered from temporal or spatial decorrelation (Ge et al., 2010, Notti et al., 2010).

SAR images acquired in X-band, contrarily that in L-band, show greater difficulties for acquisition in vegetated areas than in C-band, due to the shorter λ used. However, the reduced revisiting time on the same area of X-band sensors, reduced temporal decorrelation permitting to observe ground motions characterized by higher velocities.

Moreover, the use of a shorter wavelength allow reaching a higher precision in the deformation rates, that are measured as λ fractions, but increases ambiguity phase problems, since the probability that deformations between two consecutive acquisitions could exceed the threshold of $\lambda/4$ (the limit of maximum detectable movement in InSAR analysis) is higher.

COSMO-SKYMED

Italian Space Agency (ASI), Telespazio

Commissioned: 06/2007 - date

COSMO-SkyMed is a constellation of four satellites for both civilian and military use, the first of which was launched in June 2007.

The fourth and final satellite became operational at the end of 2010, allowing rapid repeat passes to be acquired (one image every 4 days).

This significantly reduced the time between two sequential acquisitions compared to other satellite systems, whilst also reducing the time required to create a minimum baseline of images for InSAR processing and creating data redundancy.

The satellite mounts an X-band SAR sensor, capable of acquiring high-resolution images. Cosmo-SkyMed is recommended for long-term monitoring projects.

TerraSAR-X

German Aerospace Center (DLR), Astrium

Commissioned: 06/2007 - date

TerraSAR-X, launched June 2007, is a satellite operated by both the German Space Agency (DLR) and Astrium (Infoterra) and is available for commercial purposes. TanDEM-X, a twin to TerraSAR-X, was successfully launched in June 2010.

The baseline between the two satellites is maintained between 250–500 m. Both TerraSAR-X and TanDEM-X are X-band high-resolution sensors, with 11-day repeat cycles, and are recommended for long-term monitoring projects.

3.2.3 COMPARED EVALUATION OF DIFFERENT WAVELENGTH SAR DATA

In this section, the advantages and disadvantages of C-band, X-band and L-band SAR data for ground motions mapping and monitoring are briefly summarized and described.

The choice of the best radar data stacks for a given test site is usually and mainly driven by the spatial and temporal coverage of these data. However, since many SAR images are available today, including both historical and recent data, the use of the more suitable dataset and of the best appropriate satellite geometry (ascending or descending) is fundamental for a correct PSI analysis, depending on satellite acquisitions parameters, local topography and phenomena types of the area.

C-Band satellites (ERS, ENVISAT or Radarsat) that operate at a 5.6 cm wavelength, covering wide areas at a low cost and providing data since the 1990s. They are good for the regional analysis and back monitoring of very slow-moving landslides.

X-band sensors (TerraSAR-X, COSMO-SkyMed) operate at 3 cm wavelength with higher spatial resolution up to 1 meter (1-3 m in azimuth and 1.5-3.5 in range, depending on the acquisition mode and incidence angle) and reduced revisiting time (11 or 16 days); they allow the detection and monitoring of recent movements affecting small areas with detail. X-band data are best suitable to detect and monitor urban subsidence and deformation in built-up areas. Although temporal decorrelation must be expected to be more problematic at X-band compared to longer wavelengths (C- or L-band), the high-bandwidth data is more suitable to PSI analysis, since more coherent targets could be identified in high resolution data, even in case of long time intervals. Thus, with X - band data it is expected that non-uniform deformation of fabricated infrastructure such as bridges and single buildings of urban areas can be detected in detail by PSI analysis.

Finally, the L-Band satellite (ALOS PALSAR) which operates at a 24 cm wavelength permits to detect faster landslides even in vegetated areas (table 4).

Land use	Satellite SAR data		
	L-Band	C-Band	X-Band
Artificial-built-up	YES	YES	YES
Rural-agricultural	YES	YES	YES
Forests and semi-natural	YES High radar signal penetration	PARTIALLY Moderate radar signal penetration	NO Low radar signal penetration
Damp zones	NO	NO	NO

Table 4: Application of the satellite SAR sensors spectral bands related to the land use classes, as defined by Level 1 of CORINE Land Cover 2000.

Vegetation coverage causes temporal decorrelation and makes difficult the identification of reflective stable radar targets. Deeper penetration of vegetation can be achieved using higher radar wavelengths, such as those of the L-band.

The 23 cm for ALOS PALSAR data, which turn out to be more appropriate for rural and agricultural terrain, relying on the higher signal penetration and on the lower sensitivity to temporal decorrelation of L-band with respect to X- and C-band radar data (table 4).

These characteristics with respect to L-band (ALOS) and C-band satellites (ERS, ENVISAT, RADARSAT), have enhanced PSInSAR capability for land motions mapping and monitoring, allowing the identification of more recent and faster ground movements affecting small areas with improved precision.

Regarding the velocity of the considered phenomena, according to the landslide velocity classification of Cruden and Varnes (1996) and IUGS/WGL (1995), the acquisition parameters of the currently available SAR sensors do not enable the estimation of deformations faster than few tens of cm/year, which would compromise the results of the PSI processing.

Thus, due to the phase ambiguity of SAR data processing and satellite acquisition parameters in all L-, C- and X-bands, the PSI analysis of mass movement is limited to landslide phenomena ranging from “extremely slow” (velocity < 16 mm/year) to “very slow” (16 mm/year < velocity < 1.6 m/year) (Cruden & Varnes, 1996), as we can see in table 5.

Landslide class	Typical velocity	Satellite SAR data		
		L band	C band	X band
Extremely slow	< 16 mm/year	Yes	Yes	Yes
Very slow	0.016 – 1.6 m/year	Yes	Yes	Yes
Slow	1.6 m/year - 13 m/month	No	No	No
Medium	13 m/month – 1.8 m/h	No	No	No
Rapid	1.8 m/h - 3 m/min	No	No	No
Very rapid	3 m/min - 5 m/s	No	No	No
Extremely rapid	> 5 m/s	No	No	No

Table 5: Application of different microwave bands SAR data in relation to the landslide velocity class (Cruden and Varnes, 1996).

X-band radar data are particularly suited for local detection of earth surface processes at small scales, since high resolution and density of PS point targets in X-band permit to better

understand and accurately describe deformation phenomena, entering at the level of the ground motions site-specific investigation.

The use of TerraSAR-X/COSMO-SkyMed imagery can facilitate the investigation of landslide phenomena, thanks to the higher precision of the estimated motions and the shorter revisiting time compared with the on - going medium resolution C - band SAR sensors, such as ERS1/2 and ENVISAT.

These advantages improve the level of detail of the analysis and allow studying highly localized surface displacements and their dynamic evolution patterns.

Although temporal decorrelation is more problematic at X-band compared to longer wavelengths like C-band, the high-bandwidth data permit more coherent targets to be identified in high-resolution data even in case of long time intervals, and more and faster phenomena to be detected.

Given the revisiting time δt and the wavelength λ , the maximum movement detectable between 2 consecutive acquisitions is about 0.75 cm in 11 or in 16 days, corresponding to 25 cm / year or 17 cm / year, for TerraSAR-X or COSMO-SkyMed, respectively.

Significant differences can be observed within the number and the density of C- and X-band radar targets in an area of interest. The PS density obtained from TerraSAR-X/COSMO-SkyMed dataset is significantly higher than the one of ERS/ENVISAT datasets.

Moreover, PS data in X-band usually reveal higher deformation rates than those in C-band. This is due to the shorter X-band monitoring period and to the shorter temporal sampling (11/16 days in respect to 35 days), enabling the detection of more coherent pixels that show displacements; the same pixels would not be detected over a longer monitoring period because the coherence would be lost.

Despite the potential of X-band data for detecting greater deformation gradients benefitting from their high resolution, the shorter revisiting time of 11/16 days compensates only partially the higher temporal decorrelation in vegetated areas and the atmospheric delay features take a greater portion of shorter X-band wavelength.

Therefore, decorrelation noises from vegetation and atmospheric effects are of greater importance in X-band, because of the shorter signal λ and repeat cycle.

The use of L-band allows a feasible investigation on rural areas, due to its higher penetration coefficient on the ground and the consequent lower volumetric and temporal decorrelation in vegetated zones with respect to C-band radar data.

Furthermore, another advantage of L-band SAR data (wavelength $\lambda = 23.6$ cm for ALOS) with respect to C- and X-band ($\lambda = 5.6$ cm for ERS/ENVISAT and $\lambda = 3.1$ for TerraSAR-X

and COSMO-SkyMed) is the intrinsic capability to detect faster ground movements without ambiguities, such as those related to sudden subsidence events or landslides characterized by high ground deformation rate.

Assuming the orbital repeat cycle δt of 46 days of ALOS, we have a maximum detectable displacement rate along the LOS $V_{\max} = \lambda / 4\delta t = 46.8$ cm/year.

This can be compared to the value of 14.6 cm/year valid for the C-band of ERS/ENVISAT missions, where the orbital repeat cycle is 35 days, and to the value of 25 cm/year for X-band of COSMO-SkyMed, where the revisiting time is 16 days.

The InSAR analysis can be carried out by exploiting ALOS-PALSAR data especially for the vegetated rural areas, relying on the lower sensitivity to temporal decorrelation of L-band with respect to X- and C-band radar data.

The use of L-band data is of interest also because it could allow detecting faster ground movements e.g. related to landslides or sudden subsidence events that have occasionally occurred in the recent past.

Therefore in the research studies we can extend the investigation of the areas of interests through the use of L-band ALOS data in order to cover rural or vegetated area where C-band decorrelate and PS-like targets are very few, thanks to the reduced temporal and volumetric decorrelation in L-band.

From a general point of view, it can be concluded that X-band, L-band and C-band InSAR could play synergic roles in deformation mapping and monitoring, especially in view of the following considerations.

The use of X-band imagery significantly improves the level of detail of analysis and extends the applicability of space-borne SAR interferometry to faster ground movements. This is due to higher spatial resolutions (up to 1 m), the higher PS targets density and shortest repeat cycles (11/16 days in respect to 35 or 46 days) of X-band satellites with respect to the medium resolution SAR sensors.

C-band data allow detecting precisely small displacement rates, while L-band data (ALOS) are more sensitive to strong deformation episodes, for which C band is beyond the aliasing limit.

Availability of long historical datasets enables applications of PSI techniques in C-band, thus reaching single-pixel precision, while the reduced geometrical decorrelation in L-band allows easier application of conventional differential interferometry, allowing coverage of larger areas with few fabricated features, where PSI methods fail.

3.3 A REVIEW OF THE BENEFIT OF SARA DATA

Advanced InSAR techniques, i.e. PSI - based investigations, for natural hazards and, in particular landslide processes, are successfully being carried out in the last years, demonstrating the applicability of these techniques to different environments and the flexibility to different landslide typologies and dimensions. The choice of the best radar data stacks for a given test site is usually and mainly driven by the spatial and temporal coverage of these data.

By the way, since many SAR images are available today, including both historical and recent data, the use of the more suitable dataset and of the best appropriate satellite geometry (ascending or descending), depending on satellite acquisition parameters, local topography and phenomena types of the area, is fundamental for a correct PSI analysis. The following table 6 describes the capabilities of different EO analyses, i.e. Classical DInSAR, Advanced InSAR (Multi-interferometric analysis e.g. PSI), for detecting and monitoring landslides related to the velocity classes according to [Cruden & Varnes \(1996\)](#).

<u>Landslides Class</u>	<u>Typical velocity</u>	<u>DInSAR</u>	<u>PSInSAR</u>
Extremely slow	< 16 mm/year	NO	YES
Very slow	1.6 cm/year – 1.6 m/year	PARTIALLY	PARTIALLY
Slow	1.6 m/year - 13 m/month	NO	NO
Medium	13 m/month– 1.8 m/h	NO	NO
Rapid	1.8 m/h - 3 m/min	NO	NO
Very rapid	3 m/min - 5 m/s	NO	NO
Extremely rapid	> 5 m/s	NO	NO

Table 6: Application of satellite DInSAR and PSInSAR analyses related to the landslide velocity scale as proposed by [Cruden & Varnes \(1996\)](#). Mod. From [Metternich et al., 2005](#).

Satellite SAR frames cover areas up to 100 km per 100 km with resolutions of a few tens of meters. The revisiting time of the present satellites over the same area range between 46 and 4 days.

Focusing on the Advanced InSAR, the applicability of the technique to the landslide phenomena can be exploited in relation with their velocity (table 6) and their material type and movement type (table 7), as classified by [Cruden and Varnes, 1996](#).

Within multi-interferometric analysis, PSI measures are extremely vulnerable to phase aliasing effects, due to their ambiguous nature caused by the 2π phase-wrapping.

Thus, phase unwrapping problems limit to a quarter of the wavelength, $\lambda/4$ the maximum displacement between two successive acquisitions and two close PS of the same dataset

(Ferretti et al., 2000, 2005; Hanssen, 2005; Raucoules et al., 2009; Crosetto et al., 2010). Depending on the spatial pattern of ground displacements (with respect to PS density) and their velocity (with respect to the temporal SAR sampling), some deformational phenomena that are intrinsically fast-moving e.g. fall and topple landslide types (table 6), cannot be detected or they are often underestimated due to phase unwrapping errors.

Advanced InSAR technique has been successfully applied to analyse slides, both rotational and translational phenomena (Strozzi et al., 2005; Farina et al., 2006). Regarding flows, InSAR potential applicability varies depending on the involved material type: rock flows, characterized by slow movements and regularly distributed in the dislocated mass without a well-defined slip surface, can be effectively monitored throughout SAR multi-interferometric analysis.

Earth flows can be investigated only if they are very slow-moving and poor water-bearing (Squarzoni et al., 2003).

Debris flows cannot be monitored by means of InSAR techniques, because of they are too rapid to be observed by the on-going satellite systems.

Spreads can be partially analysed by the satellite sensors, since only the sub-vertical component of the motion can be measured, related to the sinking of the upper coherent layers and induced by the lateral or sub-horizontal spreading of the lower fine-grained layers (Meisina et al, 2007).

Lateral spreads due to liquefaction cannot be monitored by satellite interferometry because of their high rapidity of occurrence.

<u>Movement type</u>	<u>Material type</u>	<u>PSInSAR</u>
Fall	Rock / Debris / Earth	NO
Topple	Rock / Debris / Earth	NO
Slide	Rock / Debris / Earth	YES
Flow	Rock	YES
	Earth	PARTIALLY
	Debris	NO
Spread	Rock / Debris / Earth	PARTIALLY

Table 7: Applicability of Advanced InSAR to landslide phenomena in relation to the material type and movement type, as classified by Cruden and Varnes (1996).

The application of satellite InSAR for the three SAR sensors spectral bands, i.e. C-band for ERS/ENVISAT/Radarsat, and X-band for TerraSAR-X and COSMOSky-Med is discussed below and summarized in figure 21, in relation to different phenomena and environment characteristics that have to be taken into account.

Overall, as pointed out before, aliasing effects limit to a quarter of the wavelength the maximum displacement between two successive acquisitions and two close PS of the same dataset due to the ambiguous nature of the 2π -wrapping of interferometric phase (Hanssen, 2005; Crosetto et al., 2010).

L - Band	C - Band	X - Band
Velocity (Cruden and Varnes, 1996)		
Extremely slow		
Very slow		
Velocity of detectable movements (mm/year)		
15 – 20 mm/year	-17 – 20 mm/year	-45 mm/year
Land use		
Artificial / built up		
Rural / agricultural		
		Forests
Map scale		
Regional		Local
Temporal range		
<u>Historical / Past (1992 – 2010)</u>		
JERS (1992 – 1998)	ERS (1992 – 2001)	
ALOS (2006 – 2008)	ENVISAT (2002 - 2010)	
	RST (1995 – 2000)	
<u>Recent (2010 – 2012)</u>		
	RST – 2 (2010 – 2012)	TSX (2010 – 2012)
		CSX (2010 – 2012)

Figure 21: Application of multi - frequency SAR data (L-, C-, X-band) in relation to different phenomena and analysis features.

Velocities compromising the PSI processing depend on the employed SAR wavelengths and satellite revisiting times; they are about 15 cm/year for ERS/ENVISAT data (C band), 21 cm/year for Radarsat (C-band), 17 cm/year for COSMO-SkyMed (X-band), 25 cm/year for TerraSAR-X (X band), 46 cm/year for ALOS/JERS (L-band).

In presence of very high deformation rates of the phenomena, there is a loss of stable reflective radar benchmarks within any PSI technique capacities (Herrera et al., 2011). Thus, higher motion rates cannot be tracked and/or interpreted correctly. Improvements of the PSInSAR can be achieved by exploiting Ground-Based InSAR techniques (Leva et al., 2003; Tarchi et al., 2003; Antonello et al., 2004; Werner et al., 2008; Casagli et al., 2010), which can extend the velocity range of applicability to slightly faster phenomena.

The use of new X-band SAR sensors, such as TerraSAR-X and COSMO-SkyMed with high spatial resolution up to 1 meter and reduced revisiting time (11 or 16 days up to 4 days) enhanced PSInSAR capability for land motions mapping and monitoring, allowing the identification of more recent ground movements affecting small areas with improved precision.

Thus, X-band radar data turn out to be particularly suited for local detection of earth surface processes at small scales, since high resolution and density of PS point targets in X-band permit to better understand and accurately describe deformation phenomena, entering at the level of the site-specific ground motions investigation.

These advantages improve the level of detail of the analysis and allow studying highly localized surface displacements and their dynamic evolution patterns.

Although temporal decorrelation is more problematic at X-band compared to longer wavelengths like C-band, the high resolution data permit more coherent targets to be identified in even in case of long time intervals, and more and faster phenomena to be detected.

Despite the potential of X-band data for detecting greater deformation gradients benefitting from their high resolution, the shorter revisiting time compensates only partially the higher temporal decorrelation in vegetated areas; additionally, the atmospheric delay features take a greater portion of shorter X-band wavelength. Therefore, decorrelation noises from vegetation and atmospheric effects are of greater importance in X-band.

Significant differences can be observed within the number and the density of C- and X band radar targets. The PS density obtained from TerraSAR-X/COSMO-SkyMed datasets is significantly higher than the one of ERS/ENVISAT datasets, due to the cell size effect.

Regarding the temporal occurrence of the investigated phenomena, C-band PS data provide historical archives dating back to 1992. Conversely, X-band PSI analysis can update phenomena mapping up to 2011 and 2012, as operating TerraSAR-X and COSMO-SkyMed satellite systems are working since 2007 and are still ongoing. Therefore, X-band SAR data can analyse and investigate recent deformation, while C-band data can perform a back monitoring of past and present displacements and can reconstruct the deformation history of the investigated areas.

The displacement time series of X-band data are better than the C-band ones, due to the shorter revisiting time. Thanks to the higher temporal sampling of TerraSAR-X and COSMO-SkyMed, it is possible to analyse the evolution of the non-linear terms of the displacement such as acceleration or deceleration. This facilitates the detection of the non-linear trends that are somehow characteristic of landslide or subsidence kinematics. From

a geological point of view, non-linear behaviours can take place because of the nature itself of the deformation phenomenon; some example are reported below.

- Subsidence processes due to sediment compaction that generally show quadratic trends.
- Slow change in the predisposing or triggering factors.
- Intense or prolonged rainfall that can cause acceleration for landslide processes.
- Water level changes.
- Loading due to new constructions and urban excavations.
- The occurrence of a rapid deformation event, such as a reactivation, a sudden sinkhole or seismic events.

Concerning the map scale of the analysis, radar remote sensing techniques can be exploited to observe subsidence and landslide-induced ground deformations, ranging from regional to local scale, i.e. 1:250,000 - 1:25,000 and 1:25,000-1:5,000, respectively (Fell et al., 2008).

From a spatial point of view, X-band data are more suitable for analysis at local scale, covering restricted phenomena and affecting small areas. The comparison of X- and C-data demonstrates the capability of X-band data for localized infrastructure and local motions monitoring, thanks to their advantages of dense PS sampling and high temporal frequency. On the other hand, C-band data are more suitable for regional investigation due to their wide coverage and medium resolution; thus, at regional scale, the use of C-band SAR images is envisaged because these data cover wide area at low cost.

The use of L-band allows a feasible investigation on rural areas, due to its higher penetration coefficient on the ground and the consequent lower volumetric and temporal decorrelation in vegetated zones with respect to C- and X-band radar data.

Besides the lower sensitivity to temporal decorrelation, especially for the another advantage of the use of L-band data, e.g. ALOS-PALSAR data, is that it allows detecting faster ground movements e.g. related to landslides or sudden subsidence events that have occasionally occurred in the recent past.

Assuming the orbital repeat cycle δt of 46 days of ALOS, we have a maximum detectable displacement rate along the LOS $V_{\max} = \lambda / 4\delta t = 45.6$ cm/year.

This value can be compared to the value of 14.6 cm/year valid for the C-band of ERS/ENVISAT missions, where the orbital repeat cycle is 35 days, and to the value of 25.7 cm/year for X-band TerraSAR-X data, where the revisiting time is 11 days.

Overall, it can be concluded that X-band, L-band and C-band InSAR could play synergic roles in deformation mapping and monitoring, especially in view of the following considerations.

The use of X-band imagery significantly improves the level of detail of analysis and extends the applicability of space - borne SAR interferometry to faster ground movements. This is due to higher spatial resolutions (up to 1 m), higher PS targets density and shortest repeat cycles of X-band satellites with respect to the medium resolution SAR sensors (11/16 days up to 4 days in respect to 35 or 46 days);

The C-band data allow detecting lower displacement rates. Availability of long historical datasets enables applications of C-band PSI techniques over large areas with a single-pixel precision at medium resolution and low cost

Finally, L-band data are more sensitive to strong deformation episodes, for which C-band is beyond the aliasing limit. The reduced geometrical decorrelation in L-band allows easier application of conventional differential interferometry where PSI methods fail.

3.4 APPLICATIONS OF SAR DATA TO GROUND DEFORMATIONS

This work is focused on surface ground deformation, especially land subsidence and landslides. Subsidence and landslides can be induced both by natural or human causes and by triggers.

These phenomena are frequent and widespread in Europe and cause extensive economic damages to private properties and public infrastructures; the social effect of these highly hazardous phenomena is relevant and not fully determined in Europe, and elsewhere.

Moreover, the impact of such natural disasters in urban areas is very high especially in highly populated and built-up areas, where the socio-economic losses and damages are stronger because of the higher value of the element at risk exposure and vulnerability.

3.4.1 LANDSLIDES

Landslide is defined as a downward movement of a mass of rock, debris, or earth that occurs down a slope under the influence of gravity. The occurrence of landslides depends on complex interactions among a large number of partially interrelated factors, such as geologic setting, geomorphologic and hydrological features, land cover characteristics, human impacts.

Landslide predisposing or preparatory variables making the slopes susceptible to failure include soil and rock geo-mechanical properties, slope gradient and aspect, elevation, land cover, lithology and drainage patterns.

Landslide triggering or dynamic factors, that initiate the movements and might be either natural or human-induced or even any combination of both (Dai and Lee, 2002), include intense or prolonged rainfall, earthquakes, volcanic eruptions, rapid snow melting and permafrost thawing, slope undercutting by rivers or sea-waves.

Human activities that are capable of acting as triggers for landslide failures are slope excavation and overloading, land use changes (deforestation), rapid reservoir drawdown, blasting vibrations, and water leakage from utilities.

The range of landslide phenomena is extremely large, making mass movements one of the most diversified and complex natural hazards.

The wide span of the spectrum of landslide phenomena makes it difficult to define a single methodology, a single product, or a unique service, to detect, map and forecast landslides, to determine landslide hazard, and to evaluate the associated risk.

Many systems have been proposed for the classification of landslides; however, the most commonly adopted system is the one by Varnes (1978).

The landslide classification based on Varnes (1978) system has two terms: the first term describes the type of movement and the second term describes the material type (table 8).

TYPE OF MOVEMENT	TYPE OF MATERIALS		
	BEDROCK	ENGINEERING SOILS	
		Predominantly coarse	Predominantly fine
FALLS	Rock fall	Debris fall	Earth fall
TOPPLES	Rock topple	Debris topple	Earth topple
SLIDES	ROTATIONAL	Rock slide	Debris slide
	TRASLATIONAL		
LATERAL SPREADS	Rock spread	Debris spread	Earth spread
FLOWS	Rock flow (deep creep)	Debris flow	Earth flow
COMPLEX	Combination of two or more principal types of movements		

Table 8: Landslide classification after Varnes (1978).

The material types are rock, earth, and debris.

Soil and mud type names are also used. All these terms should describe the displaced material in the landslide before it moved.

Rock is a hard or firm mass that was intact and in its natural place before the initiation of movement. Earth describes material in which 80% or more of the particles are smaller than 2 mm, the upper limit of sand sized particles.

Debris contains a significant proportion of coarse material; 20% to 80% of the particles are larger than 2 mm, and the remainder are less than 2 mm.

Soil is an aggregate of solid particles, generally of minerals and rocks that either was transported or was formed by the weathering of rock in place; gases or liquids filling the pores of the soil form part of the soil.

Mud describes material in which 80% or more of the particles are smaller than 0.06 mm, the upper limit of silt-sized particles.

The types of movement describe how the landslide movement is distributed through the displaced mass. The five cinematically distinct types of movement are: fall, topple, slide, spread and flow. Many landslides exhibit a combination of two or more types of movements (complex landslides).

Landslide terminology adopted, based on Cruden and Varnes (1996), classifies ground motion phenomena based on velocity, from extremely rapid shallow-seated landslide features, to extremely slow moving deep-seated landslide features, and subsidence phenomena. Landslide phenomena are also classified by velocity classes, as proposed by Cruden & Varnes (1996) (Table 9).

LANDSLIDE CLASS DESCRIPTION	TYPICAL VELOCITY
Extremely slow	< 16 mm/year
Very slow	0.016 mm/year – 1.6 m/year
Slow	1.6 m/year - 13 m/month
Medium	13 m/month– 1.8 m/h
Rapid	1.8 m/h - 3 m/min
Very rapid	3 m/min - 5 m/s
Extremely rapid	> 5 m/s

Table 9: Landslide velocity classes, as proposed by Cruden & Varnes (1996).

The SAR data can be used to identify, characterize and monitor landslides. Landslides and slope instabilities, characterized by mass surface displacement, can be detected and monitored to millimetre accuracy using the PSI technique. Ground displacement data are complimentary to traditional survey methods (GPS, tiltmeters) and provide a long-term solution to slope instability monitoring.

Landslide Characterization

Slope instability maps provide an accurate overview of differential movement occurring across landslide features. Displacement maps are used to delineate boundaries, classify morphology and detect changes in rate of movement. By detecting naturally existing ground measurement points (no in-situ instrumentation required) satellite slope monitoring provides quantitative and qualitative deformation information for mapping instabilities.

Temporal Evolution

PSI can detect millimetre-scale displacements that often precede major slope failure, providing a wide-area monitoring tool for assessing areas at elevated landslide risk. An extensive archive of radar satellite imagery allows the temporal evolution of landslides to be reconstructed, providing valuable insight into understanding and forecasting future slope behaviour.

Landslide Inventory

Given the wide-area coverage of radar satellite images the PSI technique can be used to create landslide inventories. Slope instability measurements are also used in conjunction with traditional datasets to verify, and update, existing landslide inventories.

Stabilization Program Monitoring

Satellite imagery acquired before and after the implementation of stabilization programs, can be analysed using PSI technique to monitor their effectiveness.

3.4.2 SUBSIDENCES AND UPLIFT

Subsidence is defined as the downward sub-vertical terrain movement and it describes the lowering (sinking) of a portion of the topographic surface, caused by natural or manufactured triggers. The extent of land subsidence can significantly varies from a few tens of square meters (in case of a single sinkhole in carsick areas) to several tens of hundreds of square kilometres in areas affected by mining and exploitation activities.

The extent of the spectrum of land subsidence phenomena makes it difficult to define a single methodology, product, or service, to detect and map land subsidence, and to forecast its spatial and temporal behaviour.

Anyway, subsidence phenomena can be effortlessly monitored by means of InSAR techniques, either at regional and local scale, due to low velocity of the lowering movement. Moreover, subsidence events usually occur in urbanized areas, where many stable radar benchmarks can be retrieved.

There are many possible causes for the lowering of the Earth's surface, as sediment compaction, a decrease in groundwater pressure, the intensive subsurface water withdrawal and over pumping. It is possible for subsidence to occur progressively over a long period, or to occur suddenly over a very short period and then stop.

The SAR data technique can be used to measures ground subsidence and uplift due to natural causes and anthropogenic activities. Ground deformation resulting from a variety of causes, known or unknown, can be measured with millimetre accuracy using SAR data. Imagery acquired from radar satellites can be used to remotely monitor surface displacement over wide areas.

Ground Deformation Monitoring

Remote satellite monitoring of the Earth's surface highlights the extent of ground deformation occurring over a time period of analysis. By acquiring images over an area of interest, wide areas can be analysed to produce quantitative displacement data.

Radar images available back to 1992 are used to create historic subsidence maps, which can provide insight into culpable factors of displacement onset and allow predictions to be made on future behaviour.

Displacement Modelling

SAR data can be used to refine surface and subsurface models, providing an improved overview of ground behaviour dynamics. Accurate models allow for better management of ground activities (extraction, working) and assist in minimizing the risk of damage to surface infrastructure.

3.4.3 SINKHOLE

SAR data are used to identify and monitor ground subsidence associated with sinkholes. Surface deformation maps can identify subsidence related to sinkholes, both prior to and following their collapse. As PSI is a remote sensing technique capable of identifying a high density of ground measurement points, many of the challenges in identifying and monitoring sinkholes using traditional ground based techniques can be circumvented.

Precursory Movement

SAR data can detect surface displacements to millimetre accuracy occurring prior to sudden or rapid sinkhole collapse, otherwise challenging to detect using traditional techniques. Urban and rural areas can be monitored to detect small movements and identify areas at risk of developing sinkholes. Ground deformation data can be used to identify hazards that could potentially threaten lives and damage infrastructure.

Sinkhole Characterization

Given the high density of ground measurement points detected using SAR data, sinkhole shape, extent and subsidence rate can be accurately determined. Post-collapse displacements on the ground surrounding a sinkhole can also be monitored to assess the potential of continued deformation along sinkhole borders.

3.4.4 REGIONAL MAPPING

SAR data are used to map and monitoring ground movement at broad spatial scale. The mapping of hydrogeological instabilities over wide areas provides an overview of potential risk that can threaten populations and infrastructure. The displacement maps assist in the monitoring natural hazards.

Wide Area Mapping

Given the large spatial coverage available from radar satellite imagery, surface displacement can be mapped over large areas, ranging from single counties to entire countries. Geologists, engineers, and government bodies to amalgamate numerous existing inventories into a complete dataset and make them available for entire communities, from the individual citizen to governing bodies, use instability maps.

Hazard Identification

SAR data are capable of tracking large area deformation, enabling the identification of potential risks to existing infrastructure and public safety. Countrywide inventories of ground subsidence and natural hazards are used for emergency planning and risk assessment, to assess the environmental impacts of such instabilities on the community and its economic activities.

3.4.5 EMERGENCY PREPAREDNESS

SAR data are used to identify areas of ground instability and aid the development of emergency planning. They are used by civil and environmental protection agencies to identify areas where civilians may be at risk, aiding the establishment of natural disaster response plans. Ground instability maps are used to reduce risk to acceptable thresholds and aid the establishment of guidelines for the prevention of future catastrophes.

Hazard Identification

Wide area ground instability maps assist in identifying preventative measures against natural and man-made hazards, mitigating risk to human life. By identifying ground displacement rates, SAR data are used to categorize land into areas of low to elevated risk. Where risk is deemed unacceptable, remedial action can be taken to avoid human losses and costly damage.

Risk Exposure Models

SAR data monitor the temporal evolution of potential natural hazards. Instability data are used as input to geo-hazard models for the calculation of human risk exposure and the preparation of emergency procedures.

Emergency Route Planning

By providing decision makers with an overview of surface stability, SAR data can be useful for establishing emergency evacuation routes and relocation sites.

3.5 APPLICATIONS OF SAR DATA TO ENGINEERING INFRASTRUCTURES

3.5.1 SINGLE BUILDINGS

SAR data can accurately measure displacement occurring at single buildings. Individual buildings in both urban and rural settings can be subject to surface displacement, which may cause to structural damage. These displacements can be measured and mapped to millimetre accuracy using SAR data.

Building Stability

SAR data can accurately measure displacements occurring at single buildings, providing maps that highlight building or ground instabilities.

Regular monitoring can identify differential deformation affecting infrastructure, from single buildings to entire cities, and provides an early indication of changes in surface height that could threaten structural integrity.

Historical Displacement

SAR data can reconstruct the historic displacement of a building using satellite imagery archives. Maps of historic ground movement can provide insight into future behaviour and can identify areas of stable ground for new infrastructure development.

High Resolution

The availability of high-resolution satellite imagery permits a potentially higher density of ground measurement points to be detected, thereby increasing sensitivity to building movement.

3.5.2 ROADS AND RAILWAYS

The SAR data can be used to measures ground displacement on roads, railways and surrounding embankments.

Radar imagery can detect ground displacements that could threaten the integrity and safety of road and rail infrastructure (at both grade and elevated). By identifying natural and manufactured ground measurement points, PSI maps millimetre displacements along the entire length of road and rail networks, aiding risk assessments and highlighting areas that may require maintenance.

Road, Track and Embankment Stability

PSI displacement maps highlight areas of ground movement over roads and railways, providing engineers with an overview of instabilities that could indicate infrastructure-requiring repair. Ground deformation monitoring produces quantitative and qualitative deformation maps of surrounding embankment instabilities that often precede slope failure,

providing a network-wide monitoring tool for assessing areas at elevated risk of landslides and subsidence.

Extensive Network Monitoring

SAR data are capable of measuring differential displacements over long stretches of road and track, highlighting areas of subsidence (or uplift) that may require further investigation.

Route Planning

A historic archive of satellite imagery can be used to determine stable areas for potential new routes, assisting also in the planning of network extensions and duplications. Deformation monitoring provides both historic displacement data for route planning and post-construction route stability checks.

Remote Monitoring

As radar imagery is acquired remotely, SAR data can provide surface displacement measurements in areas not suitable for ground-based fieldwork. By identifying targets already present on the ground, the interferometric data detect a significantly higher density of ground points than traditional ground-based surveys, such as GPS, levelling and tiltmeters.

3.5.3 TUNNELING ACTIVITIES

SAR data can measure ground displacement associated with tunnelling activities. Underground tunnelling can produce subsidence at ground level. The PSI technique can detect surface displacements at a millimetre scale to monitor the stability of the ground above tunnel networks and the surrounding areas.

Monitoring for Subsidence

Ground deformation due to tunnel construction can be mapped remotely using SAR data. Surface deformation over tunnelled areas is used to identify ground movement that could potentially damage surface infrastructure. SAR data use historic radar imagery to measure baseline rates of movement occurring over both existing and planned tunnel locations, as well as the surrounding areas. By mapping the temporal evolution of ground displacement occurring before and during construction, engineers can better understand the relationship between groundwork and the onset of any related ground movement.

Subsidence maps also provide data for legal disputes concerning damage claims.

Post-Construction Movement

Regular monitoring of post-construction ground movement allows engineers to identify differential displacement and subsidence (or uplift) that could indicate tunnel weaknesses.

3.5.4 BRIDGES

SAR data are used to measure displacement occurring across bridges and abutments. Deformation occurring on bridge structures and supporting abutments can be measured remotely using SAR data. Displacement can be mapped to millimetre accuracy, identifying movement that could indicate areas of bridge instability.

Stability Monitoring

SAR data can detect displacement along the entire length of a bridge, identifying differential movement that may indicate areas of structural weakness. Surface deformation data allows engineers to determine if remedial action should be taken to prevent further structural damage or potential failure.

Remote Monitoring

As radar imagery is acquired remotely, SAR data can provide displacement measurements without the need to install surface-based instruments. By identifying targets already present on structures, SAR data detect a significantly higher density of ground points than traditional methods, such as extensometers and levelling techniques.

3.5.5 AIRPORTS

SAR data are used to quantify and map ground movement over airports. By identifying a high density of ground measurement points, SAR data can be used to monitor site-wide surface deformation at airports. The high accuracy of the displacement maps can accurately identify ground deformation that could threaten infrastructure integrity.

Site Stability Mapping

The ability to monitor large areas with a single analysis allows differential displacement measurements to be calculated over the entire extent of an airport. Regular monitoring of ground movement provides an early indication in changes of subsidence or uplift rate, over all areas of an airport, including runways, buildings and surrounding areas.

Site Planning

Using a historic archive of satellite imagery, the PSI technique can determine stable ground areas for airport expansion. Maps of ground stability and movement can also assist in the development of future sites.

Remote Monitoring

By identifying natural and fabricated targets already present on the ground, the technique remotely monitors surface displacement without the need for ground-based instrumentation.

4. C-BAND DATA FOR LOCAL-SCALE MONITORING

4.1 GENERAL CONSIDERATIONS

This chapter gives an application of C-Band SAR data for monitoring ground deformation and engineering infrastructures at a local-scale. In particular, the subject of this chapter, is the SqueeSAR™ analysis carried out in the area where it is planned the construction of the Verduno gallery (CN), falling in the 2/6 lot of Asti-Cuneo motorway link.

The tunnel, length more than 3000 m (figure 22), will develop within particularly poor soils from a geotechnical point of view (marly-gypsum).

Therefore, the monitoring activities during the construction of the excavation and after the conclusion of the work will be of paramount importance for the proper management of the work and for early detection of potentially critical situations.

In this context, an essential element concerning the use of interferometric techniques for monitoring ground deformation based on satellite data is the acquisition of radar data dating back to 1992, when the ERS-1 satellite acquired regularly over vast areas of the planet.

In particular, the SqueeSAR™ analysis conducted for this purpose included the development of a dataset acquired by the Canadian satellite RADARSAT-1 in ascending geometry, between March 2003 and September 2012.

After a short introduction of the area, some notions on the technique used are reported; the data arising from the elaboration are presented and compared with those available on the National Cartographic Portal as part of the PST (Extraordinary Plan of Remote Sensing), for the periods 1992-2000 and 2003-2010.

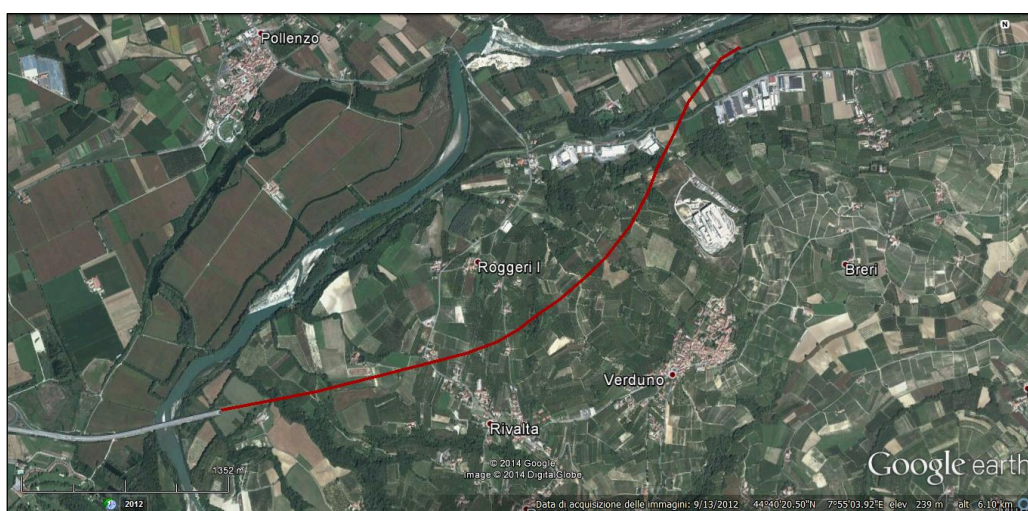


Figure 22: Track of Verduno gallery, forthcoming excavation, projected onto an optical image (Google Earth).

4.2 SqueeSAR™ PROCESSING METHOD

A further advancement of PS-InSAR technique has recently been developed by Tele-detection Europe (TRE) S.r.l., which has developed a new proprietary algorithm, SqueeSAR™, suitable for remote sensing of surface deformation even in suburban areas or poorly built, in which the density of the measures PS cannot be satisfactory (Ferretti et al., 2011).

The innovation of the new processing algorithm consists in the possibility of identifying in the monitored area two "families" of radar targets monitored by satellite:

- Point-like targets (Permanent Scatterers-PS): the interaction with the electromagnetic signal is characteristic of a single pixel of the SAR image or to more than a few other pixels connected to it;
- Distributed targets (Distributed Scatterers-DS): targets that show an interaction with the electromagnetic signal that is almost identical to a whole group of pixel of the SAR image.

The ability to detect radar target distribution (DS) is set up as a major breakthrough technology of multi-interferogram PS-InSAR, because it takes into account the fact that a SAR image contains data from targets of natural and artificial kinds, and that consequently, the electromagnetic characteristics of the radar can vary significantly, even between adjacent pixels. Figure 23 illustrates the basic principles of SqueeSAR™.

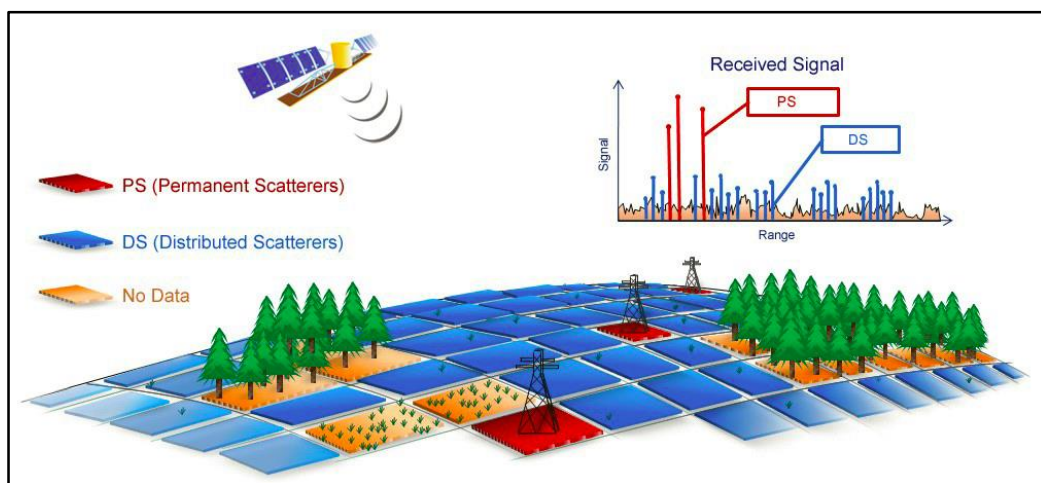


Figure 23: Scheme of SqueeSAR™ analysis. The pixels of the SAR image that are radar target points, i.e. the PS, are shown in red. The pixels corresponding to distributed radar targets, i.e. the DS, are shown in blue. The pixels that are discarded due to the low coherence of the signal, are shown in orange. Each DS, in particular, summarizes the information contained in the group of pixels that fall within "effective area", which is the area that is used during the filtering operation (TRE Srl).

Unlike a target point (PS), where the energy backscattered to the sensor is high and concentrated in reduced area, the intensity of the echo radar for a pixel belonging to a DS is usually much lower. This causes a more noisy estimate of physical parameters related to the target in question obtained from the analysis of the radar signal (for example the velocity of movement) if the estimation is at the level of single pixel.

However, the fact that the interaction with the radar signal is the same for all the pixels belonging to the same DS, allows the joint use in order to obtain a reduction of the noise inevitably present in the data (filtering operation).

The data thus filtered allow a significant improvement of the quality of the estimate of the displacement of the DS, which is thus comparable to that obtainable for a PS.

The information associated with a DS are attributed to the electromagnetic center of gravity of the area used during the filtering operation, the extension of which is generally less than one hectare. This area is called the "effective area".

From a technical point of view, similarly to what happens for a PS, an average annual velocity value and the time series of displacement along the LOS are provided for each DS. The position of the DS is calculated based on the same set of equations of the PS, but the DS does not correspond to a point, as in the case of PS, but "represents" its effective area. Its position is then defined as representative of the effective area.

4.2.1 INPUT DATA

The data Processed by TRE are used for the analysis of the deformation in the interested area relating to the periods 1992-2000 and 2003-2010 and for a comparison with those identified by the SqueeSAR technique; these data are available through the National Cartographic Portal.

Radarsat Data

For what concerns the SqueeSAR™ Radarsat data, the analysis has involved the development of a dataset consisting of 126 images acquired by the Canadian satellite Radarsat-1 in ascending geometry between March 2003 and September 2012 (Table 10). The processing of RADARSAT-1 data led to the identification of 2157 measuring points of interest in the area.

Satellite	Geometry	Number of images	Monitoring period
RADARSAT-1	Ascending	126	17/03/2003 – 25/09/2012

Table 10. Specifications of the dataset analyzed.

The area is characterized by the presence of some extensive areas used for agricultural activity and has a few fabricated structures and infrastructures; this comport a difficult detection of the stable radar targets because the radar signal is characterized by continuous changes of reflectivity.

The distribution of the measurement points identified is therefore not homogeneous: the maximum density is observed in correspondence of the populated areas and is instead rather poor in vegetated and cultivated areas.

It should be noted that the reference point is chosen during the processing, based on statistical parameters developed with the experience gained over the years, so that it appears to have high coherence, an excellent "quality radiometric" and to optimize the accuracy of the measurements.

Given the characteristics of the area of interest (extended vegetated and cultivated areas without agglomerations), a suitable radar target, from the radiometric point of view, to be selected as the reference point, was not possible to identify within the area.

The vegetated and cultivated areas are subject to continuous changes of reflectivity, which effectively limit the detection of stable radar targets, both of point (PS) and distributed point type (DS). In order to optimize the results, the area of investigation was expanded and the benchmark located at the industrial zone of Cherasco result more suitable to be.

Finally, 3181 measurement points were then identified, in a total area of 21 km².

Figure 24 shows the distribution of the measurement points identified and visualized with an average annual velocity value, in the monitored period.

All the displacement measurements are measured along the line of sight of the sensor (Line Of Sight, LOS), and are differential, or spatially related to the reference point.

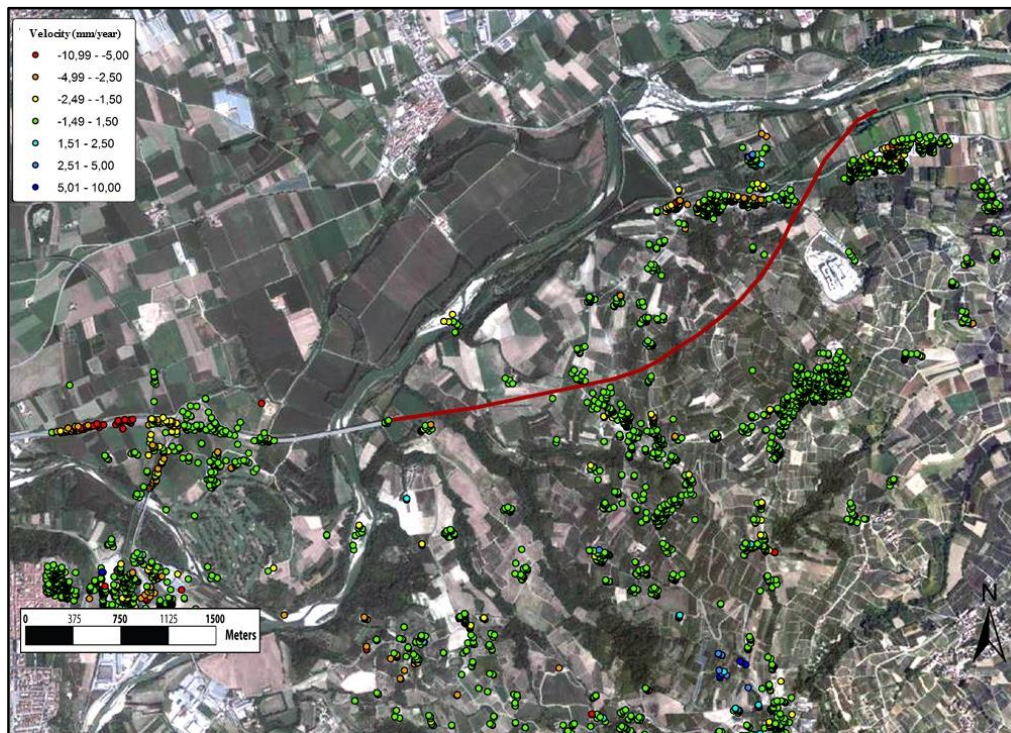


Figure 24: Distribution of measurement points identified and displayed with an annual average velocity value.

ERS and ENVISAT data

Under the project, TRE has drawn a considerable amount of satellite data ERS and ENVISAT European Space Agency (ESA) acquired over time spans from 1992 to 2002 and from 2003 to 2010 throughout the country, providing information to support the formulation of an overview of the phenomena of collapse potential or ongoing throughout the country.

In the specific case, the survey area was covered by elaborations on the following datasets:

- ERS ascending for the period 1992-2000 (Figure 25)
- ERS descending for the period 1992-2000 (Figure 26)
- ENVISAT ascending for the period 2004-2010 (Figure 27)
- ENVISAT descending for the period 2003-2010 (Figure 28)

In the same figures, the areas chosen for a detailed analysis are shown.

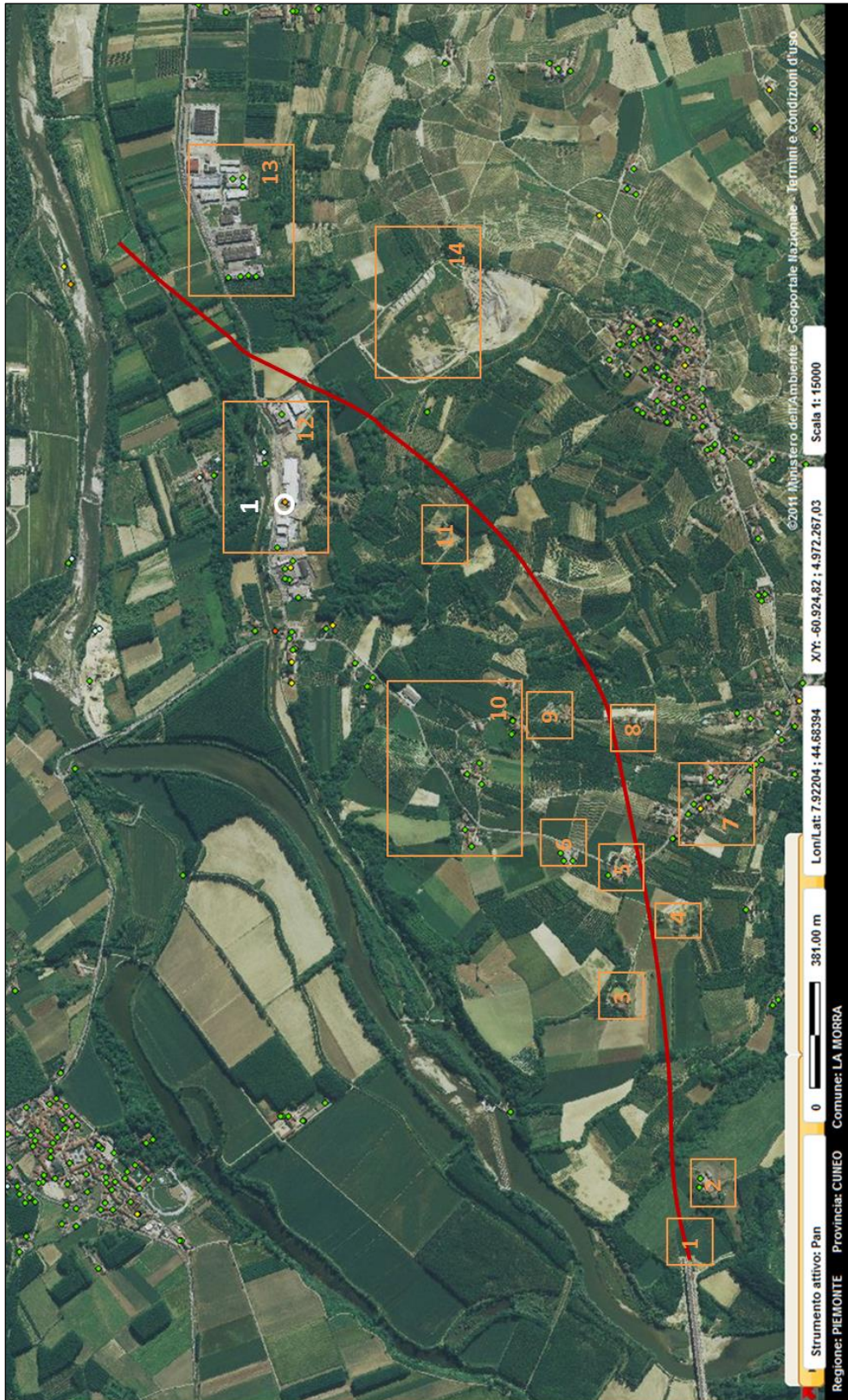


Figure 25: Dataset ERS ascending for the period 1992-2000. The orange boxes indicate the areas selected for a detailed analysis in the neighborhood of the track; the white circles show the significant targets, discussed in the text.

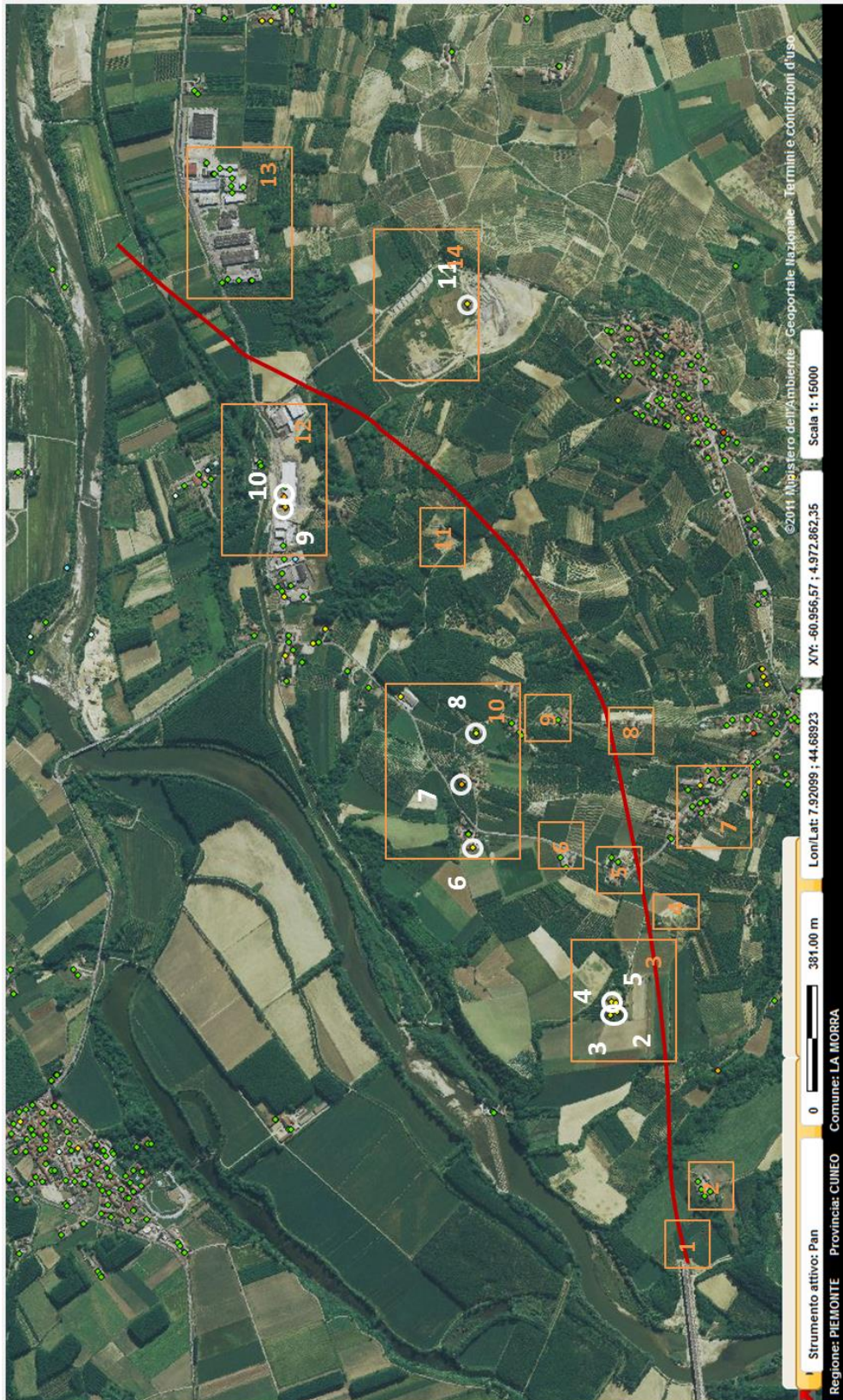


Figure 26: Dataset ERS descending for the period 1992-2000. The orange boxes indicate the areas selected for a detailed analysis in the neighborhood of the track; the white circles show the significant targets, discussed in the text.

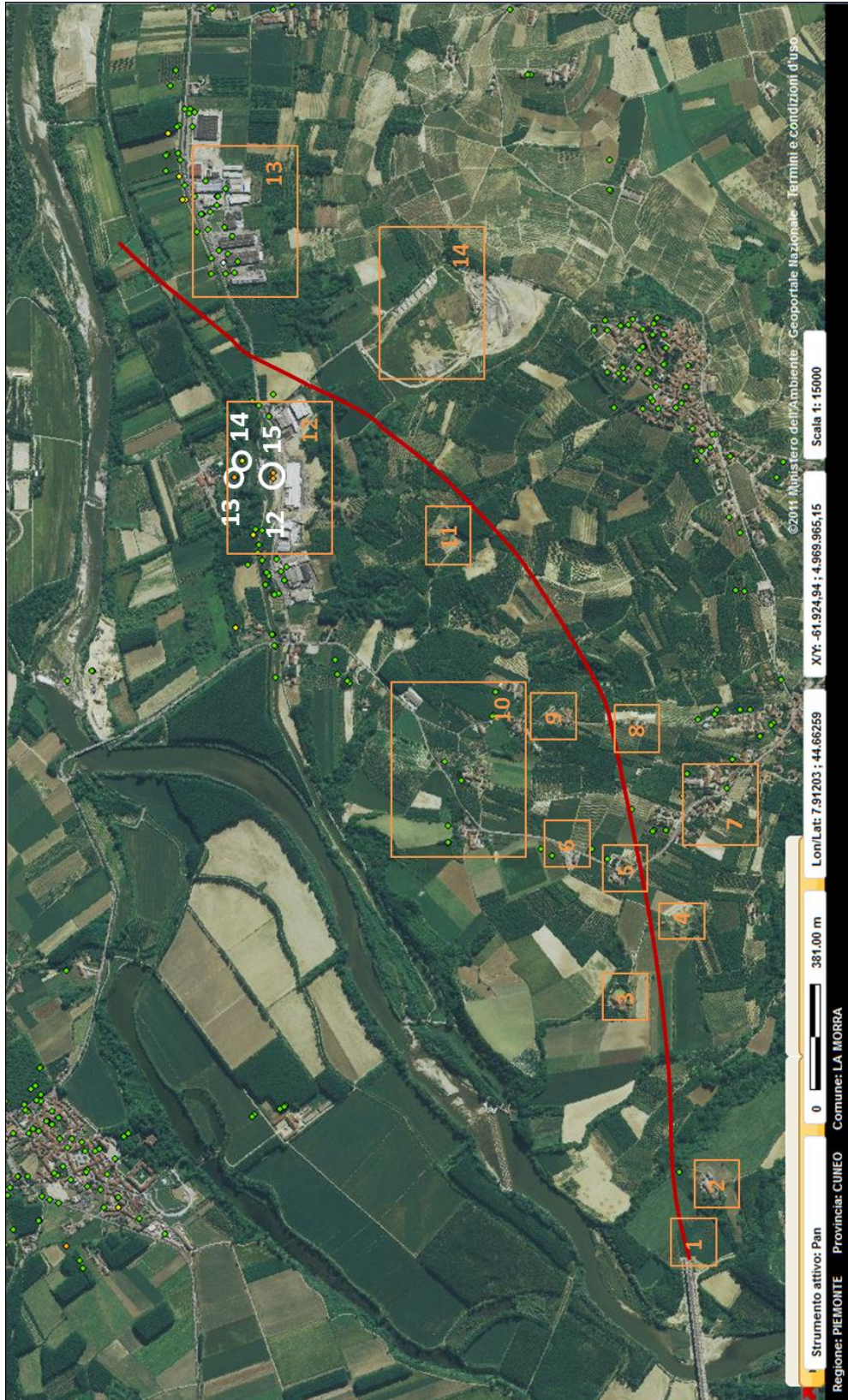


Figure 27: Dataset ENVISAT ascending for the period 2004-2010. The orange boxes indicate the areas selected for a detailed analysis in the neighborhood of the track; the white circles show the significant targets, discussed in the text.

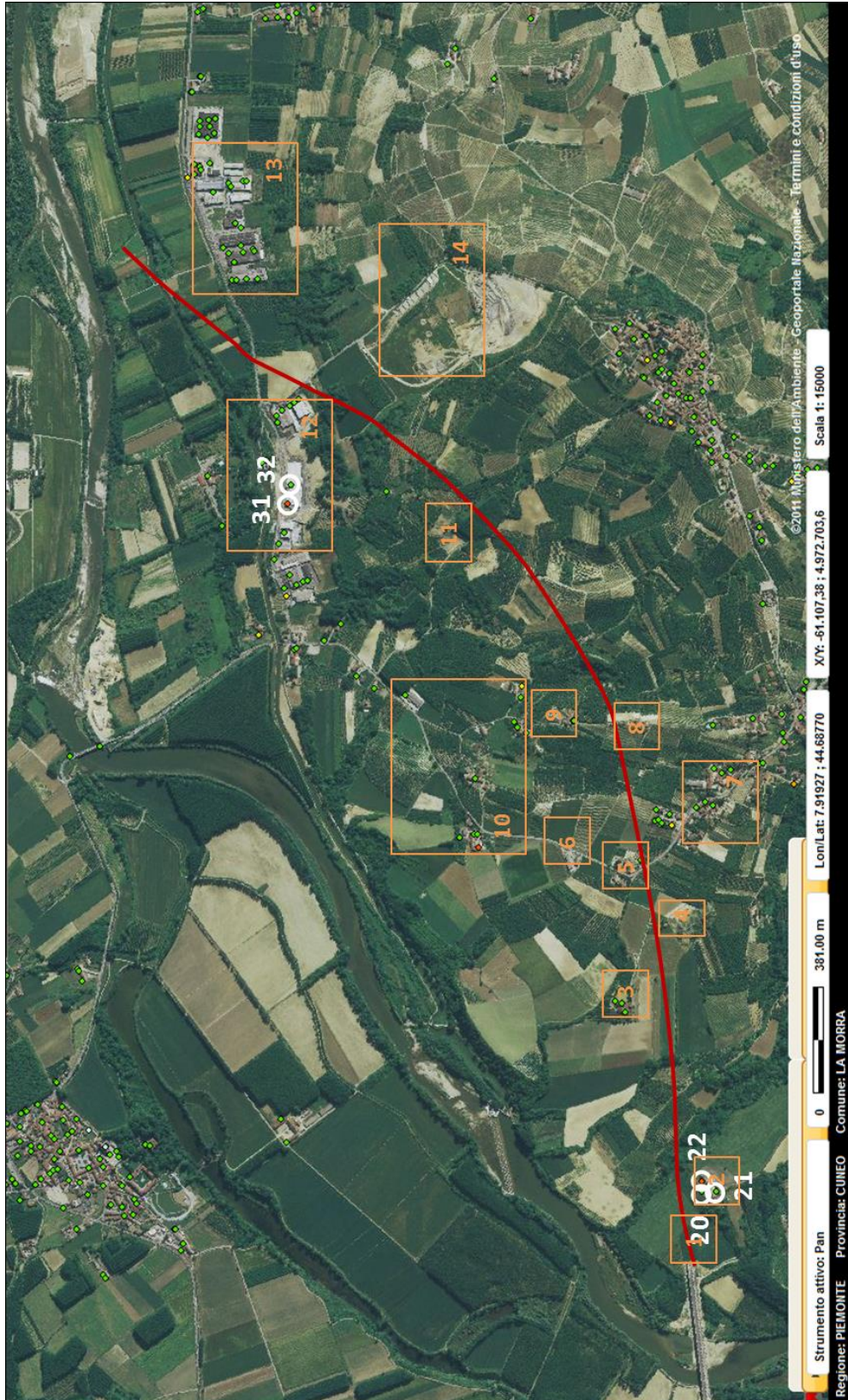


Figure 28: Dataset ENVISAT descending for the period 2003-2010. The orange boxes indicate the areas selected for a detailed analysis in the neighborhood of the track; the white circles show the significant targets, discussed in the text.

4.3 TEST SITE

4.3.1 GEOLOGICAL SETTING

The study area is located on the slopes below the village of Verduno (CN) for a total area of about 17 km². It entirely lies in the hilly area of Langhe, which is spread over an area of approximately 1000 km² in the southeast of Piedmont and is roughly bordered by the River Tanaro on the north and west, by the mountains of Liguria to the south and by the Orba River to the east (Figure 29)

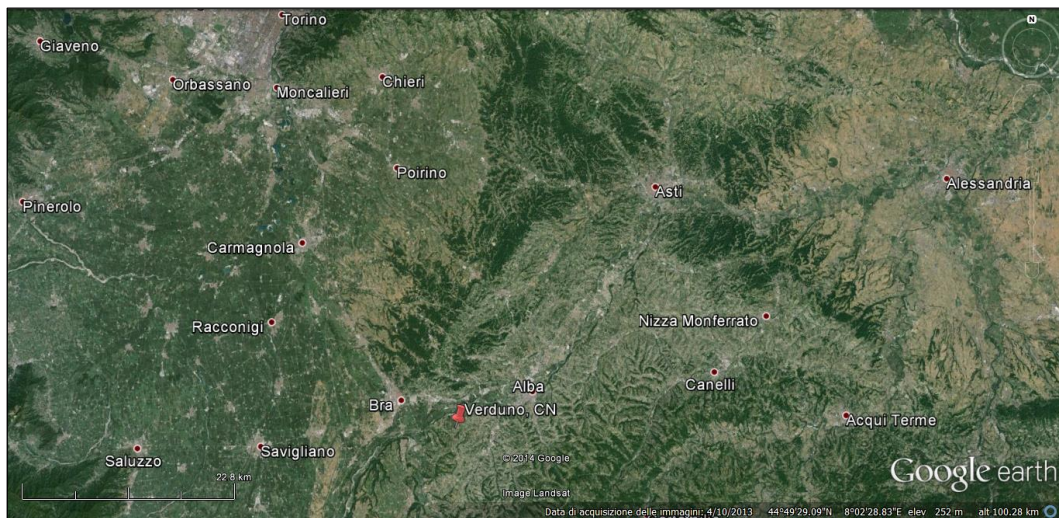


Figure 29. Location of the Verduno site.

From a geological point of view, in the territory of Langhe appears a powerful succession of sedimentary rocks belonging to the Tertiary Piedmont Basin-BTP, which includes the following geographic areas: Langhe, Monferrato, high and low hill area of Turin and Borbera-Grue area (figure 30). This sedimentary sequence, temporally extended from upper Eocene to Miocene, covers with a stratigraphic unconformity a structure (Pre Cenozoic basement) formed caused to the collision between the European plate and the micro plate Adria. This building mainly formed by tectonic units of Brianzonese and Piemontese-Ligure paleo geographic zones, since the upper Eocene tends to overlap the Adria micro plate in correspondence with a sliding surface currently dipping to south.

The relative movement along this surface has conditioned the formation of the epistuctural sedimentary basins (Bally and Snelson, 1980; Bally et al., 1985) on the back of the allochthonous units and of a foredeep on a microplate Adria (figure 31).

Within these basins and in front of fore deep the deposition of terrigenous sediments resulting from the disassembling of the chain behind it occurred.

In the object area, the sediments belonging to the Messinian succession of the BTP, emerge. This consisting of epipelagic pre-evaporitic marl of Tortonian-Lower Messinian (Fossils Sant'Agata marls) and Messinian gypsum sediments of low sea deposited during the salinity crisis of the Mediterranean (Chalky-Solfifera Formation). (Hsu et al., 1973; Cita et al., 1978; Clauzon et al., 1996; Krijgsman et al., 1999; Roveri et al., 2008).

This succession outcrops mainly along two perimeters that surround the BTP both in the north and in south side; the northern range extends for 35 km from Moncucco to Ottiglio (Monferrato Domain), the southern one, which falls within the study area, extends for about 25 km, crossing from west to east across the central Piedmont (Langhe Domain).

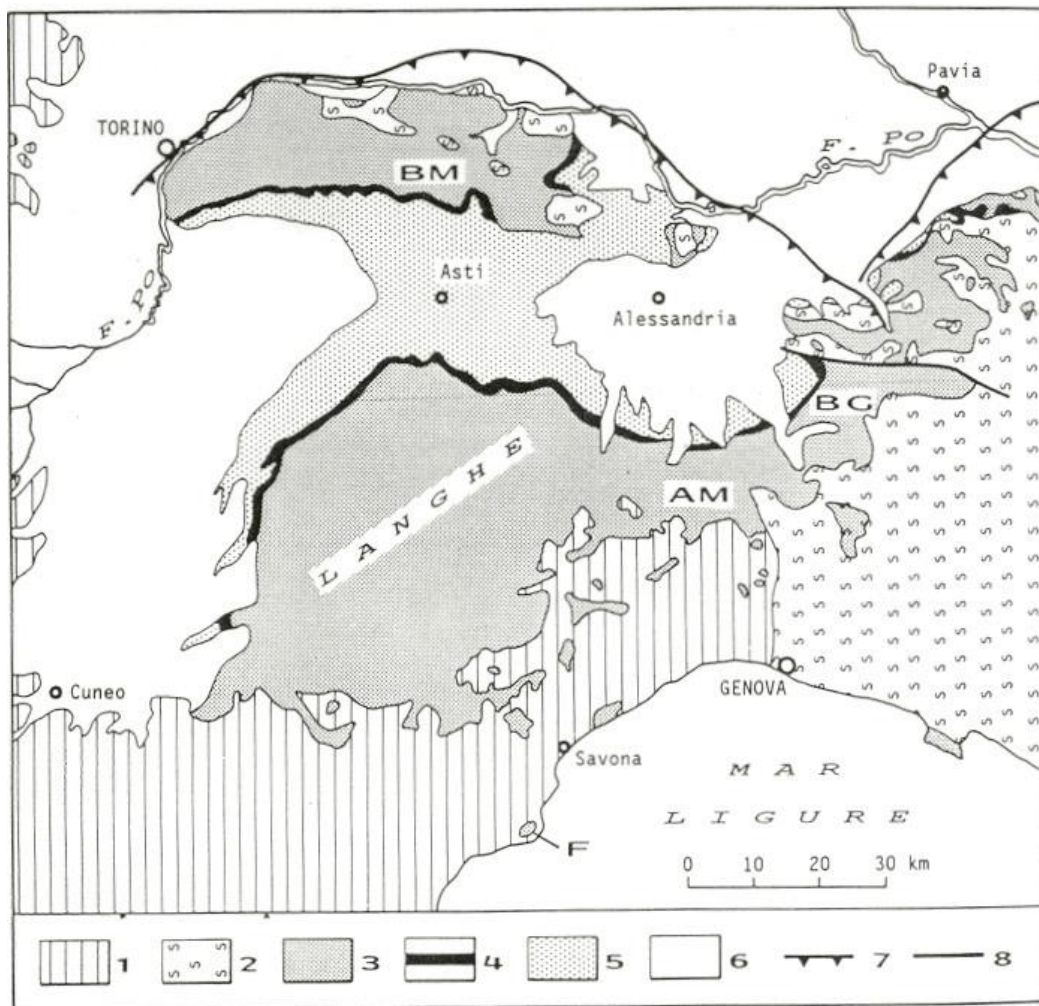


Figure 30: Geological scheme of BTP (Gelati and Gnaccolini, 1988).

Units of substrate: 1 = Units of Piedmont, Brianzoni unit; 2 = Ligurian units. Cenozoic cover; 3 = Upper Eocene Tortonian; 4 = Messinian; 5 = Pliocene. Quaternary deposits; 6 = Front of allocton; 7 = Villalvernia-Varzi Line; 8 = BM: Low Monferrato e Torino hill; AM: High Monferrato; BG = Borbera-Grue Area; F = Ligurian end.

The Chalky-Solfifera formation can reach a total thickness of about 400 m, but the portion containing the included chalky never exceeds 60-70 m in the northern side and 20-30 m in the southern side (with increasing numbers progressing from West to East).

In the object area, the horizon containing the included chalk is covered by a system of tectonic fractures with a NS orientation.

Along these lines, which also serve as preferential lines for surface runoff of the water, some karstic depressions, as result of the dissolution of sulphates by groundwater, are present; these have dimension from metric to decametric. Each depression has at its center one or more sinkholes with metric diameter and several meters deep.

Concordantly to the poor nature of the surface terrain, numerous landslides affect the area in question.

These instabilities appear to affect both the areas where the Fossils Marls of Sant'Agata outcrops, both the areas where the Chalky-Solfifera formation is the prevalent lithology.

However, it is to be noted, as the available data is somewhat discordant with one another about the perimeter of the areas subject to landslide type movements. The cartography of the IFFI inventory (figures 31 and 32), that of the PAI (figures 33) show a very limited overlap, mapping areas also very different.

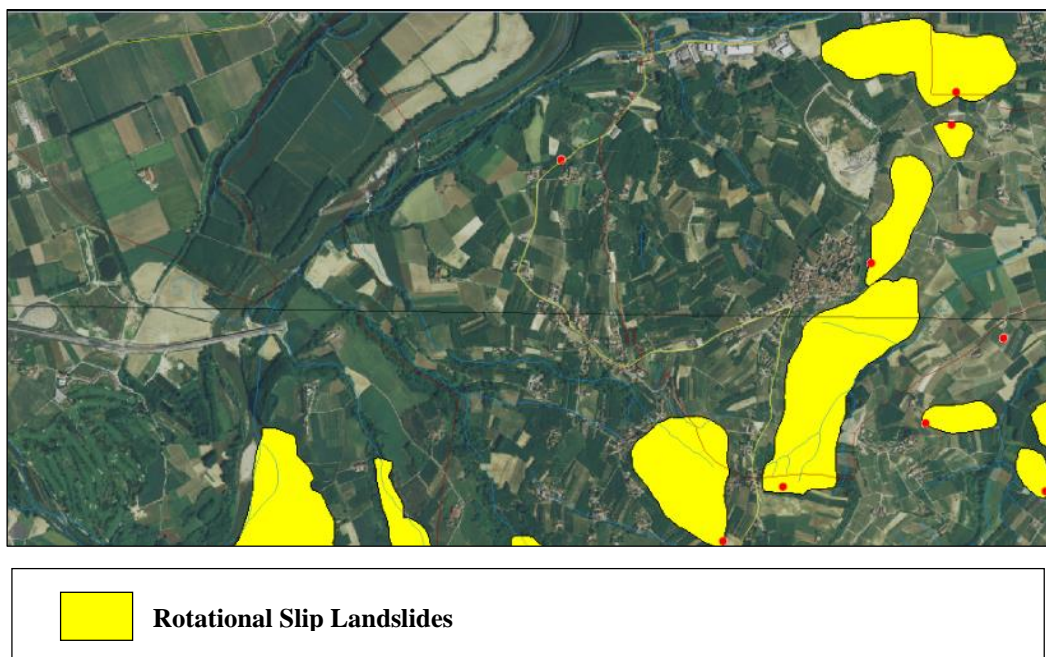


Figure 31: IFFI Landslide inventory maps (source WEBGIS Cart @ net-IFFI) on satellite photos with high detail (source Visual Earth).

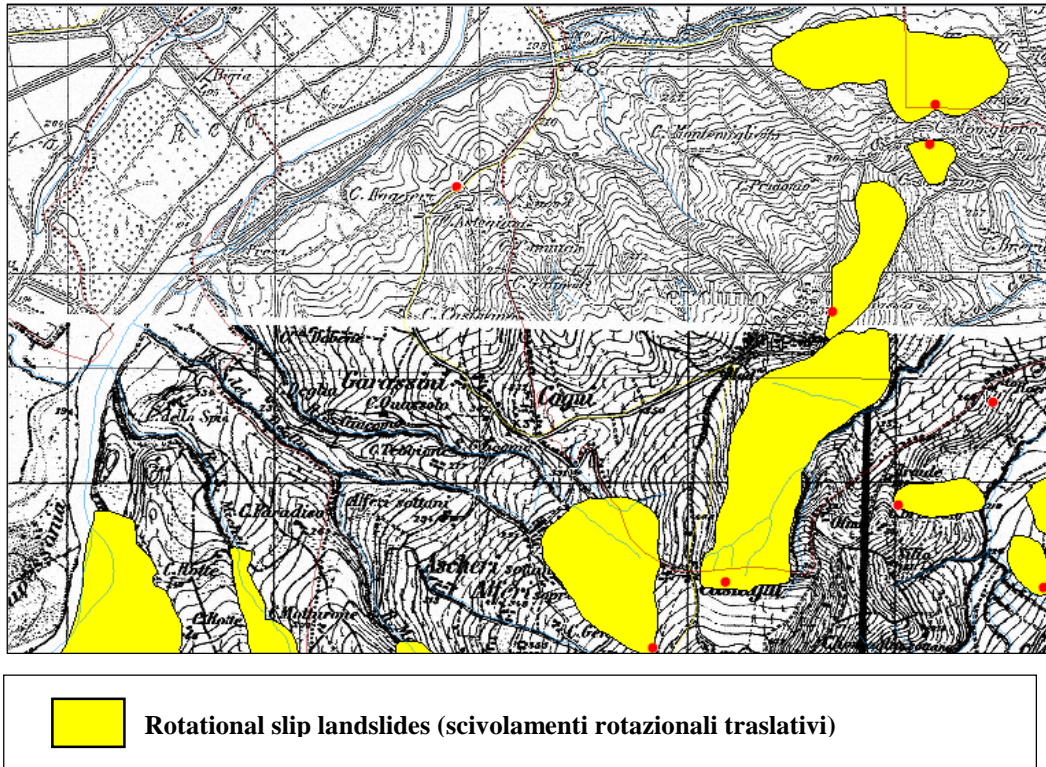


Figure 32: IFFI Landslide inventory maps (source WEBGIS Cart @ net-IFFI) on a IGM map on a 1: 25.000 scale.

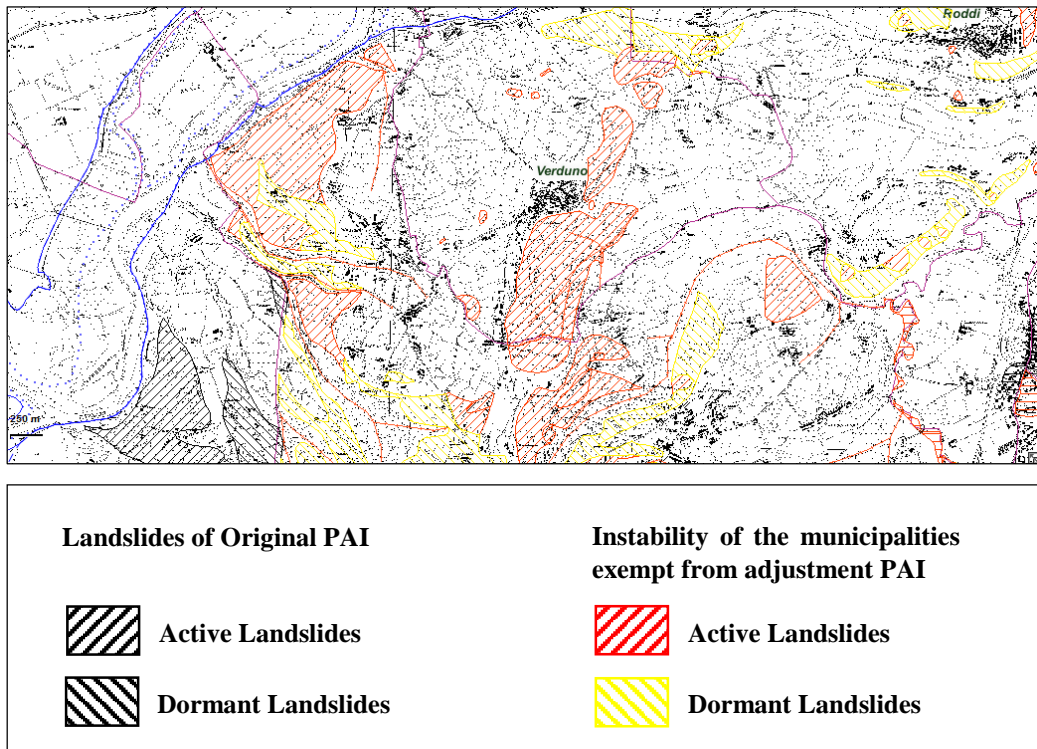


Figure 33: Mapping of landslides classified in the PAI of the Piedmont region (source <http://www.regione.piemonte.it/disuw>) on IGM map on a scale of 1: 25.000.

4.3.2 RESULTS AND DISCUSSION

The area interested by the construction of the road is divided in homogeneous areas, which are shown in figure 34, for a clearer presentation of the data.

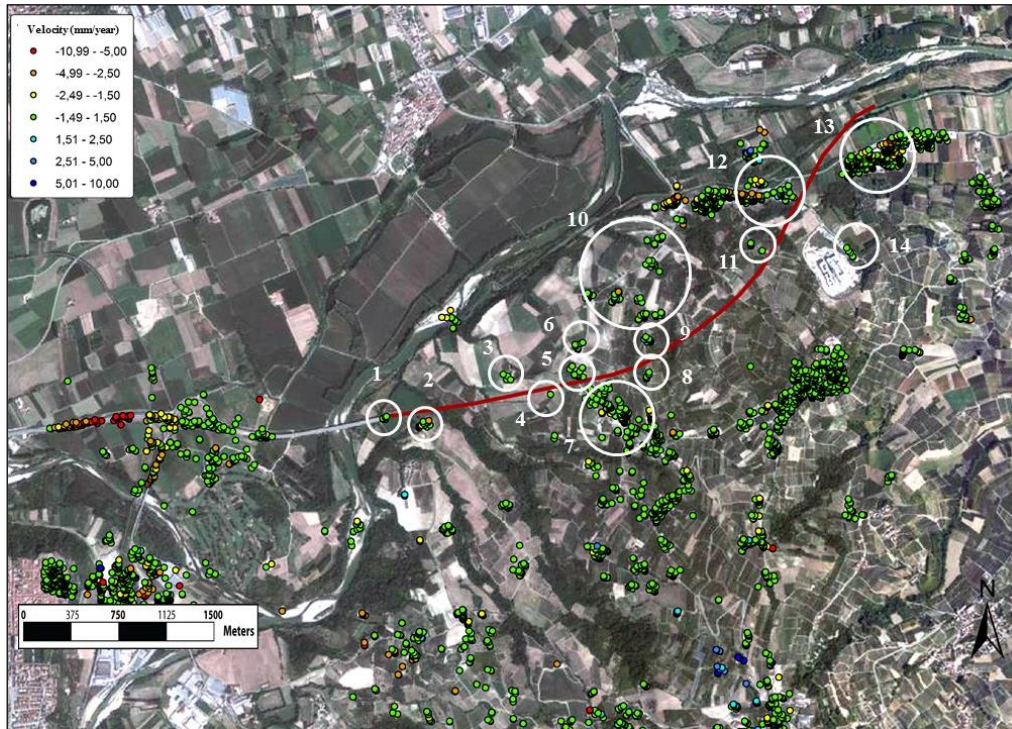


Figure 34: Delimitation of the identified areas along the area interested by the future tunnel.

AREA 1 AND AREA 2

The area 1 is located near the entry side of Cherasco (figure 35). This area identified five radar targets, focused on the final stretch of the A33 motorway, that present a slight shift away from the satellite (maximum average velocity -1.64 mm/year), probably due to the consolidation phenomena induced by the adjustment of the structures (figure 36).

The area 2 presents displacements extremely limited or equal to zero along the L.O.S. of the satellite (figure 35), with the exception of a small percentage of radar targets that show displacements going away from the satellite with an average velocity value of -2.9 mm/year (figure 37).

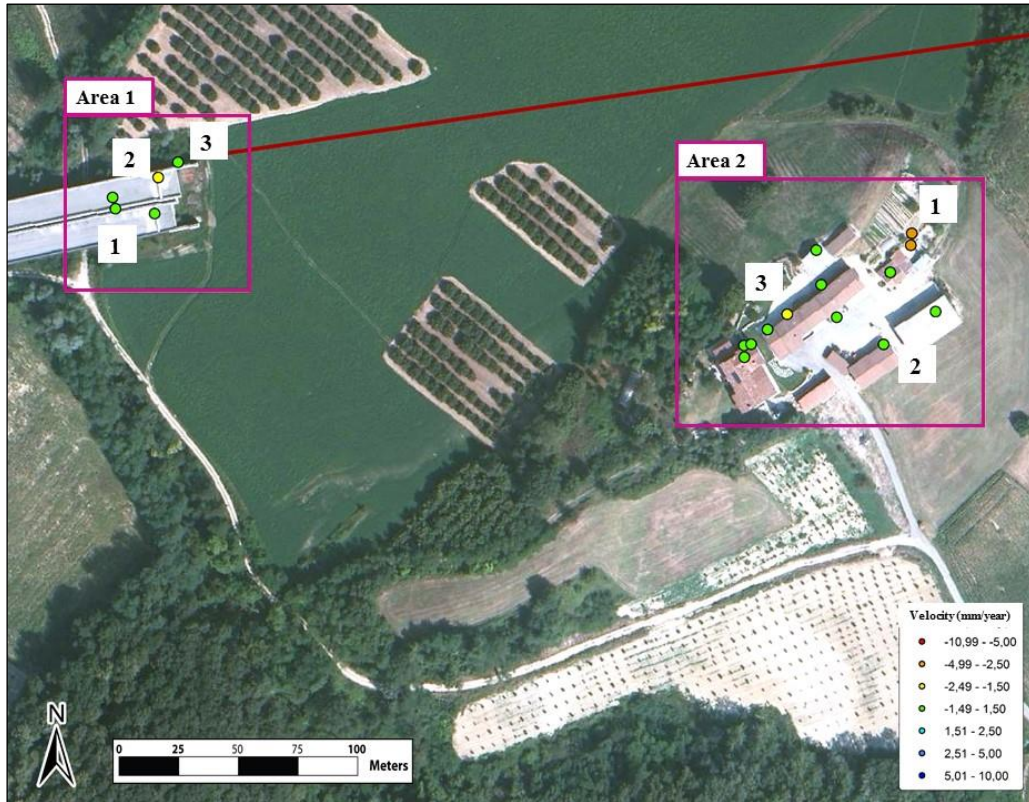


Figure 35: Localization of radar targets in the areas 1 and 2.

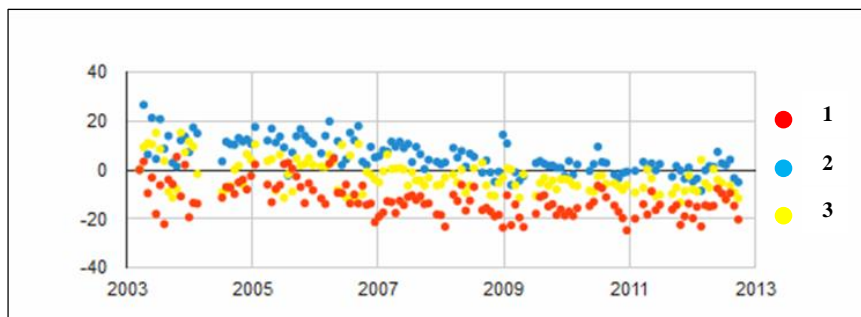


Figure 36: Time series of Radarsat targets selected for Area 1.

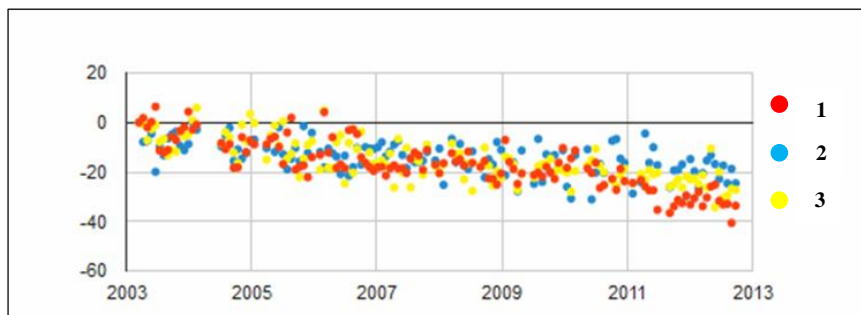


Figure 37: Time series of Radarsat targets selected for Area 2.

In this area, in addition to the Radarsat targets, some ERS and ENVISAT Permanent Scatterers fall (figure 25 - figure 28). In particular, the descending ENVISAT data confirm the trend recognized in the northeastern sector of the area (figure 39).

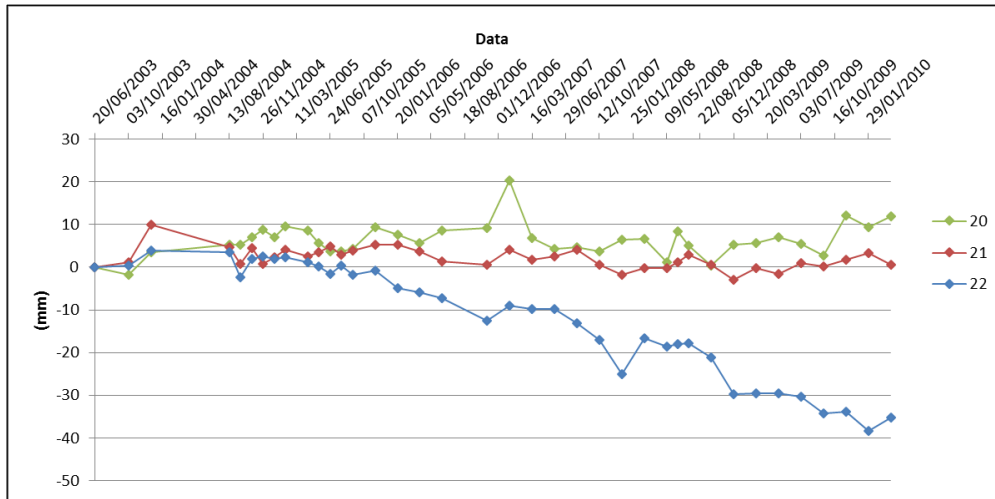


Figure 39: Time series of ENVISAT targets with descending geometry (figure 28) in the Area 2.

AREA 3 AND AREA 4

The area 3 corresponds to a farm located a few meters away from the axis of the future tunnel (figure 40), within some areas classified as active landslides mapping by the PAI (figure 33); these perimeters, however, are clearly contradictory, since they provide almost opposite directions of movement. The data show a general stability of the structures (figure 41). This trend is confirmed by the ENVISAT data with descending orbit relative to the time interval between 2003 and 2010 (figure 28). The displacements calculated by analyzing the ERS descending dataset show a slight moving away trend relatively to the period 1992-2000, (figure 42). In correspondence of the building falling within the area 4, located near the axis of the future tunnel (figure 40), only one Radarsat target is identified; it is characterized by high noise and a stable behavior (figure 43).

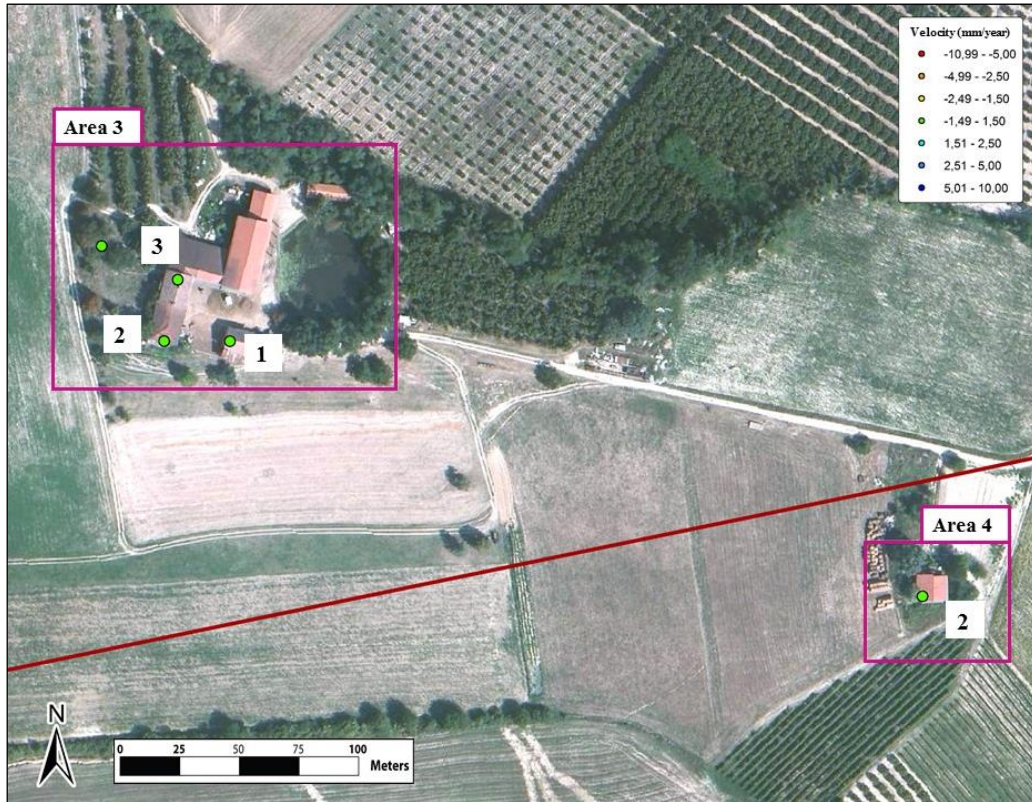


Figure 40: Localization of radar targets in the areas 3 and 4.

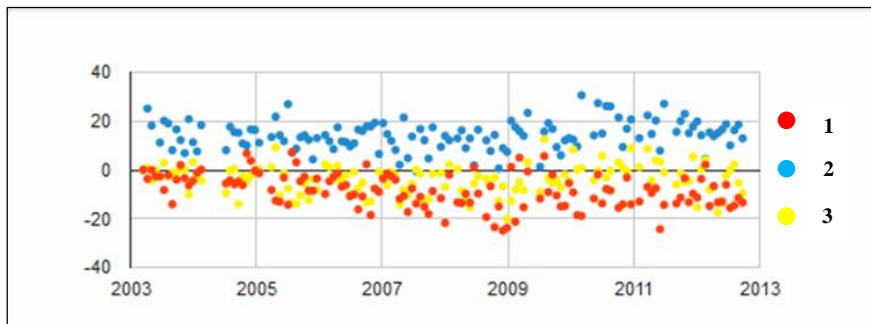


Figure 41: Time series of Radarsat targets selected for Area 3.

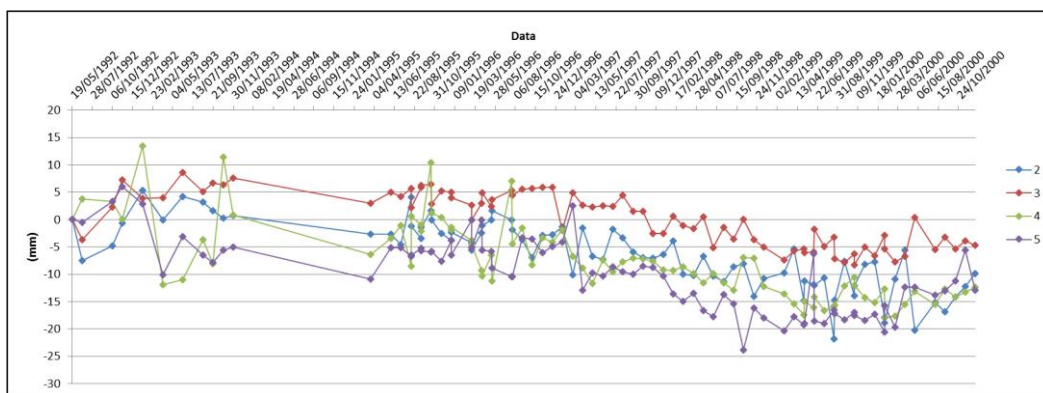


Figure 42: Time series of ERS targets with descending geometry (figure 26) falling in the Area 3.

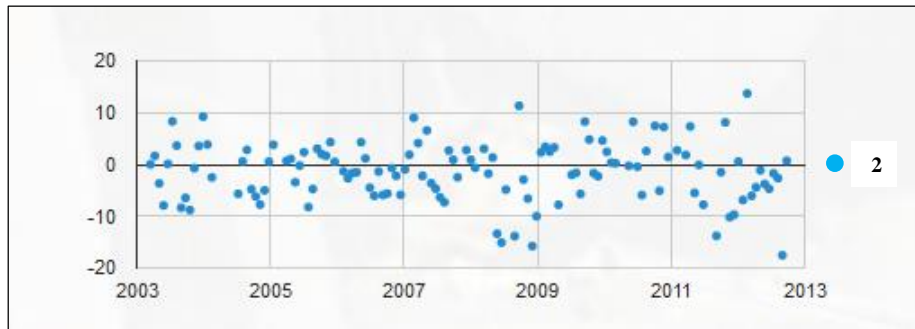


Figure 43: Time series of Radarsat targets selected for Area 3.

AREA 5 AND AREA 6

The area 5 consists of a group of residential buildings adjacent to the axis of the future tunnel (figure 44) and it is characterized by a general stability (figure 45), also confirmed by the analysis of the ERS and ENVISAT dataset (figure 25 - figure 28).

The area 6, located few tens of meters at north of the area 5 (figure 44), is characterized by irrelevant movements along the line of sight to the satellite (figure 46), confirming what has emerged from the ERS (figure 25 and figure 26) and ascending ENVISAT data analysis (figure 27).

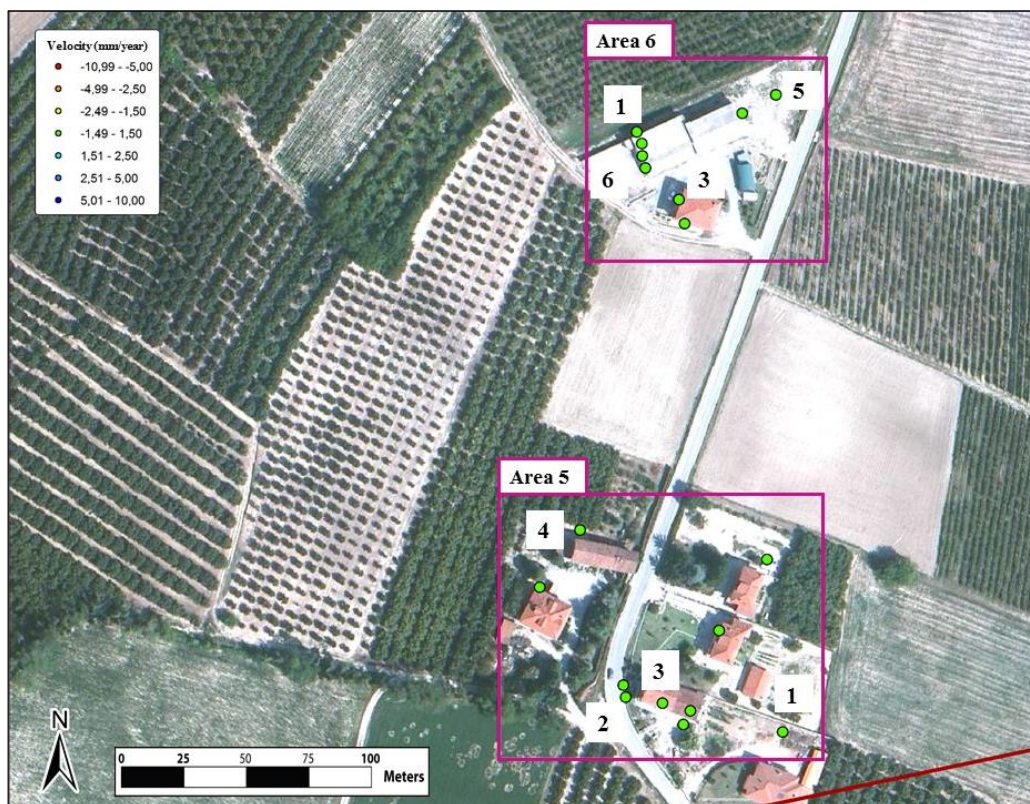


Figure 44: Localization of radar targets in the areas 5 and 6.

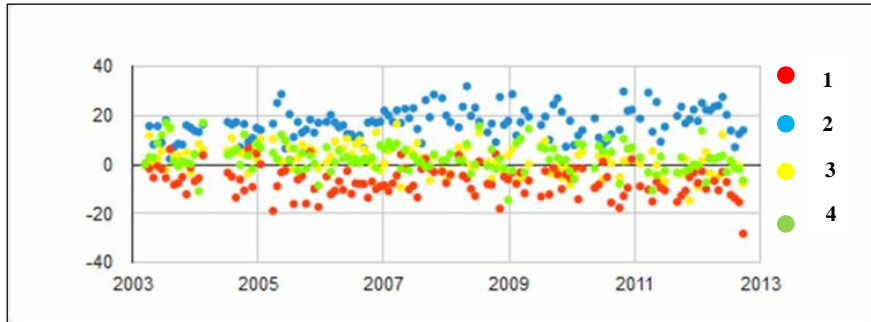


Figure 45: Time series of Radarsat targets selected for Area 5.

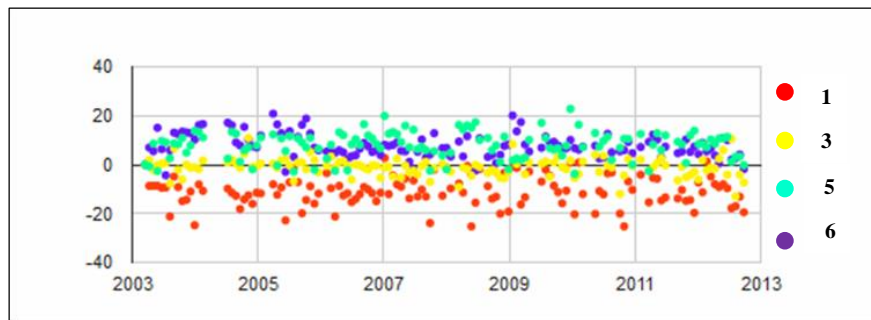


Figure 46: Time series of Radarsat targets selected for Area 6.

AREA 7

The area 7 corresponds to the fraction of Rivalta, in the municipality of La Morra, which is the largest urban center in the immediate neighborhood of the future tunnel (figure 47).

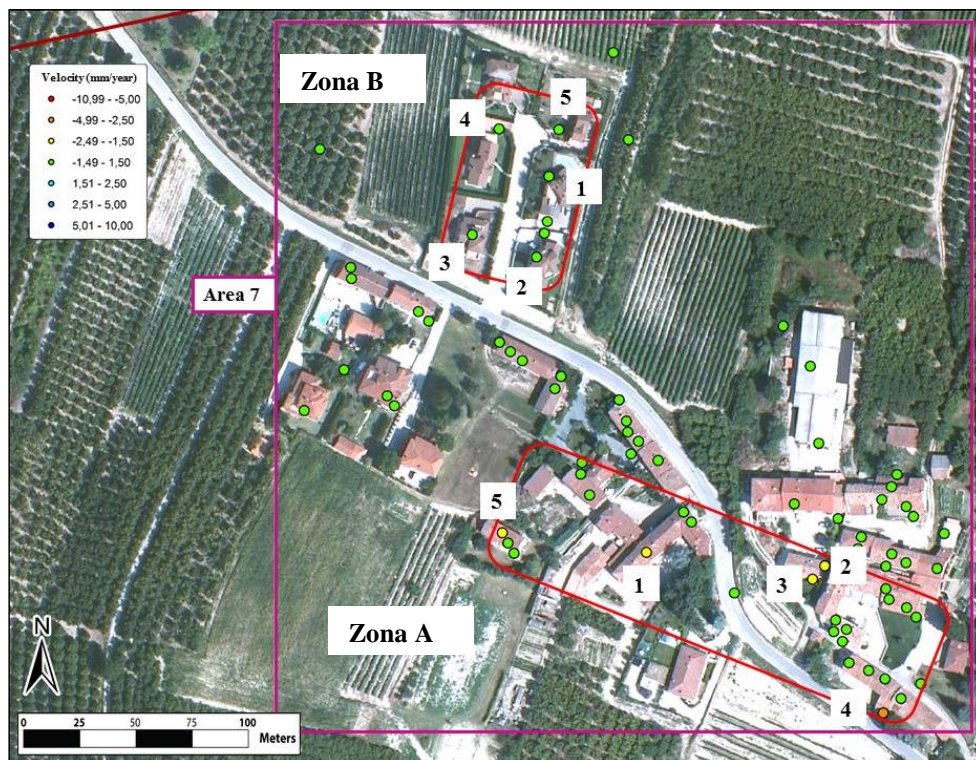


Figure 47: Localization of radar targets in the area 7

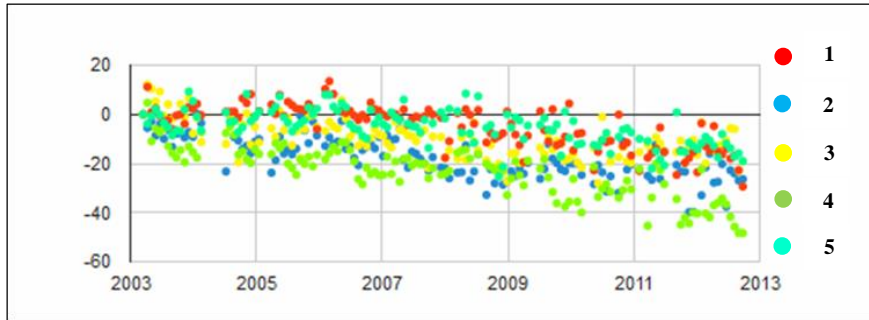


Figure 48: Time series of Radarsat targets selected for Area 7A.

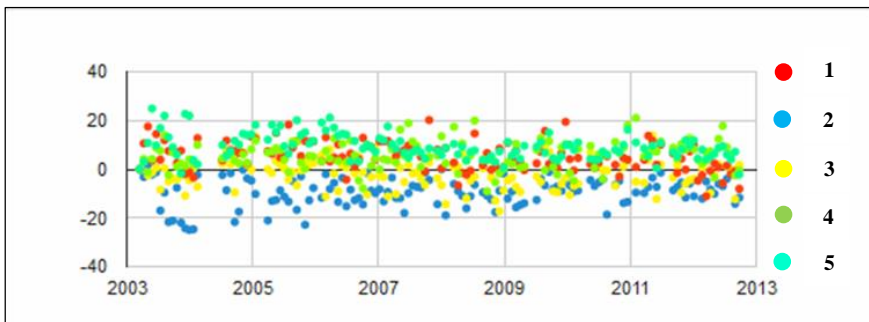


Figure 49: Time series of Radarsat targets selected for Area 7B.

AREA 8

The area 8 is located in correspondence of a village located a few tens of meters at south of the axis of the tunnel (figure 50), and is characterized by the presence of seven targets, which show a general stability (figure 51). The ERS and ENVISAT data (figure 25 - figure 28) do not have valid targets in this area.

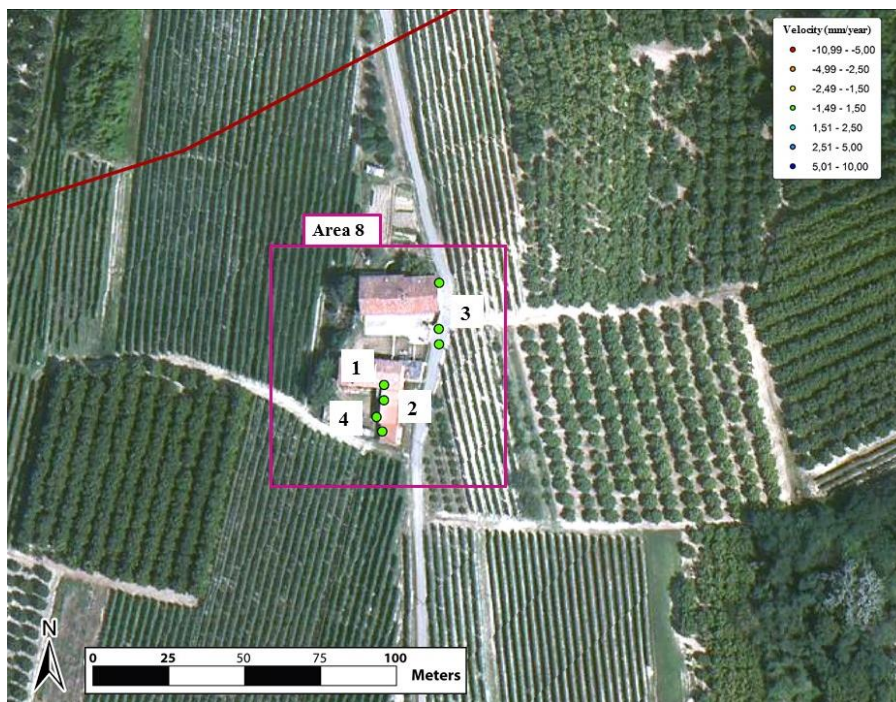


Figure 50: Localization of radar targets in the area 8.

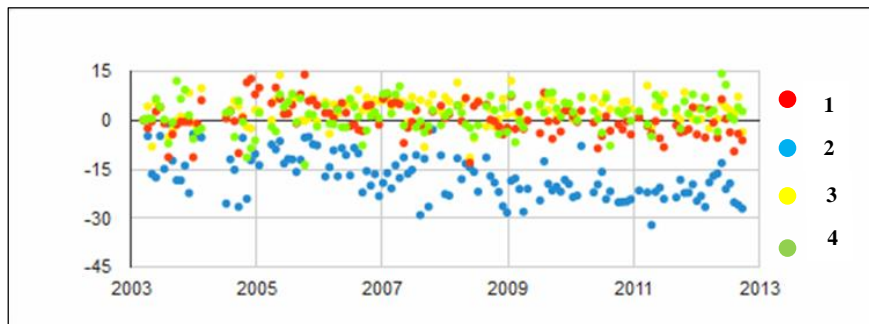


Figure 51: Time series of Radarsat targets selected for Area 8.

AREA 9

The area 9 is located in proximity of a farmhouse located few tens of meters of the axis of the tunnel (figure 52), near the top part of an area reported in the landslides inventory map of ARPA Piemonte. The Radarsat targets indicate a situation of general stability along the line of sight to the satellite, confirmed by the descending ERS (figure 26) and descending ENVISAT data (figure 28).

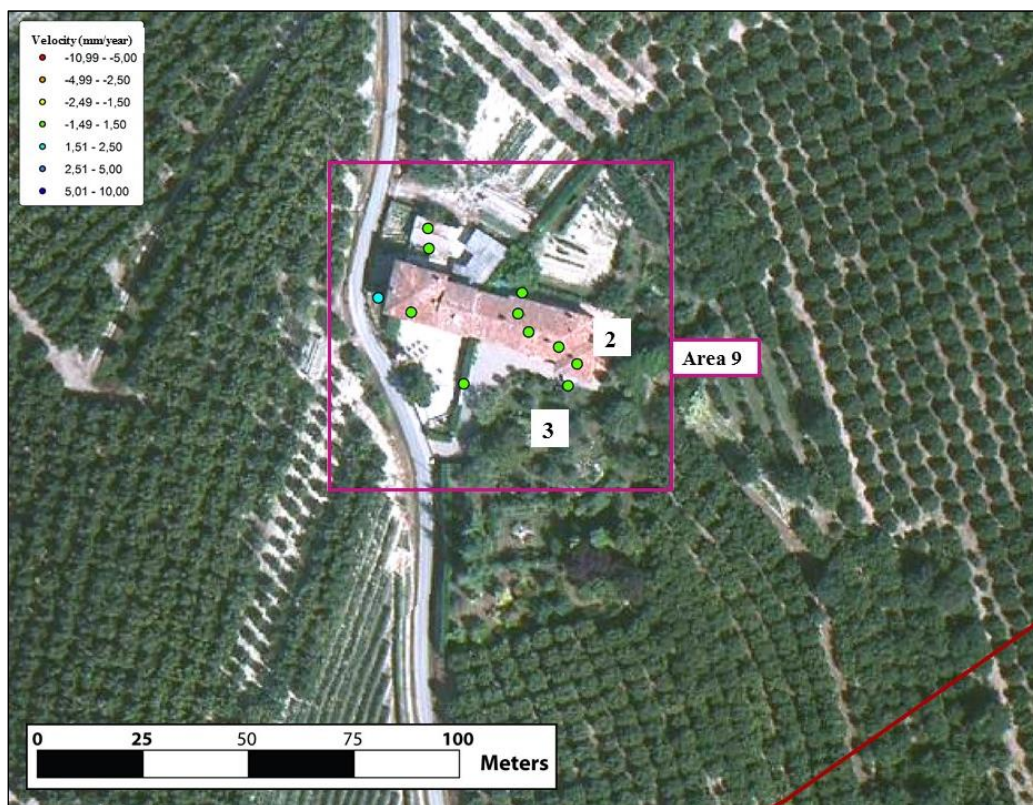


Figure 52: Localization of radar targets in the area 9.

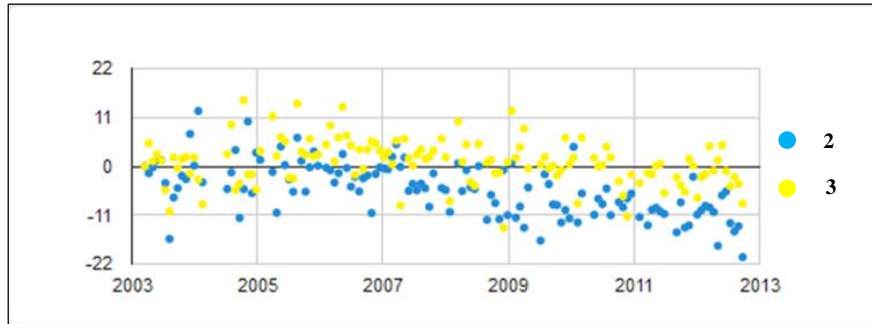


Figure 53: Time series of Radarsat targets selected for Area 8.

AREA 10

The area 10 (figure 54) is constituted by a set of buildings located within an area reported in the landslides inventory classified by ARPA Piemonte. Within this sector, there are several radar targets and only some of them have a displacement trend moving away from the satellite (figure 42), with a maximum of the average velocity values equal to -2.94 mm/year. The analysis of the ENVISAT Permanent Scatterers (figure 27 and figure 28) confirms the general stability of the area, while the descending ERS dataset has a high percent number of targets moving away from the satellite (figure 26). The apparent absence of movement in the ascending ERS dataset might suggest that the descending orbit is the more favorable to appreciate any movement in this area.

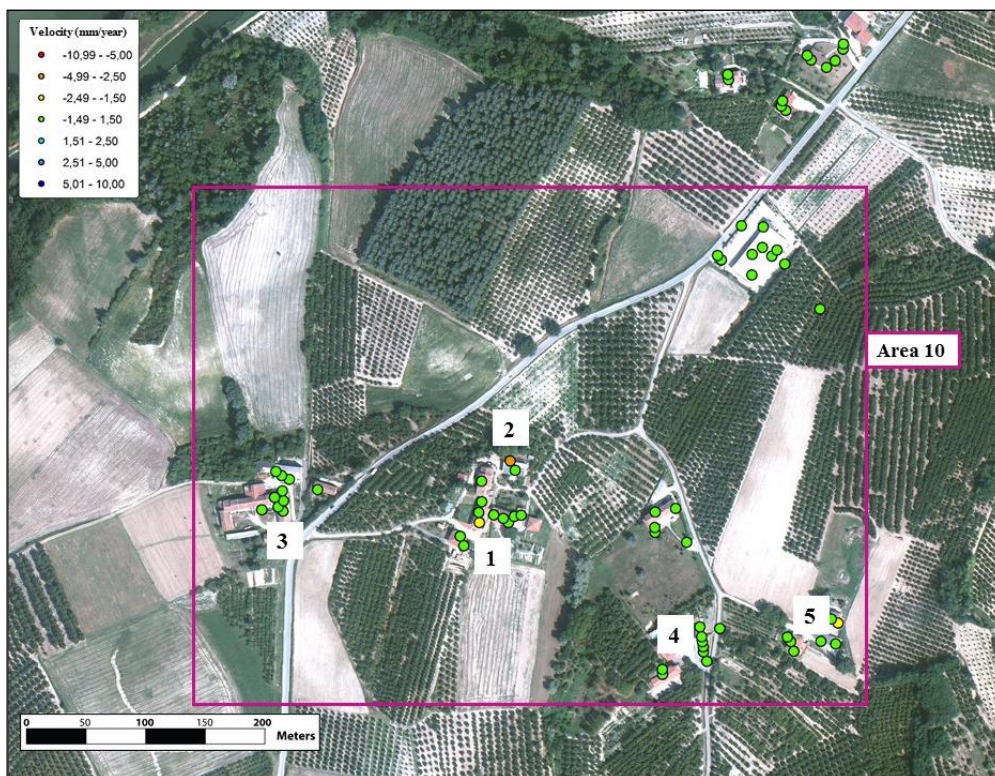


Figure 54: Localization of radar targets in the area 10.

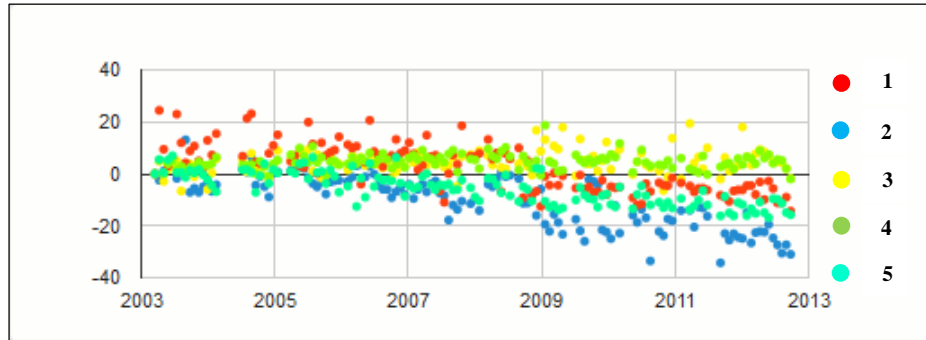


Figure 55: Time series of Radarsat targets selected for Area 10.

AREA 11

The area 11 is located at a farmhouse and some outbuildings located a few meters northwest of the axis of the future tunnel (figure 56).

All Radarsat targets have a general stability along the line of sight to the satellite (figure 57), while no one Permanent Scatterer is identified by the analysis of ERS and ENVISAT dataset (figure 25 - figure 28).

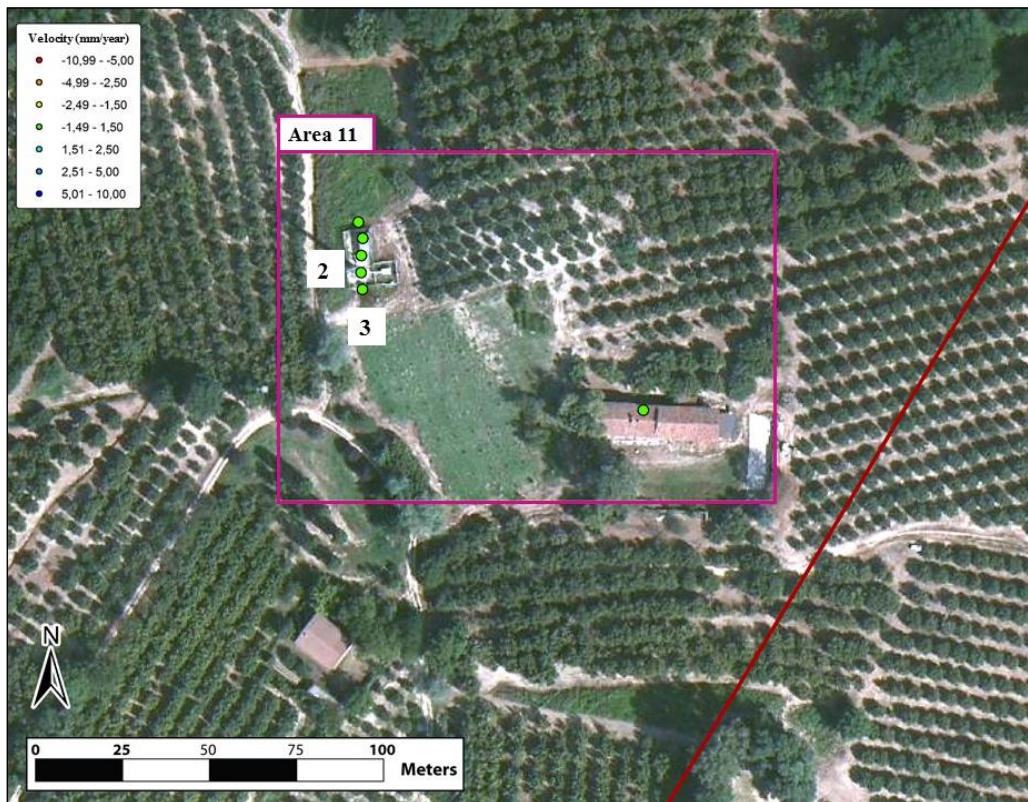


Figure 56: Localization of radar targets in the area 11.

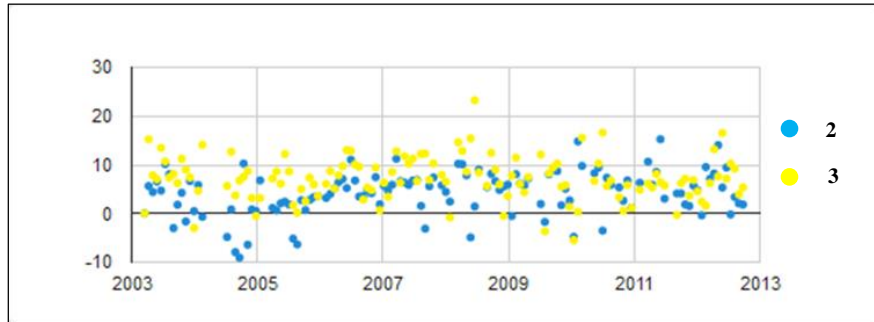


Figure 57: Time series of Radarsat targets selected for Area 11.

AREA 12

The area 12 is located in a plain area, in the west side of the Alba entrance (figure 58).

Some subsidence phenomena (with a maximum of the average velocity values up to -4.81 mm/year) are evident in correspondence of some structures in the industrial areas of the bottom valley, located on the alluvial deposits of the Tanaro River (figure 59).

Such movements may be related to the consolidation phenomena caused by the load of new structures (figure 64) and, a comparison with the ERS and ENVISAT analyzes (figure 25 - figure 28) shows a greater instability of the shed localized in the western sector of the area (figure 60 - figure 63).

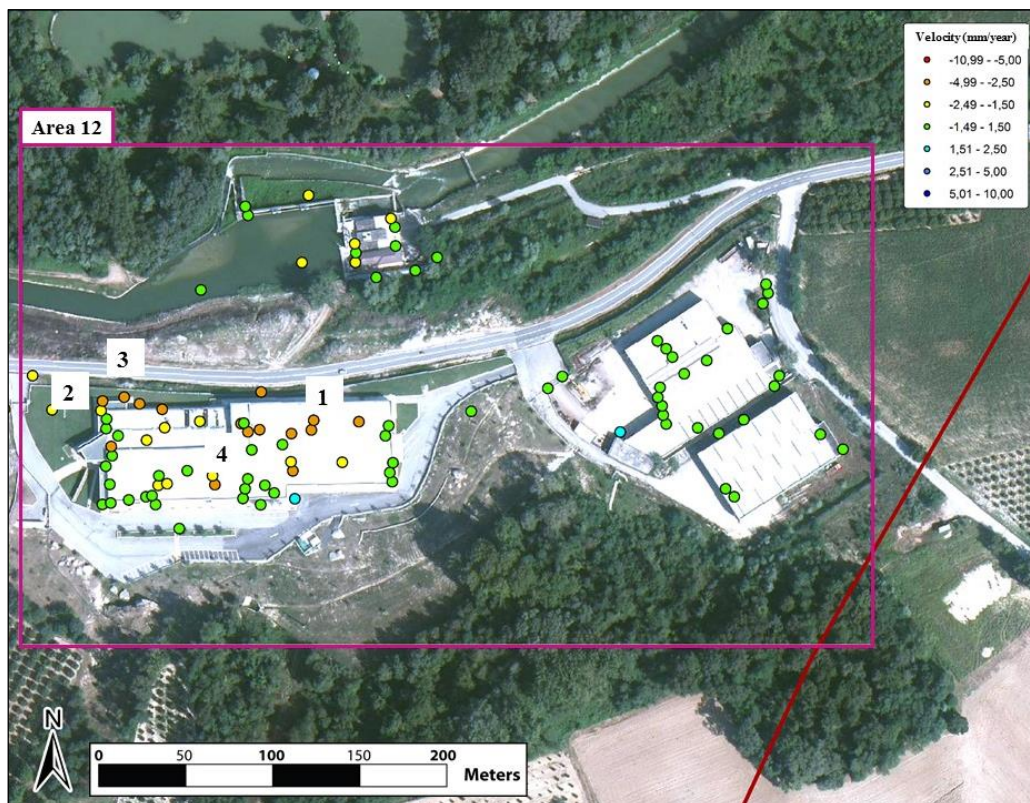


Figure 58: Localization of radar targets in the area 12.

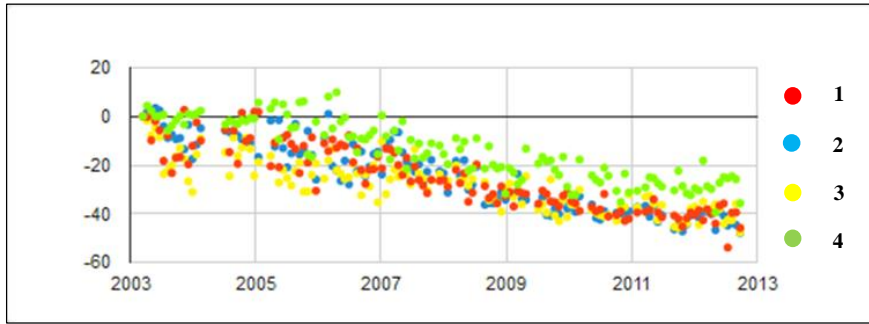


Figure 59: Time series of Radarsat targets selected for Area 12.

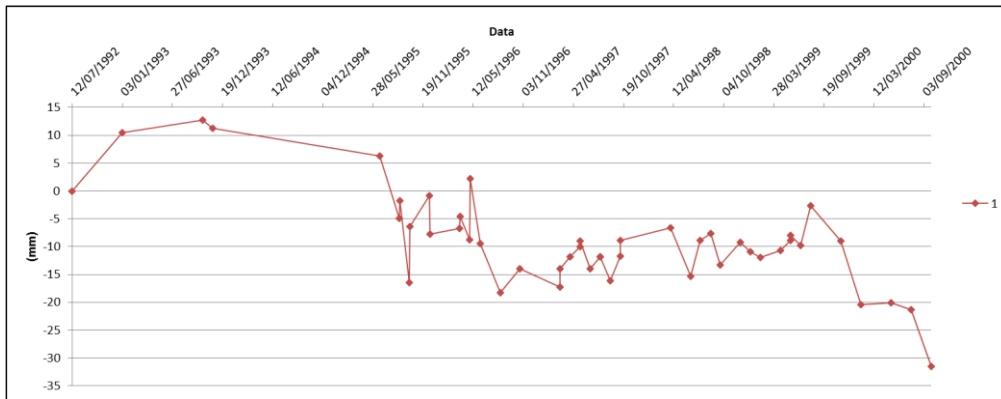


Figure 60: Time series of ERS targets with ascending orbit selected for Area 12.

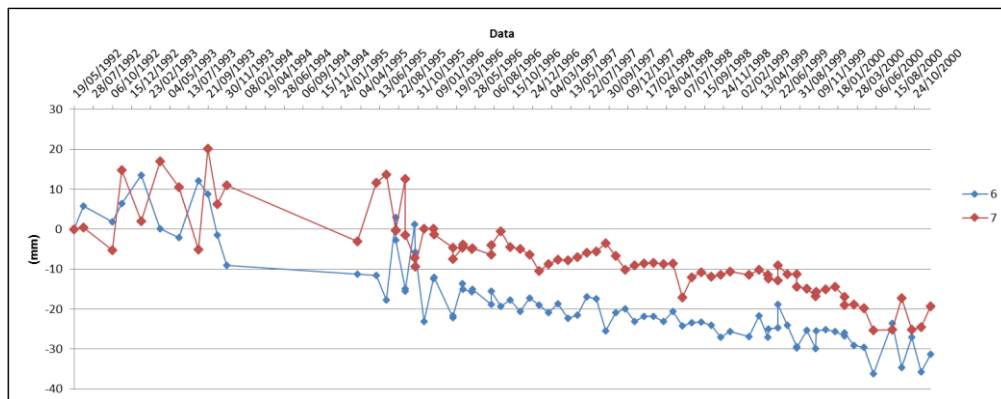


Figure 61: Time series of ERS targets with descending orbit selected for Area 12.

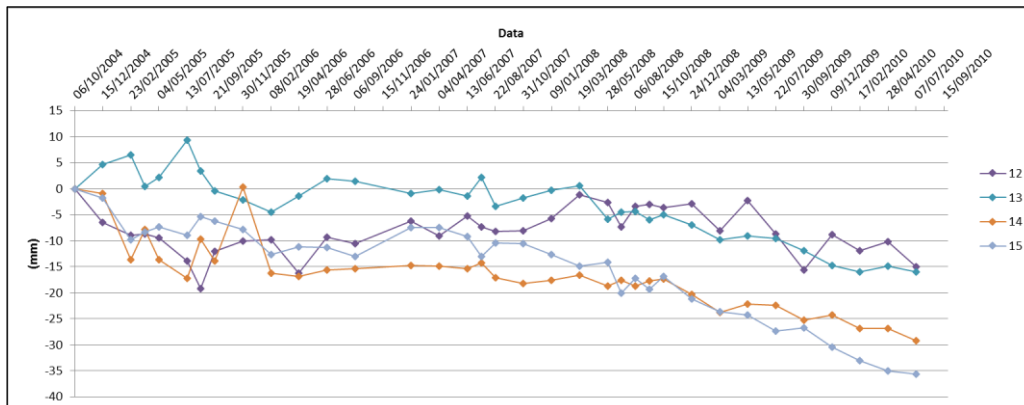


Figure 62: Time series of ENVISAT targets with ascending orbit selected for Area 12.

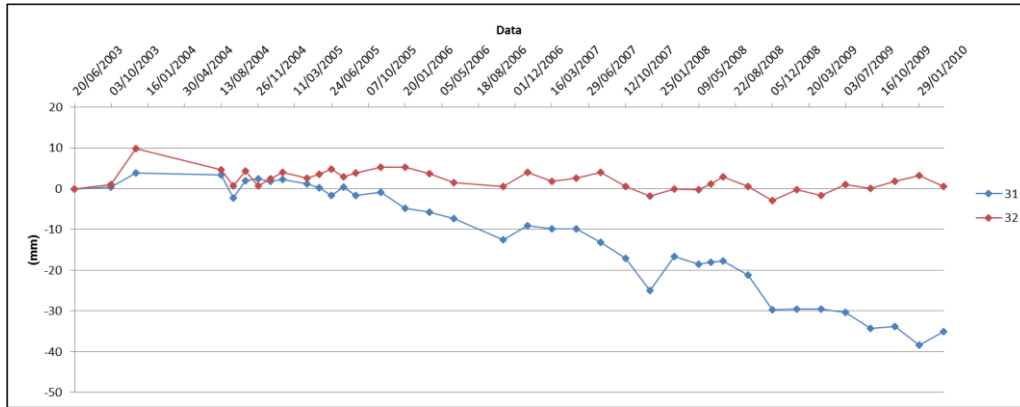


Figure 63: Time series of ENVISAT targets with descending orbit selected for Area 12.

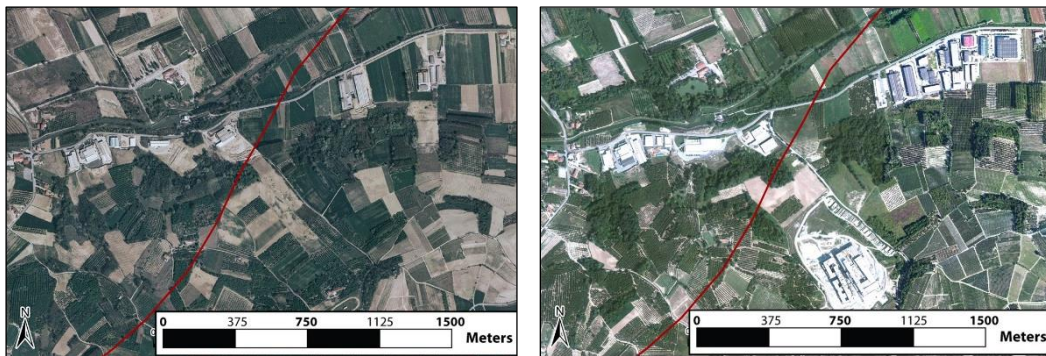


Figure 64: Entrance of the highway in the side of Alba: comparison between 2000 and 2012 orthophotos.

AREA 13

The area 13 is located at the east side of the entrance of the gallery, in the district of Alba (figure 65). It has a distribution of the deformations similar to that of the area 12 (figure 67), probably caused by the consolidation of the soil due to the load of new structures (figure 65). The analysis of ERS and ENVISAT dataset does not show significant shifts (figure 25 – figure 28).

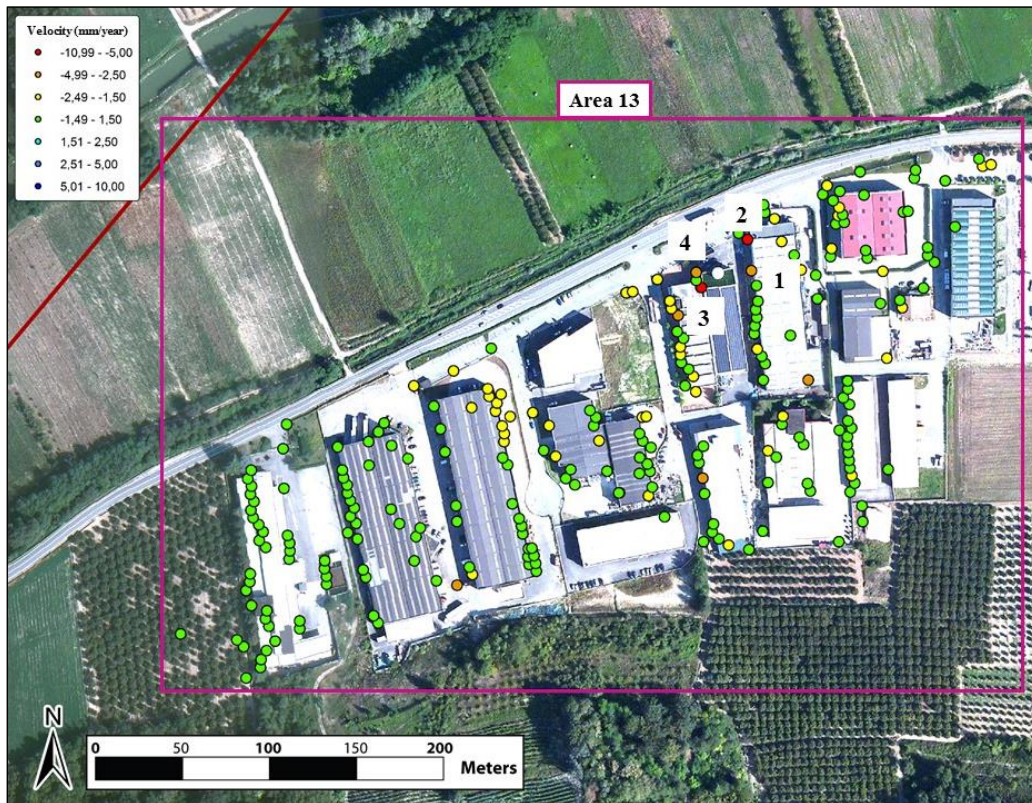


Figure 65: Localization of radar targets in the area 13.

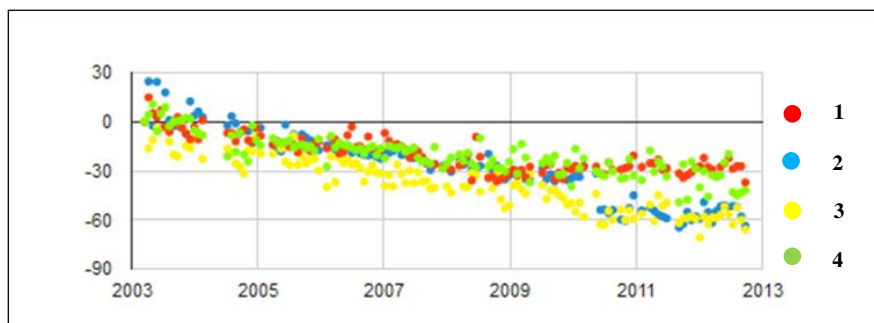


Figure 66: Time series of Radarsat targets selected for Area 13.

AREA 14

The area 14 corresponds to the site of the construction of the new hospital Alba-Bra (figure 67) that, according to the maps relative to the executive project for the construction of the tunnel, fall entirely within an active landslide (figure 33).

Given the presence of an active shipyard were not detected useful targets except for some points located in correspondence of temporary structures (figure 68).

These targets show a general stability along the line of sight to the satellite (figure 69).

From descending ERS dataset emerges a single unstable point localized in correspondence of the demolished building due to the construction of the hospital (figure 26).



Figure 67: Area of the new hospital Alba-Bra: comparison between 2000 and 2012 orthophotos.

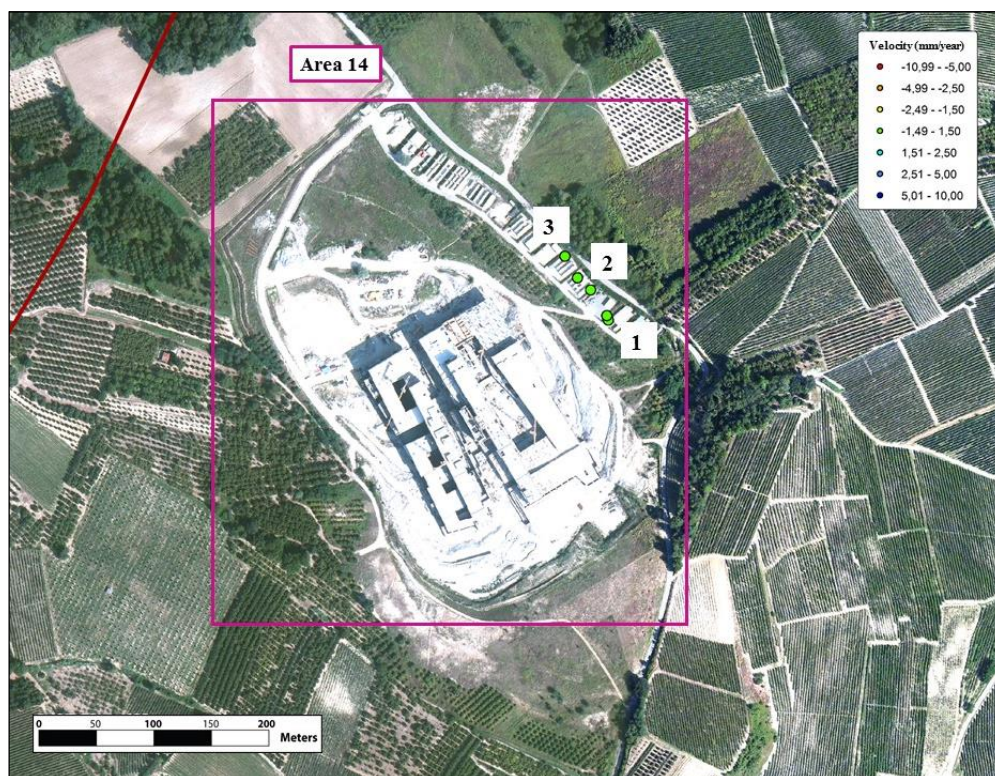


Figure 68: Localization of radar targets in the area 14.

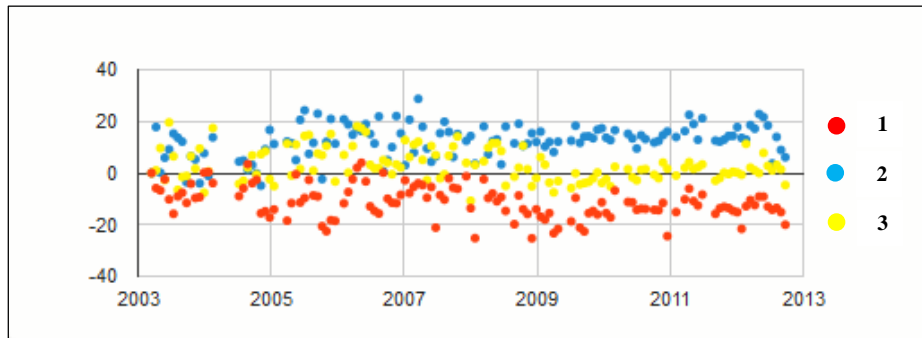


Figure 69: Time series of Radarsat targets selected for Area 14.

The SqueeSARTM processing of the ascending Radarsat-1 dataset acquired on the area of Verduno allowed obtaining quantitative information on the movements that occurred in the period between March 2003 and September 2012 within the area affected by the future construction of Verduno gallery, without any installation of in situ instruments.

Although over 3.100 measurement points have been identified on a total area of 21 km², the distribution was rather irregular, because of the extensive agricultural and/or vegetated areas that, presenting continuous variations of reflectivity, preventing the detection of radar targets stable.

The analysis, however, identified a general stability along the line of sight to the satellite in the areas identified along the track of the tunnel, except for some individual points.

Although the various maps available (IFFI, PAI) signal the presence of many of landslide phenomena in the area, the SqueeSARTM data analysis, also due to the scarcity of the radar targets on these areas, did not detect significant movements.

It should however be mentioned the lack of congruence in the maps mentioned above, which encircle areas with limited overlap and sometimes discordant meaning.

The conducted analysis is an important starting point for the possible updating of the deformation interesting the structures on the slopes investigated during the excavation of the tunnel and in the phase of post-operam.

The possibility of using images acquired from satellites of new generation, such as TerraSAR-X and CosmoSky-Med is suggested in case of SqueeSARTM monitoring, in order to obtain a more homogeneous distribution of targets during the construction phase of the gallery, given the significant extension and characteristics of the vegetated areas.

These new satellites with higher spatial and temporal resolutions guarantee the identification of measuring points even in those areas that are unfavorable to the identification of radar targets stable for the intense vegetation cover or for the presence of agricultural activities.

5. C-BAND DATA FOR BASIN-SCALE MONITORING

Remote sensed data, currently used in both near-real time and deferred timework, can give support for the creation and updating of landslides inventory maps over large areas.

Preparing landslides map is important to document the extent of landslides phenomena in region, to investigate the location, type, pattern, recurrence and statistics of slope failures, to determine landslides susceptibility, hazard, vulnerability and risk, and to study the evolution of landscapes dominated by mass-wasting processes (Guzzetti et al., 2012).

In many cases, earth observed satellite data could provide precise estimates of ground motion and indicators of landslides geometry and activity, without requiring the installation of any targets or instruments on the ground.

In particular, the Persistent Scatterers Interferometry (PSI) technique has become a widespread tool for landslides mapping properly combined with traditional geomorphological survey techniques and other monitoring instruments.

In this chapter, the spatial characterization of landslides phenomena is discussed, focusing on the landslide detection and mapping procedures by means of PSI data. In particular, in this case, the results for the use of the C-band data for basin scale monitoring are given.

5.1 GENERAL CONSIDERATIONS

The availability of the PS on wide areas can be used to update landslide inventories. The Landslides Inventory Maps (LIM) date back to the 1970's (Carrara and Merenda, 1976) and can be defined as representations of the distribution, typology, and, if possible, the date of occurrence of those mass movements that have left detectable evidence on the affected areas. Landslide inventory maps show the spatial distribution of both past and current landslides, represented as polygons or points and often include information about their state of activity (Wieczorek, 1984).

Landslide mapping activities can be performed by using a purely convention approach (stereoscopic interpretation of aerial photography) or exploiting modern and emerging technologies, mainly relied on remote sensing. Recently, (Guzzetti et al., 2012) provided a review about the various approaches for landslide identification and mapping, both the conventional and the new recent techniques.

The traditional methods most commonly used for preparing inventory maps are based on historical archives, local databases, photo-interpretation of stereo aerial photos and geomorphologic surveys (Crozier, 1984; Soeters and Van Westen, 1996).

Thus, these conventional methods rely chiefly on the visual interpretation of stereoscopic aerial photography, aided by field checks. These methods are well established, but are time-consuming and resource-intensive (Brabb, 1991; Galli et al., 2008).

Moreover, the inventory maps created with only these traditional techniques are usually subject to uncertainties and limitations related mainly to difficulties in the recognition and the subsequent mapping of morphological features and evidences related to ground instability, especially in highly vegetated and urbanized/built-up areas (Brardinoni et al., 2003). Even more problematic is the assessment of the state of activity, for which various but not resolving approaches have been proposed, such as stereoscopic multi-temporal analysis of aerial photos (Canuti and Focardi, 1986).

New and emerging techniques are mainly based on satellite, airborne, and terrestrial remote sensing technologies. These techniques have demonstrated to be valuable for the recognition of landslides (Rengers et al., 1992) and other geomorphological features, and so for facilitating the production of landslide maps reducing the time and resources required for their compilation and systematic update (Guzzetti et al., 2012).

Today, all the EO technologies are widely used by now, and more and more a landslide mapping is often performed through a combination of many techniques.

The different technologies are quite commonly employed by the researchers and operational communities of some countries, for a preliminary map of the most critical and hazardous landslide-prone areas or for a rapid production of landslide event-inventory in the emergency phase following a disaster.

In Italy, official landslide inventories exist, provided by local authorities and based on documental sources, historical archives, aerial ortophotos analysis and geomorphologic surveys (Crozier, 1984; Soeters and Van Westen, 1996). The IFFI project (Inventory of Landslide Phenomena in Italy, Inventario dei Fenomeni Franosi in Italia), carried out by ISPRA (Istituto Superiore per la Protezione e la Ricerca Ambientale) (ISPRA, 2008) and the Regions and self-governing Provinces, and PAI (Hydrogeological setting plan, Piano di Assetto Idrogeologico) are projects carried out to supply detailed picture of the distribution of landslide phenomena within Italy, aiming at identifying and mapping landslides over the whole national territory, based on standardized criteria.

5.2 PSInSAR™ PROCESSING METHOD

The PS-InSAR technique has been developed and patented by the Politecnico di Milano and exclusively licensed to Tele-detection Europe (TRE) Srl in 2000 (Colesanti et al., 2003; FERRETTI et al., 1999, 2001).

This multi-interferogram technique employs time series of satellite radar images and is an extremely effective tool for monitoring the deformation phenomena of the Earth's surface with millimeter accuracy.

In particular, the technique is based on the observation of a small subset of radar targets, denominated permanent scatterers (Permanent Scatterers, PS), which are practically immune to the effects of temporal and spatial decorrelation.

They maintain the same "electromagnetic signature" in all images, at different acquisition geometries and climatic conditions, preserving the phase information over time.

The PS typically correspond to parts of buildings, metal structures, exposed rocks, in general elements already present in the soil, whose electromagnetic characteristics do not vary significantly in the different acquisitions; this does not happen for the vegetation, whose appearance is constantly changing.

An estimate of atmospheric noise is possible, in correspondence of the PS, by means of the statistical analysis of a dataset of SAR images; then the atmosphere noise is removed and the contribution due to ground deformations isolated.

More precisely, once the atmospheric contribution has been estimated, all of the components that make up the interferometric phase are identified. Then, the terms spurious are deleted and the term that describes the variation of the optical path of the electromagnetic wave in the various acquisitions is isolated. That is the movement of the "target" in the time period between the first and the last data available.

For each PS are derived position (its geographical coordinates: latitude, longitude, altitude), the average trend of deformation (calculated as a linear interpolation of the displacement measured in the completely monitoring period) and the entire time series of the movements. All the measures, as well as in the case of differential interferometry, are differential and measured along the sensor-target joining line (LOS); these are obtained after determining one or more reference points on the ground (reference point), with known coordinates and supposed being without movement (indicated as such by measures such as GPS or optical leveling).

Negative sign indicates a shift away from the satellite; positive sign indicates a shift towards the satellite.

The strengths of the PS technique, compared to conventional DInSAR analysis, consist mainly in the ability to assess and remove the atmospheric contributions from the signal and obtain point estimations; so, the accuracy of measurements increases (up to a millimeter on each measure).

The main advantages of the technique rather than traditional instrumentation can be summarized as follows:

- ability to process the whole historical archive of radar images, from which the possibility to investigate active or reactivated instability phenomena in this period;
- generally, does not require installation of ground-based instruments;
- high spatial density of the reflector (in urban areas up to about 700 PS/km²), already present in the area;
- provides differential measurements with millimeter accuracy;
- major accuracy of the measurement in the vertical direction with respect to the GPS technique.

It is also important to note the limits of the PS technique, which can be summarized as follows:

- ability to appreciate only deformations with speeds of up to 5-6 cm/year;
- the study area needs to have a sufficient density of permanent scatterers (urbanization, or the presence of exposed rocks);
- impossible "real time" monitoring, given the frequency of the data (order of one month with the satellites in C-band acquisition) even if it is possible to integrate multiple geometries of acquisition;
- possible underestimation of deformations in case of slopes with dip direction towards North or South (due to the orbital path of the satellite).

The PS technique is the multi-configuration interferogram that has been most applied from the late 90s. The main applications concern the study of ground deformation induced by tectonic movements (Musson et al., 2004), volcanic activity (Salvi et al., 2004), subsidence due to fluid extraction from underground (Ferretti et al., 2000; Colombo et al., 2003; Canuti et al., 2005) or mining activity and landslides (Colesanti et al., 2003; Colesanti & Wasowski, 2004; Hilley et al., 2004; Ferretti et al., 2005).

5.3 SPATIAL CHARACTERIZATION

In this thesis research, the attention is focused on the PSI (Persistent Scatterer Interferometry) that has recently demonstrated its valuable suitability for the spatial detection and characterization of slow-moving landslides (Strozzi et al., 2005, Farina et al., 2006; Colesanti and Wasowski, 2006; Guzzetti et al., 2012).

In particular, the radar-interpretation conceived by Farina et al. (2003) (and then improved and integrated by Farina et al., 2006, Casagli et al., 2008, Farina et al., 2008) consists in assigning a geomorphological meaning to the scattered point-like ground displacement measurements coming from the Persistent Scatterers (PS) targets.

This analysis is possible due to the integration of PSI measures with conventional optical data (orthophotos, multi-temporal aerial photos, and VHR optical satellite images) and further ancillary geo-thematic data (topographic and geological maps). Thus, the procedure combines the photo-interpretation of aerial and satellite images with the 'radar-interpretation' of PSI data (Farina et al. 2008; Cigna et al. 2011; Righini et al. 2012), allowing the spatial extension of the point-wise ground motion measures provided by satellite data and the identification of geomorphologic and kinematic evidences related to landslide activity.

On one hand, the conventional photo-interpretation permits to recognize terrain features and landslide evidence in natural environments such as vegetated and rural areas, but not in urbanized areas where landslide-induced geomorphologic features are instead difficult to be identified, due to dense urban fabric.

On the other hand, radar-interpretation is very suitable for mapping ground displacements in urbanized and artificial areas where much more PS benchmarks (buildings, other reflective structures and urban infrastructure) are retrieved; whereas, in vegetated areas, the vegetation coverage prevent a high density of PS targets to be identified.

Thus, radar- and photo-interpretation are complementary tools to get complete information on slope instability and to map landslides (Farina et al., 2006, 2008; Meisina et al., 2007). This approach based on the radar- and photo-interpretation chain has been successfully and widely exploited and validated by several scientific applications during last years (Casagli et al., 2008; Meisina et al., 2008; Herrera et al., 2009a; Notti et al., 2010; Righini et al., 2012; Frangioni et al. 2013).

The methodology generally operates at regional or medium scales (1:100000-1:25000 and 1:25000-1:5000, respectively, according to Fell et al., 2008), and its contributions to the creation of new Landslides Inventory Maps or to the updating of pre-existing inventories consist in the following steps (figure 70).

- Detection of landslide phenomena not emerged from conventional geomorphological analyses.
- Modification of landslide boundaries;
- Assessment of representative ground displacement velocity for each landslide
- Evaluation of state of activity (explained more in detail in the next section, par 5.3.2).

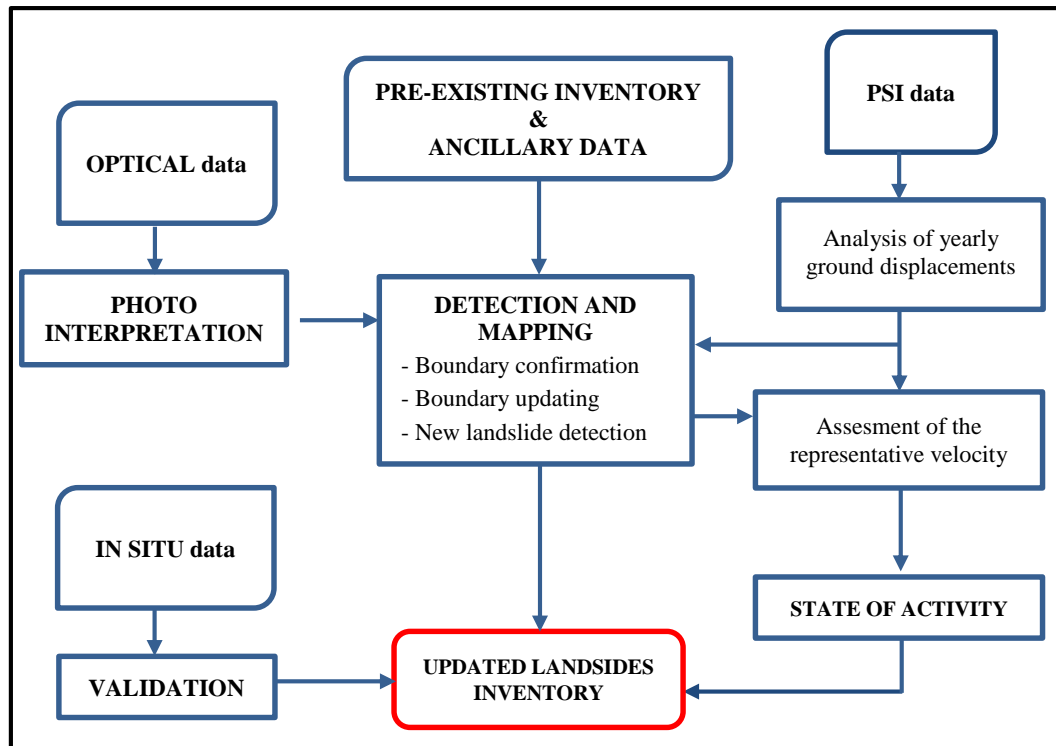


Figure 70: Flow chart describing the mapping of landslides and the evaluation of their state of activity.

In particular, as pointed out by [Frangioni et al. 2013](#), on the basis of pre-existing inventory map and PS distribution, the combined radar-interpretation and photo-interpretation procedures allow the modification of boundaries (usually enlargement) of pre-mapped phenomena and the identification of new landslides which were not previously mapped through conventional geomorphological studies.

Generally, in order to make radar-interpretation more robust, the analysis is focused on groups of at least 3-4 radar targets ([Meisina et al., 2008](#)), since measures recorded on single targets may often not be representative or indicative of a mass movement, but tied to local instability of a single infrastructure (structural fractures or settlement of building).

Moreover, the integrated PSI analyses with ancillary data, thematic maps and photo-interpretation, should be supported by field investigation and surveys, in order to confirm or even to improve all the information and evaluations performed through radar-

interpretation, to verify damage on buildings and infrastructures and other geomorphologic evidences and features connected to ground instability.

The radar interpretation presents a series of cases involving a different methodology for the analysis of the data and information that can be drawn from them. Not usually, the PSs fall within areas already mapped as landslide areas; they are often located near it, or completely outside to it. In these cases, it is important to analyze the topographic maps and the aerial image, to give an interpretation of the interferometric data. The use of ancillary data allows extending the limits of landslides already mapped and incorporating PSs that are considered part of this movement. It is also possible to detect a new area affected by a landslide, where the information provided by the interferometric data coincide with some landslide diagnostic morphologies. The updating of landslides inventories can be made in these terms:

- Detecting of “new” landslides.
- Change of the boundaries and/or the typology of old landslides.
- Determinate the state of activity of landslides for the period of satellite observation.
- Individuate the possible buildings damaged by landslides displacement.

The [Frangioni et al., 2013](#) present an updating of pre-existing landslide inventory map by means of PSI data, at a basin scale in Emilia-Romagna (Italy).

5.3.1 DETECTION OF “NEW” LANDSLIDES AND BOUNDARIES CHANGE

The PS may be very good to detect very slow landslides that are difficult to detect with traditional observation. The PS data give information only about the movement of the surface that is not possible to discriminate without other observations, if the movement is related to a shallow flow or to a deep sliding.

It is possible to define some parameters of PS data that define a slope mass movement from other localised processes; the parameters are usually: velocity; homogeneity of the movements; extension of the area with movements. These parameters can be taken in count for example to distinguish a simple debris instability from a landslide.

If the PS fall outside the areas already mapped as landslide may have the two following cases:

1. Detection of “new” landslides
2. Change of the boundaries

DETECTION OF A “NEW” LANDSLIDE: when a group of PS is moving outside of some landslides already mapped, the possibility to map a new landslide (figure 71) is evaluated. This is possible if the presence of morphological evidence and vegetation disruption is notable from the orthophotos and the topographic maps.

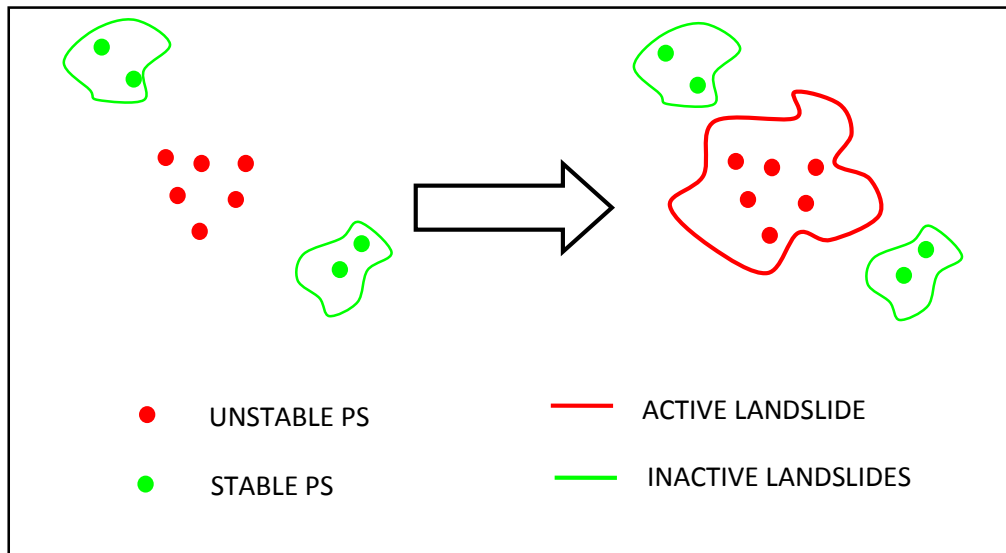


Figure 71: A new landslide mapped for the presence of moving PS away from other areas mapped as landslides.

CHANGE OF THE BOUNDARIES: it evaluates the possibility to change the limits of the landslide polygon encompassing the nearby moving PS, in case it is inferred (from orthophotos and CTR) that the movement of PS can be traced back to the same landslides mapped (figure 72)

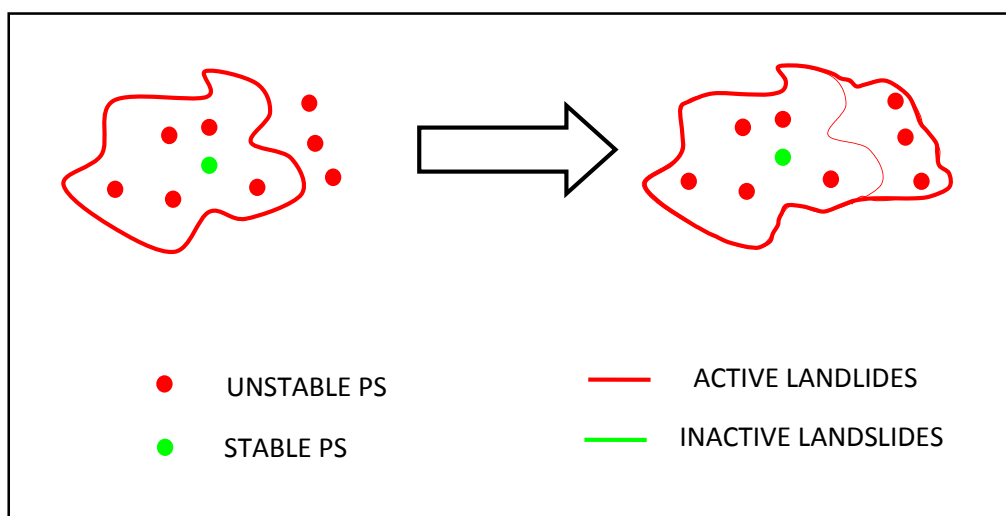


Figure 72: Change of boundaries of a landslide for the presence of moving PS, due to the same phenomenon mapped.

5.3.2 CLASSIFICATION OF THE STATE OF ACTIVITY

Some works try to compare and update the state of activity by the movements detected with SAR data (Frangioni et al., 2013). However, this presents many limitations and only for few landslides, PS data it is useful to determine the state of activity. The main limitations are described below.

- Period of observation: the activity state is referred to the interval of acquisition.
- Coverage quality of PS data: only the landslides with good PS coverage (high-density and good spatial distribution) are useful for studies on activity state; in other cases, it is possible to individuate an active or inactive sector.
- Slope aspect toward the LOS: the landslides on northern and southern slope may have movement not fully measured along the LOS directions; the projection of the velocity along the slope may solve this problem.
- Thresholds: it is not an easy task to define a sharp threshold of velocity between stable or dormant and active landslides, and this threshold depends on the type of landslides. The best way to evaluate the state of activity through PS data is the evaluation case by case for each landslide, without a fixed value of velocity or percentage of PS that show movements even if this is affected by a certain degree of subjectivity. An automatic classification of the state of activity of landslides is possible, but if the results are not validated, they should not be added to landslides inventories. Furthermore, the PS data can be considered a valid tool to determine the state of activity only for slow flow, some complex landslides and rarely rotational or translational slides because the range of movement of these processes is comparable with the range of measure of the persistent scatterer techniques.

If the PSs fall inside the areas already mapped as landslide may have the following cases:

1. Confirm the state of activity
2. Change the state of activity
3. Separation of a portion of landslides

CONFIRM THE STATE OF ACTIVITY: there is correlation between the activity state given by the existing inventory map and the activity state that can be inferred from interferometric data that fall within the landslide. In figure 73 is represented the situation. The case "A" shows moving PS that fall within a landslide classified as active, while the case "B" shows stable PS within a landslide classified as inactive. In both cases, the status of activity already present is confirmed.

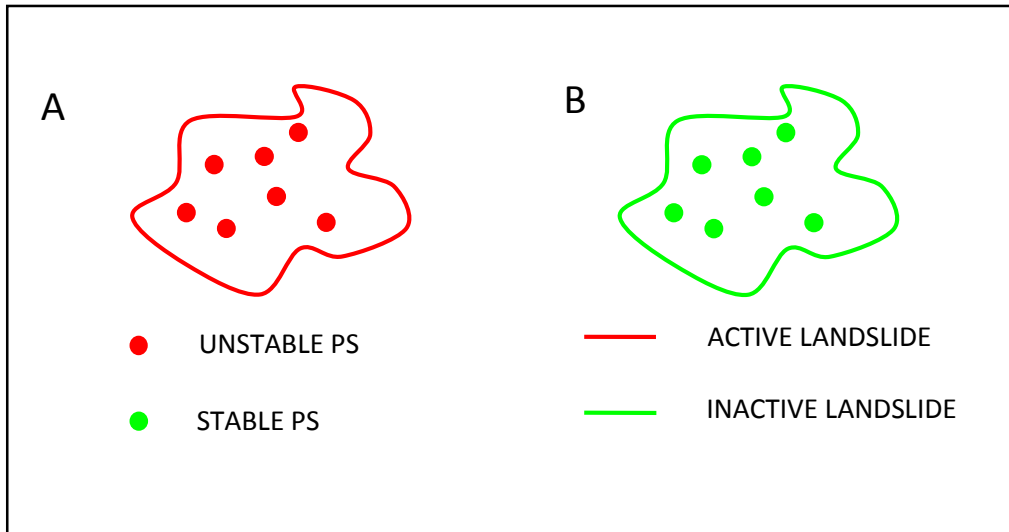


Figure 73: Cases of correlation between the activity state of the landslide indicated in the existing inventory and the information provided by the PSs. A) Confirmation of an active landslide. B) Confirmation of an inactive landslide.

CHANGE OF THE STATE OF ACTIVITY: there is no correlation between the activity status of the existing inventory map and the information derived from interferometric data. It evaluates the possibility to change the activity status of the entire landslide if the PSs supply substantially a unique velocity and are arranged in a homogeneous way within the landslide.

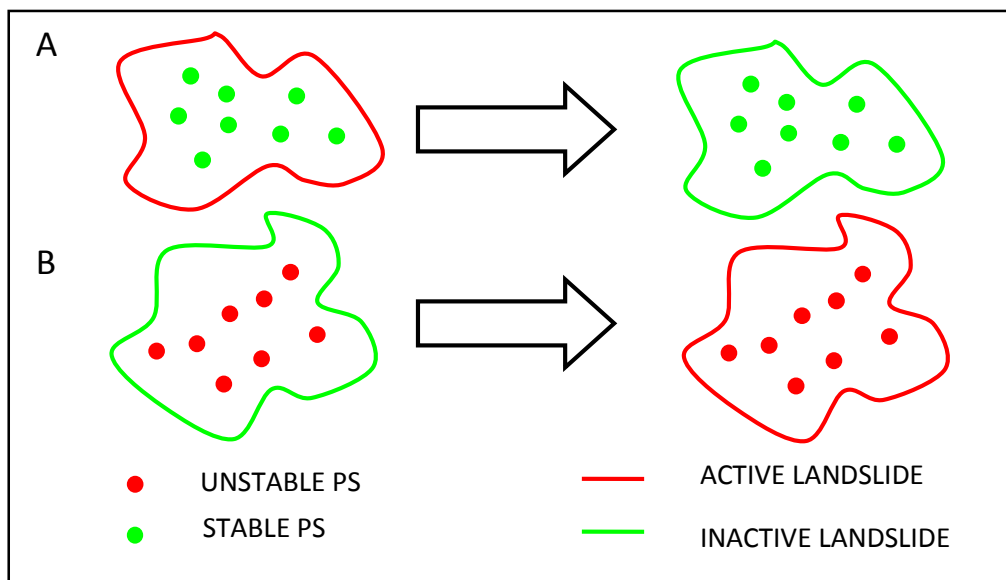


Figure 74: Cases of non-correlation between the activity state of the landslide indicated in the existing inventory and the information provided by the PS. The activity status of the landslide shown in the preexisting inventory is changed from active to inactive (A) and from inactive to active (B).

SEPARATION OF A PORTION OF LANDSLIDES: there is no correlation between the activity state of the existing inventory map and the information derived from interferometric data. In case of different thickening of PSs a part of the landslide can be isolated and considered to be independent of the starting landslide; an independent unstable area is perimeter.

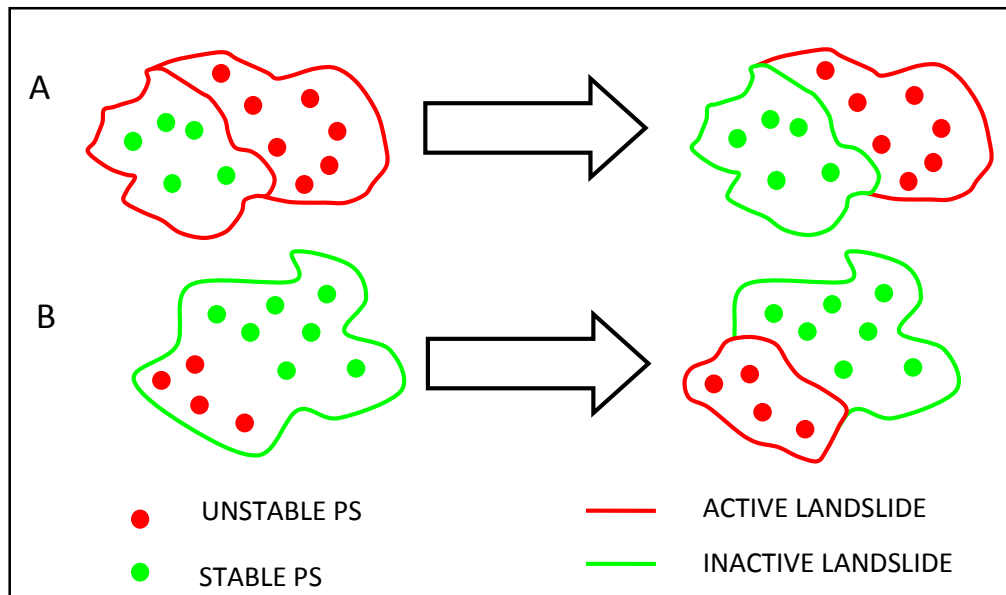


Figure 75: cases of non-correlation between the activity status of the landslide indicated in the existing inventory and the information provided by the PSs. Both stable and instable PSs are concentrated in two distinct areas of the existing landslides; the two portions are separated varying the activity status. Case A: an active landslide is separated from an inactive portion. Case B: an inactive landslide is separated from an active portion.

The classification of the activity of landslides proposed in the Multilingual Landslide Glossary (WP/WLI, 1993) includes the states reported below.

- “Active”, for a landslide that is currently moving;
- “Suspended”, for a landslide that has moved within the last 12 months (last seasonal cycle), but is not active at present;
- “Reactivated”, for a phenomenon that is now active, after being inactive;
- “Inactive”, for a landslide that is not moved within the last 12 months and can be divided into 4 more states, described below.
 - “Dormant” (an inactive landslide, which can be reactivated by its original causes or other causes).
 - “Abandoned” (an inactive landslide, which is no longer affected by its original triggering causes).

- “Stabilized” (an inactive landslide, which has been protected from its original causes by remedial measures, naturally or artificially).
- “Relict” (an inactive landslide, which developed under climatic or geomorphological conditions considerably different from those at present, i.e. a “paleo-landslide”).

An innovative methodology for the evaluation of the “state of activity” and the “intensity” of slow-moving landslides is the matrix approach, based on the use of PS measurements. It has conceived within the Earth Sciences Department of the University of Firenze, and applied on several test sites in the framework of national and international projects (Farina et al., 2006; Casagli et al., 2008).

This approach is based on the classification of the “state of activity” provided by the Multilingual Glossary for Landslides (WP/WLI, 1993) and its applicability is limited to extremely slow (velocity < 16 mm/year) and very slow landslides (16 mm/year < velocity < 1.6 m/year), according to Cruden and Varnes (1996).

The “intensity” of a landslide is a difficult parameter to be evaluated since many features must be accounted.

Hungr (1997) defines the intensity as the destructiveness of a landslide, in terms of energy volume, area, depth, movement velocity or total displacement.). Intensity expresses the geometrical and mechanical severity of a landslide, associated with its destructive power. The intensity is considered depending upon kinetic energy, mass and/or velocity (Hungr, 1995). At basin scale, the intensity is not easily measurable, due to the lack of detailed information on volume and expected velocity for a large number of landslides (Catani et al., 2005).

Usually, the landslide intensity assessment refers to range scales based on possible consequent damages (Canuti and Casagli 1996, Cruden and Varnes 1996).

Hungr (1981), in his scale, provides specific velocity thresholds associated with the different classes, modified by Cruden and Varnes (1996) and adopted by the IUGS/WGL (1995). In this context, the landslide intensity can be is assessed by PSI data in terms of movement velocity (Righini et al., 2012).

The operational methodology, which has been recently used within several scientific works (Cigna et al., 2010; Righini et al., 2012; Bianchini et al., 2012, Frangioni et al., 2013), is performed by a “PSI-based matrix”, integrating qualitative (state of activity) and quantitative information (intensity) of the phenomenon at hand.

Firstly, a representative velocity value is determined, for each landslide, through the analysis of available PS data. These representative values, in terms of LOS deformation velocity (mm/year), are referred to the coverage time of satellite acquisitions; for each landslide the values are determined by calculating the average velocity of all the PS included within its boundary.

Then, the representative ground motion rates of each landslide are compared to some displacement thresholds (± 2 mm/year in the LOS direction, away or towards the satellite), whose values depend on the characteristics of each application (landslide main typology, InSAR data, measurement accuracy, distance from reference point), for distinguishing 'moving' from 'not moving' phenomena.

Finally, the state of activity and intensity are assigned through the use of one matrix and one scale (for activity and for intensity evaluations, respectively), which are defined in terms of velocity and acquisition time and consist of cell grids with different velocity combinations, whose inputs are past or present PS velocities or/and information coming from pre-existing inventories.

The first attempt of activity matrix makes use of an activity cell-grid, whose inputs are InSAR measurements of past (ERS 1/2) and present (ENVISAT) displacement. Representative ground motion values of each landslide are compared to the velocity threshold of 2 mm/year, and finally, by means of the matrix, the state of activity is determined (figure 76).

The threshold of 2 mm/year is precautionary chosen as the minimum value exceeding the precision of the PSI technique, as found also within other works (Meisina et al. 2007, 2008; Cascini et al., 2009; Cigna et al., 2010; Righini et al., 2012).

The intensity scale is defined in terms of mean yearly velocity and consists of three different classes: 'negligible', 'extremely slow' and 'very slow' (Cruden and Varnes, 1996). It is worth to highlight that the deformation threshold discriminating the two classes of extremely slow and very slow movements is adjusted from 16 mm/year (Cruden and Varnes, 1996) to a lower value, e.g. 10 mm/year due to the underestimation of real movements produced by PSI techniques, which estimate the displacement rates along the LOS direction.

Thus, LOS measured displacements generally differ from the actual direction of landslide motion. Moreover, a further underestimation of landslide movements occurs during the assessment of landslide representative rates, which are computed as average velocities, both spatially (averaging the measures from different PS within the same landslide area) and temporally (assessing yearly rates).

An explanation and application of the results obtained with the use of the activity matrix is carried out in the Annex (Frangioni et al., 2013).

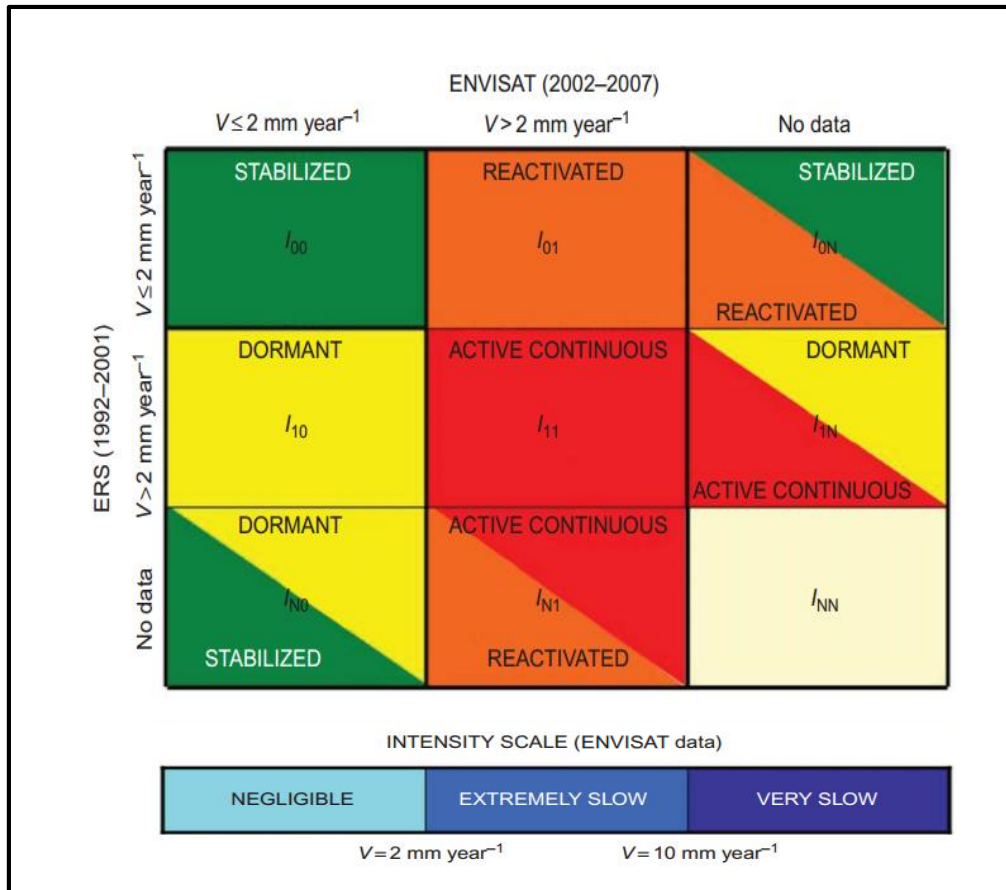


Figure 76: Activity matrix and intensity scale.

5.3.3 DETECT BUILDINGS POTENTIALLY DAMAGED BY LANDSLIDES

The buildings are one of the more suitable targets to be detected as persistent scatterer. The presence of buildings on landslides in many areas is the only possibility to have data of displacement using the SAR techniques.

At the same time PSI technique may be used in a faster way and on a large scale to detect the buildings potentially damaged by landslides movements. This requires a good inventory of buildings and PS database having good georeferencing.

The distribution of the value of the PS velocity on buildings may be also used to discriminate geological process. For instance, a strong movement distributed over all the buildings of village is probably related to a landslide; on the other hand, a pattern of irregular movements is probably related to a local geotechnical or structural problem. The correlation between damaged buildings, landslides and movement registered by PS on a regional analysis is not easy to understand because it is complex and depends from many factors. Only with the studies at a local scale, it is possible to verify this correspondence.

In relation to the area test of Le Braine, well explained in the below attached paper (chapter 5.2), an analysis on the building interested by the landslide was carried out. Along the perimeter of the building, the cracks are continuous from one side of the structure to another and which are found in the rear of the building.

On this building, an analysis of the effects that the landslide leads to the structure was made and consequently the settling of it in relation to the impact of ground motion. The classification used to represent the damages due to the landslide is of qualitative type (Alexander, 1989). Starting from the fractures on a building, that are represented using a standard symbology, (figure 77), it is possible highlight the type of tension mainly agent.

X Appendix 2			
<i>Symbols for depicting damage to building elevations</i>			
\rightleftharpoons	shearing	\rightrightarrows	unidirectional
$\leftarrow \rightarrow$	dilation (extension)	$\leftarrow \rightarrow$	(in direction of
$\rightarrow \leftarrow$	compression	$\rightarrow \leftarrow$	larger arrow)

Figure 77: Symbols used by Alexander, 1989 for a description of the fractures caused by the impact of a landslide on a building. From the top left, there are fractures for cutting; for expansion; for compression, unidirectional, in the direction of the larger arrow largest.

The qualitative analysis of the cracks is made for each of the four sides of the building (figure 78 and figure 79), in order to highlight the types of prevalent fracture and therefore to deduce the type of stress acting on the structure.

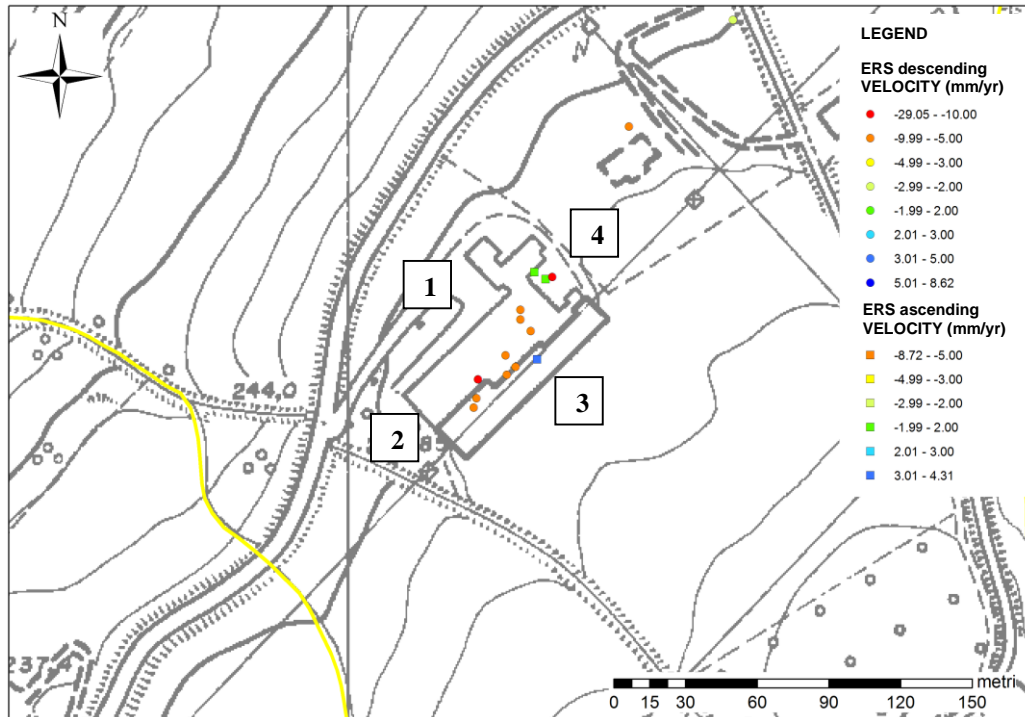


Figure 78: Building on which the analysis by impact is carried out. The numbers indicate the four sides taken into account for the analysis of fractures by impact. ERS data are represented.

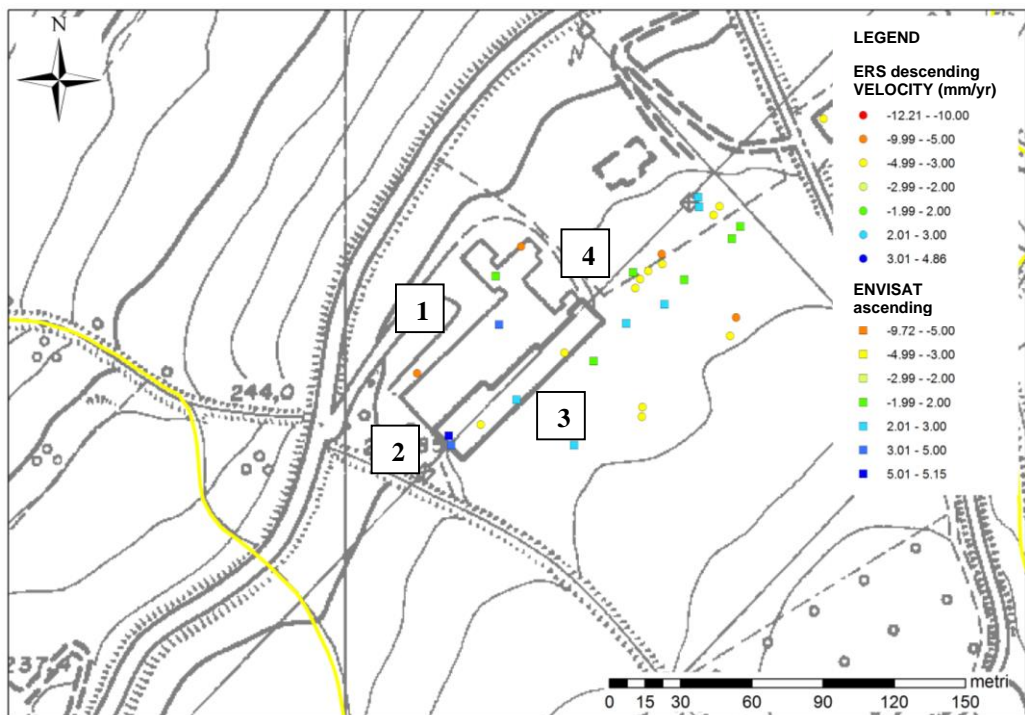


Figure 79: Building on which the analysis by impact is carried out. The numbers indicate the four sides taken into account for the analysis of fractures by impact. ENVISAT data are represented.

In 54 and 55 figures, the results of the analysis carried out are plotted.

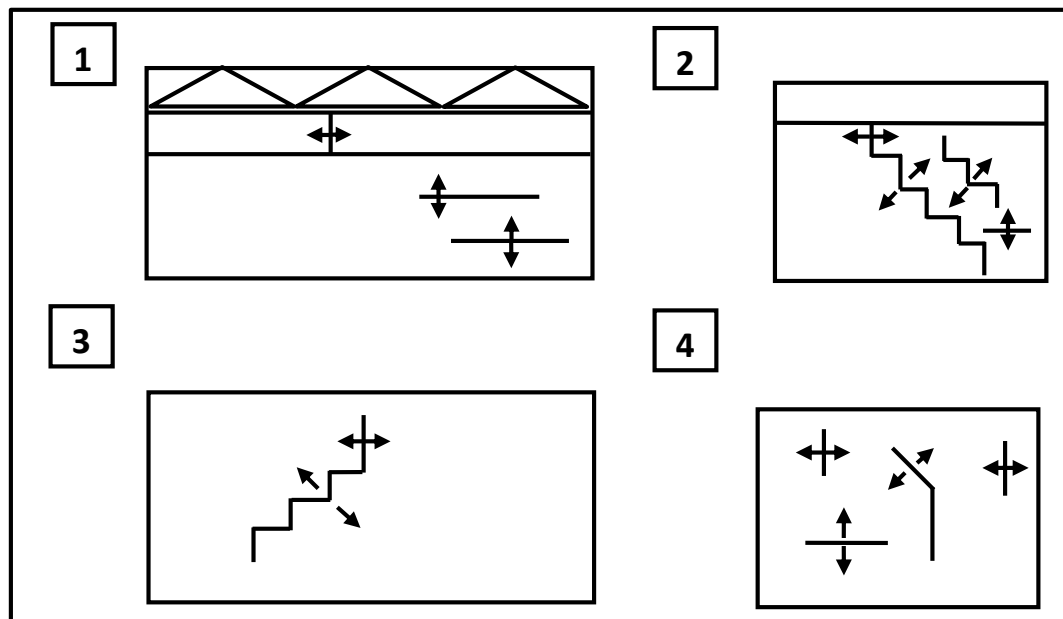


Figure 80: fractures present on each of the four sides of the building. The symbols used to represent the type of fracture refers to the one adopted by Alexander, shown in figure 51.

From the qualitative analysis of the fractures, as represented in figure 80, it is possible to construct, for each side of the building, a table of classification for every fractures (figure 81). In the above table the number of each type of fracture present (number of distension, shear, compressive fractures), of each type of trend of them (number of sub-horizontal, sub-vertical, diagonal fractures), and the summaries of the type and the number of fractures (summaries of cutting, relaxing, and sub-horizontal fractures) are inserted.

From the analysis of fractures, is evident that each of the four sides of the building is mainly affected by relaxing stress (figure 88). In particular is noted that:

- Side “1” → is the front side of the building. Bulges and horizontal and sub parallel fractures (vertical and horizontal) caused by extensional stress are predominant.
- Side “2” → diagonal fractures caused by expansion are predominant;
- Side “3” → is the backside of the building. Vertical and diagonal fractures caused by extensional forces are predominant.
- Side “4” → Vertical fractures caused by extensional forces are predominant.

For the present case, it can be concluded that the characteristic fractures induced by ground subsidence are extensive fractures, with a predominantly sub-parallel (horizontal or

vertical) and diagonal trend and tend to be zoned, concentrated in certain areas of the building; in correspondence to the horizontal fractures also some bulges are.

It can therefore be assumed that the building is located in an area of the landslide affected by prevailing extensional component, which can be located in a central sector downstream of the crown area and upstream of the accumulation zone.

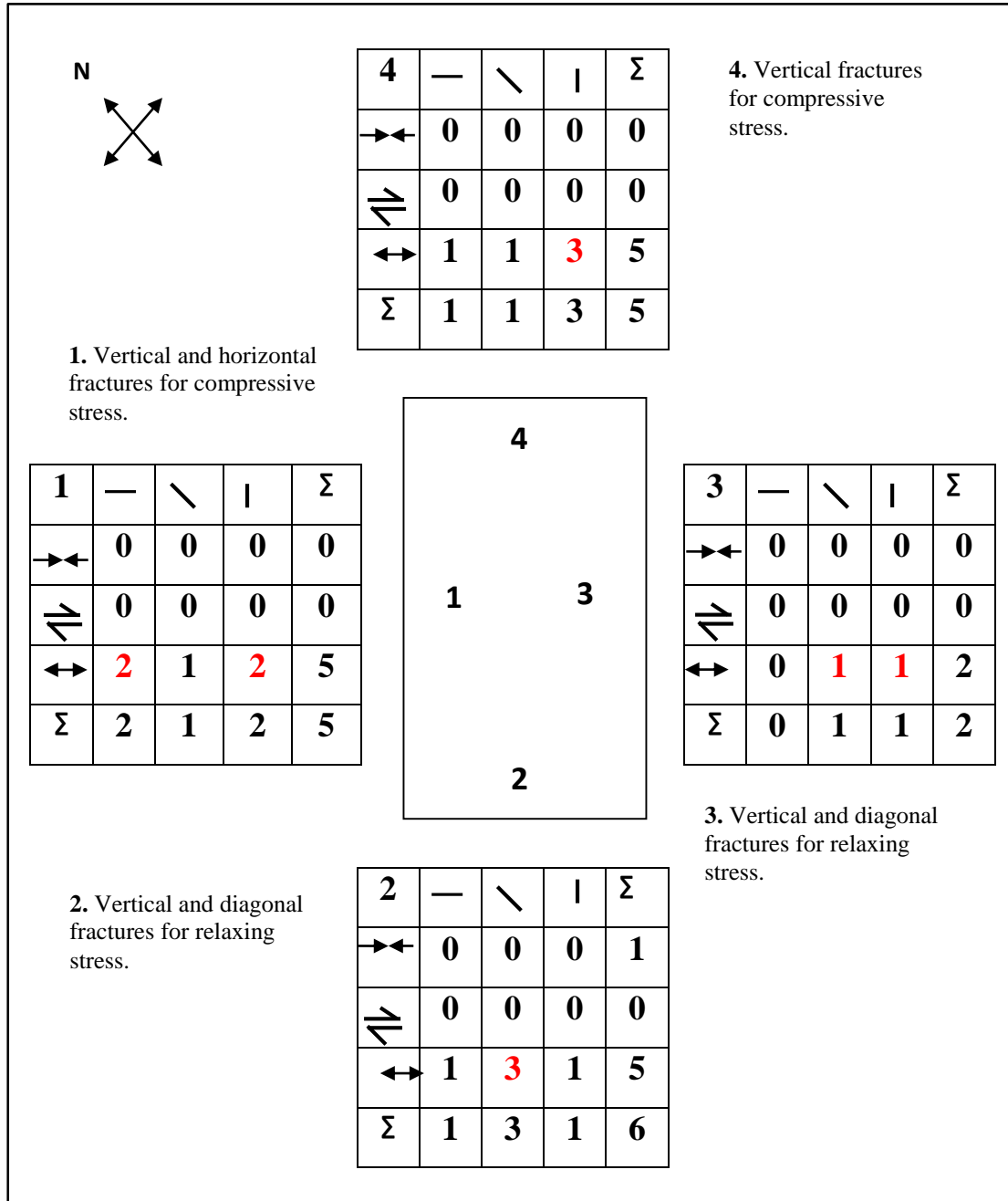


Figure 81: Graphic representation of numeric arrays that have been used to verify the type of prevalent fracture. The fracture is classified with two parameters: the first is the type of stress (relaxing, compressive, shear); the second is the type of the fracture (sub-horizontal, sub-vertical diagonal). The red numbers indicate the predominant type of fracture.

5.4 AN EXAMPLE OF UPDATING OF A LANDSLIDES INVENTORY

In this section is reported an example of updating of a landslides inventory. PS technique applied to the updating of landslides inventories.

5.4.1 Basin scale: Setta Basin

The case of study is an analysis over the wide areas of Setta Basin, Emilia Romagna Region. Considering only the mountainous and hilly sectors, the surface analysed had an extension of about 268 km².

The PS data were produced with PSInSARTM techniques using ERS and ENVISAT sensors; more than 10 thousand of PS cover the area under study.

First, we created a database and then we used the interferometric data in the landslides analysis. In particular, we updated the landslides inventory of the Setta Basin with PS data. The final updated landslide database of the Setta basin, based on Persistent Scatterer Interferometry analysis and in situ checks, consists of 1550 landslides, 236 of which have persistent scatterer information.

The landslides within the Setta basin, analysed by means of PSI technique, are 236 of which 223 were already mapped in the pre-existing landslides inventory map.

The classification of the landslides that contain PS is made with a matrix of the activity states; this matrix is well represented and explained in the attached paper "*Landslide inventory updating by means of Persistent Scatterer Interferometry (PSI): the Setta basin (Italy) case study*".

In this work, we have reclassified the state of activity of the landslides, both the 236 pre-mapped landslides and the 13 newly detected phenomena, by means of the activity matrix in relation to the PS velocities.

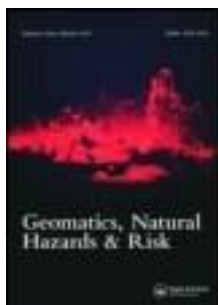
The landslide database updated with PS information includes 19 continuous active phenomena (8%), 9 reactivated (3.8%), 6 continuous active/reactivated (2.5%), 27 continuous active/dormant (11.4%), 55 reactivated/stabilized (23.3%), 14 dormant (5.9%), 26 dormant/stabilized (11.1%) and 80 stabilized (33.9%)

The aspect more interesting of the interpretation of PS data and the results of the interpretation in the Setta Basin are better described in the attached paper of [Frangioni et al., \(2013\)](#).

>5.5 ATTACHED PAPER.

“Landslide inventory updating by means of Persistent Scatterer interferometry (PSI): the Setta basin (Italy) case study” - Geomatics, Natural Hazards And Risk 2014

This article was downloaded by: [Universita Degli Studi di Firenze], [Sara Frangioni]
 On: 15 January 2014, At: 08:01
 Publisher: Taylor & Francis
 Informa Ltd Registered in England and Wales Registered Number: 1072954 Registered
 office: Mortimer House, 37-41 Mortimer Street, London W1T 3JH, UK



Geomatics, Natural Hazards and Risk

Publication details, including instructions for authors
 and subscription information:

<http://www.tandfonline.com/loi/tgnh20>

Landslide inventory updating by means of Persistent Scatterer Interferometry (PSI): the Setta basin (Italy) case study

Frangioni Sara^a, Bianchini Silvia^a & Moretti Sandro^a

^a Earth Sciences Department, University of Firenze, Via La Pira 4,

50121 Firenze, Italy

Published online: 13 Jan 2014.

To cite this article: Frangioni Sara, Bianchini Silvia & Moretti Sandro , Geomatics,
 Natural
 Hazards and Risk (2014): Landslide inventory updating by means of Persistent Scatterer
 Interferometry (PSI): the Setta basin (Italy) case study, Geomatics, Natural Hazards and
 Risk, DOI:

[10.1080/19475705.2013.866985](https://doi.org/10.1080/19475705.2013.866985)

To link to this article: <http://dx.doi.org/10.1080/19475705.2013.866985>

PLEASE SCROLL DOWN FOR ARTICLE

Taylor & Francis makes every effort to ensure the accuracy of all the information (the "Content") contained in the publications on our platform. However, Taylor & Francis, our agents, and our licensors make no representations or warranties whatsoever as to the accuracy, completeness, or suitability for any purpose of the Content. Any opinions and views expressed in this publication are the opinions and views of the authors, and are not the views of or endorsed by Taylor & Francis. The accuracy of the Content should not be relied upon and should be independently verified with primary sources of information. Taylor and Francis shall not be liable for any losses, actions, claims, proceedings, demands, costs, expenses, damages, and other liabilities whatsoever or howsoever caused arising directly or indirectly in connection with, in relation to or arising out of the use of the Content.

This article may be used for research, teaching, and private study purposes. Any substantial or systematic reproduction, redistribution, reselling, loan, sub-licensing, systematic supply, or distribution in any form to anyone is expressly forbidden Terms & Conditions of access and use can be found at

<http://www.tandfonline.com/page/termsand-conditions>

Landslide inventory updating by means of Persistent Scatterer Interferometry (PSI): the Setta basin (Italy) case study

FRANGIONI SARA*, BIANCHINI SILVIA and MORETTI SANDRO

Earth Sciences Department, University of Firenze, Via La Pira 4, 50121 Firenze, Italy

(Received 10 July 2013; accepted 12 November 2013)

This paper illustrates the contribution of Persistent Scatterer SAR Interferometry (PSInSAR) technique to landslide detection, using interferometric data acquired in C-band by European remote-sensing satellite (ERS) 1/2 and environmental satellite (ENVISAT) satellites. The main purpose is to update a pre-existing landslide inventory map, by changing or confirming the landslide geometry and state of activity and eventually, identifying new phenomena.

This work presents an application of satellite remote sensing to analyse ground displacement movements in the Setta basin, located on the northern Apennine (Bologna province, Italy) and extended up 268 km².

The proposed methodology, resting upon pre-existing works already consolidated in the scientific community, combines interferometric measures with aerial imagery and other auxiliary data, in order to detect landslide indicators, finally validated with field surveys. The use of an activity matrix allows the identification of the state of activity of landslide phenomena with respect to the velocity of the radar displacement rates. Field validations are carried out in the areas that are more relevant because of the highest ground velocities and the presence of structures extensively affected by ground movements.

The final updated landslide database of the Setta basin, based on Persistent Scatterer Interferometry analysis and in situ checks, consists of 1550 landslides, 236 of which have persistent scatterer information.

1. Introduction

Natural hazard databases, such as landslide inventories, are essential for risk management purposes, since they allow improving systems of phenomena indicators and maps on disaster vulnerability, at national and sub-national (i.e. regional and basin) scales.

Landslide inventory maps show the spatial distribution of past and current landslides and often include information about their typology and state of activity (Wieczorek 1984). Landslide databases are crucial to assess landslide hazard, susceptibility and risk within an area (Aleotti & Chowdhury 1999; Dai et al. 2002). However, landslide inventories may have different spatial resolution and detail, according to the different goals, scales and data collection methods. In Italy, the official landslide

*Corresponding author. Email: sara.frangioni@unifi.it
2014 Taylor & Francis

inventories provided by local authorities are usually based on documental sources, historical archives, aerial orthophotos analysis and geomorphological surveys (Crozier 1984; Soeters & Van Westen 1996).

The IFFI project (Inventory of Landslide Phenomena in Italy), carried out by ISPRA (Istituto Superiore per la Protezione e la Ricerca Ambientale) (ISPRA 2007) and the Regions and Autonomous Provinces, supplies a detailed picture of the distribution of landslide phenomena within Italy, aiming at identifying and mapping landslides over the whole national territory, based on standardized criteria.

An environmental analysis within the updating of these existing landslide inventory maps needs to be performed. The landslide spatial extensions are often not up to date and, moreover, landslide classification and validation strategies (Guzzetti et al. 1999; Agnesi et al. 2012) need to be optimized for phenomena assessment procedures at regional and local scales. Synthetic aperture radar (SAR) techniques, such as Persistent Scatterer Interferometry (PSI), can offer great support in the implementation of landslide inventory maps, since they provide ground displacement data that are characterized by rapid and easily updatable measurements, very high (millimetre) accuracy, great spatial resolution (up to 1 m), good temporal radar data availability (starting from 1992 up to present, with monthly acquisitions) and wide area coverage, consequently reducing efforts, fieldwork and costs.

A new approach for the updating of pre-existing landslide inventories has been recently developed and experimented (Farina et al. 2004, 2006; Righini et al. 2012), combining traditional geomorphological thematic information (e.g. topographic, geological, land use maps, optical images) and in situ observations with ground displacement data obtained through PSI analysis. This operational methodology, which has been successfully tested and used within several scientific applications (Meisina et al. 2006; Pancioli et al. 2008; Herrera et al. 2009, 2010; Cascini et al. 2009; Cigna et al. 2010, 2013; Notti et al. 2010; Bianchini et al. 2011, 2012; Righini et al. 2012) is based on the coupled radar-interpretation and photo-interpretation procedures (Casagli et al. 2008; Farina et al. 2008; Pancioli et al. 2008; Herrera et al. 2009) and on the classification of the landslide state of activity (WP/WLI 1993; Cruden & Varnes 1996), integrating qualitative and quantitative information of the phenomenon at hand.

This paper, resting upon the recent studies and scientific works carried out in the last years, shows the contribution of European remote-sensing satellite (ERS) and environmental satellite (ENVISAT) persistent scatterers (PS) data for the spatial and temporal updating of a pre-existing landslide inventory map in the Setta basin within Bologna province in central Italy.

In this work, an application of the recent matrix-based methodology (Bianchini et al. 2012; Righini et al. 2012; Cigna et al. 2013) for characterizing landslides geometry and activity throughout PS measures is performed. A field survey is carried out in the areas that showed the highest PS ground motion rates affecting buildings and manufactures: in situ checks confirmed the SAR data results, finally validating and updating the landslide inventory map within the whole Setta basin.

The updated landslide database can represent a useful tool for future landslide hazard assessment, since it could be used and integrated in land use management and civil protection policies by environmental authorities, in order to identify landslide-prone areas and eventually to prevent and mitigate landslide occurrences in the investigated basin.

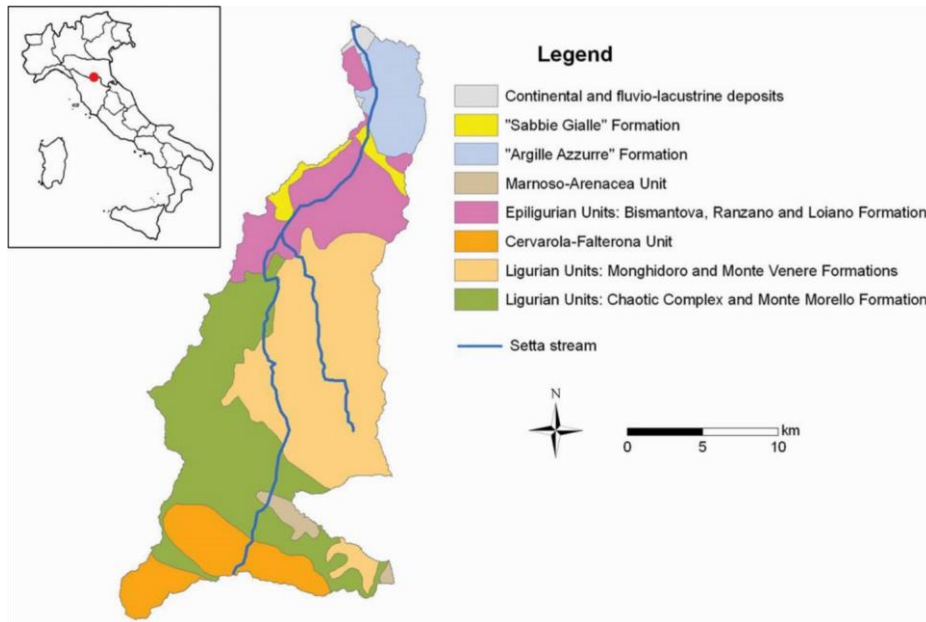


Figure 1. Study area: Location and geological sketch map of the Setta basin.

2. Case study area

The case study area, extended up 268 km², is the Setta basin, which is located in the southern Emilia-Romagna region in central Italy on the northern Apennine within Bologna province; the investigated territory includes the watershed of Setta stream, which is the right tributary of the Reno river (figure 1).

The northern Apennine belt is part of the major orogenic Apennine system of the Italian peninsula. It is composed of mostly NE-verging tectonic units piled up first during the Cretaceous–Eocene pre-collisional convergence, and then during the Oligocene–Neogene collisional steps of the Apennine orogenic development.

The terrains outcropping in the investigated area are mainly represented by metapelitic–carbonate succession belonging to the Ligurian domain, turbiditic sandstones–marls succession belonging to the Tuscanian domain (Cervarola–Falterona unit) and clay–sandy deposits of the Epiligurian domain (figure 1).

The oldest and uppermost tectonostratigraphic sequence is composed of Jurassic to Eocene–Ligurian units that were originally deposited in the Ligurian–Piedmont ocean and progressively accreted at the convergent orogenic margin (Principi & Treves 1984). Ligurian units in the test area include ophiolites, which are made of gabbros and serpentines scattered in the undifferentiated chaotic complex, and their sedimentary cover, i.e. Monte Venere and Monghidoro formations: these successions are, respectively, Paleocene calcareous–marly turbidites and arenaceous–shaly turbidites, and crop out in the eastern portion of the area of interest (figure 1).

The Ligurian units tectonically overlie the Cervarola–Falterona unit that represents the detached top of the Tuscan succession; Cervarola–Falterona sequence is made of Lower Miocene deep-sea silicoclastic sediments that accumulated in the eastward migrating foredeep basin developing in front of the Apennine orogenic wedge (Remitti et al. 2007). The tectonic Ligurian and Tuscan nappes stack in the northern Apennine is unconformably overlain by Eocene to Pliocene Epiligurian units, deposited in marine thrust-top piggyback basins (Ricci Lucchi 1986; Barchi et al. 2001; Cibi et al. 2001). Epiligurian units, which outcrop in the central-northern part of the investigated area, consist, from bottom to the top, of Bismantova formation (Lower-Middle Miocene), Ranzano sandstones (Oligocene) and

Loiano sandstones (Lower Miocene), and are mostly made of siliciclastic and bioclastic marly–silty sediments, alternating with pelitic-arenaceous and arenaceous bodies, calcarenites and sandstones (Bettelli et al. 2002).

Clay marine sediments, known as “Argille Azzurre” formation deposited in Lower-Middle Pliocene, also crop out in the northern portion of the study area. Above the “Argille Azzurre”, the Pleistocene “Sabbie Gialle” deposits, made up of yellowish sands with clays, finally close the sedimentary sequence, also outcropping in the northern portion of the investigated basin (Bargossi et al. 2004) (figure 1).

Overall, the geological setting of the Setta basin is characterized by clay and alternated clayey, silt and sandy formations that have poor geotechnical characteristics, triggering the occurrence of many shallow slow-moving ground movements.

3. Materials and methods

3.1. Methodology

Nowadays interferometric radar approaches represent a powerful tool to study movements on the Earth’s surface. Thus, classical surveying techniques have recently been complemented by satellite SAR data analysis for detecting, monitoring and mapping landslide phenomena (Gabriel et al. 1989; Bamler & Hartl 1998; Rosen et al. 2000). In particular, PSI is an advanced multi-temporal interferometric technique that analyses long temporal series of SAR images, providing annual velocities along the satellite line of sight (LOS) on a space grid of stable pointwise targets, hereafter called PS (Ferretti et al. 2001). The methodology used in this work follows the approach proposed by Farina et al. (2006) and Righini et al. (2012), based on the integration of conventional geomorphological tools with satellite radar data.

The methodology is summarized in the flow chart in figure 2.

As a preliminary phase, all the available data, i.e. radar data, landslide database and additional geo-thematic data, are collected and implemented in a GIS (geographic information system) environment. Thereafter, on the basis of pre-existing inventory map and PS distribution, the combined radar-interpretation and aerial photo-interpretation procedures (Farina et al. 2006; Casagli et al. 2008; Pancioli et al. 2008; Herrera et al. 2009) allow the detection and mapping of landslides, validated through field survey.

Once mapped the spatial distribution of landslides, the state of activity is also evaluated for each phenomenon (figure 2).

The landslide activity assessment is performed by means of a PSI-based matrix approach.

The activity matrix is defined in terms of velocity and acquisition time and follows the approach proposed by Righini et al. (2012) and Cigna et al. (2013) (figure 3).

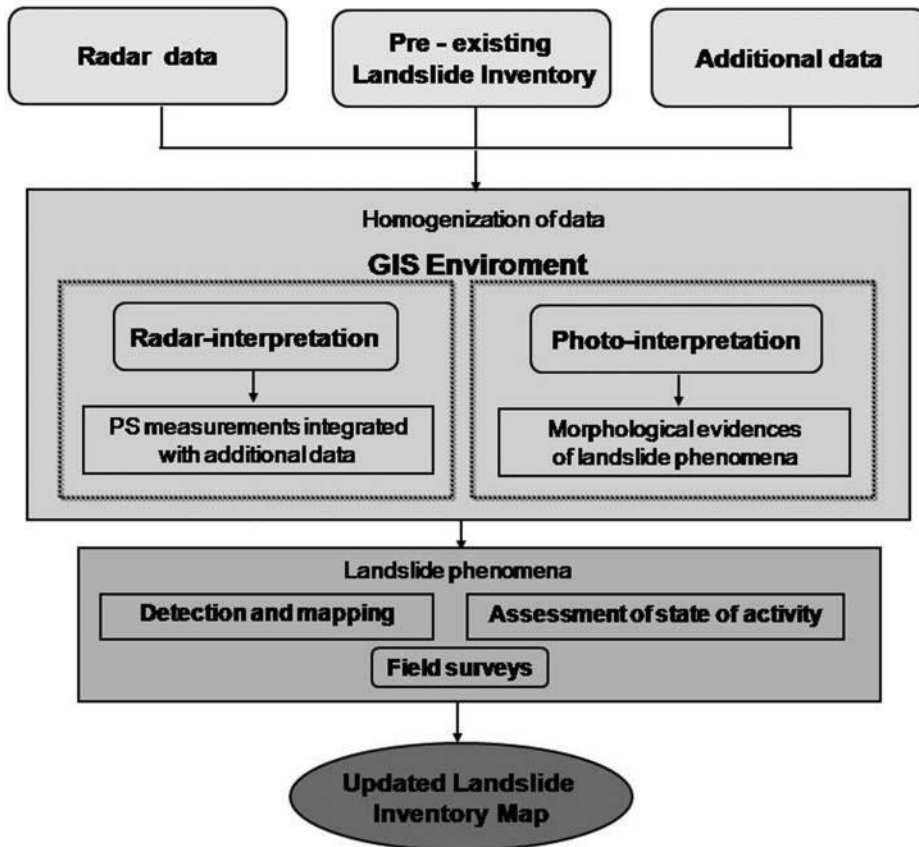


Figure 2. Flow chart of the methodology.

For every phenomenon, a representative velocity is assigned by calculating the average velocity of all the PS included within its boundaries; this velocity is compared with a threshold that is chosen as 2 mm/year to evaluate the state of activity, according to the cell grid of the matrix (figure 3). The 2 mm/year threshold corresponds to the minimum value exceeding the precision of the PSI technique. It is worth to highlight that the current satellites can only measure movements up to few decimetres per year, due to their technical parameters (i.e. signal wavelength, revisiting time).

Thus, the characterization of the landslides is only focused on extremely slow and very slow landslides, according to the velocity classification of Cruden and Varnes (1996).

The activity matrix proceeds from the combination of the landslide velocities derived from the PS ground displacement rates extracted by ERS and ENVISAT satellites for the two time periods, i.e. past and recent intervals, respectively, from 1992 to 2001 for ERS, and from 2002 to 2007 for ENVISAT.

Therefore, each landslide is characterized by two velocity rates related to the ERS data and ENVISAT data; in both cases, either the ascending or descending mean velocity is considered, whichever is higher.

		ENVISAT (2003-2008)		
		$V \leq 2$ mm/year	$V > 2$ mm/year	No Data
ERS (1992-2000)	$V \leq 2$ mm/year	STABILIZED I_{00}	REACTIVATED I_{01}	STABILIZED I_{0N}
	$V > 2$ mm/year	DORMANT I_{10}	CONTINUOUS ACTIVE I_{11}	DORMANT I_{1N}
	No Data	DORMANT I_{N0}	CONTINUOUS ACTIVE I_{N1}	CONTINUOUS ACTIVE I_{NN}

Figure 3. Landslide activity matrix based on velocity rates of ERS and ENVISAT data velocity index (I_{xy}): N → no data; 0 → $V < 2$ mm/year; 1 → $V > 2$ mm/year.

The considered velocity classes are two: one is 2 mm/year and the other is >2 mm/year. By combining the two different velocity classes and taking into account the data acquisition period, nine velocity combinations are defined, which correspond to nine different states of activity.

Each combination that identifies a specific state of activity is defined by a velocity index (I_{xy}) composed of two subscripts. The first subscript refers to the mean velocity rate of the ERS data-set, and the second one refers to the mean velocity rate of the ENVISAT data-set. Subscripts can be:

- 0 – velocity from 0 to 2 mm/year;
- 1 – velocity higher than 2 mm/year;
- N – lack of interferometric data.

In the case of missing information from ERS or ENVISAT data, the new state of activity is considered as undetermined between two states of activity, resulting in a double name in four matrix cells. If ERS data (past information) indicate velocity higher than 2 mm/year, but there is a lack of ENVISAT data (recent information), then the landslide state of activity could be either “active continuous” or “dormant” since the present behaviour of the phenomenon is unknown. If ERS data indicate velocity equal or lower than 2 mm/year and there is a lack of ENVISAT data, then the landslide state of activity could be either “reactivated” or “stabilized”. On the other hand, if a lack of ERS data exists, while ENVISAT rates indicate stability (velocity in the range of 0–2 mm/year), then the state of activity could be either “dormant” or “stabilized”. If there is a lack of ERS data, but ENVISAT data indicate a ground movement (velocity higher than 2 mm/year), then the state of activity could be either “continuous active” or “reactivated”. In these cases, further

Table 1. Interferometric data derived from SAR images of ERS 1, ERS 2 and ENVISAT

Satellite and orbit	Acquisition period	missions.		PS density (PS/km ²)
		Images number	PS number	
ERS ascending	26/07/1992 to 26/10/2000	26	1392	5
ERS descending	24/04/1992 to 01/01/2001	76	5733	21
ENVISAT ascending	16/10/2003 to 26/06/2008	25	1510	5
ENVISAT descending	25/01/2003 to 03/05/2008	25	2192	8

information related to the past or recent period is needed to solve the ambiguity.

3.2. Input data

The available input data for the study area are taken from different sources and homogenized in a GIS (figure 2).

The interferometric data derive from SAR images acquired in both ascending and descending orbits by ERS 1/2 and ENVISAT satellites, producing 7125 and 3702 PS, respectively (table 1 and figure 4).

The most significant geomorphological data of the area, useful for identifying counter lines and slope orientations, consist in the topography, which is derived from the Regional Technical Map at 1:5000 scale and the orthophotos, which are based on monoscopic aerial photos acquired by AIMA Italy flight 2000 at a 1:5000 scale (figure 4). A DTM (digital terrain model) made by IGM (Military Geographical

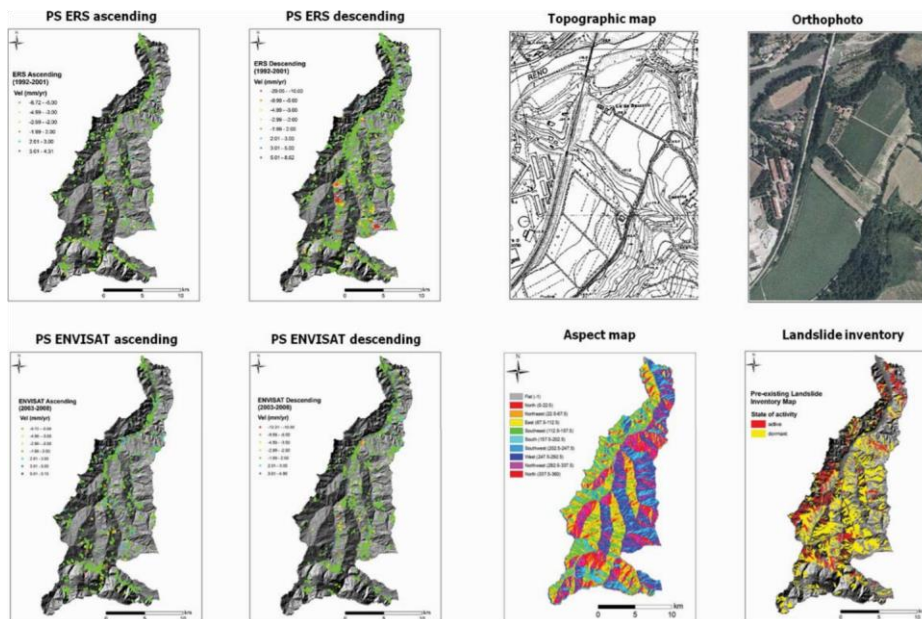


Figure 4. Available input data for the Setta basin study area.

Institute) with a 20 m resolution and a geological map on a 1:50,000 scale are also used as additional layers. From the DTM, we derive the aspect map, which shows the orientation of the slopes with respect to the north direction. The study area is mainly characterized by E–W facing slopes, while N–S-oriented slopes cover very poorly extended zones (figure

4). For this reason, the test area turns out to be suitable to be investigated through radar systems that are side-looking and can better monitor E–W slopes.

The pre-existing landslide inventory map for the Setta basin is derived from the geological survey of Emilia Romagna region at 1:10,000 scale, within IFFI (Inventario Fenomeni Franosi in Italia) project (ISPRA 2007) and dated up to 2003 (figure 4). The total number of recorded landslides is 1537, covering an area of 72 km² (26% of the total basin). The geometry, the typology and the state of activity are provided for each phenomenon. The number of dormant landslides is 886, while the active landslides are 651. The Emilia Romagna region classifies as dormant all the phenomena named “inactive” (dormant, naturally stabilized, artificially stabilized and relict), according to Cruden and Varnes (1996).

4. Field survey

Field validations are essential for verifying the reliability of the radar data interpretation and evidencing the presence of building cracks, counter slopes and geomorphological signs due to landslides. In the area of interest, the field activity was carried out on the following most relevant sites (figure 5): Creda in the municipality of Castiglione dei Pepoli; Le Braine in the municipality of Monzuno; and Pian del Voglio in the municipality of San Benedetto Val di Sambro.

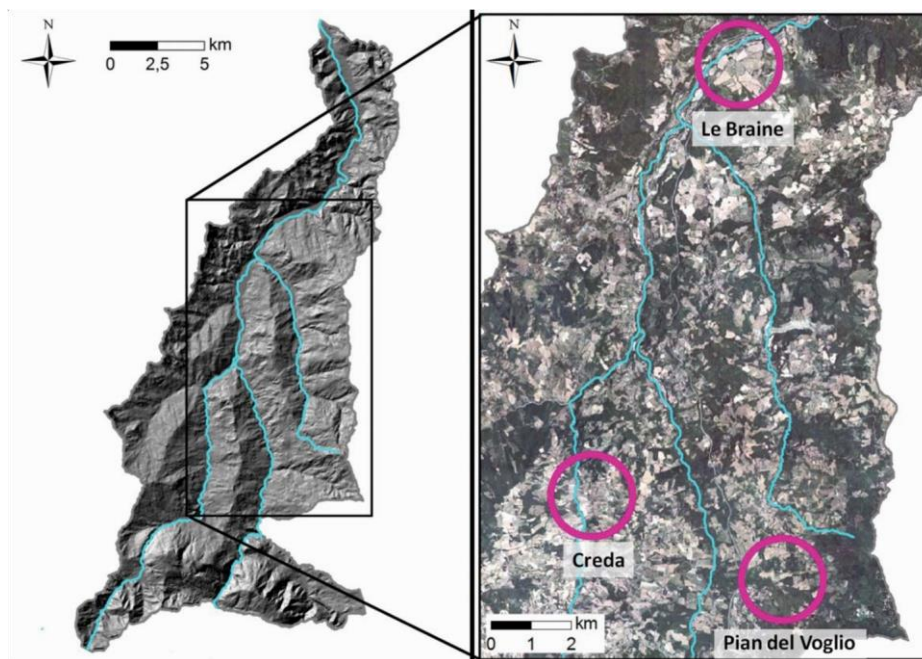


Figure 5. Location of the investigated sites.

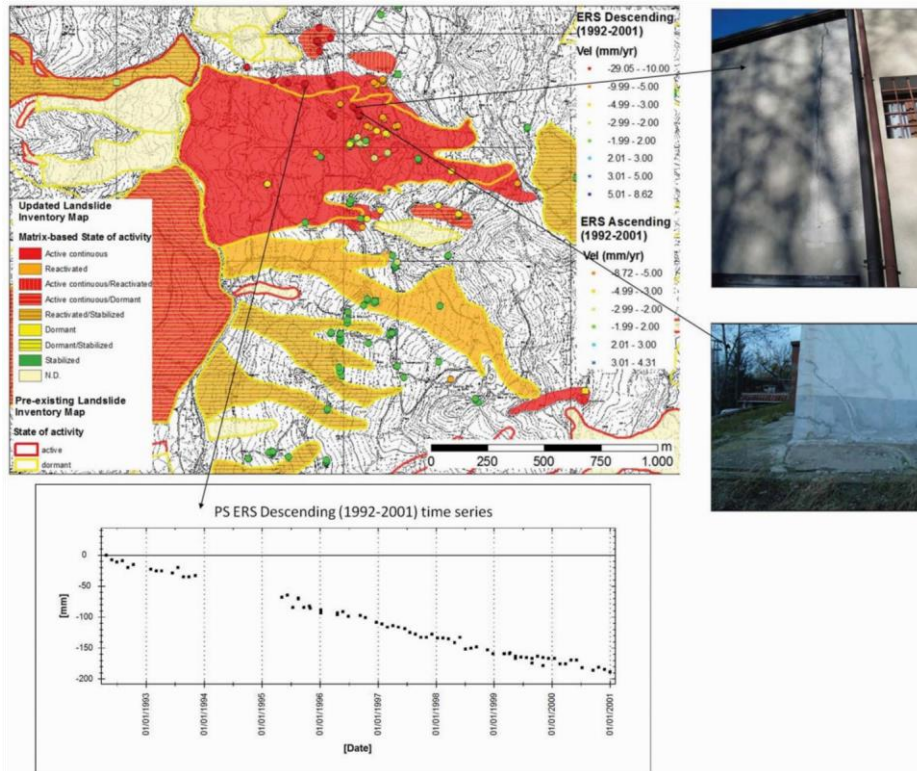


Figure 6. Updated landslide inventory map by means of ERS PS in Creda site.

4.1. Creda site

Creda is located in the municipality of Castiglione dei Pepoli, in the right side of Setta stream. The distribution of the interferometric data reveals that ground movements affect the area (figures 6 and 7). The displacement scenario obtained with ERS data shows that the area was characterized by slope instability with a mean velocity up to 28 mm/year and with a strong displacement pattern in the period 1992–2000 (figure 6). The analysis of the ENVISAT data highlights a slower ground movement with a velocity up to 8 mm/year (figure 7). The radar interpretation and the application of the activity matrix allow the enlargement of a pre-mapped dormant landslide, modified in “continuous active”, and the detection of three new active ones, one “active continuous/reactivated” and two “active continuous/dormant”. During field survey, some damaged buildings and ground surface cracks were found, corresponding to the moving radar benchmarks, which confirm these ongoing movements (figures 6 and 7).

4.2. Le Braine site

Le Braine is located in the municipality of Monzuno and a complex landslide affects the area (figures 8 and 9). The interferometric data included within its geometry show a ground motion displacement in both historical (1992–2001) and recent (2002–2007) temporal periods.

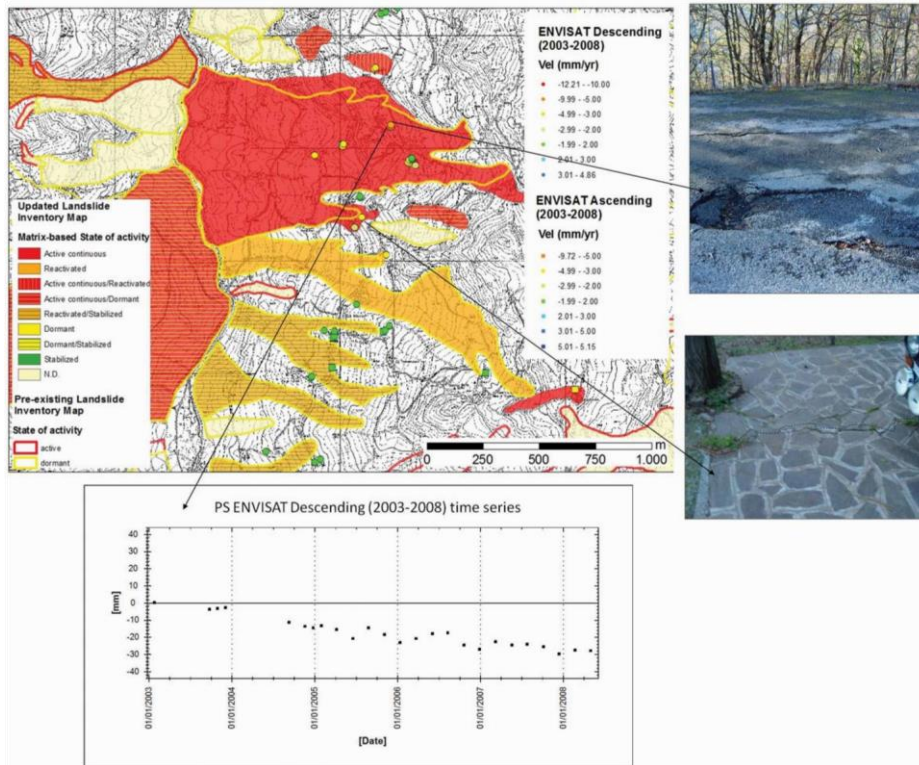


Figure 7. Updated landslide inventory map by means of ENVISAT PS in Creda site.

From 1992 to 2001, the whole area is characterized by consistent displacements with an average velocity of 6.8 mm/year, as shown by ERS data (figure 8).

The PS ENVISAT data-sets reveal not such a significant and constant pattern, but provide displacement with a mean yearly velocity of 4.6 mm (figure 9). In relation to the activity matrix, the state is changed from “dormant” to “continuous active”.

During the survey validation, many geomorphological evidences and indicators of movement (e.g. anomalies in vegetation coverage) were observed in the area; as shown in figures 8 and 9, many cracks are visible on the main road with some little scarps, revealing the instability of the area.

Some of the buildings checked in the area are characterized by many fractures due to the movement of the settlement ground. Moreover, ground motions affect mainly the road network: cracks or scarps in the surface show clear landslide evidence; sometimes the tension cracks expand, determining elongated depression.

4.3. *Pian del Voglio site*

Pian del Voglio is located in the municipality of San Benedetto Val di Sambro, in Bologna province in the right hydrographic side of Setta stream; the area is affected by a landslide phenomenon classified as “dormant” translational slide. The radar velocities within ERS and ENVISAT data-sets and the field checks

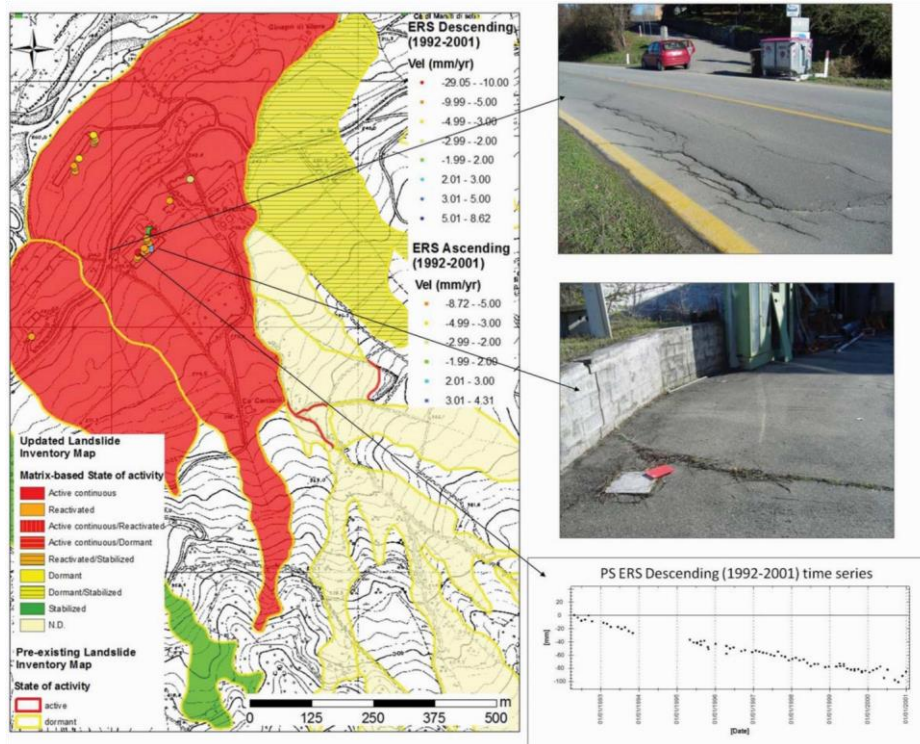


Figure 8. Updated landslide inventory map by means of ERS PS in Le Braine site.

allow confirming this stability, but permit to delineate two active portions at the toe of the main landslide movement, identified as independent from it. The displacement rates reach up values of 10–29 mm/year in the period 1992–2001 (figure 10) and 5–9.99 mm/year in the following period 2002–2007 (figure 11). The PS time series of these two time intervals show a strong temporal evolution trend (figures 10 and 11). The in situ observations show cracks that are clearly referred to the terrain movement. Thus, the two active phenomena are identified as “continuous active”, while the larger already mapped landslide is classified as “stabilized”.

5. Final results

The applied state of activity classification of landslides takes benefit from the effective radar ground motion data. The landslides within the Setta basin, analysed by means of PSI technique, are 236 of which 223 were already mapped in the pre-existing landslides inventory map. In this work, we have reclassified the state of activity of the landslides, both the pre-mapped and the 13 newly detected phenomena, by means of the activity matrix in relation to the PS velocities.

The landslide database updated with PS information includes 19 continuous active phenomena (8%), 9 reactivated (3.8%), 6 continuous active/reactivated (2.5%), 27 continuous active/dormant (11.4%), 55 reactivated/stabilized (23.3%), 14 dormant (5.9%), 26 dormant/stabilized (11.1%) and 80 stabilized (33.9%) (figure 12).

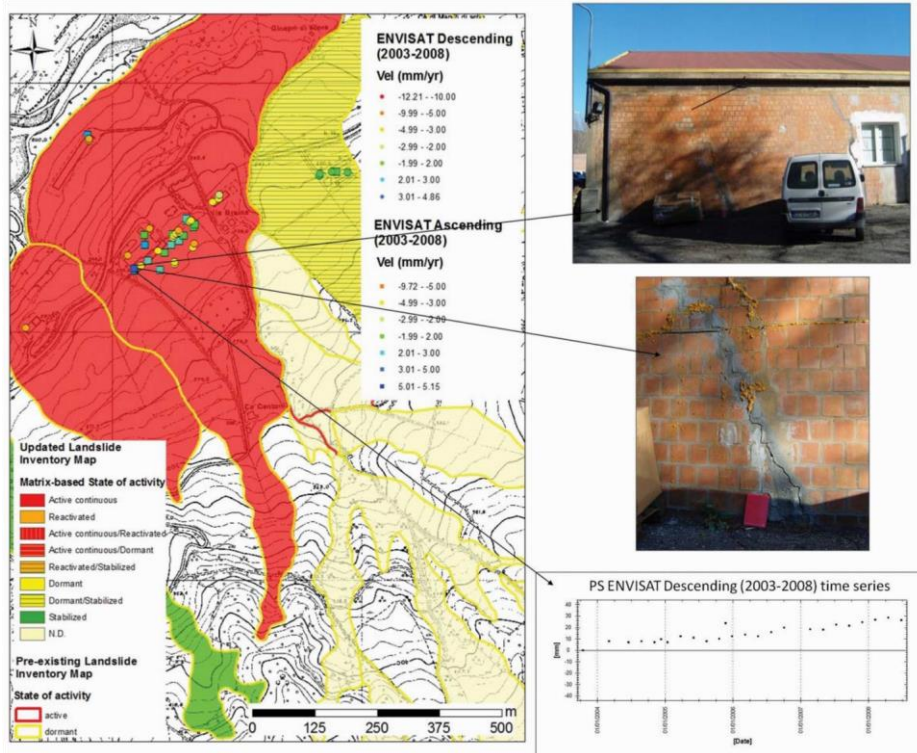


Figure 9. Updated landslide inventory map by means of ENVISAT PS in Le Braine site.

The 28 landslides classified as “active” in the pre-existing landslides database of Emilia Romagna region are reclassified, as we can see in figure 13. In particular 7 landslides are confirmed in the state of activity and boundaries, while 21 landslides are modified both in the state of activity and boundaries.

The 195 landslides classified as dormant by Emilia Romagna region are reclassified as we can see in figure 14. In particular, 82 are the landslides varied in the state of activity and boundaries and 113 confirmed.

Among the 236 landslides with PS information, 134 phenomena are confirmed and 89 modified. Moreover 13 new phenomena were detected and classified as continuous active (3), reactivated (1), continuous active/reactivated (1) and continuous active/ dormant (8). In figure 14, for each state of activity the recorded landslides are counted according to the type of updating (confirm, variation and new detection).

In conclusion, we can summarize that:

- new landslide perimetrates are all “active”;
- there are few confirms for “active” landslides;
- between “inactive” landslides there are many confirms;
- there are many landslides that vary the activity status in “reactivated/ stabilized” and “continuous active/dormant” due to the lower number of ENVISAT data available;
- there are many variations to an “active” status (82).

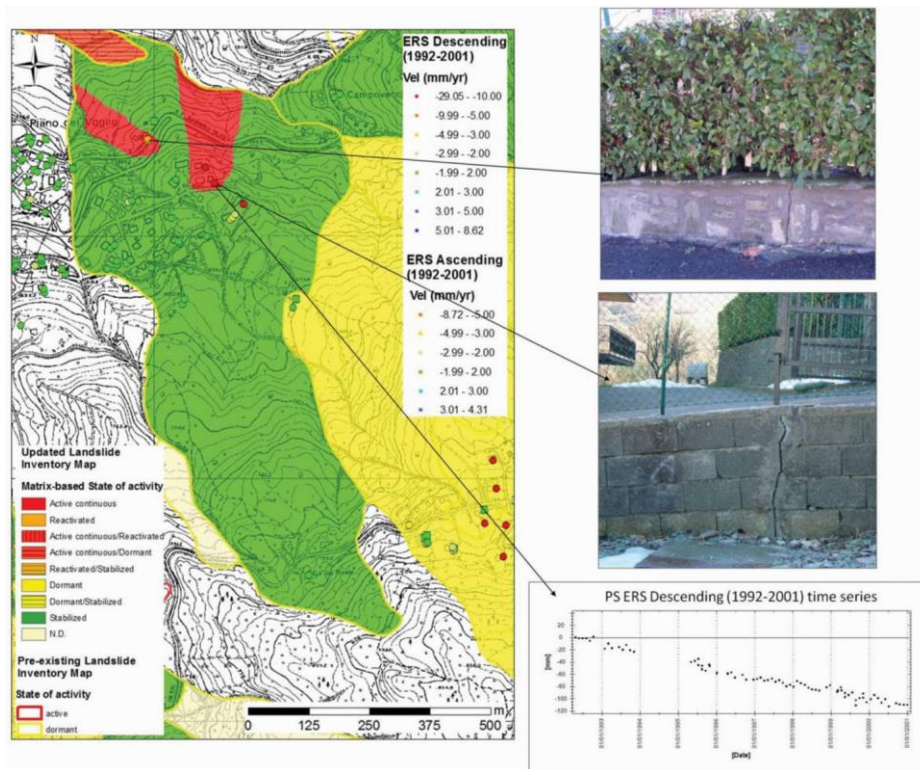


Figure 10. Updated landslide inventory map by means of ERS PS in Pian Del Voglio site.

6. Discussion

This work represents an application of slope instability mapping and updating by means of PSI analysis.

The Setta basin is a typical widespread situation in the Appennine chain in Italy: many small villages are built on hills characterized by soft sediments and affected by landslides that can experience sudden reactivation and acceleration of ground movements, triggered by rainfall and seismic activity.

The satellite orbit (approximately N–S) strongly limits the technique capabilities for detecting processes with N–S direction of movement, because the velocity measured along the LOS can be an underestimate of the real velocity. The study area is characterized by E–W facing slopes and, assuming that mass movements occur along the maximum slope direction, the LOS velocities are reliable for measuring the real displacements. Regarding the availability of radar point targets in the investigated area, the number of SAR images and the consequent low PS density obtained with ENVISAT data, especially for descending orbits, are lower than the ERS one (25 images and 9.23 PS/km² for ENVISAT versus 76 images and 26.27 PS/km² for ERS). Thus, the number of ERS PS within the mapped landslides is significantly higher (1749) than the amount of ENVISAT PS (931). Consequently, the number of the landslides containing ERS PS is 205 with an area of 34 km², while the landslides with ENVISAT PS are 155 covering an area of 27 km².

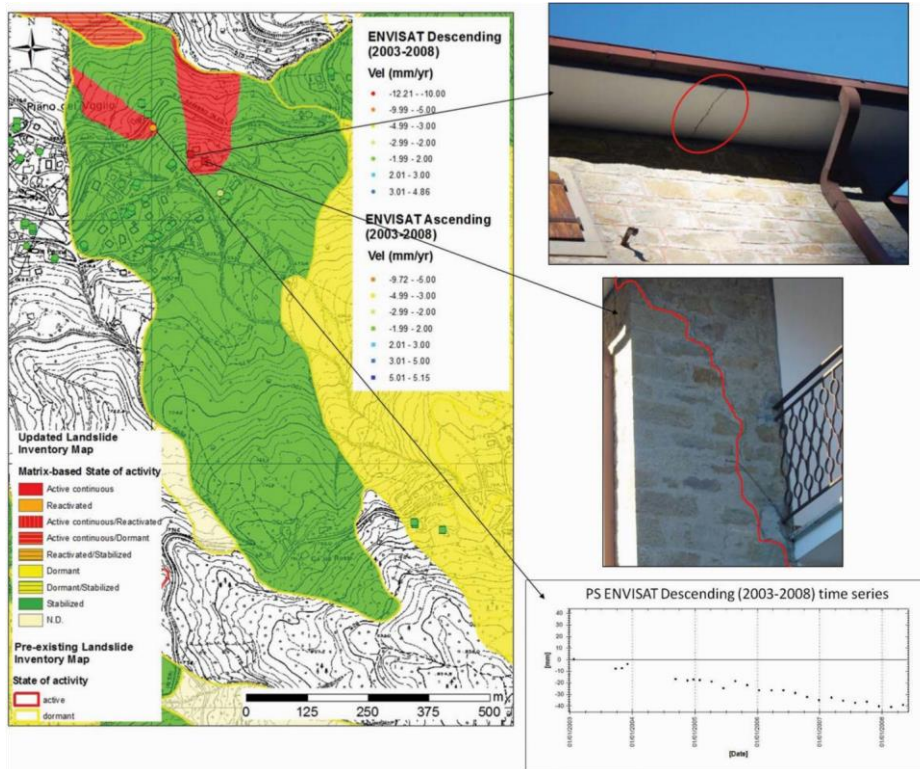


Figure 11. Updated landslide inventory map by means of ENVISAT PS in Pian Del Voglio site.

The recent launches of space-borne SAR missions, such as the X-band missions COSMO-SkyMed (Constellation of small Satellites for Mediterranean basin Observation) and TerraSAR-X, are providing acquisitions with a shorter revisiting time and higher spatial resolution, being more suitable for landslide investigations and reducing some of the PSI limitations. The updating of the product using new satellite missions, such as COSMO-SkyMed and TerraSAR-X (or even Sentinel that will be launched in 2014), could be a further potential perspective, deeply encouraged.

The radar interpretation demonstrates the usefulness of quantitative information that can be obtained from PSI technique in analysing and characterizing landslide phenomena at basin scale.

The distribution of PS inside a landslide cannot be homogeneous and the interferometric data can have different density (PS/km²). ERS and ENVISAT medium resolution data can detect a low amount of radar scatterers on the ground. Nevertheless, even few PS benchmarks can be significant if they are integrated and validated with field survey and additional geo-thematic information. This work is carried out at a basin scale, so the radar interpretation is site specific and performed singularly. Thus, all the available ERS and ENVISAT data in the investigated area are taken into account, even if few PS are retrieved, despite the PS density.

One of the main pending issues of this kind of investigation is the choice of the velocity threshold that must be selected to distinguish moving from not moving PS

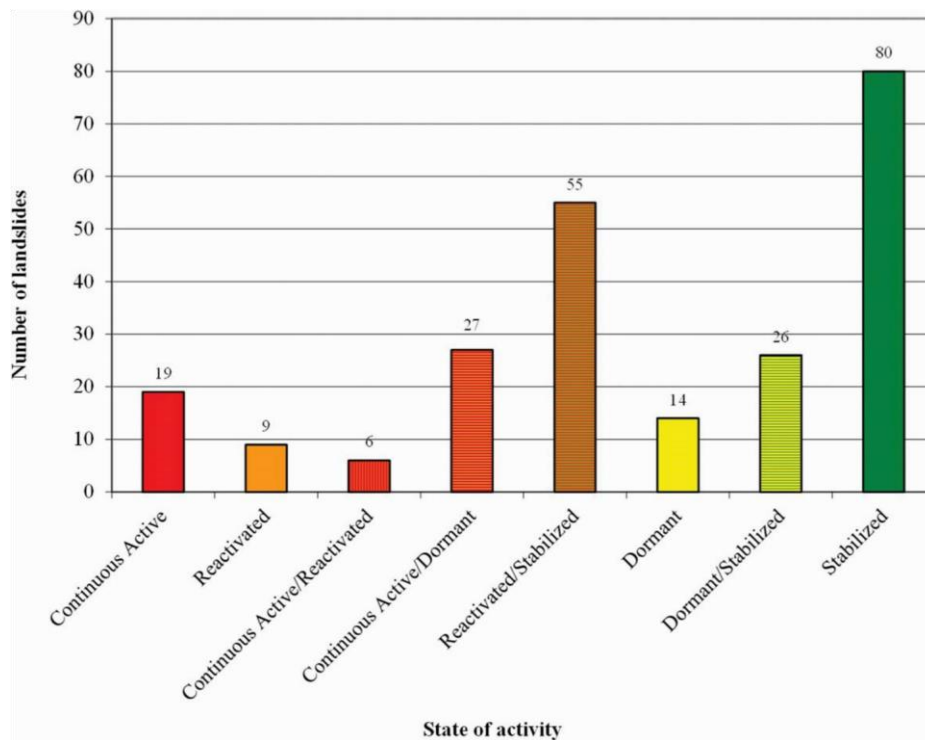


Figure 12. State of activity of 236 landslides with PS information classified according to the used activity matrix.

and consequently active from no-active landslide phenomena. There are no fixed rules to define stable velocity value thresholds. The choice is usually based on visual or statistical parameters, bearing in mind that these velocity thresholds are site specific and empirically determined taking into account the characteristics of the phenomena we are investigating (types, velocity) and the precision technique (e.g. the velocity threshold must be higher than the errors and noises within the measurements). In the study area of this work, PS populations of ERS and ENVISAT sensors are characterized by an almost Gaussian (normal) distribution, with coincident mean and median values and with standard deviation values ranging 1.5–2. As a result, we decided to establish the stability threshold of velocity at 2 mm/year, since this is the widely and mostly used value in literature for this type of analysis with Cband radar data (Wasowski et al. 2002; Meisina et al. 2008; Righini et al. 2012) and since it fits our data and case study well.

The activity matrix used in this work is the outcome of several previous approaches and represents an appropriate tool when managing PS data for landslide state of activity assessment (Righini et al. 2012; Bianchini et al. 2012; Cigna et al. 2013).

The new classification based on the activity matrix permits not to underestimate the activity when there is a lack of interferometric data. Thus, for example, in the case of absence of ENVISAT data where it is not possible to assign a state of activity to a certain phenomenon due to the lack of data, we preserve the two possible states of activity, not to discard those that may be the probable causes of the absence of

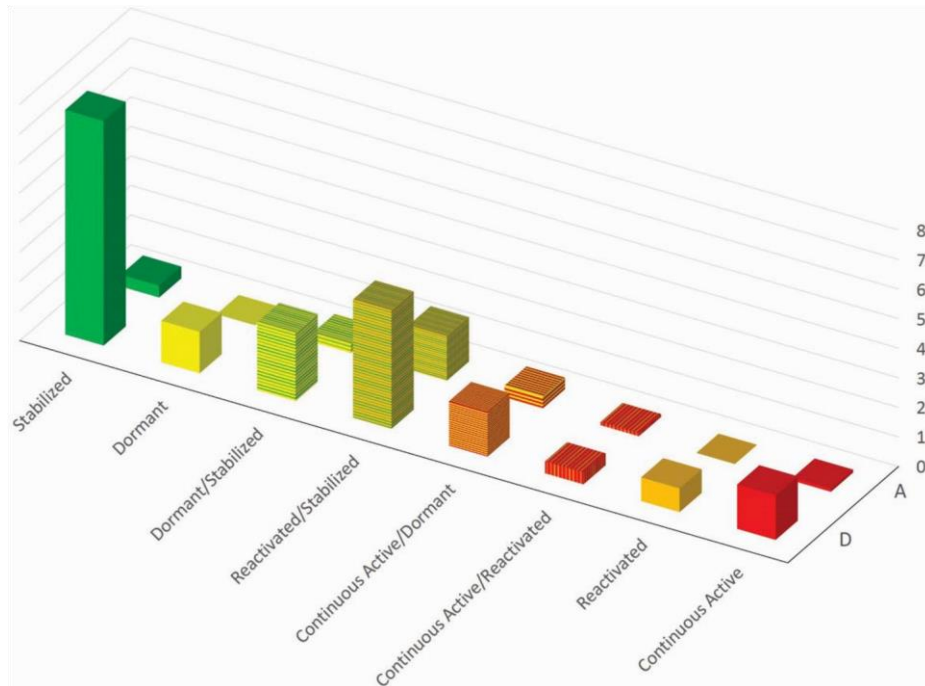


Figure 13. Reclassification of the 28 “active” (A) and 195 “dormant” (D) landslides in relation to the activity matrix used.

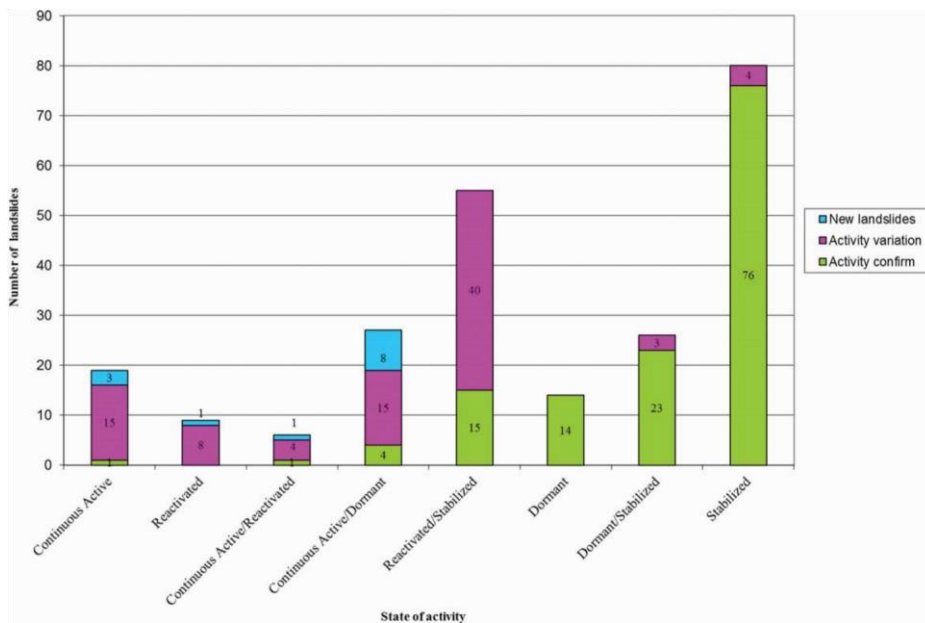


Figure 14. Variations for the 236 landslides updated with PS data. For each state of activity the number of landslides is given and divided in relation to the type of updating (variation, confirm and new detection).

data. The lack of ENVISAT data accompanied by PS ERS that record velocities lower than 2 mm/year could lead to considering a landslide as “inactive” for the period 2000–2007, but it is not excluded that in the presence of ENVISAT data it could be a reactivated landslide.

Therefore, it is useful to have some classification parameters taking into account the origin of the interferometric data; in fact, the presence of both or only one of the data-sets gives a different weight to the final classification of the state of activity.

A landslide classified as “inactive” in relation to the presence of both stable ERS and ENVISAT PS has a higher reliability than a landslide classified as “inactive” for the presence of only stable ERS PS, bearing in mind that in this last case they give an information only for the temporal period between 1992 and 2000.

A better identification of the geometry of unstable areas and of their state of activity by means of radar data, especially in urban sectors, improves the quality of the urban and environmental planning in the areas characterized by a high hydrogeological hazard.

The PSI technique can only measure slow displacements so far: this fits well with the high number of extremely slow processes that affect the study area, characterized by clay, silt and sandy formations, prone to slow-moving ground movements.

Field surveys mainly confirm PSI analysis outcomes, since several damaged buildings were pointed out in correspondence with moving radar benchmarks; moreover, many signs of instability such as cracks, depressions and evidences of new layers of road fills were found on road networks.

In the area of interest, the number of landslides with no PS targets is 1314; this lack of PS information should be efficiently integrated by further other traditional geomorphological techniques, for example, ground-truth systems.

The distribution of PS is higher in urbanized areas than in agricultural and seminatural areas; anyhow, the number of retrieved target points is quite satisfying as it ranges from 5 to 21 points per km² in the two different data-sets.

7. Conclusion

This work focuses on landslides inventory map updating in the Setta basin (Emilia Romagna region, Italy), integrating the interpretation of information retrieved from PSI with thematic maps and field survey. The results highlight the capabilities of multi-interferometric InSAR data, combined with conventional techniques, to support landslides investigation over large areas.

In particular, the contribution of this work relies on the use of a landslide activity matrix, which allowed us to reclassify the state of activity of landslides newly detected or already recorded in the pre-existing landslide database.

The outcomes demonstrate the usefulness of the PSI technique to update landslide inventories at basin scale, thanks to the available archives of historical and recent satellite data with monthly sampling and millimetre-scale accuracy.

This work represents a valuable tool that can be exploited by national agencies and local authorities for environmental planning in landslide-prone areas.

Acknowledgements

This work was carried out in the framework of the Terrafirma project (www.terrafirma.eu.com) which is one of the initiatives run by the European Space Agency under the Global Monitoring for Environment and Security (GMES) Service Element Program (GSE).

ERS and ENVISAT data were provided and processed by Tele-Rilevamento Europa (TRE) through the PSInSAR technique.

Access to IFFI (Inventario Fenomeni Franosi in Italia) landslide database was performed through the ISPRA's web map service (WMS), while the landslide phenomena map (Carta Inventario dei fenomeni franosi) for the test area was provided by Emilia Romagna region through region portal website and both inventories were homogenized and imported into GIS.

References

- Agnesi V, Angileri S, Arnone G, Cali M, Calvi F, Cama M, Cappadonia C, Conoscenti C, Costanzo D, Lombardo L, Rotigliano E. 2012. A multi-scale regional landslide susceptibility assessment approach: the *sufra_sicilia* (susceptibilita da frana in sicilia) project. In: Proceedings of the 7th EUREGEO. Bologna: Centro Stampa Regione EmiliaRomagna.
- Aleotti P, Chowdhury R. 1999. Landslide hazard assessment: summary review and new perspectives. *Bull Eng Geol Environ.* 58:21–44.
- Bamler R, Hartl P. 1998. Synthetic aperture radar interferometry. *Inverse Probl.* 14:R1–R54.
- Barchi M, Landuzzim A, Minellim G, Piallim G. 2001. Outer northern Apennines. In: Vai GB, Martini IP, editors. *Anatomy of an orogen: the Apennines and adjacent Mediterranean basins*. Dordrecht: Kluwer Academic Publishers; p. 215–254.
- Bargossi GM, Gamberini F, Gasparotto G, Grillini GC, Marocchi M. 2004. Dimension and ornamental stones from the Tosco-Romagnolo and Bolognese Apennine. *Periodico di Mineralogia - LXXIII*, special issue 3: 171–195.
- Bettelli G, Boccaletti M, Cibin U, Panini F, Poccianti C, Rosselli S, Sani F. 2002. Note illustrative della carta geologica d'Italia alla scala 1:50.000 Foglio 252 [Illustrative notes of the geological map of Italy, 1:50,000 scale, sheet 252]. Barberino del Mugello (Florence): Servizio Geologico d'Italia; p. 15–94.
- Bianchini S, Cigna F, Casagli N. 2011. Improving landslide inventories with multi-temporal measures of ground displacements retrieved through persistent scatterer interferometry [abstract]. In: Catani F, Margottini C, Trigila A, Iadanza C, editors. *The Second World Landslide Forum. Putting Science into practice*. Rome: FAO Headquarters.
- Bianchini S, Cigna F, Righini G, Proietti C, Casagli N. 2012. Landslide hotspot mapping by means of persistent scatterer interferometry. *Environ Earth Sci.* 67:1–18.
- Casagli N, Colombo D, Ferretti A, Guerri L, Righini G. 2008. Case study on local landslide risk management during crisis by means of remote sensing data. In: Proceedings of the First World Landslide Forum; Tokyo, Japan; p. 125–128.
- Cascini L, Fornaro G, Peduto D. 2009. Analysis at medium scale of low-resolution DInSAR data in slow-moving landslide affected areas. *ISPRS J Photogrammetry Remote Sens.* 64:598–611.
- Cascini L, Fornaro G, Peduto D. 2010. Advanced low- and full-resolution DInSAR map generation for slow-moving landslide analysis at different scales. *Eng Geol.* 112:29–42.
- Cibin U, Spadafora E, Zuffa GG, Castellarin A. 2001. Continental collision history from arenites of episutural basins in the northern Apennines, Italy. *Geol Soc Am Bull.* 113:4–19.
- Cigna F, Bianchini S, Casagli N. 2013. How to assess landslide activity and intensity with persistent scatterer interferometry (PSI): the PSI-based matrix approach. *Landslides.* 10:267–283.
- Cigna F, Bianchini S, Righini G, Proietti C, Casagli N. 2010. Updating landslide inventory maps in mountain areas by means of persistent scatterer interferometry (PSI) and photo-interpretation: central Calabria (Italy) case study. In: Malet JP, Glade T, Casagli N, editors. *Mountain risks: bringing science to society*. Florence: CERIG Editions; p. 3–9.
- Crozier MJ. 1984. Field assessment of slope instability. In: Brunsten D, Prior DB, editors. *Slope instability*. London: Wiley; p. 103–142.
- Cruden DM, Varnes DJ. 1996. Landslide types and processes. In: Turner AK, Schuster RL, editors. *Landslides: investigation and mitigation, Volume 247 of special report, Transportation Research Board, National Research Council Series*. Washington (DC): National Academy Press; p. 36–75.
- Dai FC, Lee CF, Ngai YY. 2002. Landslide risk assessment and management: an overview. *Eng Geol.* 64:65–87.

- Farina P, Casagli N, Ferretti A. 2008. Radar-interpretation of InSAR measurements for landslide investigations in civil protection practices. In: Proceedings of the 1st North American Landslide Conference; 2007 Jun 3; Vail, CO; p. 272–283.
- Farina P, Colombo D, Fumagalli A, Marks F, Moretti S. 2006. Permanent scatterers for landslide investigations: outcomes from the ESA-SLAM project. *Eng Geol.* 88:200–217.
- Farina P, Moretti S, Colombo D, Fumagalli A, Manunta P. 2004. Landslide risk analysis by means of remote sensing techniques: results from the ESA-SLAM project. In: Proceedings of the International Geoscience and Remote Sensing Symposium; 2004 Sep 20–24; Anchorage, Alaska; Vol. 1, p. 62–65.
- Ferretti A, Prati C, Rocca F. 2001. Permanent scatterers in SAR interferometry. *IEEE Trans Geosci Remote Sens.* 39:8–20.
- Gabriel AK, Goldstein RM, Zebker HA. 1989. Mapping small elevation changes over large areas: differential radar interferometry. *J Geophys Res.* 94:9183–9191.
- Guzzetti F, Carrara A, Cardinali M, Reichenbach P. 1999. Landslide hazard evaluation: an aid to a sustainable development. *Geomorphology.* 31:181–216.
- Herrera G, Davalillo JC, Mulas J, Cooksley G, Monserrat O, Pancioli V. 2009. Mapping and monitoring geomorphological processes in mountainous areas using PSI data: central Pyrenees case study. *Nat Hazards Earth Syst Sci.* 9:1587–1598.
- [ISPRA] Istituto Superiore per la Protezione e la Ricerca Ambientale. 2007. IFFI, Inventario dei Fenomeni Franosi in Italia. <http://www.isprambiente.gov.it/it/progetti/iffi-inventariodei-fenomeni-franosi-in-italia>
- Meisina C, Zucca F, Fossati D, Ceriani M, Allievi J. 2006. Ground deformation monitoring by using the permanent scatterers technique: the example of the Oltrepo Pavese (Lombardia, Italy). *Eng Geol.* 88:240–259.
- Meisina C, Zucca F, Notti D, Colombo A, Cucchi G, Giannico C, Bianchi M. 2008. Geological interpretation of PSInSAR data at regional scale. *Sensors.* 8(11):7469–7492.
- Notti D, Davalillo JC, Herrera G, Mora O. 2010. Assessment of the performance of X-band satellite radar data for landslide mapping and monitoring: upper Tena Valley case study. *Nat Hazards Earth Syst Sci.* 10:1865–1875.
- Pancioli V, Raetzo H, Campolmi T, Casagli N. 2008. TerraFirma landslide services for Europe based on spaceborne InSAR data. In: Proceedings of the First World Landslide Forum; Tokyo, Japan; p. 81–84.
- Principi G, Treves B. 1984. Orogenic belts as accretionary prism: the examples of the northern Apennines. *Ofioliti.* 9:557–618.
- Remitti F, Bettelli G, Vannucchi P. 2007. Internal structure and tectonic evolution of an underthrust tectonic melange: the Sestola-Vidiciatico tectonic unit of the northern Apennines, Italy. *Geodinamica Acta.* 20:37–51.
- Ricci Lucchi F. 1986. The Oligocene to recent foreland basins of the northern Apennines. In: Allen PA, Homewood P, editors. *Foreland basins.* International Association of Sedimentologists. Oxford (UK): Blackwell Publishing; p. 105–140.
- Righini G, Pancioli V, Casagli N. 2012. Updating landslide inventory maps using persistent scatterer interferometry (PSI). *Int J Remote Sens.* 33:2068–2096.
- Rosen PA, Hensley S, Joughin IR, Li FK, Madsen SN, Rodriguez E, Goldstein RM. 2000. Synthetic aperture radar interferometry. *Proc IEEE.* 88:333–382.
- Soeters R, Van Westen CJ. 1996. Slope instability recognition, analysis and zonation. In: Turner AK, Schuster RL, editors. *Landslides: investigation and mitigation*, Volume 247 of special report, Transportation Research Board, National Research Council Series. Washington (DC): National Academy Press; p. 129–177.

Wasowski J, Refice A, Bovenga F, Nutricato R, Gostelow P. 2002. On the applicability of SAR interferometry techniques to the detection of slope deformations. In: Proceedings of 9th IAEG Congress; Durban, South Africa.

Wieczorek GF. 1984. Preparing a detailed landslide-inventory map for hazard evaluation and reduction. IAEG Bull. 21:337–342.

[WP/WLI] Working Party on World Landslide Inventory. 1993. Multilingual glossary for landslides. Richmond (BC): The Canadian Geotechnical Society, BiTech.

6. X-BAND DATA FOR LOCAL-SCALE MONITORING

6.1 GENERAL CONSIDERATIONS

This chapter gives some applications of the X-Band SAR data for monitoring ground deformation and engineering infrastructures at a local scale. In particular, the subject of this chapter, is the IG interferometric processing chain for small areas and the consequently analysis of the obtained results; all these steps are carried out in the area within and around Barcelona, capital city of the autonomous community of Catalonia in Spain.

The monitoring activities in the area will be of paramount importance for early detection of potentially critical situations, especially in proximity of the roads and highways of the area. In this context, an essential element concerning the use of interferometric techniques for monitoring ground deformation based on satellite data is the acquisition of 26 interferometric radar image acquired in X band.

In particular, the IG processing chain and analysis conducted for this purpose included the development of a dataset acquired by the German satellite TerraSAR-X, in ascending geometry, ranging from December 2007 to November 2009.

After a short introduction of the processing technique used, some notions on the study area are given; the data arising from the elaboration are subsequently presented and analyzed.

The second paragraph describes the input data, the methodology used to produce the ground deformation maps, and the method adopted for the interpretation of the results. In particular, the second section, reproduce the chronological order of the PSI processing method of the Institute of Geomatics.

The third paragraph gives a general description of the main geological features of the study area. In particular, an examination of the geographical aspect of the Llobregat River is given; also, it is analyzed from the geological point of view. The last section of this paragraph examines, in general, the main aspects that characterize the movement of hydro-geological instability in the Catalan area.

The fourth paragraph illustrates some examples of land deformation detection based on the IG processing method for small areas and analyzes some areas close to Barcelona city. It describes the results obtained from the processing step; in particular, three cases of study are analyzed. For each site, there is a short geological overview of the study, a summary of processing performed and the analysis of the results obtained from the PS processing and analysis. For the sites, the results obtained with the field trip validation and those relating to the calculation of real velocity, are presented.

6.2 THE IG PROCESSING FOR SMALL AREAS

This chapter focuses on the application of X-Band data for local scale monitoring; it describes the methodology used to produce ground deformation maps and the method adopted for the interpretation.

The study area covers some areas placed on the banks of the Llobregat River and reported by Dr. Ramon Copons, geologist of the area, in relation to their possible predisposition to hydro-geological phenomena: landslides and subsidence (figure 82).

These areas were considered interesting because urbanized and major exposed to the risk due to a possible occurrence of these phenomena; in particular with regard to the landslides that occur as reactivation of pre-existing landslide bodies.

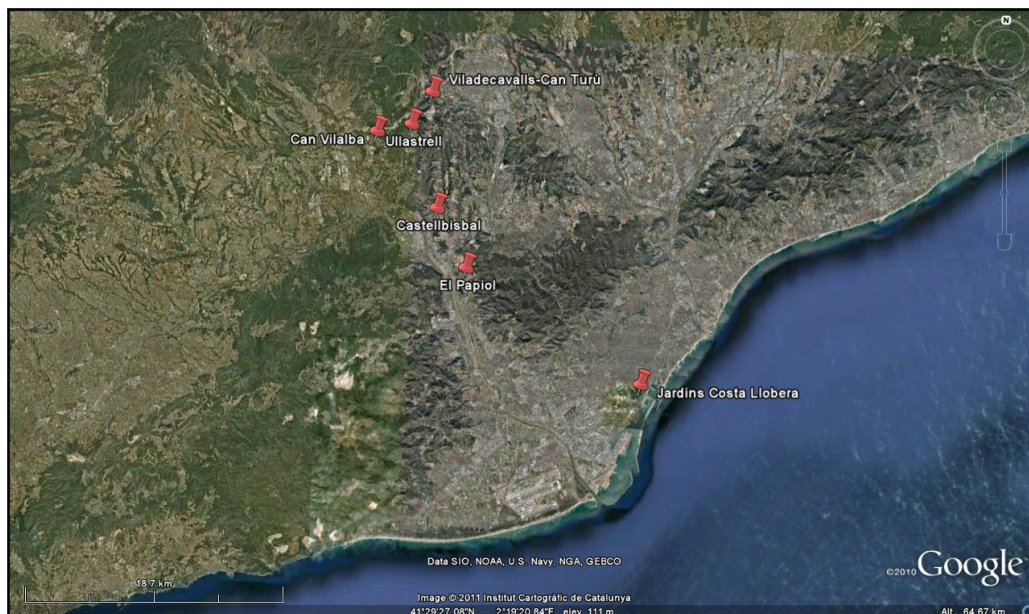


Figure 82: Area of study. The area covers some urban settlements surrounding the city of Barcelona. These fall within the Llobregat delta.

The chapter presents the data used, describes the type of data processing used, explaining a part of the technique of the Institute of Geomatics for data processing. The methodology used, has as objective the construction of ground deformation maps and the recognition of landslides.

The individuation of landslides and subsidence is based on a combination of interferometric TerraSAR-X data and observations of satellite remote sensing images; the entire work environment is developed in ENVI (the Environment for Visualizing Images) and Google Earth.

The methodology, which consists of several steps described below, has as its goal the identification of hydrogeological instability on six test sites in Catalan area.

1 Data acquisition

The process of acquiring information is about the following data: the interferometric data of the ground displacement detected by TerraSAR-X satellite; the ancillary data, including orthophotos acquired by Institut Cartogràfic de Catalunya (ICC), topographic maps on a 1:5.000 scale.

2 Data processing

The methodology adopted for the processing of interferometric data is that developed by the Institute of Geomatics based on the algorithm developed by Mora and others (Mora et al, 2003). A detailed explanation of the processing work done is given.

3 Photo and radar-interpretation

The photo-and radar-interpretation, designed to extract content information from the data above, is conducted with ENVI and Google Earth. It uses topographic maps on a 1:5000 scale. In particular, the photo-interpretation is used to identify any diagnostic morphology of a landslide and particular characteristics as indexes of the ground motion.

The radar interpretation is used to spatially extend the detailed information of a permanent scatterer and recognize any areas of instability.

4 Validation

The validations are essential to verify the results obtained; we examine the areas considered significant for the study area, both for their situation (the proximity of villages) and finally to the particular interferometric information contained in.

The work, which has as its purpose the processing of the data, can be summarized as follow. Within the scheme, the blue blocks on the left show the input data which are then expressed on the same line. As a cyclical process, the output of the first step is used as initial data for the next step.

The yellow blocks represent the operations used; the names of the operations are those corresponding to the steps of the processing method.

The orange blocks concisely explain what the different operations are.

Finally, the blue blocks on the right define the results of each operation.

Except for the first operation, starting from 26 radar images, the result of each step represents the beginning of the next step.

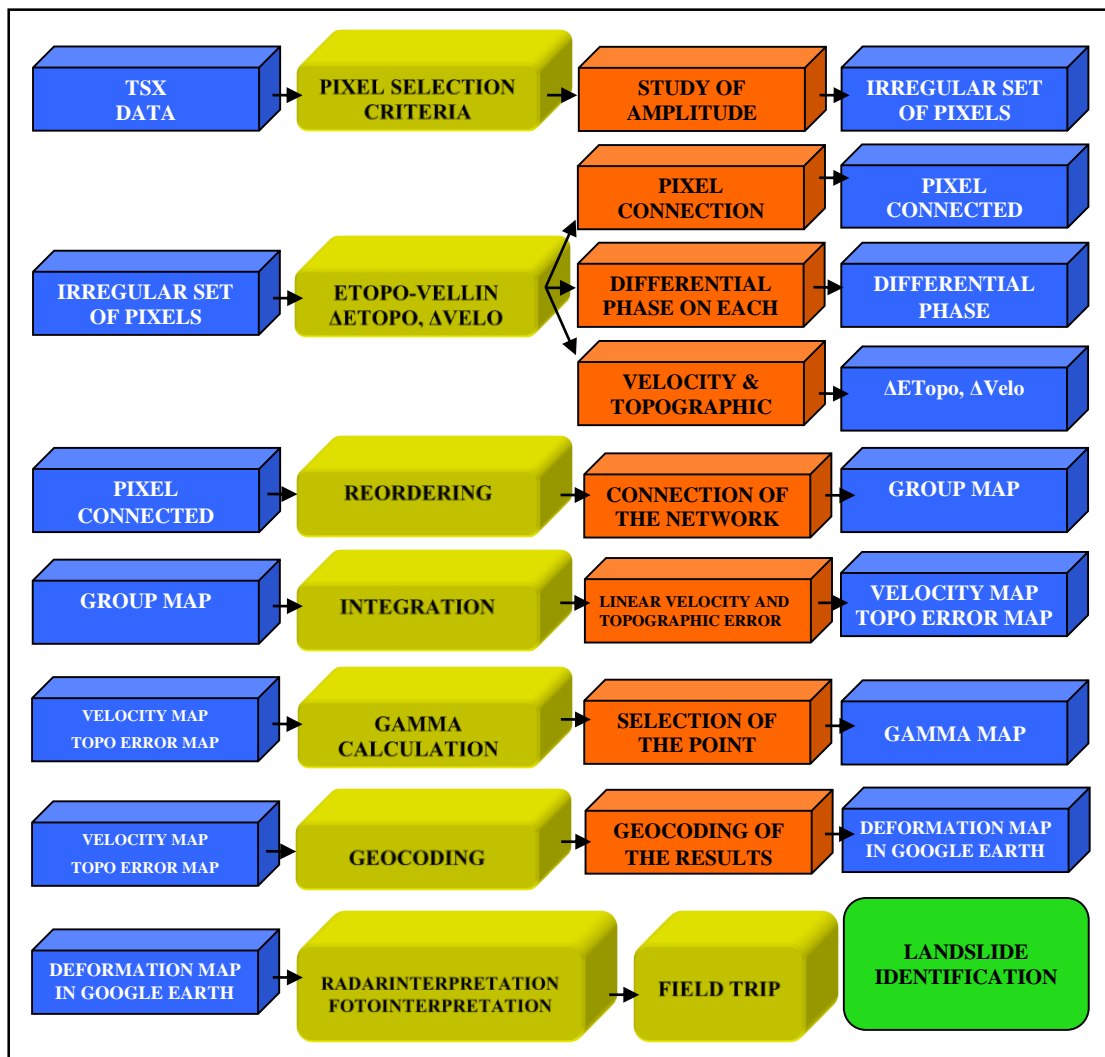


Figure 83: Schematic representation of the methodology adopted for the preparation of this work.

The recognition of landslides is done through radar- and photointerpretation step, supported by ancillary data, such as digital orthophotos, topographic maps, digital terrain models, geological maps.

6.2.1 INPUT DATA

Input data were processed in the coordinate system WGS 1984 UTM zone 31 N, and are the following: the interferometric data of the annual average rate of land displacement recorded by satellites, the Google Map images, the ortophoto (1:5000), the topographic maps (1:5000), the geological map (1:50.000) and the digital terrain model with its output files (slope and aspect).

Interferometric Data

The algorithm used is able to provide good results even with a reduced set of SAR images. In this work, a set of 26 TerraSAR-X images with ascending orbits, ranging from December 2007 to November 2009 has been used, as shown in table.

FID	Pol_Chn	Orbit Name	Start Date	Start Time	Orbit
19881	VV	3016	20071230	17:41:06,0	ascending
20143	VV	3183	20080110	17:41:04,0	ascending
20262	VV	3350	20080121	17:41:05,0	ascending
13336	VV	3684	20080212	17:41:05,0	ascending
13622	VV	3851	20080223	17:41:03,0	ascending
13954	VV	4018	20080305	17:41:03,0	ascending
14230	VV	4185	20080316	17:41:03,0	ascending
15844	VV	4853	20080429	17:41:04,0	ascending
16241	VV	5020	20080510	17:41:05,0	ascending
16602	VV	5187	20080521	17:41:06,0	ascending
10001	VV	5521	20080612	17:41:07,0	ascending
10393	VV	5688	20080623	17:41:08,0	ascending
10886	VV	5855	20080704	17:41:08,0	ascending
11177	VV	6022	20080715	17:41:09,0	ascending
12491	VV	6523	20080817	17:41:11,0	ascending
20367	VV	6857	20080908	17:41:14,0	ascending
	VV	7692	20081102	17:41:16	ascending
	VV	8360	20081216	17:41:13	ascending
	VV	8861	20090118	17:41:11	ascending
	VV	9028	20090129	17:41:10	ascending
	VV	9362	20090220	17:41:10	ascending
	VV	9696	20090314	17:41:11	ascending
	VV	10197	20090416	17:41:12	ascending
	VV	10865	20090530	17:41:14	ascending
	VV	11533	20090713	17:41:16	ascending
	VV	12034	20090815	17:41:18	ascending
	VV	12535	20090917	17:41:19	ascending
	VV	13036	20091020	17:41:21	ascending
	VV	13537	20091122	17:41:20	ascending

Satellite data used in this work were processed with the method of the Institute of Geomatics for the areas of interest. The images are chosen to form 56 interferograms with

short spatial baseline. The displacement measurements are differential, related to a ground point of known coordinates (reference point); temporal measures are related to the acquisition date of the first image (master image).

Topographic Map

The base map used is the Regional Technical Map on a 1:5000 scale, in raster format, which was acquired by the Institute Cartographic of Catalunya. The topographic map represents the surface considering the position, shape, dimensions and the identification of ground accidents and specific objects that are located there. The topographic mapping products are made from direct photointerpretation of aerial photography or digital orthoimages or by existing cartographic databases. The data map are obtained in two and three dimensions. The accuracy of the information depends on the scale of the product, but always remains within the cartographic standards.

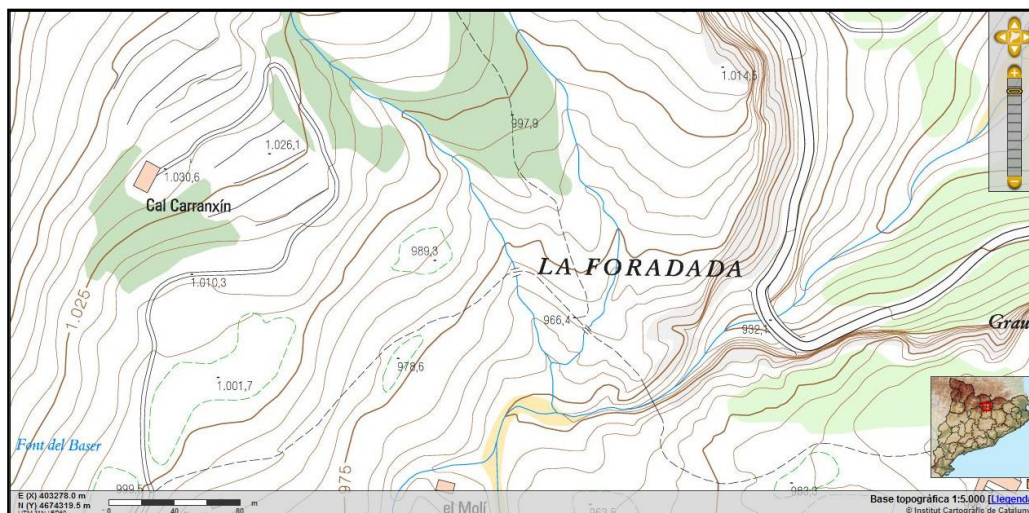


Figure 84: Topographic Map on a 1:5000 scale acquired by the Institute Cartographic of Catalunya.

Ortophoto

The orthophoto or orthoimage are based on aerial photos or satellite image and therefore elements of the earth's surface are visible. They are obtained by scanning the original negatives of aerial photographs and therefore in a shooting there are different scales in relation to the target point of the various portions of the territory.

The photographs or images, or mosaic image, are geometrically rectified and converted into orthophoto or orthoimage. This correction is particularly useful in the presence of hills and mountains. More the aerial photos were made at low altitude, greater does the lens of the camera create the cone strain during the acquisition; this gives the impression that the objects tend to lean towards the outside of the frame. The process of orthorectification

corrects this error bringing everything on a reference plane, so that a certain distance on the valley floor matches the same distance on the top of the relief. The orthophotos are then georeferenced.

The operation consists in taking the digital photos in a reference system where each object and area correspond to geographic coordinates, lengths and surfaces calculated in according to the type of projection used as a geographical reference.



Figure 85: Orthophoto in scale 1:5000 acquired by the Institute Cartographic of Catalunya.

Google earth

Through the Google Earth application the satellite images has been observed (figure 86). As a continuously update work the images are not visible on the same date and may have a temporal discrepancy from three to four years to less than one.



Figure 86: Google map image.

Geological Map:

The geological map used is acquired by Institute of Geomatics of Catalunya on a 1:50000 scale.

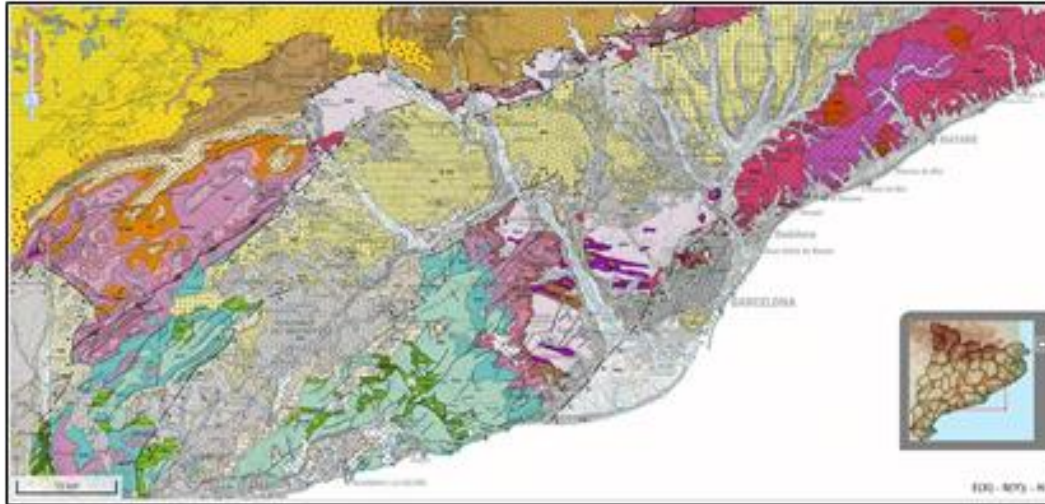


Figure 87: Geological Map on a 1:50.000 scale acquired by the Institute Cartographic of Catalunya.

DTM

It is the representation of heights of an area in digital format. The DTM is produced in a raster format by associating at each pixel the absolute height attribute. The DTM (Digital Terrain Model) made by IG (Institute of Geomatics) with a resolution of $35\text{ m} \times 35\text{ m}$ is used.

The DTM is a raster data structure where they are stored altitude information inherent to a given area, from this we can extract information such as slope, curvature and exposure of the slopes.

The view of the slopes is useful to highlight anomalies in the morphology (terracing), to recognize the landslide deposits (low slope values) and detachment (sharp increases in the gradient).

In this paper, two calculations are made using the digital terrain model: the slope and the aspect calculation. In particular, the slope is measured in degrees with the convention of 0 degrees for a horizontal plane; the aspect angle is measured with the convention of 0 degrees to the north (up) and the angle increasing clockwise.

The DTM has been used in the processing to remove the topographic component.

6.2.2 METHODOLOGY

The paragraph is organized as follows, trying to reproduce the chronological order of the PSI method of the Institute of Geomatics processing. The first section describes the pixel selection criteria and after a description of pixel connection and differential phase calculation is given; the second section describes the differential velocity and topographic error calculation and after presents the integration step. Finally, in the last section, the geocoding step for the map of ground motion is showed. To start de PS processing the following images are required: the mean amplitude image, the dispersion of amplitude image used for pixel selection and the interferogram files.

Mean Amplitude

The amplitude of a SAR image represents the terrain response to the microwave pulses transmitted by the radar; it includes the transmission effects (dispersions, refraction) in the two-way antenna-ground travel. The detected SAR image is generally visualised by means of grey scale levels as shown in the example of figure 88. Bright pixels correspond to areas of strong backscattered radiation (urban areas), whereas dark pixels correspond to low backscattered radiation (a quiet water basin).



Figure 88: TerraSAR-X detected image of Castellbisball (Barcelona, Spain). Image of the average amplitude. Light colors indicate high reflectivity of the signal. Conversely, dark colors indicate low reflectivity signal.

The amplitude depends on two groups of parameters: those depending on the radar (carrier wavelength, polarization, incidence angle); those related to the physical characteristics of the terrain (reflectance, humidity, surface roughness, terrain slope). The mean amplitude of a stack of images is computed in order to get a general idea of the study area. In fact the amplitude is a function of the wave-terrain interaction on the surface of the imaged scene and it depends more on the roughness and on the chemical composition of the scatterers on the terrain. It can be used to identify key features as streets, buildings, infrastructures; typically, exposed rocks and urban areas show strong amplitudes, whereas smooth flat surfaces (like quiet water basins) show low amplitudes.

The M_A images will be used to select the pixels to work with.

Dispersion of the Amplitude

The dispersion of the amplitude is computed as $D_A \approx \sigma_A/m_A$ where m_A and σ_A are the mean and the sqm of the amplitude. D_A is a parameter of the phase stability (for a high signal to noise ratio are obtained negative values). The dispersion is also a measure of the degree of correlation between the values of the radiation fed back to the ground at two different moments, separated by a time t .

The D_A image will be used to select the pixels to work with (figure 89)



Figure 89: Image of the D_A . Dark colors are associated with low amplitude dispersion and therefore the signal is of good quality. Conversely, light colors are signs of a high amplitude dispersion; the signal is not good.

Interferograms

The interferograms are the result of the difference between two images with two different phase values (figure 90). The interferometric phase variation can be explained by a phase shift proportional to the altitude difference between the point targets, referred to horizontal reference plane and a phase variation proportional to the slant range displacement of the point target in and with a shift in slant range of the reflector on the ground.

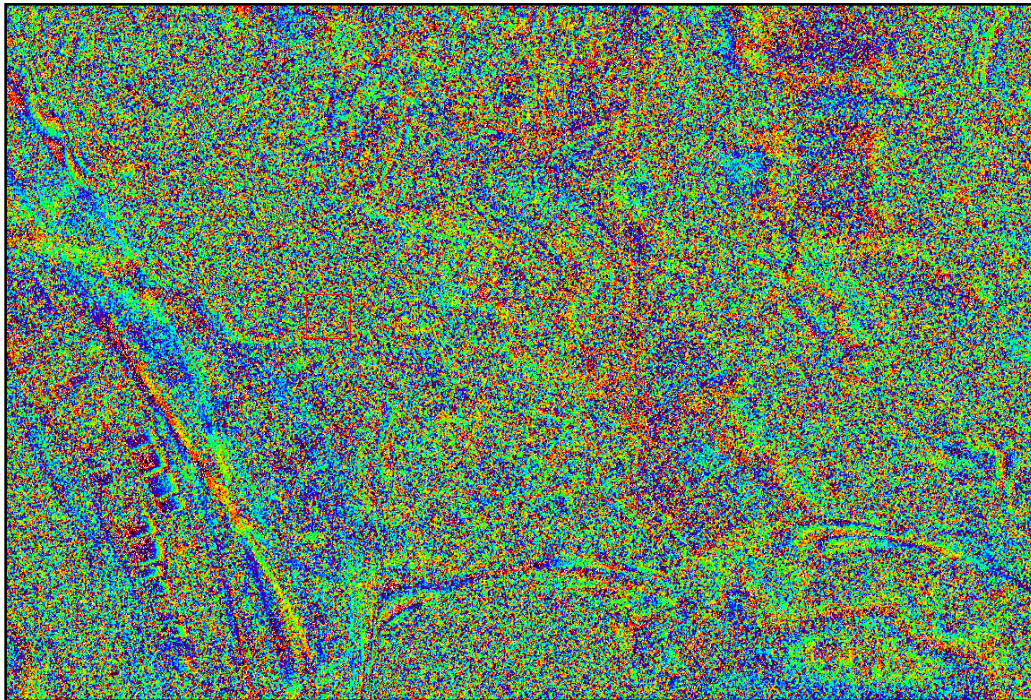


Figure 90: TerraSAR-X detected image of Castellbisball (Barcelona, Spain). Image of differential interferogram. From this image, you cannot find the shift, too small for differential interferometry.

Two key features (Biescas et al., 2007) characterize the proposed PS-InSAR approach for slow deformation measurement. It works with multiple interferometric observations: its main input is a stack of N interferograms acquired over a given deformation area; it makes use of an appropriate modelling of the PS-InSAR observations, which enables the joint estimation of the terrain deformation and the topographic error. The method uses areas of limited size (3km-3km) to prevent the atmospheric effect, since it is not removed but only reduced at one infinitesimal contributions, which can be neglected.

The algorithm used in this work is able to retrieve the linear components of movement from a set of interferograms, estimating only the DEM error and not the atmospheric artefacts. The basis for the linear estimation of movement is the adjustment of a linear model, which considers the linear velocity of displacement and the DEM error, to the available data in a similar way as done in the preceding methods (Ferretti et al., 2000, 2001).

In summary, the processing main steps of the proposed method include five parts. Firstly is the identification of the pixels candidates (those presenting a good phase quality) with a criterion based on a low value of the dispersion of amplitude along the interferogram stack. Secondly the more suitable pixels of an interferogram stack are selected and connected by a network with a triangulation to establish phase relations among them, adjustment of a linear model, which considers linear deformation and DEM error, to those phase relations for the whole set of interferograms. For each edge of the network, a phase difference is computed by differentiating the phases of the two corresponding pixels. Then, the differential terrain deformation and the differential topographic error are estimated for each edge. Finally, these differential values are integrated and interpolated over the entire set of selected pixels, to generate the movement maps. The most relevant stages of the procedure are briefly described in the following.

Pixels Selection

The linear deformation model cannot be applied to all the pixels within the area under study since only a part of them have sufficient phase quality due to decorrelation. Therefore, a first selection based on their phase quality estimation has to be performed before computing their deformation velocity. This selection can be done with two methods, one based on pixel amplitude stability and the other on spatial coherence. In this case the criterion is based on the study of the amplitude dispersion (D_A); only those pixels that have a D_A lower than a certain threshold in a minimum number of interferograms are selected (Blanco et al, 2006). The selection based on amplitude (Ferretti et al., 2000, 2001) estimates the phase standard deviation of every pixel from its temporal amplitude stability, which preserves the maximum spatial resolution of the images and allows detecting single isolated scatterers smaller than a resolution cell. Infact if the PS are smaller than the resolution cell, they are stable. The following step consists in selecting those pixels which have a minimum phase quality to be processed and extract temporal deformation series. This is done in order to guarantee a good quality of the input phases, discarding the bad pixels in term of phase of noise. Note that this step is only a selection of candidates, and some of them will be rejected later if they do not adjust to the linear model.

Pixels Connections and Phase Calculation

The result of the previous step is an irregular set of pixels. When generating an interferogram by combining two SAR images, its phase variation between neighbouring pixels can be expressed as (Mora et al., 2003):

$$\Delta\phi_{\text{int}} = \Delta\phi_{\text{flat}} + \Delta\phi_{\text{topo}} + \Delta\phi_{\text{mov}} + \Delta\phi_{\text{atm}} + \Delta\phi_{\text{noise}}$$

where: $\Delta\phi_{\text{flat}}$ is the flat earth component related with range distance; $\Delta\phi_{\text{topo}}$ is the phase related with topographic component; $\Delta\phi_{\text{mov}}$ is the component due to the displacement of the terrain in range direction [line of sight (LOS)] between both SAR acquisitions; $\Delta\phi_{\text{atm}}$ is the phase related with atmospheric artefacts; and $\Delta\phi_{\text{noise}}$ comprises degradation factors related with temporal and spatial decorrelation and thermal noise. Three of the terms are analytically well known ($\Delta\phi_{\text{flat}}$, $\Delta\phi_{\text{topo}}$ and $\Delta\phi_{\text{mov}}$) (Mora et al., 2003).

$$\Delta\phi_{\text{flat}} = \frac{4\pi}{\lambda \cdot r} \cdot \frac{b \cdot \Delta r}{\tan \theta} \quad (2)$$

$$\Delta\phi_{\text{topo}} = \frac{4\pi}{\lambda \cdot r} \cdot \frac{b \cdot \Delta h}{\sin \theta} \quad (3)$$

$$\Delta\phi_{\text{mov}} = \Delta\phi_{\text{linear}} + \Delta\phi_{\text{nonlinear}} = \frac{4\pi}{\lambda} \cdot \Delta v \cdot T + \Delta\phi_{\text{nonlinear}} \quad (4)$$

where λ is the wavelength; r the range distance; b the normal baseline (normal component of the separation between the position of satellites in both acquisitions respect to the incident angle); Δr is the range increment between pixels; θ the incidence angle; Δh and Δv are the height and velocity increments between neighboring pixels respectively; and T is the temporal baseline between both SAR acquisitions. Note that the deformation term has two contributions: linear and nonlinear displacement.

By removing the flat earth and topographic terms, we obtain the DInSAR phase:

$$\Delta\phi_{\text{int}} = \Delta\phi_{\text{mov}} + \Delta\phi_{\text{errortopo}} + \Delta\phi_{\text{atm}} + \Delta\phi_{\text{noise}} \quad (5)$$

As the DEM used to cancel the topography is not perfect, $\Delta\phi_{\text{errortopo}}$ is the phase component associated to the height error

$$\Delta\phi_{\text{errortopo}} = \frac{4\pi}{\lambda \cdot r} \cdot \frac{b \cdot \Delta \varepsilon}{\sin \theta} \quad (6)$$

where $\Delta \varepsilon$ is the height error increment expressed in meters. If a set of differential interferograms of the same area is used, the topographic error and the linear deformation are correlated in all the images following (4) and (6). As the atmospheric conditions change from acquisition to acquisition, the atmospheric contribution behaves as a white process in time (Mora et al., 2003).

Consequently, we can consider the atmospheric contribution and noise temporally decorrelated along the whole set of interferograms.

With this approach, a model, which considers linear velocity deformation and DEM error, can be fitted to the set of differential interferograms with different temporal baselines.

Pixel connection

The phase of individual pixels is not of practical utility due to the presence of different phase offsets among differential interferograms.

As the information contained in the PS-InSAR phase is differential, it can be exploited only by considering pairs of the previous pixels. For this reason two neighbouring pixels, (x) and (y), are connected by edges, computing the phase difference of each edge and cancelling then the offsets effect.

Several methods to connect an irregular set of points can be used, e.g., the Delaunay triangulation. This kind of triangulations relates all the neighbouring pixels of irregularly gridded data generating no overlapped triangles and computing the phase difference of each edge (figure 91)

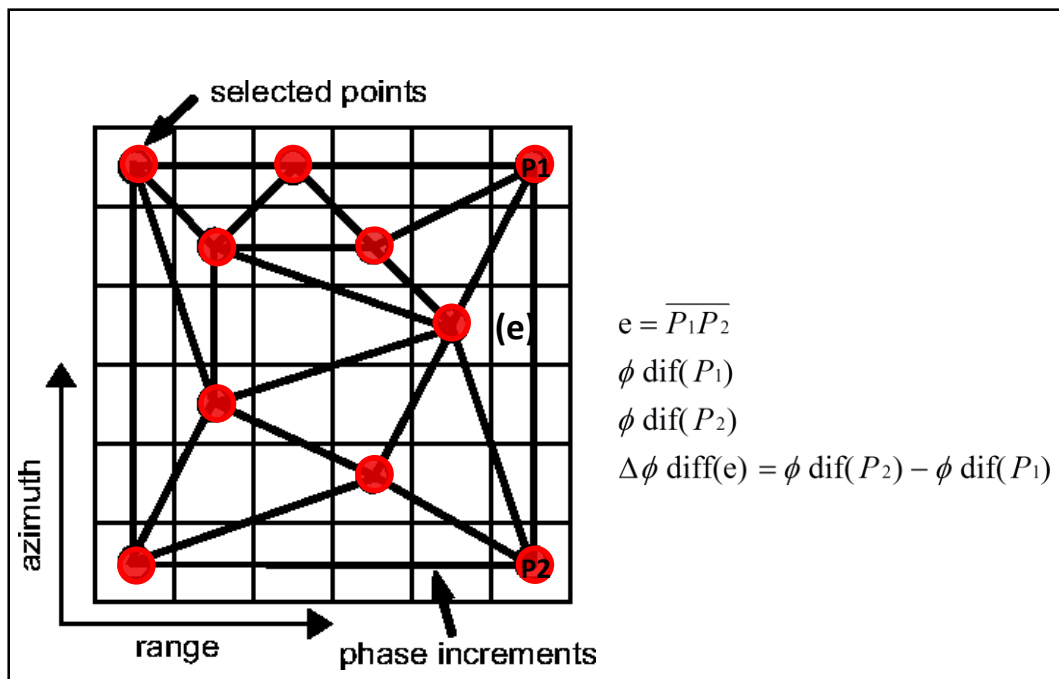


Figure 91: Pixels connection; example of Delaunay triangulations. The selected pixels are connected by edges. The differential wrapped phase value over each edge is calculated by subtracting the wrapped phase values over its extremes. Each edge has one differential phase value for each of the N interferograms. [Adapted from Mora et al., 2003].

These edges have to be as short as possible in order to minimize the atmospheric effects in the phase difference; the edges are selected with a minimum/maximum criterion of distance. Usually during the triangulation, the maximum distance allowed to connect two separate pixels is limited to approximately 1km, which is a reasonable correlation distance of the atmosphere. In some cases, non-connected isolated areas will have to be studied independently.

Phase calculation

Then a differential wrapped phase value is assigned to each edge and for each interferogram, obtaining for each edge a stack of N differential interferometric wrapped phases. As it is shown in figure 94 this is done by computing the difference of the wrapped phases over P_1 and P_2 for the edge $e = \overline{P_1 P_2}$ (Crosetto et al., 2009)

Then, the differential phase increments can be expressed as (Mora et al., 2003):

$$\begin{aligned} \Delta\phi_{\text{diff}}(x_m, y_m, x_n, y_n, T_i) &= \frac{4\pi}{\lambda} \cdot T_i \cdot [v(x_m, y_m) - v(x_n, y_n)] + \frac{4\pi}{\lambda} \cdot \frac{b(T_i)}{r(T_i) \cdot \sin(\theta_i)} \cdot [\varepsilon(x_m, y_m) - \varepsilon(x_n, y_n)] \\ &+ [\beta(x_m, y_m, T_i) - \beta(x_n, y_n, T_i)] \\ &+ [\alpha(x_m, y_m, T_i) - \alpha(x_n, y_n, T_i)] \\ &+ [n(x_m, y_m, T_i) - n(x_n, y_n, T_i)] \end{aligned} \quad (8)$$

where x and y are the pixel position coordinates within the image; T_i is the time baseline of the i th interferogram; λ is the wavelength; v is the constant velocity of the linear model of displacement; b the spatial baseline of the i th interferogram; r the range distance; θ the incidence angle; ε the topographic error; β the nonlinear component of velocity; α the atmospheric phase artefacts; n and decorrelation noise.

Another advantage of relating neighbouring pixels is that the atmospheric component is minimized for every relationship due to their spatial proximity.

Taking into account that the atmospheric perturbation is a spatial small wave number signal, we can consider for neighbouring pixels that (Mora et al., 2003):

$$\alpha(x_m, y_m, T_i) \approx \alpha(x_n, y_n, T_i) \quad (9)$$

The assumption considered in (9) holds if during triangulation the maximum distance allowed to connect two separate pixels is limited to approximately 1 km, which is a reasonable correlation distance of the atmosphere (Hassen, 2001). In some cases, no connected isolated areas will have to be studied independently.

Differential Velocity and Topographic Error

The differential velocity and differential topographic error are computed over each edge by using N differential wrapped phases and some geometrical parameters of each interferogram. As the linear velocity and DEM error are constants in the whole set of differential interferograms, it is possible to retrieve a good estimation of them adjusting the following phase model to data (Ferretti et al., 2000, 2001):

$$\begin{aligned} \Delta\phi_{\text{model}}(x_m, y_m, x_n, y_n, T_i) &= \\ &= \frac{4\pi}{\lambda} \cdot T_i \cdot [v_{\text{model}}(x_m, y_m) - v_{\text{model}}(x_n, y_n)] + \frac{4\pi}{\lambda} \cdot \frac{b(T_i)}{r(T_i) \cdot \sin(\theta)} \cdot [\mathcal{E}_{\text{model}}(x_m, y_m) - \mathcal{E}_{\text{model}}(x_n, y_n)] \end{aligned} \quad (10)$$

This can be performed maximizing the following model coherence function [11]:

$$\begin{aligned} \gamma_{\text{model}}(x_m, y_m, x_n, y_n) &= \\ &= \frac{1}{N} \cdot \left| \sum_{i=0}^N \exp[\Delta\phi_{\text{diff}}(x_m, y_m, x_n, y_n, T_i) - \Delta\phi_{\text{model}}(x_m, y_m, x_n, y_n, T_i)] \right| \end{aligned} \quad (11)$$

Where N is the number of interferograms. This function is equal to one when the adjustment to data is perfect and zero in case of total decorrelation.

In this work, the maximization of function is done numerically; to find the values Δv e $\Delta\mathcal{E}$ that give the maximum γ , a discrete grid is used (figure 92)

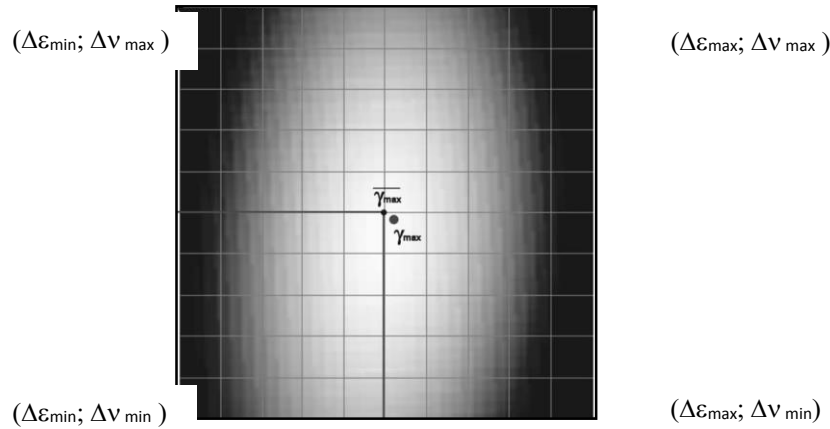


Figure 92: Estimation of the differential velocity and the differential topographic error. For each edge, γ is a function which depends on the variables Δv and $\Delta\mathcal{E}$. To find the maximum value of γ several pairs $(\Delta v, \Delta\mathcal{E})$ are proved. The estimated values $(\Delta v_{\text{estimated}}, \Delta\mathcal{E}_{\text{estimated}})$ are given by the pair which gives the maximum value of γ . This solution does not give exactly the absolute maximum γ_{max} but the best approximation γ_{max} due to the used discrete network. As much dense is the discrete network, the better is the approximation, but at the same time, more expensive is the computation time [Taken from Biescas, 2007].

A reduced set of interferograms can cause an erroneous estimation of the unknown frequencies as different combinations of velocity and DEM error can generate similar phases. The larger the number of interferograms, the better will be the estimation as the range of multiple solutions is reduced. There is not a clear minimum number of images as results depends on each case, but we found that seven interferograms can provide good results and it is very difficult to work with less than five. Once this maximization process

has been done for each relationship, the result is the following set of velocity and topographic error increments:

$$\Delta v_{\text{estimated}}(x_m, y_m, x_n, y_n) = [v_{\text{model}}(x_m, y_m) - v_{\text{model}}(x_n, y_n)]_{\text{maximize}} \quad (12)$$

$$\Delta \mathcal{E}_{\text{estimated}}(x_m, y_m, x_n, y_n) = [\mathcal{E}_{\text{model}}(x_m, y_m) - \mathcal{E}_{\text{model}}(x_n, y_n)]_{\text{maximize}} \quad (13)$$

At this point, a new quality test is performed and all the connections with a model coherence below a threshold are rejected. Good results have been obtained with coherence thresholds larger than 0.7. Because of the quality test, some pixels will be left isolated and eliminated.

Integration Step

An integration process is necessary to obtain absolute values for each pixel; it consists on the reconstruction of the velocity and the topographic error on the selected pixels using the result obtained over the edges. This is done by least square adjustment, considering the linear velocity and the topographic error over each pixel as unknowns, and the estimated differential velocities and differential topographies as observations (Biescas et al., 2007). The integration starts from different points, chosen from those presenting links with better model coherences, and calculates the absolute value of velocity for each pixel using

$$v_{\text{estimated}}(x_m, y_m) = \frac{1}{\sum_i \gamma_{\text{model}}(x, y, x_i, y_i)} \cdot \sum_i [v_{\text{estimated}}(x_i, y_i) + v_{\text{estimated}}(x, y, x_i, y_i)] \cdot \gamma_{\text{model}}(x, y, x_i, y_i)$$

where index i corresponds to those neighbouring pixels connected to the one that is being integrated. Each contribution reaching a pixel is weighted with its associated model coherence to reduce the contribution of the less reliable connections. As the integration only involves differential values, it is necessary to fix the velocity values of at least one pixel (reference point). The same has to be done for the topographic error. The outcomes of this step are a velocity map and a topographic error map, whose values are relative to the chosen reference point.

The larger the ratio is between edges and pixels the more reliable are the integrations results. A similar procedure is performed for the DEM error. During the integration step is very important to choose the stable area: it is a stable point of the investigation to which are reported all the other points. The integration process is aimed to calculate the speed of points in reference to the absolute speed of a given point that is the stable zone. It need to have the following features: the stable area shall not be affected by ground motion; the area must be a stable area resting on the ground and it cannot be chosen at the top of a building; the stable area must be inside the area affected by movement, cannot fall outside it

Geocoded ground deformation map

The geocoding of the result allows representation of the PS in ground geometry. In that way we can visualize the PS on a ortophoto, a GIS or a web map service (like Google Erath).

The geocoding is a transformation from radar geometry to ground geometry. A “ground control point” (GCP) is needed for a first shift calculation (line and coloumn, geographic coordinates).

The result is a file to open in Google Earth (.kml) containing the geocoded PS (figure 93).

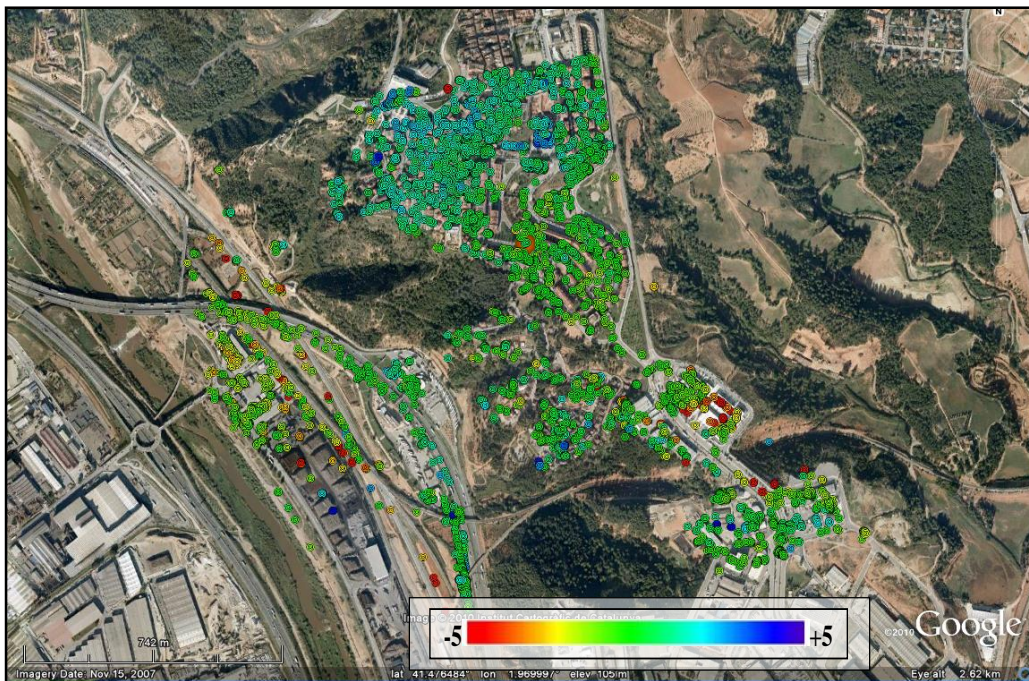


Figure 93: Example of geocoded deformation map. The colour scale is saturated between -5 and +5 mm/year.

6.3. OVERVIEW OF THE STUDY AREA

This chapter gives a general description of the main geological features of the study area. In particular, the Llobregat River basin is examined in terms of geographical aspect and subsequently analyzed by the geological point of view. The last section examines, in general, the main aspects that characterize the movement of hydro-geological instability in the Catalan area.

The Llobregat River, whose head is in the Pyrenees, has a length of 156.5 km and a drainage area of 4948.4 km². It is a Mediterranean river with little flow, a marked dry season, severe flooding and high irregularity (Marquis, 1984). Many streams from Garraf and Collserola flow into the delta plain and are reflected by the flooded areas and wetlands.

The Llobregat River delta, south of the city of Barcelona, is an example of Mediterranean delta began in the postglacial period, which prograde over a narrow marine platform, and is sandwiched between mountainous terrain. It is highly modified by coastal processes such as littoral drift to the southwest, with currents of about 30 cm/s (Font et al., 1987; Chiocci et al., 1997), which redistributed these sediments to the southwest and brought sediments from the north coast of Barcelona. To a lesser extent, the wave (low energy) and the tide (a few centimetres) contributed to the redistribution of sediment.

In the prodelta and the slope, numerous synsedimentary failures and canyons that redistribute the sediment gravitationally are present (Maldonado et al., 1986). Probably the same processes were active during the Pleistocene.

Superpose to deltaic sedimentary processes, coastal and continental shelf margin must be added the temporal variation of sediment and Quaternary eustatic changes affecting the vertical and lateral facies. The result of eustatic changes is an amalgamation of deltas, now submerged, separated by multiple surfaces of erosion.

The modern delta is part of a complex of Pleistocene submerged deltas that today have placed their deltaic fronts at depths of more than 80 m away from the current shoreline, of at least 12 km.

6.3.1 GENERAL GEOLOGICAL SETTING

The Llobregat delta is developed at the foot of the Mediterranean side of the Catalan coast, part of NE–SW set known with the Catalanides name. This set is made up of large morphostructural units: the pre-coastal mountain and the coastal mountain. The Llobregat River (figure 94) crosses the Coastal range and two very different fields are distinguished and separated by the failure of a horizontal displacement that matches the Llobregat River valley.

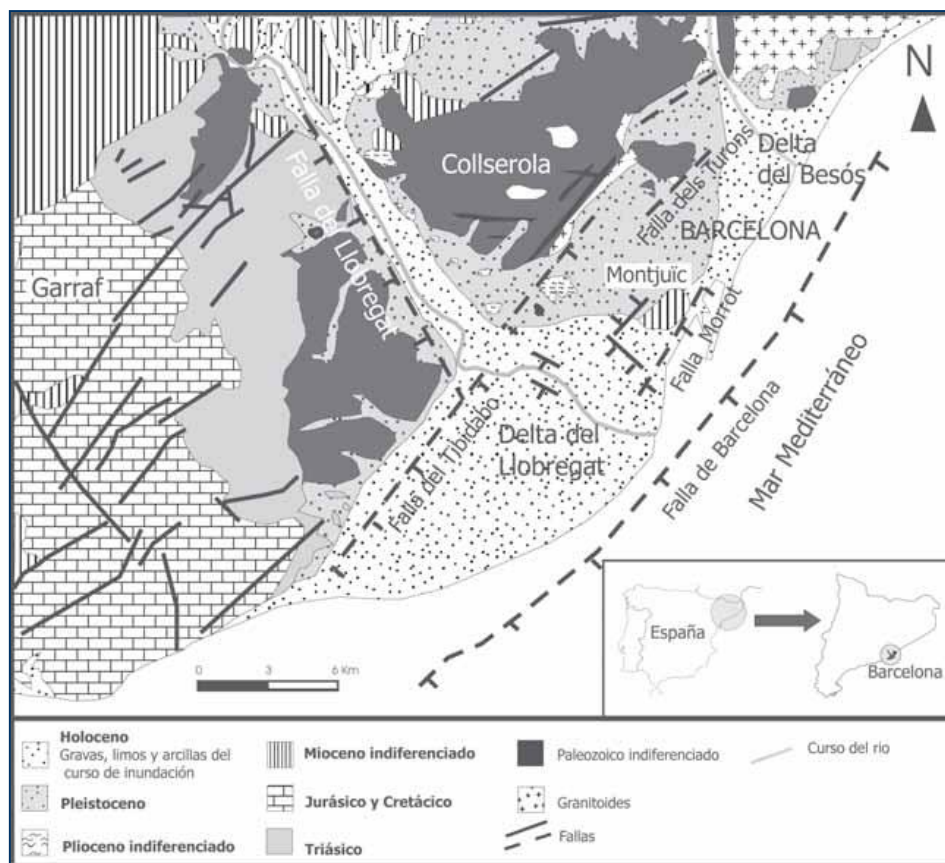


Figure 94: Schematic Geologic map of the Llobregat delta region (modified from Almera, 1891) [SIMÒ et al. 2005].

The northernmost unit corresponds to the Sierra de Collserola, which in the southernmost part, includes Paleozoic materials. The unit in the SW Llobregat valley is formed by the Garraf massif, where the Paleozoic goes smoothly under Mesozoic materials. The Llobregat River valley, which spans the pre-coastal mountain range and the coastal mountain range, is a long narrow hallway filled of Holocene sediments. The mound called Montjuic lies parallel to the mountain ranges of the Sierra de Collserola and it is separated from it by a depression, which consists of Miocene sediments. This mound is the NE limit of the delta and separates Llobregat and Besos deltas. The central depression between the

Montjuic and the Sierra de Collserola is called the Plain of Barcelona, and is covered with Pleistocene materials, which in the area of the Sierra de Collserola rely directly on the granite and Paleozoic shales and in the rest of the plain on tertiary materials. In this area, there are three morphotectonic units: Part of the Hercynian Massif, which forms the Collserola Mountains; The Garraf Massif; The depression of the Valles - Penedes, a graben filled with Miocene sediments. The pre Triassic discordance is among the basement in the Mesozoic cover. This base was strongly folded during the Hercynian orogeny, which in its main phase gave rise to a flow foliation. The last episode of metamorphic materials of this sector of the Catalanides are associated with green schist facies. Hercynian tectonics is represented by the intrusion of a mass of granodiorite, which outcrops at the foot of Tibidabo. This intrusion appears accompanied by an aureole of contact metamorphism. In the Mesozoic cover, which forms the Garraf massif, are distinguished, in addition to the pre Triassic discordance, two less pronounced. One at the base of the Jurassic, and other in the Cretaceous. The Mesozoic cover is affected in its entirety by folds of large radius of curvature, and crossed by a dense network of fractures of variable direction (Marques, 1984). In the network of fractures, which sometimes affects the base, notably with NE-SW, there is another family with NW-SE direction, and a third with NS direction.

6.3.2 STRATIGRAPHY

Paleozoic

In the area around the Llobregat delta, Paleozoic outcrops are divided into two areas; one located east of the river Llobregat, which form the bulk of the Sierra de Collserola and the other is located west of the same river, on the eastern edge of Garraf massif, sinking to W under Mesozoic materials. The following materials (Sabarís et al., 1957), ranging from the Ordovician to Carboniferous, form the Paleozoic in this area.

- a) *Ordovician*: Shale and sandy shale with less powerful quartzite beds and carbonate rocks.
- b) *Silurian*: Quartzite beds alternating with Phyllites.
- c) *Upper Silurian-Devonian*: Massive limestone and shale.
- d) *Carboniferous*: Shale, sandy shale and greywacke.

Mesozoic

- *Triassic*

It outcrops forming a continuous band which is the western edge of the massif of Garraf. As in the other of Catalanides consists of three Triassic floors of Germanic facies.

- a) *Buntsandstein*: conglomerates, sandstones and red clay.
- b) *Muschelkalk inferior*: dolomites and limestone.

Medium Muschelkalk: sandstones and red clays.

Upper Muschelkalk: limestone, dolomite and limestone marl.

c) *Keuper*: limestone, dolomite and marly limestone.

- *Jurassic and Cretaceous*

On the variegated marls of the Keuper, we develop a robust calcareous - dolomite set, which is the Garraf massif. There are various levels within this complex.

- *Lias*: dolomitic layers.

- *Dogger and Malm*: black dolomites.

- *Valanginian - Hauterivian*: gray limestone with dolomite interbedded.

- *Barremian*: Gray compact limestone.

- *Aptian - Albian*: Marls with calcareous levels interbedded.

Cretaceous materials are arranged under the Quaternary in the area of Castelldefels.

Cenozoic

- *Miocene*

Miocene materials are located on both the pre-coastal depression and in the coastal shelf.

In the pre-coastal depression are clay, which reach a thick exceeding 2200 m in the center of the rift valley of the Valles - Penedes. In the coastal shelf, the Miocene forms the small hill of Montjuic, consisting of conglomerates and sandstones of siliceous cement, intercalated with marls, sandy marls and loose sands.

- *Pliocene*

The Pliocene is small outcrops along the Llobregat lower valley, including Castellbisbal and Esplugues. Several facies are distinguished in the Pliocene.

a) Conglomerates with sandy matrix: This facies is exposed in the base and the high deposits, and only at the edges of the basin of sedimentation. [Valenciano \(1967\)](#) relates to the Pliocene estuary of the lower Llobregat and calls this formation Gravels of Castellbisbal. The material differs from the upper terrace of Llobregat River located at the same topography for the different composition.

b) Blue clay, called in the country "fetge cow". Are very homogeneous clays with minor interbedded dark and very fine sand.

c) Sand and yellowish sandy clay: oblique-stratified or massive medium-grained sand interbedded with weak blue marl. Recognized in various outcrops on both banks of the lower Llobregat valley.

- *Quaternary*

The Quaternary has a great variety of deposits, classified as follows([Sabariés et al., 1963](#)):

- a) Fluvial terraces. Four distinct river terraces, corresponding to different periods of glaciations. They are located at different altitudes, both above and below the current course of the river Llobregat. The lithology is formed by gravel and is uniform.
- b) Torrential deposits. Fragments of local origin, mixed with red clay. As the materials are further away from the mountains are seen lateral facies changes, and coarse material passes to clay matrix.
- d) Deltaic deposits. They consist of a fluvial series, deltaic and marine complex, partly due to lateral facies changes that occur in deltaic environments.

6.3.3 GEOMORPHOLOGICAL SETTING

At the catchment scale, the tectonic control on the landscape is highlighted by the performance of the main features of hydrography; the course of the river Llobregat, as with most rivers in the surrounding area, has a trend NW-SE.

Relief

The basin of the Llobregat River, from W to E is delineated by a sharp morphological jump; a high-energy relief, steep slopes, narrow and paid valleys and a high drainage density, characterizes the most northwestern part. In this area, the landscape evolution is controlled by the erosive action of rivers and processes related to the collapses.

In the other part of the basin there is a landscape characterized by broader valleys and forms of gentler slopes; the drainage density also decreases significantly. As for the shape of the landscape, looking at the hills, you can recognize the presence of rocks with different alterability on which the weather have shaped a landscape of contrasting characteristics.

The profiles and the ridges of slopes identify the rocks more resistant to erosion, at which the slopes are steeper and sometimes you can see the rock outcropping.

Landslides

The climate is the most influencing factor on the stability of the slopes and existing landslides in Spain. Relief, together with the lithological component, contribute to the geographic distribution of the slope failures. The relationship between climate and slope instability is complex due to the great variety of failure mechanisms. In the twentieth century, the most notorious episodes of widespread slope instability occurred in Catalonia in October 1907 and 1940, and November 1982. High-intensity, short-lasting rainfall episodes generally cause shallow landslides, debris flow and rock falls. Prolonged low or moderate-intensity rainfall lasting for several days or weeks reactivate landslides and mudslides.

The behaviour of large landslides is very dependent on the geological and geomorphologic context, but their reactivation is frequently associated with abnormally rainy seasonal periods. In any case, anthropogenic modifications like leaks and overloading are a decisive cause of new, apparently spontaneous, slope failures (Corominas, 2006). The Catalan area concentrates the largest number of ruptures due to the coincidence of pronounced relief, the presence of susceptible grounds and a regime of torrential rainfall. Two factors that favor instability stand above the others: the steep slope of the versant because of the excavation of the Pleistocene glaciers and the engagement of the actual river network. In figure 95, the susceptibility of the territory to generate landslides is shown. Susceptibility classes have been defined in four levels based on ground relief and its typology; these are below exposed:

- High susceptibility zones. Those with a very steep relief and lithology prone to generate landslides. Their range is approximately 27% of the territory.
- Medium susceptibility zones. Those with a steep relief but a relatively low drop level. They take approximately 22% of the territory.
- Low susceptibility zones. Mountainous areas of smooth hills and depressions with a certain topographic level drop. These account for 45% of the territory.
- Undetected susceptibility zones. These are the great interior plains and the coastal plains with practically horizontal relief that take 6% of the total territory.

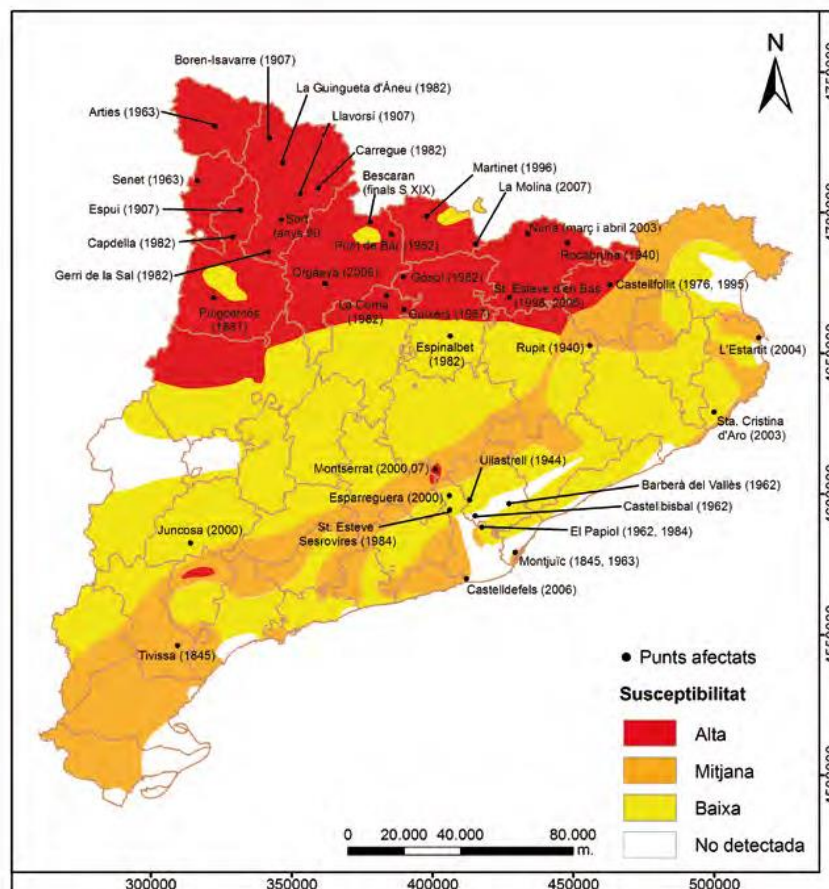


Figure 95: Landslide susceptibility map in Catalonia with the localization of major events with recorded damage sometime in history [Taken from RISKCAT: Els riscos naturals a Catalunya].

The break of the slope in a precise moment requires the presence of an external action whose effect is to increase the destabilizing tensions or reduce the strength of field. The areal erosion and channeled erosion that are fully developed and accompanied by many phenomena of mass movement, such as rotational slides and flows, affecting most of the slopes. The fluvial erosion, acting deepening the furrows and valleys displacing the foot sides, also governs all the processes of shaping of the slopes. This, together with the action of other factors, including human intervention, can trigger landslides that take on major importance in the nature of clay slopes. The landslides also occur spontaneously without any apparent trigger as a result, for example, of tension relax or by the progressive loss of the resistance of the materials making up the hillside, because of weathering. Earth flows and rock falls have a great incidence and a wide territorial distribution in Catalonia. The slope instability occurs where conditions are favorable. The lithology and the relief, among others, are the main constraints of the appearance of cracks. The infiltration of rainwater into the hillside increases the pores pressure and ground cracks, reducing their resistance. The relationship between the amount of infiltrated water and flowing regulates the slope

changes in water pressure of groundwater. When the interstitial pressure increases to a critical level, failure occurs. The topographic slope, vegetation cover, and terrain permeability and saturation degree regulate the infiltration rate. On the other hand, the instability is determined by the terrain resistance, which varies depending on the nature of materials, the geological structure and geometry of the slope. There are different types of landslide movement (Corominas, 2006):

Shallow landslides and debris flows

The most characteristic landslides of rainfall in all regions of the planet are small breaks (translational landslides and debris flows); these are triggered by heavy and short rain events. Depending on the permeability of materials making up the slope, there are two types of behavior. The first takes place in permeable slopes covered with colluvium where the generation and dissipation of pore pressures positive is very fast, even less 24 hours. The rupture occurs at the contact between surface formation with the waterproof substrate because of heavy rains while the effect of antecedent rainfall is, general, little decisive. This pattern is most common in all colluvial formations dominated by coarse fraction (pebbles and gravel) with permeable sandy-silty matrix. A different behavior occurs on the slopes consisting of low permeability materials (clays and shales), where pre-saturation is a necessary condition for the occurrence of debris flows and landslides. Antecedent rainfall reduces the suction in the soil and stimulates the increase in interstitial pressure of subsequent rains, decreasing soil strength. In the presence of antecedent rainfall, the failure of the slope occurs for rainfall intensities lower than required in the case of permeable soils. Shallow failures, mostly debris flows, debris slides and small slumps take place on colluvium and on weathered layers of claystones and marls. Failure surfaces often develop within the colluvium or in the boundary between weathered and unweathered rock usually at depths up to 3 m. Slopes affected by shallow sliding range between 25° and 45° (Corominas and Moya, 1999). Colluvial deposits are composed of silty and sandy gravels, with angular clasts. Animal burrows and roots form high permeability macropores, very frequent in the upper half meter of the deposits. These macropores are responsible for the rapid increase of the pore water pressures in the soil.

Earth flows

Medium landslides and earth flows tend to be common in clay materials and low permeability lithologies. The most reported cases are reactivation of existing cracks, and antecedent rainfall is of great importance.

Rock falls

The water pressure increasing in cracks and fissures causes the instability. It arises from the cumulative effect of freeze - thaw cycles that weaken rock and propagate cracks. Strong bedrock outcrops of limestone and conglomerates are almost unaffected by sliding and only isolated rock falls occur on cliffs during heavy rains, although some are induced by freeze - thaw mechanisms and the wedging effect of roots. Source areas for rock falls are steep rockwalls with slope angles over 60° (Corominas and Moya, 1999).

Earth slide

First, we must distinguish between new generation breaks and reactivation of existing landslides. Historical records show that the majority of first breaks large landslides have been triggered by non-climatic factors (Corominas, 2000). Geometric changes in the rock mass can be displaced modify the hydrological and mechanical properties of the slope. The cracks opening and closing due the distortion of the rock mass breaks new ground for groundwater flow and produce significant changes in the generation of water pressures. In some slopes, accelerating movement leads to a fragile break, in others, the foot sliding forward on the valley floor acts as a buttress, which leading to the gradual deceleration and stabilization movement. The exceptional rainfall events are not always a necessary condition for the break. By contrast, rainfall is the most common cause of reactivation of latent landslides and acceleration of the already active. Large rotational slides, mudslides and mudflows affect mostly clay stones and marls that form gentle slopes. Failure surfaces are frequently found more than 3 to 4 m deep.

Subsidence Phenomena

Subsidence is the motion of a surface as it shifts downward relative to a datum such as sea level. Land collapses are vertical movements of the ground, more or less sudden, associated with the existence of subsoil cavities close to the ground surface. Subsidence is a process of slow, gradual collapse of an area of the ground. The opposite of subsidence is uplift, which results in an increase in elevation. There are many types of subsidence associated with different causes as follow explained

Groundwater-related subsidence

The habitation of lowlands, such as coastal or delta plains, requires drainage. The resulting aeration of the soil leads to the oxidation of its organic components and this decomposition process may cause significant land subsidence. This applies especially when ground water levels are periodically adapted to subsidence, in order to maintain desired unsaturated zone depths. In addition to this, drained soils consolidate because of increased effective stress.

In this way, land subsidence has the potential of becoming self-perpetuating; having rates up to 5 cm/yr.

Mining

Several types of sub-surface mining and specifically methods that intentionally cause the extracted void to collapse will result in surface subsidence. Mining induced subsidence is relatively predictable in its magnitude, manifestation and extent. Mining-induced subsidence is nearly always much localized to the surface above the mined area, plus a margin around the outside.

Extraction of natural gas

If natural gas is extracted from a field the initial pressure in the field will drop over the years. The gas pressure also supports the soil layers above the field. If the pressure drops, the soil pressure increases and this leads to subsidence at the ground level.

Seasonal effect

Many soils contain significant proportions of clay, which because of the very small particle size are affected by changes in soil moisture content. Seasonal drying of the soil results in a reduction in soil volume and a lowering of the soil surface. If building foundations are, above the level to which the seasonal drying reaches, they will move and this can result in damage to the building in the form of tapering cracks.

Dissolution of limestone

Subsidence frequently causes major problems in karst terrains, where dissolution of limestone by fluid flow in the subsurface causes the creation of voids (i.e. caves). If the roof of these voids becomes too weak, it can collapse and the overlying rock and earth will fall into the space, causing subsidence at the surface. This type of subsidence can result in sinkholes that can be many hundreds of meters deep. In the area of interest, the main causes of subsidence are due to the water extraction, mining and extraction of natural gas. In the picture below (figure 96) are shown the subsidence susceptibility in relation to the lithology.

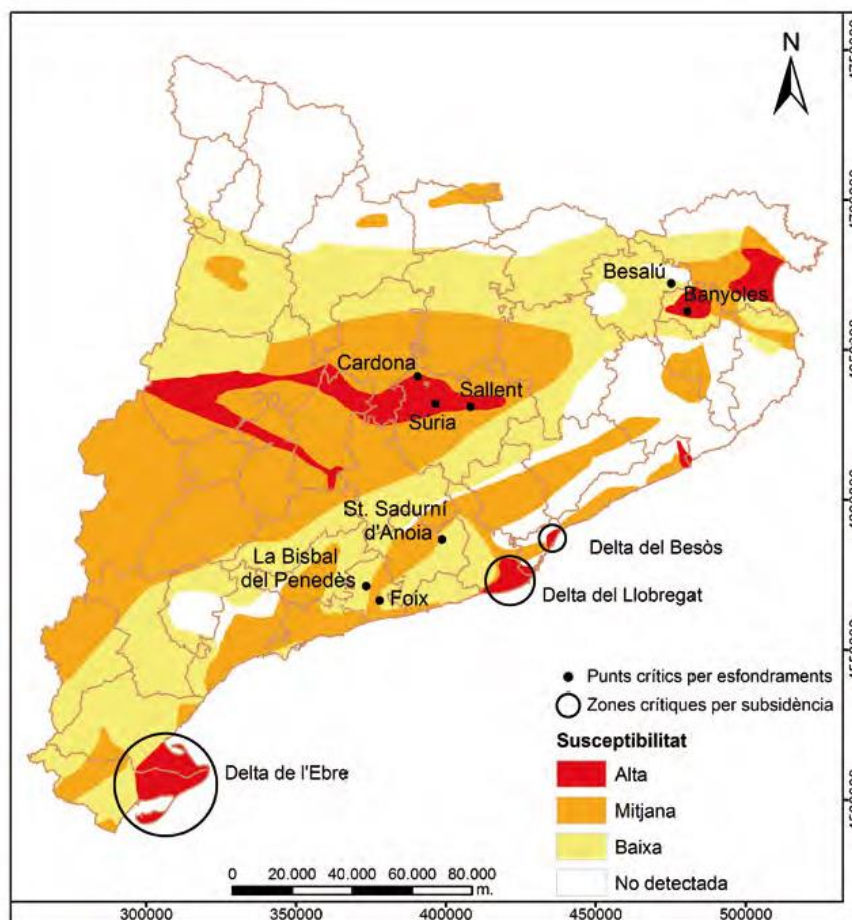


Figure 96: Susceptibility map to the collapses and subsidence in Catalonia. The most affected zones are highlighted. [Taken from RISKCAT: Els riscos naturals a Catalunya].

There are four levels of susceptibility.

- High susceptibility zones. They occupy approximately 10% of the territory.
- Medium susceptibility zones. Represent the areas of the terrain where powerful lutitical formations occur. They account for approximately 30% of the territory.
- Low susceptibility zones, where powerful calcareous and conglomerate formations are found. They constitute 40% of the territory.
- Undetected susceptibility zones. They account for 20% of the territory, where granitic and metamorphic formations that will not produce land collapses and subsidence appear.

6.4 TEST SITES

This section illustrates some examples of land deformation detection based on the IG processing method for small areas and analyzes some areas close to Barcelona city.

The three cases of study are presented: for each site, there is a short geological overview of the study, a summary of processing performed and the analysis of the results obtained from the PS processing and analysis. For the sites, the results obtained with the field trip validation and those relating to the calculation of real velocity, are presented.

In order to estimate the deformation over these areas, 26 ascending SAR images are used; these cover the period from December 2007 to November 2009 and are acquired by the TerraSAR-X sensor with a strip map mode.

By processing the 26 TerraSAR-X *stripmap* image acquired and elaborated at the Institute of Geomatics, 56 interferograms have been developed and a PSI data stack has been computed, making possible to carry out an accurate detection of all the main ground deformation processes active in the area between 2007 and 2009.

The first step of the processing is the selection of the pixels that present amplitude stability in time. In this case, pixels having a mean amplitude value higher than 0.25 have been selected. The result is a set of pixels distributed all over the image. Obviously, the density of points is higher in the urban areas than in vegetated ones. All the pixels are related using the Delaunay triangulations.

After the data processing using the algorithm for linear deformation estimation, the remaining number of points are selected. In addition to noisy pixels, some very nonlinearly moving quality points could have been eliminated and consequently lost.

The maps of the PS identified in the image and their coordinates (latitude, longitude and precise elevation) are the result of the multi-interferogram Permanent Scatterers approach. The PSI technique for the landslides detection has been made by integrating the PS information with the ancillary data in Google Earth and ENVI. The procedure followed can be summarized in visualization and classification of PS and overlapping with ancillary data. The PS in .kml formats were displayed in Google Earth; the available dataset is already cut on the area with the previous processing operation. For viewing in Google environment PS were classified according to the velocity with different colors.

- red, identifies the land moving away from the radar sensor;
- blue, identifies the land moving towards to the radar sensor;
- green, identifies stable points.

The stability values are grouped into classes ranging from -5mm/year e +5mm/year.

The class corresponding to the stable PS is chosen between -2mm/year e $+2\text{mm/year}$.
 The intermediate classes are from -5 mm / year to -3 mm / year and -3 mm / year to -2 mm / year for the movement detected moving away from the satellite.
 From $+2\text{ mm / year}$ to $+3\text{ mm / year}$ and $+3\text{ mm / year}$ to $+5\text{ mm / year}$ for the movement detected moving towards to the satellite.



Figure 97: Colorscale for the ground deformation map visualization in Google Earth

In this chapter, we consider all the cases of study in term of analysis and interpretation of deformation map. For each of them the first part gives a geological framework of the study area, then describes the processing work and finally are analyzed the deformation maps trying to explain the causes of the main phenomena identified.

Two most relevant areas are analyzed to carry out a more detailed investigation as well as a campaign validation. For these cases some calculations have been done, including the calculation of the aspect affected by landslide, the calculation of the slope of the same and calculation of the real rate of soil movement.

The campaign validation was carried out as a last analysis, to verify the results obtained from radar interpretation and highlight possible injury to buildings, the presence of counter slopes of the ground and other geomorphological phenomena related to slope instability.

The field trip was carried out in sample areas, most significant for the good satellite information, for the presence of built-up areas of interest and for the presence of major road links.

The results obtained can be summarized in the table below.

AREAS OF STUDY	COMMENTS
1. EL PAPIOL	Ground movement is detected
2. CASTELLBISBALL	Ground movement is detected
3. JARDINS COSTA I LLOBERA	Ground movement is detected

6.4.1 EL PAPIOL

El Papiol is a municipality in the comarca of the Baix Llobregat in autonomous region of Catalonia, Spain. It is on the left of the confluence of the Rubí River with Llobregat River, under the foothills of the Collserola; some streams drained by the river Llobregat cut the northern and southern slopes of the hills.

The slopes are steep slopes, which favors the formation of soil creep. Small vertical slopes characterize the hill, while the slope is clearly milder in other areas. These scarps are evidence of the contrast between lithological easily erodible material (clay) and others stronger that have the tendency to be fragmented into blocks (limestone), causing the presence of landslides and landslide deposits.

The active erosion on the softer lithologic sections by streams and because of gravitational processes influence clearly the physical geography of this small area.

The village places on the hydrographic left side of the Llobregat river valley at an averaged altitude of 110 meters above the sea level; an old village centre and other recently built areas compose it. In addition, an industrial zone and an important cement plant are placed downslope the village.

Old landslides, reactivated during a flood in October 1962, affect the most part of the urban area of El Papiol. All the further reactivations have occurred following intense rainfall events such as in 1971, November 1983 and March 1984.

In all of these cases, the massive rainfalls have been the triggering factor but the diffuse water losses from the flawed sewage system have accelerated the effects.

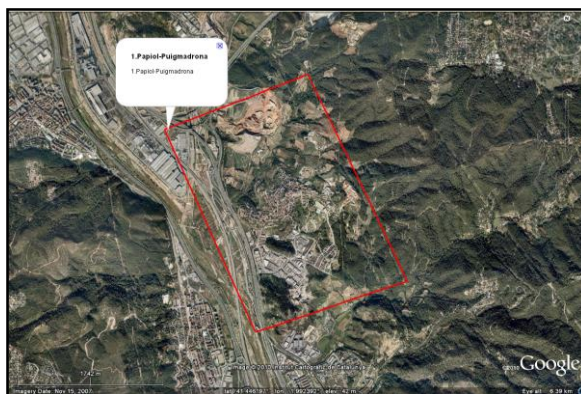


Figure 98: El Papiol.

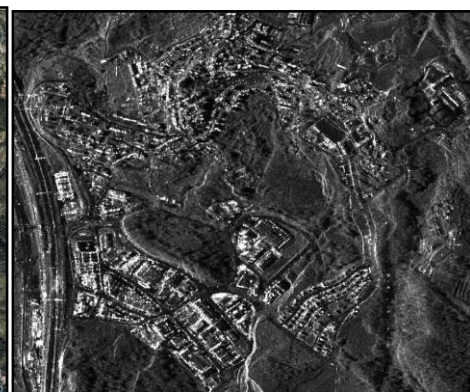


Figure 99: Mean Amplitude image

6.4.1.1 Geological Setting

The area of El Papiol shows a geological setting where the marine and fluvial Pliocene sediments are prevalent (figure 100). In particular, on the valley floor, near to the industrial area, the subsoil is characterized by very plastic clays whereas the main part of the village is built on an older sandstone formation, on which the aforementioned landslides have occurred. The succession of Papiol is located on the southern margin of the Neogene basin of the Vallès - Penedès.

This basin is bounded by normal faults oriented ENE-WSW (figure 100).

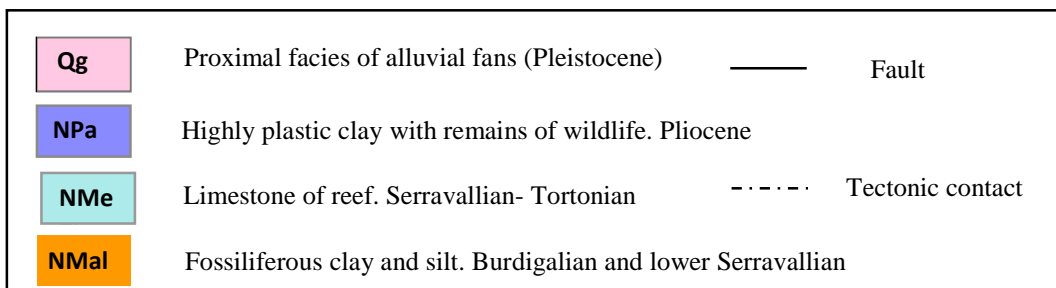
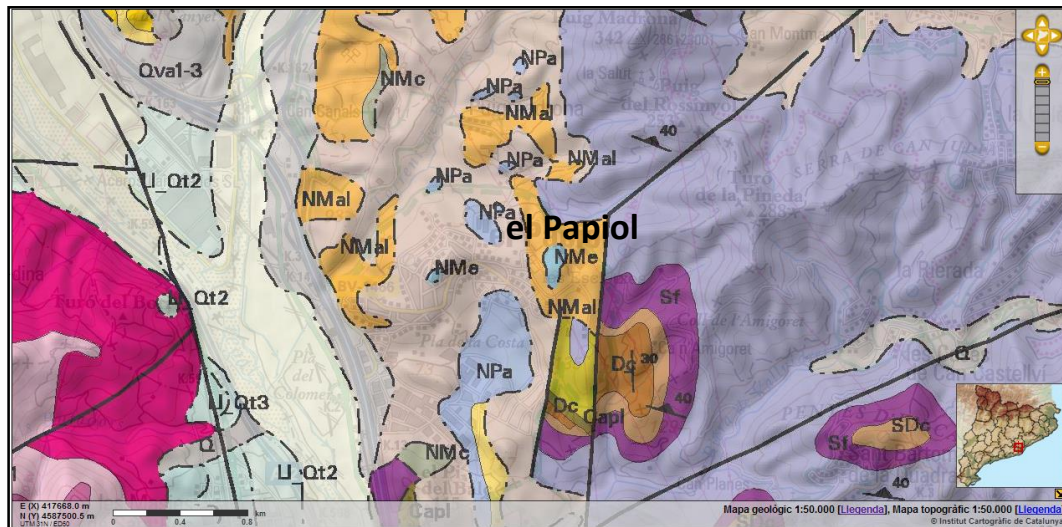


Figure 100: Geological map on a 1:50.000 scale of El Papiol. Taken from the cartographic portal of ICC (Institut Cartogràfic de Catalunya).

The described sequences deposited at the foot of the Tibidabo Mountain, which constituted a margin basin during the Miocene; the small alluvial fans, with a radius close to 1 km, leading to the sedimentation of conglomerates, breccia, sands and clays.

During the medium Miocene, an important transgression affected the basin (Font J. et al., 1987). This outcrop shows the development of a sequential organization of the alluvial

system of the lower and middle Miocene and the subsequent Langhian marine transgression.

The sedimentary record in the Vallès-Penedès basin includes mainly succession of the Lower Miocene age (Aquitanian-Burdigalian) to higher (Tortonian).

Two complex of sedimentary and continental environments constitute this register: the lower continental complex (lower Miocene-middle Miocene) and the superior continental complex (middle Miocene-upper Miocene).

Terrigenous rocks originated by the action of alluvial fans systems, mainly of northern provenance, that from the Tibidabo Mountain gave rise to deposits observable in the bottom of the hill of Papiol village, composed the Continental complexes.

During some stages of the basin (mainly middle Miocene) were formed (between the continental deposits) terrigenous and carbonate deposits corresponding to deposits of marine and transitional environments, which recognized the influence of Miocene transgressions.

During the Langhian marine transgression, sedimentary deposits of carbonate platforms formed and expanded in the basin of Valles Penedes (Sole et al., 1963).

The Les Escletxes geotop shows the development of a retrograde sequential organization of the lower and middle Miocene alluvial systems and the subsequent Langhian marine transgression (middle Miocene). The possible performance of extensional faults that control the accumulation of appreciable thick (some hundred meters) of lutites of the alluvial fans can be seen very clearly in this place.

Thus, the subsequent sedimentation of marine facies resulted in the formation of a not very powerful stratigraphic unit that covers the continental deposits; this demonstrates the filling of a paleorelief, possibly of tectonic origin and related with the performance of small faults. The Langhian marine transgression resulted in the formation of limestone deposits and do not show significant changes in thickness, because they were not influenced by the performance of any significant tectonic structure.

6.4.1.2 Result And Discussion

The first step of the processing is the selection of pixels with an amplitude stability. In this case, pixels having a mean amplitude value lesser than 0.3 have been selected. The figure 101 shows the results of the processing step.

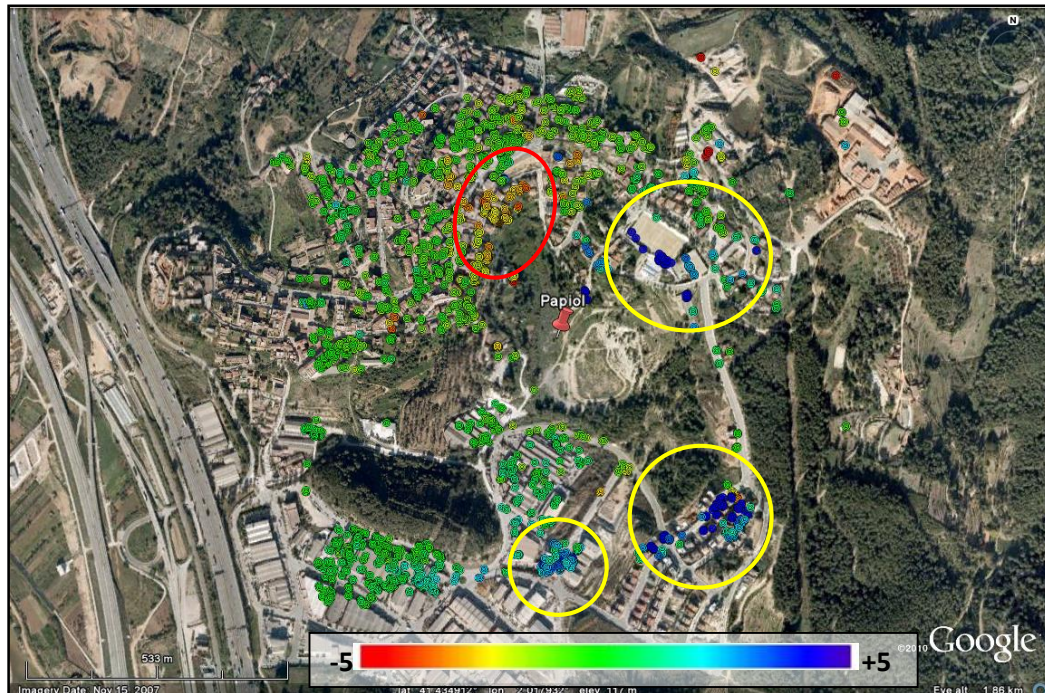


Figure 101: Deformation map. The PS that indicate significant movements are in four different areas. In particular, PS with negative velocity values characterizes the area labeled as one as result of a west-facing slope; this implies that the movement is detected moving away from the satellite. The other 3 areas show positive values, because the motion is detected approaching the satellite. The velocity values refer to the Line of Sight of the SAR; there is a minimum value of -8.5 mm/year and a maximum of 12.2 mm/year . The color scale is saturated between -5 mm/year and $+5 \text{ mm/year}$.

The processing of TerraSAR-X data have permitted to delimit four main areas affected by slope processes (figure 101). The positive velocity values are movements on direction toward from the satellite whereas the negative ones have strong component away the satellite LOS. Taking into account the morphological features of the slopes, the phenomena have been delimited and thanks to the velocity values measured by the PS, these have been characterized with an average velocity value. An uplift with displacement ratios up to 10 mm/year affects the industrial area placed on the valley floor; it could be due to the swelling of the underlying plastic clays resulting from a suspension of underground water extraction.

The morphological features that characterize the area are two gravitational movements of considerable importance.

The first phenomenon coincides with the movement detected by the interferometric data and it is a landslide sets to clay lithology and interesting the urban village of El Papiol.

The detected movement is a slump that had its last reactivation in 1983 due to intense precipitation phenomena and it occurred because to the overcome of the cutting resistance; the water pressure and the presence of overloads (buildings) influence these phenomena. Secondary areas are often associated with the main sliding surface.

The interferometric data show that the satellite detect in a different way the movements that occur in the four areas reported in the figure 101.

Ground motions that are registered moving away from the satellite affects the area 1 that is exposed to the east; this could correspond to the destabilization of the sandstones that are subjected to the movement of clay. Some ground displacements that are recorded close to the satellite, characterize the other three areas that are respectively oriented to NW.

The second phenomenon interests an area within the center of the village and called Les Escletxes; from the photos, it is clear the presence of an intensely fractured zone.



Figure 102: Image of Google Earth of the Les Escletxes (zone A).

The presence of two different lithologies, clay and limestone, characterizes the area affected by instability. The cross section of the examined area is visible in figure 103.

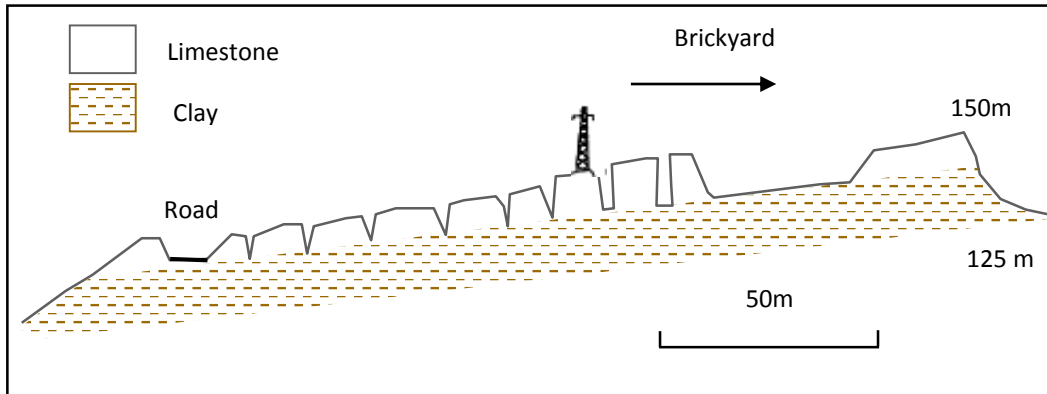


Figure 103: Cross section of the Les Escletxes landslides.

The figure above show that the phenomenon is due to a competent plaque of fractured limestone sliding on a deformable substrate of clay; we consider the substrate as a flexible and plastic mass easily deformable. The liquefaction phenomena due to the water infiltration, coming from the fractures in the overlying plate, cause the movement.

Blocks of limestone (competent and fragile) and intensely fractured characterized the plate; the motion in this case is related to the deformations that occur in the clayey substratum.

Obviously, the two movements are closely related to each other. The outcrop is characterized by the presence of numerous trenches as can be seen in figure 104.



Figure 104: Pictures of the trenches in the geotope of Les Escletxes.

The phenomenon is attributable to a plate-substrate system (Casagli, 1993): the rock mass that forms the top of the plaque has a high fracture permeability; the substrate of the plate is made of clay and is characterized by a low permeability to primary porosity.

These conditions are predisposing factors to instability because the constant presence of water at the substrate-plaque contact, promotes softening phenomena; these phenomena are located at the discontinuities of the hilltop of the plaque. The extrusion and softening of the clay can cause the fracturing of the rock mass and the onset of mechanical instability that causes the gradual increase in the opening of the fractures and the increased of the vertical permeability. This phenomenon is actually inactive as there is no evidence of movement visible from the photo interpretation and the interferometric data does not report useful informations.

Synthetically can be made a reconstruction of the history that led to the origin of this geotp. The outcrop was not as it is today; the limestone was characterized by some small cracks and holes and the water had not yet reached the clay. It is a stable situation with a competent plate on the shale substrate.

The water penetration into the fractures in relation to rainfall and thaw phenomena, promotes the alteration of the shale substrate. The softening of the clay causes the instability of the plaque and the fracturing of the rock mass

In relation to the orientation of the existing joints to the main stress, to the shear strength of joints and to the possibility of deformation in the substrate to allow the movement, may form: opening of the joints with cracking, or shear sliding along the joints with the formation of trenches

The rock mass slightly eroded is broken down into some isolated blocks. Some trenches, which are preferential ways for water flow, separate them.

6.4.1.3 Field Trip Validation

During the validation field, survey diffuse damages to the buildings and roads have been detected in the other four areas (figure 105).

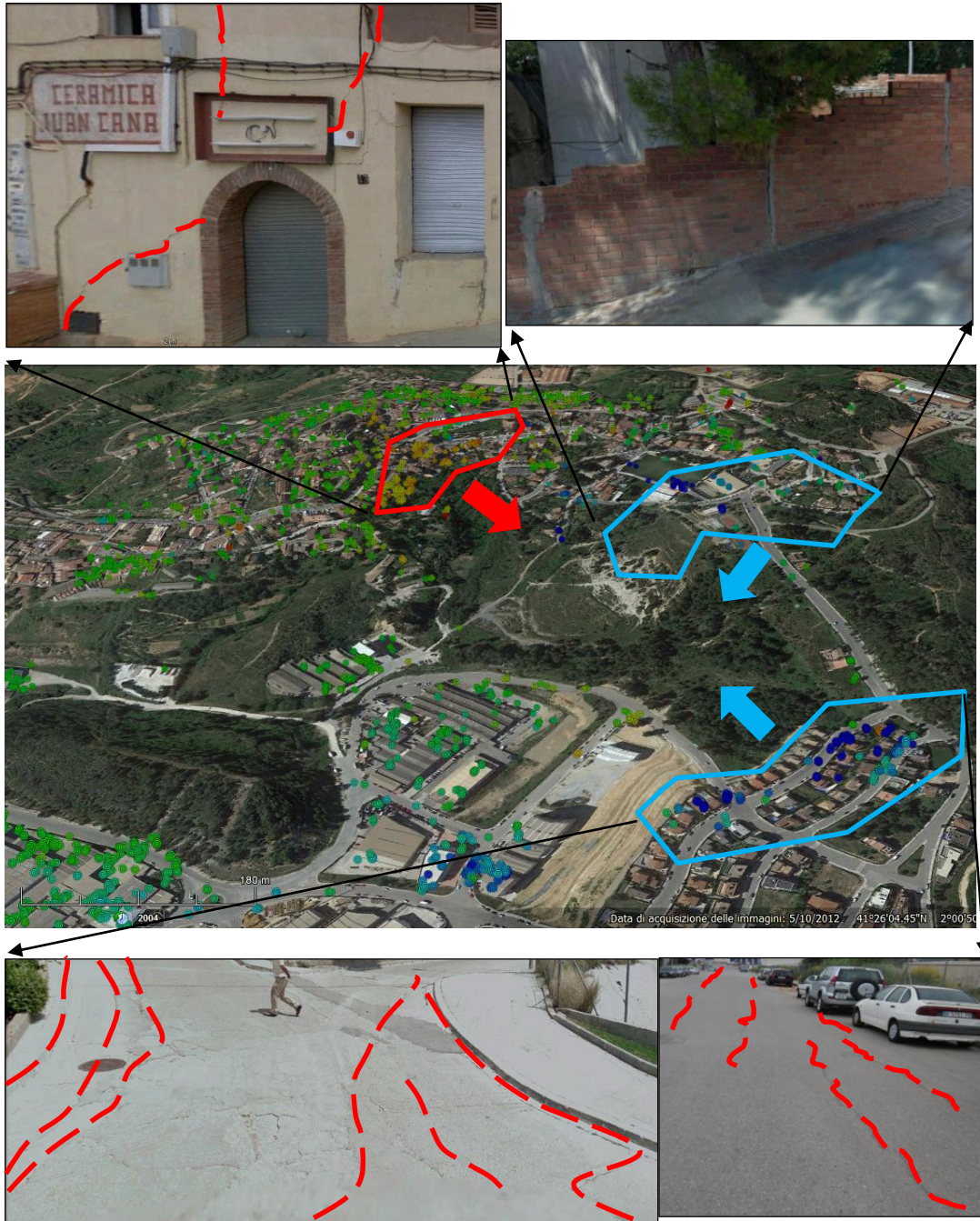


Figure 105: Slope processes delimited on the village of El Papiol. The pictured were taken during a field survey when diffuse damages to the buildings and roads have been detected.

6.4.2 MONTJUÏC

Barcelona's Montjuïc is a broad shallow hill with a relatively flat top overlooking the harbour, to the southwest of the city centre. The eastern side of the hill is almost a sheer cliff, giving it a commanding view over the city's harbour immediately below. The profile is steeper on the east slope, gentle on the west slope, and has a maximum altitude of 191.7 m (Montjuïc Castle) and a minimum of 7.8 m and a length of approximately 360 ha.

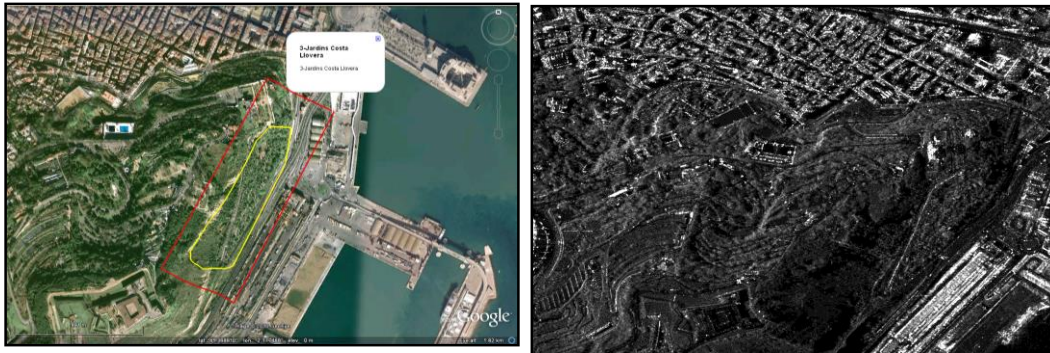


Figure 106: Jardins Costa i Llobera and Mountjuïc and Mean Amplitude image of Mountjuïc

6.4.2.1 Geological Setting

From a geological point of view Montjuïc represent an “island” among the surrounding areas, that are characterized by recent alluvial sediments, mainly of the Llobregat river delta in the southern part and other minor streams coming from the surrounding hills (Sierra de Collserola) in the northern part.

The lithology of the hill is characteristic and different from the surrounding reliefs like Sierra de Collserola, the hills of Monterols, and El Putget that are composed by metamorphic rocks and sandstones of the Paleozoic age (between 500 and 300 millions of year). In fact, Neogenic sedimentary rocks compose Montjuïc (figure 107), in particular Miocene arcoss sandstones with levels of marls with abundant fossils of marine fauna and plants, locally covered by more recent fluvial terrace deposits.

Due to this lithological setting and composition an intense mining activity have been performed until the early seventies of ‘900 with the development of many sandstone quarries, some of which visible even now, which have been for a long time the main source of building material of the city (figure 107)

The formation of Montjuïc, during the Miocene period, is associated with an intense period of extension that caused the opening of the Balearic Sea (Solc de Valencia).

Due to this extensive system, a rift (depressed area due to crustal extension) consisting of several sedimentary basins or Graben (Vallès-Penedès, Barcelona) separated by structural

elevations or Horst (Collserola, Garraf) was formed at the NW boundary of the Solc de Valencia. The structure of this rift is dominated by normal faults oriented generally NE-SW (Villalta and Rosell 1965).

The mountain of Montjuïc is part of a Neogene Horst and of a Graben of the Catalan Coast Mountains in the far northwest of the depression of Valencia.

It consists of about 200 m thickness of sedimentary rocks (clays, sandstones and conglomerates) deposited in a delta during the Miocene (15 million years ago).

The SE side of the mountain is the one providing the best outcrops of the Miocene. His abrupt profile (carved by a fault that has led part of the mountain under the sea) shows a NE-SW trend and cuts Miocene material from the base to the roof.

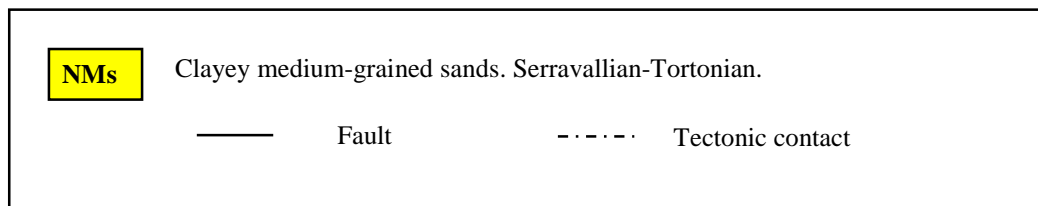
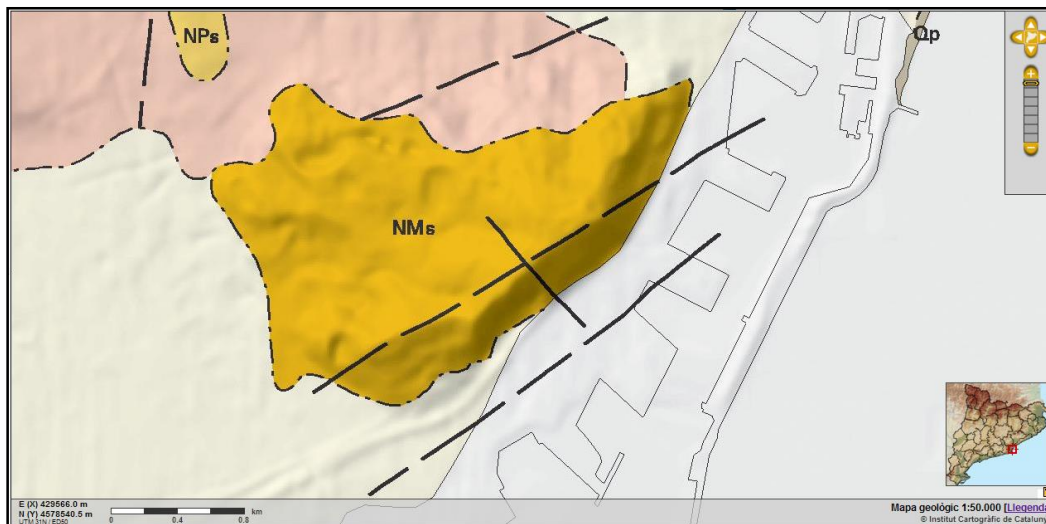


Figure 107: Geological map on a 1:50.000 scale. Taken from the cartographic portal of ICC (Institut Cartogràfic de Catalunya).

The base of the mountain is composed of massive and well cemented sandstones and conglomerates. Above this, from the lighthouse to below Montjuïc Castle are outcropping massive sandstone layers very powerful in some points. All these materials are what, 15 million years ago, was a delta (Delta Montjuïc) formed by a river that borne on massif Collserola. Within the stratigraphic series of Montjuïc is easy to observe the different sedimentary environments that characterize a delta (Vía and Padreny, 1972).

The first 75 meters of the series correspond to delta plain deposits, above these the front delta deposits and above the pro deltaic deposits.

The western side of the mountain has few natural outcrops, because its soft slope is caused by the same layers of Miocene that sink in the city of Barcelona and the materials are covered by Pliocene and Quaternary materials of Llobregat delta (Villalta and Rosell 1965). Montjuïc is not an isolated outcrop in the geology of Catalonia, since its genesis is associated with all the sediments that fill the Catalan Miocene sedimentary basins. The geological context that relates the formation of these basins is extensive phase of the Neogene, which produces the structure of the coastal Catalan margin and depressions, as can be seen today (figure 108).

Four main formations characterize the Montjuïc (Pacerisa, 1999).

- unit of Mirador: constituted by sands
- unit of Miramar: constituted by marls
- unit of Castle: constituted by clay and sandstones
- unit of Morrot: constituted by sandstones and conglomerates

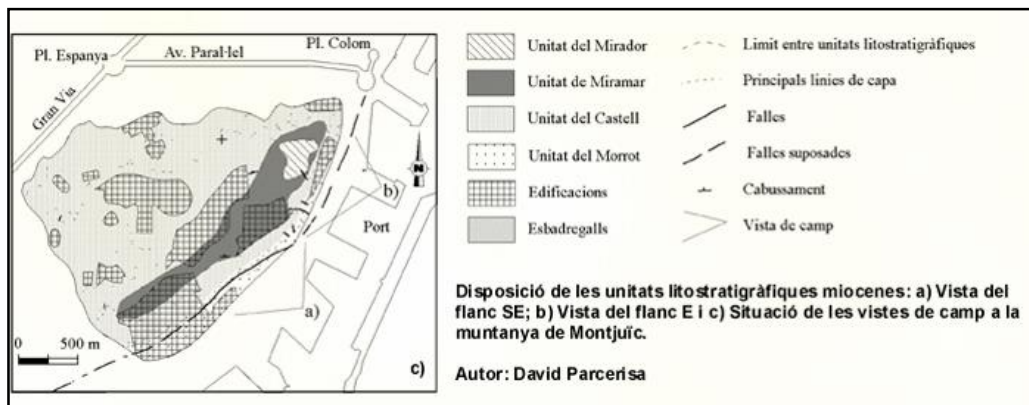


Figure 108: Layout of the lithostratigraphic units of the Miocene. Adapted from Pacerisa, 1999.

6.4.2.2 Results And Discussion

The result of pixels selection is a set of 12072 pixels distributed all over the image; looking at the amplitude image, a higher density of PS on populated area and on the port rather than the slope is expected to have. Therefore, since the area of interest concerns the area with less coherence, a densification of the pixels on the side of interest is done.

For this, the pixel selection described previously is repeated in this stage but relaxing the selection thresholds; the objective is to obtain a denser set of pixels. For the operation of densification, we take a dispersion of amplitude value of 0.3. The result is an increase of 7570 pixels for the only area of interest, the slope of Mountjuć.

A very important thing to keep in consideration in the processing step is the choice of the stable area; it is a stable point of the investigation to which are reported all the other points. It need to have some features like not to be affected by ground motion; the area must be a stable area resting on the ground and it must be inside the area affected by movement, cannot fall outside it. The result of processing is shown in figure 109; in our case the stable area falls within the port and is represented by an orange spot.



Figure 109: Land deformation map after the processing. The orange spot indicates the stable area in which all the points refer. The velocity value are saturated within a range between -5 mm / year and $+5$ mm / year. The velocity values refer to the Line of Sight of the SAR; there is a minimum value of -6.9 mm / year and a maximum of 1.2 mm / year.

By analysing the ground deformation map obtained, two areas with remarkable surface displacement have been detected on the hill; in particular on the east side in correspondence with the area of Jardins de Costa I Llobera (figure 109). In these areas, an accurate exam on the SAR data has highlighted displacements with velocity values up to several millimetres per year, measured along the Line-Of-Sight (LOS) of the satellite, and in direction away from the satellite (orange and reddish points in figure 109).

In the area of Jardins de Costa I Llobera evidences of superficial displacements have been detected in two sites (figure 110).



Figure 110: two different sites have been detected as interested by deformation. The first one interests the Carretera Miramar and a portion of the underlying gardens. The mean velocity is 4 – 5 mm / year. The second site, placed near a small car park next to the entrance of the tunnel on Carretera Miramar has a mean velocities are around 4.8 mm / year.

The first one (the lower in the right box of figure 110 near the gardens) interests the Carretera Miramar and a portion of the underlying gardens. The average LOS velocity values are around 4-5 mm/year measured along the LOS of the satellite but, the presence of a dense vegetation, did not allow increasing the density of PSI points in the area of the gardens, but only on the road.

The second site (the upper in the right box of figure 110) is placed near a small car park next to the entrance of the tunnel on Carretera Miramar. In this site, the measured velocities are around 4.8 mm/year.

It is worth to underline that the displacement direction in this side of the hill is particularly favourable to be detected by a satellite with a polar orbit like TerraSAR-X indeed in this case the velocity values could be considered as very near to the real ones.

6.4.2.3 Field Trip Validation

A rocky cliff (figure 111) and an underlying steep slope characterize this side of Montjuïc where the gardens are located. As seen during a field survey performed, the cliff is a wide outcrop of weakly consolidated sandstones, sands and clays, whose rock fall sediment have originated a large deposit at the foot. Furthermore, in some parts of the cliff, quarry activities have took place in the past, whose waste materials have contributed to increase the thickness of the deposits at the foot.



Figure 111: In A in the interferometric data indicate that the area affected by soil deformation. The area is under a scarp. In B is visible the alternation of clay lithology's resting upon cementified sandstone layers. In C the effects of the soil movement on the sidewalk.

From the photo B is evident the presence of a slope characterized by the alternation of clay resting on cemented sand; in particular, the clay give rise to the formation of gully

structures. The eroded material, accumulated at the foot of the slopes, tends to cause soil movement confirmed by interferometric data (photo A).

In the photo C is the result of ground motion that create the instability on the sidewalk along the road. With regard to the road on which fall the PS there were no fractures.

The road was recently resurfaced. It is clear that those two landslides involve those instable slope deposits, which are moving with an extremely low deformation rate (Cruden and Varnes, 1996).

The second site, placed near a small car park next to the entrance of the tunnel on Carretera Miramar, shows an area predisposed to rock fall and topple; to reduce that risk, some gabions are were put.

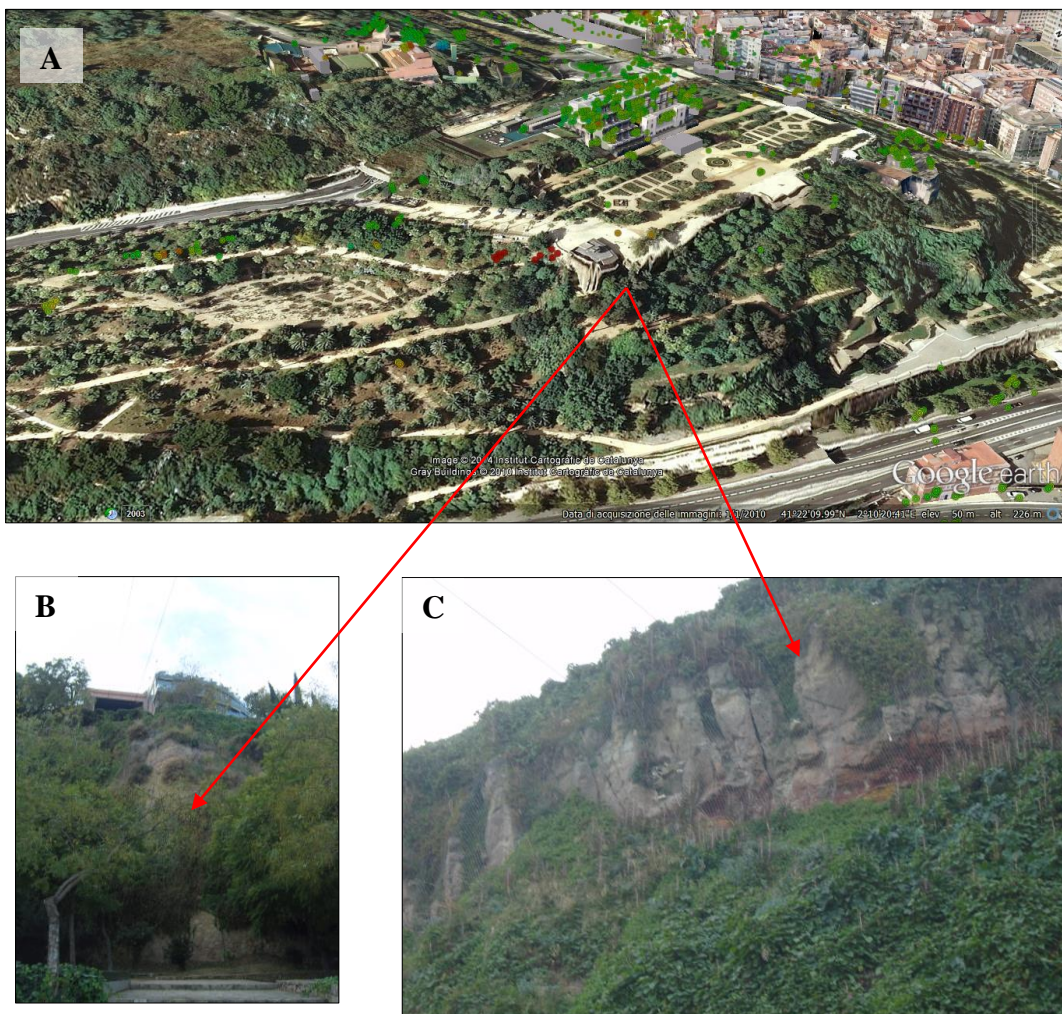


Figure 112: In A in the interferometric data indicate that the area affected by soil deformation. In B and in C the effects of the soil movement on the scarp.

6.4.2.4 Real Velocity Calculation

In relation to the slope of figure 113, an analysis to calculate the real velocity of the soil deformation in the area, was done.

To obtain the values of Slope and Aspect have been made some elaboration of the DTM (Digital Terrain Model).

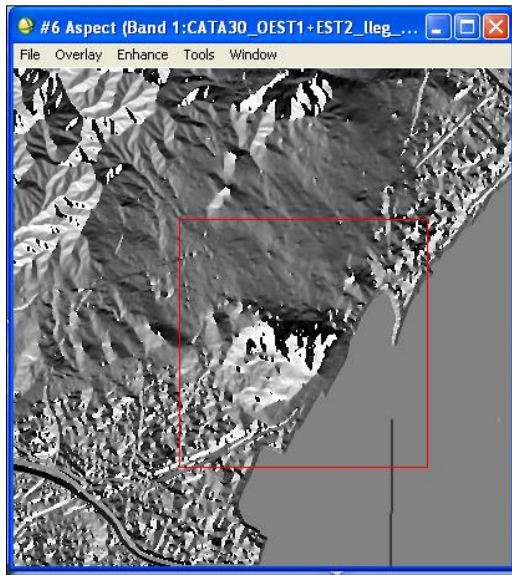


Figure 113: Aspect Image of Montjuïc

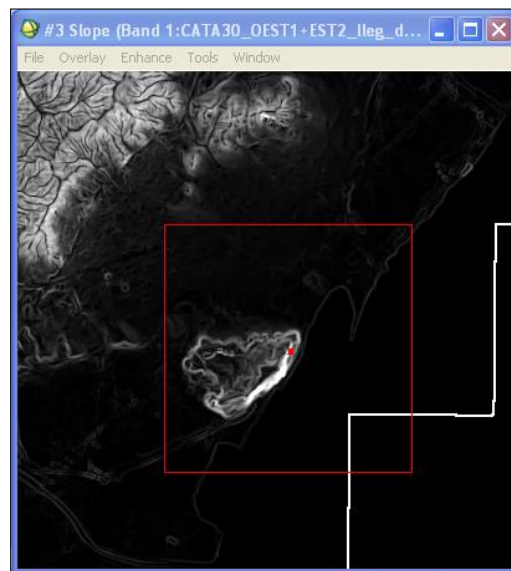


Figure 114: Slope image of Montjuïc

The slope that we are analyzing has an orientation of 130° from the north and therefore the slope is exposed to the southeast; usually PS ascending give a higher information to the east and southeast slopes facing.

The slope image (figure 114) gives us information on the slope of the versant. The slope is measured in degrees with the convention of 0 degrees horizontal.

The images of Aspect and Slope clearly emphasize the scarp of the mountain facing the port; the numerical values obtained allow us to make a calculation of the real velocity.

The calculation of the real velocity is based on the decomposition of the velocity values into two components: the horizontal and the vertical one.

On the next page are shown the patterns with their correction formulas to calculate the real velocity; it requires an estimate of the mean velocity of PS. In this case, the value is 6.6 mm/year.

The PS on which the real velocity calculation was made are surrounded by a circle in figure. The Aspect value to insert is 130° .

The results are shown in table .

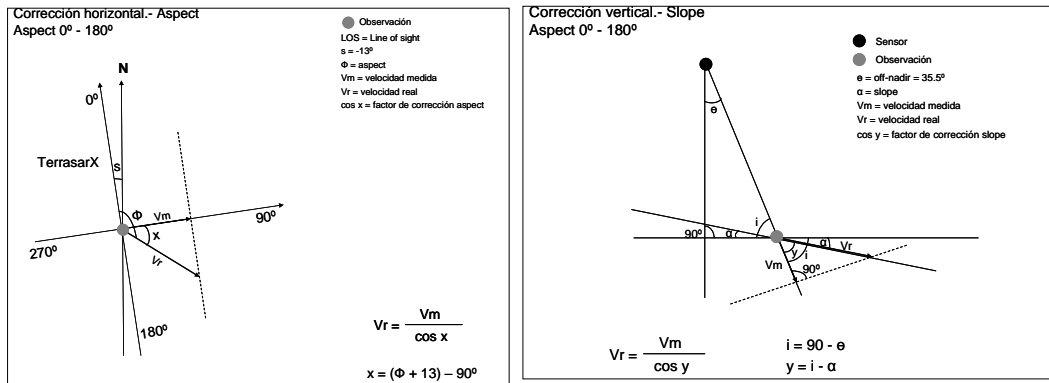


Figure 115: Pictures explain the procedure to correct the measured velocity along the line of sight to calculate the real velocity. It takes into account the two components of movement: horizontal and vertical.

Variables	Units	Value
Incidence (off-nadir) angle	degrees	35.5
Mean Velocity (Vm)	mm/year	6.6
Slope	degrees	30
Aspect	degrees	130
Aspect correction factor (cos x)		0.6
Slope correction factor (cos y)		0.9
Total correction factor		0.5
REAL VELOCITY	mm/year	12.05

From the value of 12 mm/year the movement can be said underestimated; although, for the geometry of exposure is closer to the real value.

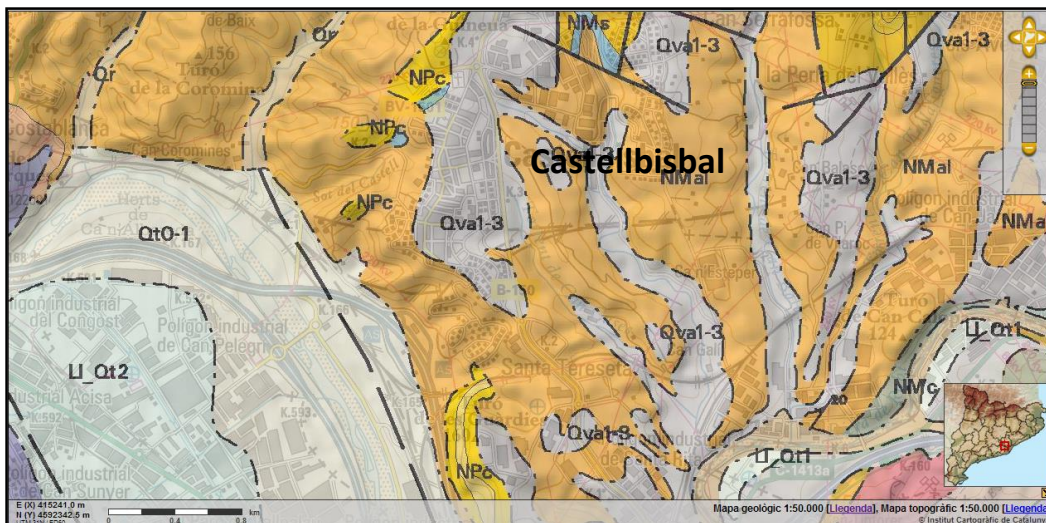
6.4.3 CASTELLBISBAL

Castellbisbal is a municipality and town in the country of Vallés Occidental, located in the province of Barcelona in the autonomous community of Catalonia, Spain (figure 116). Castellbisbal name comes from two Catalan words: "Castell" and "Bisbe", which are "castle" and "bishop" respectively.

6.4.3.1 Geological Setting

From the geological point of view, the area is characterized by a major lineament trending NW-SE, which coincides with the trend of the Llobregat river.

From the lithological point of view, the presence of sediments of fluvial origin of a period from Serravallian to Holocene characterizes the area.



— — —	Fault	- - -	Uncertain Fault	- · - ·	Tectonic contact
LI_Qt1	Terrace and tributaries of the Llobregat. Holocene	Qva1-3	Terrace and tributaries of the Llobregat. Terminal Pleistocene - basal Holocene		
Qr	Deposits of extra current streams and rivers. Holocene	NPc	Conglomerates with sandy matrix. Pliocene		
LI_Qt2	Terrace and tributaries of the Llobregat. Terminal Pleistocene - Holocene basal	NMal	Fossiliferous clay and silt. Burdigallian-Serrvallian		

Figure 116 Geological map on a 1:50.000 scale of Castellbisbal. Taken from the cartographic portal of ICC (Institut Cartogràfic de Catalunya).

6.4.3.2 Results And Discussion

The first step of the processing is the selection of those pixels that present an amplitude stability in time. In this case, pixels having a mean amplitude value lesser than 0.25 have been selected.



Figure 117: Image of Castellbisbal.

Figure 118: Mean Amplitude image of Castellbisbal.

The result of the data processing in the deformation map in figure 119.

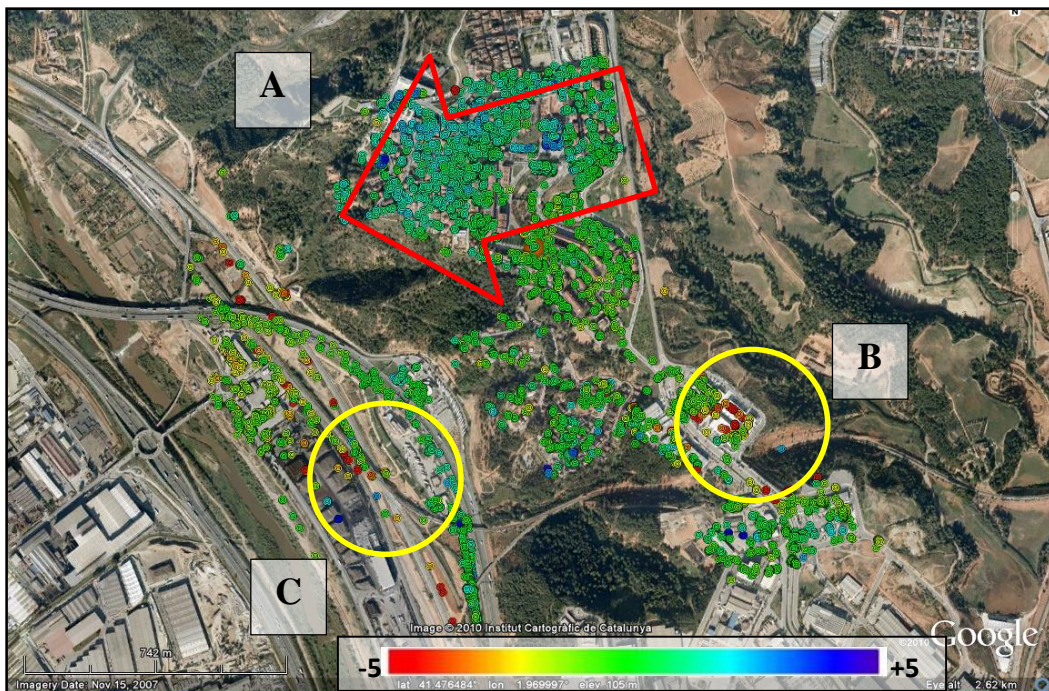


Figure 119: Land deformation map after the processing. The orange point indicate the stable area in which all the points refer. The velocity value are saturated within a range between -5 mm / year and $+5$ mm / year. The PS that indicate significant movements are in three different areas. In particular, the area labeled as A shows positive values. The other areas are characterized by PS with negative velocity values as result of a probably subsidence. This implies that the movement is detected moving away from the satellite.

From the values retrievable from the cursor location value of ENVI, we can know the values of amplitude and the pixels that are selected for processing. We expected a density of points higher in the urban area, over the industrial areas near to the village and over the highway. The preliminary result was a set of 6503 pixels distributed all over the image; after the quality test the remain number of points after the, is 5445 from the initial 6503 selected. From the LOS deformation velocity map, three areas interested by land deformation are visible.

In particular, probable subsidence phenomena interest the areas labeled as “B” and “C” in relation to the presence of a large number of industries. Castellbisbal rises on the banks of Llobregat; the aquifer represents a strategic water resource. A heavy exploitation, for industrial use and water supply, together with periods of drought, with the consequent land impermeabilization and the decrease of natural recharge of the aquifers, may have caused the lowering of the ground. The measurements show a maximum of subsidence of about 7.5 mm / year projected in the slant range direction.

The result over the city in the upper part of the image and labeled as “A” correspond to a landslide phenomenon.

The horizontal deformation component cannot be calculated using only one orbital direction. This term could be estimated using ascending and descending orbits.

6.4.3.3 Field Trip Validation

The ground deformation map have been identified three unstable areas, as is shown in figure 120.

The areas labeled as “B” and “C” are interested by subsidence phenomena; in the area labeled as B we can have also problems with the thermal expansion of the warehouse roof. The area labeled as “A” coincide with a landslide; the following factors should mentioned in determining the instability.

- The area corresponds to a high moving area located above a scarp (figure 120).
- The substrate consists of lutites and sandstones in form of strata (figure 121).
- The plans of stratification are about inclined to favor the slope of the escarpment, which would favor the displacement of the area (figure 121).
- Near the houses next to the escarpment there are cracks in buildings and relocation of the asphalt (figure 122).



Figure 120: image of the slope on which a real velocity calculation was made; the PS used to estimate the value are in the red area. They show positive values; this implies that the movement is detected moving close to the satellite. The velocity value are saturated within a range between -5 mm / year and $+5$ mm / year.



Figure 121: Image of the scarp; near the escarpment is visible an alteration of plant tissue.



Figure 122: Image of building conditions. In correspondence of PS were found fractures along the road and the walls surrounding the house.

6.4.3.4 Real Velocity Calculation

In relation to the slope of figure 120, an analysis to calculate the real velocity of the soil was done; the motion detected by the satellite, is along its line of sight and in some cases can underestimate the real movement. In general, the following assumption can be made: if the slope of the landslide is lesser than the incidence angle of the sensor, the movement of the land is underestimated. On the other hand, if the slope of the landslides is greater than the incidence angle of the sensor, the movement of the soil is overestimated. For the landslides affecting this area, the slope is generally below 35° , and therefore the movement is underestimated. To calculate the value of the real velocity it is necessary to know some values: the aspect, the slope and the mean velocity of PS considered. To obtain the values of Slope and Aspect some elaboration of the digital terrain model have been made.

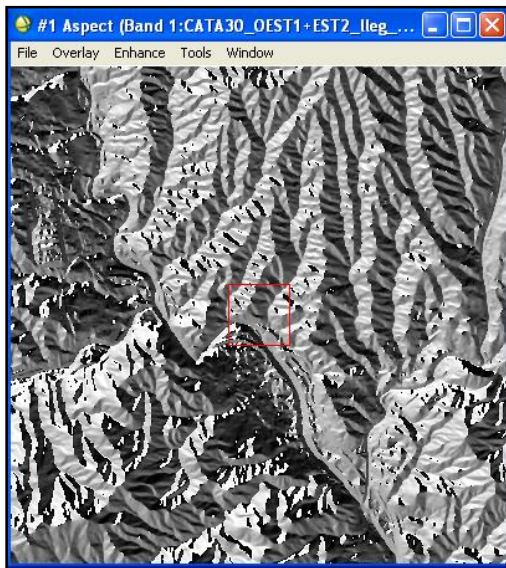


Figure 123: Aspect Image of Castellbisbal

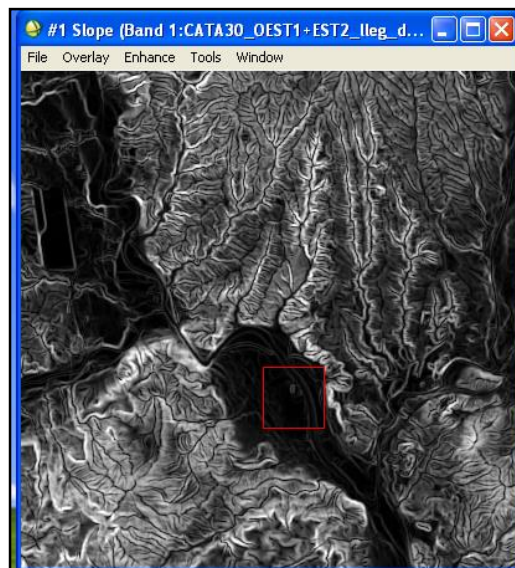


Figure 124: Slope image of Castellbisbal

The Aspect image (figure 123) gives us information on the orientation of the slope. In fact, in relation to the acquisition geometry of the satellite, some slopes are more suited to the use of this technique and other less. The aspect angle is measured with the convention of 0 degrees at north (above) and with angles increasing clockwise. The slope that we are analyzing has an orientation of 270° from the north and therefore the slope is exposed to the west. The descending orbit would be a better geometry of recovery to the west facing slopes; in fact usually, PS ascending give a higher information to the east and southeast slopes facing. The Slope image (figure 124) gives us information on the slope of the versant. The slope is measured in degrees with the convention of 0 degrees horizontal. Both the Slope and Aspect image not give us much visual help to the interpretation because the

resolution of the terrain digital model is 35 m and therefore low; the numerical values obtained, however, allow us to make a calculation of the real velocity. The calculation of the real velocity is based on the decomposition of the velocity values into two components: the horizontal and the vertical one. To calculate it there are several corrections to be used in relation to the different values of the Aspect that can vary between from 0° to 180° or from 180° to 360°. The aspect value of 270 °.

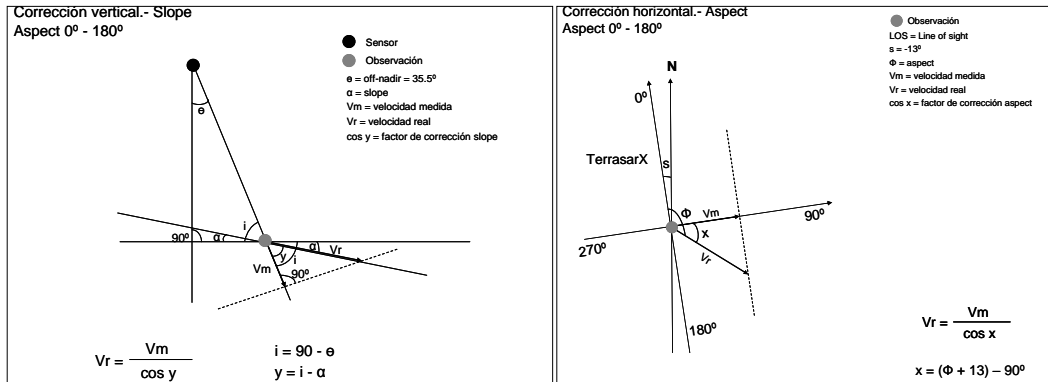


Figure 125: Pictures explain the procedure to correct the measured velocity along the line of sight to calculate the real velocity. It takes into account the two components of movement.

The mean velocity was calculated based on the PS places on the versant and surrounded by a circle in figure. The results are shown in table:

Variables	Units	Value
Incidence (off-nadir) angle	degrees	35.5
Mean Velocity (Vm)	mm/year	2.3
Slope	degrees	25
Aspect	degrees	270
Aspect correction factor (cos x)		0.97437006
Slope correction factor (cos y)		0.18223553
Total correction factor		0.17756484
REAL VELOCITY	mm/year	13

From this value equal to a rate of land movement of 13 millimeters per year can be said that the movement was significantly underestimated.

7. X-BAND DATA FOR BASIN-SCALE MONITORING

7.1 GENERAL CONSIDERATIONS

This chapter gives an application of X-Band SAR data for monitoring ground deformation and engineering infrastructures at a basin scale. In particular, the subject of this chapter, is the IG interferometric processing chain for wide areas and the consequently analysis of the results obtained; all these steps are carried out in two test areas. The first is located within and around Burgos, a city in northern Spain and the historic capital of Castile; it is situated on the confluence of the Arlanzón river tributaries, at the edge of the Iberian central plateau. It is the capital of the province of Burgos, in the autonomous community of Castile Y León. The second is located within the Barcelona city, capital city of the autonomous community of Catalonia in Spain. The monitoring activities in the area will be of significant for early detection of potentially critical situations, in proximity of the major infrastructures of the area, for examples: airport, roads and highways, harbors and villages.

In this context, an essential element concerning the use of interferometric techniques for monitoring ground deformation based on satellite data is the acquisition of respectively 12 and 26 interferometric radar image acquired in X band. In particular, the IG processing chain and the analysis conducted for this purpose included the development of two different dataset. The first dataset, used for the analysis of Burgos city, is acquired by the German satellite TerraSAR-X, in ascending geometry, from January 2013 to July 2013. The same German satellite TerraSAR-X, in ascending geometry, acquired the second dataset used for the analysis of Barcelona city, for the period between December 2007 and November 2009. After a short introduction of the IG processing technique used, some notions on the study areas are given; the data arising from the elaboration are presented and analyzed. The second paragraph describes the input data, the methodology used to produce the ground deformation maps, and the method adopted for the interpretation of the results. In particular, the second section, reproduce the chronological order of the PSI method of the Institute of Geomatics processing. The last two sections of this paragraph examine the main ground deformations and engineering infrastructures instabilities for the two examined areas. These give some examples of land deformation detection based on the IG processing method for wide areas and describe the results obtained. For each site, there is a short geological overview of the study, a summary of processing performed and the analysis of the results obtained from the PS processing and analysis.

7.2 IG PROCESSING CHAIN FOR WIDE AREAS

The interferometric procedure is a set of sequential steps, which is carried out to estimate displacement velocity from a set of Synthetic Aperture Radar (SAR) Single Look Complex (SLC) images. This procedure involves the use of several software and scripts and allows the description of the displacement and the estimation of the contribution of the atmosphere to the SAR images.

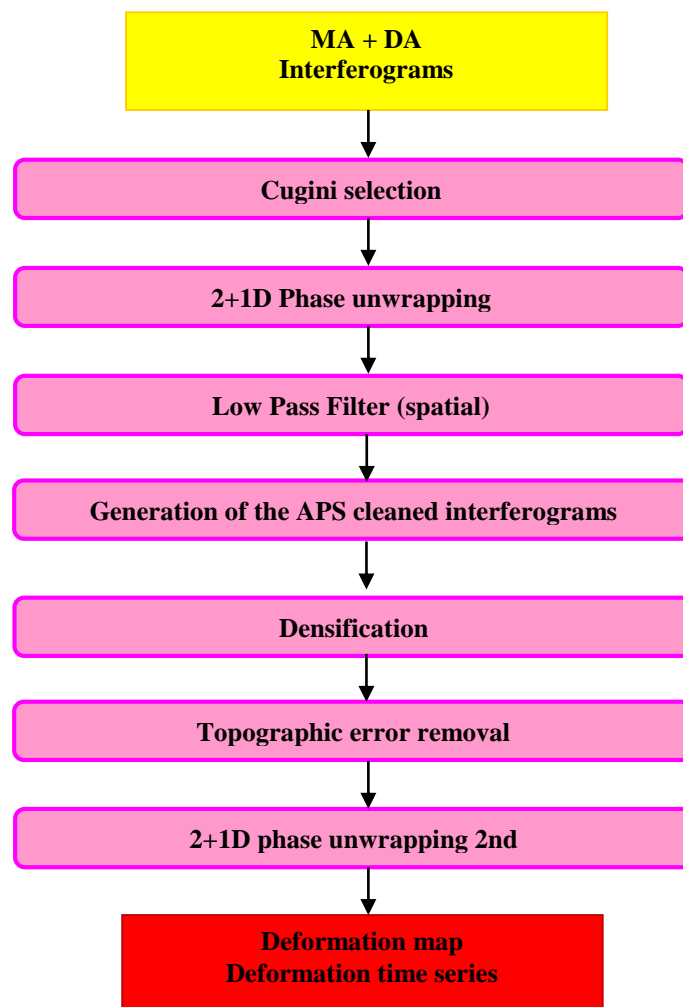


Figure 126: Flow diagram of the methodology used for the data processing in the wide areas.

7.2.1 INPUT DATA

Input data were processed in the coordinate system WGS 1984 UTM, and are the following: the interferometric data of the annual average rate of land displacement recorded by satellites, the Google Map images, the geological map (1:50.000).

The algorithm used for the interferometric data processing is able to provide good results even with a reduced set of SAR images. In particular, in this work, two dataset acquired in ascending orbit are used.

The first is a set of 12 TerraSAR-X images with ascending orbits, ranging from January 2013 to July 2013 that has been used to monitor ground deformation and engineering infrastructures Burgos.

The second is a set of 26 TerraSAR-X images with ascending orbits, ranging from December 2007 to November 2009 that has been used to monitor ground deformation and engineering infrastructures in the city of Barcelona.

The satellite data used in this work were processed with the IG processing chain for wide areas at the Institute of Geomatics.

The images are chosen to form 55 and 56 interferograms respectively with short spatial baseline. The displacement measurements are differential, related to a ground point of known coordinates (reference point); temporal measures are related to the acquisition date of the first image (master image).

Through the Google Earth application the satellite images has been observed. As a continuously update work the images are not visible on the same date and may have a temporal discrepancy from three to four years to less than one.

The geological map used is acquired by Institute of Geomatics of Cataluña on a 1:50000 scale.

The photo-and radar-interpretation, designed to extract content information from the data above, is conducted with ENVI and Google Earth. In particular, the photo-interpretation is used to identify any diagnostic morphology of a landslide and particular characteristics as indexes of the ground motion.

The radar interpretation is used to spatially extend the detailed information of a permanent scatterer and recognize any areas of instability.

7.2.2 METHODOLOGY

Cugini Selection

The cugini selection is a new PS selection procedure elaborated from the Institut of Geomatic team, in which the selected points have to fulfil some requirements set out below.

- Full frame coverage.
- Low level of ϕ_{Noise} in order to ensure a high quality of the interferometric phase along the whole period of study.
- Low etopo value to avoid an important source of phase unwrapping errors.
- Negligible thermal dilation contribution to the interferometric phase.

It is known that the points with thermal dilation effects are usually located in fabricated structures usually with a certain height, as skyscrapers, buildings, etc. This requirement is directly related to the previous one.

The algorithm *Cousin_Finder_fast_DA_Kdtree_oneshot.exe* find points with similar phase behaviour than a previous selected point (seed) (figure 127).

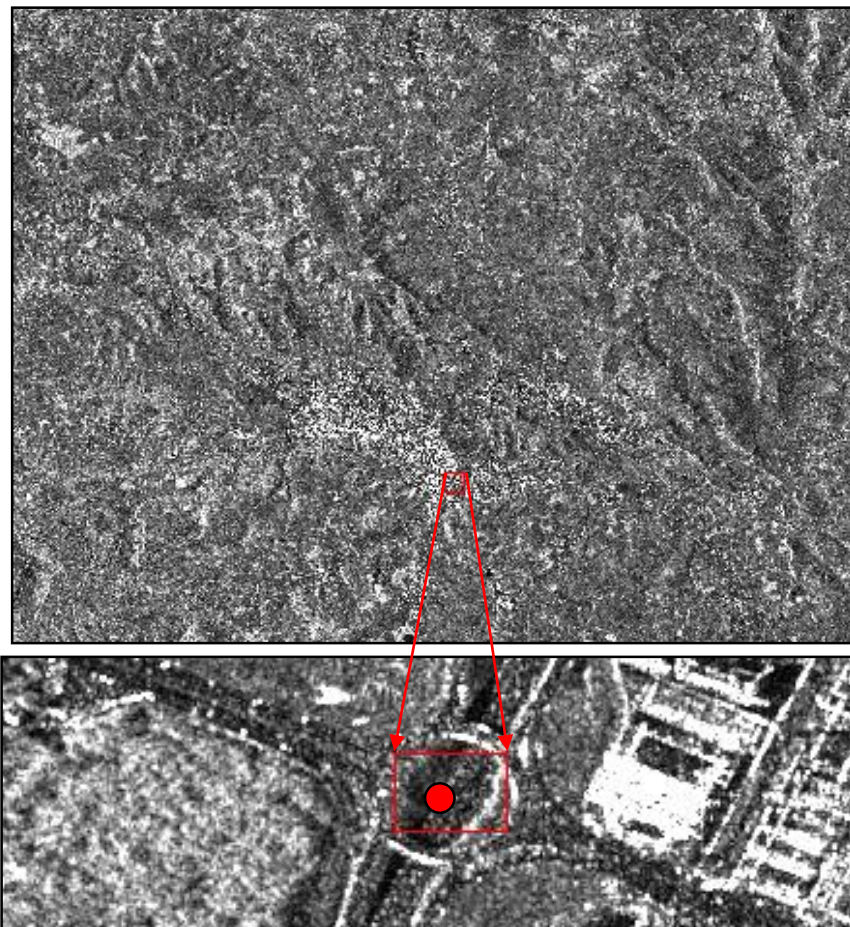


Figure 127: Mean amplitude image of the interested area of Burgos and location of the seed chosen for the propagation step within the interferometric procedure.

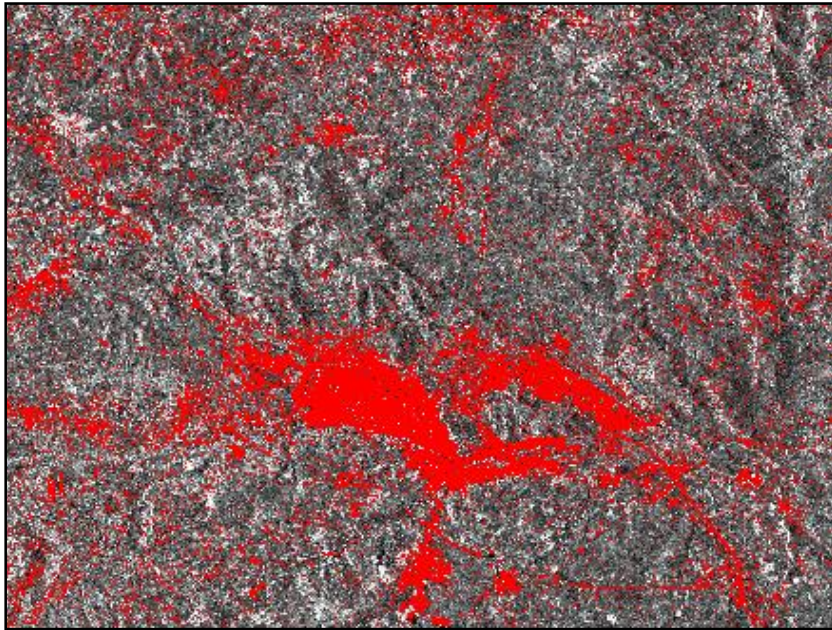


Figure 128: Mean amplitude image and results of the seed propagation along the frame using the Kd-tree propagation for the interested area of Burgos.

To propagate along the frame it uses kd-tree propagation. The condition for a point to be selected and become a seed itself is that in 90% (input) of the interferograms the phase differences between the point and the seed must be smaller than a given threshold. This threshold is the sum of a threshold for the noise + a threshold for the atmosphere effects (that depends on the distance to the seed).

2D+1 Phase Unwrapping

The phase unwrapping is the fundamental problem in the construction of elevation maps from a SAR image. The phase unwrapping consists of a decryption, that is the reconstruction of the phase difference of the radiation received by the two SAR systems, as a function of the coordinates of slant range and azimuth (figure 129).

The data available to reconstruct the phase difference are a measure of the difference of 2π module. In this case, a method that makes use of the equivalent of the irrotational property of a vector gradient field, within a discrete space, was used. This property is used primarily to identify areas in which the discrete vector field defined based on the available data must be corrected. Then to perform the correction needed to obtain a useful estimate of the discrete gradient of the phase difference function, with the knowledge of some a priori information. The function of phase difference is reconstructed from the estimation of the discrete gradient. The use of the Fourier transform makes possible the realization of a fast algorithm, which is to process an image of N pixels in $O(N \log N)$ elementary operations.

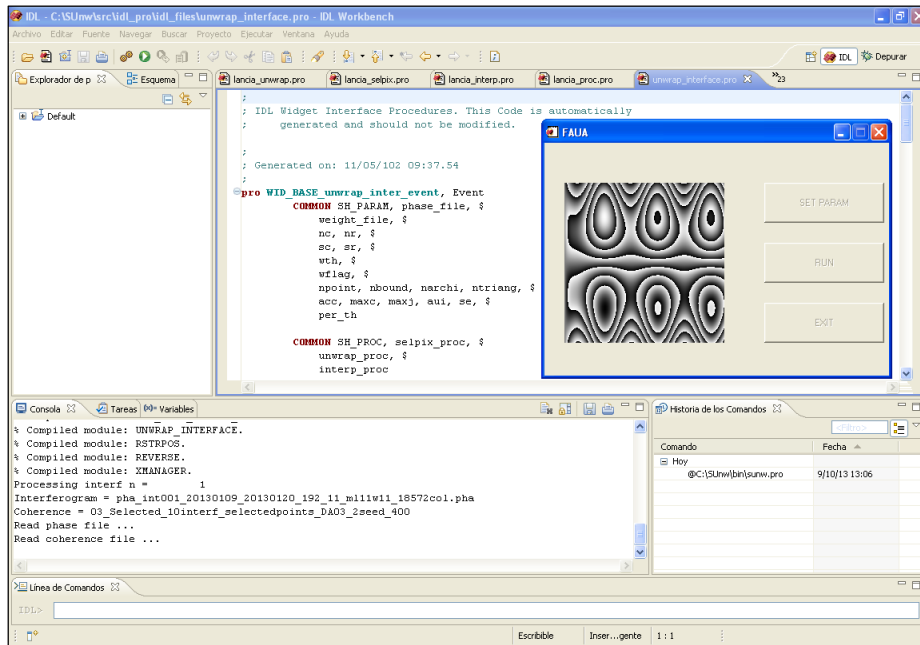


Figure 129: Image of the 2D Phase Unwrapping step conducted in IDL environment. In particular the IDL unwrapping general window and the IDL window for procedure setting are shown in the image.

Prelinea ed Int2ima

In this step of the procedure, all of the interferometric phases are determined in relation to the same reference point for comparing the phase differences. The Int2ima is a software developed by the team of the Institute of Geomatic for transforming the interferometric phase in a phase of image. A key task is to make a correction of the errors of wrapping phase that were not corrected during the phase unwrapping. Through an iterative process, we determine the phase values associated with each SAR image, starting from a stack of interferograms. If we have a network of L -interferograms and M -images, for each pixel can write L -equations for $M-1$ variables. The estimate of the phase is made assuming the phase value of the first image of the time series equal to zero.

There are two key parameters that drive this process; the first is the “residual” R , which represents the difference between the interferometric phase ($\Delta\Phi$) and the value of the phases estimated a posteriori Φ_M and Φ_S . $\rightarrow \rightarrow R = \Delta\Phi - (\Phi_M - \Phi_S)$.

The second parameter is given by the redundancy of the network of interferograms and images. For each image is important to consider the number of interferograms that are directly connected with it, such as the number of interferograms where a given image appears, does not matter if it is master or slave.

Low pass filter

The purpose of the low pass filter is to identify, within the interferometric phase, the contribution due to the atmosphere and then estimate and remove it from the phase to obtain the contribution due to the soil deformation (figure 130). This step is necessary to obtain the time series of ground deformations.

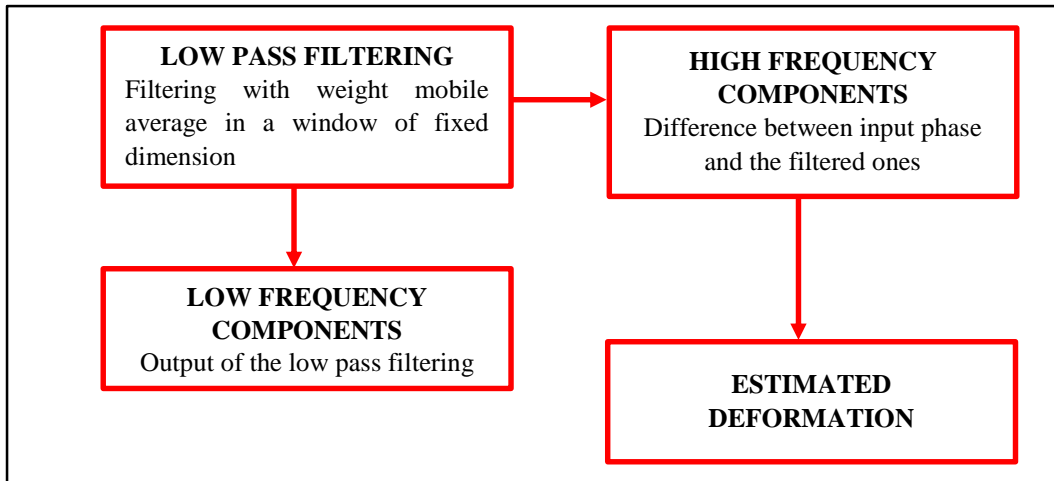


Figure 130: Flux diagram that shows the different passages useful to obtain a deformation map without the atmosphere contribution.

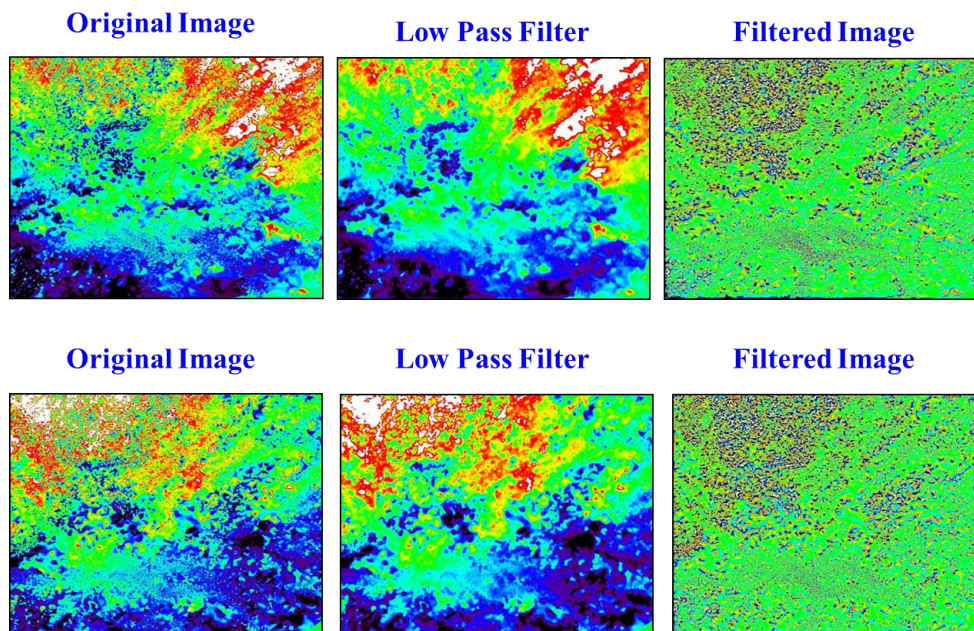


Figure 131: Images show the different passages useful to obtain a deformation map without the atmospheric contribution. The first image correspond to the original image with the atmosphere contribution; the second image is the filter that is used to remove the atmosphere. The third image is the first image without the atmosphere contribution.

Densification

In summary, the "densification" consists of five main parts. First of all the identification of the candidate pixels (those that have a high quality of the interferometric phase) with a criterion based on a low value of the amplitude dispersion along the interferometric track. Secondly, the most appropriate pixels of the track are selected and connected to form a network of points; for this, is useful the triangulation of Delaunay in order to establish the phase relations over the different points and build a model that takes into account the linear velocity of displacement and the average topographic error.

For each side of the network the phase difference between two corresponding points is determined.

After, the differential ground deformation and the differential topographical error on each side are estimated. Finally, an integration and an interpolation of these differential values over the entire set of selected pixels generate deformation maps.

The densification process was already explicate in the paragraph 6.2.2.

7.3 TEST SITES

This section illustrates some examples of land deformation detection based on the IG processing method for wide areas and analyzes some areas of Barcelona city and of Burgos, in Castilla Y Leon. The two cases of study are presented: for these sites, there is a short geological overview of the study, a summary of processing performed and the analysis of the results obtained from the PS processing and analysis. In order to estimate the deformation over these areas, two dataset acquired in ascending orbit by the TerraSAR-X sensor with a strip map mode are used.

The first is a set of 12 TerraSAR-X images with ascending orbits, ranging from January 2013 to July 2013 that has been used to monitor ground deformation and engineering infrastructures for Burgos city. The second is a set of 26 TerraSAR-X images with ascending orbits, ranging from December 2007 to November 2009 that has been used to monitor ground deformation and engineering infrastructures for Barcelona city.

By processing the 12 and 26 TerraSAR-X strip map images, acquired and elaborated at the Institute of Geomatics, 56 interferograms have been developed and a PSI data stack has been computed, making possible to carry out an accurate detection of all the main ground active deformation processes. The maps of the PS identified in the image and their coordinates (latitude, longitude and precise elevation) are the results of the multi-interferogram Permanent Scatterers approach. The PSI technique for the landslides detection has been made by integrating the PS information with the ancillary data in Google Earth and ENVI. The PS in .kml formats were displayed in Google Earth; the available dataset is already cut on the area with the previous processing operation. For viewing in Google environment PS were classified according to the velocity with different colors: red, identifies the land moving away from the radar sensor; blue, identifies the land moving towards to the radar sensor; green, identifies stable points.

The stability values are grouped into classes ranging from -5mm/year e $+5\text{mm/year}$.

The class corresponding to the stable PS is chosen between -2mm/year e $+2\text{mm/year}$.

The intermediate classes are from -5 mm / year to -3 mm / year and -3 mm / year to -2 mm / year for the movement detected moving away from the satellite.

From $+2\text{ mm / year}$ to $+3\text{ mm / year}$ and $+3\text{ mm / year}$ to $+5\text{ mm / year}$ for the movement detected moving towards to the satellite. In this chapter, we consider all the cases of study in term of analysis and interpretation of deformation map. For each of them the first part gives a geological framework of the study area, then describes the processing work and finally are analyzed the deformation maps trying to explain the causes of the main phenomena identified.

7.3.1 BURGOS

The city of Burgos is located in the center of Burgos province, in the autonomous community of Castilla y Leon (Spain). It has an area of 107.08 km² and is located 856 meters above the sea level, according to the National Geographic Institute (figure 132).



Figure 132: Burgos city. Location of the interested area of study.

Burgos is a city in northern Spain and the historic capital of Castile. It is situated on the confluence of the Arlanzón river tributaries, at the edge of the Iberian central plateau. It has about 180.000 inhabitants in the actual city and another 20.000 in the metropolitan area. The city forms the principal crossroad of northern Spain along the Camino de Santiago, which runs parallel to the River Arlanzón.

7.3.1.1 Geological Setting

The study area lies within a geological context in which the Sierra de Atapuerca appears. The Sierra de Atapuerca is a large hill of limestone. The limestone was formed on the sea floor 85 million years ago during the last period (Cretaceous) of the Mesozoic, the era of the dinosaurs. Later, back in the Cenozoic, in the period called the Tertiary, and in the Oligocene age, the gigantic forces that move the earth's crust produced the emergence and the deformation of the limestone that formed a small mountain, which is actually a fold (or anticline) lying.

Once withdrew the sea water, erosion has paved the summit of the Sierra de Atapuerca, which now has a flat top with a maximum altitude of 1082 m above the sea level.

As a result, in the successive epoch (the Miocene), what is now the Meseta of Duero turned into a giant hollow landlocked. This is a large continental basin that went filling up with sediments derived from the erosion of the mountains such as a wall, surrounded it: the Cantabrian Range to the north, the Iberian system to the east, the central System to the south and the mountains of León and Trias at west. The Sierra de Atapuerca is located at the northeastern part of the great basin of the Duero, a few kilometers from the Sierra de la Demanda, which is part of the Iberian System. Precisely, it is located in one of the gorges that give access to the Castilla: the corridor of La Bureba. The other two entrances are located in the southeast, in the territory of Soria, and in south-west, in the territory of Ciudad Rodrigo, where the Duero opens the way to the sea, entering in Portugal through the border region of Los Arribes.

A little over the Sierra de Atapuerca, after the pass of Pedraja (1130 m), is located in the Ebro basin. The Sierra de Atapuerca is surrounded by the amount of sediment accumulated in the basin of the Duero at the end of the Miocene. Continental rather than marine limestones were deposited then, in shallow lakes that extended throughout the basin.

The limestone of the final phase of sedimentation are today horizontal mesa (flat, dry and uncovered terrain), which are located at almost the same level as the top of the Sierra de Atapuerca.

The filling of the basin of the Duero ended in the Pliocene (the epoch that follows the Miocene), when cause the lift in the center of the peninsula, a river network, that began to erode and drag to the Atlantic sediments accumulated in millions of years, formed, as it continues to happen still. Across the river basin the erosion has cut the limestone mantles of the horizontal mesas and dug the soft sediments, clay and marl, which are found below. The Castilian plateau thus has two levels: the old surface of the plateau, limestone rock and

with little arable land in general, and the new surface of the valley, the most fertile and inhabited area. Both surfaces are connected by strong inclinations.

These forms of relief (plateaus and slopes) can be observed in the left margin of the river Arlanzón, near the village of Ibeas de Juarros and in front of the Sierra de Atapuerca, which is located on the right bank. The river Arlanzón flows a short distance from the southern slopes of the Sierra de Atapuerca, a few kilometers upstream of the city of Burgos

As in all the rivers in the upper reaches uproots and drags large boulders, which rounds and turns in rolling stones. When the major floods of Arlanzón are produced, even today many of these gravels are deposited in the floodplain. As mentioned above, the river is gone digging deeper the soft sediment, in the course of time; these are clay and marl type, which filled the basin of the Duero during the Miocene. In the transition remain suspended elements, which in geology are called terraces, ancient stony plains.

The highest deposits are located in the 85 m above the present level of the river, and a total level of 994 m, very close to the top of the Sierra. By studying the terraces we can know the track of the river Arlanzón in prehistory. The marine limestone, which constitutes the substrate of the Sierra de Atapuerca, is a rock that water dissolves easily. In this way long underground pipes filled were formed and formed what is called a karst phenomenon. When the water level or water table is lowered because the river network went deeper and deeper into the valley, the high karst cavities were dry and, at the same time, they produced collapses that have opened the covers. Even the relegation of the slopes by erosion affecting the galleries, has given rise to new entries. From this moment carnivores and humans could visit the caves. The whole city sets on the flood of the river Arlanzón, on whose left bank (right in picture) there are several terraces; below the alluvial soils, formations dating back to Tertiary are based on the Mesozoic tectonized levels. On top of these, the limestone plateau of the Tortonian (Upper Miocene) represents the last sequence of Tertiary lacustrine deposits, which protect the lower marl and clay, less competent, forming the Cuestas.

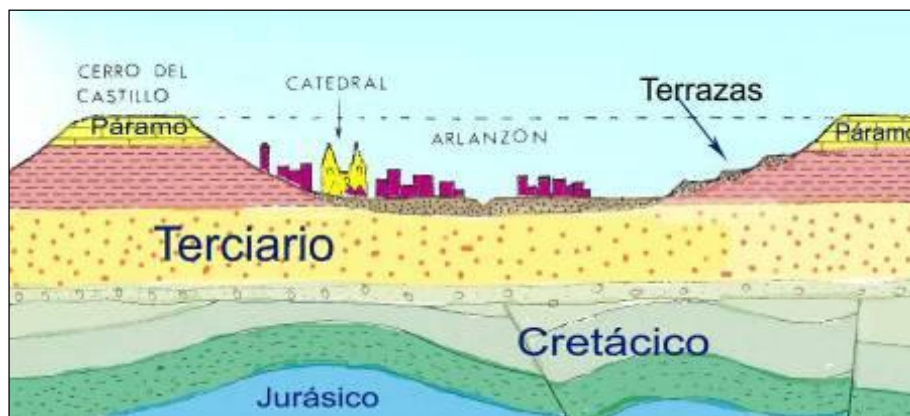


Figure 133: Geological set of Burgos city.

7.3.1.2 Results And Discussion

Burgos is located in Castilla y Leon, Spain; it is situated on the confluence of the Arlanzón river tributaries, at the edge of the Iberian central plateau. For the study area are 12 TerraSAR-X images acquired in ascending geometry in the time interval January 2013–July 2013 are used. From the images, 55 interferograms were obtained and through the methodology set out in Chapter 3, a map of ground deformation is obtained (figure 134).

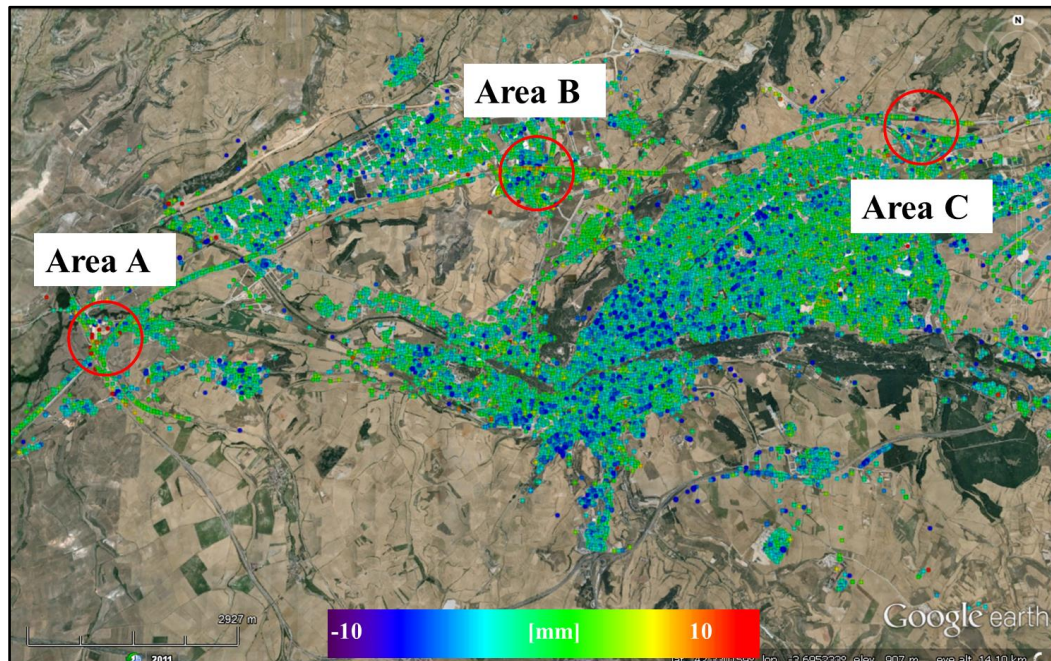


Figure 134: Deformation maps of Burgos. The PS that indicate significant movements are in three different areas. The color scale is saturated between -10 mm / year and $+10$ mm / year.

The deformation map identifies three areas affected by deformation related to localized subsidence of roads and roadways under construction. Some of the other deformations are most likely due to thermal phenomena for the high temperature range that we have in this area.

For the three areas of interest, the time series have been extracted and analyzed, but the acquisition period is temporally limited to 6 months (January to July).

In particular, the PS were produced using data from high-resolution satellite in X-band; the density of PS is ten times greater than traditional C-band satellite.

The number of images used is few (only 12) and on short period (6 months). Because of this, a lot of noise affects the data. The geological setting and kinematics of the displacement are more homogeneous all over the area, so the interpretation of PS data is easier.

Area A

The area A is located near the intersection between the Autovia Camino de Santiago and the Carretera de Logrono-Vigo. During 2011, some works have been carried out along the stretch of highway; this has led to some excavations and construction of new facilities.

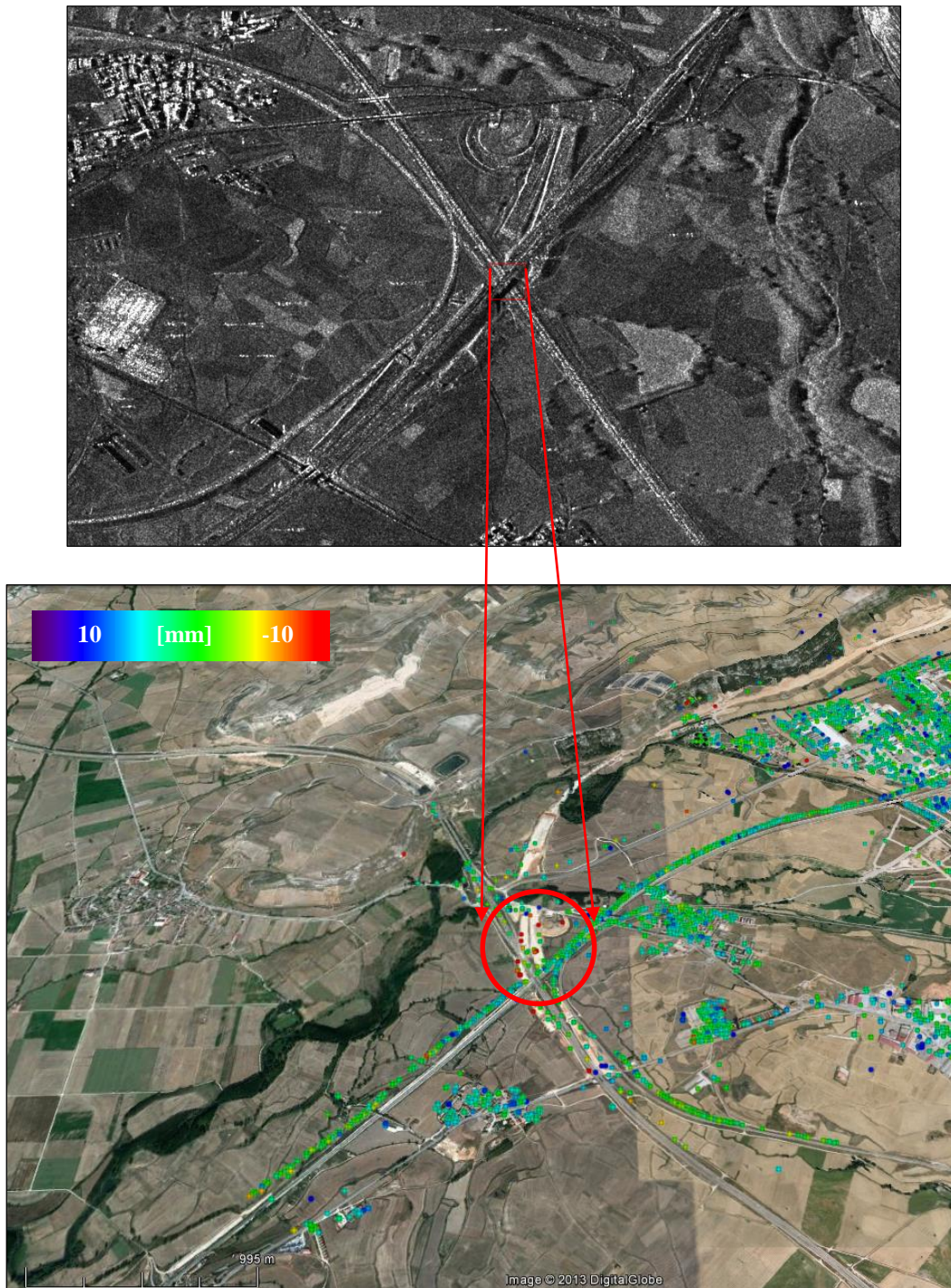


Figure 135: Mean amplitude image of the study area and localization of radar targets in the area A. The velocity value are saturated within a range between -10 mm / year and $+10$ mm / year. The velocity values refer to the Line of Sight of the SAR.

In the following figures, the time series of the interest points are presented for the area A.

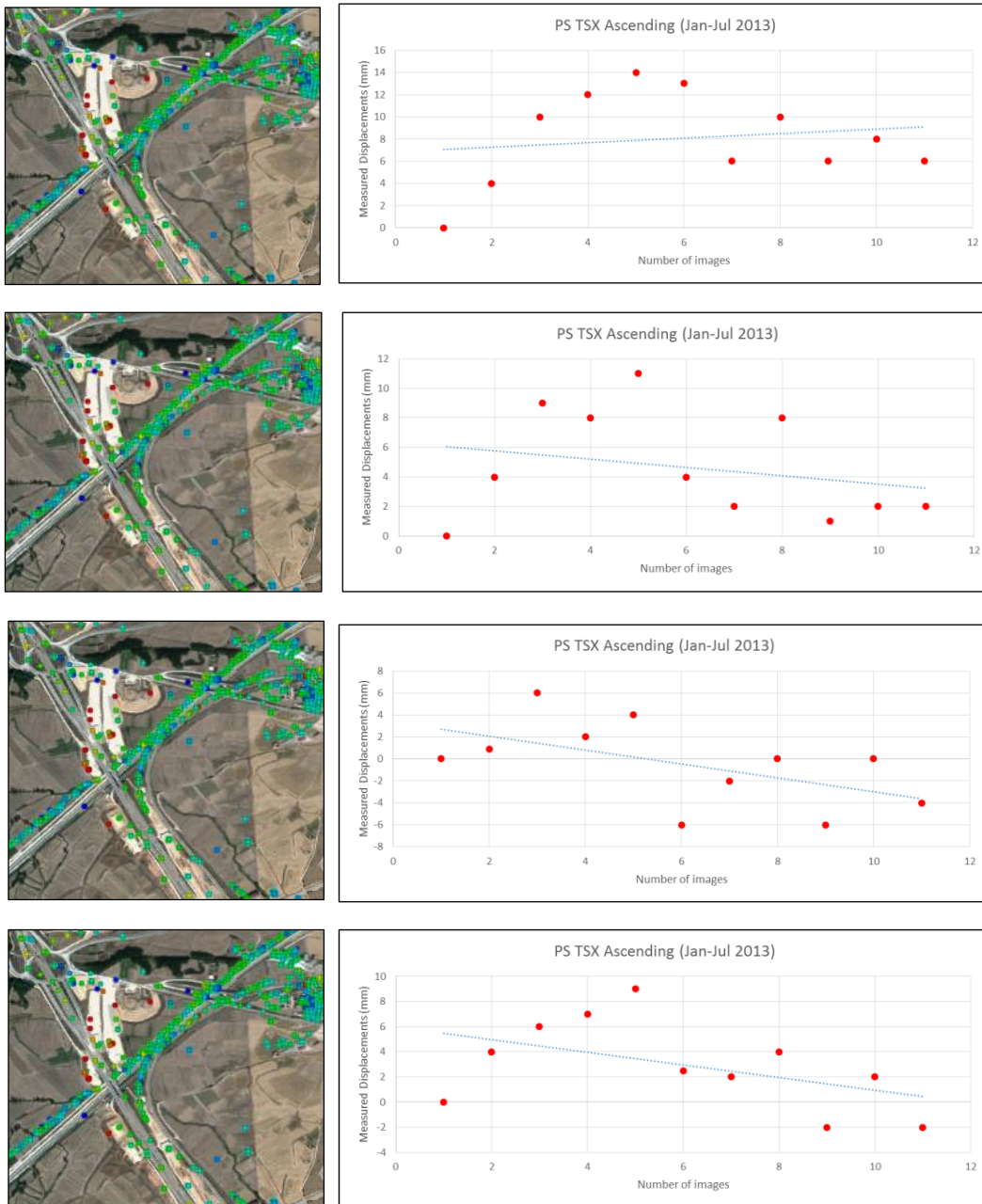


Figure 136: Time series of the interested points for the area A.

The radar targets, identified, present both a movements close to and away from the satellite; the maximum velocity recorded is 12 mm/year. The movement recorded by the interferometric data is due to some yards going down the stretch of the highway. In addition, some movements are probably due to the consolidation phenomena induced by the structures adjustment (figure 136). The area A presents displacements with an average velocity value of -2.5 mm/year.

Area B

The area B is located along a track of the Autovia in the nearness of the Rio Vena.

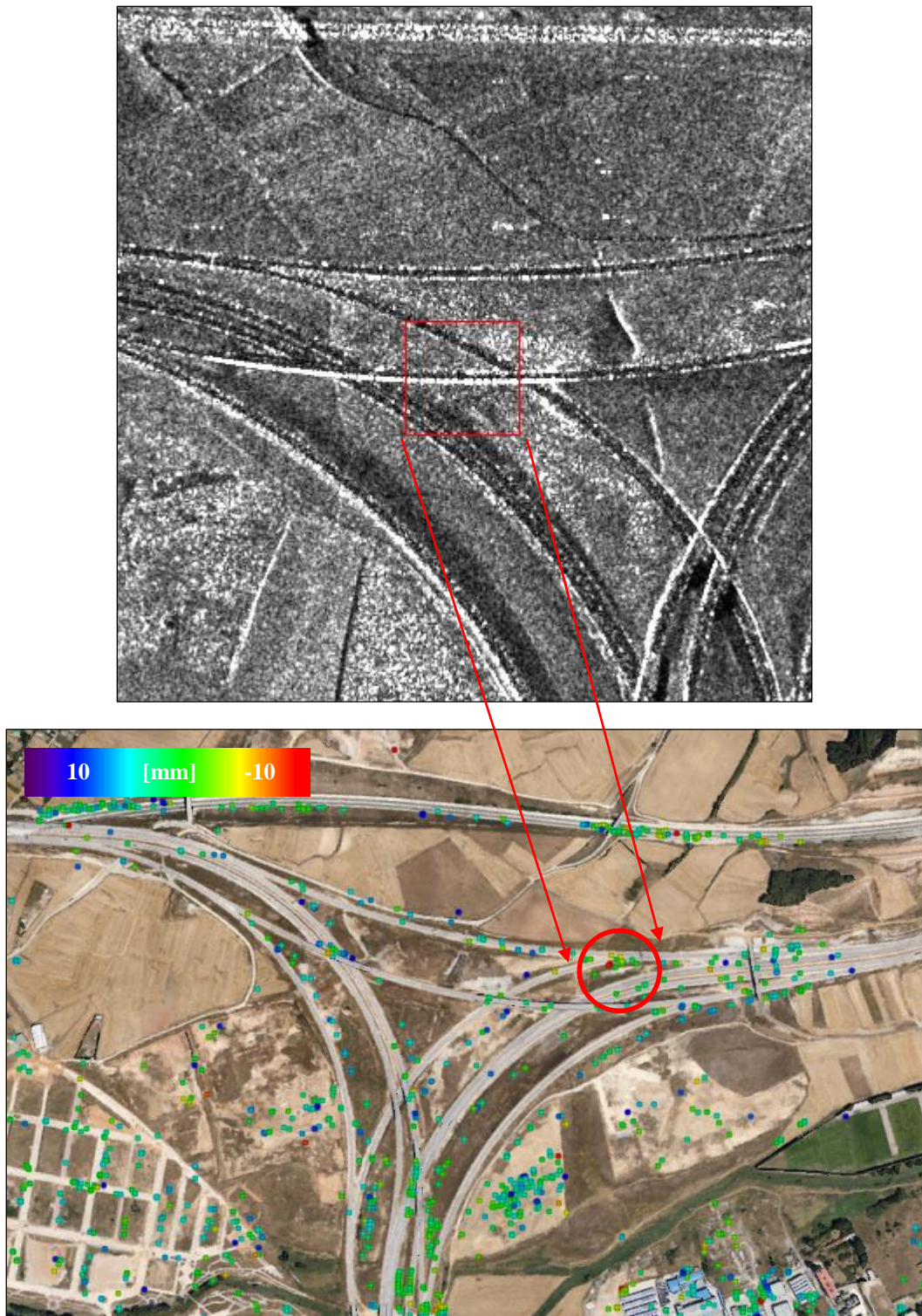


Figure 137: Mean amplitude image of the study area and localization of radar targets in the area B. The velocity value are saturated within a range between -10 mm / year and $+10$ mm / year. The velocity values refer to the Line of Sight of the SAR.

In the following figures the time series of the interest points are presented for the area B.

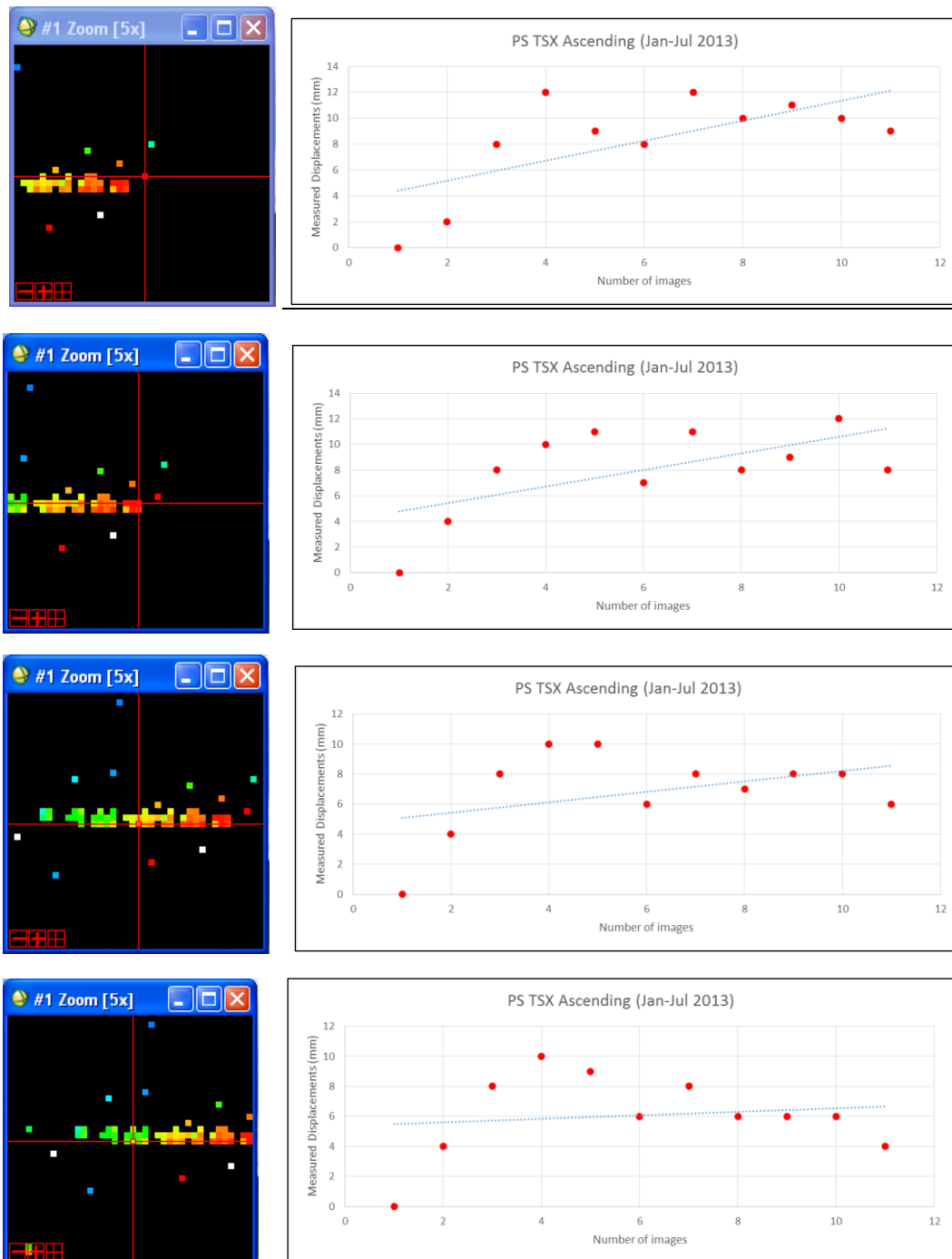


Figure 138: Time series of the interested points for the area B.

The identified radar targets, present only movements away from the satellite; the maximum velocity recorded is 12 mm/year. The movement registered by the interferometric data is probably due to an assessment of some structural part of the highway. The area B presents displacements with an average velocity value of 4 mm/year.

AREA C

The area C is located in the area of nearness of the Villalonquéjar polygon, crossed by the new railway ring. In particular, the area is located near the intersection between Calle Merindad de Cuesta Urria and Calle Merindad de Sottocuevas. The interested area is an industrial polygon formed by groups of prefabricated.

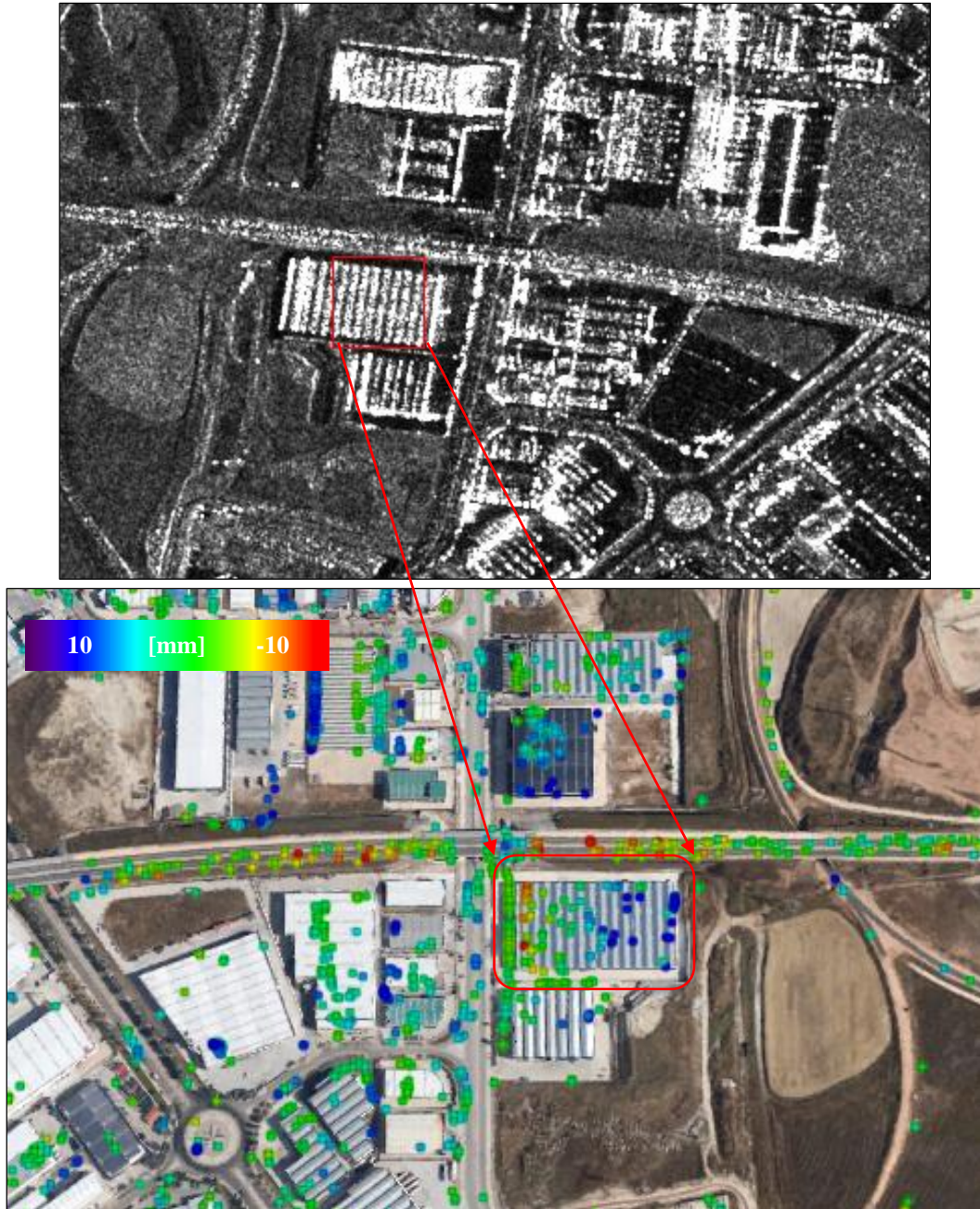


Figure 139: Mean amplitude image of the study area and localization of radar targets in the area B. The velocity value are saturated within a range between -10 mm / year and $+10$ mm / year. The velocity values refer to the Line of Sight of the SAR.

In the following figures, the time series of the interest points are presented for the area C.

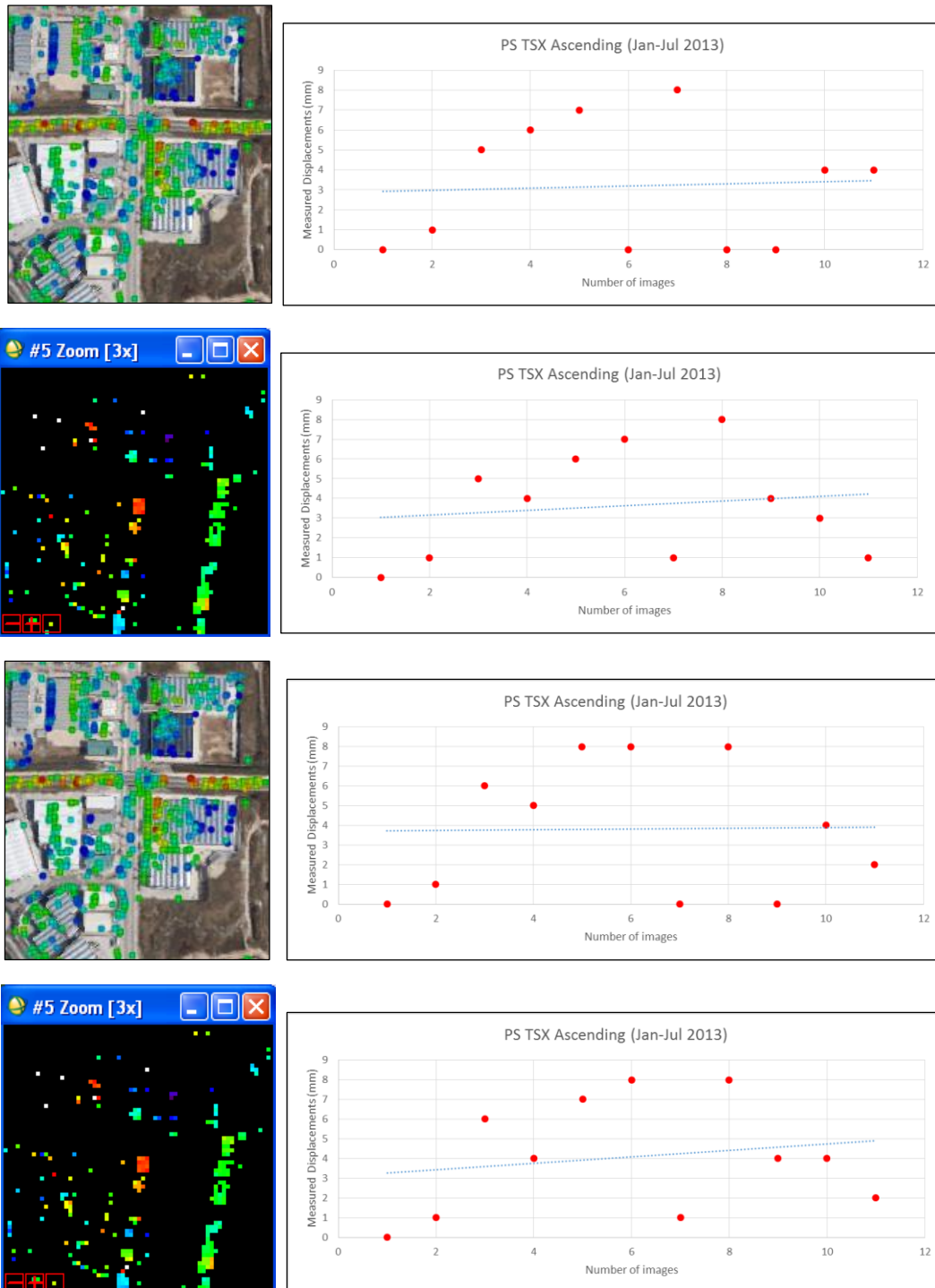


Figure 140: Time series of the interested points for the area C.

The radar targets, identified, present both a movements close to and away from the satellite. The area C consists of a group of prefabricated. The displacement registered can be due to a thermal dilation as an effect of a high temperature change between January and July.

7.3.2 BARCELONA

Barcelona is a Spanish city, capital of the autonomous community of Catalonia and the second largest city in the country as well as the largest metropolis on the Mediterranean Sea. Barcelona is located on the northeast coast of the Iberian Peninsula, facing the Mediterranean Sea, on a plain approximately 5 km wide limited by the mountain range of Collserola at west, the Llobregat river delta to the southwest and the Besòs River to the north.

This plain covers an area of 170 km² of which 101 km² are occupied by the city itself.

The main relief that borders the city is the Tibidabo, a 512 m high hill part of the Collserola range, offers striking views over the city.

Barcelona is characterized by small hills, most of them urbanised, that gave their name to the neighbourhoods built upon them, such as Carmel (267 m), Putxet (181 m) and Rovira (261 m).

The escarpment of Montjuïc (173 m) is situated to the southeast, overlooking the harbour and topped by Montjuïc castle and some of the most important sports structures and monuments (built for the 1992 Olympic Games) such as the sports arena “Palau St. Jordi”, the Olympic Stadium and other sports venues.

Montjuïc houses also some of the biggest park and gardens of the city, such as the botanical gardens of “Jardins de Costa I Llobera”, matter of study in this research as affected by slope movements.

Barcelona has a Mediterranean climate (Köppen climate classification: Csa) with mild, humid winters and warm, dry summers (Kottek et al., 2006).

Groundwater resources in deltaic aquifers are essential in the Mediterranean region to sustain the socioeconomic development of coastal communities and shallow-water ecosystems.

Understanding the geological connection between coastal aquifers and the offshore sedimentary record is important to better predict consequences in terms of water management.

The coast overlooking the river Llobregat shows a strong retreat between the 1950 and 1968 and that was estimated to be 10 m/year (Marques and Jul Hi, 1983).

An ancient shoreline between the ages of 11 century B.C. and the first century A.C., located 3 km within the area of the Llobregat delta confirms a constant progradation up to the middle of this century. Localized phenomena of strong growth are reported as due to the realization of artificial structures along the coast.

7.3.2.1 Geological Setting

The study area is located along the Catalan Coastal Range, eastern Iberian Margin, and represents a Neogene rifted margin associated with the opening of the Valencia Trough (Maillard and Mauffret, 1999). In the course of the Neogene extension, normal faults trends ENE–WSW as well strike-slip faults trends NW–SE deforming the area.

There are two Neogene half-grabens in the central part of the Catalan Coastal range: the onshore Vallés–Pendés half-graben and the offshore Barcelona half-graben (figure 141 and figure 142) (Roca and Guimerà, 1992; Roca, 1994).

The Barcelona plain and Llobregat delta are depressions between two horsts and are at the edge of the Barcelona half-graben (figure 141 and figure 142).

The modern Llobregat River has a typical Mediterranean regime, influenced by intense seasonal rainfall. The Llobregat delta plain covers an area of 97 km², and has a shoreline about 23 km long.

The Barcelona shelf is up to 60 km long and 16 km wide, with slopes that dip between 0.3 and 0.7° (figure 141) (Bartrina et al., 1992). Low-energy waves and tidal ranges of a few centimetres with a strong southward outer shelf current (30 cm /s) affect the shelf (Chiocci et al., 1997). The depth of the shelf break varies from 90–95 m to 75–85 m north to south and the slope angle is 21°.

Several deeply incised submarine canyons (perpendicular to the shoreline) are located on the outer shelf (Amblàs et al., 2006) and numerous shoreline-parallel faults cut the continental slope (Medialdea et al., 1986, 1989). Apparently, the canyons are disconnected from fluvial sources suggesting a tectonic control (figure 141) (Canals et al., 2004; Amblàs et al., 2006).

Earlier studies on the Llobregat delta plain include work from Almera (1891), Llopis (1942a, b, 1946), Solé-Sabaris et al. (1957) and Solé-Sabarís (1963). The Ministerio de Obras Públicas, (1966), first described the main hydrogeological units of the delta plain. Later Marques (1984) defined a Pleistocene (Flandrian) Lower Detrital Complex and a Holocene Upper Deltaic Complex (figure 3). Manzano et al. (1986 1987), Lafuerza et al. (2005) and Gamez (2007) more recently studied Holocene sedimentary facies.

The offshore Quaternary sedimentary record was subdivided into at least four high frequency depositional sequences (figure 143) (Medialdea et al., 1986; Checa et al., 1988; Medialdea et al., 1989; Liqueste et al., 2008).

Simó et al. (2005) provided a preliminary correlation between onshore and offshore deltaic units (figure 141).

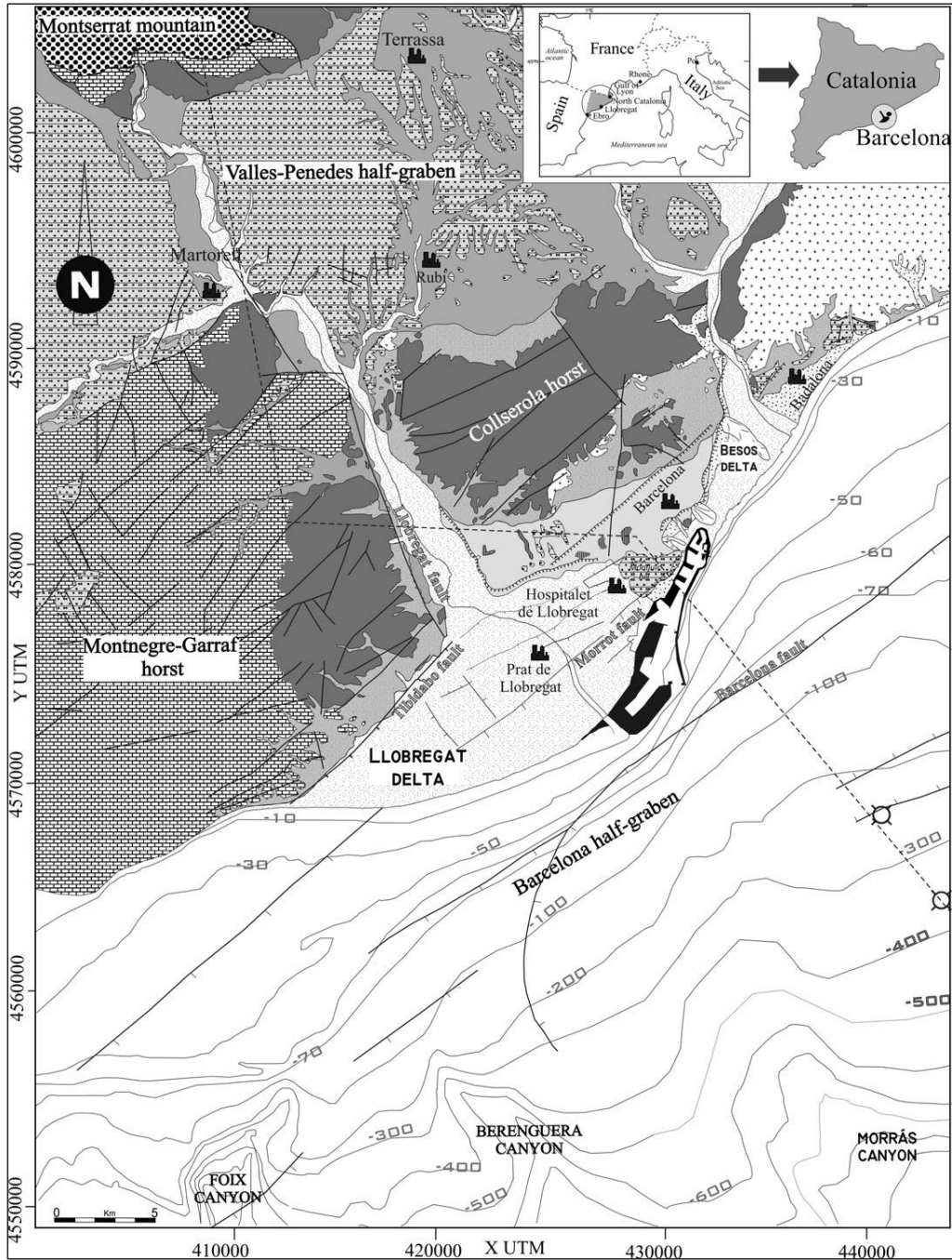


Figure 141: Onshore–offshore geographical and geological settings of the Llobregat and Besòs deltas (northeast Spain, northwestern Mediterranean Sea). After ICC (2005), Medialdea et al. (1986, 1989), and Perea (2006).

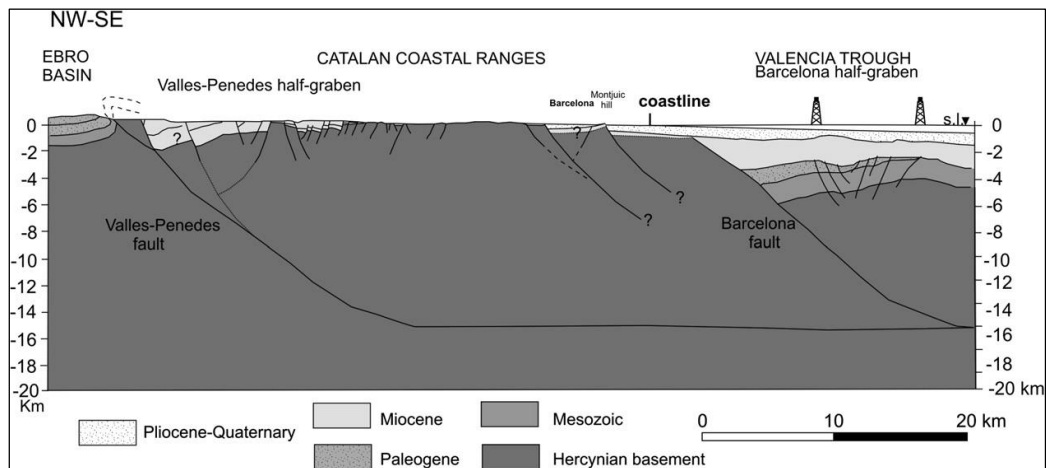


Figure 142: Cross-sectional structural sketch of the Catalan Coastal Ranges showing the tectonic structure of central plain and shelf off Barcelona. See figure 141 for location. From Parcerisa (2002).

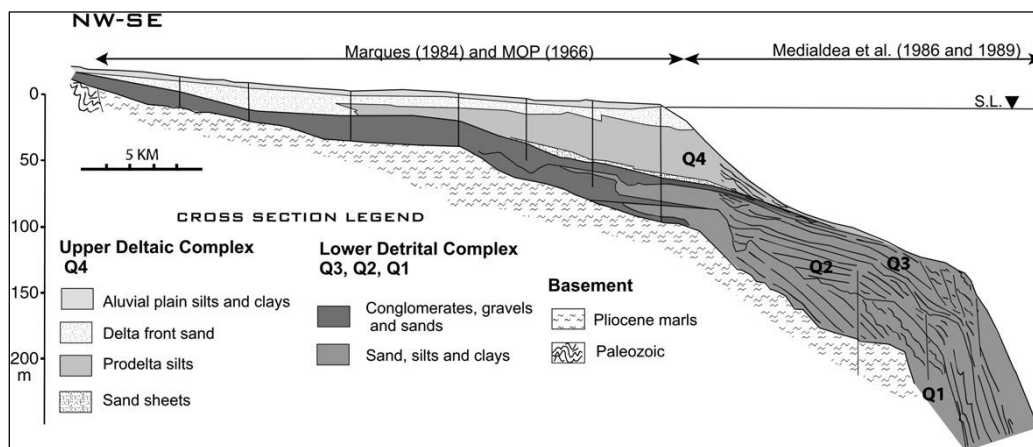


Figure 143: Previous geologic cross section of the onshore and offshore of the Llobregat deltas based on Ministerio de Obras Públicas (1966), Marques (1984), and Medialdea et al. (1986, 1989). The lower Quaternary deltas (Q1–3) correlate with the Lower Detrital Complex and the Holocene delta (Q4) with the Upper Deltaic Complex. After Simó et al (2005).

Understanding the distribution in time and space of sedimentary packages in coastal areas is relevant to the exploitation and protection of groundwater resources. Different properties of the sedimentary packages and their lateral and vertical connectivity with other units define the reservoir/aquifer potential and the susceptibility to contamination. Of special interest are deltas that contain deep aquifers. These aquifers are susceptible to seawater intrusion, which produce a risk of quality deterioration of the water resources.

7.3.2.2 Results And Discussion

By processing 26 TerraSAR-x strip map image over the urban area of Barcelona, acquired and elaborated by the Institute de Geomàtica team, 56 interferograms have been developed and a PSI data stack has been computed making possible to carry out an accurate detection of all the main ground deformation processes active in the area between 2007 and 2009.

In the following paragraph, some results of the analysis are reported and described.

The available TerraSAR-X data have allowed detecting some local subsidence phenomena that occurred in Barcelona during the satellite acquisition time (2007-2009).

In the urban area of Barcelona, the analysis of the velocity map obtained by the interferometric analysis of the TerraSAR-X images have highlighted some areas where significant ground deformations were ongoing during the acquisition period.

This analysis have been very important in order to point out how some human activities, can deeply modify the environment, generating risk conditions especially in densely populated urban areas.

Due to the gentle and flat topography of the urban area (except Montjuïc), almost the detected ground motions have been classified as subsidence, relative to underground works, underground water exploitation and some other local causes.

The capability of the Satellite SAR remote-sensing technique to detect millimetre displacements have proven itself as a perfect tool to monitor and map areas affected by slow ground motions that can cause serious injuries to the building and structures on the surface, generating potential situations of risk.

The Llobregat Delta is of great ecological and economical value for the following reasons.

- It is the major centres of population and agriculture.
- It provide challenges to geotechnical engineering.
- There is a presence of soft soils.
- The distribution of materials is complex.
- There is a high water table.
- It need to preserve ecosystems.

A Llobregat River with 156.6 km long and draining a 5045 km² basin, characterizes the Llobregat delta. It has a Delta extension of 97 km², 23 km of shoreline and it is confined by the Garraf (SW), Montjuïc (N) and Collserola mountains (NW). The history and mechanisms of delta formation control and explain the succession and structure of the different deposition units. An approach based on an understanding of the mechanisms of delta formation provides a richer geological picture than pure lithological correlations. The flood plain and pro-delta deposits exhibit a high degree of lateral uniformity. Alluvial and

beachfront deposits are much more dependent on the vagaries of the river flow channels. The various aquifers play a key role in the geotechnical appraisal of the area: the upper aquifer ensures a high water table throughout; the exploitable lower aquifer require protection measures and may constraint some construction procedures; the variation of the piezometric levels of the lower aquifer may affect the consolidation state of the intermediate pro-delta deposits.

As mentioned previously, the city of Barcelona, in its majority, is placed on a flat territory characterized by fluvial sediments related to all the river streams that runs from the Collserola mountain ridge to the Llobregat river delta.

A complex pattern of paleo- and recent riverbeds, in many instances occupied by roads (the Ramblas) or obliterated by buildings and structures characterize the underground geological setting of the city. This complex system and the intrinsic high permeability of fluvial sediments represent an ideal condition for the development of dense sub-surface flow net and potentially exploitable aquifers. The underground water exploitation is one of the most common causes of subsidence in flat areas and valley floors, because of the compaction of the sediments due to the removal of the internal water.

Here, in addition to the exploitation for the water supply and the aqueduct/network one other cause of sub-surface drainage is the tunnel excavation: indeed one of the main problems of this kind of works is seepage that can considerably weaken the sides and face of the gallery (Lee et al., 1992).

The groundwater flow passing through soil grains occurs in response to an energy gradient and a measure of this gradient is provided by the difference in hydraulic head (Freeze and Cherry, 1979). When a tunnel is excavated below the groundwater level, the groundwater flows into the excavated surface of the tunnel and there exists a difference in hydraulic head around the tunnel (Lee & Nam, 2004). In the areas significant subsidence motions have been detected, related to causes such as underground water exploitation or soil compaction due to superficial weights. In particular the areas are described.

1. The airport of El Prat de Llobregat.
2. An industrial polygon near the Llobregat River.
3. A new embankment area near the harbour.

Since only data acquired in ascending orbit were available, a combination of the velocity vectors in both the acquisition geometries is not possible. In order to solve this problem, the ground motions in these areas have been assumed as vertical due to the flat topography. Some interesting results are shown below.

AIRPORT OF EL PRAT DE LLOBREGAT

The area is placed directly on the Llobregat river delta and the hydrogeological setting of the area is almost completely characterized by fluvial sediments of delta system (figure 144 and figure 145), with the exception of the area near the coastline occupied by littoral sands. Furthermore, the construction of the airport have severely modified the surface drainage system that was composed by a complex fluvial channel network.

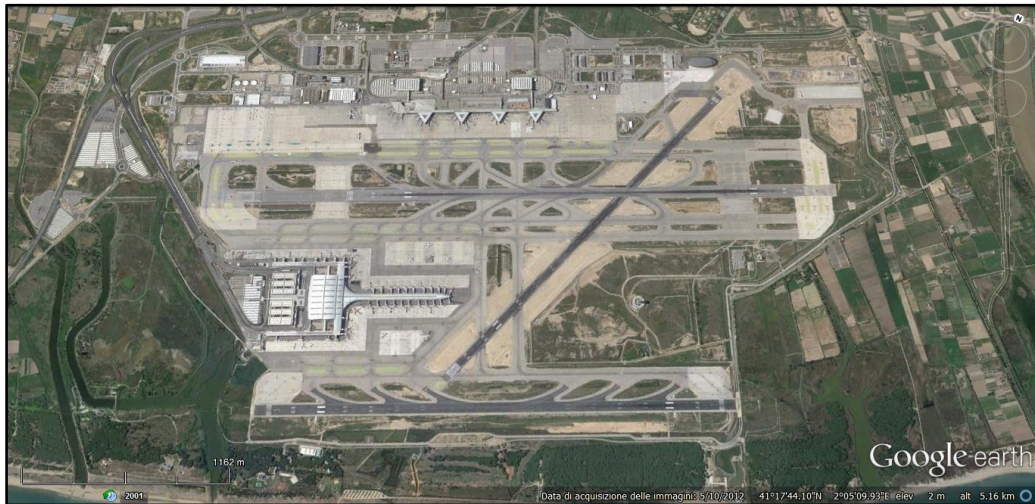


Figure 144: El Prat del Llobregat airport taken from Google Earth.

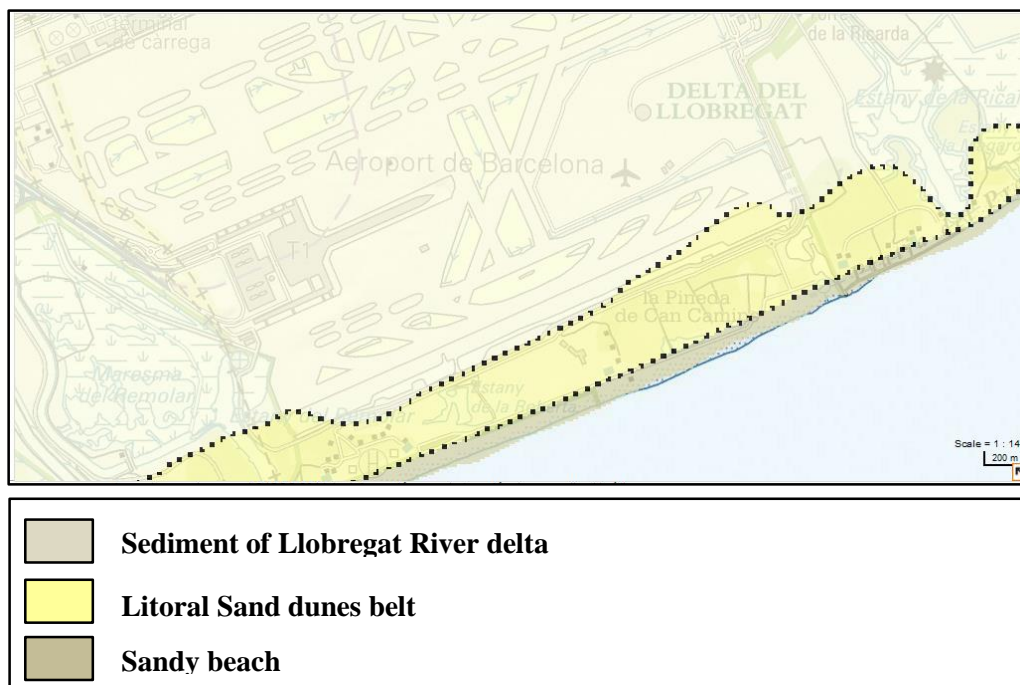


Figure 145: Geological setting of the airport area. Taken from <http://siurana.icgc.cat/visorIGC/geotreballs.jsp>.

The airport El Prat de Llobregat is affected by diffuse vertical displacements, concentrated in four zones (figure 146). The velocity values measured by the PS indicate evident deformations around the terminals (zones 1 and 4), outside of the landing area, where the control tower is placed (zone 3) and directly on the landing stripes (zone 2).

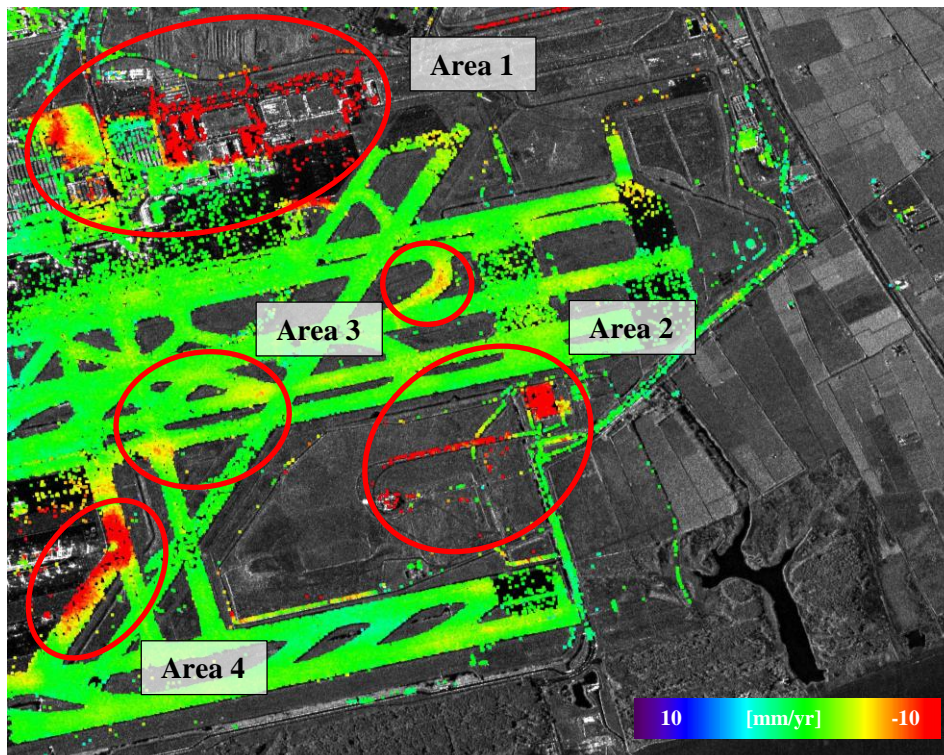


Figure 146: Mean amplitude image and deformation map after the TerraSAR-X processing data on El Prat Airport of Barcelona. The velocity value are saturated within a range between -10 mm / year and $+10$ mm / year. The PS that indicate significant movements in four different sectors. The PS are characterized by negative velocity values. This implies that the movement is detected moving away from the satellite. The registered movement can be due to the construction of new structures as well as some subsidence phenomena.

The area 1 is characterized by new structures that have been built recently; probably the velocity map shows ground deformations in correspondence with these areas.

The subsidence also, could locally be due to the presence of wells from which a large quantity of water have been pumped out during the acquisition time.

A grassland and a generalized absence of structures, except for the presence of the control tower of the airport characterize the area 2; this area is affected by a subsidence phenomenon. The deformation is probably due to the weight of the buildings, together with a possible presence of active wells for the water supply.

The area 3, is characterized by some areas affected by subsidence, located in the central part of the stripes, that show a very peculiar shape and deformation pattern.

The deformative contribution related to the weight of the aircraft is evident analysing the deformation pattern that shows the major values on the centre of the stripes where all the aircrafts are located. The weight of the aircrafts is probably sufficient to produce this deformation rates on the asphalt.

The area 4 is a large zone in deformation that surrounds the recently built Terminal 1 of the airport; the subsidence phenomena can be due to a combination of some causes as aquifer exploitation; weight of the new terminal; weight of the aircrafts.

As supposed for the areas 3 here the effects of the weight of the aircrafts on the asphalt are clearly visible. In all of those areas, the velocity values increase progressively from zero (at the borders of the stripes) to the maximum values in the centre.

This effect is not visible in all the landing stripes of the airport due to the periodic replacement of the asphalt, performed for maintenance and to the differential subsoil resistance properties.

Furthermore, the areas with older asphalt have been proved as more affected by displacement as well as the areas where the aircraft usually stand or move them.

In conclusion, the displacements in these areas are clearly visible from the PS data.

Very recent alluvial sediments related to the delta system of the Llobregat River characterize the geological setting of the area. It is an area extremely favourable to the underground water extraction due to its fluvial pertinence, with a subsoil characterised by a complex channel-bed structure.

The extraction of underground water often generate subsidence phenomena (Raucoules et al., 2003; Canuti et al., 2005; Canuti et al., 2006) and the presence of diffuse agricultural and industrial activities ensure a massive exploitation of this resource, originating a wide settlement of the entire area of the delta.

In the area of the airport, new buildings have been recently constructed, whose weight have generated local settlements due to the compaction of the underground sediments.

The recent construction, in combination with underground water extraction, have generated several subsidence areas, with high deformation rates in the examined areas (zones 1, 2 and 4).

The deformation rates might slightly decrease until the soil compaction process is complete. However, a continuous monitoring of some structures could be needed in order to assess their stability.

BARCELONA HARBOUR

The area is placed directly on the Llobregat river delta and the hydrogeological setting of the area is almost completely characterized by fluvial sediments of delta system (figure 147 and 148). Furthermore, the construction of the harbour has severely modified the structural asset of the delta.

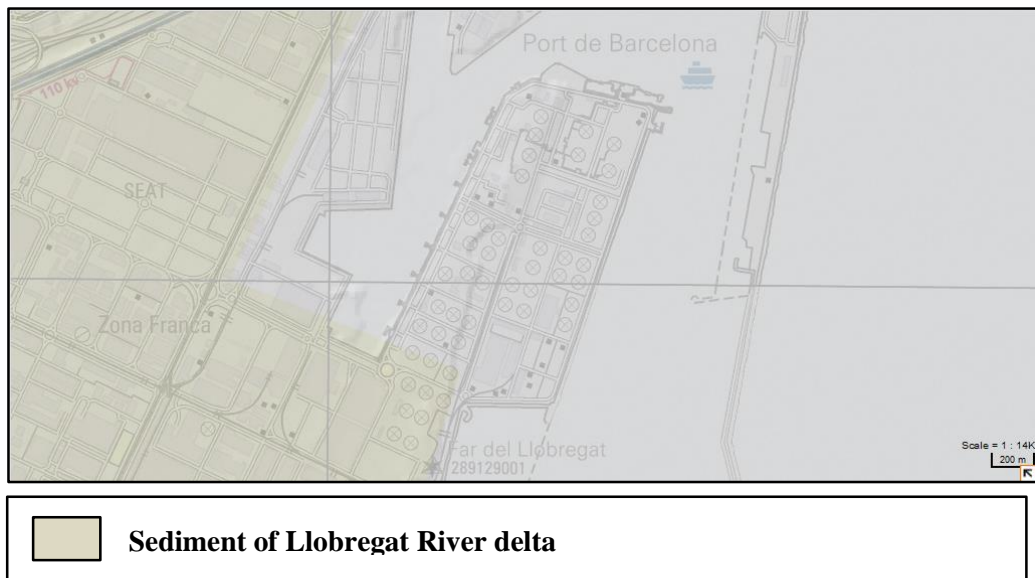


Figure 147: Geological setting of the harbour area. Taken from <http://siurana.icgc.cat/visorIGC/geotreballs.jsp>.

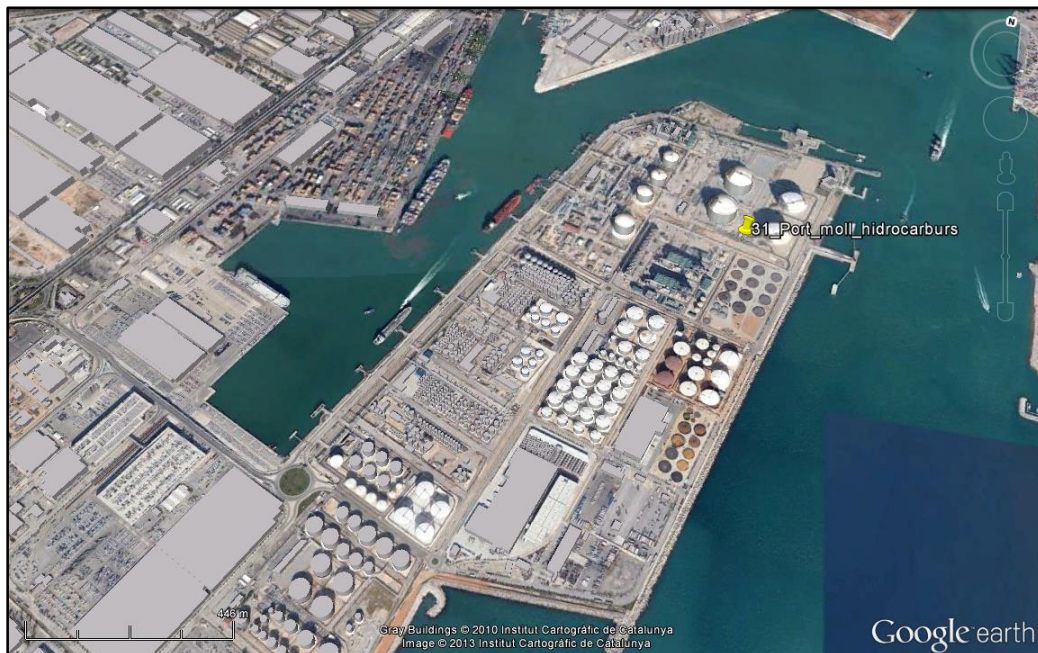


Figure 148: Image of the Barcelona Harbour taken from Google Earth.

The Barcelona harbour is affected by diffuse vertical displacements, concentrated in the eastern part of the harbour (figure 149).

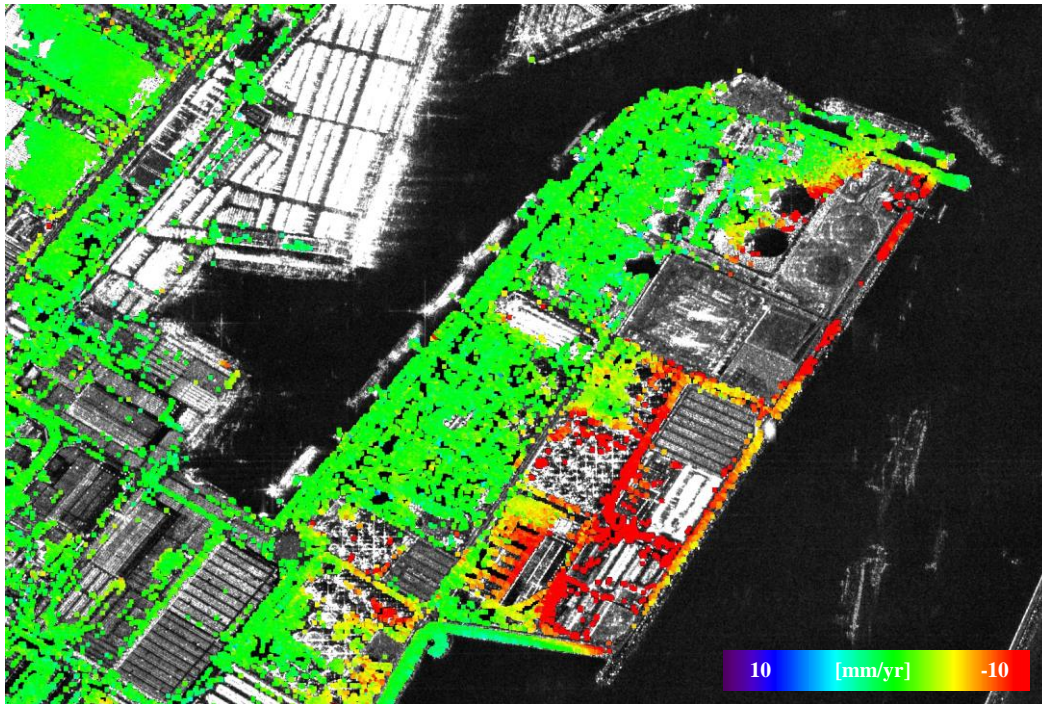


Figure 149: Mean amplitude image and deformation map after the TerraSAR-X processing data on Barcelona Harbour. The velocity value are saturated within a range between -10 mm / year and $+10$ mm / year. The PS that indicate significant movements in the eastern part of the harbor. The PS are characterized by negative velocity values because of a probably subsidence. This implies that the movement is detected moving away from the satellite.

The radar targets identified, only movements away from the satellite. The movement registered by the interferometric data is probably due to an assessment of some structural part of the harbor.

Heavy maritime structures may exhibit potential instability problems when founded on soft deltaic deposits. Stability is always controlled by undrained conditions.

Deltaic deposits often have low stiffness and may cause significant movements during excavations. Those movements can be reduced to very small values adopting adequate control measures of the displacements. The soft nature of many deltaic deposits leads to potential stability problems for heavy structures founded on them. They can be overcome by staged construction/preloading supported by adequate instrumentation systems.

INDUSTRIAL POLYGON

The area is placed directly on the Llobregat river delta and the hydrogeological setting of the area is almost completely characterized by fluvial sediments of delta system (figure 150 and 151), with the exception of the area near the coastline occupied by littoral sands. Furthermore, the construction of the industrial polygon have severely modified the surface drainage system that was composed by a complex fluvial channel network.

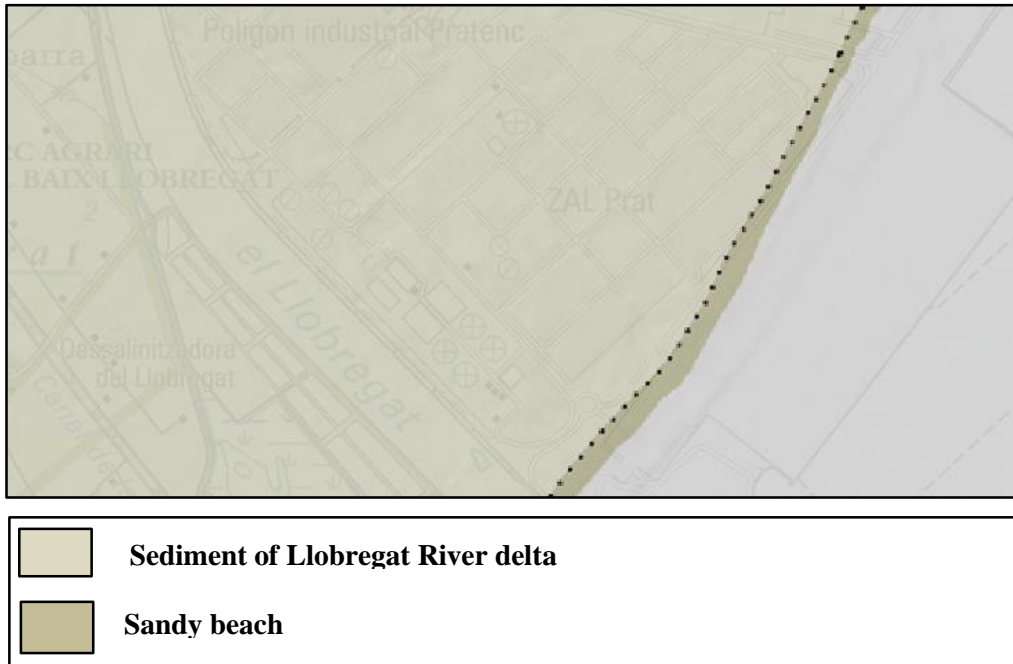


Figure 150: Geological setting of the industrial polygon. Taken from <http://siurana.icgc.cat/visorIGC/geotreballs.jsp>



Figure 151: Image of the Industrial Polygon of Pratenc taken from Google Earth.

The industrial polygon of Barcelona is affected by diffuse vertical displacements, concentrated in the left part of the river where the hydrocarbons deposit are concentrated (figure 152). The velocity values measured by the PS indicate evident deformations along the Llobregat river track and the certain structures that make up the industrial polygon.

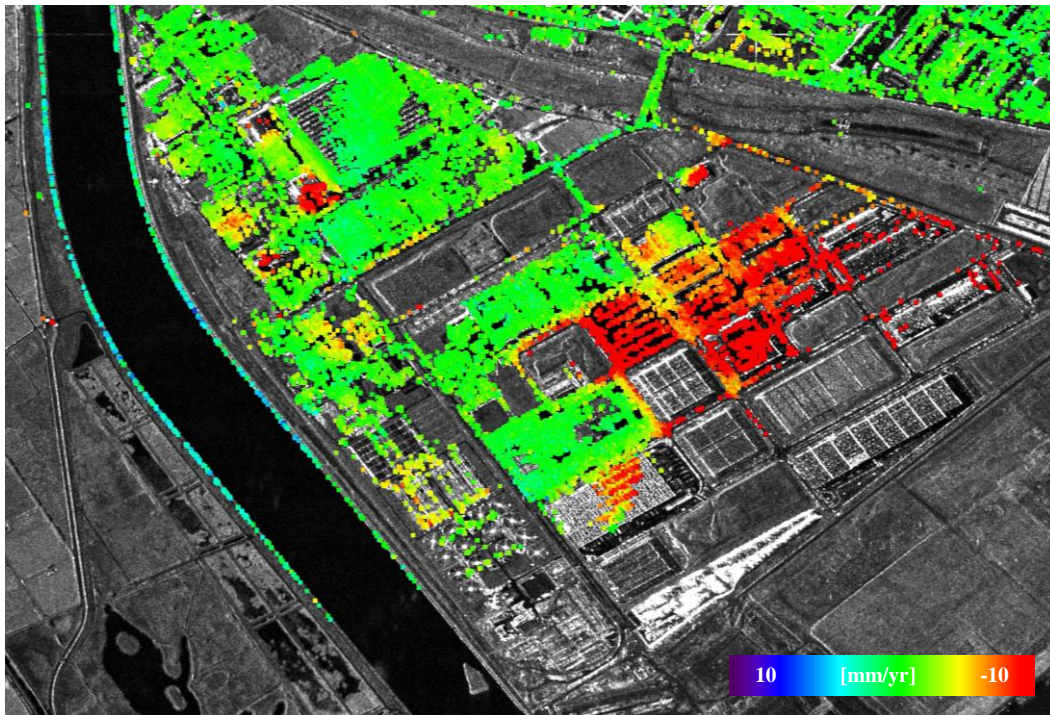


Figure 152: Mean amplitude image and Deformation map after the TerraSAR-X processing data on the industrial Polygon of Barcelona. The velocity value are saturated within a range between -10 mm / year and $+10$ mm / year. The PS that indicate significant movements are in two different areas. In particular, the area along the track of the Llobregat River shows positive values. The other areas are characterized by PS with negative velocity values as result of a probably subsidence. This implies that the movement is detected moving away from the satellite.

The radar targets present both movements close to and away from the satellite.

In particular, along the river, there are ground movements close to the satellite that indicate an uplift movement. They are probably due to swelling phenomena that characterize the clays materials and that occur along the Llobregat River. The other part of the Industrial Polygon consist of a group of prefabricated; here, the displacement registered can be due to some subsidence phenomena due to the presence of soft deltaic deposits. Deltaic deposits often have low stiffness, may cause significant movements of the heavy structures, and may exhibit potential instability problems when ounded on these types of sediment. In addition, the displacement it can be due to a thermal dilation as an effect of a high temperature change.

8. C and X-BAND DATA FOR LOCAL-SCALE MONITORING

8.1 GENERAL CONSIDERATIONS

This chapter gives an application of C and X-Band SAR data for monitoring ground deformation and engineering infrastructures at a local scale. The subject of this chapter is the SqueeSAR™ analysis carried out in some areas within the Province of Messina.

The monitoring will be of paramount importance for early detection of potentially critical situations.

This application represents an element concerning the use of interferometric techniques for monitoring ground deformation based on satellite data. The acquisition radar data dating back to 1992, when the ERS-1 satellite acquired regularly over vast areas of the planet is of paramount importance in this context.

The SqueeSAR™ analysis conducted for this purpose included the development of various datasets acquired by different satellites in different band of acquisition.

The second paragraph, after some notions on the geological setting of the areas of study, describes the data arising from the elaboration and the mainly results and discussions.

In particular, the data acquired in C-band are compared with those available in X-band. The interferometric data in C-band are these acquired by the ERS, ENVISAT and by the Canadian satellite RADARSAT-1. The available interferometric data in X-band are these acquired by the COSMO-SkyMed satellite.

The recent COSMO-SkyMed, launched in November 2010, is able to capture up to 1800 images a day. This allows operating also in emergency situations with asynchronous operating mode in order to obtain images in the shortest possible time.

The study shows a use of the most recent interferometric data and of ancillary data available for the risk analysis.

It intends to take advantage of the existing archives of satellite data acquired C-band.

The temporal continuity and the geometric compatibility between the time series of ERS-1, ERS-2 and ENVISAT represents an unprecedented opportunity to generate long time series of ground deformation.

This allows providing exclusive information for a better understanding of the long-term behavior of the slow kinematic phenomena of terrain deformation.

The last section of this paragraph examine the main ground deformations and instabilities for the examined areas. These give some examples of land deformation detection and describe the results obtained.

8.2 OVERVIEW OF THE STUDY AREA

The geological history of Sicily is very complex, both because of its location in a Mediterranean area characterized by extreme tectonic mobility, both because of the nature of the sedimentary rocks deposited in different domains paleo-geography and both because of the tectonic difficulties that have occurred by Upper Paleozoic to Quaternary.

Sicily, in relation to its geological-structural, is schematically divided into three structural elements (figure 153) which follow from north to south, are presented.

1. A sector of the chain, which runs along the northern coast of the island, from Peloritani Mountains to the archipelago of Egadi, consisting of a set of stratigraphic and structural structures resulting from deformation of the paleo-geographic domains of the Mesozoic and Paleocene period converging towards the S-SE.
2. A sector of the foredeep, which occupies almost the entire south-central portion of the island, articulated in two sedimentation basins (Caltanissetta Basin and Castelvetro) separated from the Sicani Mountains representing the southern spur of the chain.
3. One area of foreland, located at the southern tip of the island. Consists mainly of carbonate rocks (Plateau Iblean).

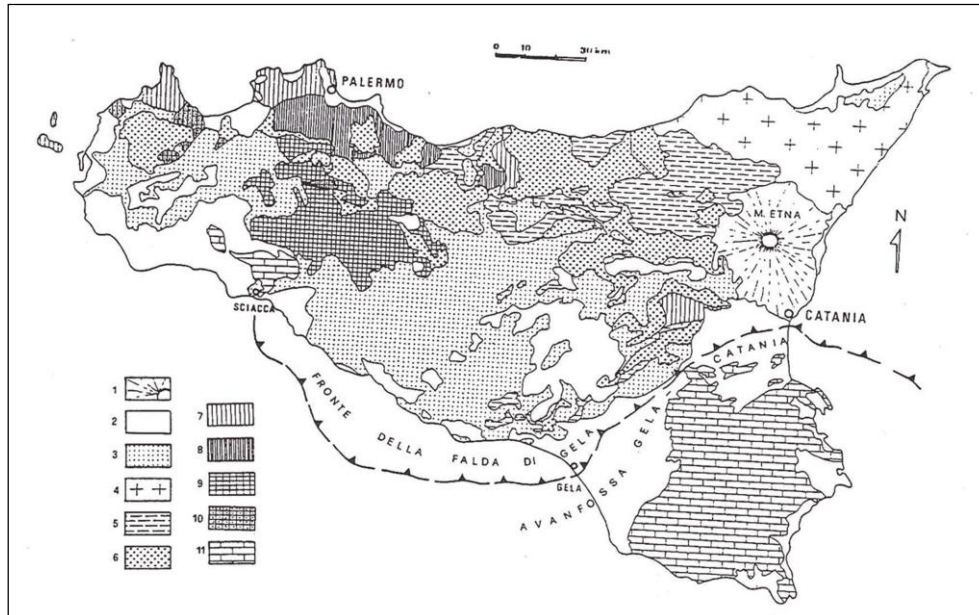


Figure 153: Tectonic scheme of Sicily *Gasperi (1995)*. 1. Etna volcanic rocks; 2. Succession of the Pliocene and Pleistocene; 3. Succession of the Tortonian and Pliocene; 4. Unit of the Arco Calabro-Peloritano; 5. Unit of Sicilidi; 6. Flysch Numidico; 7. Unit Panormidi; 8. Imeresi units; 9. Sicane units 10. Unit of Trapani; 11. Iblee and Saccensi units.

The sector of the chain runs along the northern coast and is the result of tectonic deformation suffered by geological bodies belonging to different paleo-geography domains, because of compression movements associated with the Oligo-Miocene counterclockwise rotation of the Sardo-Corso block and the collision of this with the African continental margin.

The area of the chain, in western Sicily is represented by the thrust of several units that are collocated with a southern tectonic convergence.

In the paper entitled “Evoluzione Paleotettonica della Sicilia Nord-Occidentale (Giunta e Liguori, 1973) have constructed a model for the chain that from north to south include: an Inner Zone, a Panormid platform and, a Imerese Basin, an Intermediate platform, a Trapanese Basin, a basin, and finally a Sicano Basin and an External Platform.

One of the most important works on the geology of Sicily, still considered a good reference point, is the “Schema Geologico della Sicilia (Catalano e D’argenio, 1982).

The authors divide the units that make up the chain in dislocated unit (Saccensi units, Sicane and Trapanesi units), strongly displaced units (Imeresi units, Panormidi, Prepanormidi), indoor units (Sicilidi) and units of the Calabro-Peloritano Arc.

Today, according to the most recent views, it must be deemed that the Imerese units and Sicane units and are superimposed on the Trapanesi and Saccensi units of platform. Different opinions have instead are about the geometric position of the Panormidi and Imeresi unit, with some authors (Lucchesi and Agnesi, 2007) that believe that the Imerese Unit tectonically overlapped on the Panormidi unit and with other which sustain the over thrust of the basin succession (Imeresi units) above the sequences of low sea (Panormidi unit).

The foreland area is located in the southeastern portion and consists of predominantly carbonate rocks outcropping in the iblean area.

This sector is characterized by the presence of a weakly deformed substrate that has allowed the development of extensive flat areas located at high altitudes, dissected by deep canyons.

8.3 TEST SITES

The choice of test areas is due on the availability of relevant thematic data, including information useful for the validation of the results obtained. Other important aspects are the relevance and the variability of these known phenomena, with particular attention to those phenomena that can be a source of potential risk. The study area is located along the northeaster part of Sicily region in south Italy and includes the Monti Nebrodi range within Messina Province (figure 154).



Figure 154: Analysed areas within Messina province, Sicily (Italy).

From a geomorphological point of view, the area is influenced by the geo-structural conditions, by the crystalline competence of the outcropping rock and by the recent tectonic activity. The coastal landscape is typical of the recently uplifted areas, characterized by steep slopes, narrow valleys and high topographical gradient and relief energy. The area was highly affected by several landslide events in the period from October 2009 to February 2010 and landslide-induced phenomena kept on occurring up to nowadays. The main triggering factors of the slope movements along the Monti Nebrodi are the geomorphological features and the occurrence of intense and seasonally high precipitation. Referring to the IFFI (Inventario Fenomeni Franosi in Italia) database, which is the available and most updated landslide inventory map, 816 landslides are mapped until 2003 in Messina Province, covering an area of 140 Km². The mapped phenomena are predominantly complex events, roto-translational slides and slow flows.

8.3.1 NASO

8.3.1.1 Geological Setting

The relief on which it stands Naso is a prominent structural element in the topographic context of the area; the nature of the lands constituting the morphologic high and the steepness of the slopes contribute to determine geomorphological processes.

These are attributable to the classical phenomena of degradation of the edges (fractures, collapse) which then evolve into complex landslides because the debris is caught by visco-plastic deformation phenomena. The set of acquired data and the analysis step allow some statements about the instability affecting the south area of Naso.

The geomorphological features indicate the presence of gravitational deformation that affected the entire width of the south side; it is probably a reactivation of a phenomenon that occurred centuries ago (figure 155).

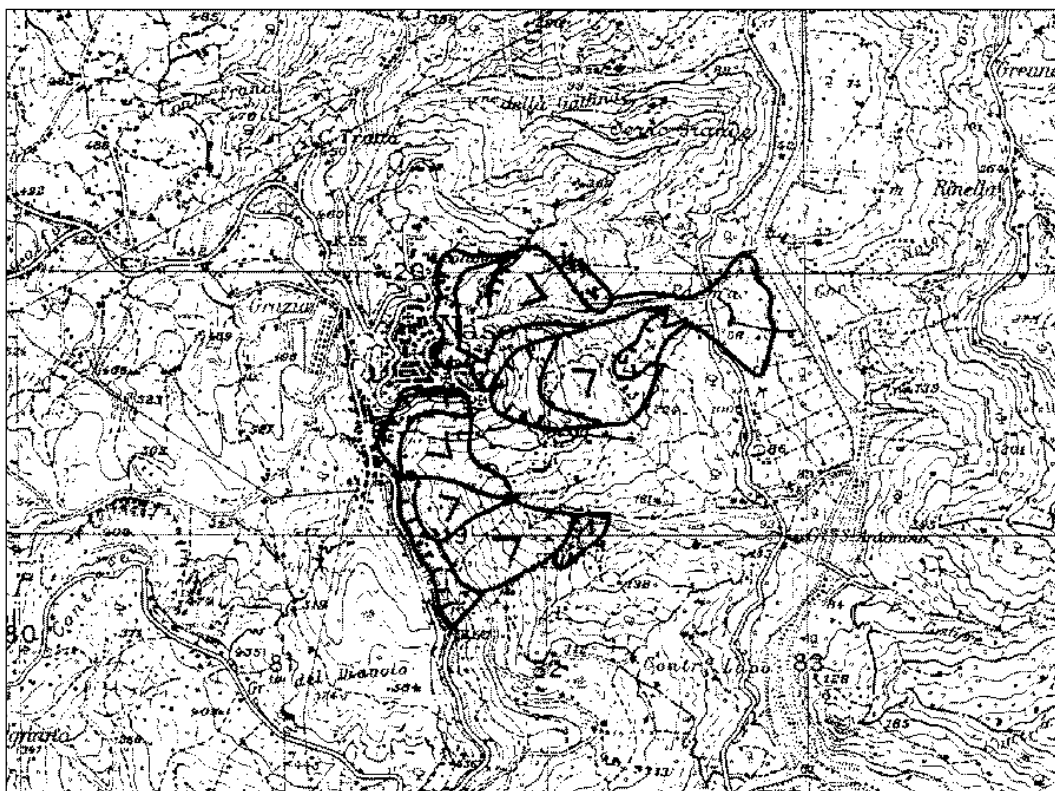


Figure 155: carta geomorfologica tratta dall'Atlante del Progetto AVI (<http://avi.gndci.cnr.it/docs/schedes3/sicilia/>).

The geology of Naso is characterized by the presence of land belonging to the late orogenic post-collisional cover (Middle Pleistocene), represented by a sequence of calcarenites and sands eteropic with argillitic levels to the higher portions of the sequence. The sequence is

called “Calcareniti di San Conrado” in the cartography of the CARG project and rests on Flysch of Capo d’Orlando; in turn, it rests on metamorphic core (figure 156).

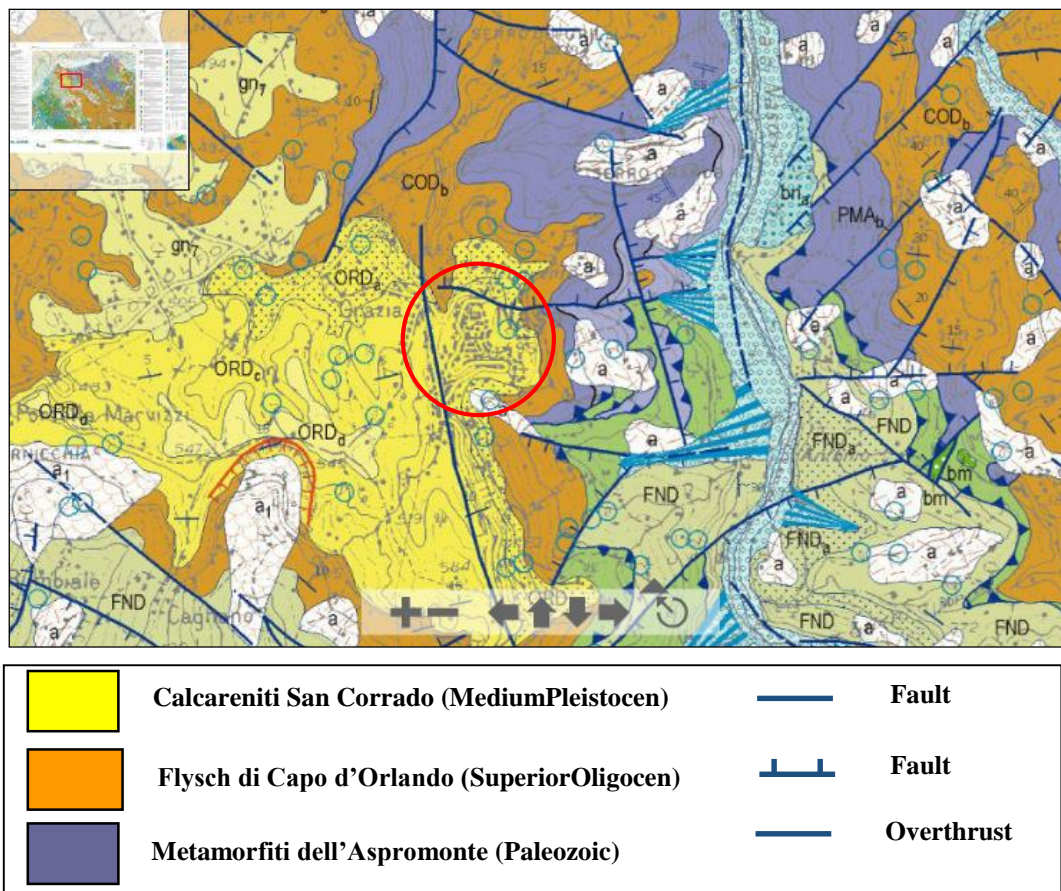


Figure 156: Geological map (stralcio CARG – ISPRA, 2009). **CALCARENITI DI SAN CORRADO:** ORDa e ORDb: alternating of yellowish limestones and ocher sands, etheropic each other in layers of 20 50 cm, fossils, containing sometimes decimeter levels of quartz micro-conglomerates grayish uncemented (ORDc); maximum thickness of 130 m. **FLYSCH DI CAPO D’ORLANDO:** CODb: predominantly sandstone facies (Oligocene).

8.3.1.2 Results and Discussion

The available C-band PS data within the test area are the following data:

- ERS data acquired in the spanning time 1992-2001.
- ENVISAT data acquired in the spanning time 2003-2010.
- RADARSAT data acquired in the spanning time 2005 - 2010

The acquisitions in both ascending and descending geometry are available for all datasets.

The available X-band PS data within the test area are the following data:

- COSMO-SkyMed data acquired in the spanning time May 2011-May 2012

The acquisitions in both ascending and descending geometry are available for the dataset.

The ground deformation map of Naso derived from PS data acquired in the spanning time 1992-2001 by the C-band satellite ERS 1/2, in ascending geometry, is shown in figure 157.

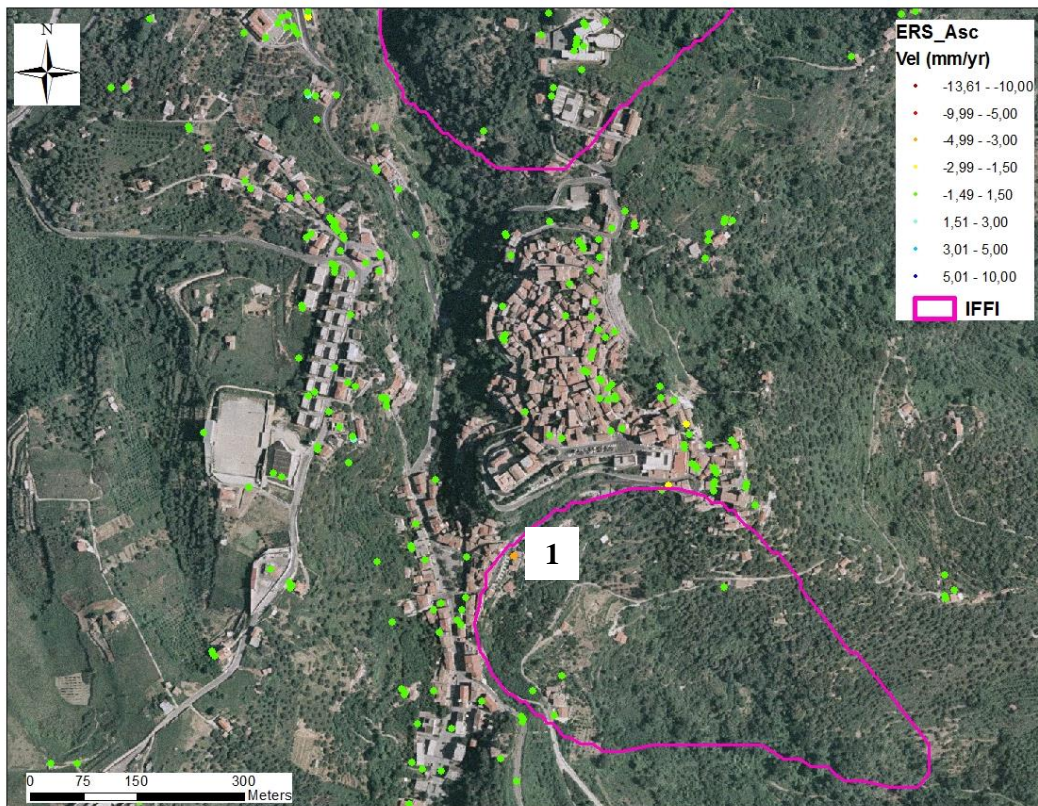


Figure 157: Ascending ERS data in the Naso area.

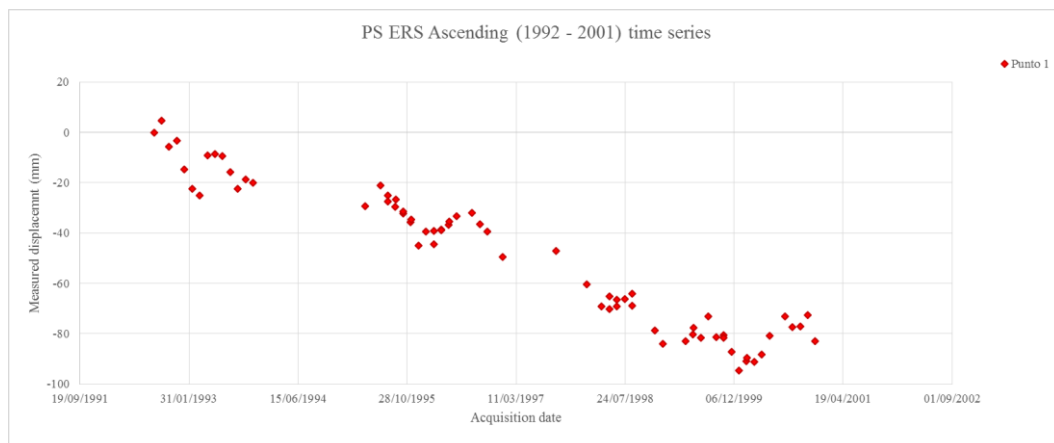


Figure 158: Time series of ascending ERS target selected.

The selected area, in general, presents displacements extremely limited or equal to zero along the L.O.S. of the satellite. The ascending selected PS presents a displacement going away from the satellite with an average velocity value of -4.50 mm/year (figure 158).

The ground deformation map of Naso derived from PS data acquired in the spanning time 1992-2001 by the C-band satellite ERS 1/2, in descending geometry, is shown in figure 159.

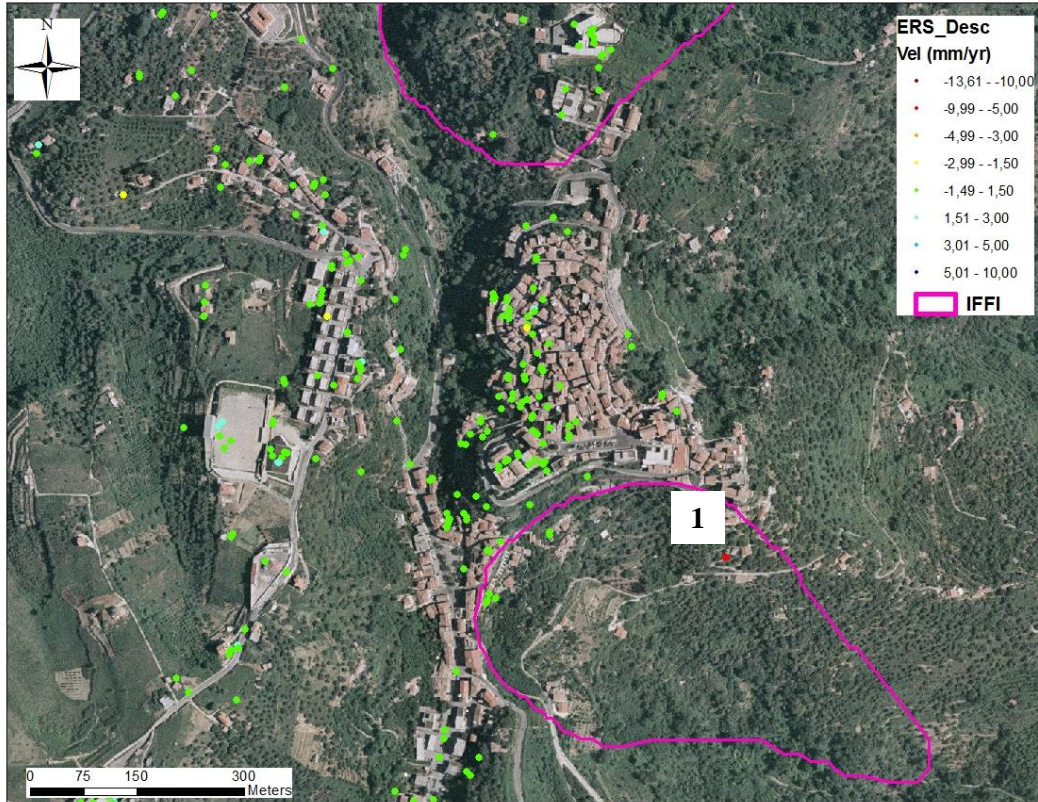


Figure 159: Descending ERS data in the Naso area.

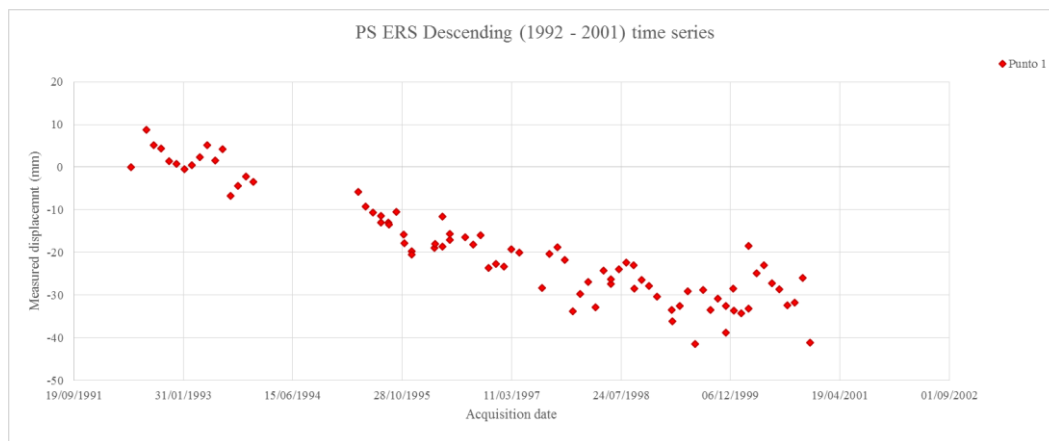


Figure 160: Time series of descending ERS target selected.

Also for the descending ERS data, the selected area, presents, in general, displacements extremely limited or equal to zero. The time series of the selected target show an average deformation rate of 8.50 mm/year (figure 160).

The ground deformation map of Naso derived from PS data acquired in the spanning time 2003-2010 by the C-band satellite ENVISAT, in ascending geometry is shown in figure 161.

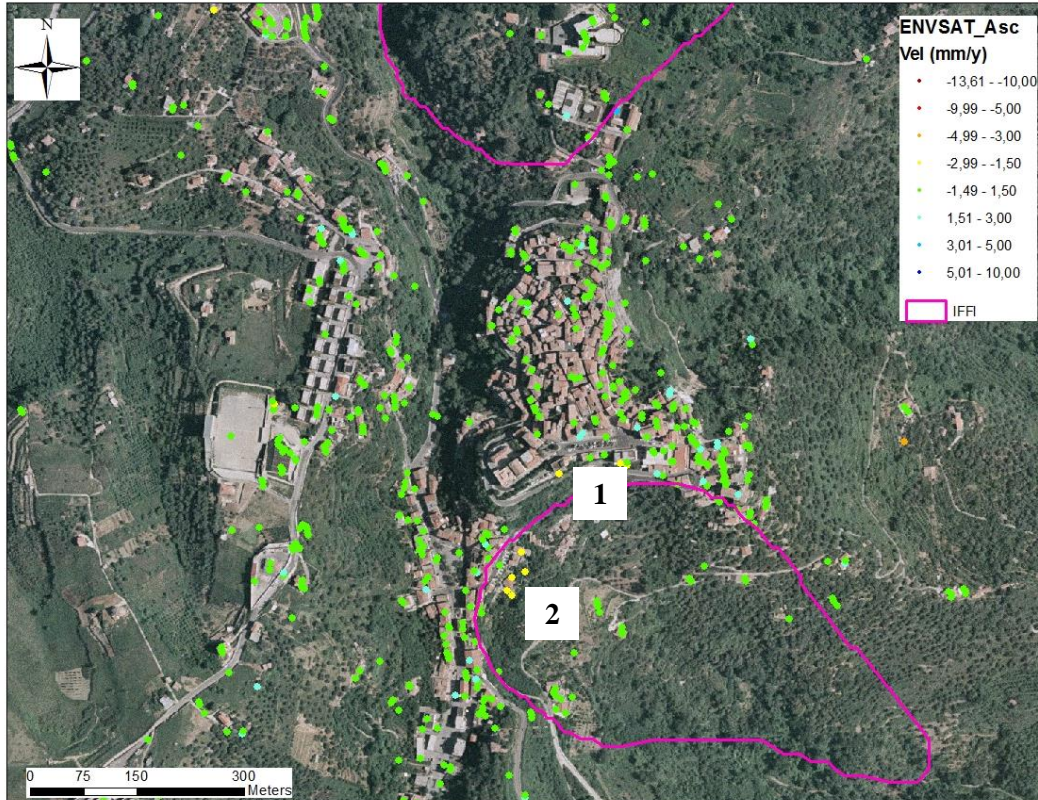


Figure 161: Ascending ENVISAT data in the Naso area

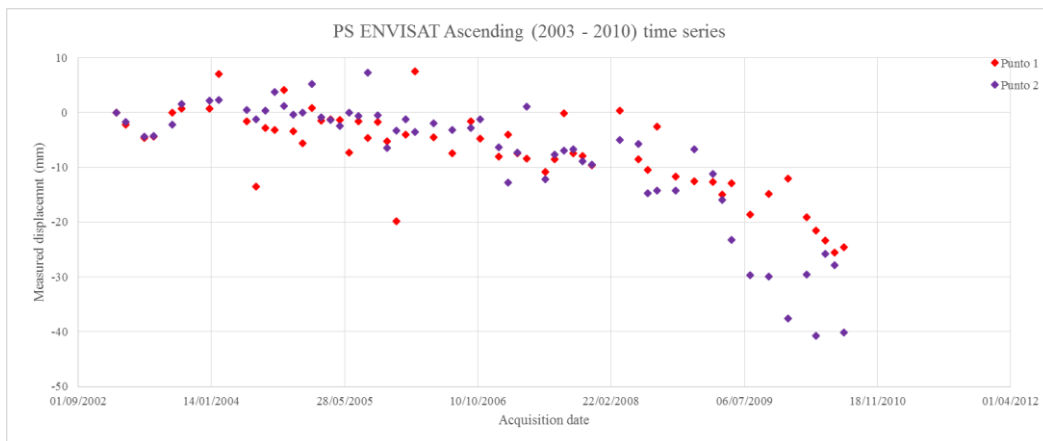


Figure 162: Time series of ascending ENVISAT targets selected.

The interferometric data acquired by the ascending ENVISAT satellite present a general instability. In particular, the time series of the selected target presents a displacement going away from the satellite with an average velocity value of -2.50 mm/year (figure 162).

The ground deformation map of Naso derived from PS data acquired in the spanning time 2003-2010 by the C-band satellite ENVISAT, in descending geometry is shown in figure 163.

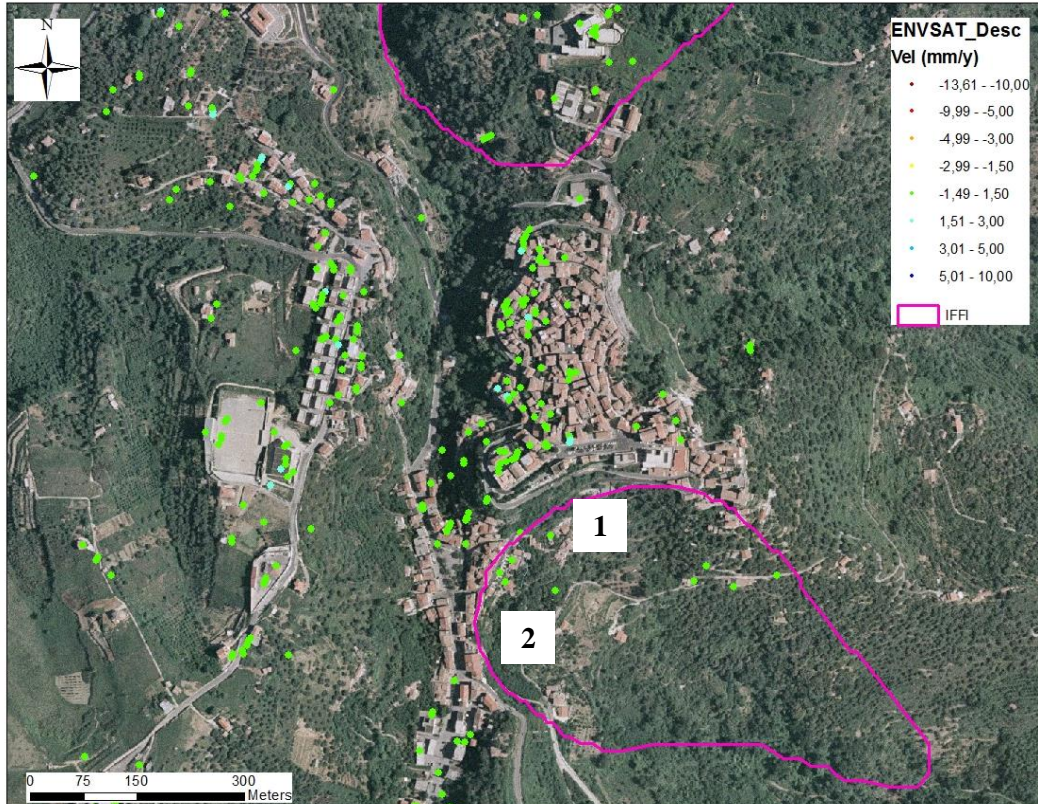


Figure 163: Descending ENVISAT data in the Naso area.

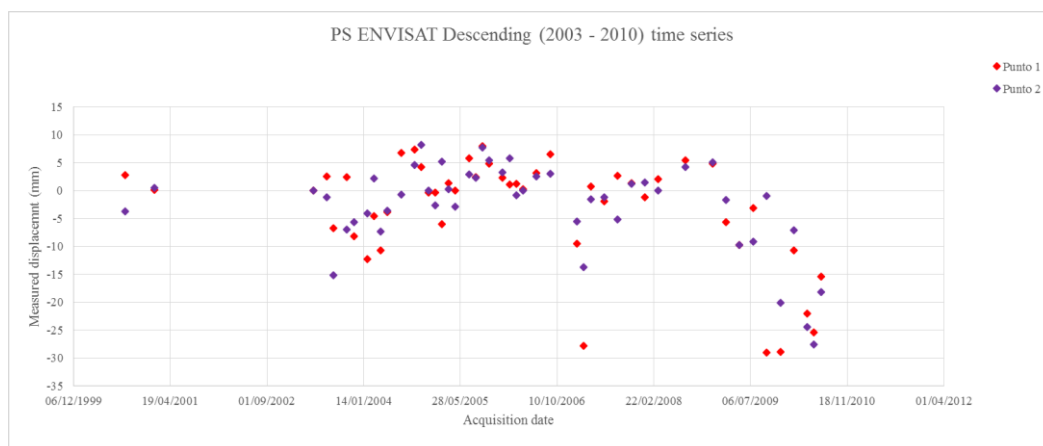


Figure 164: Time series of descending ENVISAT target selected.

The descending ENVISAT data, presents displacements extremely limited or equal to zero along the L.O.S. of the satellite. The time series of the selected target presents a

displacement that is within the stability threshold. In particular the average velocity value registered by the satellite of -1.50 mm/year (figure 164).

The ground deformation map of Naso derived from PS data acquired in the spanning time 2005-2010 by the C-band satellite RADARSAT, in ascending geometry, is shown in figure 165.

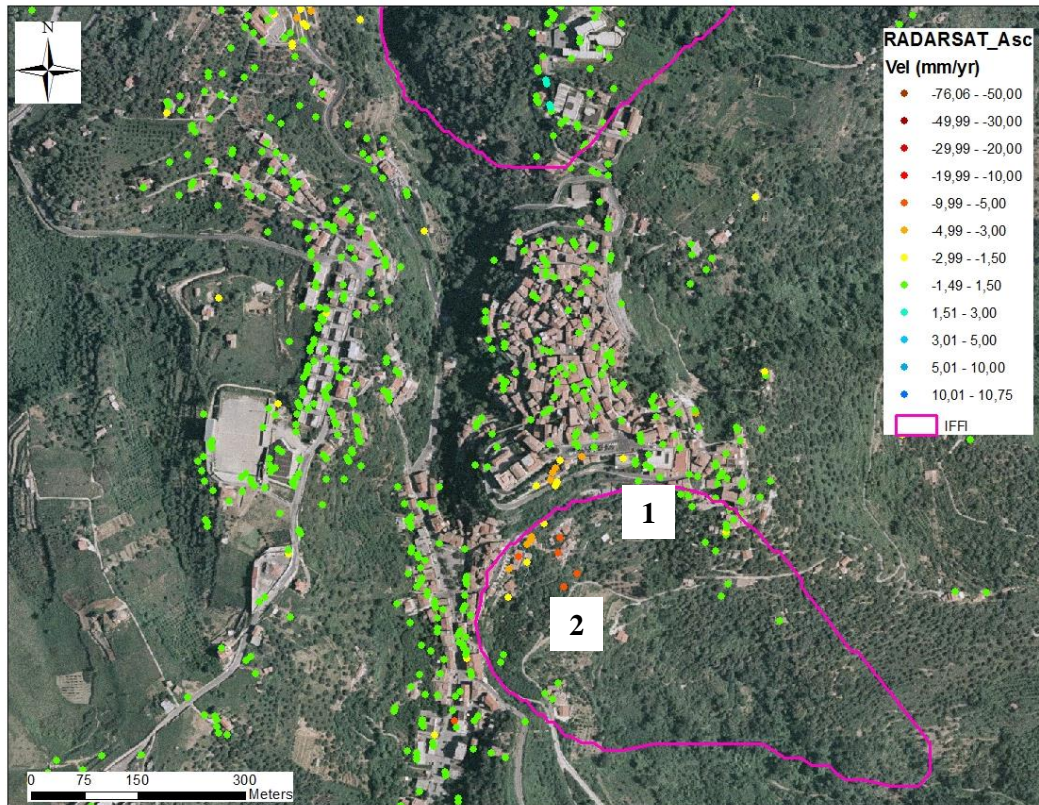


Figure 165: Ascending RADARSAT data in the Naso area.

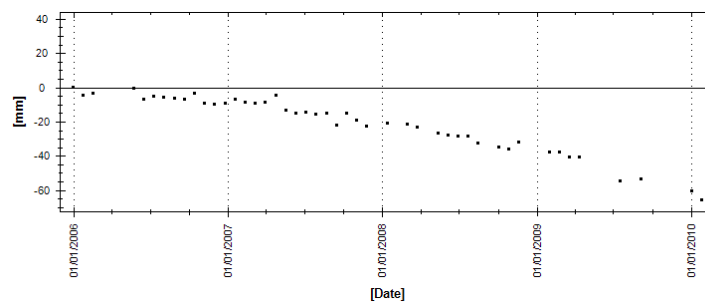


Figure 166: Time series of ascending RADARSAT target selected.

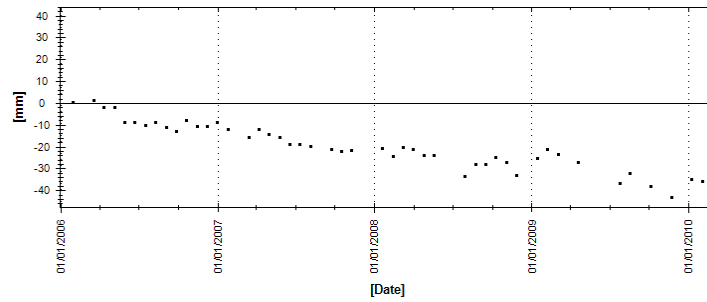


Figure 167: Time series of ascending RADARSAT target selected.

The ground deformation map of Naso derived from PS data acquired in the spanning time 2005-2010 by the C-band satellite RADARSAT, in descending geometry, is shown in figure 168.

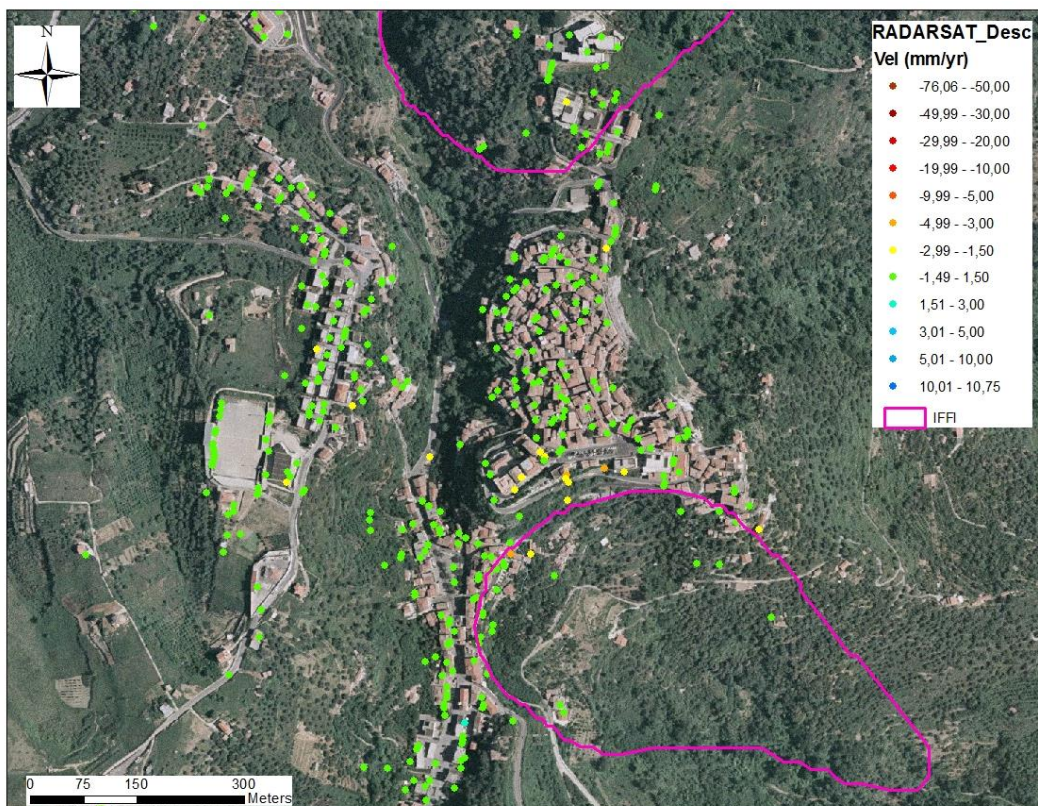


Figura 168: Descending RADARSAT data in the Naso area.

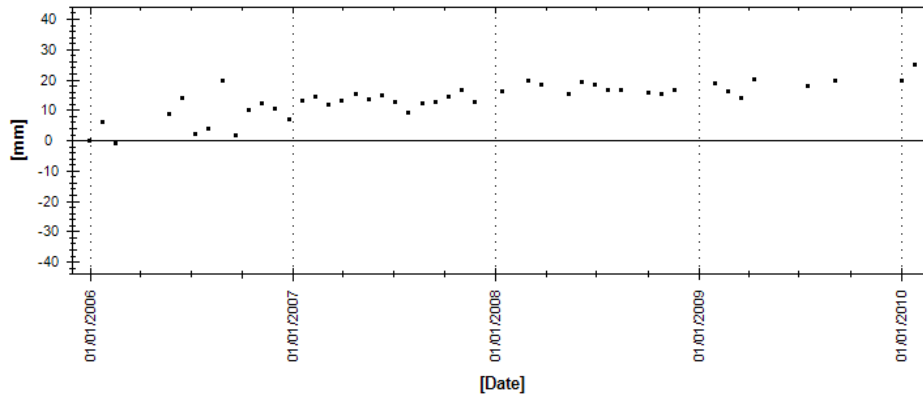


Figure 169: Time series of descending RADARSAT target selected.

The interferometric data acquired by the RADARSAT satellite present a general instability. In particular, the time series of the selected targets present both movement close to and away from the satellite. The average velocity values registered for the selected target are proximally of -7 mm/year and 2 mm/year (figures 165 - 168).

The ground deformation map of Naso derived from PS data acquired in the spanning time May 2011-May 2012 by the X-band satellite COSMO-SkyMed, in ascending geometry, is shown in figure 170.

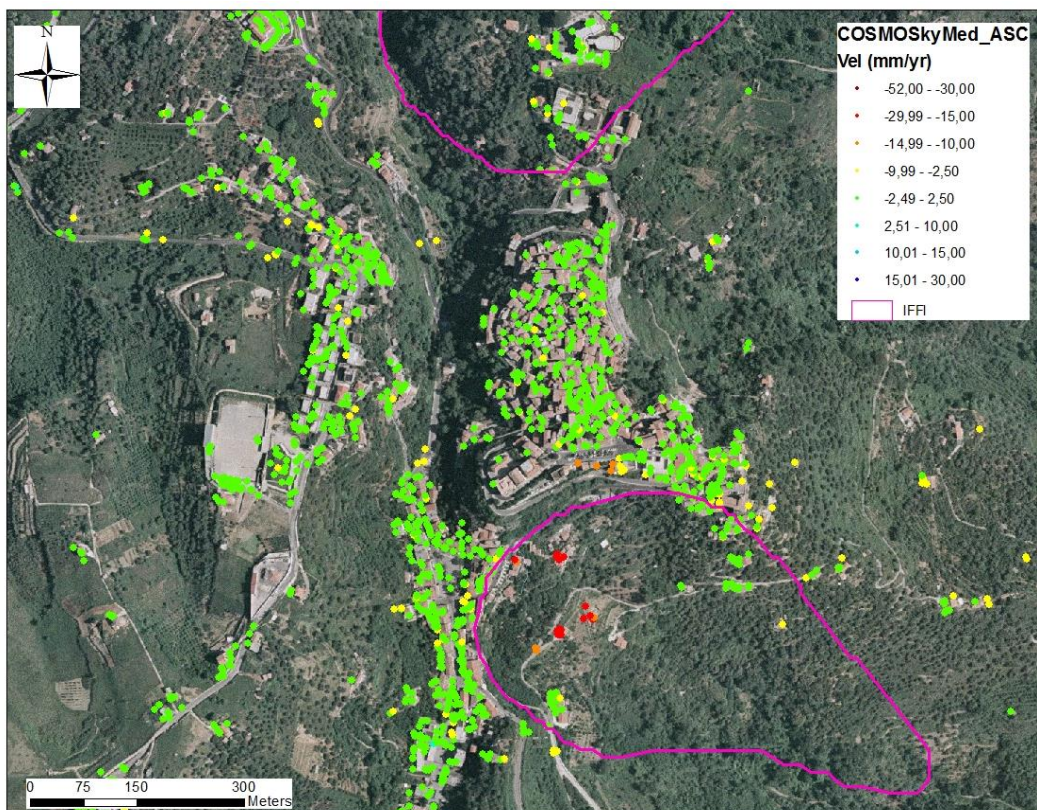


Figure 170: Ascending COSMO-SkyMed data in the Naso area.

The ascending COSMO-SkyMed deformation map shows a general instability for the selected area. The displacement, starting from the ERS acquisition period has been increasing over time until reaching values of 15 mm/year, as shown in figure 170.

By the way, PS targets that show high deformation rates that are significantly more frequent than those of C-band satellites are.

This is due to the dense sample of X-band data and to the short monitoring period of only one year (2011-2012) which allows the detection of a high number of PS in areas affected by active superficial processes.

Over longer acquisition time, these natural processes could be not identified at all.

The descending COSMO-SkyMed deformation map shows a general instability for the selected area with very high deformation rate.

The selected targets present both movement close to and away from the satellite. In particular, in correspondence with the yielding of the SS 116 deformation rate of 35 mm/year are reached (figure 170 and figure 171).

The ground deformation map of Naso derived from PS data acquired in the spanning time May 2011-May 2012 by the X-band satellite COSMO-SkyMed, in descending geometry, is shown in figure 171.

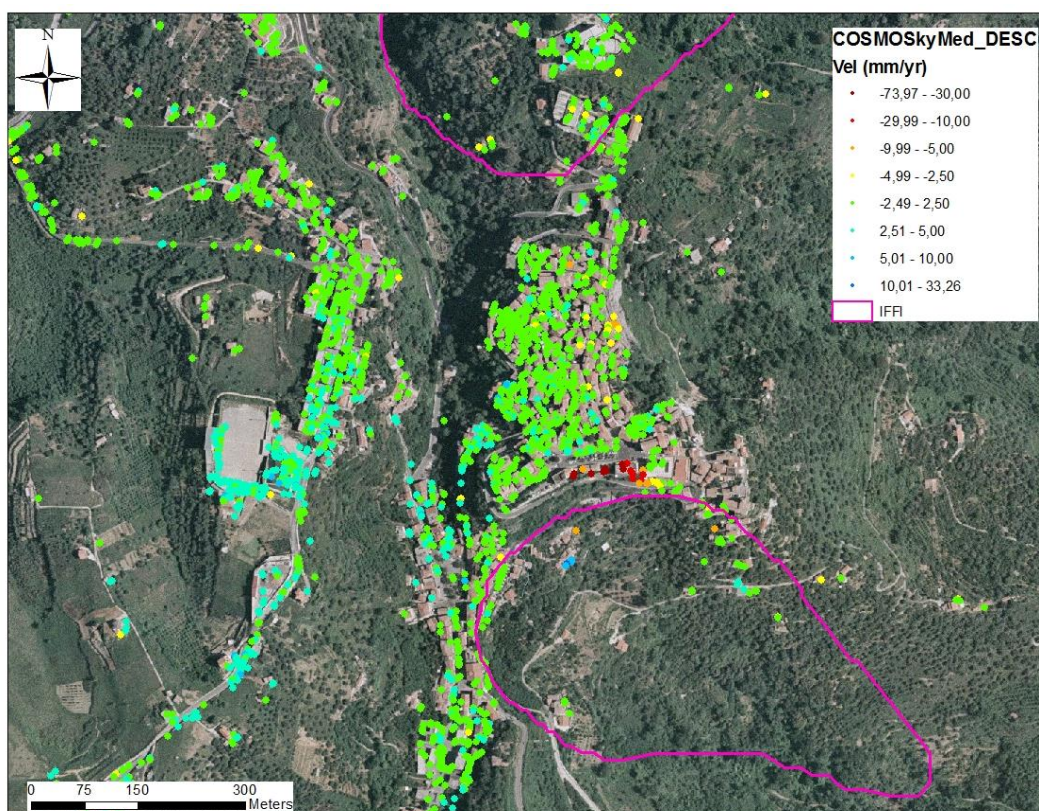


Figure 171: Descending COSMO-SkyMed data in the Naso area.

The hydrogeological, is the main problem of Naso. The risk that the situation could literally fall is clear and it is visible noting the most of the streets. In the hubs of the country, the floor is uneven in different parts but what is most striking is the trend, highly irregular, of the tiles. The PS data denote a recent activity of the phenomenon that manifests itself mainly with fractures and settling of the road of the main street (Via G. Amendola -Piazza Roma), with the collapse of the SS 116 downstream of the town and with fractures of the factories (buildings, walls) in the district of the Spirito Santo.

The analysis shows how the movement has gradually increased from 1992 to 2012, in particular the most significant considerations can be made by examining the data from 2005 to today. As shown by the ascending RADARSAT data, an average displacement rate of 7 mm/year affects the south sector of the suburb. This has been increasing over time until reaching values of 15 mm/year, as shown by the ascending and descending COSMO-SkyMed data. In particular, in correspondence with the yielding of the SS 116 deformation rate of 35 mm/year were reached.

8.3.2 CASTELL'UMBERTO SFARANDA

8.3.2.1 Geological Setting

The area in question, from the geological point of view, is located on the Flysch of Capo d'Orlando, constituted by an alternation of metric sandstone benches and decimetric layers of silt clayey sands.

The sandstones are highly fractured, confirming the numerous tectonic activity that affected this area (figure 172).

The alternation between sandstone layers with good permeability due to fracturing and the sandy-clay levels, characterized by a low permeability, facilitates the presence of multi groundwater aquifers. Numerous water sources are present as confirmation of this aspect.

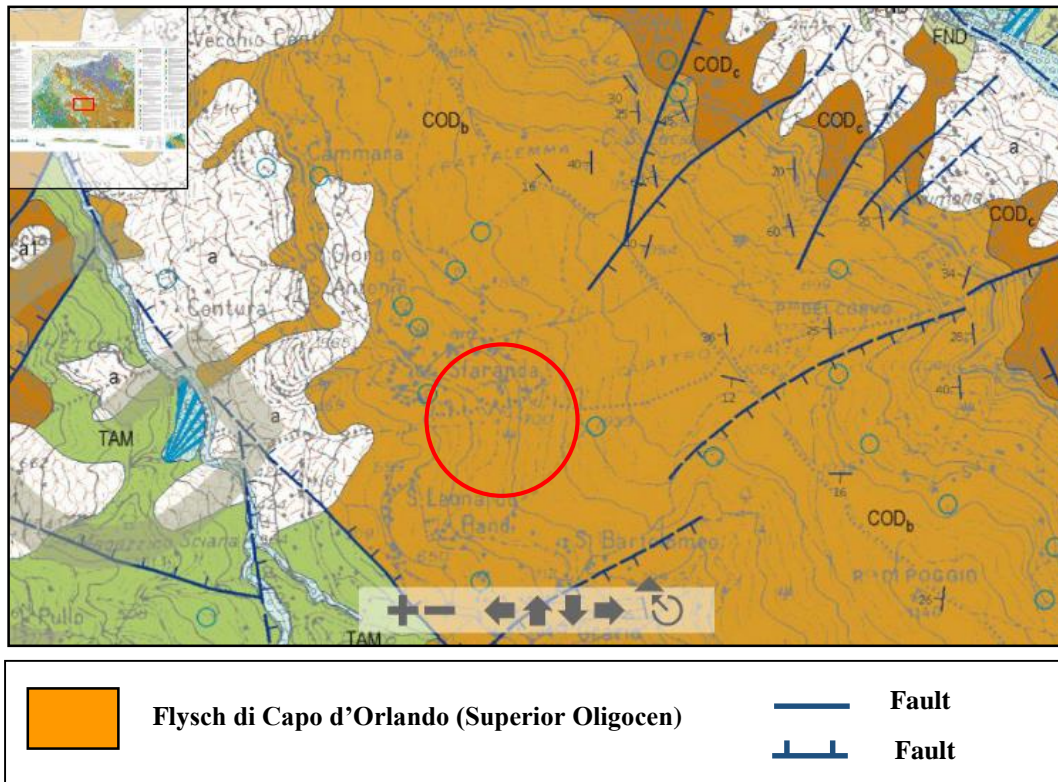


Figure 172: Geological Map (stralcio CARG – ISPRA, 2009) and location of the area affected by the landslide.

The PAI identifies an active slide phenomenon; the landslide body seems to involve both the debris cover and the flyschoid substrate (figure 173). The Sfaranda landslide, falling in the basin of the river Cavalieri, affects a whole side for a total area of 15 ha, a width of the central zone of 470 m and a crown-foot length of 600 m.

The instability has no obvious geomorphological signs: no slope instability or landslide body and the foot is barely mentioned (for past events); the phenomenon manifests itself through fractures in the soil and damage to numerous buildings along the slope.

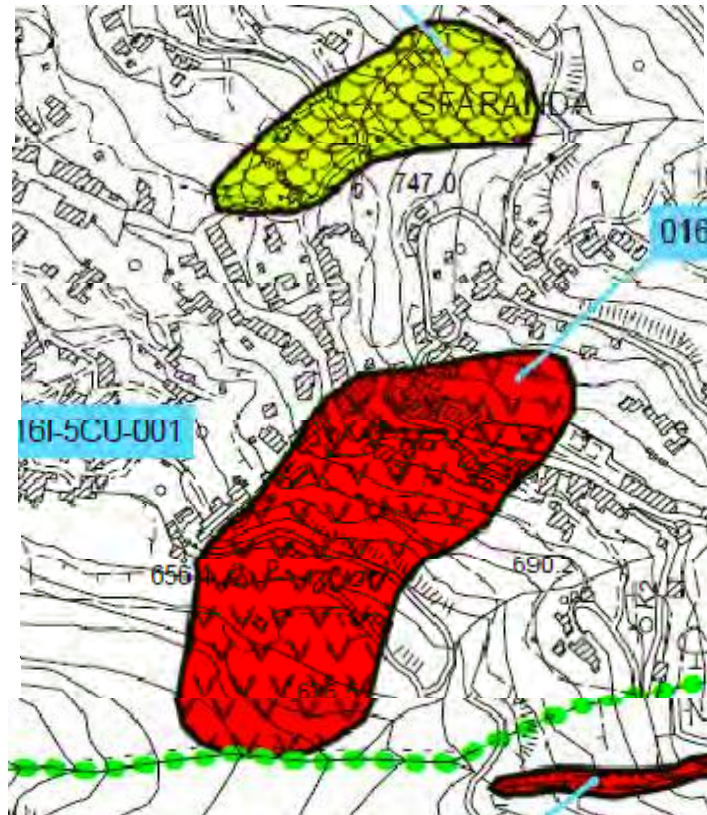


Figure 173: Geomorphological map from the Atlante of the AVI Project (<http://avi.gndci.cnr.it/docs/schedes3/sicilia/>).

8.3.2.2 Results and Discussion

The available C-band PS data within the test area are the following data:

- ERS data acquired in the spanning time 1992-2001.
- ENVISAT data acquired in the spanning time 2003-2010.
- RADARSAT data acquired in the spanning time 2005-2010.

The acquisitions in both ascending and descending geometry are available for all the three datasets.

The available X-band PS data within the test area are the following data:

- COSMO-SkyMed data acquired in the spanning time May 2011-May 2012.

The acquisitions in both ascending and descending geometry are available for the datasets.

The ground deformation map of Sfaranda derived from PS data acquired in the spanning time 1992-2001 by the C-band satellite ERS 1/2, in ascending geometry, is shown in figure 174.

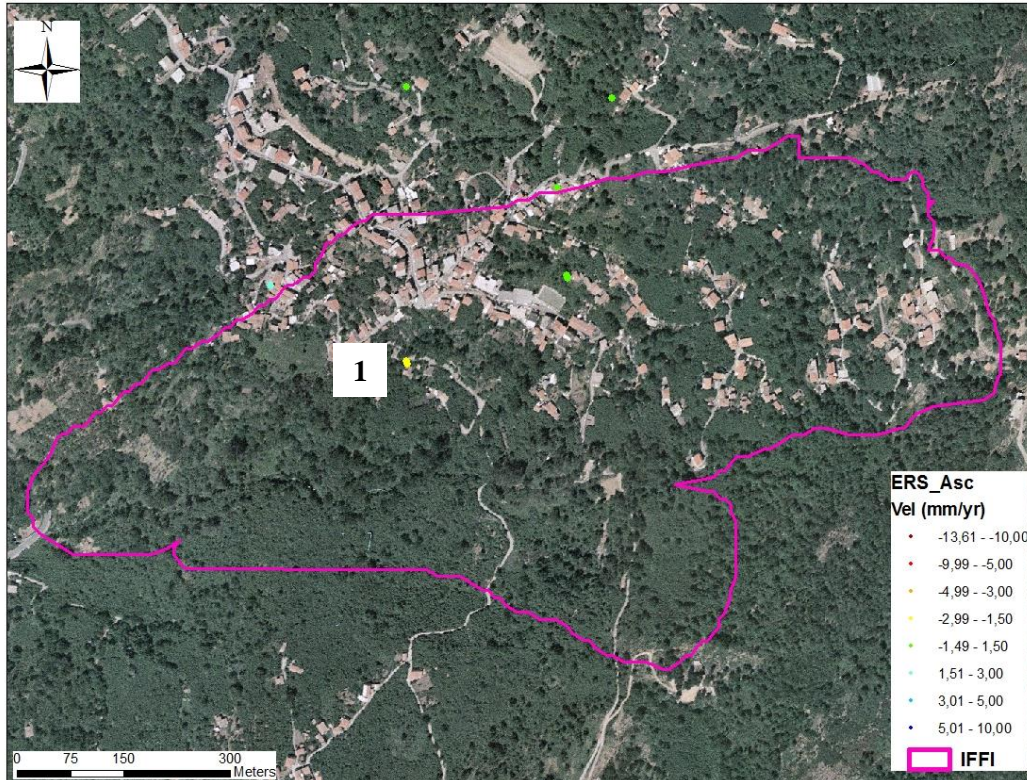


Figure 174: Ascending ERS data in the Sfaranda area.

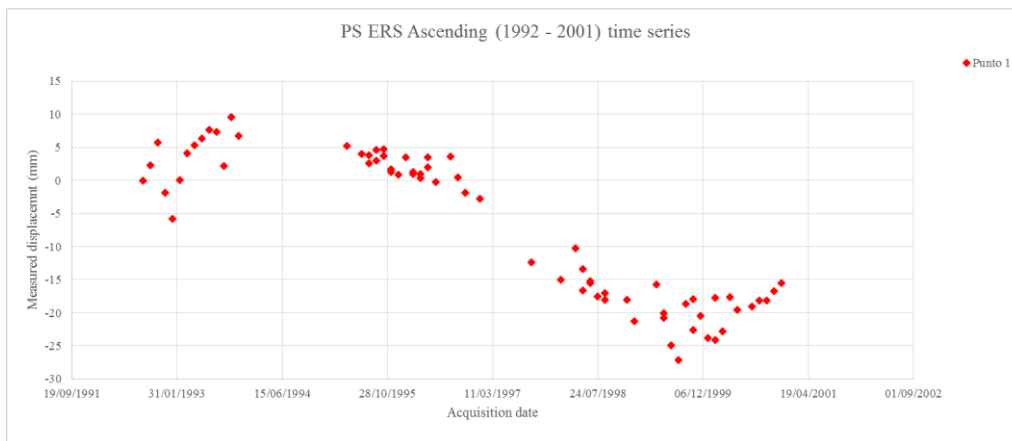


Figure 175: Time series of ascending ERS target selected.

The exposure of the landslide, south-west oriented does not make it suitable to be analyzed with data acquired in ascending geometry, more useful to examine the east-facing slope. In any case, the time series of the selected target presents a displacement going away from the satellite with an average velocity value of -2.50 mm/year (figure 175).

The ground deformation map of Sfaranda derived from PS data acquired in the spanning time 1992-2001 by the C-band satellite ERS 1/2, in descending geometry, is shown in figure 176.

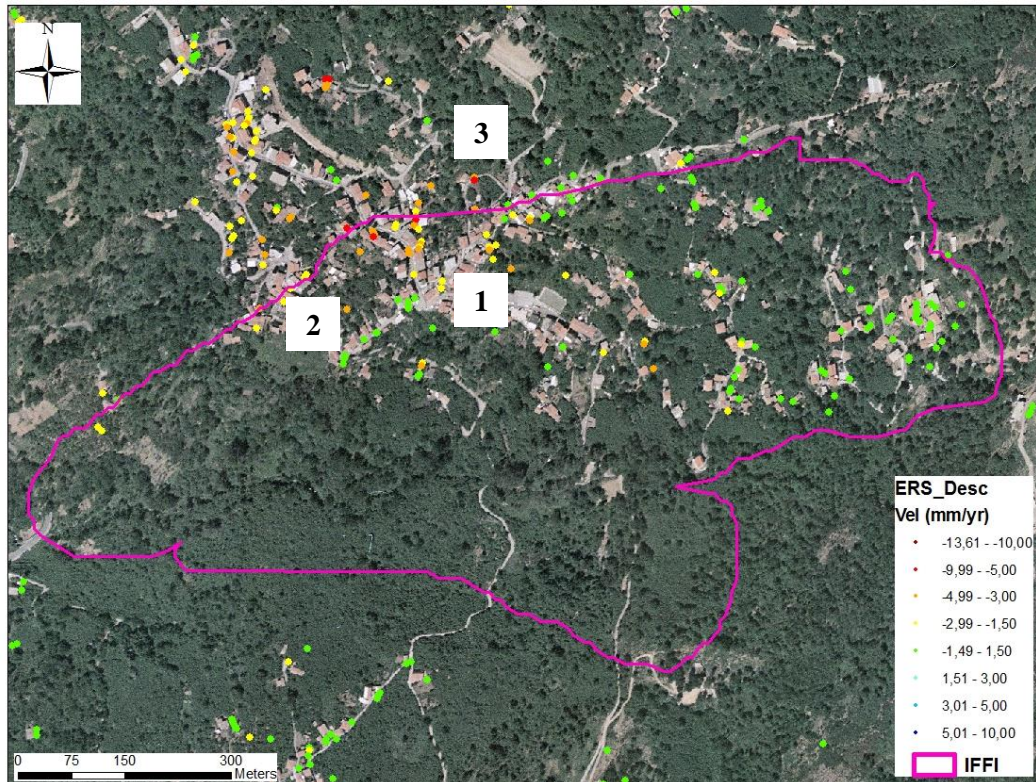


Figure 176: Descending ERS data in the Sfaranda area.

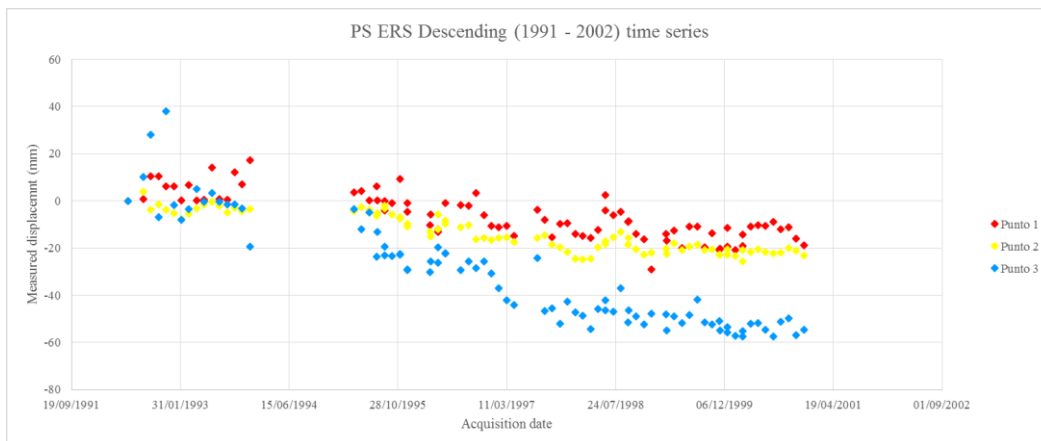


Figure 177: Time series of descending ERS targets selected.

The interferometric data acquired by the descending ERS satellite present a general instability. In particular, the time series of the selected targets present a displacement going away from the satellite with average velocity values of -2.50 mm/year and -3.50 mm/year (figure 177).

The ground deformation map of Sfaranda derived from PS data acquired in the spanning time 2003-2010 by the C-band satellite ENVISAT, in ascending geometry, is shown in figure 178.

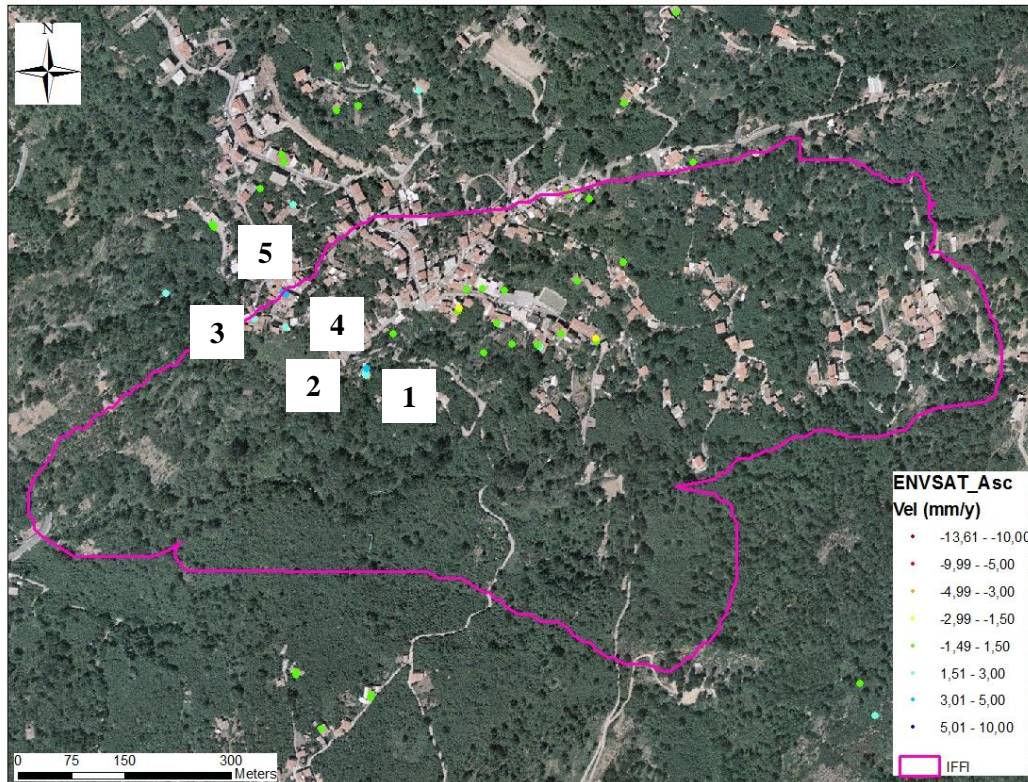


Figure 178: Ascending ENVISAT data in the Sfaranda area

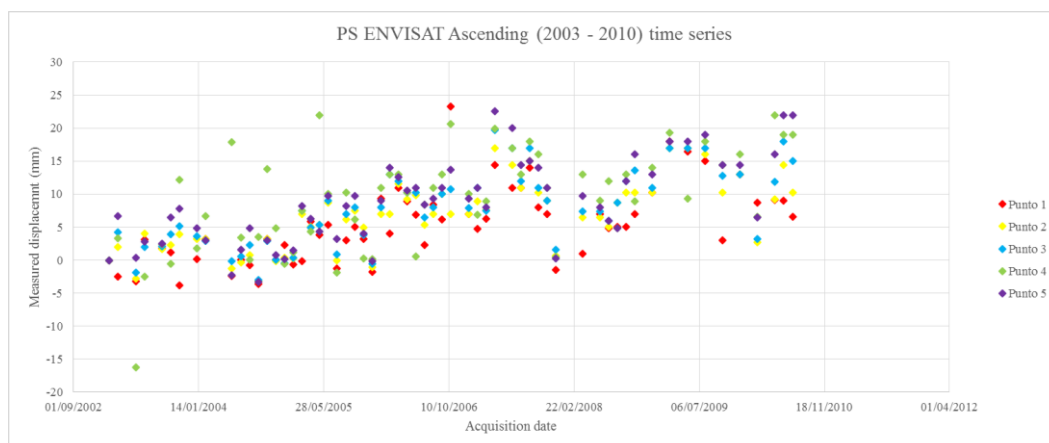


Figure 179: Time series of ascending ENVISAT targets selected.

The interferometric data acquired by the ascending ENVISAT satellite present a general instability of the area. In particular, the time series of the selected targets present a displacement close to the satellite with average velocity values of 5 mm/year (figure 179).

The ground deformation map of Sfaranda derived from PS data acquired in the spanning time 2003-2010 by the C-band satellite ENVISAT, in descending geometry, is shown in figure 180.

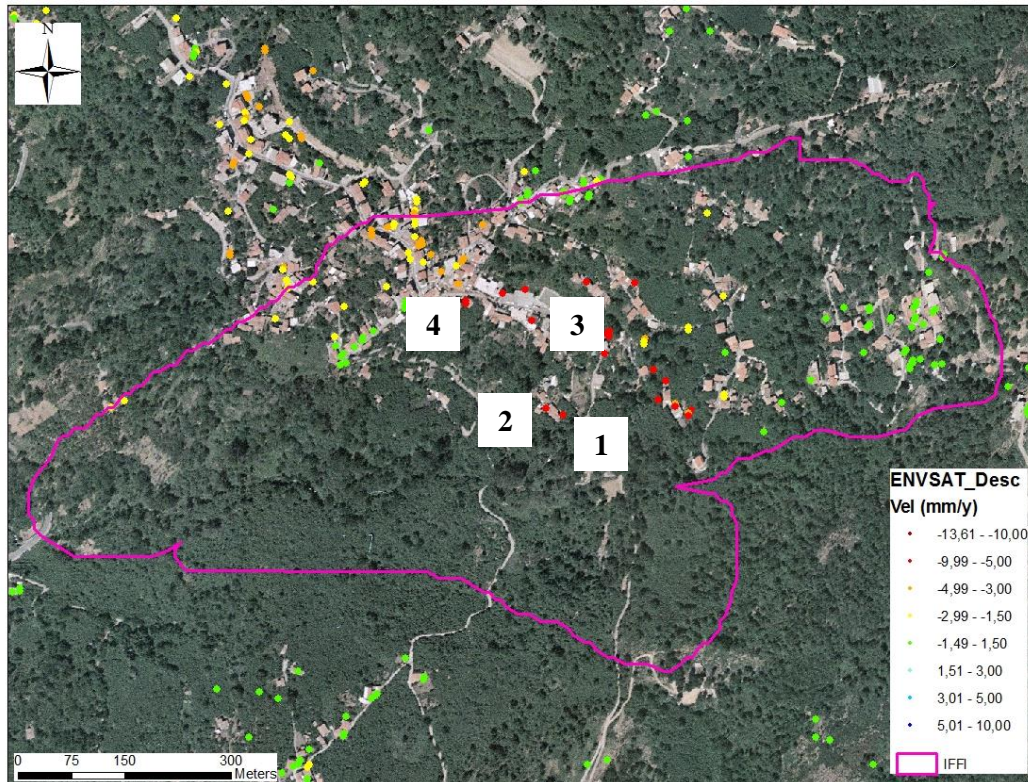


Figure 180: Descending ENVISAT data in the Sfaranda area.

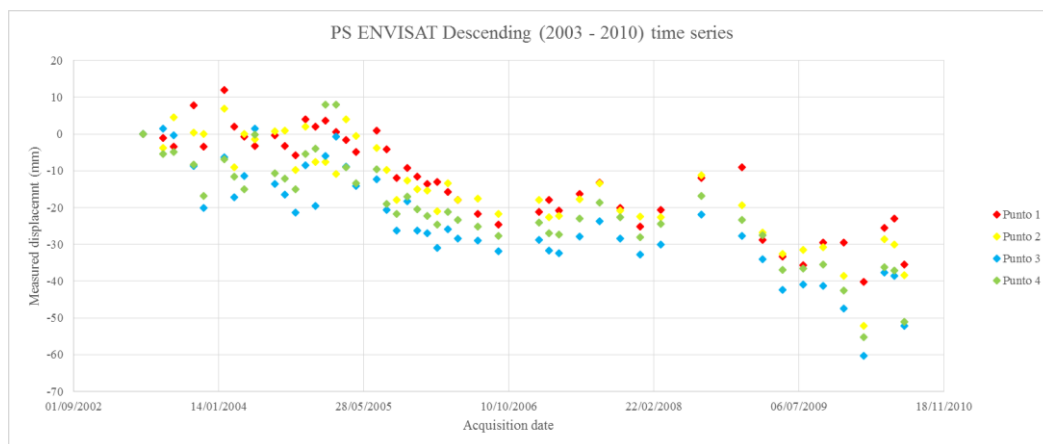


Figure 181: Time series of descending ENVISAT targets selected.

The interferometric data acquired by the descending ENVISAT satellite present a general instability. The average velocity value registered for the selected target is of -8 mm/year (figures 180 and 181).

The ground deformation map of Sfaranda derived from PS data acquired in the spanning time 2005-2010 by the C-band satellite RADARSAT, in ascending geometry, is shown in figure 182.

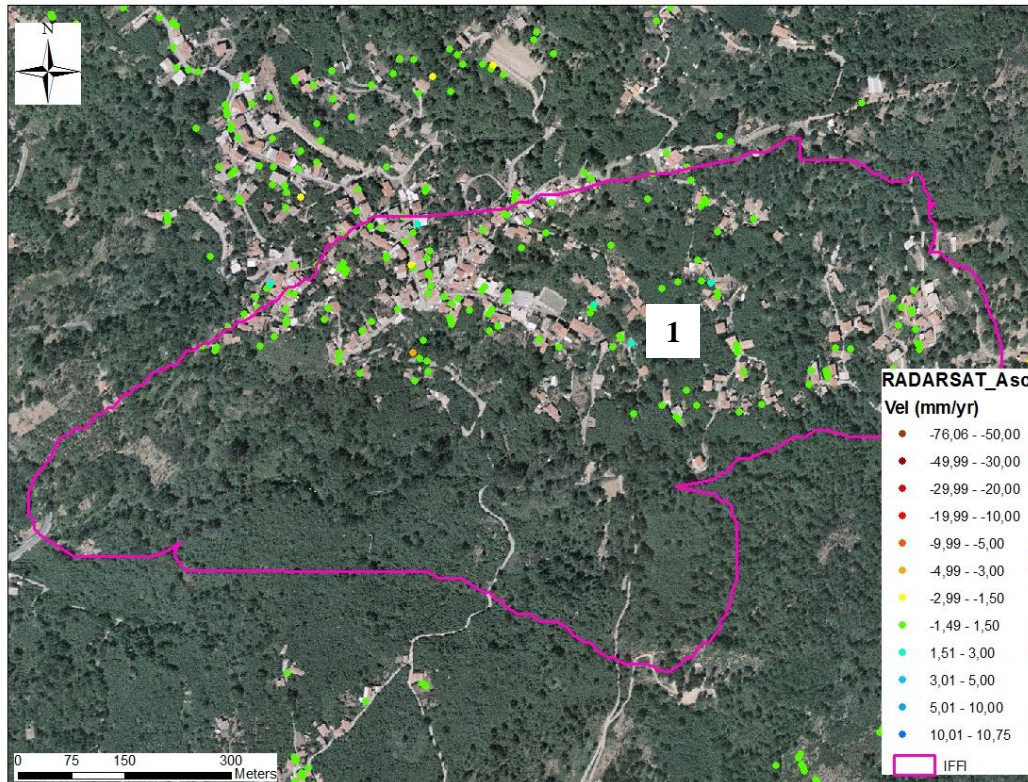


Figure 182: Ascending RADARSAT data in the Sfaranda area

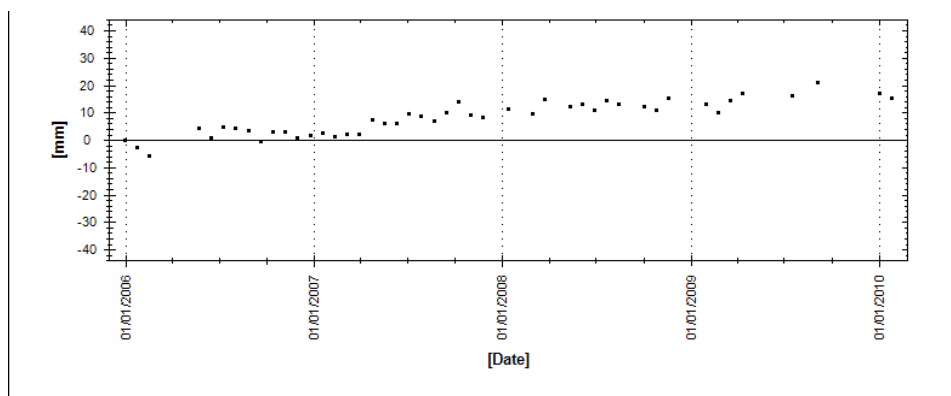


Figure 183: Time series of ascending RADARSAT targets selected.

The interferometric data acquired by the ascending RADARSAT satellite present a general stability. In particular, the targets present an average velocity values within the threshold of stability. The average velocity value registered for the selected target is of 2 mm/year (figure 183).

The ground deformation map of Sfaranda derived from PS data acquired in the spanning time 2005-2010 by the C-band satellite RADARSAT, in descending geometry, is shown in figure 184.

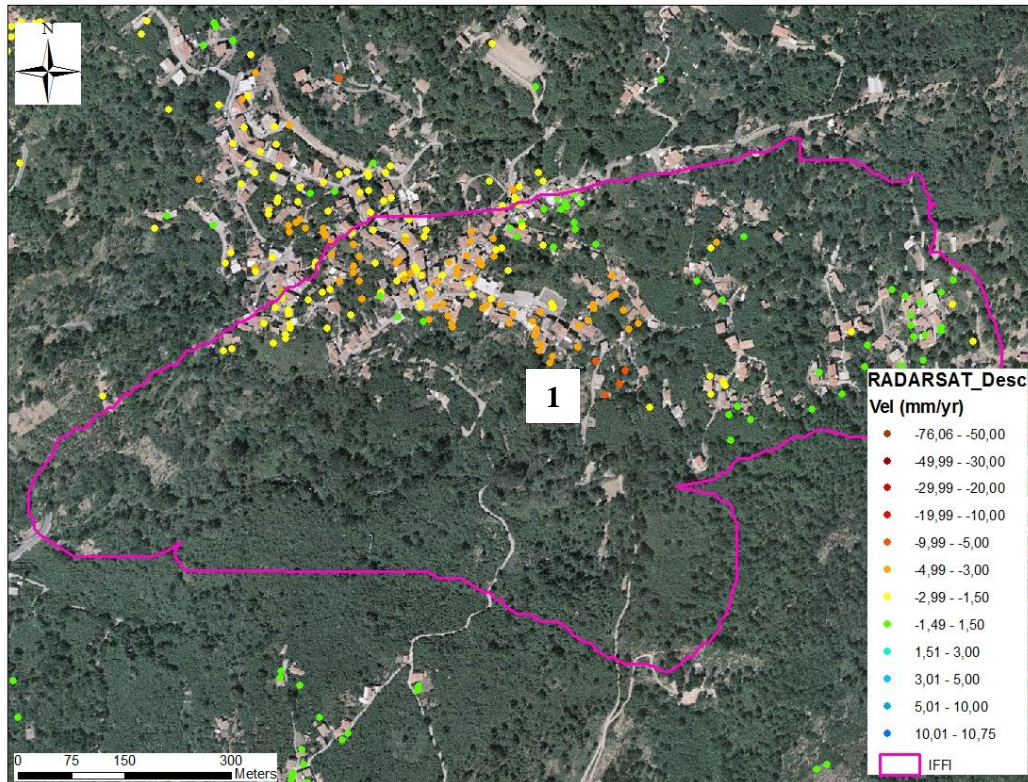


Figure 184: Descending RADARSAT data in the Sfaranda area.

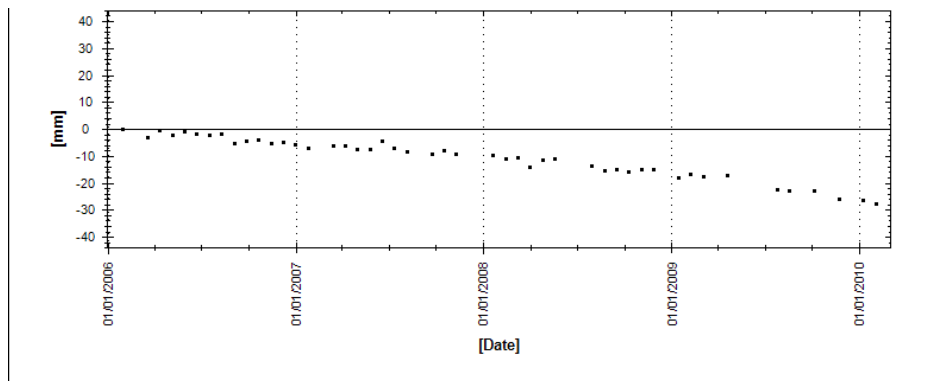


Figure 185: Time series of descending RADARSAT targets selected.

The interferometric data acquired by the descending RADARSAT satellite present a general instability. In particular, the time series of the selected targets present movement going away from the satellite. The average velocity values registered for the selected target are proximally of 3 mm/year (figures 185). In some radar targets, the deformation rate is of 8.50 mm/year.

The ground deformation map of Sfaranda derived from PS data acquired in the spanning time May 2011-May 2012 by the X-band satellite ERS 1/2, in ascending geometry, is shown in figure 186.

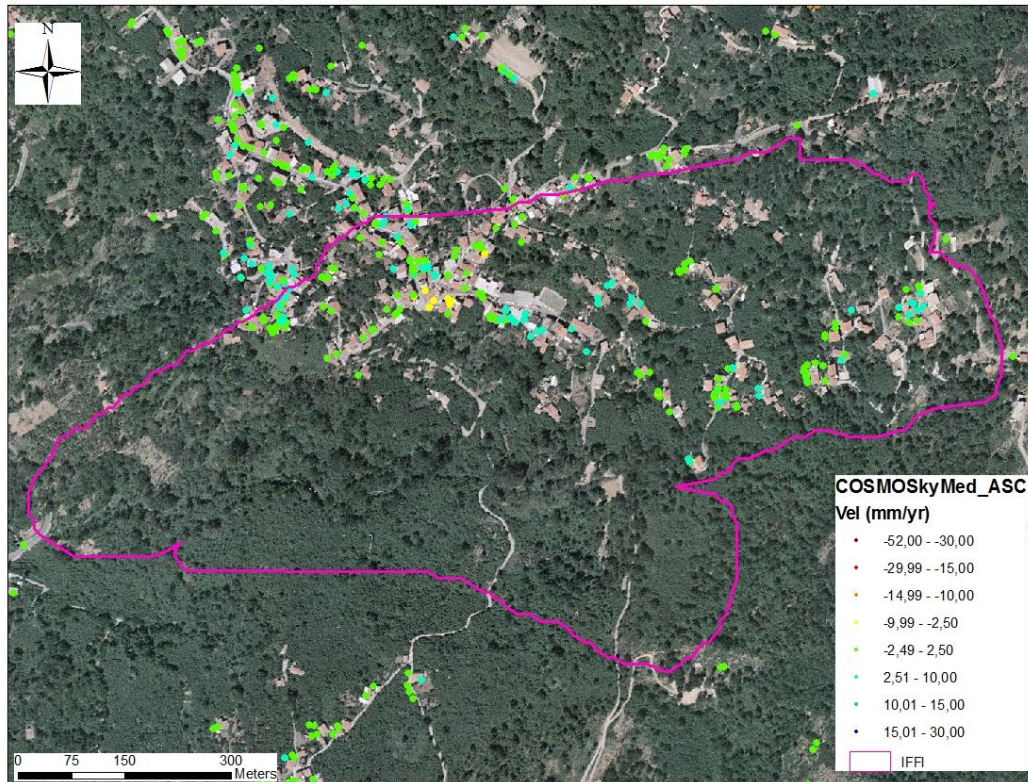


Figure 186: Ascending COSMO-SkyMed data in the Sfaranda area.

The exposure of the landslide, south-west oriented does not make it suitable to be analyzed with data acquired in ascending geometry, more useful to examine the east-facing slope. From the thematic maps, we can see that the density of permanent reflectors identified by ascending datasets is significantly lower when compared to radar targets identified in the descending datasets. With the exception of data relating to the acquisition in ascending orbit of the COSMO-SkyMed satellite, with a different angle of view and thus able to investigate the side so oriented.

The ascending COSMO-SkyMed deformation map shows a general instability for the selected area. The displacement, starting from the ERS acquisition period has been increasing over time until reaching values of 15 mm/year, as shown in figure 184.

By the way, PS targets that show high deformation rates that are significantly more frequent than those of C-band satellites are. This is due to the dense sample of X-band data and to the short monitoring period of only one year (2011-2012) which allows the detection of a high number of PS in areas affected by active superficial processes.

The selected targets present both movement close to and away from the satellite. In particular, in correspondence with the yielding of the SS 116 deformation rate of 35 mm/year are reached (figure 187).

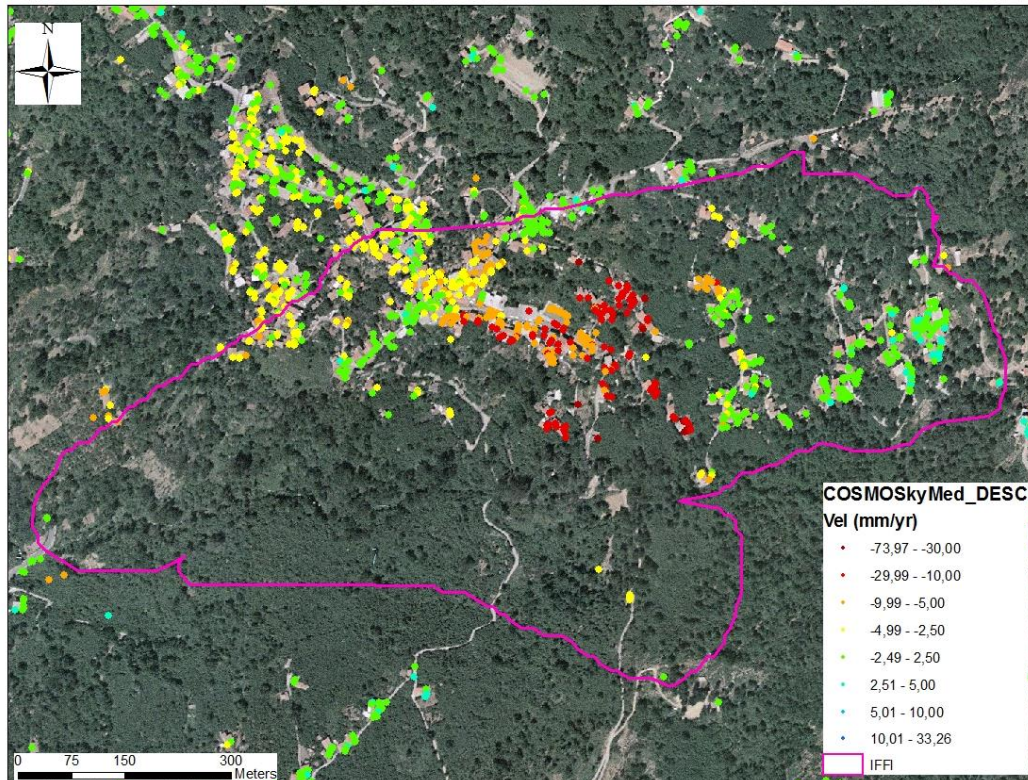


Figure 187: Descending COSMO-SkyMed data in the Sfaranda area.

The descending COSMO-SkyMed deformation map shows a general instability for the selected area with very high deformation rate reaching values of 30 mm/year, as shown in figure 187. The exposure of the landslide, south-west oriented does not make it suitable to be analyzed with data acquired in ascending geometry, more useful to examine the east-facing slope. In fact, not all the thematic maps listed above indicate significant deformation rates. An exception are the ascending Cosmo-SkyMed data, characterized by a different angle of view and therefore able to investigate the side so oriented.

The data acquired in descending geometry instead, show and confirm the instability of the area. In particular, the average annual rate recorded is 7 mm/year for the ENVISAT data, 3.5 mm/year for the RADARSAT data and 12 mm/year for the COSMO-SkyMed data.

The geomorphological instability is part of an active dynamic morphological context due to a geological situation denoted to one side by the presence of tectonic structures that have led layers with considerable inclinations and on the other side a deterioration of mechanical properties of the soil.

9. C and X-BAND DATA FOR BASIN-SCALE MONITORING

9.1 GENERAL CONSIDERATIONS

This chapter gives an application of C and X-Band SAR data for monitoring ground deformation and engineering infrastructures at a basin scale. In particular, the subject of this chapter is the Province of Messina on which an analysis in terms of spatial prediction of the hydrogeological risk was conducted.

A spatial prediction much more precise than can say, for example, which area can be affected, joint most likely, within the areas of alert, can be done with the preparation of landslide susceptibility maps. The landslide susceptibility maps, therefore, are useful documents for land use planning, management of natural hazards and the development of mitigation measures.

In this respect, the second paragraph describes the methodology used for the spatial prediction with a landslide susceptibility map in the province of Messina. In particular, a methodology for the landslide susceptibility map preparation is described. First, the predisposing factors are introduced by geological, structural-geological and geomorphological point of view. After the main results of the elaboration are discussed. These provides, usually in the format of digital maps, the probability of occurrence of a certain type of landslides in a given area, but without taking into account the time factor. In this context, an essential element is the use of interferometric techniques for monitoring ground deformation based on satellite data, which can give an idea of what are the deformations occurred in the time.

The third paragraph, after some notions on the geological setting of the study area, describes the data arising from the elaboration and the main results and discussions.

In particular, the data acquired in C-band are presented and compared with those available in X-band; the acquisition of radar data, dated back to 1992, when the ERS-1 satellite acquired regularly over vast areas of the planet.

In particular, the PSInSAR technique is conducted on the datasets acquired by the ERS and ENVISAT satellites, while the SqueeSAR™ analysis is conducted both on the dataset acquired by the Canadian satellite RADARSAT-1, for what concern the C-Band and on the dataset acquired by the COSMO-SkyMed satellite for what concern the X-Band.

The last section of this paragraph examine the main ground deformations and instabilities for the examined areas. These give some examples of land deformation detection and describe the results obtained.

9.2 SPATIAL PREDICTION WITH A LANDSLIDES SUSCEPTIBILITY MAP

The landslide susceptibility can be defined as the predisposition to landslides. It is a function of the intrinsic stability degree of a slope (defined according to the safety factor or to the peak strength) combined with the presence of predisposing factors capable of reducing the resistance peak and trigger the movement. The predisposing factors are represented by geological, structural-geological and geomorphological factors. Some examples are:

- the shapes, sizes and the nature of geological bodies;
- the structure and the texture of the coverage of the substrate;
- the arrangement of the layers;
- the presence of fractures, faults, stratification surfaces, schistosity;
- the type and degree of chemical weathering and the mechanical degradation;
- the permeability (which disturbs the circulation of surface water and groundwater; the last one being connected to the size and distribution of pore pressures);
- the slope angle (inclination more high of the topographical surface because an increase of the shear stress applied to the slope and the speed with which the landslide movement tends to explicate).

The structural causes are the "quasi-static" variables, in other word they are affected by contained temporal variations and they disturb mainly on the spatial distribution of the landslides and on the susceptibility to slopes instabilities. The prediction of susceptibility is, therefore, an assessment of the relative hazard that is an estimation of the instability degree of one slope with respect to another, without expressing the probability of occurrence of landslides in absolute terms or in temporal sense. Various methods for assessing the susceptibility based on different types of approach have been developed over the years. [Soeters and Van Western \(1996\)](#), [Van western et al. \(1997\)](#) [Aleotti and Chowdhury \(1999\)](#) proposed to classify the existing procedures in four main ways: Landslides inventories; Heuristic methods; Deterministic methods; Statistical analysis. Here, by means of multivariate statistical analysis of morphological, geological, hydrological, vegetation and hydrographic indicators it was possible to obtain a model for the relative hazard zonation. There are numerous examples of statistical analysis of the slope stability factors, often associated with the use of geographic information systems and digital mapping. The statistical analysis techniques most commonly used are the regressive and discriminant analysis. [Varnes and Iaeg \(1984\)](#); [Brabb \(1984\)](#); [Hanses \(1984\)](#); [Einstein \(1988\)](#) and [Hartlen and Viberg \(1988\)](#) present some revisions on the methodologies. The discriminant analysis has been used for the present work.

9.2.1 A METHOD FOR THE LANDSLIDES SUSCEPTIBILITY MAP

The discriminant analysis (Discriminant Function Analysis) is a multivariate classification technique, which is useful in situations where you want to create a predictive model of the membership of a group based on the characteristics observed in each case (Davis, 1970 Klecka, 1980). The discriminant analysis is conducted to define an assignment mode of the cases to different groups, in function of a set of variables related to each other. The interest is to define a model that allows assigning a case to a predefined group, depending on a number of variables. Discriminant analysis assumes that n variables Y_1, \dots, Y_n were measured on observations from two or more groups: $G_1, \dots, G_k, k \geq 2$. The purpose of the analysis is to find one or more combinations of the parameters that make it possible to optimally discriminate between groups. In this way, it possible to assign an observation to a given group based on the measures Y_1, \dots, Y_p . Discriminant analysis is a linear combination of the variables used to calculate the coefficient of discrimination (D):

$$D = b_0 + b_1x_1 + \dots + b_nx_n + \sum b_ix_i$$

Where:

- D = coefficient of discrimination
- b_0 = constant of the model
- x_i = the i -th independent variable selected by the model
- b_i = the i -th coefficient of the discriminant function

The number of discriminant functions is equal to $(k-1)$ where k is the number of groups. In the case of landslide hazard, only two groups (territorial units in active landslide or non-active landslide) are normally used. For each case analyzed by the model, the discriminant coefficient is calculated. This meta-variable should optimize the difference between two groups defined a priori. One possibility that is very important in the discriminant analysis is to operate with a stepwise procedure that select the variables that must to be included in the prediction model based on a statistic (Huberty, 1994). The basic idea of the discriminant function is to determine if two groups or more groups are different with regard to the average of a variable and then use that variable to predict the membership to a group. This means that is necessary to define if the groups are significantly different in relation to the mean of a particular variable. In the discriminant analysis, the predictor variables should have a multivariate normal distribution. However, it is important to emphasize, that violations of normality in the discriminant analysis are not fatal, unlike other statistical methods. This feature of the discriminant analysis makes it very suitable to the hazard problems where the variables are rarely normal.

9.2.2. PREDISPOSING FACTORS

Landslides belonging to different types have neither the same intensity nor the same destructive power nor are equally affected by the factors of land sliding considered (Zézere, 2002).

This limitation can be solved by differentiating the types of events prior to the assessment of susceptibility. This, not only because different movements occur under different environmental conditions (Yan, 1988; Aste, 1991; Carrara et al., 1992; Leroi, 1996), but also because the impact that these have on the environment and on the elements at risk is different and must be estimated separately for each individual type.

The assessment of the susceptibility at the catchment scale has limitations related to the difficulty of acquiring the necessary data for this scale for all of the predisposing factors. Considering these limitations and taking into account the main works at the international level (Suzen et al., 2004; Zézere 2002; Ermini et al., 2005; Aleotti and Chowdhury, 1999), we selected the following parameters.

1. Slope angle
2. Curvature of the slope
3. Drained area
4. Lithology
5. Land cover

The first three are morphometric parameters and can be obtained through GIS processing starting from a DTM of the Province of Messina provided by the Region of Sicily.

The landslide susceptibility can be defined as the propensity of a given area to the triggering of mass movements, in relation to the characteristics of the land cover and the substrate, of the morphological characteristics and of the increased exposure to the morphogenetic agents. It is therefore function of the degree of inherent stability of the slope combined with the presence of certain factors capable of triggering the landslide (predisposing factors or parameters) (Glade et al., 2005).

The choice of the predisposing factors or parameters is therefore a crucial step in the evaluation procedure of the landslide susceptibility. Some of these parameters have been widely used in studies of landslide susceptibility (lithology and slope), while the effect of other parameters (higher order derivatives of elevation, exposure, structural setting) is still debated. It can depend on the method used, on the physical disposition of the study area and on the type of landslides. (Carrara and Guzzetti, 1995; Baeza and Corominas, 1996; Segoni et al., 2012; Catani et al., 2013).

It also discusses the number of parameters to be adopted. Effective evaluation of landslide susceptibility were made both with a few parameters (Ohlmacher and Davis, 2003; Dahl et al., 2010; Akgun, 2012; Pereira et al., 2012) that with a large number of parameters (Guzzetti et al., 1999, Lee et al., 2003; Gorevski et al., 2006; Lee and Pradhan., 2007; Nefeslioglu et al., 2011; Felicísimo et al., 2012).

In any case, a higher number of parameters not guarantee the quality of the result. It can be shown that an increase in the number of model parameters may also worsen the accuracy of the susceptibility map (Pradhan and Lee, 2010; Floris et al., 2011; Manzo et al., 2012; Catani et al., 2013)

Before the processing, however, the parameters must be appropriately processed by a point of view of their spatial representation according to the procedure described below. Two different types of parameters were initially selected: the topographic attributes and the thematic attributes.

The topographic attributes are quantitative parameters used to characterize the landslides forms. Each of these parameters can be put into relation with some physical processes or used as an indicator of the presence or absence of a landslide.

Landslide Inventory Map

To prepare of the landslide susceptibility map of the Messina Province were used the landslides collected as part of the IFFI Project (Landslides Inventory in Italy), which collects on a national scale about 486.000 landslides affecting an area of about 20.721 km² (6.9% of the Italian territory). ISPRA, the Regions and Autonomous Provinces developed this inventory, following a common protocol both in terms of the geometric representation and of attributes description of the phenomena and provides a detailed picture of the distribution of landslides on the Italian territory.

The landslides were identified through field studies, historical documents, and interpretation of aerial photographs and were mapped in a GIS environment using polygons (78%), lines (11%) and points (11%), according to the form, type and size of landslides.

Regarding the Sicily Region mapping IFFI was initially carried out at a scale of 1: 25.000 to then move in a second phase of the project to a more detail resolution (1: 10.000) and it has determined that the phenomena recordable amounted to 3657; the area affected by these phenomena is of almost 500 km².

In particular, only the slow landslides are considered in developing of susceptibility the map cause to the other typologies are not in sufficient numbers to carry out a significant and reliable statistics.

In detail, between the movements belonging to the group of slow kinematics landslide, the region of interest includes the vast majority of the phenomena of the following types: debris flow and debris avalanches, and shallow and deep-seated landslides (figure 188).

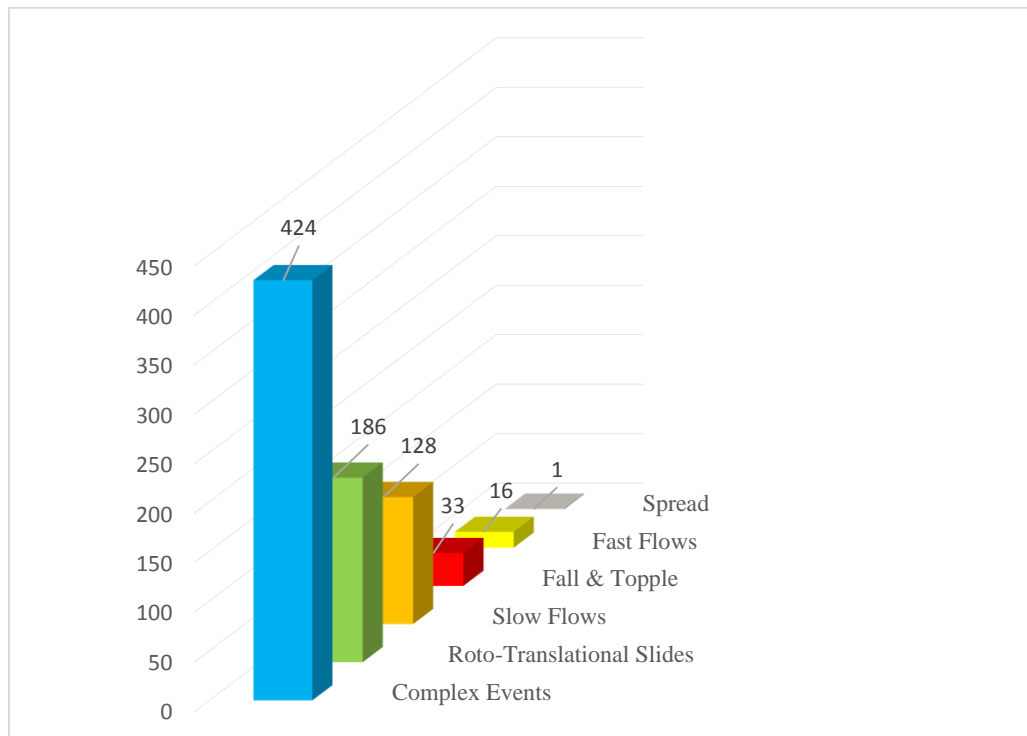


Figure 188: Histogram of the type of landslides in the area.

Referring to the IFFI (Inventario Fenomeni Franosi in Italia) database, which is the available and most updated landslide inventory map, 788 landslides are mapped until 2003 in the province of Messina, covering an area of 140 Km² and mainly involving flyches, sandstones and pelitic litotypes. The mapped phenomena are predominantly complex events (424), roto-translational slides (186), slow flows (128), fast flow (16) and spread (1), according to [Varnes, 1978](#) classification system (figure 188). This was the starting point for the realization of the susceptibility map: the landslides database is of fundamental importance in this type of analysis since the information of the presence or absence of a landslide is compared with a series of input data (predisposing parameters) and has the function of train and validate the analysis model.

DTM

The original resolution of the DTM (Digital Terrain Model) of the study area is 20 m (figure 189). From this, the output raster is created: it was made a resampling of the parameters at a resolution of 100 m using the software of ESRI ArcGIS™ 9.3 of the ESRI®.

Some parameters were resampled using the average of the values in cells of 5x5 pixels (using the “aggregate” of ArcMap), while others were grouped according to the most recurrent value (Majority) using the command “block statistic” always in a window of 5x5 pixels.

Moreover, given the spatial variability of the topographic attributes, other variables were defined: in fact, the standard deviation (for numeric attributes) or the variance (for categorical attributes), calculated within windows of 5x5 pixels, again with the command “block statistic”, has been considered for each “topographic attribute”

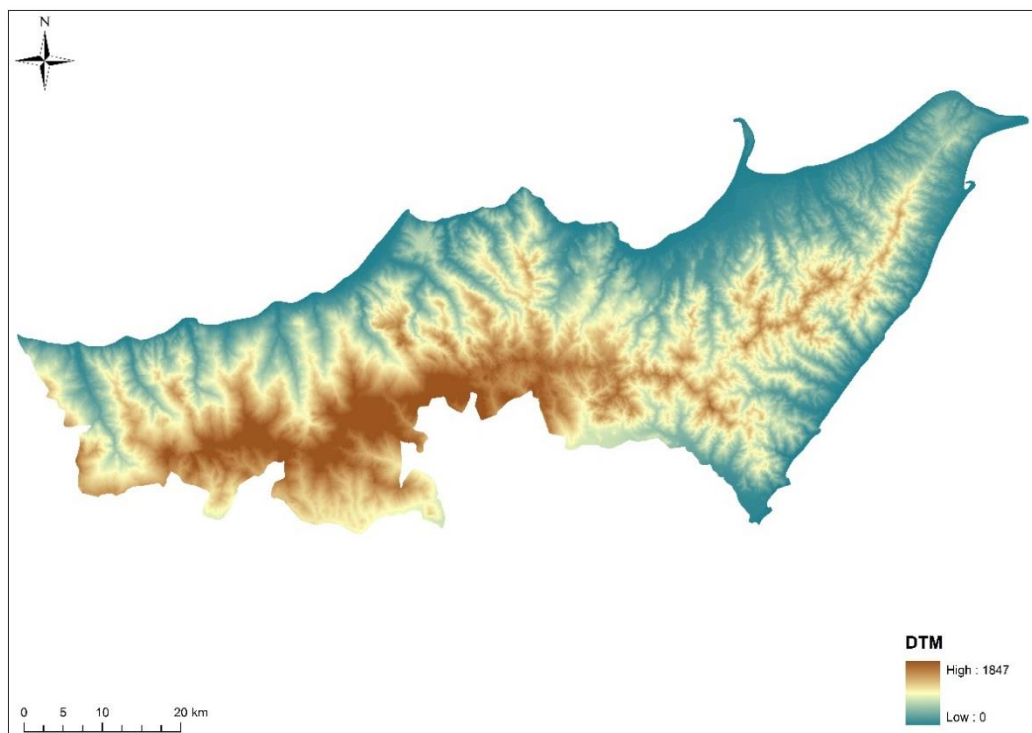


Figure 189: Digital terrain model (DTM) with 20m resolution of the mountain-hilly area of Messina Province; it was used to derive the topographic attributes of the terrain at a resolution of 100m.

Aspect

The aspect is the spatial orientation of each pixel. In practice, it indicates where each portion of the slope is facing. This parameter can play a key role in the estimation of the susceptibility defined as the exposure of the soil to a different amount of rainfall and solar radiation, and consequently affects the soil moisture and the presence of vegetation in the same soil. (Guzzetti et al., 1999; Dai and Lee, 2002; Demir et al., 2013).

In this case the parameter has been obtained using the "aspect" within the module "spatial analyst" of ArcGIS 9.3 that allows to realize an exposure raster with some angular measurements (from 0° to 360 °) that indicate the exposure with respect to the north (for

example, 0° = north-facing slope, 90° = east-facing slope). The raster resolution is 20 m (figure 190)

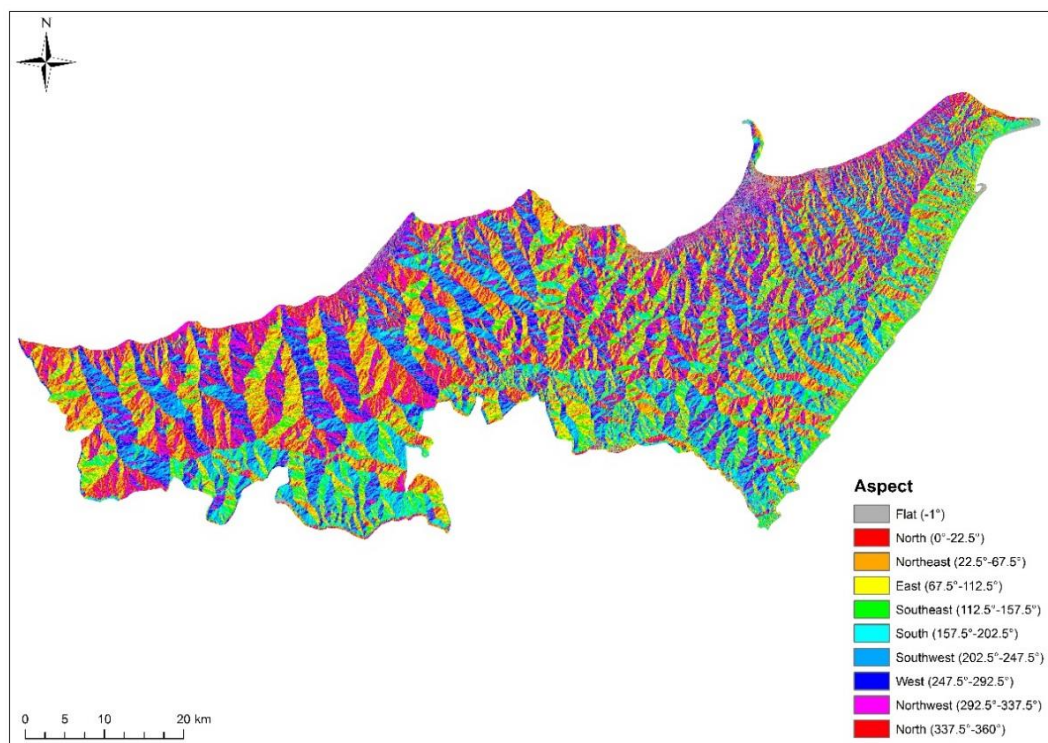


Figure 190: Image of the Aspect map derived from digital terrain model (DTM) with 20m resolution of the Messina Province.

Given the difficulty of treating angular measurements (the average of measurements of direction does not correspond to the arithmetic average of the measures of the angles); the exposure was reclassified in nine different categories, based on the angular values. Eight of them represent the main cardinal directions and one indicate a flat morphology area (table 11)

Class of exposure	Cardinal central point	Width of the class
1	N	$337.5^\circ - 22.5^\circ$
2	NE	$22.5^\circ - 67.5^\circ$
3	E	$67.5^\circ - 112.5^\circ$
4	SE	$112.5^\circ - 157.5^\circ$
5	S	$157.5^\circ - 202.5^\circ$
6	SO	$202.5^\circ - 247.5^\circ$
7	O	$247.5^\circ - 292.5^\circ$
8	NO	$292.5^\circ - 337.5^\circ$

Table 11: Table of the classes in which the Aspect map is divided.

Elevation

The elevation is directly obtained from the DTM. This is one of the parameters commonly used in the susceptibility evaluations as different altitudes are related to different environmental features (vegetation, temperature, rainfall). (Dai e Lee, 2002; Costanzo et al., 2012; Felicísimo et al., 2012; Günther et al., 2012; Sabatakakis et al., 2012).

The standard deviation, in this case, is closely related to the energy of the relief and then with the potential erosive capacity. (Oguchi, 1997; Günther et al., 2012; Kayastha et al., 2012).

Slope

The slope is one of the main parameters, because the cutting forces acting on the slope depend from this angle. It is widely used in studies of susceptibility (Aleotti and Chowdhury, 1999; Guzzetti et al., 1999). The DTM has a homogeneous structure with square cells with the side of 20 m. Through a morphological analysis of the digital elevation model, it is possible to perform a parameterization of the surface that is used to describe numerically the continuous shape of the surface itself (Wood, 1996). Between the topographical attributes most commonly calculated from a DTM, the slope gradient, used for the evaluation of various parameters involved in many geological and geomorphological processes, assumes a fundamental role. In a raster format, if you consider a tangent plane to the digital model in every point, it is possible to identify a vector composed of a gradient in the maximum gradient direction (slope gradient) and of an azimuth or an aspect of the direction in which we have the maximum gradient (slope aspect) (Evans, 1998). Considering the slope such as slope gradient, it therefore represents the gradient of the tangent plane to the surface at the desired point in the direction of maximum slope, while from the analytical point of view it is equivalent to the first derivative of the function, which expresses the variation in altitude along the same direction. This derivative is generally obtained for each cell based on the value of the cells within a window of nine elements, which is made sliding on the digital model. The calculation may be accomplished by various methods. Zevenbergen and Thorne (1987) have proposed to utilize a second order polynomial surface bound to the four cells adjacent to the cell in question:

$$\tan\theta = [(\delta z/\delta x)^2 + (\delta z/\delta y)^2]^{0.5}$$

Where z is the altitude and x and y are the coordinates of the axes of the grid. An efficient implementation of this system is present within ArcGIS using the "SLOPE" within the module for raster calculations (spatial analyst). Since it appears that, the final slope calculated for each cell of the DEM, is equal to:

$$\tan\theta = [(\delta z/\delta x)^2 + (\delta z/\delta y)^2]^{0.5}$$

where

$$[(\delta z/\delta x)^2] = [(z_{i+1,j+1} + 2z_{i+1,j} + z_{i+1,j-1}) - (z_{i-1,j+1} + 2z_{i-1,j} + z_{i-1,j-1})] / 8 \delta x$$

Where

is the gradient in the east-west direction, while:

$$[(\delta z/\delta y)^2] = [(z_{i+1,j+1} + 2z_{i+1,j} + z_{i+1,j-1}) - (z_{i+1,j-1} + 2z_{i,j-1} + z_{i+1,j-1} + z_{i-1,j-1})] / 8 \delta x$$

is the gradient in the North-South direction. In these expressions, z_i is the altitude of the i -th point while δx is the width of the cell in the DTM.

When the slope for each cell of the DTM was determined, we proceeded to the classification of the same, with some suitably according classes defined for each type of phenomenon, as a function of some considerations deduced from the literature.

In figure 191, the slope map derived from the DTM is shown. To realize the raster of the slope the special command "slope" within reach "spatial analyst" of ArcMap was used.

The maximum value, the average value and minimum value were used for a more complete information. Five classes of gradient were defines as follows: $0^\circ - 5^\circ$; $5^\circ - 10^\circ$; $10^\circ - 15^\circ$; $15^\circ - 33^\circ$; $33^\circ - 90^\circ$

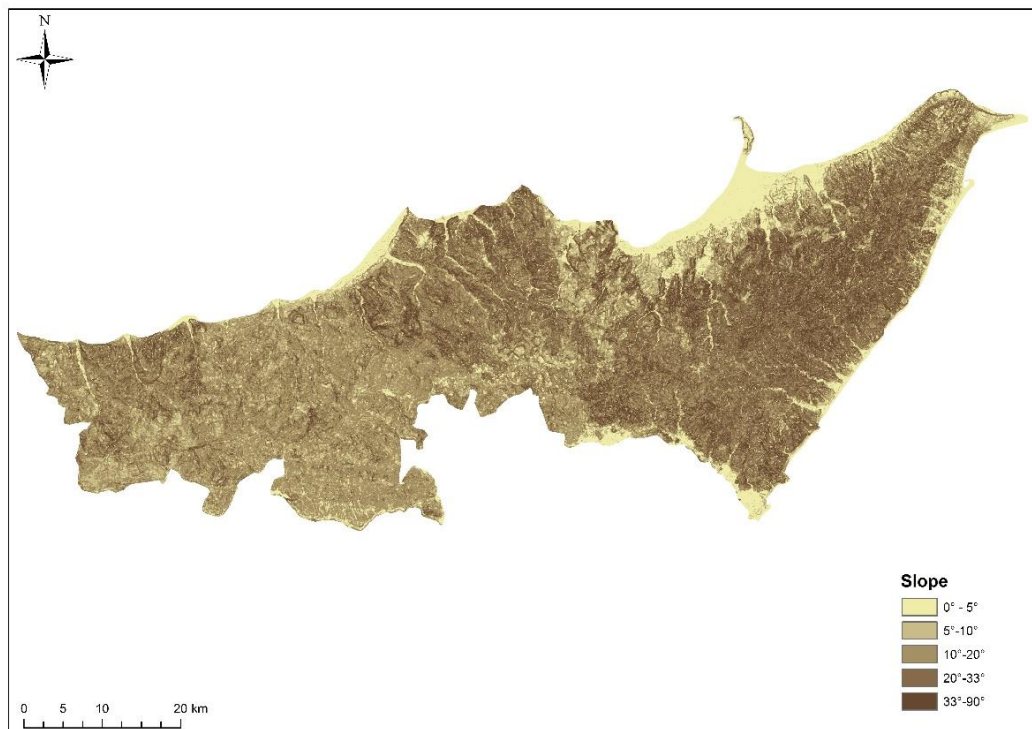


Figure 191: Image of the Slope map derived from digital terrain model (DTM) with 20m resolution of the mountain-hilly area of Messina Province.

Curvature

It is commonly used to describe the physical characteristics of an area with respect to erosion and runoff (Zeverbergen and Thorne, 1987) and to identify the morphologies related to landslide bodies (Evans, 1998; Ohlmacher, 2007; Catani et al., 2010). The curvature is the change of the slope in the space and it is expressed as the gradient of the slope. There are many ways to calculate the curvature of the topographic surface. The three types of curvature have been selected as predisposing parameters to landslides. All raster curvature described below have been filtered with a moving average filter (5x5 pixels). The curvature is obtained by the command "curvature" of the ArcGIS software, which takes into account the central cell of the DTM input and the eight neighboring cells, interpolating the quadratic surface that best approximates the nine heights.

Various types of curvature can be derived as the second derivatives of the topographic surface. In this study, four type of curvature were given.

Profile curvature

Obtained using the "curvature" of ArcGIS, is the second derivative of the DTM calculated in 5x5 windows. The profile curvature is obtained by performing the discrete derivatives in the direction of maximum slope. This procedure is used to calculate the profile curvature for each cell in the input DTM.

The analysis of the profile curvature indicates whether any point along the profile, belongs to a concave or convex area: the profile curvature is convex when in plan the contour lines are close to each other and concave when the contour lines move away from each other. In a longitudinal section, the profile curvature is convex if the slope increases towards the valley and concave in the opposite case (figure 192)

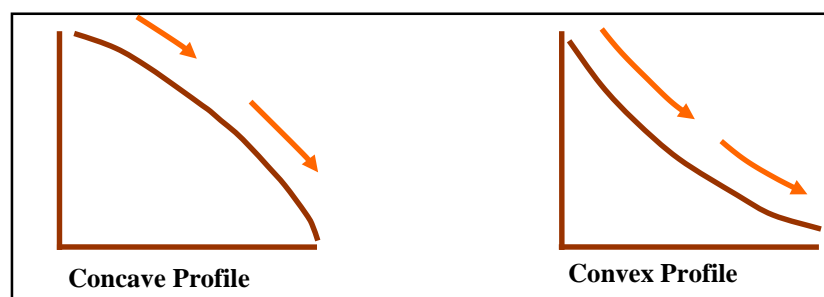


Figure 192: Planar curvature.

It expresses the rate of change of the slope gradient along the direction of maximum slope. It affects acceleration/deceleration of the flow surface and consequently erosion/deposition of the material of the slope.

Curvature s.s.

Obtained using the "curvature" of ArcGIS, is the second derivative of the DTM calculated in 5x5 windows.

Planar curvature

The planar curvature is calculated by performing the discrete derivative in the direction perpendicular to that of maximum slope. This procedure is used to calculate the planar curvature for each cell of the input DTM. The analysis of the planar curvature allows identifying and characterizing the flow areas: the convex contour lines (positive curvature) indicate a divergent flow, while the concave contour lines (negative curvature) alludes to a convergent a flow (figure 193). The planar curvature is calculated orthogonally with respect to the direction of maximum slope and can be used to characterize the convergence and divergence of the flow and to recognize real watersheds.

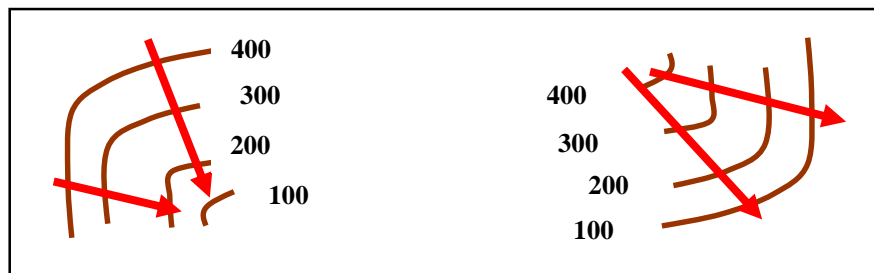


Figure 193: Planar curvature: convergence and divergence according to the trend of contour lines.

Type of slope

It is a categorical variable obtained by combining the values of the planar and profile curvature. The two raster have been reclassified in accordance with the following criteria: values smaller than -0.02 = concavity; values greater than 0.02 = convexity; intermediate values = slope plane (constant slope). The three different classes for the two curvatures give rise to nine different combinations. Through some appropriate procedures for the reclassification and calculation, starting from the curvature, a raster where each pixel is classified has been created.

Drained area

This parameter expresses the portion of an area, drained by a specific pixel in the map. It is used in the analysis of susceptibility to estimate the water flow and the potential saturation of a portion of the soil (Catani et al., 2005; Felicísimo et al., 2012; Xu et al., 2013). These raster were made with the commands in the toolbox "hydrology" of ArcMap 9.3. First, the closed depressions were removed from the DTM with the "sink" command,

and then the raster of flow direction (command "flow direction") has been calculated. This last one was used to calculate drained the area (command "flow accumulation ").

Topographic Wetness Index (TWI)

This parameter is defined as (Beven e Kirby, 1979):

$$\ln (A/tg\beta)$$

where

A is the area drained by each pixel, as described above and β is the slope.

This index is commonly used for the characterization of the spatial distribution of soil moisture. The thematic attributes are derived with the use of GIS from specific thematic maps. The raster of this index has been achieved by setting the "raster calculator" the following operation:

$$TWI = \ln \left(\frac{(Acc + 1) \times 400}{\tan(slope + 0.0001)} \right)$$

Acc is the raster of the drained area to which one is added (to count the pixel in question, otherwise excluded from the calculation) and which is multiplied by 400m² (the area of each pixel).

slope is the raster of the slope, to which a very small scalar quantity is added; this, to avoid indeterminate forms and null values (flat pixel) in the denominator of the fraction.

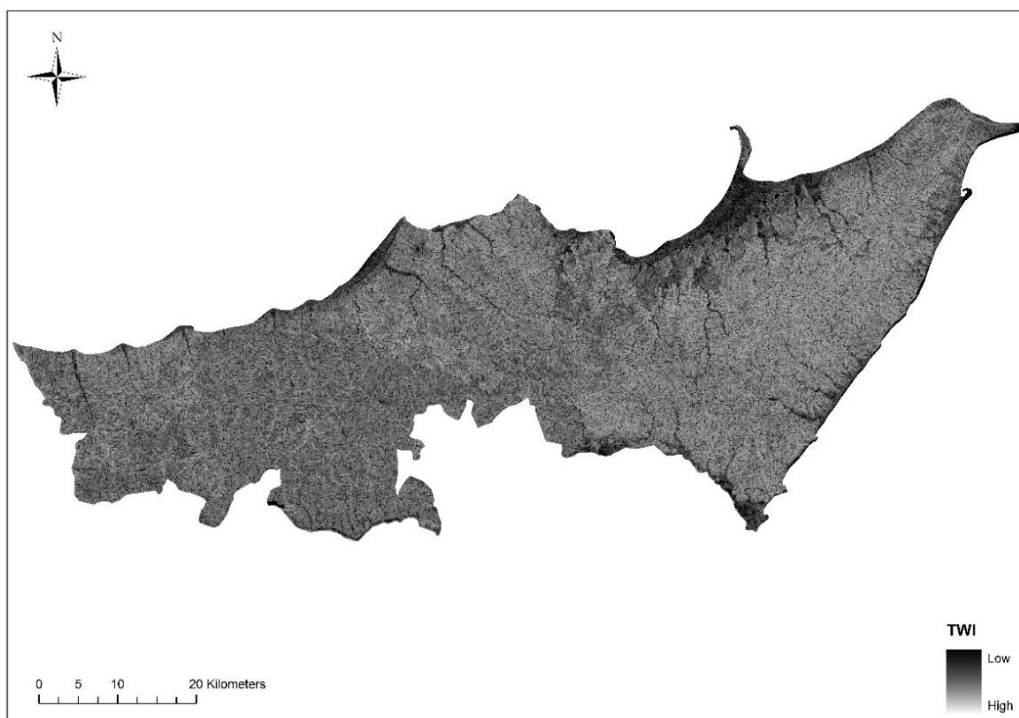


Figure 194: Image of the TWI map derived from digital terrain model (DTM) with 20m resolution.

Lithology

The lithology is one of the most important variable in the evaluations of landslides susceptibility, as it contains the geotechnical and hydraulic properties of the bedrock and influences the characteristics of the cover soil overlying (Dai e Lee, 2002; Catani et al., 2005; Costanzo et al., 2012). The material available to derive a complete lithological mapping of the area under study is the “lithotechnical map” of the Sicilia region on a 1: 10.000 scale. This paper, as mentioned, does not focus on the recognition of different formations from the only descriptive geological point of view, but on a geotechnical characterization and on the type of soil, which are the parameters that are most popular when you search for a correlation with landslides. The result of this processing is represented, in figure 195.

The classification adopted is a specific, not necessarily coincident with a geological or formational classification. For example, we do not care so much if this is the rock formation belonging to the X formation rather than the Y formation, but what lithology can influence the trigger of a landslide in a given area; for example if there is a “rock mass” or a “cohesive soil”. Compared to the classification given by the Italian lithotechnical map on a 1: 100.000 scale, some changes has been made. The lithological classes taken are as follows: argillites; crystalline rocks; alluvial deposits; limestone; flysch; pyroclastic.

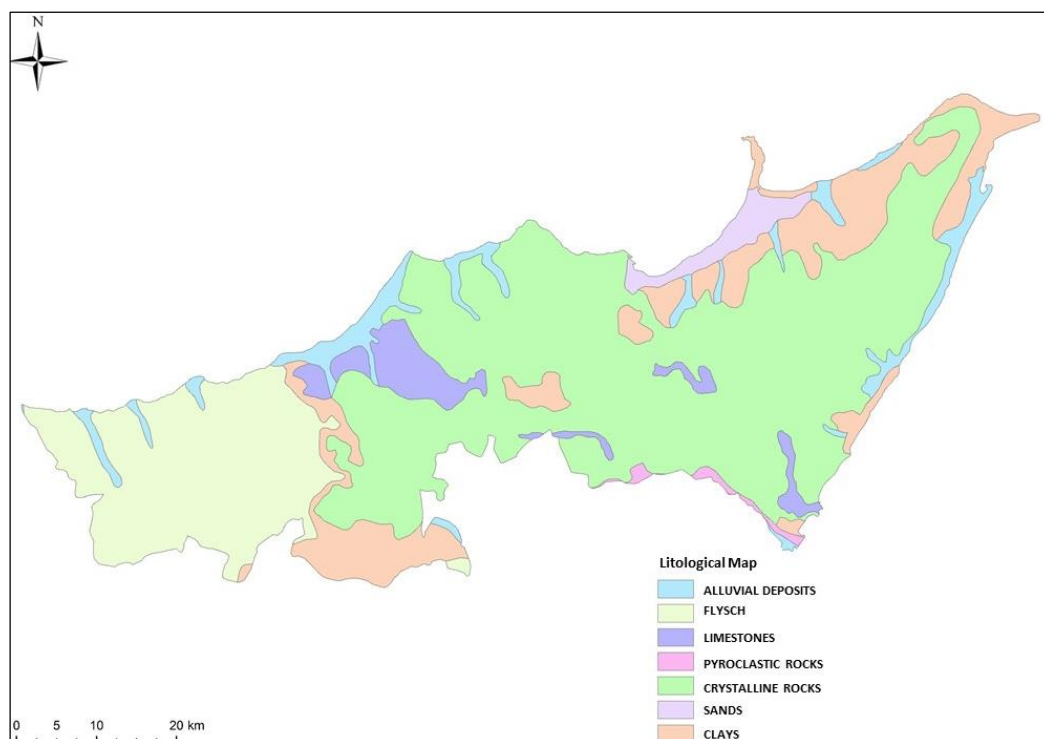


Figure 195: Lithological map of the Messina Province obtained after the work of unification and reclassification.

Land use

The susceptibility is strongly influenced also by the vegetation cover and, in addition, the use of soil parameter can be used to indirectly to determine the human factor on the slopes (Varnes and IAEG 1984; Costanzo et al., 2012; Pereira et al., 2012). The land use map on a 1:25.000 scale was derived from the map provided by Sicilia Region. This uses, as regards the first three levels, the method of classification derived from the European specifications of the European project “Corine Land Cover”(CLC), complemented by a fourth level. The map follow the specifications defined at the national level by the Land Use Working Group of CISIS (Interregional Centre for computer systems, geographic and statistical) and focused on specific issues. This map was reclassified on GIS environment following the guidelines provided by the Department of Earth Sciences, University of Florence, making some changes to better adapt the result to the peculiarities of the area investigated. The fourth level was not considered as far too detailed.

The new classes are nine and synthesize the information, giving a general indication of the employment of regional soil surface (figure 196). The land use was derived from the digital map Corine Land Cover 2000. The classes of land use adopted in the areas covered are as follows: wetlands and water bodies; artificial surfaces; agricultural areas; arable no vegetation zones; perennial crops.

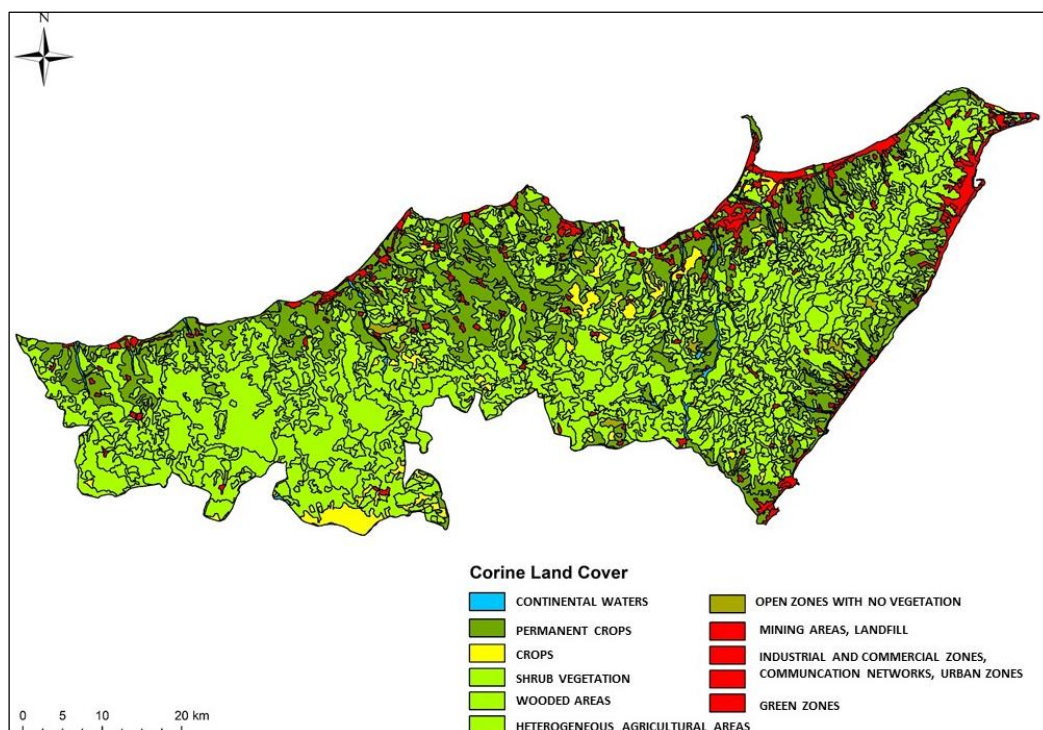


Figure 196: Land Use map in the Messina Province after the reclassification work of the Corine Land Cover map (CLC).

9.2.3. DATA ANALYSIS AND RESULTS

As previously mentioned, the purpose of this paper is to produce a map of landslide susceptibility for the Messina Province and to do this it was decided to use a method of classification and regression based on a specific version of Random Forest the algorithm, the tree bagger.

The Random Forest classification consists of a machine-learning algorithm for a non-parametric multivariate classification, first developed by Breiman (2001).

The RFtb approach is usually used in sociological studies (Strobl et al., 2009) and in the classification of remote sensing images (Ham et al., 2005; Pal, 2005).

However, it is used more frequently, even in the modeling environment (Prasad et al., 2006; Strobl et al., 2008; Bachmair and Weiler, 2012).

The algorithm uses random binary trees that use a subset of the spatial parameters through techniques bootstrapping.

Each tree has the aim to minimize the errors of classification, but the random components influence the result and, for this, a single shaft classifier would be very sensitive to random variables in the choice of the data input.

For this reason, instead of a single classification or of a regression tree, the RFtb method uses a set of trees (hence forest) aimed at ensuring the stability of the model.

The RFtb technique has several advantages over other techniques of regression and classification.

First, this technique does not require assumptions about the distribution of the explanatory variables, and also allows the use of mixed categorical and numerical variables; finally is able to quantify the interrelationship and the non-linearity between the variables.

These are great advantages when working with variables of land with a certain degree of approximation and with an intrinsic uncertainty in assigning the correct class even in previously investigated areas.

A further advantage is the ability of the RFtb model to provide information on the statistical weight of each variable on the overall result.

This is obtained in the phase of pruning, during which the variables, which weigh so less or even negative on the elaboration of the susceptibility maps of are excluded.

In the present work, the RFtb model was implemented in Matlab environment: in this implementation, the relative importance of the predisposing parameters is estimated using the out-of-bag error (OOBE), which is the error that is made in the classification excluding the parameter less significant from the final ensemble.

Negative OOB errors indicate the variables that worsen the forecast. Positive OOB errors instead, indicate variables that are more important as the higher the value of OOB error is. The output of the model indicates the probability of belonging to one of two classes “landslide” or “no-landslide”.

The overall result of the model, however, can be evaluated through the misclassification probability (MP) that represents the classification error in a specific RFtb configuration.

On the basis of previous publications and in particular of the information contained in [Catani et al. \(2013\)](#) a 200 trees model is used to minimize the error resulting from the random components, and 10 runs were made for the calculation of the average OOBE of each parameter. This choice regards the optimal configuration of the model and the number, the importance and the scale of the detection of predisposing parameter,

As first thing for the training and the subsequent validation of the statistical model is necessary to find an area for the training phase (training) of the model and one for testing (testing) of the same. It was decided to use the 10% of the survey area for the training and the 10% for the test, because this configuration has shown good results ([Catani et al., 2013](#)), also in consideration of the fact that the parameters have a spatial resolution of 100 m.

Sampling points were created on the software ArcMap using the "create random points" within Messina Province.

Two datasets consisting of 102540 points were created. A sampling was carried out on each of these, using the software ArcMap, with the command "sample".

Another important issue in the landslide susceptibility studies is how many and which parameters are needed to get a better result

This does not only depend on the number of parameters that you intend to use, but also by the resolution at which the analysis is performed ([Catani et al., 2013](#)).

It is necessary to start from a configuration where the parameters described above are included in.

At this point, the process of pruning of the RFtb begins, which, as the word itself indicates (pruning, i.e., cutting), cuts off one parameter at a time, starting from the least significant (minor OOBE) until you get to a configuration with a single parameter that will, on the contrary, be the one with the higher relevance (greater OOBE).

The susceptibility map, obtained as described in the previous sections, gives a value of susceptibility continuous throughout the considered study area.

The values range, from zero to 81%, indicate the percentage probability that in the pixels with this value, a landslide can occur (figure 197).

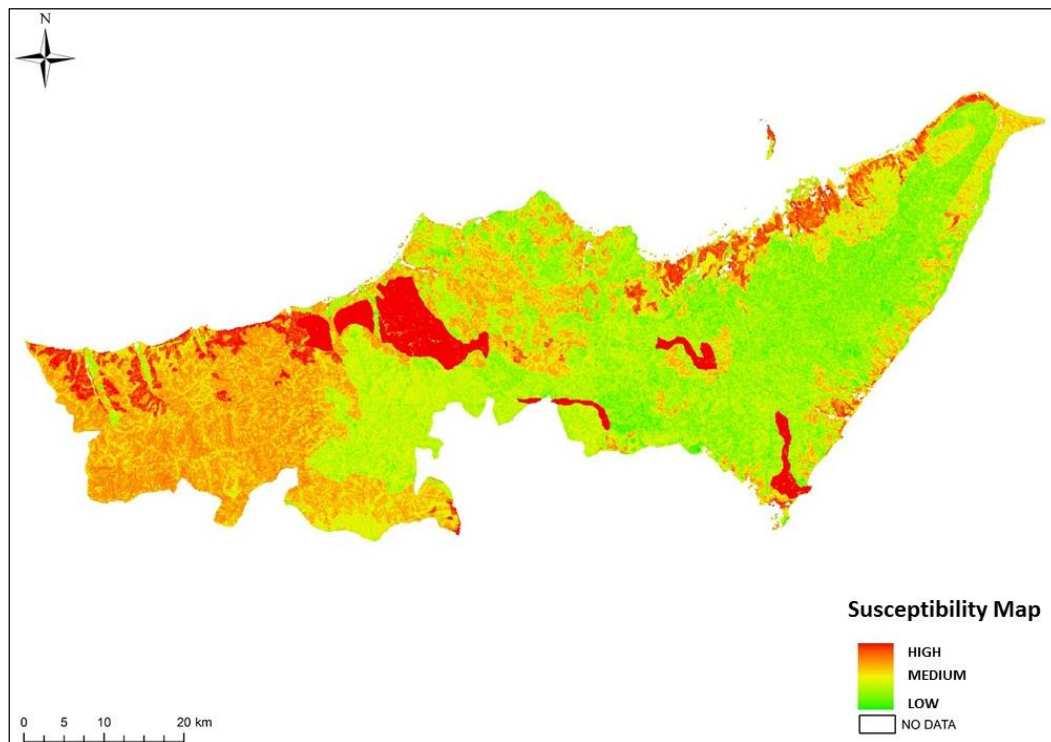


Figure 197: Susceptibility map of Messina Province.

This information is not very useful for this purpose since it does not give an immediate information on the state of risk of the area and it is difficult to interpret.

To obviate these problems, it is therefore necessary a classification of the susceptibility map of landslides to indicate more clearly the level of risk in the territory and that gives information easy to read and interpret.

The classification appears to be a critical step because the map can be considered reliable. [Catani et al. \(2005\)](#) provided by previous works and in particular indications to this effect. Besides the method described above, for a more accurate classification, it is also taken into account the histogram of the distribution of values of susceptibility, which shows the percentage probability value in the abscissa and the number of pixels presenting for each value in the ordinate. It is therefore assumed a classification according to the Natural Breaks of the distribution pixels (figure 198).

The Jenks optimization method, also called the Jenks natural breaks classification method, is a data clustering method designed to determine the best arrangement of values into

different classes. This is done by seeking to minimize each class's average deviation from the class mean, while maximizing each class's deviation from the means of the other groups. In other words, the method seeks to reduce the variance within classes and maximize the variance between classes.

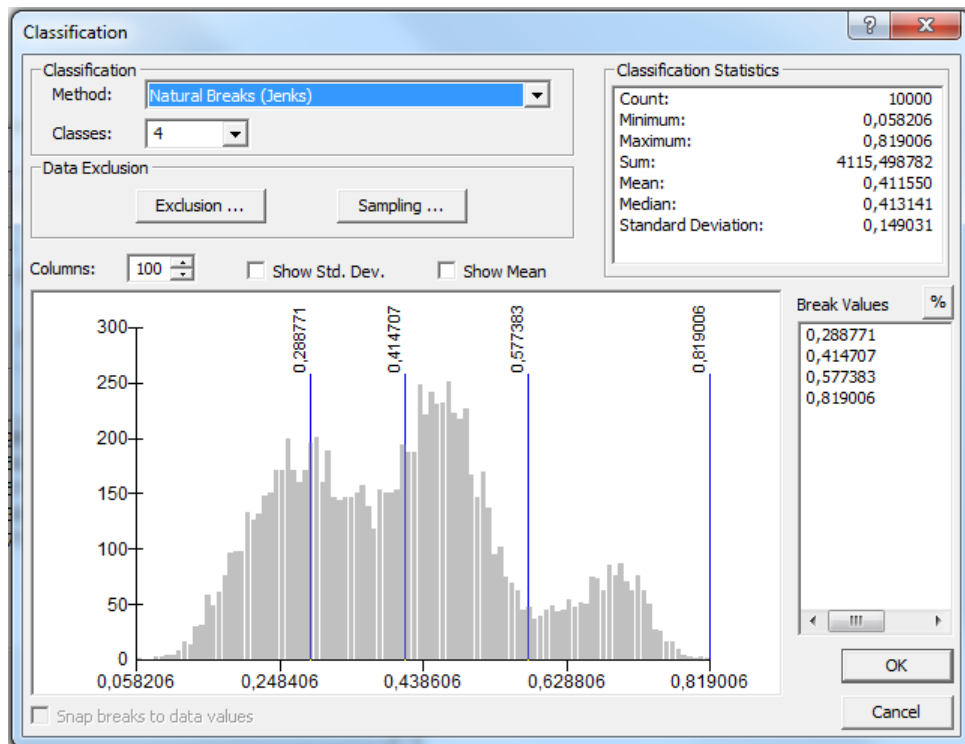


Figure 198: Frequency histogram of the values of susceptibility classified according to the Natural Breaks.

The Jenks scheme determines the best arrangement of values into classes by iteratively comparing sums of the squared difference between observed values within each class and class means. The best classification identifies breaks in the ordered distribution of values that minimizes within-class sum of squared differences.

Jenks' goal in developing this method was to create a map that was accurate, in terms of the representation of data's spatial attributes. By following this process, Jenks claims, the "blanket of error" can be uniformly distributed across the mapped surface. He developed this with the intention of using relatively few data classes, less than seven, because that was the limit when using monochromatic shading on a choroplethic map.

Unlike the optimal method, which uses a numerical measurement to separate data classes objectively, the natural breaks method classifies data subjectively.

9.3 TEST SITE: NEBRODI

The investigated area covers ca. 1500 km² in the province of Messina (northeast Sicily) and crosses the territory of Nebrodi. The area was affected during the period between October 2009 and February 2010 by several landslides over the entire area in question, which involved several settlements and infrastructure.

The backbone of the Nebrodis, that with the Madonie Mountains to the west and the Peloritans to the east constitute the Sicilian Apennine, in ENE - WSW direction for a length of about 70 km.

The Nebrodes Mountains are made up of a group of mountains high over 1500 meters sloping down to the Tyrrhenian coast to the north. The Monte Soro represents the main peak of the ridge, which reach an altitude of 1847 m.

In the western, part the flysch formations with a prevalent marl-clay component outcrop extensively (Flysch Di Reitano and Numidian Flysch).

In the central part is dominated by shales (Unit of Monte Soro, Unit of Superior Clays), while in the east we find sandstone formations in outcrop (Flysch of Capo d'Orlando). In the area between San Fratello (to the west), Longi (North) and Frazzanò (east) we find calcareous marl formations and dolomite formations.

Nebrodes Mountains, along with the Madonie Mountains to the west and with Peloritans to the east constitute the Siculo-Maghrebian Apennine, extending to the Tyrrhenian coast at north and to Etna Mount at south, from which it is separated by the valley of the Alcantara River.

The orography of Sicily shows clear contrasts between the northern portion, and the south central and southwestern portions. The first one is mostly mountainous, represented by Peloritani, Nebrodes Mountains, the Madonie, Trabia Mountains, the mountains of Palermo and of Trapani. Typical hilly reliefs modest, with the exception of the mountain range of the Sicani, characterize the second one.

The southeast area has a plateau morphology, and the eastern is dominated by Etna volcano (PAI, 2004).

The general orography of the study shows relatively mild reliefs, consisting of shales and sandstones, with rounded sides that open into wide valleys crossed by numerous rivers, which flow into the Tyrrhenian Sea. The landscape takes irregular profiles with most rugged shape and heavily fissured rocks where the limestone predominate.

In general, the morphology is affected by the asymmetry of the slopes and the rich vegetation cover. The surface drainage network is predominantly torrential with an average modest runoff and strongly influenced by seasonality: moderate or zero during the periods

of the year when rainfall is scarce or absent, they become significant during the rainy season. The characteristics of these streams are typical of the regions of Calabria and northeastern Sicily, allowing you to define with the peculiar term "Fiumare."

Specifically, in the area of northeastern Sicily, the rivers are predominately in NW-SE direction, with course almost perpendicular to the Apennines; this suggests a possible tectonic control on waterways, which would set on fractures or faults with an anti-Apennine trend. The catchment areas are articulated and rugged valleys in the upstream part, to become larger in the terminal (APAT, 2008).

9.3.1. GEOLOGICAL SETTING

The geological history of Sicily is very complex, both for its location in an area of the Mediterranean that is characterized by extreme tectonic mobility, both for the characteristics of sedimentary rocks deposited in different paleo geographic domains, both for the tectonic events that have occurred from the upper Paleozoic to Quaternary (PAI, 2004). The geo-tectonic structure of the island is heavily influenced by the result of the collision between the crustal sectors of the African and European plates, related to the closure of the large oceanic basin of the Tethys Ocean.

The collision has created, starting from the Tertiary, the Apennine-Maghreb orogeny; this corrugated chain constitutes the Apennines, continues beyond the Strait of Sicily to North Africa, through the Calabrian Arc and Sicily. Sicily is located exactly along the orogenic suture, in a still active geodynamic system, as you can verify from the analysis of seismic and volcanic activity present, as well as, indirectly, from the observation of a number of surface deformation phenomena, sometimes associated with crustal imperceptible movements.

Everything began with the sliding of the crustal sector of Tethys Ocean under the European continent to the African margin; the portion of the oceanic crust is progressively moved below to the European continent because of its lesser thickness and of higher density.

The original oceanic sedimentary cover have been subject to partial separations and overlaps and account for a large part of the corrugated areas of the orogen (Lentini et al., 1996).

The result is the current geological structure of Sicily, as amended by subsequent tectonic movements that occurred in the Tertiary, and consists of a chain-foreland system.

The corrugated areas of the chain are the most abundant portion of the territory; foreland areas (Pelagian Block) are present in the most southern parts of the region, not yet deformed

and advancement front of the chain. These are found in the outcrops of the Hyblaean Mountains (Lentini et al., 2000).

Within such an orogenic system is therefore possible to distinguish three main structural domains: the Foreland Dominion represented by the area of the Afro-Adriatic plates not reached by the compressive deformation. The Orogenic Domains, and the Tyrrhenian Basin, partly made up of oceanic crust, the opening of which has intervened in the final stages of the orogeny, to change the general tectonic appearance.

The Apennine-Maghrebian orogeny and the opening of the Tyrrhenian Basin are therefore the two main causes of the current geological structure of Sicily, which is therefore the result of the superposition of a tectonic cycle of compressive nature and one of extensional nature (Lentini et al., 1995).

The deeper domain, of Foreland, form the so-called “external thrust system”, which creeps below to the orogen and is constituted by crustal and oceanic sectors; it outcrops in the southeastern Sicily and is present in the Sicilian Channel.

In this context, however, it is necessary to focus attention on the orogenic domains, consisting of an allocton portion, the Kabilo-Calabride Chain, and from the Apennine Maghreb Chain. This complex chain has a convergence towards the East and Southeast and presents thicknesses locally close to 15 km; the geological-structural setting is shown schematically in figure 199.



Figure 199: Outline of the major structural domains of the Apennine-Maghrebian orogen; identifies a thrust system composed of the unit of foreland to the South, from the Maghrebids units and the from the Kabilo-Calabridi units to north (Lentini et al., 1995).

The Apennine-Maghrebian Chain has developed, mostly at the expense of the Tethys Ocean, from the Upper Oligocene to Middle-Upper Miocene.

Being predominantly of oceanic nature, the successions of the Maghreb Apennine chain consist of several tectonic scales belonging to Numidian flysch unit and Sicilide unit, according to the classification of Ogniben (1960).

A list of such units has described follow, according to the stratigraphic order of surfacing, from the top down (APAT, 2008).

APENNINE MAGHREBIAN UNITS

- Sicilide Complex:

- Unit of Troina: marl alternating with marly limestones; Varicoloured clays.
- Unit of Superiors Scagliose Clays (Cretaceous), consisting of clays marls, with decimetric levels of limestones and marly limestones.
- Unit of Nicosia: marly clays and clayey marls.
- Unit of Monte Soro (Cretaceous) in quarzoarenitic-clay facies.
- Unit of Mount Salici-Mount Castelli: clays with micro faunas.

The Kabilo Calabride Chain is the result of the deformation of the European margin of the Tethys Ocean; currently appears as an item on Apennine-Maghrebids units.

These units are made up of fragments of continental crust consisting of Hercynian crystalline rocks with Mesozoic-Tertiary sedimentary covers.

Originated from the upper Eocene suffered a first orogenic transport to the roof of the Maghrebids domains in accord with the opening of the Balearic-Provencal basin and the rotation of the Corsica-Sardinia block (De Jong et al., 1973; Dewey et al., 1989).

Again, here is a list of units making up the Kabilo-Calabride chain, according to the stratigraphic order of surfacing (APAT, 2008).

KABILO-CALABRIDE UNITS

- Calabride Complex:

- Unit of Aspromonte constituted by lithological associations of various kinds, in metamorphic facies of various degree.
- Unit of Mandanici: dolomite, crystalline limestone and pseudo-olitic, calcareous breccia
- Units of Ali: lithological associations of various kinds, in varying degrees of metamorphic facies.
- Unit of San Marco d'Alunzio (Lower Cretaceous): limestone and dolomitic limestone.
- Unit of Longi-Taormina, constituted by: Flysch of Frazzanò (Superior Eocen), a sandstone and clay alternation with conglomeratic levels interbedded in phyllitic clasts, sandstone and gneiss. Marl and marly limestone in facies of "throws" (Inferior Eocene): Biomicrites with arenitic layers. Whitish-gray marly limestones and calcareous marl (Inferior Cretaceous).
- Unit of Capo Sant'Andrea: red nodular limestone in "Red Ammonite" facies, massive gray limestones, sandstones and conglomerates in the red facies "Verrucano".

The Kabilo-Calabridi Units emerge in the entire ridge of the Peloritans Mountain and extend southwards to San Fratello-Gardens alignment, oriented NW-SE and is exposed along the tectonic contact of overlap of these units on the Apennine-Maghrebids. This alignment is known in the literature as “Line of Taormina” (Amodio Morelli et al., 1976). The Apennine Maghreb units form the backbone of the Nebrodi Mountains, extending southward to form the sedimentary substrate of the Mount Etna.

A system of normal faults displaces the chain, with particular emphasis in the south area of Sicily; it is the result of the opening of the Tyrrhenian Basin, which took place from Serravallian and resulting in the structures belonging to the so-called “South Tyrrhenian System” (Finetti et al., 1996). The welding of these domains is sanctioned by common horizons of Burdigalian age, after which the two allochthonous elements have acted as a unique building (Lentini et al., 1995).

The territory of Messina, Italy is one of the areas at greatest hydrogeological risk; according to the latest survey conducted by Legambiente and Civil Protection, the 84% of the provincial capital of Sicily is characterized by centers at risk (www.protezionecivile.it). The causes are to be found in the geological and geomorphological features of the area, in the strong anthropization and in the peculiar weather conditions, with rainfalls characterized by a strong seasonality.

The geology of the area, which sees the tectonic contact between the formations of the Superior Clays belonging to the Apennine-Maghrebids Units and the overlying the Kabilo-Calabridi Units, made up of rock terms, promotes the slipping phenomena.

The instability also affects the overburden, favored by the presence of the water table at a ground level or close to it, especially during periods of high rainfall.

The anthropic system interacts through the transformation of the territory, the works of regulation and water drainage plumbing, the wells and the profound sources.

The natural disasters that occurred in Sicily in recent years are the proof of the alarming developed by Legambiente and Civil Protection; there are 48 municipalities in the province of Messina and 43 in the province of Palermo where landslides have damaged the roads networks, while landslides and mud hit civilian homes and public buildings (www.blogsicilia.it).

In 2001, the National Geological Service (now APAT) has in fact initiated a project to bring together and standardize the data collected throughout the national territory, in relation to landslides.

The IFFI Project was carried out in Sicily during the years 2002-2003, by the Department of Geology and Geodesy, University of Palermo, on behalf of the Regional Administration-Department of Land and Environment.

During the IFFI project, all those landslides present in the archives, were controlled, through the interpretation of ATA flight Sicily 1997 (medium scale 1: 20.000) and mapped based on IGM scale of 1: 25.000 and computerized with software Arcview.

A total of 360 landslides have been inventoried, divided into nine provinces in Sicily, as shown in figure 200. The landslides were then classified according to size, their activity status and type in the project IFFI

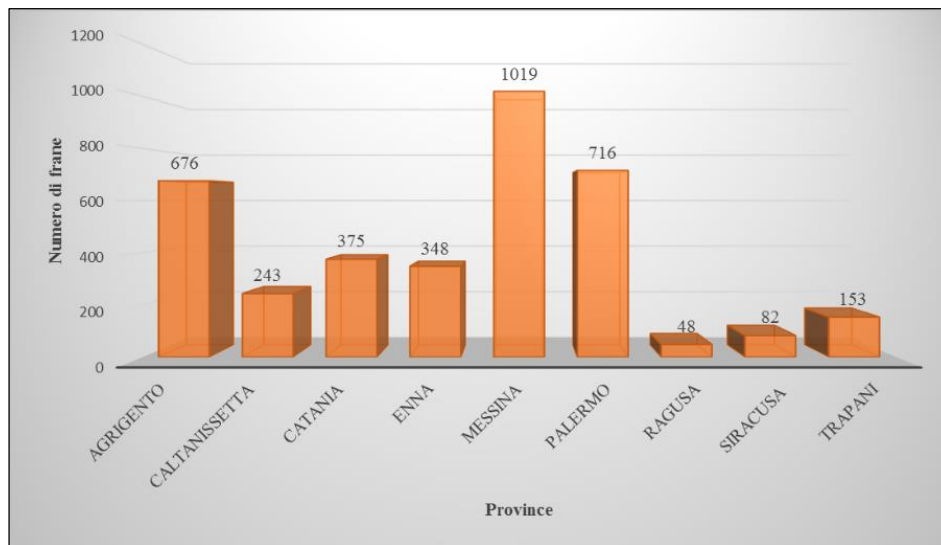


Figure 200: Landslide Inventory in Sicily; IFFI, 2004.

9.3.2. RESULTS AND DISCUSSION

The available C-band PS data within the test area are as follows; acquisitions both in ascending and descending geometry are available for all the three datasets. The ground deformation map of Messina province derived from PS data acquired in the spanning time 1992-2001 by the C-band satellite ERS 1/2, in ascending geometry, is shown in figure 201.

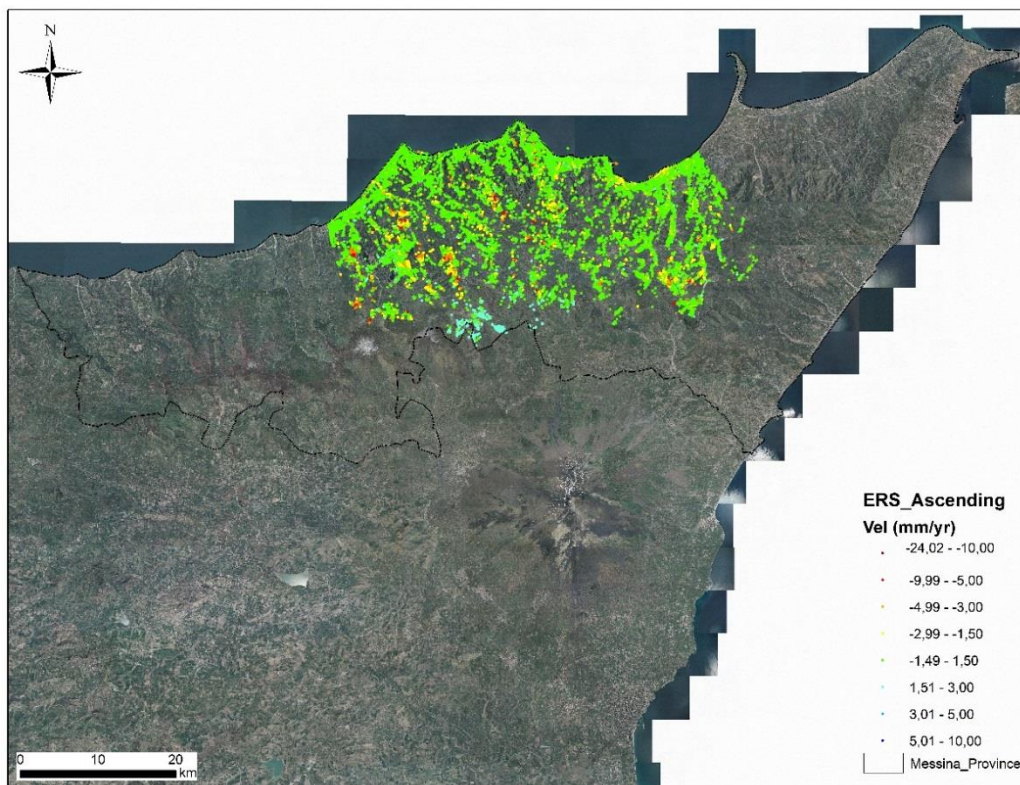


Figure 201: Ground deformation velocity map: PS ERS data in ascending pass.

The PS ERS ENVISAT ascending derived from three different data stacks as follows:

Dataset	Temporal Range	Number of scenes	Number of PS	Density PS/km ²
Floresta	23/08/92 - 13/12/00	54	26282	16.91 PS/km ²
S. Fratello	11/09/92 - 05/06/00	34	8068	6.55 PS/km ²
Naso	23/08/92 - 13/12/00	50	9055	46.19 PS/km ²

The PS total number identified in the area is 43.405, in ascending geometry (figure 201). These derive from three different data stacks of 54, 34 and 50 images processed with the SqueeSARTM technique. From the first data stack, 26282 points were obtained for an area of 1554 km². From the second data stack, 8068 points were obtained for an area of 1230 km². From the third data stack, 9055 points were obtained for a total area of 196 km². Based on the histogram velocity distribution and standard deviation of all the values, eight

velocity classes were created, with a threshold ± 1.5 mm/year for distinguishing moving from not moving. Stable PS that fall into this stable range are 32.463 (75% of the total number of points) in this area. Point motion statistics show that extreme outlier PS with very high deformation rates, i.e. < -10 mm/year and $> +10$ mm/year, are respectively 1212 and 1274.

The ground deformation map of Messina province derived from PS data acquired in the spanning time 1992-2001 by the C-band satellite ERS 1/2, in descending geometry, is shown in figure 202.

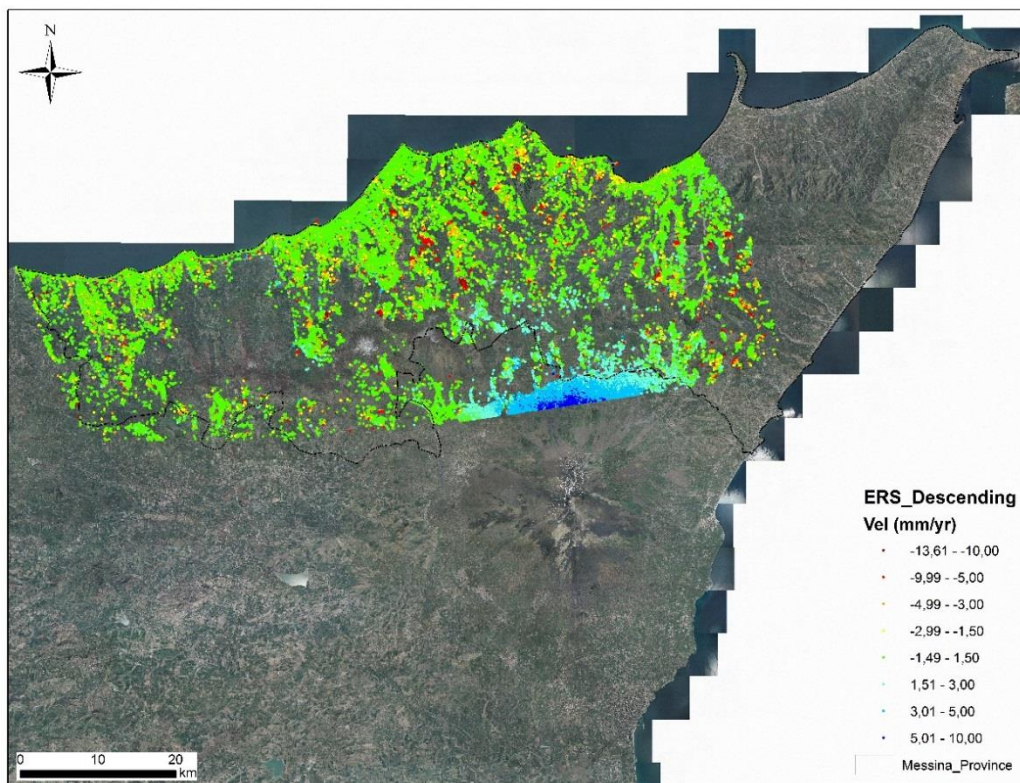


Figure 202: Ground deformation velocity map: PS ERS data in descending pass.

The PS PS ERS descending derived from two different data stacks as follows:

Dataset	Temporal Range	Number of scenes	Number of PS	Density PS/km ²
Caronia	01/05/92 - 08/01/01	70	23452	2.25 PS/km ²
Raccuja	01/05/92 - 08/01/01	70	81302	46.45 PS/km ²

The images in ascending orbit were acquired from May 1992 to January 2001. The PS total number identified in the area is 104.754 in descending geometry (figure 202). These derive from two different data stacks of 70 and 70 images processed with the SqueeSARTM technique. From the first data stack, 23452 points were obtained for an area of 1042 km².

From the second data stack, 81302 points were obtained for an area of 1750 km². Based on the histogram velocity distribution and standard deviation of all the values, eight velocity classes were created, with a threshold ± 1.5 mm/year for distinguishing moving from not moving. Stable PS that fall into this stable range are 69.227 (66% of the total number of points) in this area. Point motion statistics show that extreme outlier PS with very high deformation rates, i.e. < -10 mm/year and $> +10$ mm/year, are respectively 2674 and 1453.

The ground deformation map of Messina province derived from PS data acquired in the spanning time 2003-2010 by the C-band satellite ENVISAT, in ascending geometry is shown in figure 203.

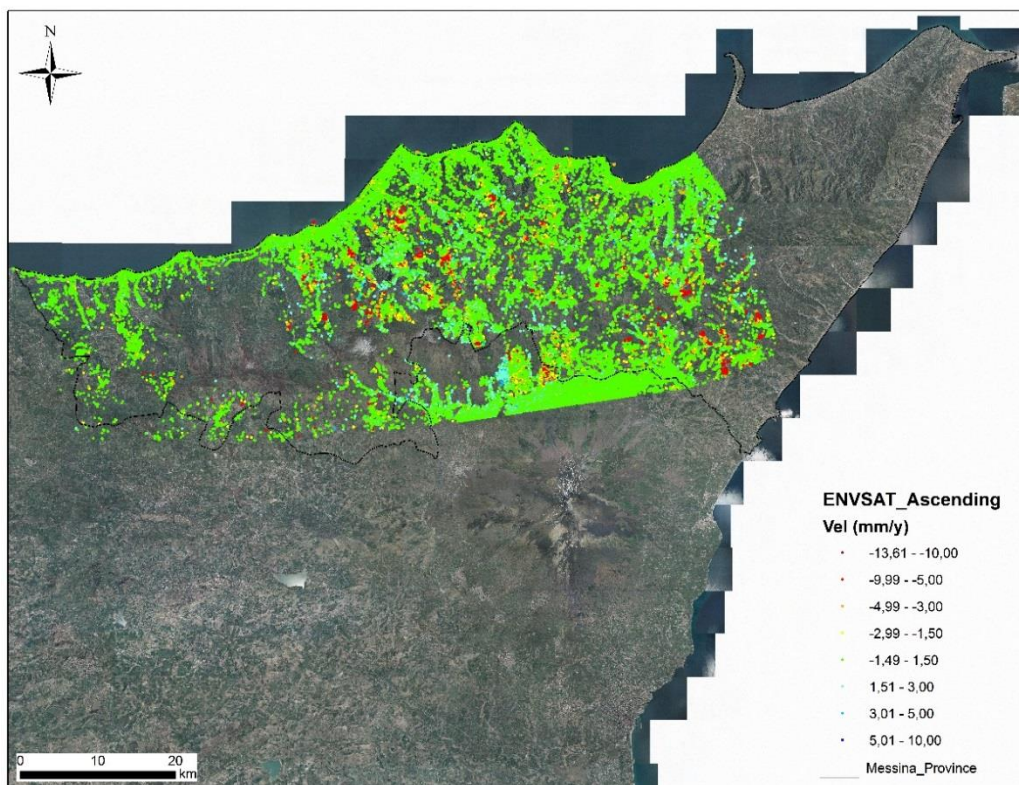


Figure 203: Ground deformation velocity map: PS ENVISAT data in ascending pass.

The PS ENVISAT ascending derived from two different data stacks as follows:

Dataset	Temporal Range	Number of scenes	Number of PS	Density PS/km ²
Floresta	22/01/03 - 22/09/10	65	128584	64.74
S. Fratello	30/06/03 - 11/10/10	42	9186	11.39

The PS total number identified in the area is 137.770 in ascending geometry (figure 203). These derive from two different data stacks of 65 and 42 images processed with the

SqueeSAR™ technique. From the first data stack, 128584 points were obtained for an area of 1986 km². From the second data stack, 9186 points were obtained for an area of 806 km². Based on the histogram velocity distribution and standard deviation of all the values, eight velocity classes were created, with a threshold ± 1.5 mm/year for distinguishing moving from not moving. Stable PS that fall into this stable range are 115.057 (84% of the total number of points) in this area. Point motion statistics show that extreme outlier PS with very high deformation rates, i.e. < -10 mm/year and $> +10$ mm/year, are respectively 3477 and 31.

The ground deformation map of Messina province derived from PS data acquired in the spanning time 2003-2010 by the C-band satellite ENVISAT, in descending geometry is shown in figure 204.

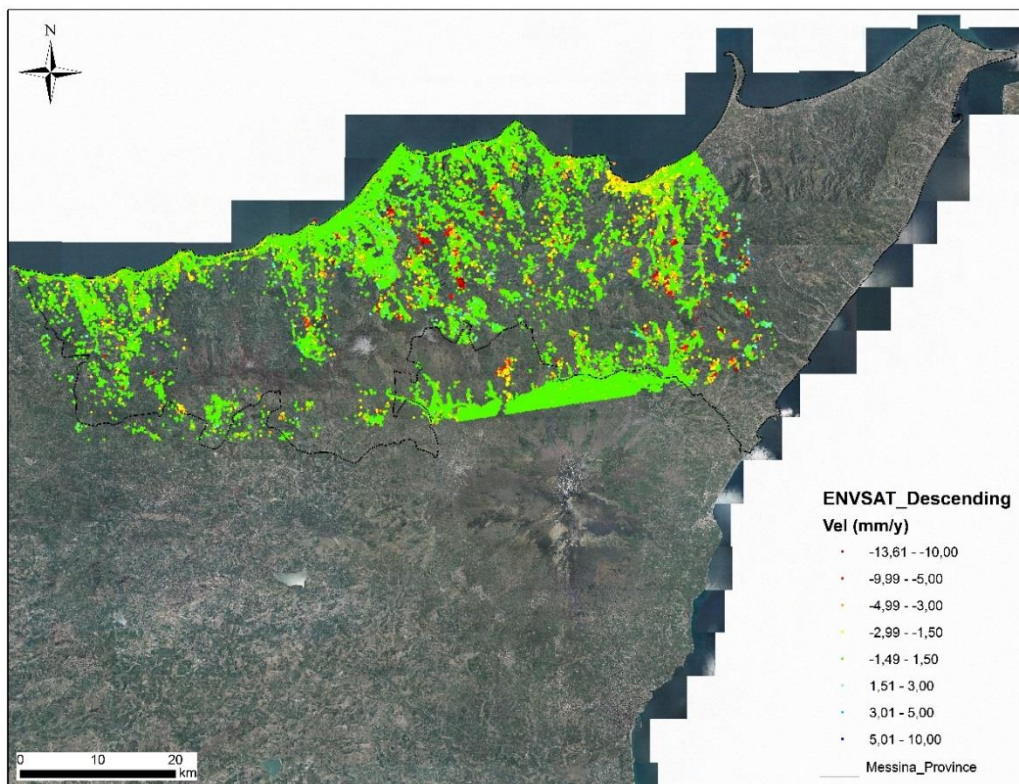


Figure 204: Ground deformation velocity map: PS ENVISAT data in descending pass.

The PS ENVISAT descending derived from two different data stacks as follows:

Dataset	Temporal Range	Number of scenes	Number of PS	Density PS/km ²
Caronia	07/07/03-13/09/10	49	21277	20.41
Raccuja	07/07/03-13/09/10	49	77898	44.51

The images in descending orbit were acquired from July 2003 to September 2010. The PS total number identified in the area is 99.175 in descending geometry (figure 204). These derive from two different data stacks of 49 and 49 images processed with the SqueeSARTM technique. From the first data stack, 21277 points were obtained for an area of 1042 km². From the second data stack, 77898 points were obtained for an area of 1750 km². Based on the histogram velocity distribution and standard deviation of all the values, eight velocity classes were created, with a threshold ± 1.5 mm/year for distinguishing moving from not moving. Stable PS that fall into this stable range are 81.441 (82% of the total number of points) in this area. Point motion statistics show that extreme outlier PS with very high deformation rates, i.e. < -10 mm/year and $> +10$ mm/year, are respectively 2418 and 7.

The ground deformation map of Messina province derived from PS data acquired in the spanning time 2005-2010 by the C-band satellite RADARSAT, in ascending geometry, is shown in figure 205.

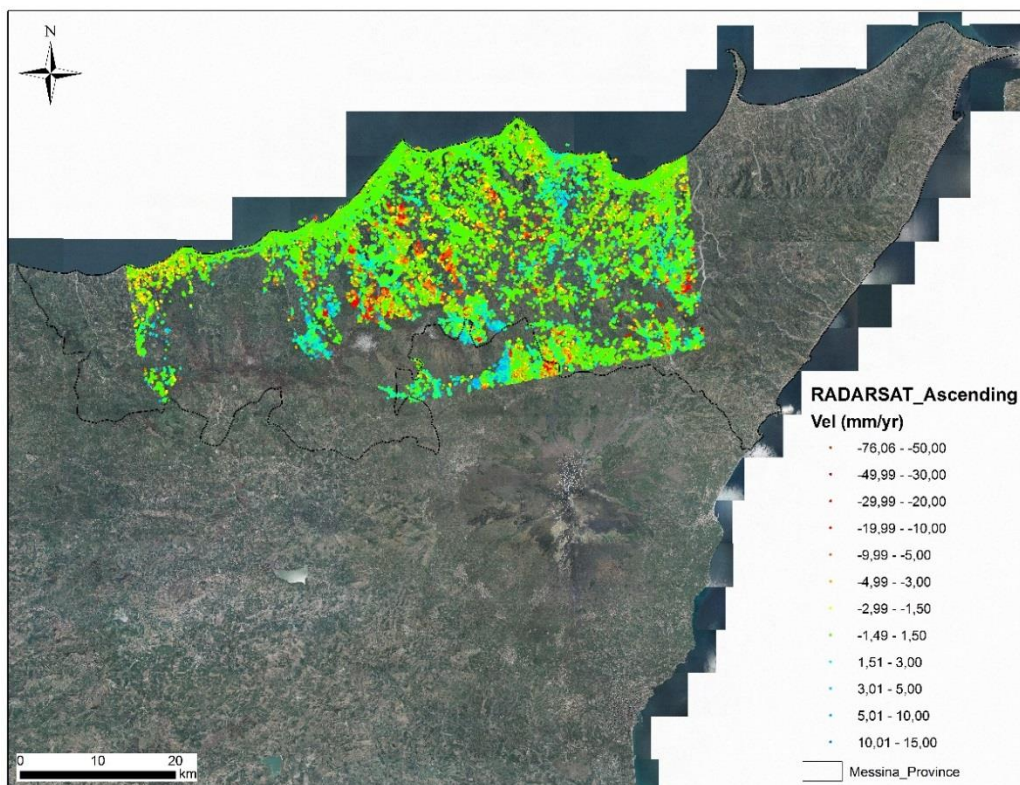


Figure 205: Ground deformation velocity map: PS RADARSAT data in ascending pass.

The PS RADARSTAT ascending derived from one data stack as follows:

Dataset	Temporal Range	Number of scenes	Number of PS	Density PS/km ²
Nebrodi	30/12/05 - 26/01/10	46	225465	112.73

The 46 images in ascending pass were acquired from December 2005 to January 2010. The number of points is 225 465 PS in an area of about 2000 km² (density 112 PS/km²). It was possible to take a rapid mapping of the sites with the highest criticism for the hydrogeological risk, identified by radar satellite data available.

For the PS classification and in order to distinguish between stable and motion areas, a threshold of ± 2 mm/year in the direction concordant or discordant with respect to that of the satellite was chosen. The choice of this value of velocity is closely related to the type of movement of the phenomena identified, which are mainly complex landslides and slips roto-translational as well as the precision of the technique PSI.

The ground deformation map of Messina province derived from PS data acquired in the spanning time 2005-2010 by the C-band satellite RADARSAT, in descending geometry, is shown in figure 206.

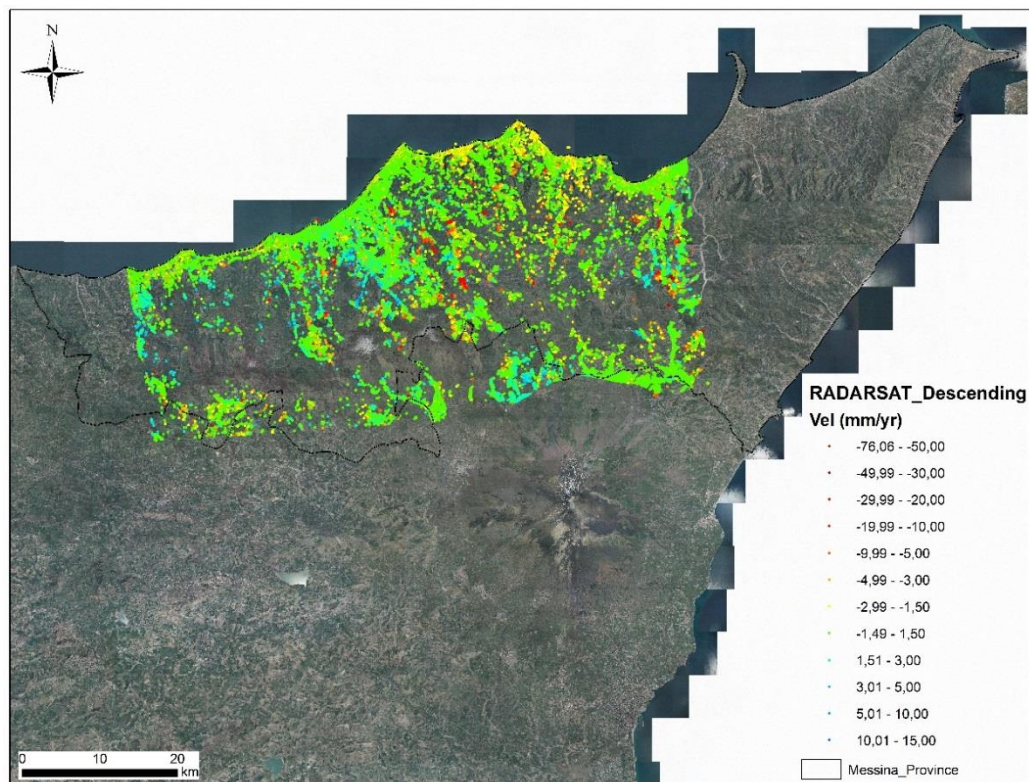


Figure 206: Ground deformation velocity map: PS RADARSAT data in descending pass.

The PS RADARSTAT descending derived from one data stack as follows:

Dataset	Temporal Range	Number of scenes	Number of PS	Density PS/km ²
Nebrodi	31/01/06 - 03/02/10	47	95045	86.40

The 47 images in ascending orbit were acquired from January 2006 to February 2010.

The number of points is 95045 PS in an area of 1100 km² (density 86 PS/km²). It was possible to take a rapid mapping of the sites with the highest criticism for the hydrogeological risk, identified by radar satellite data available.

For the PS classification and in order to distinguish between stable and motion areas, a threshold of ± 2 mm/year in the direction concordant or discordant with respect to that of the satellite was chosen. The choice of this value of velocity is closely related to the type of movement of the phenomena identified, which are mainly complex landslides and slip roto-translational as well as the precision of the technique PSI.

The available X-band PS data within the test area are as follows; acquisitions both in ascending and descending geometry are available for the datasets. PS data acquired in the spanning time May 2011-May 2012 by the X-band satellite COSMO-SkyMed in ascending and descending geometries are being analyzed for the area of interest within Messina province. These data consist of four datasets (Brolo, Randazzo, Maniace and Naso datasets), 2 in ascending and 2 in descending pass, processed by TRE by means of advanced SqueeSAR technique. The mean PS density is estimated about 250-350 PS/Km² in ascending orbit and about 400 PS/Km² in descending orbit; in some areas, a point targets density greater than 1000 PS/km² has been detected; for example on the SE Etna mountainside within the Maniace descending dataset. The ground deformation map of Messina province derived from PS data acquired in the spanning time May 2011-May 2012 by the X-band satellite COSMO-SkyMed, in ascending geometry, is shown in figure 207.

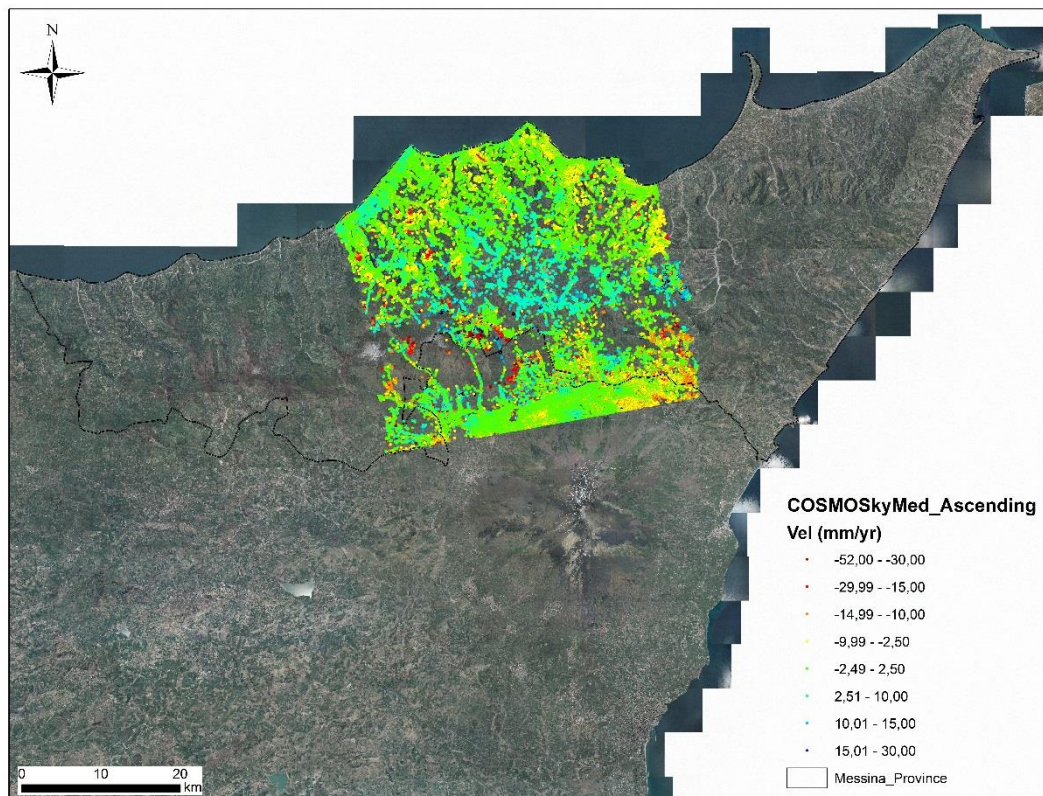


Figure 207: Ground deformation velocity map: PS COSMO-SkyMed data in ascending pass.

The PS COSMO-SkyMed ascending derived from two different data stacks as follows:

Dataset	Temporal Range	Number of scenes	Number of PS	Density PS/km ²
Brolo	01/05/11 - 03/05/12	26	197888	219.85
Randazzo	01/05/11 - 03/05/12	27	255443	356.76

The PS total number identified in the area is 453.331 for a total area of 1616 km², in ascending geometry (figure 207).

These derive from two different data stacks of 26 and 27 images processed with the SqueeSAR™ technique.

From the first data stack, 197.888 points were obtained for an area of 900 km².

From the second data stack, 255.443 points were obtained for a total area of 716 km².

The analysis of the velocity of the detected PS, show that, using a threshold of ± 3 mm/year for points that are thought to be motionless, the stable PS are 342.562 that means 75% of the total amount.

Point motion statistics (mm/year velocity classes) reveal that PS that greatly exceed the velocity stable range, showing deformation greater than ± 15 , are few (1869 PS with average velocity < -15 mm/year and 47 PS with average velocity $> +15$ mm/year).

By the way, PS targets show deformation rates up to -50 mm/year that are significantly higher than those of C-band satellites are.

This is due to the dense sample of X-band data and to the short monitoring period of only one year (2011-2012) which allows the detection of a high number of PS in areas affected by active superficial processes. Over longer acquisition time, these natural processes could be monitored in a lower amount or not identified at all.

Some moving PS clusters with yearly average velocity of about -10 up to -15 mm/year can be observed in the western northern-central portions of the investigated area (figure 207).

The negative sign stands for a decreasing distance with time from the satellite sensor and, given the ascending LOS geometry and the general N-NE facing direction of the slopes, this can imply the presence of some significant local downward movements.

The ground deformation map of Messina province derived from PS data acquired in the spanning time May 2011-May 2012 by the X-band satellite COSMO-SkyMed, in descending geometry, is shown in figure 208.

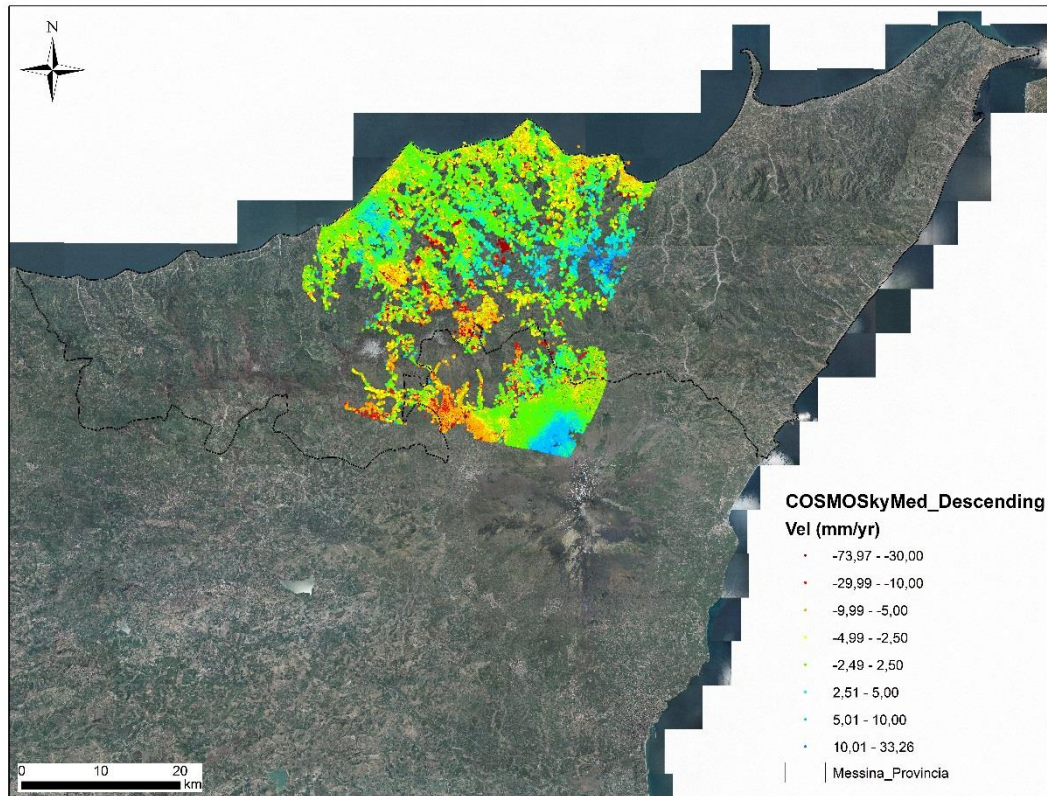


Figure 208: Ground deformation velocity map: PS COSMO-SkyMed data in descending pass.

The PS COSMO-SkyMed descending derived from two different datastacks as follows:

Dataset	Temporal Range	Number of scenes	Number of PS	Density PS/km ²
Naso	16/05/11-02/05/12	32	383793	400.62
Maniace	16/05/11-02/05/12	32	409932	1059.26

With regard to the data acquired in descending geometry, the processing has given rise to 793.725 PS within an area of 1345 km². These are derived from two different data stacks of 32 and 32 images processed with the SqueeSARTM technique.

From the first data stack 383.793 points were obtained for an area of 958 km²; from the second we have obtained 409.932 for a total area of 387km².

In descending geometry (figure 208), 793.725 PS were identified in the area of interest. Based on the histogram velocity distribution and standard deviation of all the values, eight velocity classes were created, with a threshold ± 3 mm/year for distinguishing moving from not moving.

Stable PS that fall into this stable range are 458.096 (58% of the total number of points) in this area. Point motion statistics show that extreme outlier PS with very high deformation rates, i.e. < -10 mm/year and $> +10$ mm/year, are respectively 14.142 and 3.844.

PS motion data show mean LOS velocities -5 mm/year up to about -30 mm/year, especially in the southern western part of the area of interest, while some zones are characterized by positive sign of the LOS movement, particularly toward the eastern and southern portions of the area.

The use of PS COSMO-SkyMed in comparison with the analyzes carried out by means of ERS, ENVISAT and RADARSAT data ensures a shorter time revisiting (baseline temporal up to 4 days) and a higher spatial density of the points PS (from 400 to 1000 PS/km²).

This significantly increases the possibility of identifying landslides.

Significant differences can be observed by comparing the number and the density of PS in C-band and X-band obtained for the study area.

The density of the PS obtained by COSMO-SkyMed data is significantly higher than that obtained from the data in band C.

Another difference relates to the rate of deformation recorded that is much higher as regards the data in X band.

This is due to the smaller amount of time monitored (12 months) and the shortest revisit time (ten days prior to the monthly satellites of the European Space Agency).

This allows the identification of pixels that show consistent movement of the soil; the same pixel, consistent for this time interval, not would be better if it was considered a longer period, because the consistency would be lost.

10. DISCUSSION AND CONCLUSION

This work have tasted and analysed the potential applicability and exploitation of Space–Borne interferometric SAR data for monitoring ground deformation and engineering infrastructures. The interferometric radar approach represent a powerful tool to detect movements on the Earth’s surface. Thus, mapping and monitoring slope instability can greatly benefit from remote sensing and satellite data analysis, due to the high precision and great cost – benefit ratio.

Space-borne InSAR (Synthetic Aperture Radar Interferometry) techniques can offer a useful support in detecting and characterizing slow-moving surface displacements: they provide rapid and easily updatable ground velocity measurements over large areas, along the satellite LOS, with great accuracy (up to 1 mm), high spatial resolution, cost-effectiveness, non-invasiveness, good temporal coverage (from 1992 up to present) and good sampling (monthly acquisitions).

In the last years, different InSAR techniques have been developed in many research studies to analyse different geological processes from regional to local scales, such as subsidence, landslides, tectonic and volcanic activity (Massonnet and Feigl, 1998; Singhroy et al., 1998; Hilley et al. 2004).

The potential of remote sensing techniques is particularly relevant for wide mountainous areas, where conventional in situ surveys are not always economically and practically suitable for carrying out a systematic investigation of deformation phenomena, due to difficult accessibility and huge extension of such environments.

Differential InSAR (DInSAR), a technique that exploits the phase difference of two SAR images gathered at different times on the same area from slightly different positions, has been widely used since late ‘80s (Zebker et al., 1986; Gabriel et al., 1989) to detect surface deformation over large areas (Costantini et al., 2000). By the way, atmospheric effects, temporal and geometrical decorrelation, limit conventional DInSAR.

Multi-temporal interferometric approaches, like PSI (Persistent Scatterer Interferometry), overcome these limitations, analysing long temporal series of SAR data, and providing annual velocities and deformation time series on grids of stable reflective point-wise targets, called Persistent Scatterers or PS (Ferretti et al., 2001).

Advanced multi-temporal interferometric techniques, for example the PSI, are being carried out in the last years for natural hazards and in particular for landslide processes, demonstrating their applicability to different environments and the flexibility to different

landslide-induced movements. PSI analysis has been mainly used for mapping and monitoring slow - moving landslides (“extremely slow” and “very slow” phenomena, Cruden and Varnes, 1996) and for evaluating their state of activity and intensity (Righini et al., 2012; Frangioni et al., 2013: par. 5.5).

In particular, in this PhD work, PSI-based investigations have been successfully performed to detect and monitor ground deformation and engineering infrastructures.

The PSI data have allowed to map and monitor ground displacements at both regional and local scales, dealing with different landslide typologies and dimensions.

However, InSAR techniques yield both advantages and constraints, as reported in several works (Singhroy, 2002; Rott, 2004; Crosetto et al., 2005; Metternicht et al., 2005). The potential and effectiveness of space-borne InSAR techniques mainly rely on wide area coverage, cost efficiency and a good cost/benefit ratio, data availability, accuracy, systematic acquisition and updating, density of measurements.

Satellite InSAR provide precise ground motion measures even on areas that are usually not economically and practically accessible. Moreover, radar data can identify localized zones characterized by high movement rates (and so by an high potential hydrological hazard) over regional areas, consequently reducing efforts and time-consuming in situ surveys, and permitting to a priori know the most critical areas to which attention must be focalized and further investigation carried out.

The very high resolution (0.1-1 mm/year for LOS average velocity and 1-3 mm on single measures at each times acquisition) of SAR data increases the geomorphological information on slopes, generating more reliable landslide inventory maps (Metternicht et al., 2005). The availability of large data stacks of SAR data covering almost more than 20 years with monthly sampling allows reconstructing the extent and the magnitude of ground motion over target areas back to the early 90s, providing an unprecedented and concurrent historical and updated overview of the investigated phenomena. In particular, both historical archives of SAR images (ERS1/2, ENVISAT and JERS data) and currently operational SAR missions (RADARSAT1/2, TerraSAR-X, COSMO-SkyMed) can be exploited to carry out the “back-monitoring” (Cigna et al., 2011) of past and recent ground displacements and to reconstruct the deformation history of the observed scene, with millimetre precision.

InSAR techniques show up some constraints and limitations, including satellite configuration in SAR image acquisition, the limitation in measuring “fast” deformation phenomena, the impact of the linear deformation model assumption made in many PSI approaches.

Velocity

The most significant drawback of PSI data refers to the technical acquisition parameters of the satellites. Overall, all the presently available SAR data, from both historical archives and currently operational missions, do not allow the measurement of deformations faster than few tens of cm per year.

The acquisition parameters and characteristics of the currently available SAR sensors do not enable the estimation of deformations faster than few tens of cm/year, which would compromise the results of the PSI processing.

Thus, due to the phase ambiguity of SAR data processing and satellite acquisition parameters in all, C- and X-band, the PSI analysis of mass movement is limited to phenomena ranging from “extremely slow” ($v < 16$ mm/year) to “very slow” (16 mm/year $< v < 1.6$ m/year), according to the velocity classification of Cruden & Varnes, 1996 (IUGS, 1995) (table 12).

LANDSLIDE CLASS DESCRIPTION	TYPICAL VELOCITY	SATELLITE SAR	
		C-BAND	X-BAND
Extremely slow	< 16 mm/year	Yes	Yes
Very slow	0.016 – 1.6 m/year	Yes	Yes
Slow	1.6 m/year - 13 m/month	No	No
Medium	13 m/month – 1.8 m/h	No	No
Rapid	1.8 m/h - 3 m/min	No	No
Very rapid	3 m/min - 5 m/s	No	No
Extremely rapid	> 5 m/s	No	No

Table 12: Application of the satellite SAR sensors spectral bands related to the landslide velocity scale as proposed by Cruden & Varnes (1996).

Aliasing effects, due to the ambiguous nature of the 2π -wrapping of interferometric phases, limit to a quarter of the wavelength the maximum displacement between two successive acquisitions and two close PS of the same dataset (Hanssen, 2005; Crosetto et al. 2010). Velocities compromising the PSI processing depend on the employed SAR wavelengths and satellite revisiting times; they are about 15 cm/year for ERS/ENVISAT data (C band), 20 cm/year for RADARSAT (C-band), 17 cm/year for COSMO-SkyMed (X-band), 25 cm/year for TerraSAR-X (X band), 45 cm/year for ALOS/JERS (L-band).

As we can see, L-band sensors can measure faster ground motions, up to 45 cm/year, that cannot be detected with C- or X-band satellites.

In presence of very high deformation rates of the phenomena, there is a loss of stable reflective radar benchmarks within any PSI technique capacities.

Consequently, rapid surface movements characterized by higher motion rates cannot be correctly detected and interpreted. Higher motion rates cannot be tracked and interpreted correctly.

Improvements of the PSInSAR can be achieved by exploiting Ground-Based InSAR (Casagli et al., 2010; Antonello et al. 2004; Tarchi et al., 2003) techniques, which can extend the velocity range of applicability of approach to include faster phenomena.

Future missions like Sentinel by ESA will allow monitoring faster movements: the higher discernible velocity will be up to 42.6 cm/year for Sentinel satellite, thanks to its shorter revisiting time (14 days).

Moreover, the launch of new satellite systems (Sentinel 1 and Radarsat Constellation Mission) will facilitate the research and analysis of land surface phenomena, ensuring the continuity of C-band SAR data and coupling wide coverage, high precision and short revisiting time.

Geometry of acquisition

An important limit of satellite InSAR is referred to the solely LOS measurement capability. Space-borne InSAR only measures displacement in slant range (the displacement in the direction of the radar illumination).

The component of velocity vector in the flight direction (N-S direction since the satellite has a near polar orbit and a side-looking acquisition) cannot be measured (Rott, 2004).

For instance, the LOS displacement projection along the local steepest slope can be performed to compare different PS data (from different sensors with different acquisition angles and from ascending and descending orbits) and consequently landslide velocities with different aspects. This is because when we measure the displacement from the satellite we can only detect the component of the motion that is parallel to the satellite LOS, but the real displacement can actually occurs in all three dimensions (Cascini et al., 2009).

The combination of ascending and descending SAR data is an attempt to homogenize all the PS acquired by different satellite systems or in different acquisition. This in order to retrieve the vertical and the approximately East-to-West horizontal components of deformation for each available multi-band datasets.

It is not always possible due to the requirement of both acquisition geometries on the same area, which is usually quite rare. As already mentioned, SAR satellites are blind to South-to-North horizontal deformation components due to their polar orbiting.

Type of Satellite

Different satellites and SAR data are available nowadays, each one bearing specific characteristics mainly depending on the employed wavelength and technical acquisition parameters.

The main features and opportunities can be summarized as follow:

- C-band satellites (ERS and ENVISAT missions) provide the availability of long temporal archives of rates and time series, covering wide areas at a low cost and providing data since the 1990s at medium resolution.
- X-band SAR systems can facilitate the research and application of terrain-related phenomena with high precision and short revisiting cycle compared with the medium resolution SAR systems in C-band. This high spatial resolution and the short repeat cycle (up to 4 days with COSMO-SkyMed) allow studying highly localized surface displacements. The use of a short wavelength such as X-band ($\lambda \approx 3.1$ cm) on one hand allows reaching a higher precision in the deformation rates, but on the other hand increases ambiguity phase problems, since the probability that deformations between two successive acquisitions could exceed the threshold of $\lambda/4$ (the limit of maximum detectable movement in InSAR analysis) is higher.
- L-band data reduce temporal decorrelation effects induced by the vegetation coverage, due to the major penetration capacity of the radar signal. Moreover, L-band SAR data have the intrinsic capability to detect faster ground movements without ambiguities: the use of a greater wavelength ($\lambda \approx 23$ cm for ALOS) allow reducing InSAR problems related to phase ambiguity. In fact, assuming a repeat pass interval (δt) coincident with the ALOS orbital repeat cycle (46 days), the maximum detectable displacement rate along the LOS (Line Of Sight) is $V_{max} = \lambda/4\delta t = 46.8$ cm/year, compared to the threshold value of 14.6 cm/year valid for the C-band ERS/ENVISAT missions, where the orbital repeat cycle is 35 days. This increases the probability that, between two successive acquisitions, if operating in L-band the displacements occurred in the investigated area do not exceed the threshold.

The different available radar datasets show different temporal coverage and this is an important facet to account for, when performing PSI analysis.

Each PS dataset has a different temporal coverage and when the detection and monitor landslides activities have the purpose to generate landslide inventory or landslide activity maps, these products are referred only to a single specific temporal interval.

This is coincident with the temporal coverage of the satellite acquisition and sometimes, when more than one dataset area available, they are not “continuous” in time and some gaps are present in the PS temporal distributions.

Therefore, we obtained results for each available dataset necessarily pointing out the different temporal period they are referred.

A further analysis could include a comparison of historical, recent and current radar rates and the application of activity matrices (Frangioni et al. 2013) in order to provide, when it is possible, the more accurate evaluation of the state of the activity (WP/WLI, 1993) of the detected phenomena.

Temporal occurrence and observation of the phenomena

X-band PSI analysis can update phenomena mapping and monitoring up to 2011 and 2012, as operating TerraSAR-X and COSMO-SkyMed satellite systems are working since 2007 and are still ongoing. Therefore, on one hand these X-band SAR data can analyse and investigate recent deformation.

On the other hand, C-band data characterized by historical archives can perform a back monitoring of past and present displacements and can reconstruct the deformation history of the investigated areas.

Number of processed SAR images

The number of processed SAR images and the spatial resolution in azimuth and range of the satellite acquisition, also contribute to influence the targets density on the areas of interest. This is critical especially when focusing on specific critical area or dealing with a single phenomenon at local scale, which needs to be investigated at high detail.

Radar targets density

Significant differences can be observed when comparing the number and the density of C- and X-band PS datasets detected on the same area of interest.

The PS density obtained from TerraSAR-X dataset is higher than the one of C-band satellites datasets. Moreover, TerraSAR-X or COSMO-SkyMed radar data show higher deformation velocities than those of ERS and ENVISAT.

In X-band results, the percentage of PSs with greater mean velocity is higher than that of ENVISAT or ERS data. That indicates the information gaps for low resolution and coherence in ENVISAT data.

Another aspect is that the dense samples of TerraSAR-X or COSMO-SkyMed data permits to obtain more details of the deformation, which is related to cell size effect.

Land use

Interferometry can be complicated by changes on vegetation canopy across time. Decorrelation caused by dense vegetation (forest) that prevents many stable coherent scatterers to be retrieved, is the main limiting factor for PSInSAR applications in natural environments. Thus, in urbanized zones and cities, PSI gets a reasonably good sampling, while in vegetated, rural and forested areas, benchmarks are very few and PSI tends to fail. This is particularly true when using higher frequencies (C-band), while lower frequencies (L-band sensors) are characterized by less opacity in the atmosphere, a less attenuation in the vegetation canopy, and higher penetration in the soil.

In order to overcome this low target density, the concept of DS (Distributed Scatterers) has been introduced, as exploited in SqueeSAR algorithm (Ferretti et al., 2011).

Vegetation coverage causes temporal decorrelation and makes difficult the identification of reflective stable radar targets. Deeper penetration of vegetation can be achieved using higher radar wavelengths, such as those of the L-band.

The 23 cm for ALOS PALSAR data, which turn out to be more appropriate for rural and agricultural terrain, relying on the higher signal penetration and on the lower sensitivity to temporal decorrelation of L-band with respect to X- and C-band radar data (table 13).

Land use	PSInSAR	
	Banda C	Banda X
Artificial - built-up	YES	YES
Rural - agricultural	YES	YES
Forests and semi-natural	PARTIALLY	PARTIALLY
Damp zones	NO	NO

Table 13: Application of the satellite SAR sensors spectral bands related to the land use classes, as defined by Level 1 of CORINE Land Cover 2000.

X-band data are best suitable to detect and monitor urban subsidence and deformation in built-up areas. Although temporal decorrelation must be expected to be more problematic at X-band compared to longer wavelengths (C- or L-band), the high-bandwidth data is more suitable to PSI analysis, since more coherent targets could be identified in high resolution data, even in case of long time intervals.

Thus, with X - band data it is expected that non-uniform deformation of fabricated infrastructure such as bridges and single buildings of urban areas can be detected in detail by PSI analysis.

Scale map of the analysis

Radar remote sensing techniques can be exploited to observe subsidence and landslide-induced ground deformations, ranging from regional to local scale. i.e. 1:250,000-1:25,000 and 1:25,000-1:5,000, respectively (Fell et al., 2008).

From a spatial point of view, X-band data are more suitable for analysis at local scale, covering restricted phenomena and affecting small areas. In fact, the higher spatial resolution and shorter repeat interval of X-band radar data allow studies of highly localized surface displacements with a dynamic temporal evolution that have previously suffered from temporal or spatial decorrelation.

The comparison of X- and C-data demonstrates the capability of X-band data for localized infrastructure and local motions monitoring, thanks to their advantages of dense PS sampling and high temporal frequency.

On the other hand, C-band data are more suitable for regional investigation due to their wide coverage and medium resolution; thus, at regional scale, the use of C-band SAR images is envisaged because these data cover wide area at low cost.

Typology of the phenomena

Only slow-moving phenomena (<100 mm/year) can be detected and monitored. Therefore, some types of landslides, for example, rock falls and topples, are intrinsically fast movement, and PSI analysis is not useful. PS data in some cases can be maybe considered at least as precursors of local rupture (Notti et al. 2010; Herrera et al., 2010).

Displacement time series

The displacement time series of X-band data are better than the C-band ones, due to the shorter revisiting time. Thanks to the higher temporal sampling of TerraSAR-X and COSMO-SkyMed, it is possible to analyse the evolution of the non-linear terms of the displacement such as acceleration or deceleration of the moving mass.

This facilitates the detection of the non-linear trends that are somehow characteristic of landslide or subsidence kinematics.

From a geological point of view, non-linear behaviours can take place because of the nature itself of the deformation phenomenon; some examples are follow explain.

The subsidence processes due to sediment compaction that generally show quadratic trends. A slow change in the predisposing or triggering factors (intense or prolonged rainfall), that can cause acceleration for landslide processes or water level changes. The occurrence of a rapid deformation event, reactivation, sudden sinkhole, seismic event. Loading due to new constructions, urban excavations.

Back analysis

Another limit that encompasses all the multi-frequency PSI data is the possibility to improve detection and monitoring of hydrogeological events not in real-time.

Only the mainly in the deferred time, and, partially, in the near-real time, e.g. allowing analysing the evolution patterns of deformations across time and the temporal reconstruction of ground motions back in time, up to 1992 in case of availability of ERS 1/2 satellite imagery (“back-monitoring”).

Suitability of PSI in different environments

The areas investigated offer a wide range of geological–geomorphological settings, typology of landslides and different land use.

The PS analysis for the updating of landslides inventories work well only in some conditions. An a priori knowledge of this information allows to decide if PS analysis will be useful or not over a specific area.

The more suitable areas for PS are characterised by the presence of slow landslides, many scatterers and a good orientation of the slope towards the LOS.

The Setta Basin have these characteristics: many scatterers and the presence of slow landslides, complex landslides or creeping process.

The Barcelona Province is also suitable for the PS analysis: the presence of shale formations cause a favourable condition for slow processes and the presence of many debris fields without vegetation over these landslides represent a source of potential scatterer.

On the other hands there are some vegetated area and hills where the presence of potential scatterers is not so good; also, areas in which the main processes are shallow and rapid landslides that affect colluviums are not detectable by SAR.

The reported studies show different results in landslides detections, and in the updating of landslides inventories. These differences are related with many factors following described. The extensions of the area under study.

Over small area (small river basin) the percentage of landslides detected by PS is homogeneous and, if the conditions are favourable, may be rather high.

Over wide areas due to different conditions related to geology, geomorphology, land use, the percentage of landslide detected change in each sectors.

The sensors used and the methodology of SAR image processing used.

The sensor with a higher temporal and spatial resolution and new methodology of SAR images processing increase the number of landslides detectable.

The availability of two geometries of acquisitions.

Having both, ascending and descending data increase the number of landslides detectable.

The presence of scatterers. This factor is related to land use.

The type of landslides that affected the studied area.

For the updating of a landslide inventory it is clear that an area covered by slow flow processes it is more suitable than an area affected by rock-fall.

The quality of pre-existing landslides inventory.

If an inventory is well done the majority of landslides detected by PS should be already mapped, on the area with partial or incomplete inventory SAR data may identify many “new” landslides.

The methodologies and criteria used to interpret the PS data and to update landslides inventories. This factor is affected by the subjectivity used by each group of research.

For instance, the decision of update the state of activity or choose if an “anomalous areas” is to classify as landslide is not related to a fixed criteria or to threshold.

Moreover, we have to remind the importance of the availability of other geo information or analysis to support the PS data in order to make a good improvement of the inventory.

For instance, a field survey or an analysis of aerial photos is usually fundamental to confirm the state of activity or the boundaries of landslides detected by PS.

In spite of these differences, the most notable results is that different groups of research, using different criteria and different approach demonstrate that PS data it is a valid tool to update landslides inventories.

Velocity of the stability threshold

A key point of PSI analysis for landslide studies is the choice of the velocity stability thresholds, necessary to firstly distinguish moving from not moving PS and, consequently, moving areas from stable ones.

The choice of velocity thresholds has always to be performed taking into account both the characteristics of investigated processes (geometry, expected velocity, typology) and the technical characteristics of available PSI measures (LOS direction, measurement precision, relativity of PSI measures with respect to the reference point).

There are no fixed rules to define stable velocity values and the choice is usually based on visual or statistical parameters of the PS population. In literature, the “standard” stability threshold of ± 2 mm/year is usually used in C-band, since the chosen velocity threshold must be the minimum value exceeding the precision of the technique, which is about few millimetres per year (Colesanti and Wasowski, 2006; Righini et al., 2012).

By the way, this threshold is suitable usually when the PS velocity distribution is Gaussian (normal) with coincident mean and median values and when PS data show almost no dispersion.

Other works used, for projected LOS velocities along the slope, a threshold of ± 5 mm/year, obtained by a calibration procedure (Cigna et al., 2013) or a stable threshold that has to contain a certain percentage of PS data.

For example the 68% that corresponds to the percentile of standard deviation in a data population (Herrera et al., 2013), found at the same distance from 0 for all the available PS data, since the PS velocity values projected along the steepest slope show a negatively skewed distribution (Bianchini et al., 2013).

Another threshold could also be 10 mm/year because of dealing with potential damages occurrence at given ground displacement rates, as proposed by Mansour et al., 2012 from a literature review.

This threshold establishes that landslides to buildings and infrastructures produce moderate damages when the displacement velocity is between -10 and -100 mm/year, whereas major damages occur in the 100 to 1600 mm/year velocity range.

It is worth to highlight that the velocity threshold values are typically site-specific since they are strictly dependent on the case studies at hand, and are empirically determined, bearing in mind that the chosen velocity threshold must be always higher than the errors and noises within the measurements.

SAR data and interferometric techniques demonstrated to have a fundamental role to play for studying geohazard-related events at different risk prediction, prevention and emergency stages, such as detection, mapping, and monitoring and hazard zonation. Nowadays, InSAR-based applications are widely accepted and consolidated in Europe thanks to the efforts spent by the scientific community and end-users (geological surveys, local authorities and Civil Protection Authorities) in the last decade.

This PhD research programme exploited advanced satellite interferometric techniques for monitoring ground deformation and engineering infrastructures, also for spatial and temporal ground displacement detection and mapping, and for quantitatively and qualitatively analysis of landslide movements at basin and local scale.

The research was mainly based on the combined use of PSI (Persistent Scatterer Interferometry) data with geo-thematic and in situ information.

Some PSI-based procedures were elaborated to successfully update landslide inventory and to evaluate the state of activity of landslide phenomena. In particular, PSI data were used for the identification of localized areas affected by high ground motion rates within wide regions and for the improvement of pre-existing landslide inventory maps, throughout the assessment of qualitative (state of activity) and quantitative (velocity movement)

information of each identified phenomenon. In some cases, radar-interpretation of PSI data also allow mapping additional new phenomena not previously identified by means of conventional investigations.

Time series of displacement, available for each PS, are ideally appropriate for defining the temporal behaviour of landslides, in order to monitor ground motion trends and to observe kinematic dynamics of the investigated phenomena. In-depth analysis of PS time series in selected sites demonstrated to be a significant tool for supporting the study of temporal evolution patterns of ground movements.

SAR data from different wavelength bands and from different satellite systems were used, i.e. historical C-band SAR archives from ESA Missions, as well as new generation SAR satellites acquiring in X-band (TerraSAR-X and COSMO-SkyMed), to properly monitor ground deformations at local and basin scale.

Radar data exploitation in landslide-prone and -affected areas also deal with damage assessment.

In particular, the combined use of radar data with traditional geomorphological tools like field surveys and in situ campaigns gave useful efforts to the mapping of the impacts of landslide phenomena on buildings and manufactures of the affected sites, and to the monitoring of displacements in urbanized areas.

All the case studies of the work, dealing with test sites affected by slope instability in Italy and in Spain, were studied and critically analysed, attesting the reliability and effectiveness of SAR data exploitation to support geo-hazard investigations.

Thus, in conclusion, SAR data processed through interferometric approaches, especially PSI data, demonstrated their usefulness and suitability for landslide investigations within different activities such as mapping, monitoring and damage assessment, for different end-users in charge of risk management (local authorities, Civil Protection Department), in various environments and both at local and large scale.

REFERENCES

AKGUN A. (2012) - “A comparison of landslide susceptibility maps produced by logistic regression, multi- criteria decision and likelihood ratio methods: case study at Izmir”- *Turkey, Landslides*, 9, 93–10106,.

ALEOTTI P., CHOWDHURY R. (1999) - “Landslide hazard assessment: summary review and new perspectives” – “*Bulletin. Engineering. Geological. Environment.* 58, pp. 21-44.

ALEXANDER D. (1989) – “Urban landslides. An international review of geographical work in the natural and environmental sciences” - *Progress in Physical Geography*. Volume 13 (2), 157-191.

ALMERA, J., (1891). – “Mapa geológico-topográfico de la provincia de Barcelona. Región I o de contornos de la capital. Escala 1:40.000. 1ª, Barcelona.”.

AMBLÀS, D., CANALS, M., URGELES, R., LASTRASA, G., LIQUETE, C., HUGHES-CLARKE, J.E., CASAMOR, J.L., CALAFAT, A.M., (2006). – “Morphogenetic mesoscale analysis of the northeastern Iberian margin.” - *NW Mediterranean Basin Marine Geology* 234 (1–4), 3–20.

AMODIO-MORELLI L., BONARDI G., COLONNA V., DIETRICH D., GIUNTA G., IPPOLITO F., LIGUORI V., LORENZONI F., PAGLIONICO A., PERRONE V., PICCARRETA G., RUSSO M., SCANDONE P., ZANETTIN-LORENZONI E., ZUPPETTA A. (1976). – “L'Arco Calabro-Peloritano nell'orogene appenninico-maghrebide.” - *Memorie della Societa Geologica Italiana*, 17: 1-60.

ANTONELLO G., CASAGLI N., FARINA P., LEVA D., NICO G., SIEBER A. J., TARCHI D. (2004) – “Ground-based SAR interferometry for monitoring mass movements.” - *Landslides*, 1, 21-28.

APAT (2007) – “Rapporto sulle frane in Italia – Il Progetto IFFI - Metodologia risultati e rapporti regionali” - Agenzia per la Protezione dell’Ambiente e per servizi tecnici. Rapporto 78/2007

APAT (2008) – “Note illustrative della Carta Geologica d’Italia alla scala 1:50.000 (Messina-Reggio Calabria).” S.EL.CA., Firenze.

ARNAUD A., ADAM N., HANSSSEN R., INGLADA J., DURO J., CLOSA J., EINEDER M. (2003) – “ASAR ERS interferometric phase continuity.” *Proceedings of IGARSS 2003*, Toulouse, France.

BALLY A.W. & SNELSON S. (1980) – “Realms of subsidence”, *Can. Soc. Petrol. Geol. Mem.*, 6, 1-94.

BALLY A.W., CATALANO R. & OLDOW J. (1985) – “Elementi di tettonica regionale”, Pitagora, Bologna, 276 p.

- BACHMAIR, S., WEILER, M. (2012)** – “Hillslope characteristics as controls of subsurface flow variability” - *Hydrol. Earth Syst. Sci.*, 16, 3699–3715.
- BAMLER R., P. HARTL (1998)** – “Synthetic aperture radar interferometry.” - *Inverse Problems*, 14 (4), R1-54.
- BAEZA C. AND COROMINAS J. (1996)** – “Assessment of shallow landslide susceptibility by means of statistical techniques” - in: *Proceedings of the Seventh International Symposium on Landslides*, edited by: Balkema, A. A., Trondheim, Norway, 17–21 June, Vol. 1, 147–152.
- BARTRINA, M.T., CABRERA, L., JURADO., M.J., GUIMERÀ, J., ROCA, E., (1992).** – “Evolution of the central Catalan margin of the Valencia trough (western Mediterranean).” - *Tectonophysics* 203, 219–247.
- BASILICO M. (2000)** – “Algoritmi per l’allineamento di immagini SAR interferometriche” - Tesi di Laurea in Ingegneria Elettronica. Politecnico di Milano.
- BEGNI G. ESCADAFAL R. FONTANNAZ D. AND HONG-NGA NGUYEN A.-T. (2005)** – “Remote sensing: a tool to monitor and assess desertification.” - *Les dossiers thématiques du CSFD*. Issue 2. 44 pp.
- BERARDINO P., COSTANTINI M., FRANCESCHETTI G., IODICE A., PIETRANERA L., RIZZO V. (2003)** - “Use of differential SAR interferometry in monitoring and modelling large slope instability at Maratea (Basilicata, Italy).” *Engineering Geology*, 68 (1–2), 31–51.
- BEVEN K. J., KIRKBY M. J. (1979)** – “A physically based, variable contributing area model of basin hydrology” - *Hydrol. Sci. Bull.*, 24, 43–69.
- BIESCAS E., CROSETTO M., AGUDO M., MONSERRAT O., CRIPPA B. (2007)** – “Two radar interferometric approaches to monitor slow and fast land deformations.” - *Journal of Surveying Engineering*, 133, 66-71.
- BOVENGA F., NUTRICATO R., REFICE A., WASOWSKI J. (2006)** – “Application of multi-temporal differential interferometry to slope instability detection in urban/peri-urban areas.” - *Engineering Geology*, 88, 218-239.
- BRABB E.E. (1984)** – “Innovative approaches to landslides hazard mapping”. – “Proc. IV Int. Symp. On Landslides, Toronto”, 1, 307-324
- BRABB, E., (1991)** – “The world landslide problem”. *Episodes*, 14(i): 52-61.
- BRARDINONI, F., SLAYMAKER, O., HASSAN, M. A. (2003)** – “Landslide inventory in a rugged forested watershed: a comparison between air-photo and field survey data.” - *Geomorphology*. 54, p. 179–195.
- BREIMAN L. (2001)** – “Random forests” - *Mach. Learn.*, 45, 5–32. Brunetti
- CANALS, M., CASAMOR, J.L., LASTRAS, G., MONACO, A., COSTA, J., BERNÉ, S., LOUBRIEU, B., WEAVER, P., GREHAN, A., DENNIELOU, B., (2004).** – “The role of canyons in strata formation.” - *Oceanography* 17 (4), 80–91.

- P. CANUTI E P. FOCARDI (1986)** – “Slope stability and landslides investigation in Tuscany.” - *Memorie della Societa Geologica Italiana*, 31, 1986, pp. 307-315.
- CANUTI P., CASAGLI N., FARINA P., FERRETTI A., MARKS F., MENDUNI G. (2005)** – “Land subsidence in the Arno river basin studied through SAR interferometry.” - *Proc. of SISOLS 2005, Seventh International Symposium on Land Subsidence*. - Shanghai, China, 23-28 October 2005, 1, pp 407-416.
- CARRARA A., and MERENDA L. (1976)** – “Landslide inventory in northern Calabria, southern Italy. – *Geological Society of America Bulletin* 87: 1153-1162
- CARRARA A. (1983)** – “Multivariate methods for landslide hazard evaluation” - *Math. Geol.*, 15, 403–426. 99
- CARRARA A., GUZZETTI F. (1995)** – “Geographical Information Systems in Assessing Natural Hazards” - *KLUWER Academic Publisher*, Dordrecht, The Netherlands.
- CARNEC C., MASSONNET D., KING C. (1996)** – “Two examples of the application of SAR interferometry to sites of small extent.” - *Geophysical Research Letters* 23, 3579-3582.
- CASAGLI N., FARINA P., FERRETTI A. (2004)** – “Radar-interpretation of InSAR measurements for landslide investigations in civil protection practices” – 272-283.
- CASAGLI N., COLOMBO D., FERRETTI A., GUERRI L., RIGHINI G. (2008)** – “Case Study on Local Landslide Risk Management During Crisis by Means of Remote Sensing Data.” - *Proceedings of the First World Landslide Forum*, Tokyo, Japan, 125-128
- CASAGLI N., CIGNA F., DEL CONTE S., LIGUORI V. (2009)** – “Nuove tecnologie radar per il monitoraggio delle deformazioni superficiali del terreno: casi di studio in Sicilia.” - *Geologi di Sicilia, Anno XVII*, 3, 17-27.
- CASAGLI N., CATANI F., DEL VENTISETTE C., LUZI G. (2010)** – “Monitoring, prediction and early-warning using ground-based radar interferometry. - *Landslides*, 7(3), 291-301.
- CASCINI L., FORNARO G., PEDUTO D. (2009)** – “Analysis at medium scale of low-resolution DInSAR data in slow-moving landslide affected areas.” - *Journal of Photogrammetry and Remote Sensing*, 64(6): 598–611
- CATALANO R., D'ARGENIO B. (1982)** – “Schema geologico della Sicilia.” - In Catalano R. & D'Argenio B.: In Guida alla geologia della Sicilia occidentale. *Soc.Geol.It., Guide Geologiche Regionali*, 9 - 41,.
- CATANI F., FARINA P., MORETTI S., NICO G., STROZZI T. (2005)** – “On the application of SAR interferometry to geomorphological studies: estimation of landform attributes and mass movements.” - *Geomorphology*, (66), 119–131.
- CATANI F., LAGOMARSINO D., SEGONI S., TOFANI V., (2013)** – “Exploring model sensitivity issues across different scales in landslide susceptibility” - *Nat. Hazards Earth Syst. Sci. Discuss.*, 1, 583–623.

- CHECA, A., DÍAZ, J.I., FARRÁN, M., MALDONADO, A., (1988).** – “Sistemas deltaicos holocenos de los ríos Llobregat, Besós y Foix: modelos evolutivos transgresivos.” - *Acta Geologica Hispánica* 23, 241–255.
- CHIOCCI, F.L., ERCILLA, G., TORRES, J., (1997).** – “Stratal architecture of Western Mediterranean Margins as the result of the stacking of Quaternary lowstand deposits below ‘glacioeustatic fluctuation base-level.’” - *Sedimentary Geology* 112 (3–4), 195–217.
- CITA M.B., WRIGHT R.C., RYAN W.B.F. & LONGINELLI A. (1978)** – “Messinian paleoenvironments”. Init. Rep. DSDP, 42A, 1003-1035.
- CLAUZON G., SUC J.P., GAUTIER F., BERGER A. & LOUTRE M.F. (1996)** – “Alternate interpretation of the Messinian salinity crisis: controversy resolved” - *Geology*, 24, 363-366.
- COLESANTI C., FERRETTI A., PRATI C., ROCCA F. (2003A)** – “Monitoring landslides and tectonic motion with the Permanent Scatterers technique.” - *Engineering Geology* 68(1–2), 3–14.
- COLESANTI C., WASOWSKI J. (2006)** – “Investigating landslides with space-borne Synthetic Aperture Radar (SAR) interferometry.” - *Engineering Geology*, 88, 173–199.
- COSTANTINI M., IODICE A., MAGNAPANE L., PIETRANERA L. (2000)** – “Monitoring terrain movements by means of sparse SAR differential interferometric measurements.” In: *Proceedings of IGARSS 2000, 20th IEEE international Geoscience and Remote sensing symposium*, Honolulu, Hawaii, USA, July 24–28, p 3225–3227.
- COSTANZO D., ROTIGLIANO E., IRIGARAY C., JIMENEZ-PERALVAREZ J. D., CHACON J. (2012)** - “Factors selection in landslide susceptibility modelling on large scale following the gis matrix method: application to the river Beiro basin (Spain)” - *Nat. Hazards Earth Syst. Sci.*, 12, 327–340.
- CROSETTO M., MONSERRAT O., IGLESIAS R., CRIPPA B. (2010)** – “Persistent scatterer interferometry: potential, limits and initial C and X-band comparison.” - *Photogrammetric Engineering and Remote Sensing*, 76, 9, pp. 1061–1069.
- CROSETTO M., MONSERRAT O., CUEVAS M., CRIPPA B. (2011)** – “Spaceborne Differential SAR Interferometry: Data Analysis Tools for Deformation Measurement.” - *Remote Sensing*, 3, pp. 305-318; doi: 10.3390/rs3020305
- CROZIER MJ (1984)** – “*Field assessment of slope instability*”. Brunsten D and Prior DB (Eds.) *Slope Instability*. London, John Wiley & Sons Ltd: 103-42.
- CRUDEN D.M., VARNES D.J. (1996)** – “Landslide types and processes.” In: Turner AK, Schuster RL (eds) *Landslides: investigation and Mitigation*, Sp. Rep. 247, Transportation Research Board, National research Council. National Academy Press, Washington DC, 36–75.n
- CUMMING I.G., WONG F.H. (2005)** – “2Digital processing of synthetic aperture radar data: Algorithms and implementation.” - Artech House, 660 p.

- DAHL M. P. J., MORTENSEN L. E., VEIHE A., JENSEN N. H. (2010)** - “A simple qualitative approach for 5 mapping regional landslide susceptibility in the Faroe Islands” - *Nat. Hazards Earth Syst. Sci.*,10, 159–170.
- DAI F.C., LEE C.F., (2002)** – “Landslide characteristics and slope instability modelling using GIS, Lantau Island, Hong Kong.” - *Geomorphology*, 42, 213-228.
- DAVIS, JC (1973)** – “Statistics and Data Analysis in Geology”. Wiley, New York.
- DEMIR G., AYTEKIN M., AKGUN A., IKIZLER S. B., TATAR O. (2013)** – “A comparison of landslide susceptibility mapping of the eastern part of the North Anatolian Fault Zone (Turkey) by likelihood-frequency ratio and analytic hierarchy process methods” - *Nat. Hazards*, 65, 1481–1506.
- DEWEY J.F., HELMAN M.L., TURCO E., HUTTON D.H.W. AND KNOTT S.D. (1989)**. – “Kinematics of the Western Mediterranean.” M.P.D. Coward, D. Park, R.G. (Editor), *Alpine Tectonics*. Geological Society, pp. 265-283.
- DE JONG K.A., MANZONI M., STAVENGA T., DIJK F.V., VAN DER VOO R., ZIJDERVELD, J.D.A., (1973)**. – “Palaeomagnetic Evidence for Rotation of Sardinia during the Early Miocene.” *Nature*, 243: 281-283.
- DE ZAN F., MONTI GUARNIERI A. (2006)** - “TOPSAR: Terrain Observation by Progressive Scans.” - *IEEE Transaction on Geoscience and Remote Sensing*, 44(9).
- EINSTEIN H.H. (1988)** - “Special lecture: Landslide risk assessment procedure”. - *Proc. 5th Int. Symp. On Landslides*, Lausanne, 2, 1075-1090.
- ERMINI L., CATANI F., AND CASAGLI N. (2005)** – “Artificial neural networks applied to landslide susceptibility Assessment” - *Geomorphology*, 66, 327–343.
- EVANS, I. S. (1998)** - “What do terrain statistics really mean?” - in: *Landform Monitoring, Modelling and Analysis* - edited by: Lane, S., Richards, K., and Chandler, J., John Wiley & Sons, Chichester, UK, 119–138.
- FARINA P., COLOMBO D., FUMAGALLI A., GONTIER E., MORETTI S. (2003)** – “Integration of Permanent Scatterers analysis and high resolution optical images within landslide risk analysis.” In: *FRINGE*, Frascati, Italy, 1–8.
- FARINA P., COLOMBO D., FUMAGALLI A., MARKS F., MORETTI S. (2006)** – “Permanent Scatterers for landslide investigations: outcomes from the ESA-SLAM project.” - *Engineering Geology*, 88, 200–217.
- FELL R., COROMINAS J., BONNARD C., CASCINI L., LEROI E., SAVAGE W.Z., ENG J-J-TCL (2008)** – “Guidelines for landslide susceptibility, hazard and risk-zoning for land use planning.” - *Engineering Geology*, 102, 85–98.
- FELICISIMO A., CUARTERO A., REMONDO J., QUIROS E. (2012)** - “Mapping landslide susceptibility with logistic regression, multiple adaptive 101 regression splines, classification and regression trees, and maximum entropy methods: a comparative study” - *Landslides*.

- FERRETTI A., PRATI C., ROCCA F. (2000)** – “Non-linear subsidence rate estimation using Permanent Scatterers in differential SAR interferometry.” - *IEEE Transactions on Geoscience and Remote Sensing*, 38 (5), 2202–2212.
- FERRETTI A., PRATI C., ROCCA F. (2001)** – “Permanent Scatterers in SAR interferometry.” - *IEEE Transactions on Geoscience and Remote Sensing*, 39 (1), 8–20.
- FERRETTI A., PRATI C., ROCCA F., CASAGLI N., FARINA P., YOUNG B. (2005)** – “Permanent Scatterers technology: a powerful state of the art tool for historic and future monitoring of landslides and other terrain instability phenomena.” - *Proceedings of 2005 International Conference on Landslide Risk Management*, Vancouver, Canada.
- FERRETTI A. & JURINA L. (2007)** – “Permanent Scatterers technology: a powerful tool for historic and future monitoring of landslides and building settlements” – Università di Milano.
- FINETTI I., LENTINI F., CARBONE S., CATALANO S., DEL BEN A. (1996)**. – “Il sistema Appennino meridionale-Arco Calabro-Sicilia nel Mediterraneo centrale: studio geologico-geofisico.” - *Boll. Soc. Geol. It.*, 115: 529-559.
- FLORIS M., IAFELICE M., SQUARZONI C., ZORZI L., DE AGOSTINI A., GENEVOIS R. (2011)** - “Using on-30 line databases for landslide susceptibility assessment: an example from the Veneto Region(northeastern Italy)” - *Nat. Hazards Earth Syst. Sci.*, 11, 1915–1925.
- FORNARO G., FRANCESCHETTI G., LANARI R. (1996)** – “Interferometric SAR phase unwrapping using Green’s formulation.” - *IEEE Transactions on Geoscience and Remote Sensing*, 34, 720-727.
- FRANCESCHETTI G. (1999)** – “Synthetic Aperture Radar Processing”, pp. 9-17.
- FRANGIONI S., BIANCHINI S., MORETTI S. (2013)** – “Landslide inventory updating by means of Persistent Scatterer Interferometry (PSI): the Setta basin (Italy) case study.” - *Geomatics, Natural Hazards and Risk*, doi: 10.1080/19475705.2013.866985.
- FREEZE, R.A., CHERRY. J.A. (1979)** – “Groundwater.” - *Prentice-Hall, Inc. Englewood Cliffs*, NJ. 604 p.
- GABRIEL A.K., GOLDSTEIN R. M., ZEBKER H.A. (1989)** – “Mapping Small Elevation Changes Over Large Areas: Differential Radar Interferometry.” - *Journal of Geophysical Research*, 94, 9183–9191.
- GALLI P., GALADINI F., PANTOSTI D. (2008)** – “Twenty years of paleosismology in Italy. *Earth-Science Reviews*, 88, 89 – 117.
- GAMEZ, D., -(2007)**. – “Sequence Stratigraphy as a tool for water resources management in alluvial coastal aquifers: application to the Llobregat delta (Barcelona, Spain).” - Ph'D Thesis. Technical University of Catalonia, Barcelona, pp. 177. (<http://www.tdx.cesca.es/>).
- GASPERI G. (1995)** – “Geologia Regionale - Geologia dell’Italia e delle regioni circummediterranee.” - *Pitagora Editrice Bologna*. p. 316 - 358,.

- GE D., WANG Y., ZHANG L., GUO X. AND YE XIA Y., (2010)** – “Mapping urban subsidence with TerraSAR-X data by PSI analysis.” - IEEE International Geoscience and Remote Sensing Symposium, Honolulu, Hawaii, USA, 25-30 July 2010. pp. 3323 – 3326. ISSN: 2153-6996.
- GELATI R. & GNACCOLINI M. (1988)** – “Sequenze deposizionali in un bacino episaturale in una zona di raccordo tra Alpi e Appennino Settentrionale.” - Atti Ticin. Sci. Terra, 31, 340-350.
- GIUNTA G., LIGUORI V. (1973)** – “Evoluzione Paleotettonica della Sicilia Nord - Occidentale.” *Boll. Soc. Geol. It.*, 92, 903 – 824.
- GLADE T., CROZIER M. (2005)** – “The nature of landslide hazard impact.” - In: *Landslide hazard and risk*. Glade T., Anderson M. and Crozier M. (Eds), Wiley, Chichester, 43–74.
- GOLDSTEIN R. M. (1995)** – “Atmospheric limitations to repeat-track radar interferometry” - *Geophys. Res. Lett.*, 22.
- GORSEVSKI P. V., GESSLER P. E., FOLTZ R. B., AND ELLIOT W. J. (2006)** – “Spatial prediction of landslide hazard using logistic regression and ROC analysis” - *Trans. GIS*, 10, 395–415.
- GRAHAM L.C. (1974)** – “Synthetic interferometric radar for topographic mapping.” - Proceedings of the IEEE. 62, 763–768.
- GREIF V., VLCKO J. (2012)** – “Monitoring of post-failure landslide deformation by the PS-InSAR technique at Lubietova in Central Slovakia.” - *Environmental Earth Sciences*, 66, 1585–1595.
- GUNTHER A., REICHENBACH P., MALET J.-P., VAN DEN EECKHAUT M., HERVAS J., DASHWOOD C., GUZZETTI F. (2012)** – “Tier-based approaches for landslide susceptibility assessment in Europe” - *Landslides*, doi:10.1007/s10346-012-0349-1, 2012.
- GUO, HUADONG; HUANG, QINGNI; LI, XINWU; SUN, ZHONGCHANG; ZHANG, YING (2013)** – “Spatiotemporal analysis of urban environment based on the vegetation–impervious surface – soil model (Full text article available).” - *Journal of Applied Remote Sensing* 8: 084597. doi:10.1117/1.JRS.8.084597
- GUZZETTI F., CARRARA A., CARDINALI M., AND REICHENBACH P. (1999)** – “Landslide hazard evaluation: a review of current techniques and their application in a multiscale study, Central Italy” - *Geomorphology*, 31, 181–216.
- GUZZETTI F., MANUNTA M., ARDIZZONE F., PEPE A., CARDINALI M., ZENI G., REICHENBACH P., LANARI R., (2009)** – “Analysis of ground deformation detected using the SBAS-DInSAR technique in Umbria, Central Italy.” - *Pure and Applied Geophysics*, 166.
- GUZZETTI, F., MONDINI, A.C., CARDINALI, M., FIORUCCI, F., SANTANGELO, M., CHANG, K.T. (2012)** - Landslide inventory maps: New tools for an old problem. *Earth-Science Reviews*, 112(1-2), 42-66.

- HAM J., CHEN Y., CRAWFORD M., AND GHOSH J. (2005)** – “Investigation of the random forest framework for classification of hyperspectral data” - *IEEE T. Geosci. Remote Sens.*, 43, 492–501.
- HANSEN A. (1984)** - “Landslides Hazard Analysis”. - John Wiley & Sons. Chp. 13, 523-602
- HANSSEN R.F. (2005)** – “Satellite radar interferometry for deformation monitoring: a priori assessment of feasibility and accuracy.” - *Int. J. Appl. Earth Obs.*, 6, 253–260.
- HASSEN R. (2001)** – “Radar Interferometry” – Amsterdam, the Netherlands. Kluwer, 2001.
- HARTLÈN J. & VIBERG L.(1988)** – “General report: evaluation of landslide hazard”. Proc. 5 th. Int Symp. On Landslides, Lausanne, 2, 1037-1058.
- HERRERA G., FERNÁNDEZ-MERODO J.A., MULAS J., PASTOR M., LUZI G., MONSERRAT O. (2009A)** – “A landslide forecasting model using ground based SAR data: The Portalet case study.” - *Engineering Geology*, 105, 220–230.
- HERRERA G., FERNANDEZ J.A., TOMAS R., COOKSLEY G., MULAS J. (2009B)** – “Advanced interpretation of subsidence in Murcia (SE Spain) using A-DInSAR data - modelling and validation.” - *Natural Hazards Earth System Science*, 9, 647-661.
- HERRERA G., TOMÁS R., MONELLS D., CENTOLANZA G., MALLORQUI J.J., VICENTE F., NAVARRO V.D., LOPEZ-SANCHEZ J. M., CANO M., MULAS J., SANABRIA M. (2010)** – “Analysis of subsidence using TerraSAR-X data: Murcia case study.” - *Engineering Geology*, 116, 284-295.
- HILLEY G.E., BÜRGMANN R., FERRETTI A., NOVALI F., ROCCA F. (2004)** – “Dynamics of Slow-Moving Landslides from Permanent Scatterer Analysis.” - *Science*, 304, 1952-1955.
- HOLZNER J., BAMLER R. (2002)** - “Burst-mode and ScanSAR interferometry.” *IEEE Transaction on Geoscience and Remote Sensing*, 40(9), 1917–1934.
- HOOPER A., ZEBKER H.A., SEGALL P., KAMPES B. (2004)** – “A new method for measuring deformation on volcanoes and other natural terrains using InSAR persistent scatterers.” - *Geophysical Research Letters*, 31.
- HOOPER A., SEGALL P., ZEBKER H.A. (2007)** – “Persistent scatterer interferometric synthetic aperture radar for crustal deformation analysis, with application to Volcán Alcedo, Galápagos.” - *Journal of Geophysical Research*, 112.
- HSÜ K.J., RYAN W.B.F. & CITA M.B. (1973)** – “Late Miocene desiccation of the Mediterranean.” - *Nature*, 242, 240-242.
- ICC, (2005).** – “Mapa geològic de Catalunya. Barcelonès. 1:50 000.” - *Institut Cartogràfic de Catalunya, Barcelona*.
- IUGS/WGL-INTERNATIONAL UNION OF GEOLOGICAL SCIENCES WORKING GROUP ON LANDSLIDES (1995)** – “A suggested method for describing the rate of movement of a landslide.” - *IAEG Bull.* 52, 75–78 Hamburg, pp. 1993–1939.

- KAMPES B.M. (2006)** – “Radar interferometry: Persistent Scatterer technique.” - Springer ed., Netherlands.
- KAMPES B. M., ADAM N. (2006)** – “The STUN Algorithm for Persistent Scatterer Interferometry.” In: Fringe 2005 Workshop, Proceedings of the Conference held 28 November - 2 December, 2005 in Frascati, Italy, H. Lacoste and L. Ouwehand (eds), ESA SP-610. European Space Agency, 2006. Published on CDROM., p.16.1.
- KAYASTHA P., DHITAL M. R., DE SMEDT F. (2012)** - “Landslide susceptibility mapping using the weight of evidence method in the Tinau watershed” - *Nepal, Nat. Hazards*, 63, 479–498.
- KLECKA WILLIAM R. (1980)** – “Discriminant Analysis”
- KLEES R., MASSONNET D. (1999)** – “Deformation measurements using SAR interferometry: Potential and limitations.” - *Geologie en Mijnbouw*, 77, 161–176.
- KOTTEK, M., GRIESER, J., BECK, C., RUDOLF, B. AND RUBEL, F., (2006)** – “World Map of the Köppen-Geiger climate classification updated.” - *Meteorologische Zeitschrift*, Vol. 15, No. 3, 259-263
- KRIJGSMAN W., HILGEN F.J., RAFFI I., SIERRO F.J. & WILSON D.S. (1999)** – “Chronology, causes and progression of the Messinian salinity crisis.” - *Nature*, 400, 652-655.
- LAFUERZA, S., CANALS, M., CASAMOR, J.L., DEVINCENZI, J.M., (2005).** – “Characterization of deltaic sediment bodies based on in situ CPT/CPTU profiles: a case study on the Llobregat delta plain, Barcelona, Spain.” - *Marine Geology* 222–223 (1–4), 497–510.
- LANARI R., MORA O., MANUNTA M., MALLORQUÌ J.J., BERARDINO P., SANSOSTI E. (2004)** – “A Small Baseline Approach for Investigating Deformation on Full resolution Differential SAR Interferograms.” - *IEEE Transaction on Geoscience and Remote Sensing*.
- LEE S., PRADHAN B. (2007)** - “Landslide hazard mapping at Selangor, Malaysia using frequency ratio and logistic regression models” - *Landslides*, 4, 33–41, 2007.
- LEE S., RYU J. H., LEE M. J., WON J. S. (2003)** – “Use of an artificial neural network for analysis of the susceptibility to landslides at Boun, Korea” - *Environ. Geol.*, 44, 820–833.
- LEE, I.-M., NAM S.-W., (2004)** – “Effect of tunnel advance rate on seepage forces acting on the underwater tunnel face.” - *Tunneling and Underground Space Technology*. 19, 273-281.
- LENTINI F., CARBONE S., CATALANO S., GRASSO M., MONACO C. (1990).** – “Principali elementi strutturali del thrust belt appenninico-maghrebide in Sicilia centro-orientale.” - *Mem. Soc. Geol. It.* 45: 495-502.

- LENTINI F., CARBONE S., CATALANO S., GRASSO M. (1995).** – “Principali lineamenti strutturali della Sicilia nord-orientale.” *Studi Geol. Camerti*, Vol. Spec. (1995/2), 319-329.
- LENTINI F., CARBONE S., CATALANO S., GRASSO M. (1996).** – “Elementi per la ricostruzione del quadro strutturale della Sicilia orientale.” - *Mem. Soc. Geol. It.*, 51, 145-156.
- LENTINI F., CATALANO S., CARBONE S. (2000).** – “Carta Geologica della provincia di Messina scala 1:50.000.” - S.EL.CA., Firenze.
- LENTINI F. (2008).** – “Note illustrative della Carta Geologica d'Italia alla scala 1:50.000 (Messina-Reggio Calabria).” Firenze, S.EL.C.A.
- LENTINI F. (2008)** – “Note illustrative della Carta Geologica d'Italia alla scala 1:50.000 (Messina-Reggio Calabria).” Firenze, S.EL.C.A.
- LILLESAND T. M., KIEFER R.W. (1987)** – “Remote Sensing and Image Interpretation.” - Wiley, New York, NY. 1987. 10
- LIQUETE, C., CANALS, M., DE MOL, B., DE BATIST, M., TRINCARDI, F., (2008).** – “Quaternary stratal architecture of the Barcelona prodeltaic continental shelf (NW Mediterranean).” - *Marine Geology* 250 (3–4), 234–250.
- LLOPIS, N., (1942a).** – “Los terrenos cuaternarios del llano de Barcelona.” - *Publicaciones de la Diputación Provincial de Barcelona* 6, 52.
- LLOPIS, N., (1942b).** – “Tectomorfoloía del Macizo del Tibidabo y valle inferior del Llobregat.” - *Estudios Geograficos III* (7), 321–383.
- LLOPIS, N., (1946).** – “Los movimientos verticales intracuaternarios del NE de España.” - *Estudios Geologicos II*, 181–236.
- LUCCHESI T., AGNESI V. (2007)** – “Analisi del dissesto da frana in Sicilia.” In APAT – AGENZIA PER LA PROTEZIONE DELL’AMBIENTE E PER I SERVIZI TECNICI. Rapporto sulle frane in Italia. Vol. unico. pp. 633 - 649. ROMA. APAT. ISBN: 978 - 88 - 448 - 0310 - 0.
- LU P., CASAGLI N., CATANI F. (2010)** – “PSI-HSR: a new approach of representing Persistent Scatterer Interferometry (PSI) point targets using hue and saturation scale.” - *International Journal of Remote Sensing*, 31, 2189-2196.
- MAILLARD, A., MAUFFRET, A., (1999)** – “Crustal structure and riftogenesis of the Valencia Trough (north-western Mediterranean Sea). Basin.” - *Research* 11, 357–379.
- MANTOVANI, F., SOETERS, R. AND VANWESTEN, C.J., (1996)** – “Remote sensing techniques for landslide studies and hazard zonation in Europe.” - *Geomorphology* 15 (3–4), 213–225.
- MANZANO, M., PELAEZ, M.D., SERRA, J., (1986–1987).** – “Sedimentos prodeltaicos en el Delta emergido del Llobregat.” - *Acta Geologica Hispánica*, vol. 21–22, pp. 205–211.

- MANZO G., TOFANI V., SEGONI S., BATTISTINI A., AND CATANI F. (2012)** – “GIS techniques for regional- scale landslide susceptibility assessment: the Sicily (Italy) case study” - *Int. J. Geogr. Inf. Sci.*
- MARQUES, M.A., (1984)**. – “Las formaciones cuaternarias del delta del Llobregat LXXI. Institut d'Estudis Catalans.” - *Barcelona*, pp. 1–280.
- MASSONNET D., FEIGL K.L. (1998)** – “Radar interferometry and its application to changes in the Earth’s surface.” - *Reviews of Geophysics*, 36.
- MEDIALDEA, J., MALDONADO, A., ALONSO, B., DIAZ, J.I., FARRÁN, M., GIRÓ, S., VAZQUEZ, A., SAONZ- AMOR, E., MARTÍNEZ, A. AND MEDIALDEA, T., (1986)**. – “Mapa geológico de la plataforma continental española y zonas adyacentes. E 1:200000.” - *Tarragona. Memoria*. - Hojas 41 and 442 Instituto Geológico y Minero de España (IGME), Madrid.
- MEDIALDEA, J., MALDONADO, A., DIAZ, J.I., ESCUTIA, C., FERRAN, M., GIRO, S., SERRA, M., MEDIALDEA, T. AND VAZQUEZ, J.T., (1989)**. – “Mapa geológico de la plataforma continental española y zonas adyacentes. E 1:200000.” - *Barcelona. Memoria*. - Hojas 35 and 42. Instituto Geológico y Minero de España (IGME), Madrid.
- MEISINA C., ZUCCA F., CONCONI F., VERRI F., FOSSATI D., CERIANI M., ALLIEVI J. (2007)** – “Use of Permanent Scatterers technique for large-scale mass movement investigation.” - *Quaternary International*, 171–172, pp.90-107.
- MEISINA C., ZUCCA F., NOTTI D., COLOMBO A., CUCCHI G., GIANNICO C., BIANCHI M. (2008)** – “Geological Interpretation of PSInSAR Data at Regional Scale.” - *Sensors*, 8(11), 7469-7492.
- META A., MITTERMAYER J., PRATS P., SCHEIBER R., STEINBRECHER U. (2010)** – “TOPS imaging with TerraSAR-X: Mode design and performance analysis.” - *IEEE Transaction on Geoscience and Remote Sensing*, 40(2), 759–769.
- METTERNICHT G., HURNI L., GOGU R. (2005)** – “Remote sensing of landslides: an analysis of the potential contribution to geospatial systems for hazard assessment in mountain environments.” - *Remote Sensing of Environment*, 98, 284-303.
- MINISTERIO DE OBRAS PÚBLICAS, (1966)**. – “Estudio de los recursos hidráulicos totales de las cuencas de los ríos Besós y Bajo Llobregat.” - *Comisaria de Aguas del Pirineo Oriental y Servicio Geológico de Obras Públicas*, p. 4.
- MONTI GUARNIERI A., PRATI C. (1996)** – “ScanSAR focusing and interferometry.” - *IEEE Transaction on Geoscience and Remote Sensing*, 34(4), 1029–1038.
- MONTI GUARNIERI A., ROCCA F. (1999)** – “Combination of low- and highresolution SAR images for differential interferometry.” - *IEEE Transaction on Geoscience Remote Sensing*, 37, 2035–2049.
- MORA O., MALLORQUÌ J.J., BROQUETAS A. (2003)** – “Linear and nonlinear terrain deformation maps from a reduced set of interferometric SAR images.” *IEEE Transactions on Geoscience and Remote Sensing*, 41, 2243-2253.

- NEFESLIOGLU H. A., GOKCEOGLU C., SONMEZ H., GORUM T. (2011)** - “Medium-scale hazard mapping for shallow landslide initiation: the Buyukkoy catchment area” - (Cayeli, Rize, Turkey), *Landslides*, 8, 459–483.
- NOTTI D., DAVALILLO J.C., HERRERA G., MORA O. (2010)** – “Assessment of the performance of X-band satellite radar data for landslide mapping and monitoring: Upper Tena Valley case study.” - *Natural Hazards Earth System Science*, 10, 1865-1875.
- OGNIBEN L., (1960).** - *Nota illustrativa dello schema geologico della Sicilia nord-orientale*. Riv. Min. Sicil.vol. 11, n. 64-65, pp. 183-212.
- OGUCHI T. (1997)** - “Drainage density and relative relief in humid steep mountains with frequent slope failure” - *Earth Surf. Proc. Land.*, 22, 107–120.
- OHLMACHER G. C., DAVIS J. C. (2003)** - “Using multiple logistic regression and GIS technology to predict landslide hazard in northeast Kansas” - *USA, Eng. Geol.*, 69, 331–343.
- OHLMACHER G. C. (2007)** – “Plan curvature and landslide probability in regions dominated by earth flows and earth slides” - *Eng. Geol.*, 91, 117–134.
- PELTZER G., ROSEN P. (1995)** – “Surface displacement of the 17 May 1993 Eureka Valley earthquake observed by SAR interferometry.” *Science*, 268, 1333-1336.
- P.A.I. (2004)** - Piano Stralcio di Bacino per l'Assetto Idrogeologico - *Relazione Generale* - Anno 2004.
- PAL M. (2005)** – “Random forest classifier for remote sensing classification” - *Int. J. Remote Sens.*, 26, 217–222.
- PARCERISA, D., (2002).** – “Petrologia i diagènesi en sediments de l'Oligocè superior i del Miocè inferior i mitjà de la Depressió del Vallès i del Pla de Barcelona. Evolució de l'àrea font i dinàmica dels fluids.” - *Ph'D Thesis*, Universitat Autònoma de Barcelona, Bellaterra, pp. 288.
- PEREA, H., (2006).** – “Falles actives i perillositat sísmica al marge nord-occidental del solc de València.” - *Ph'D Thesis*. - Faculty of Geology, University of Barcelona, Barcelona, pp. 332.
- PEREIRA, S., ZEZEZE, J. L., BATEIRA, C. (2012)** - “Technical Note: Assessing predictive capacity and conditional independence of landslide predisposing factors for shallow landslide susceptibility models”- *Nat. Hazards Earth Syst. Sci.*, 12, 979–988.
- PRADHAN B., LEE S. (2010)** – “Landslide susceptibility assessment and factor effect analysis: back-propagation artificial neural networks and their comparison with frequency ratio and bivariate logistic regression modelling” - *Environ. Model. Softw.*, 25, 747–759.
- PRASAD A. M., IVERSON L. R., LIAW A. (2006)** – “Newer classification and regression tree techniques: bagging and random forests for ecological prediction” - *Ecosystems*, 9, 181–199.

- RAUCOULES D., LE MOUÉLIC S., CARNEC C., KING C. (2003)** – “Urban subsidence in the city of Prato (Italy) monitored by satellite radar interferometry.” - *International Journal of Remote Sensing*, v.24 (4), pp 891-897.
- RAUCOULES D., BOURGINE B., DE MICHELE M., LE COZANET G., CLOSSET L., BREMMER C., VELDKAMP H., TRAGHEIM D., BATESON L., CROSETTO AGUDO M., ENGDahl M. (2009)** – “Validation and Intercomparison of Persistent Scatterers Interferometry: PSIC4 project results.” - *J. Appl. Geophys.*, 68 (3), 335–347.
- ROCA, E., (1994)** – “La evolución geodinámica de la cuenca Catalano-Balear y áreas adyacentes desde el Mesozoico hasta la actualidad.” - *Acta Geologica Hispánica* 29, 3–26.
- ROCA, E., GUIMERÀ, J., (1992)** – “The Neogene structure of the eastern Iberian margin: structural constraints on the crustal evolution of the Valencia trough (western Mediterranean).” - *Tectonophysics* 203, 203–218
- ROSEN P. A., HENSLEY S., JOUGHIN I. R., LI F. K., MADSEN S. N., RODRIGUEZ E., GOLDSTEIN R.M. (2000)** – “Synthetic aperture radar interferometry” - *Proc. I.E.E.E.* 88 (3).
- ROTT H. (2004)** – “Requirements and applications of satellite techniques for monitoring slope instability in Alpine areas.” Workshop on risk mitigation of slope instability. Ispra, Italy’ JRC-Institute for the Protection and Security of the Citizen.
- ROVERI M., MANZI V., GENNARI R., IACCARINO S.M. & LIGLI S. (2008)** – “Recent advancements in the Messinian stratigraphy of Italy and their Mediterranean-scale implications.” *Boll. Soc. Paleont. It.*, 47(2), 71-85.
- SABATAKAKIS N., KOUKIS G., VASSILIADES E., LAINAS S. (2012)** - “Landslide susceptibility zonation in Greece” - *Nat. Hazards*, 65, 523–543.
- SANDWELL T., PRICE E.J. (1998)** – “Phase gradient approach to stacking interferograms.” - *Journal of Geophysical Research*, 103.
- SCHOWENGERDT, ROBERT A. (2007)** – “Remote sensing: models and methods for image processing. (3rd ed.).” Academic Press. p. 2. ISBN 978-0-12-369407-2.
- SCHOTT, JOHN ROBERT (2007)** – “Remote sensing: the image chain approach. (2nd ed.).” *Oxford University Press*. p. 1. ISBN 978-0-19-517817-3.
- STROBL C., BOULESTEIX A. L., KNEIB T., AUGUSTIN T., ZEILEIS A. (2008)** – “Conditional variable importance for random forests” - *BMC Bioinformatics*, 9, 307.
- STROBL, C., MALLEY, J., TUTZ, G. (2009)** – “An introduction to recursive partitioning: rationale, application, and characteristics of classification and regression trees, bagging, and random forests” - *Psychol. Methods* - 14, 323–348.
- SEGONI, S., ROSSI, G., CATANI, F. (2012)** - “Improving basin-scale shallow landslides modelling using reliable soil thickness maps” - *Nat. Hazards*, 61, 85–101.
- SIMÓ, J.A., GÀMEZ, D., SALVANY, J.M., VÀZQUEZ-SUÑÉ, E., CARRERA, J., BARNOLAS, A., ALCALÀ, F.J., (2005.)** – “Arquitectura de facies de los deltas cuaternarios del río Llobregat, Barcelona, España.” - *Geogaceta* 38, 171–174.

- SINGHROY V., MATTAR K., GRAY A. (1998)** – “Landslide characterization in Canada using interferometric SAR and combined SAR and TM images.” - *Adv. Space Res.*, 21(3), 465-476.
- SINGHROY, V. (2005)** – “Remote Sensing of Landslides.” In *Landslide Hazard and Risk* cap. 16 John Wiley & Sons Ltd ISBN 0-471-48663-9
- SKOLNIK M. L. (2001)** – “Introduction to RADAR systems”. 3 edn. 1221 Avenue of the Americas, New York, NY 10020: Tata McGraw-Hill.
- SQUARZONI C., DELACOURT C., ALLEMAND P. (2003)** – “Nine years of spatial and temporal evolution of the La Valette landslide observed by SAR Interferometry.” - *Engineering Geology*, 68.
- SOETERS, R. & VAN WESTEN, C.J. (1996)** – “Slope instability recognition, analysis, and zonation.” In A.K. Turner & R.L. Schuster (eds), *Landslides—Investigation and Mitigation: 129-177*. Washington, D.C.: National Academy Press. National Research Council. Transportation Research Board Special Report 247.
- SOLÉ-SABARÍS, L., (1963).** – “Ensayo de interpretación del Cuaternario Barcelonés. Miscel.” - *Barcilonensia II*, 7–54.
- SOLÉ-SABARIS, L., VIRGILI, C., I., Z., (1957).** – “Livret guide d'excursions: Environs de Barcelone et Montserrat.” - In: *INQUA (Ed.), V Congress Inter INQUA*, Barcelona, p. 38.
- SOUMEKH M. (1999)** – “Synthetic Aperture Radar Signal Processing with MATLAB Algorithms.” - *Ed. Wiley-Interscience*, 616 pp.
- STROBL, C., MALLEY, J., TUTZ, G. (2009)** – “An introduction to recursive partitioning: rationale, application, and characteristics of classification and regression trees, bagging, and random forests.” - *Psychol. Methods*” - 14, 323–348.
- STROZZI T., FARINA P., CORSINI A., AMBROSI C., THÜRING M., ZILGER J., WIESMANN A., WEGMÜLLER U., WERNER C. (2005)** – “Survey and monitoring of landslide displacements by means of L-band satellite SAR interferometry.” - *Landslides*, 193-201.
- TARCHI D., CASAGLI N., FANTI R., LEVA D., LUZI G., PASUTO A., PIERACCINI M., SILVANO S. (2003)** – “Landslide monitoring by using ground-based SAR interferometry: an example of application to the Tessina landslide in Italy.” *Engineering Geology*, 68, 1–2.
- VAN WESTEN, C.J., CASTELLANOS, E. AND KURIAKOSE, S.L. (2008)** – “Spatial data for landslide susceptibility, hazard, and vulnerability assessment: an overview.” - *Engineering Geology* 102 (2008) 112–131.
- VARNES D. J. & IAEG COMMISSION ON LANDSLIDE (1984)** – “Landslide hazard zonation - a review of principle sand pratique”. UNESCO, Paris 63 pp.

WERNER C., WEGMULLER U., STROZZI T., WIESMANN A. (2003) – “Interferometric Point Target Analysis for deformation mapping.” - *Proceedings of IGARSS 2003*, Toulouse (Francia).

WIECZOREK, G.F. (1984) – “Preparing a detailed landslide-inventory map for hazard evaluation and reduction.” - *Association of Engineering Geologists Bulletin*, v. 21, no. 3, p. 337–342.

XU W., YU W., JING S., ZHANG G., HUANG J. (2013) – “Debris flow susceptibility assessment by GIS and information value model in a large-scale region, Sichuan Province (China)” - *Nat. Hazards*, 65, 1379–1392.

ZEBKER H.A., GOLDSTEIN R.M. (1986) – “Topographic Mapping From Interferometric Synthetic Aperture Radar Observations.” - *Journal of Geophysical Research*, (91), 4993–4999.

ZEBKER H. A., ROSEN P. A., HENSLEY S. (1997) – “Atmospheric effects in interferometric synthetic aperture radar surface deformation and topographic maps.” – *Journal of Geophysical Research.*, 102.

ZÊZERE, J.L. (2002) – “Landslide susceptibility assessment considering landslide typology. A case study in the area north of Lisbon (Portugal).” - *Natural Hazards and Earth System Sciences*, vol. 2, 1/2, European Geophysical Society, p.73-82.

ZEVEBERGEN, L. W., C. R. THORNE. (1987) – “Quantitative Analysis of Land Surface Topography” - *Earth Surface Processes and Landforms* 12: 47–56.